AWARD NUMBER: W81XWH-14-1-0228

TITLE: Biomechanical Modeling and Measurement of Blast Injury and Hearing Protection Mechanisms

PRINCIPAL INVESTIGATOR: Rong Z. Gan, Ph.D.

CONTRACTING ORGANIZATION: University of Oklahoma, Norman, OK

REPORT DATE: December 2020

TYPE OF REPORT: Final

PREPARED FOR: U.S. Army Medical Research and Development Command
Fort Detrick, Maryland 21702-5012

DISTRIBUTION STATEMENT: Approved for Public Release;
Distribution Limited

The views, opinions and/or findings contained in this report are those of the author(s) and should not be construed as an official Department of the Army position, policy or decision unless so designated by other documentation.

REPORT DOCUMENTATION PAGE

Form Approved
OMB No. 0704-0188

Public reporting burden for this collection of information is estimated to average 1 hour per response, including the time for reviewing instructions, searching existing data sources, gathering and maintaining the data needed, and completing and reviewing this collection of information. Send comments regarding this burden estimate or any other aspect of this collection of information, including suggestions for reducing this burden to Department of Defense, Washington Headquarters Services, Directorate for Information Operations and Reports (0704-0188), 1215 Jefferson Davis Highway, Suite 1204, Arlington, VA 22202-4302. Respondents should be aware that notwithstanding any other provision of law, no person shall be subject to any penalty for failing to comply with a collection of information if it does not display a currently valid OMB control number. **PLEASE DO NOT RETURN YOUR FORM TO THE ABOVE ADDRESS.**

1. REPORT DATE	2. REPORT TYPE	3. DATES COVERED
December 2020	Final Report	30 Sept 2014 – 29 Sept 2020

4. TITLE AND SUBTITLE

Biomechanical Modeling and Measurement of Blast Injury and Hearing Protection Mechanisms

5a. CONTRACT NUMBER
W81XWH-14-1-0228

5b. GRANT NUMBER
13063031

5c. PROGRAM ELEMENT NUMBER

6. AUTHOR(S)

Rong Z. Gan, Ph.D.

E-Mail: rgan@ou.edu

5d. PROJECT NUMBER

5e. TASK NUMBER

5f. WORK UNIT NUMBER

7. PERFORMING ORGANIZATION NAME(S) AND ADDRESS(ES)

University of Oklahoma, Norman,
Oklahoma, 73019

8. PERFORMING ORGANIZATION REPORT NUMBER

9. SPONSORING / MONITORING AGENCY NAME(S) AND ADDRESS(ES)

U.S. Army Medical Research and Development Command
Fort Detrick, Maryland 21702-5012

10. SPONSOR/MONITOR'S ACRONYM(S)

11. SPONSOR/MONITOR'S REPORT NUMBER(S)

12. DISTRIBUTION / AVAILABILITY STATEMENT

Approved for Public Release; Distribution Limited

13. SUPPLEMENTARY NOTES

14. ABSTRACT

Objectives of the project are to determine middle ear protective mechanisms and develop the finite element (FE) model of the human ear for simulating blast injury and assisting design/evaluation of HPDs. There are three aims: quantify middle ear injury in relation to blast overpressure (BOP) level and wave direction using human cadaveric ears; identify middle ear protection mechanisms and hearing damages in animals exposed to blast and the changes of mechanical properties of ear tissues after exposure; develop FE model of human ear to predict BOP transmission through the ear and the prevention mechanisms of acoustic injury for HPDs. Major findings include: 1) blast waveforms recorded at the ear canal entrance, near the tympanic membrane (TM), and inside the middle ear under different wave directions; 2) movements of the TM and stapes during blast exposure measured with dual lasers; 3) EMG measurements of middle ear muscle reflex in response to blast exposure in animals; 4) identified hearing damage and cochlear injury caused by repetitive blast exposure at low BOP or single blast at high BOP level (mild or moderate TBI) in animals; 5) blast-induced TM microstructure and mechanical property changes; 6) 3D FE model of the entire ear for modeling blast wave transmission from the ear canal to cochlea; 7) 3D printed human ear/temporal bone and its application for HPDs evaluation.

15. SUBJECT TERMS

Blast overpressure transmission, ear biomechanics, tympanic membrane rupture, middle ear muscle reflex, finite element modeling of human ear, hearing protection devices

16. SECURITY CLASSIFICATION OF:			17. LIMITATION OF ABSTRACT	18. NUMBER OF PAGES	19a. NAME OF RESPONSIBLE PERSON
a. REPORT	b. ABSTRACT	c. THIS PAGE			USAMRMC
Unclassified	Unclassified	Unclassified	Unclassified	312	19b. TELEPHONE NUMBER *(include area code)*

Table of Contents

Page

1. Introduction……. 2

2. Keywords……. 2

3. Accomplishments……..……... 2

4. Impact……...…… 77

5. Changes/Problems...….…… 78

6. Products…….…….…..……. 79

7. Participants & Other Collaborating Organizations…… 86

8. Special Reporting Requirements…… 88

9. Appendices…… 89

A Quad chart

Copies of 21 Published Journal Articles

1. INTRODUCTION

The objectives of this research project are to determine middle ear protective mechanisms in the conductive path of impulse noise or blast wave into cochlea and to develop the finite element model of the human ear for simulating blast injury and assisting the design and evaluation of personal hearing protection devices. To our knowledge this state-of-the-art approach has not been experimentally applied to evaluating the mechanical basis for middle and inner ear damage relevant to high intensity sound or blast exposure. Our **long-term goal** is to understand ear biomechanics in response to blast overpressure and impulse noise and to provide the prevention mechanism of acoustic injury for development of effective hearing protection devices. To reach the objectives and long-term goal, we have a series of tasks under three specific aims to test our **general hypothesis**: the biomechanical response of the middle ear and inner ear (or cochlea) to impulse noise or blast exposure can be characterized in our 3D comprehensive finite element model of the human ear.

2. KEYWORDS

Blast overpressure transmission, ear biomechanics, tympanic membrane rupture, middle ear muscle reflex, finite element modeling of human ear, hearing protection devices

3. ACCOMPLISHMENTS

● What were the major goals of the project?

The project has three specific aims with 7 tasks as listed below.
Aim 1: To quantify middle ear injury in relation to blast overpressure (BOP) level and impulse wave direction using human cadaver ears or temporal bones.
Task 1-1. To identify blast-induced damage of the tympanic membrane and middle ear ossicles when the ear is exposed to different blast overpressure levels at several incident wave directions.
Task 1-2. To characterize the transfer functions of the ear canal and middle ear in response to impulse sound or blast overpressure applied at the ear canal entrance.

Aim 2: To identify middle ear protection mechanisms using the chinchilla model and the dynamic properties of ear tissues.
Task 2-1. To detect the middle ear muscle reflex in awake chinchillas during the blast exposure.
Task 2-2. To identify changes of mechanical properties of middle ear tissues after high impulse noise/blast exposure in human temporal bones.

Aim 3: To continue the development of our 3-dimensional (3D) finite element (FE) model of the human ear with militarily relevant applications.
Task 3-1. To improve the current 3D FE model of the human ear by including middle ear nonlinearities.
Task 3-2. To develop the active FE model of the ear associated with middle ear muscle functions.

Task 3-3. To provide prevention mechanisms of acoustic injury for personal hearing protection devices (HPDs, passive and active) by using our 3D FE model of the human ear.

- **What was accomplished under these goals?**

(1) Major activities:

Aim 1:

1) Developing the "head block" mounted with human cadaveric ear or temporal bone (TB) to measure blast pressure transmission from the ear canal into the middle ear and cochlea;
2) Conducting blast tests at three incident wave directions with respect to the head block: from the top of the head - the vertical setup, from lateral to the ear – horizontal setup, and from the front of the face - the front setup;
3) Performing the impulse pressure energy spectra analysis of the waveforms at the ear canal entrance (P0), near the tympanic membrane in the canal (P1), and inside the middle ear cavity (P2) recorded from blast tests at three blast wave directions;
4) Conducting the front tests of HPDs: the military earplugs (Combat Arms and battle earplugs), standard foam earplug, and Lyric hearing aid/earplug in human cadaver ears;
5) Performing multiple blast tests in human TBs to identify the changes of tympanic membrane (TM) surface vibration behavior and TM microstructure and to prepare ear tissues for mechanical testing in Aim 2;
6) Developing new methodology with two laser Doppler vibrometers (LDVs) to measure the movement of the TM and earplug (e.g. Lyric earplug) during blast exposure;
7) Extending new methodology with dual LDVs to measure the movement of stapes footplate in human cadaver ears with and without earplug during blast exposure;
8) Performing blast tests in 3D printed TB to verify the printed TB can be used for standardized testing of HPDs to blast exposure;
9) Conducting data analyses of the completed experiments in human TBs and preparing journal manuscripts.

Aim 2:

1) Developing surgical procedure to access the stapedius muscle, insert the electrode into the muscle, and design the animal holder used in blast testing chamber;
2) Conducting electromyography (EMG) measurements in chinchillas during acoustic stimulation and blast exposure and determining the threshold and latency of the recorded EMG signals of the stapedius muscle;
3) Detecting the effect of high intensity noise exposure on middle ear muscle reflex (MEMR) in chinchillas;
4) Determining the TM rupture threshold under the open and shielded conditions or different waveforms in chinchillas;
5) Identifying the hearing damage (auditory brainstem response (ABR) threshold and distortion product otoacoustic emission (DPOAE) level changes) and central auditory system damage (immunohistochemistry study) in chinchillas after repetitive blast exposure at the mild BOP or mild traumatic brain injury (mTBI), named as G2 level, and observed over the time course;
6) Identifying the hearing damage (ABR threshold and DPOAE level changes) and the central auditory injury (middle latency response (MLR)) in chinchillas after repetitive blast

exposure at the low BOP (below mTBI), named as G1 level, and observed over the time course;
7) Conducting scanning electron microscopy (SEM) imaging of the chinchilla and human TMs and SEM imaging of chinchilla hair cells or stereocilia before and after blast exposure;
8) Measuring mechanical properties of human and chinchilla TM samples after blast exposure using a series of dynamic and quasi-static mechanical testing methodologies: the acoustic loading with LDV measurement over the frequency domain, the split Hopkinson tension bar (SHTB) for measurement at high strain rate, the micro-fringe protection technique, and surface 3D digital image correlation (DIC) technique;
9) Conducting a novel study in chinchillas using 3D printed chinchilla "helmet" as a head protection device associated with the HPDs (e.g. earplugs) to investigate the blast-induced damage in the peripheral auditory system (PAS) and central auditory system (CAS) and the protective functions of the HPD and helmet;
10) Conducting data analyses of the animal experiments and mechanical property tests of ear tissues and preparing journal manuscripts.

Aim 3:

1) Developing the 3D FE model of the human ear including the external ear, TM, middle ear, middle ear cavity, and cochlear load within the ANSYS Workbench and conducting the FE analyses on blast pressure transmission through the ear using two strongly coupled Fluid-Structure Interactions (FSIs) as calculated by Fluent and ANSYS Mechanical;
2) Validating the FE model by comparing the model derived P1 and P2 waveforms with the experimentally recorded waveforms in human cadaver ears or TBs during blast tests;
3) Utilizing the FE model to predict the mechanism of TM rupture in relation to blast wave direction with respect to the head;
4) Simulating the earplugs in human FE model to predict their protective function to the blast overpressure;
5) Including the uncoiled cochlea to the FE model of the human ear to simulate the BOP transmission from the ear canal to the cochlea – the first FE model of entire human ear for computing blast wave transduction;
6) Improving the FE model of the entire human ear with the simulation of middle ear muscle active function (stapedius muscle);
7) Developing the comprehensive FE model of the entire ear by including the spiral cochlea – the final goal for FE modeling of human ear biomechanics in response to blast exposure
8) Developing the 3D FE model of the chinchilla ear, including the ear canal, middle ear, bulla, and spiral cochlea, which can serve as a tool for correlating animal hearing test results to the humans;
9) Utilizing the 3D printing system (Object350, Stratasys) to provide the 3D printed human ear model or TB for standardized testing of HPDs to blast exposure;
10) Participating in the DoD BIPSR Process of Candidate Standard Champion for our FE model on the "Biomechanical Modeling and Measurement of Blast Injury" and preparing journal manuscripts.

(2) Specific objectives:

Aim 1:

- Investigate the BOP wave transduction from the environment through the ear canal into the middle ear and cochlea and quantify the TM or middle ear injury in relation to BOP level and blast wave direction;
- Evaluate the HPDs (e.g. earplugs) in human cadaveric ears by determining the attenuation of blast pressure reaching the TM and the reduction of middle ear ossicular chain (e.g. stapes) movement;
- Develop new technologies to measure blast-induced movements of the TM and middle ear ossicles, particularly the stapes footplate, the primary source causing the hair cells' damage or sensorineural hearing loss.

Aim 2:

- Complete the EMG measurement of middle ear muscle reflex induced by acoustic stimulation and blast overpressure in chinchillas and investigate the effect of pre-noise exposure (130 dB) on EMG signals of the stapedius muscle reflex;
- Determine hearing damage in relation to the number of blast exposures and the intensity of BOP over the recovery time course with the assessment of the PAS and CAS injuries;
- Evaluate the protective function of HPDs (e.g. earplugs) for repeated exposures at low BOP or mild TBI level;
- Conduct a novel study on prevention of blast-induced auditory injury using the helmet and earplugs in animal model of chinchilla;
- Determine blast-induced microstructure and mechanical property changes of the TM and middle ear tissues and develop new techniques for measuring dynamic properties of ear tissues.

Aim 3:

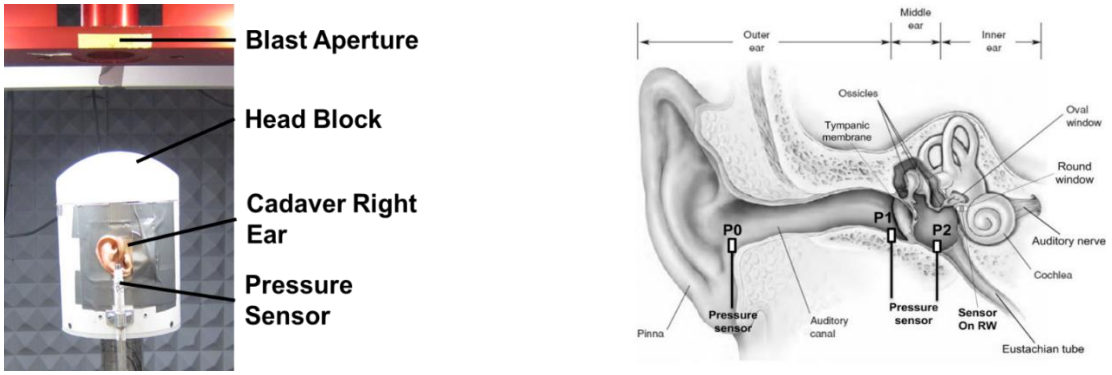
- Develop the 3D FE model of the human ear with cochlear load which can be used for predicting the middle ear injuries to BOP waves and evaluating the design and protective function for HPDs;
- Develop the 3D FE model of the human ear with uncoiled cochlea for simulating BOP wave transmission from the ear canal through the middle ear to the cochlea and predicting the cochlear function changes and middle ear muscle contraction;
- Improve the 3D FE model of the entire human ear with spiral cochlea of three fluid chambers separated by the basilar membrane (BM) and Reissner's membrane (RM);
- Improve the 3D FE model of chinchilla ear or bulla with spiral cochlea for simulating blast wave transmission from the ear canal to cochlea and blast-induced hearing damage in the PAS;
- Develop the 3D printed physical model of the human ear or temporal bone for assessing HPDs' design and protection mechanisms to blast waves.

(3) Significant results or key outcomes:

Aim 1:

(1-1) **<u>Development of new methodologies to measure blast overpressure transmission through the human ear from the entrance of the ear canal (P0) to near the TM in the canal (P1) and inside the middle ear cavity (P2) under three blast wave directions with respect to the head</u>**

A “head block” attached with human cadaver ear or temporal bone and mounted with two pressure sensors, one near the TM in the ear canal and one inside the middle ear cavity, was developed in our lab to measure the transfer functions of the ear canal and middle ear in response to blast overpressure. In addition to two pressure sensors inside the ear, the third sensor is placed at the entrance of the ear canal (Fig. 1A). The three pressure sensors are simultaneously monitoring the blast pressure at the entrance of the ear canal (P0), near the TM in the canal (P1), and behind the TM in the middle ear (P2) as shown in Fig. 1B. A compressed nitrogen-driven blast apparatus was utilized to produce blast overpressure by rupturing a polycarbonate film.



(A) **(B)**

Figure 1. (A) Picture of experimental setup with the head block along the vertical blast wave direction inside the test chamber (Gan et al., 2019B); (B) Schematic of simultaneously measuring blast overpressure transduction through the ear with three pressure sensors (Gan et al., 2018A).

The “head block” was exposed to open-field blast inside an anechoic test chamber along three directions: the vertical, horizontal, and front with respect to the head as shown in Fig. 2. Blast overpressure waveforms were recorded at the ear canal entrance (P0), near the TM (P1), and inside the middle ear (P2). Thirteen to fourteen human cadaver ears were tested in each wave direction and the TM rupture thresholds were identified. Results were published in *Military Medicine*, Vol. 183 (Gan et al., 2018A) and are reported here in Figs. 3-5.

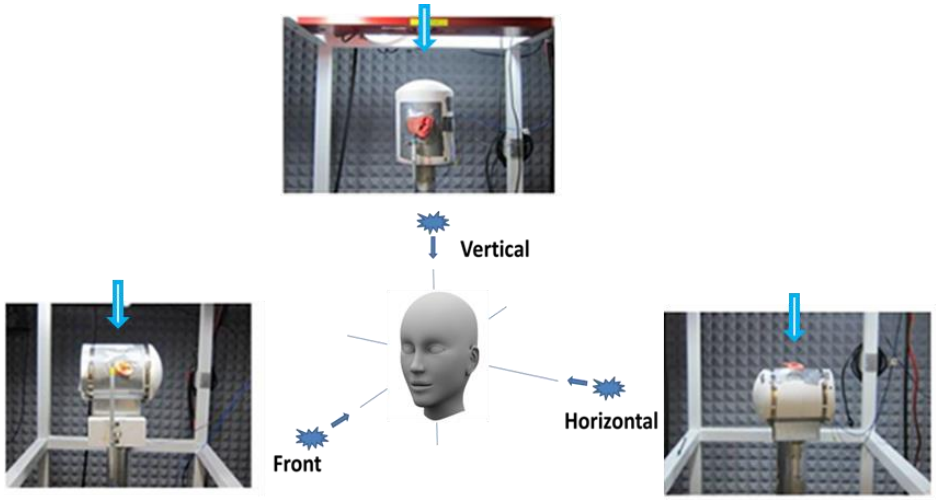


Figure 2. Schematic of three blast wave directions with respect to the head and the pictures of experimental setup with the head block along the vertical, horizontal, and front wave directions inside the test chamber. The blue arrow in each picture shows blast wave origination for the vertical, horizontal, and front setup test, respectively (Gan et al. 2018A).

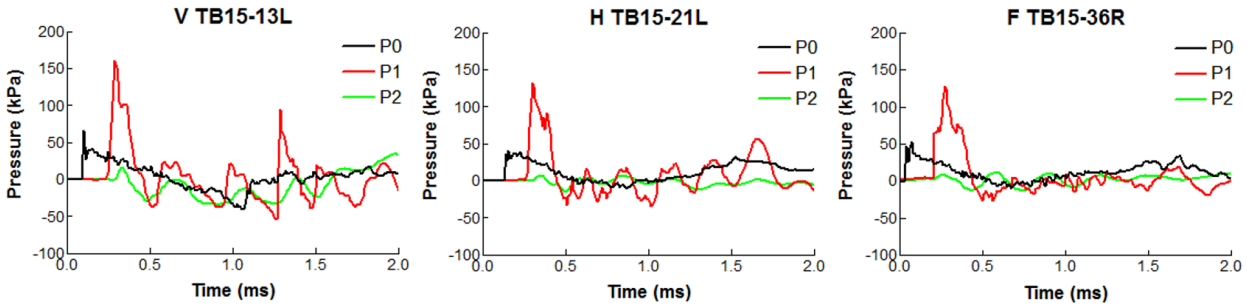


Figure 3. Overpressure waveforms of P0 (black), P1 (red), and P2 (green) recorded from three cadaver ears or temporal bones under the vertical (V, left), horizontal (H, medium), and front (F, right) tests. TB15-13L, TB15-21L, and TB15-36R represent the TB samples.

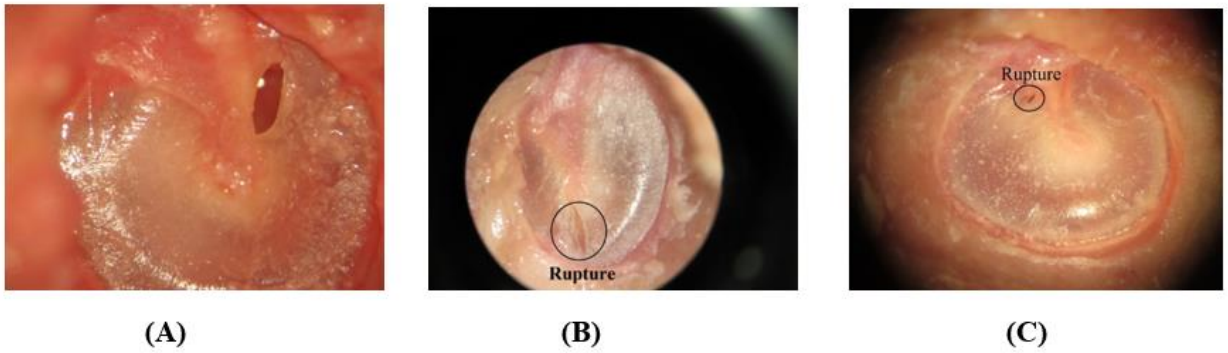


Figure 4. Otoscopic pictures of human TMs ruptured after blast exposure. (A) Vertical test, left ear, TM ruptured in the superior-posterior region; (B) horizontal tests, left ear, TM ruptured in the inferior side; (C) front test, right ear, TM ruptured in the superior-posterior region.

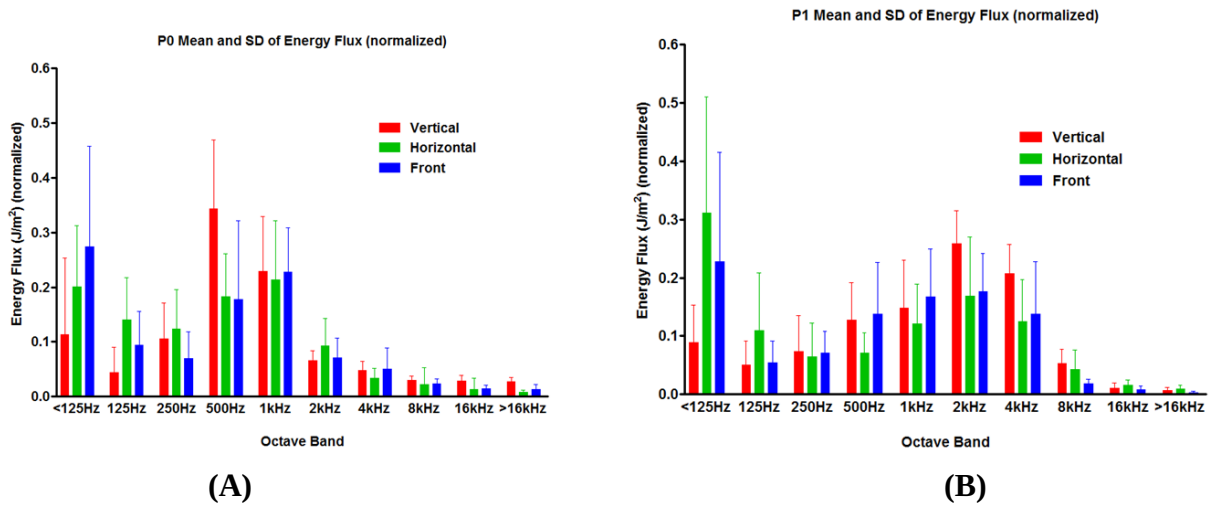


Figure 5. Comparison of normalized energy flux over 10 octave bands from below 125 Hz to above 16 kHz between the waveforms recorded in vertical, horizontal, and front tests. (A) Mean and standard deviation (SD) of energy flux for P0 waveforms; (B) mean and SD of energy flux for P1 waveforms.

Results indicated that blast wave direction affected the peak P1/P0 ratio, TM rupture threshold, and energy flux distribution over frequencies. The front wave resulted in lowest TM rupture

threshold and the horizontal wave resulted in highest P1/P0 ratio. To investigate the mechanisms of TM injury in relation to blast wave direction, we have employed the 3D FE model of the human ear to simulate the BOP transmission through the ear which are reported under Aim 3.

(1-2) Evaluation of various HPDs (military earplugs and other earplugs) in human cadaver ears to determine HPDs' protective function against blast exposure

Hearing damage induced by blast exposure is a common injury in military personnel involved in most operation activities. Personal hearing protection devices such as earplugs come as a standard issue for Service members; however, it is not clear how to accurately evaluate the protection mechanisms of different HPDs for BOP. We have used the head block to characterize earplugs (EPs) protective function to BOP as the attenuation of P1, the blast pressure reaching to the eardrum or TM. Different earplugs including two types of military EPs: Combat Arms earplug (CAE) and Battle Plug, the standard foam EP, and the Lyric hearing aid or EP were inserted into the cadaver ear and then assembled to the head block inside the blast chamber as shown in Fig. 6. This study resulted in a journal article published in *Military Medicine*, Vol. 184 (Gan et al., 2019B).

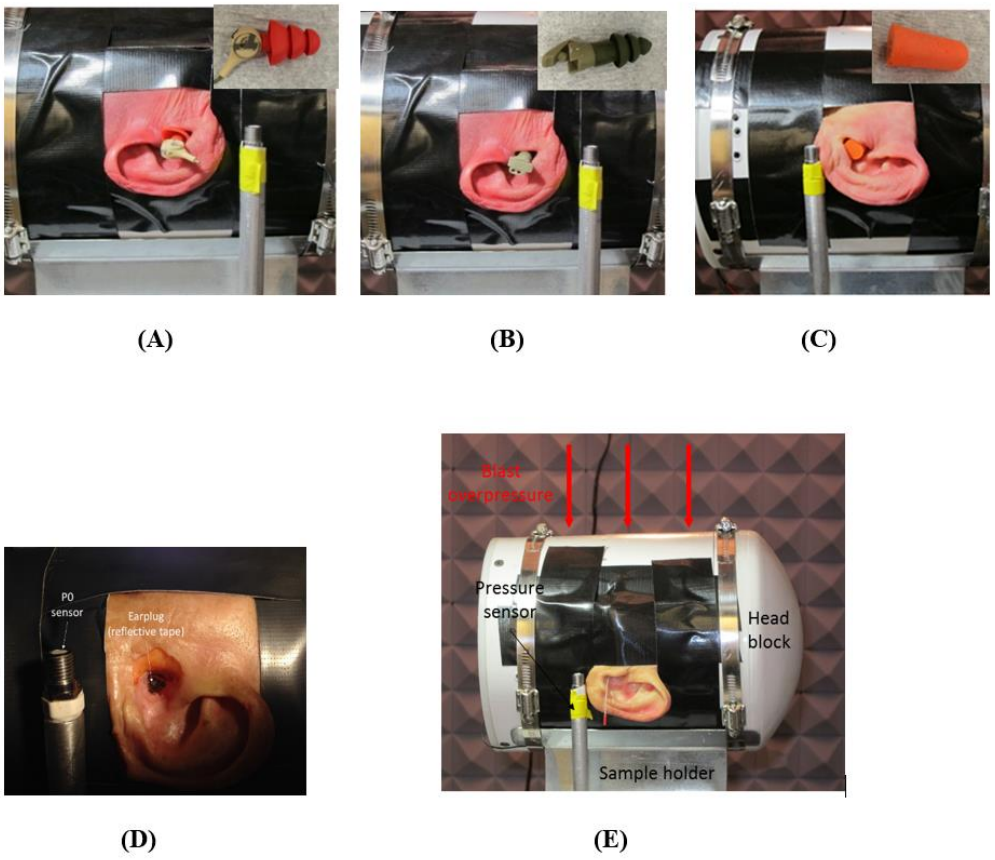
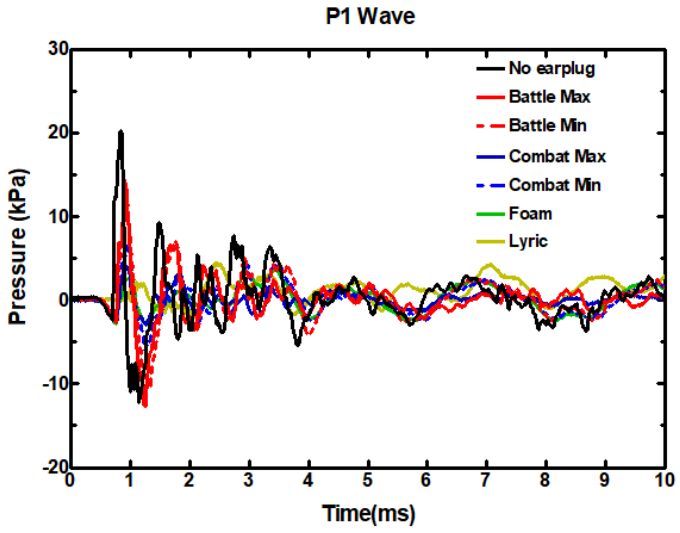
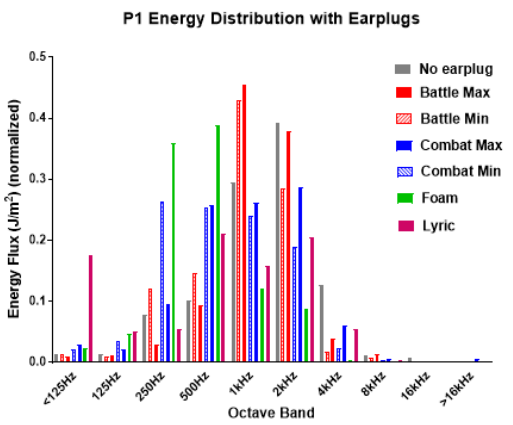


Figure 6. Pictures of the experimental setup with earplug in human cadaver ear attached to the head block in front setup (blast wave from the front of the face). (A) Combat Arms, (B) Battle Plug, (C) Foam, (D) Lyric earplug, (E) entire head block attached with the human ear inside the blast chamber. Note that the yellow taped pole was the P0 pressure sensor and the reflective tape pointed on the Lyric earplug was used for laser measurement of Lyric's movement under blast exposure, which is not included in this paper (Gan et al., 2019B).

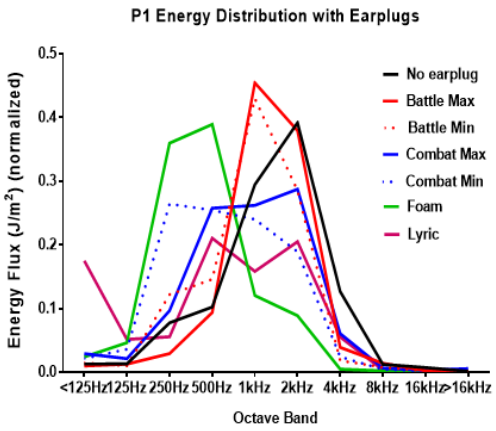
Figure 7A displays the P1 waveforms recorded from ears without earplugs and ears with different earplugs or attenuation settings, including the Battle plugs, CAE, foam, and Lyric. The waveform variation indicates the different effects of earplugs on the pressure wave reaching to the TM in the canal. Figures 7B and 7C illustrate the comparison of impulse energy fluxes of P1 waves over 10 octave frequency bands obtained from seven ear cases in bar curves and in line curves, respectively. The P1 energy distribution over octave bands was altered when the earplug was placed in the ear canal. Table 1 lists the mean and standard deviation of experimental data obtained from human cadaver ears with 6 earplug cases, including the peak values of P0, P1, and P0-P1 in ears with earplug, the peak P1 and the ratio of P1/P0 in ears without earplug, and the P1 reduction induced by the earplug. This is the first time of using cadaver ears to evaluate HPDs' function indicating that different earplugs showed variations in pressure waveforms transmitted to the eardrum, which determine the protection level of earplugs.



(A)



(B)



(C)

Figure 7. (A) Comparison of P1 waveforms measured from the ear without earplug and the ears with earplugs: Battle plug at max and min settings, Combat Arms at max and min settings, foam earplug, and Lyric earplug. (B) Normalized P1 wave energy flux distribution over 10 octave bands from below 125 Hz to above 16 kHz in bar curves. (C) Normalized P1 wave energy flux distribution over 10 octave bands from below 125 Hz to above 16 kHz in line curves (Gan et al., 2019B)

TABLE I. Experimental Results of EPs Tested in Human Cadaver Ears During Blast Exposure

Earplug Type	P0 (dB) w/Earplug	P1(dB) w/Earplug	P0 – P1 (dB) w/Earplug	P1 (dB) w/Out earplug	P1/P0 ratio w/Out earplug	P1 (dB) Reduction
Battle maximum ($N = 15$)	188.9 ± 1.8	176.1 ± 7.5	12.8 ± 7.1	194.3 ± 2.9	1.7 ± 0.4	18.2 ± 6.9
Battle minimum ($N = 13$)	188.1 ± 1.4	175.7 ± 8.1	12.4 ± 8.4	193.8 ± 3.0	1.6 ± 0.4	18.1 ± 7.4
Combat Arms maximum ($N = 14$)	189.8 ± 1.3	176.5 ± 6.9	13.4 ± 6.7	194.5 ± 2.6	1.7 ± 0.4	18.0 ± 7.0
Combat Arms minimum ($N = 12$)	188.3 ± 1.8	176.3 ± 6.5	11.9 ± 5.7	193.6 ± 3.1	1.7 ± 0.4	17.3 ± 5.9
Foam ($N = 13$)	189.1 ± 1.7	176.8 ± 7.2	12.3 ± 6.4	194.2 ± 3.1	1.7 ± 0.4	17.3 ± 6.8
Lyric ($N = 6$)	189.1 ± 1.3	172.8 ± 2.1	16.3 ± 1.7	193.7 ± 3.2	1.8 ± 0.8	20.9 ± 5.3

Note that the P0-P1 without earplug can be derived from the P0 and P1/P0 ratio.

we have also employed the 3D FE model of the human ear to simulate the earplugs inside the ear canal to predict the EP protective function to the BOP, which are reported under Aim 3.

(1-3) 3D printed human ear or temporal bone for standardized testing of HPDs to blast exposure

Due to the technology's versatility and relatively inexpensive manufacturing cost, 3D printing technology provides an intriguing tool for customized solutions for otolaryngology applications. We have utilized 3D printing's versatility to create a human TB model that reproduces the responses observed in blast testing of human TBs with and without HPDs. The 3D printed TB model was created based on our published human ear FE model (Fig. 8a) consisting of the ear canal, TM, middle ear, and cochlea load. Figure 8b displays a sectional view of the CAD model of 3D printed TB showing how the human ear model was encased in the outer TB structure. A Stratasys Objet350 3D printer supported by the DURIP award from the US Army Research Office was used to print the ear's soft and hard tissues with flexible and rigid polymers, respectively.

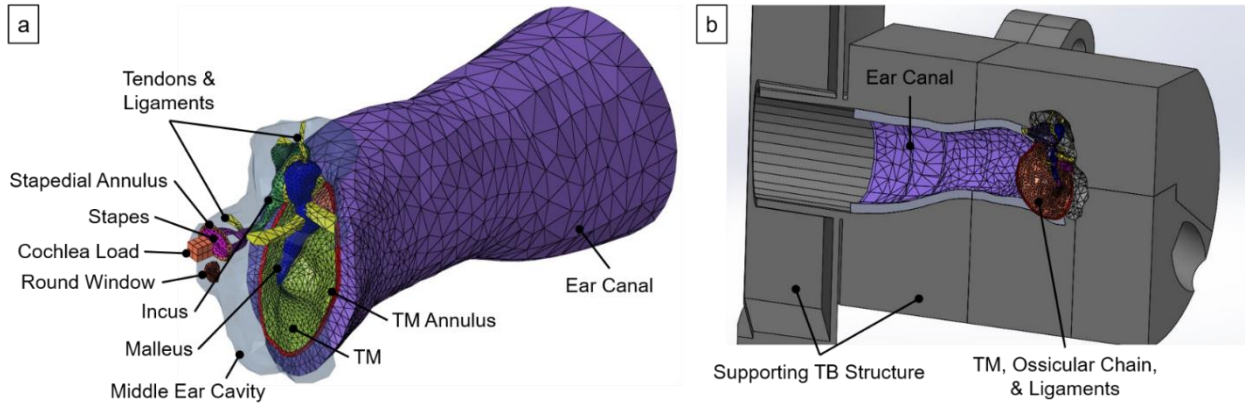


Figure 8. (a) FE model of the human ear with the ear canal, middle ear, and cochlear load (Gan et al., 2004). (b) Sectional view of the assembled CAD model showing the enclosed ear canal and middle ear tissues (Brown et al., 2020A).

An assembled CAD model of the 3D printed TB is shown in Fig. 9. The outer ear portion contained most of the ear canal and was designed to attach to the "head block" used in blast exposure tests (Fig. 9a), and the middle ear portion contained the TM, ossicular chain with joints

and suspensory ligaments, as well as ports for measuring the air pressure near the TM (P1) and in the middle ear cavity (P2) and allowing access to the stapes footplate (Fig. 9b). The 3D printed TB was printed as two main sections: outer and middle ear (Fig. 9c), and the cavity seals (Figs. 9b and 9c) were initially printed separately from the middle ear portion to facilitate cleaning of the support material within the middle ear cavity then fastened to the middle ear portion to enclose the middle ear cavity.

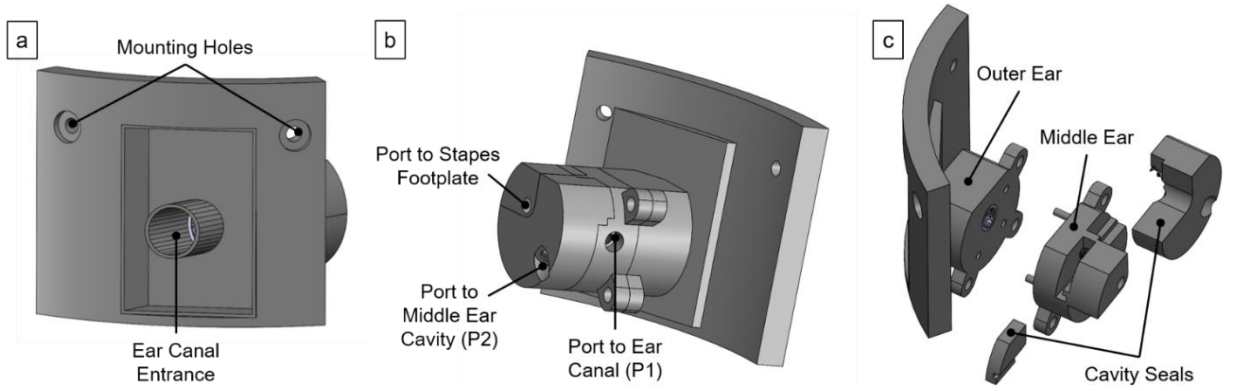


Figure 9. (a) Lateral view of the CAD model of the 3D printed TB highlighting the ear canal entrance. The model's shape was designed to mount into the head block for blast exposure tests. (b) Medial view of the CAD model of the 3D printed TB. The pressure ports to the ear canal near the TM (P1) and middle ear cavity (P2) are shown where pressure sensors are threaded for measurements. A port for access to the stapes footplate for future studies is also shown. (c) Exploded view of the 3D printed TB's CAD model showing the parts to be printed separately: outer ear, middle ear, and cavity seals.

Blast exposure tests in 3D printed TB were performed similar to the HPD characterization in human TBs tests performed by Gan et al. (2019B). The 3D printed TB was exposed to blast while fixed to the "head block" in an anechoic chamber with a blast apparatus designed for open-field blasts (Figs. 10a and 10b) at the BOP level of 6 – 8 psi. Figure 10c illustrates where pressures were monitored: P0, at the entrance of the ear canal, and P1, in the ear canal near the TM. Either a 3M foam earplug (3M Co., St. Paul, MN) or Lyric hearing aid (Phonak, LLC, Warrenville, IL) was used to as HPDs during BOP exposure as shown in Fig. 10d left and Fig. 10d right, respectively).

Figure 11 displays the measured pressures during BOP exposure for the human and 3D printed TBs with earplugs equipped. The P0 and P1 pressures recorded while the 3D printed TB had either the foam or Lyric earplug inserted into the ear canal can be seen in 11a, and 11b plots the similar data for that in a human TB sample. Results indicated that in the 3D printed TB, the attenuated peak pressures at P1 induced by HPDs ranged from 0.92 – 1.06 psi (170 – 171 dB) with blast peak pressures of 5.62 – 6.54 psi (186 – 187 dB) at P0 which were well within the mean and standard deviation of published data from tests in human TBs. The developed 3D printed TB model accurately evaluated HPDs' protective function during blast and potentially performed as a TB model for research in ear biomechanics for acoustic transmission. Details of 3D printed human ear model or TB for standardized testing of HPDs to blast exposure has been presented in several conferences and included in Marcus Brown's Ph.D. dissertation at the University of Oklahoma, May 2021.

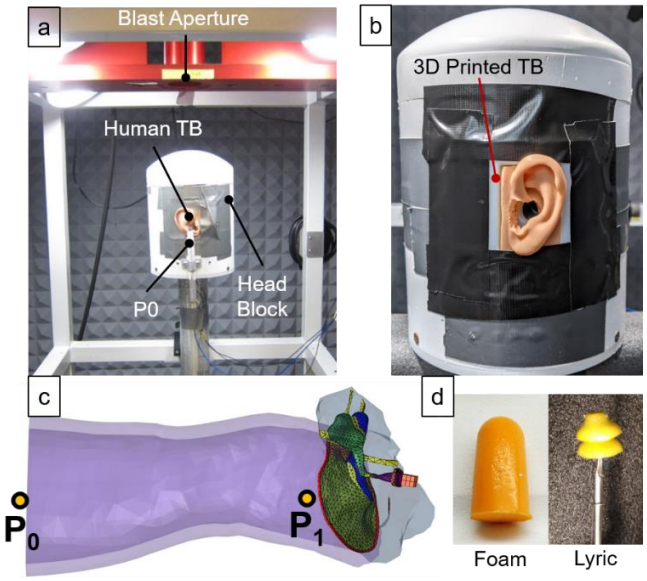


Figure 10. (a) Image of the blast test setup within an anechoic chamber where the "head block" sits below the blast aperture. A human cadaveric TB is mounted to the head block and the pressure sensor P0 is mounted outside of the ear canal entrance. (b) Image of the 3D printed TB mounted to the head block. (c) The FE model highlighting where the pressures were monitored during blast exposure: at the entrance of the ear canal, P0, and in the ear canal near the TM, P1. (d) Images of the foam earplug (left) and Lyric earplug with a stick holder (right) used in blast exposure tests.

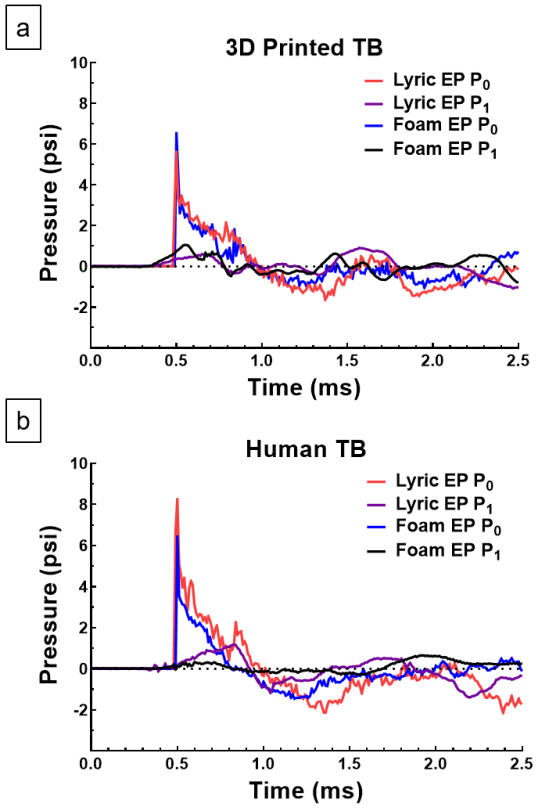


Figure 11. Plots of the P0 and P1 pressures measured in blast tests of the 3D printed TB (a) and human cadaveric TBs (b) protected with a foam earplug (blue line for P0 and black line for P1) or Lyric earplug (red line for P0 and green line for P1).

(1-4) Innovative techniques of using dual laser Doppler vibrometers to measure the movements of the TM and stapes footplate in real time domain during blast exposure

New methodologies to measure the TM and ossicular chain movements during blast exposure have be recently developed in our lab by using two laser Doppler vibrometers. At first, a novel dual-laser setup was first ever established based on a blast chamber and two LDVs to make the real-time measurement on the movement of TM under blast exposure. By measuring vibrations of the TM and "head block" simultaneously using two LDVs under blast, the head block vibration can be eliminated from the movement of the TM. Figure 12 is a schematic diagram of the experimental setup. The "head block" attached with human TB and mounted with two pressure sensors for measuring the response of the middle ear to the blast overpressure. The shaded square represents the location of the TB whose inner structure is shown in the block on the right. LDV1 (single beam laser) aimed at the target placed on the head block to measure the movement of the entire TB specimen while LDV2 (scanning LDV) aimed at the TM at the umbo to measure the movement of the TM which includes both the TM and head block movements. Figure 13 illustrates the pictures of dual laser experiment to measure TM movement during blast exposure. This innovative study has been published in *Hearing Research*, Vol. 378 (Jiang et al., 2019).

Figure 14 shows the results obtained from one TB including the pressure data of P0 and P1 (Fig. 14a), velocity data measure by LDV1 and LDV2 (Fig. 14b), TM velocity after subtracting head block velocity (Fig. 14c), and the converted TM displacement (Fig. 14d). Results from 5 fresh human TBs indicated that the maximum TM velocity was 12.62 ± 3.63 m/s (mean ± SD) and the displacement was 0.78 ± 0.26 mm. The peak-to-peak displacement normalized by the P0 pressure (35 kPa or 5 psi) was 22.9 ± 6.6 μm/kPa. The frequency domain analysis indicated that the spectrum peaks were located at frequencies below 3 kHz.

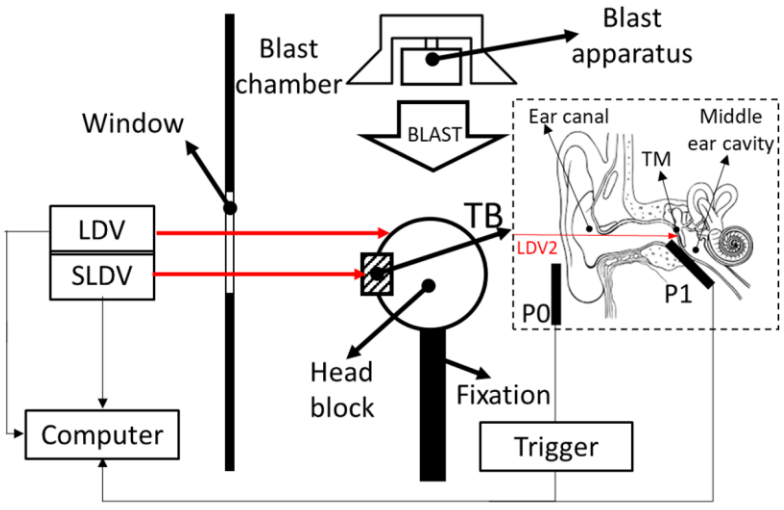


Figure 12. Schematic of the experimental setup showing the blast chamber and LDVs. The inside structure of the TB specimen and the location of the pressure sensors are shown in the dashed square.

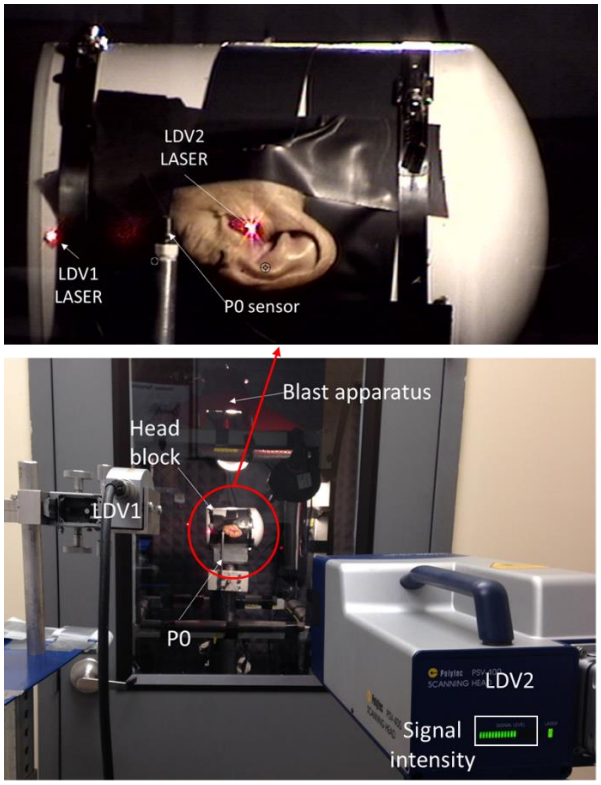


Figure 13. Experimental setup: upper panel shows the zoomed-in view of the "head block" showing two lasers aiming at their targets; lower panel shows the blast chamber and two LDVs viewed from the outside of the blast room.

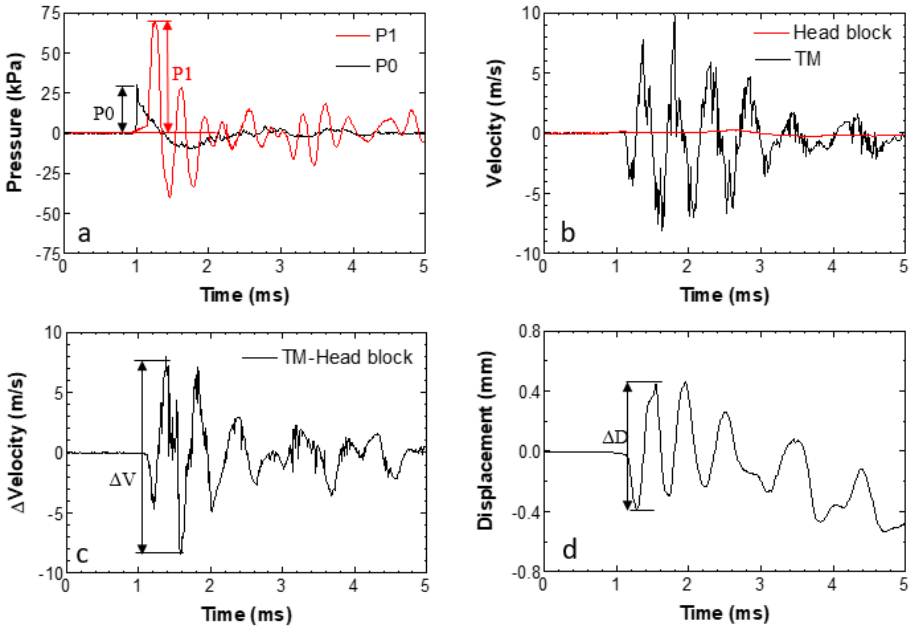


Figure 14. Typical results from TB #5: (a) Pressure curves obtained from P0 and P1 sensor; (b) raw velocity data obtained from LDV1 and LDV2; (c) TM velocity after the subtracting head block velocity from the TM velocity; (d) TM displacement curves.

Following the success of TM measurement with dual lasers, we have extended the techniques to measure the movement of stapes footplate, the end part of the ossicular chain, which directly contacts the cochlear fluid. This is a significant development toward to quantitatively characterize the response of the middle ear and the energy entering the cochlea during blast exposure. A journal paper submitted to *Hearing Research* is currently under the 2nd review (Jiang et al., 2020).

Figure 15 shows the schematic of experimental setup which is similar to the TM measurement of Fig. 12 except that the LDV2 was aimed at the states footplate (SFP) and LDV1 aimed at the TB as a reference. To expose the SFP, the facial recess surgical approach was performed (Fig. 16a) and a reflective tape was placed at the footplate as the laser's target (Fig. 16b). Pictures in Fig. 17 show the experimental setup. Eight TBs were used in this study for open ear tests (without earplug) and 5 TBs were tested with foam earplug (3M, Inc.).

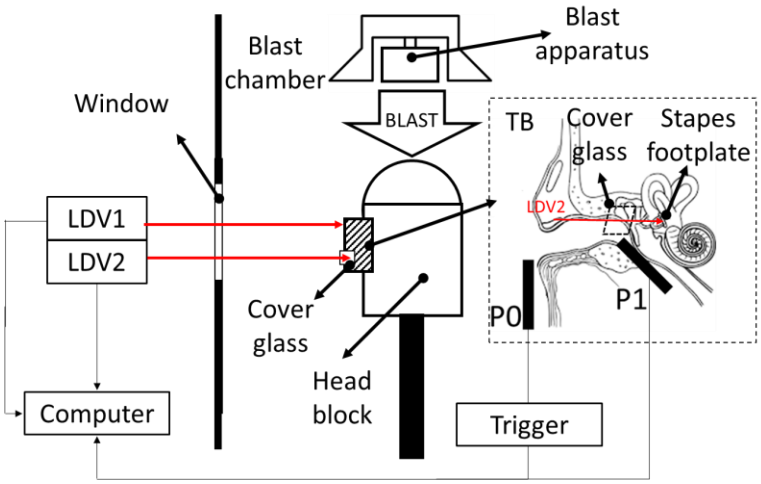


Figure 15. Schematic diagram of the experimental setup showing the blast chamber, head block, LDVs, and the data acquisition system. The zoomed-in view (dashed square) shows the inside structure of the TB specimen and locations of the pressure sensors. The LDV2 reached the SFP through the facial recess surgical approach.

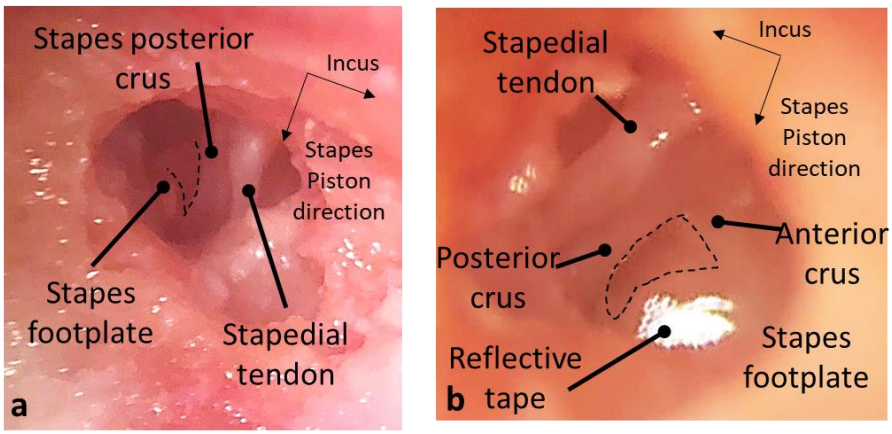


Figure 16. Facial recess surgical approach to reach SFP. (a) Deep opening of middle ear to expose the SFP; (b) placing the reflective tape on the center of the SFP. Note that the two pictures were obtained from different specimens. The stapes piston direction and the long process of incus were used as references to demonstrate anatomic directions. The visible edges of stapes cruses and SFP were highlighted by black broken lines.

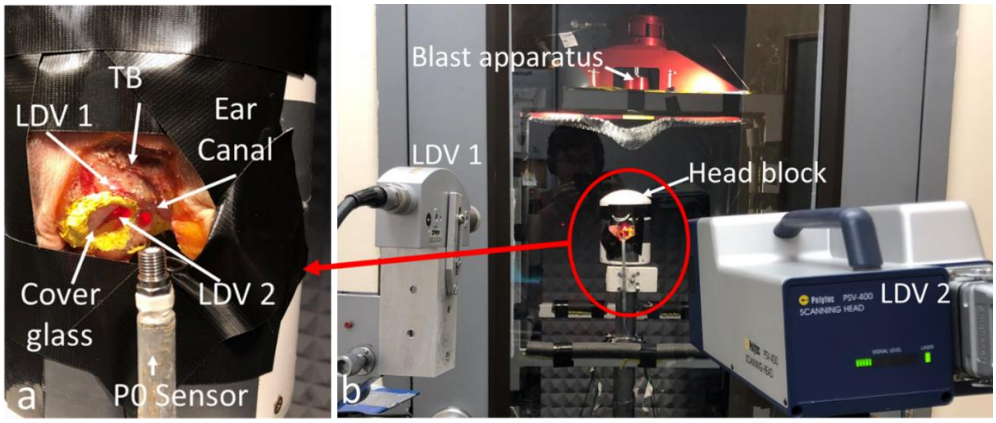


Figure 17. Experimental setup: (a) The zoomed-in view of the head block during the experiment showing two lasers aiming at their targets; (b) the blast apparatus inside the test chamber and two LDVs viewed from the outside of the blast room. The blast was generated by the apparatus.

The waveforms over 5-ms duration measured from 3 TBs with open ear are displayed in Fig. 18. Column 1 in Fig. 18 represents the P0 and P1 pressure waveforms; Column 2 represents the velocity of stapes footplate and TB measured from two LDVs; Column 3 shows the velocity of the footplate by subtracting the TB (reference) velocity; and Column 4 shows the displacement of the footplate converted from the velocity data. The peak-to-peak SFP displacement of 68.7 ± 31.6 μm (mean ± SD) measured from all eight TBs without HPDs.

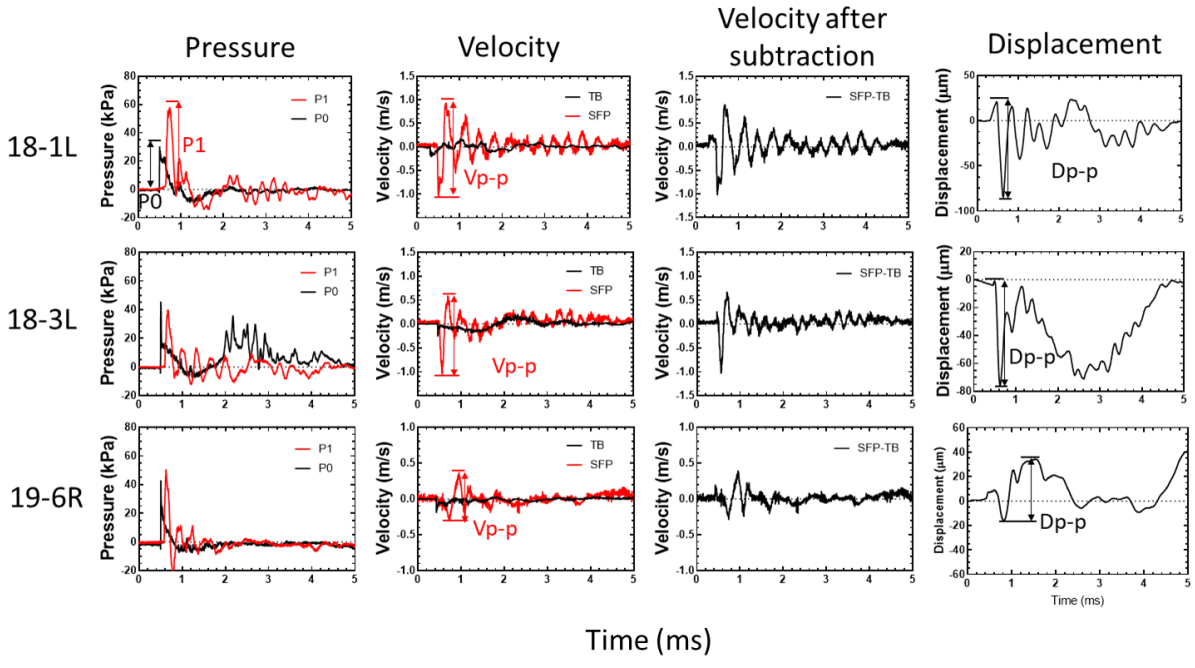


Figure 18. Typical time-domain results measured from three TBs exposed to blasts at a P0 level of 5-8 psi (34-55 kPa). The four columns from left to right present the pressures, velocities of the SFP and TB, SFP velocities after subtraction, and SFP displacement.

Figure 19 shows the waveforms recorded in 3 plugged or protected ears. As shown in this figure, the pressure reaching the TM in the ear canal (P1) was reduced very much due to the earplug and the velocity or displacement of the footplate showed huge reduction compared to the open ears. In five of the TBs, the insertion of the foam earplug reduced the SFP displacement from 48.3 ± 6.3 μm to 21.8 ± 10.4 μm. In conclusion, the reduced footplate displacement with earplug indicates that the earplug significantly reduced the energy entering the cochlea by reducing the P1, which further reduce the vibration of the stapes footplate. This is a technology innovation on biomechanical measurement of blast-induced auditory injury and a significant step toward simultaneously measuring the TM and stapes footplate movements during blast exposure.

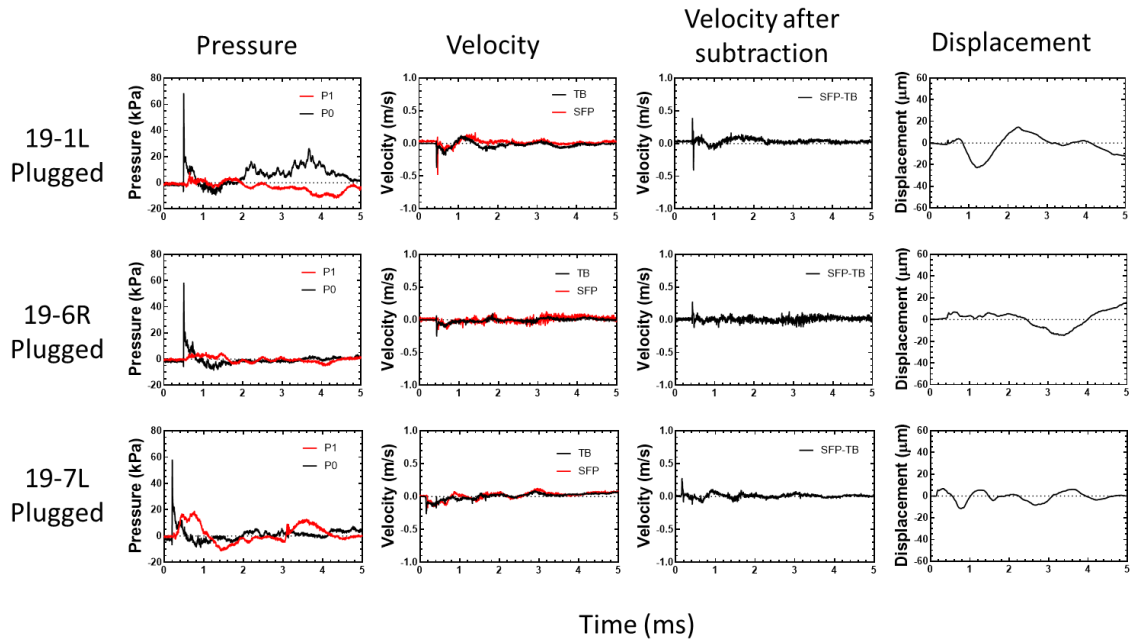


Figure 19. Typical time-domain results measured from three TBs with the protection of HPDs under a P0 level of 5-8 psi (34-55 kPa). The four columns from left to right present the pressures, velocities of the SPF and TB, SFP velocities after subtraction, and SFP displacement.

(1-5) Measurement of TM surface motion changes damaged by blast waves

Measurement of the entire TM surface motion has been used to explore the relationships between the structure and acoustic function of the middle ear in animals and human cadaveric temporal bones. However, the impact of biomechanical changes of the TM after blast exposure on TM's movement for sound transmission has not been investigated until our study that the full-field surface motion of the human TM was measured using the scanning LDV (SLDV) in 4 human TBs under normal and post-blast conditions. Figure 20A is the schematic diagram showing the experimental setup for measuring the TM surface motion and Fig. 20B shows a typical view of a TM sample captured by the SLDV and the scanning grids of 400-500 measurement points were distributed evenly over the entire surface of the TM. Note that the scanning LDV (PSV-500, Polytec, Inc.) was supported by the DURIP award from the Office of Naval Research. This study resulted in a journal article published in *J. Biomechanical Engineering*, Vol. 141 (Gan and Jiang, 2019A) which was selected as one of the JBME Editors' Choice papers for 2019.

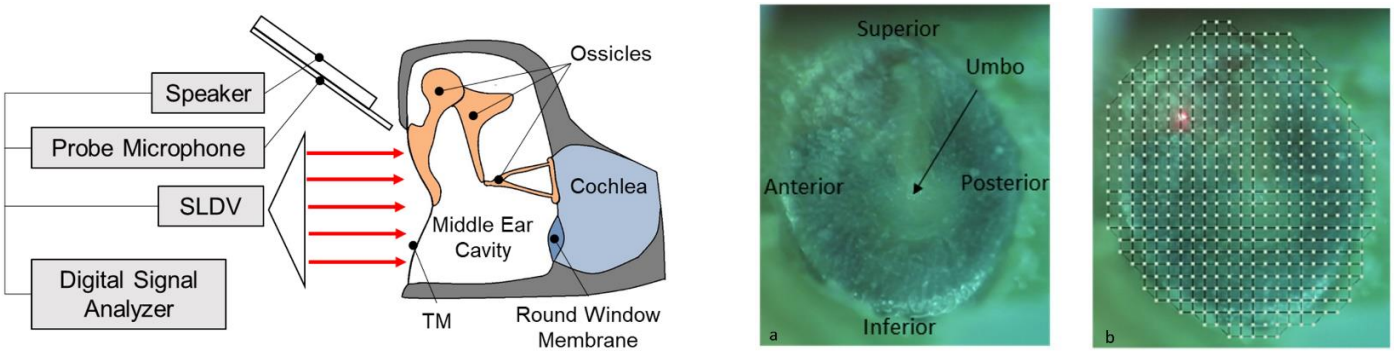


Figure 20. (A) Schematic diagram of the experimental setup showing the SLDV and a human temporal bone. (B) Left panel: One exposed TM sample image (left ear) captured by the SLDV; Right panel: the typical scanning points defined on the TM surface with a laser spot shown.

Figure 21 shows the full-field surface motion of specimen TB-60 (right ear) at five frequencies before and after four repeated blasts at the level of 53 kPa. The color bars on the right side of images represent the displacement amplitude normalized by the input sound pressure in nm/Pa.

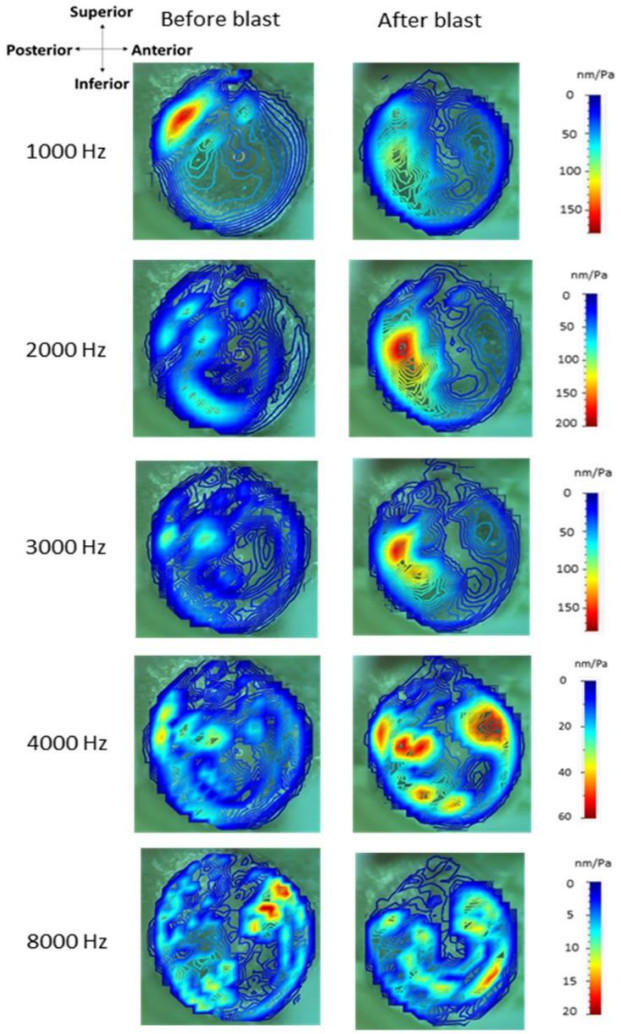


Figure 21. Deflection shapes of TM surface motion measured by SLDV on specimen TB-60 (right ear) at five frequencies of 1, 2, 3, 4, and 8 kHz before and after four repeated blasts. The orientation of the right ear TM is shown in the upper left-hand corner.

The deflection shapes of 4 TMs from all TBs at 3 kHz are presented in Fig. 22. The left column of this figure displays the shapes of TM deflection before blast exposure, and the right column shows the TM deflection shapes after blast exposure. Results indicated that the TM displacement after blast exposure increased in the posterior region of the membrane between 3 and 4 kHz in all tested TBs. An FE model of human TM with multilayer microstructure and orthogonal fiber network was created to simulate the TM damaged by blast waves which will be reported in Aim 3. The consistency between the experimental data and the model-derived TM surface motion suggests that the tissue injuries were resulted from a combination of mechanical property change and regional discontinuity of collagen fibers. This study provides the evidences of surface motion changes of the TM damaged by blast waves and possible fiber damage locations.

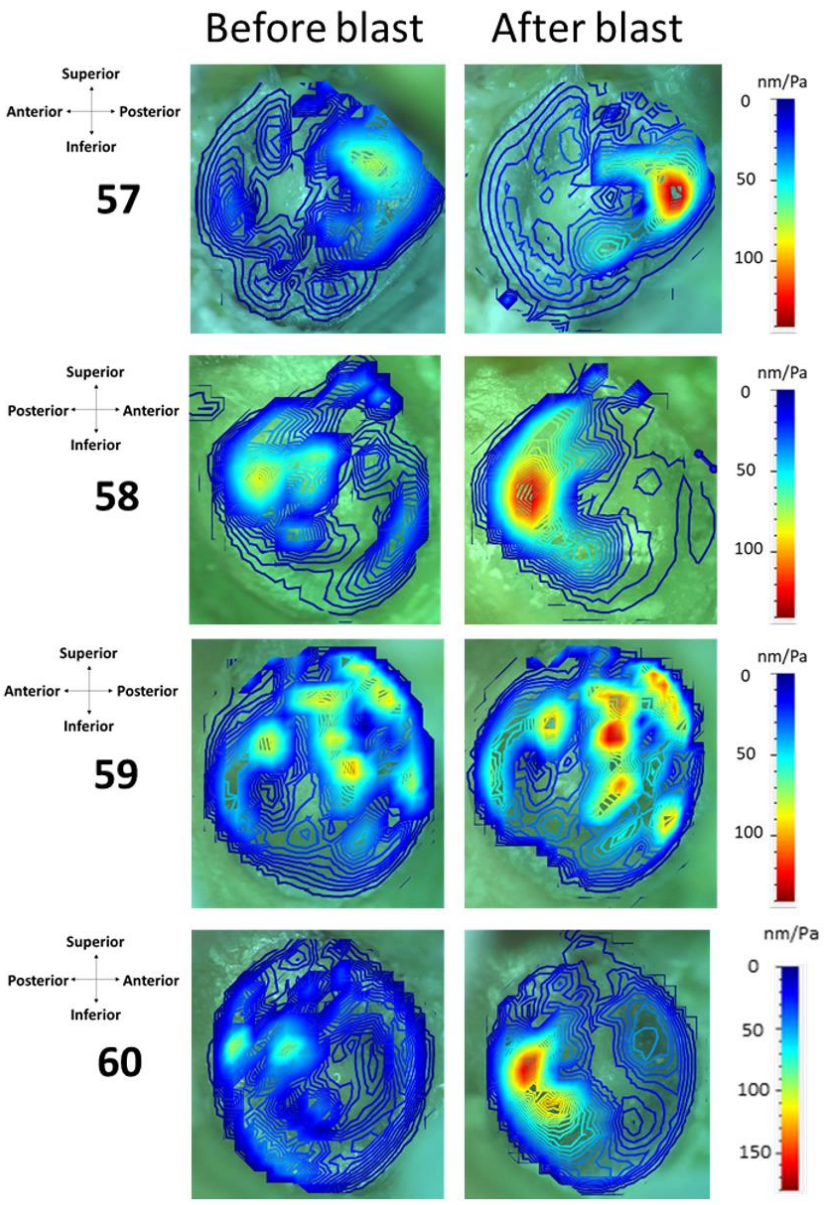


Figure 22. Deflection shapes of TM surface motion measured by SLDV on all TBs at 3 kHz.

Aim 2:

(2-1) <u>Measurement of middle ear muscle reflex or electromyography in chinchillas during the blast exposure</u>

The stapedius muscle and tensor tympany muscle are two muscles in the middle ear as shown in Fig. 23. Stapedius muscle is activated in the middle ear muscle reflex (MEMR) as a protective function in response to high intensity sound exposure. When a sound is of enough amplitude to elicit the MEMR, the reflex damps the stapes's motion and mitigates the high ossicular motion transmitted from the stapes to the cochlea. The measurement of MEMR commonly used in the clinics using tympanometry is an indirect method to test MEMR. Electromyography (EMG) is an invasive procedure that gives a direct measurement of the behavior of a muscle over the time domain. In this project, we successfully developed the EMG technique in chinchilla blast model to study the MEMR for the first time, particularly for a stimulus of blast exposure no EMG stapedius data exist in any animal model. Results were presented in several conference papers by Yokell et al. and the Ph.D. Dissertation by Zachary Yokell at University of Oklahoma, May 2019.

Figure 24 shows the surgical opening in a chinchilla (A) and the insertion of a bipolar electrode fabricated in our lab into the stapedius muscle (B). Figure 25 displays the recorded EMG amplitude signals from four chinchillas exposed to different blast pressure levels. The waveform varied with the BOP exposure level and the EMG amplitude almost lineally increased as the blast intensity increased.

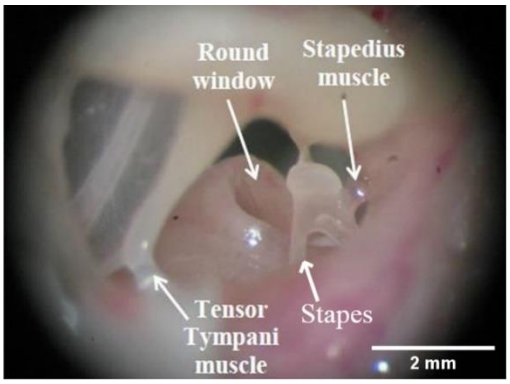
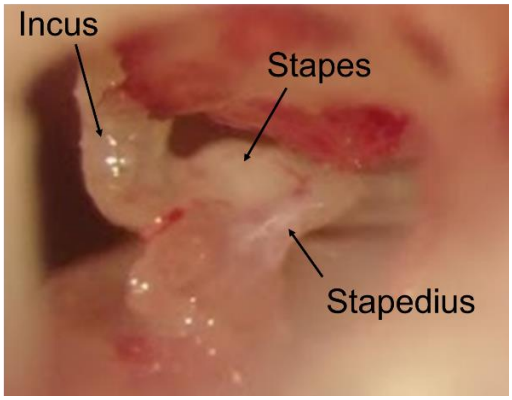
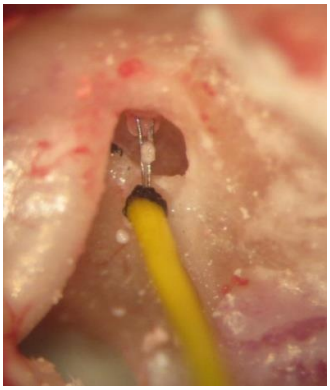


Figure 23. Chinchilla ossicles and middle ear muscles.



(A)



(B)

Figure 24. (A) View of surgical opening of chinchilla stapedius muscle; (B) the electrode inserted into the chinchilla stapedius muscle.

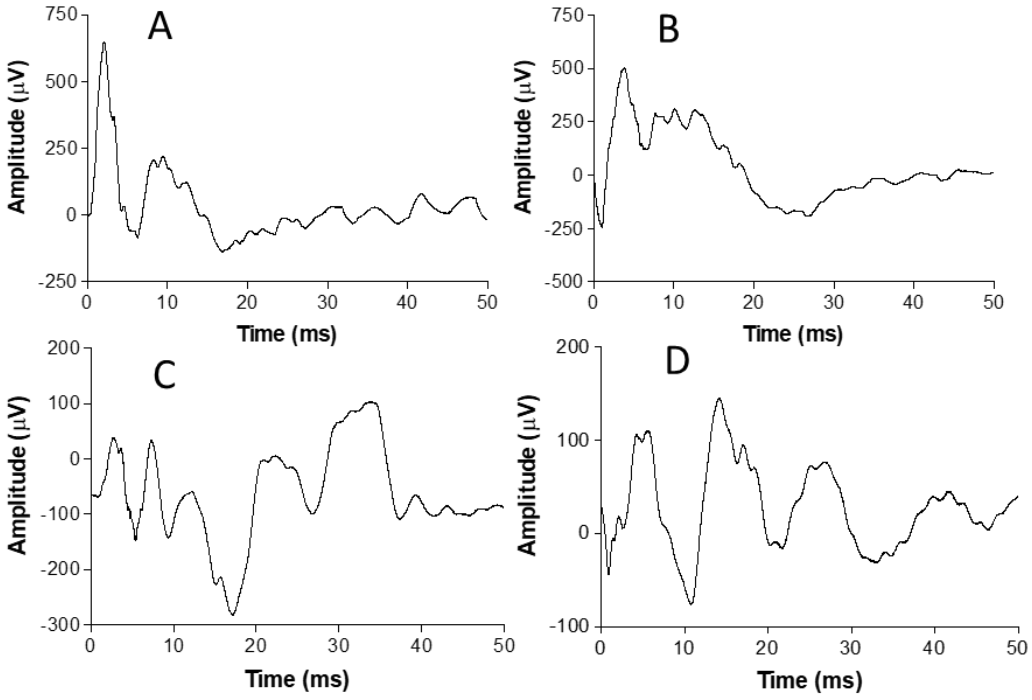


Figure 25. EMG signals recorded from four chinchillas at different blast overpressure levels. (A) and (B): BOP level at 8.3 psi; (C) and (D): BOP level at 2.5 psi.

Figure 26 shows the EMG latency defined as the time difference between the BOP peak and the first EMG peak. The average latency time from 10 animals between blast overpressure onset and muscle activation was determined to be 4.75 ± 3.19 ms. As this is shorter than the time course of a blast event, this confirmed that the MEMR activates too slowly in chinchillas to provide a mitigative function against blast overpressure waves.

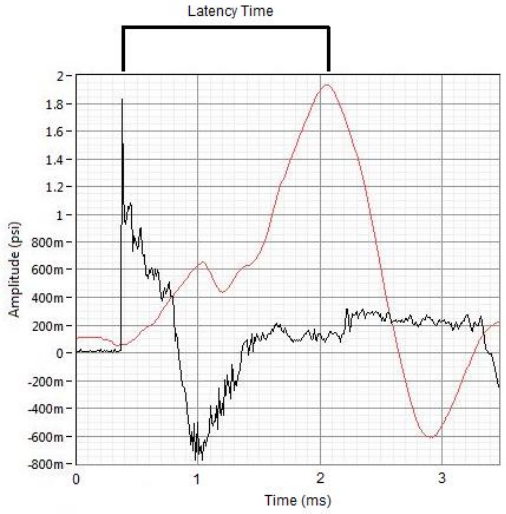


Figure 26. Blast MEMR latency as the difference between the overpressure peak (black) and the first EMG peak (red).

An acute hearing damage model in chinchilla was established to determine the changes of MEMR threshold after noise exposure to 130 dB SPL. The MEMR thresholds and hearing levels of these chinchillas (n=8) were tested before and after noise exposure to quantify the resultant level of hearing damage. Figure 27 shows the thresholds of stimulus levels measured from the EMG data (A) and the auditory brainstem response (ABR) (B). Across all frequencies tested, pre-exposure animals had an average MEMR threshold of 68.8 dB and ABR of 37.2 dB. After one hour of exposure these increased to 123.4 dB and 103.6 dB, respectively, and after two hours they increased to 124.5 dB and 105.8 dB. While there was not a statistically significant difference between the damage caused by the two exposure durations, the one-hour case caused an average of 65.1 dB shift in the animals' hearing levels and 54.7 dB shift in MEMR activation levels. Figure 28 displays the shift in MEMR and hearing level threshold after exposure. Across all frequencies, the average MEMR threshold shift was 54.7 dB for one hour and 55.9 dB for two hours. For ABR, the shift was 65.1 dB for one hour and 67.3 dB for two hours. In conclusion, this acute hearing damage model can be used to assess protective interventions in a single day of experimentation.

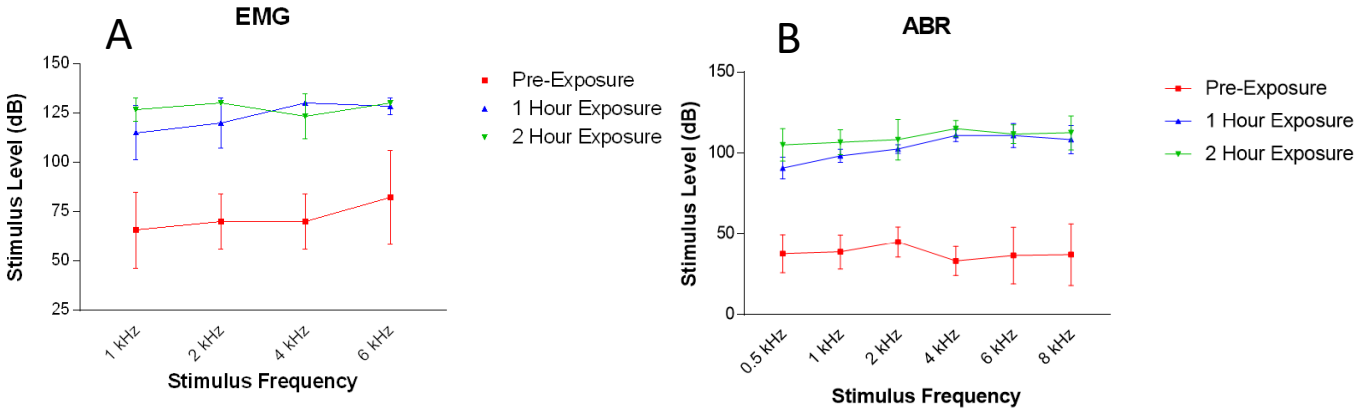


Figure 27. (A) EMG-determined MEMR threshold levels before and after noise exposure. (B) Hearing or ABR threshold levels before and after noise exposure.

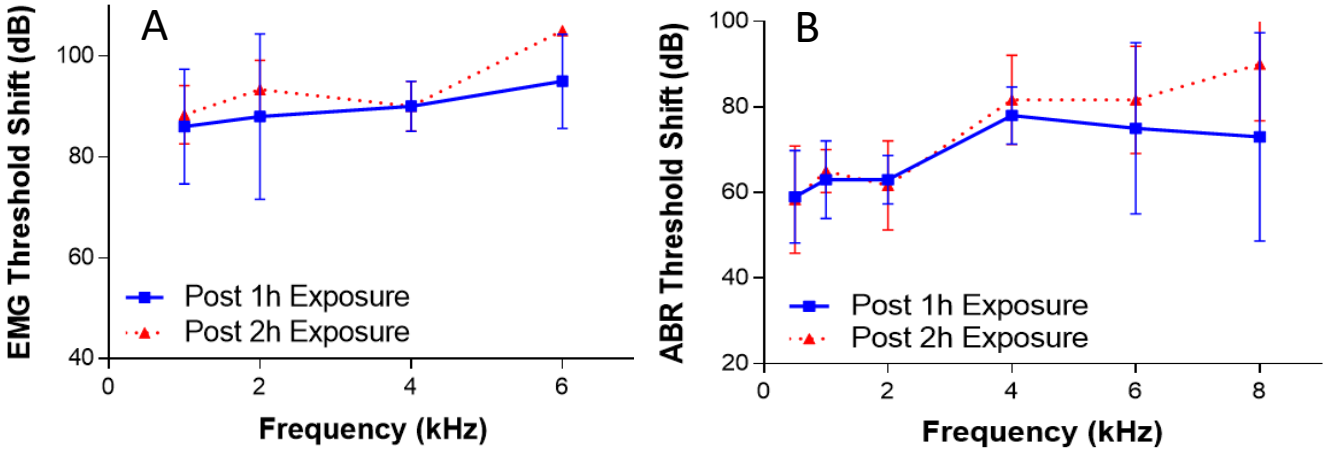


Figure 28. (A) EMG threshold shift after noise exposure. (B) Hearing or ABR threshold shift after noise exposure.

(2-2) Blast-induced peripheral and central auditory injuries measured in chinchillas including mechanical damage of the TM and middle ear and the changes of hearing threshold, cochlear function, and immunofluorescence images

Mechanical damage to middle ear components in blast exposure directly causes hearing loss, and the rupture of the TM is the most frequent injury of the ear. We used chinchilla model to investigate that the severity of injury graded by different patterns of TM rupture is related to the BOP waveforms created by two conditions: open field and shielded a stainless-steel cup covering the animal head. Figure 29A shows the overpressure waveforms recorded in a chinchilla exposed to open field tests and Fig. 29B shows the waveform recorded from an animal in shielded testing. The sound pressure signal in the open field is a shock wave-like impulse and the pressure signal in the shielded case is a complex wave-like waveform as observed in our experiments. The impulse wave is completely changed under the shield. The results from this study were published in *Hearing Research*, Vol. 340 (Gan et al., 2016).

Table 1 lists the measured TM rupture thresholds (positive-peak in both psi and dB SPL) for animals tested in open field. The mean value of the TM rupture threshold measured from 9 animals in open field was 9.1 psi or 190 dB SPL or 62.7 kPa with a standard deviation (S.D.) of ±1.7 psi (N=9). Table 2 lists the measured TM rupture thresholds for animals tested with the shielded. The mean value of the TM rupture thresholds measured from 9 animals with the shield was 3.4 ±0.7 psi (N=9) or 181 dB SPL. Comparing the results listed in Tables 1 and 2, a significant difference in the TM rupture thresholds between the open and shielded cases was revealed. With the shield, the TM rupture occurred at a much lower impulse pressure than that in the open field. This difference shows the biphasic nature of the shielded impulse.

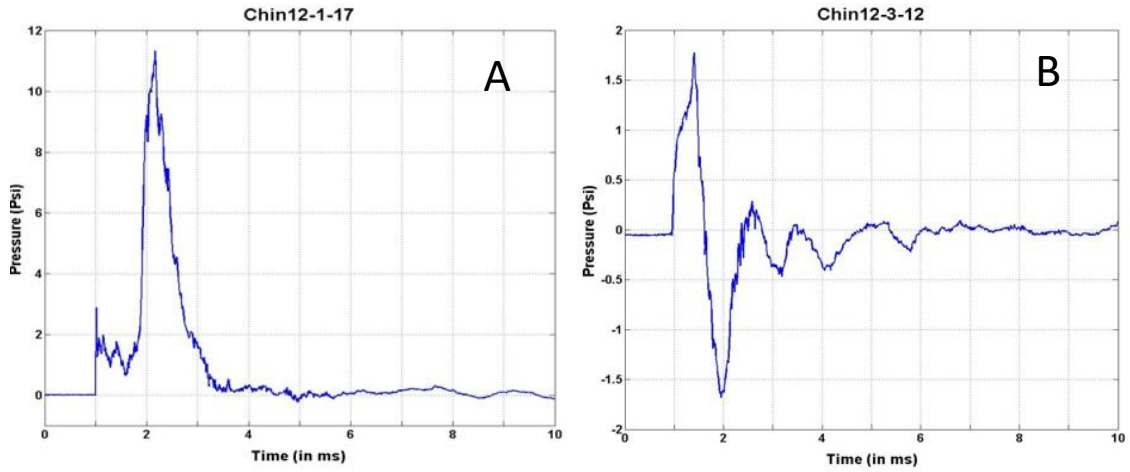


Figure 29. (A) The overpressure waveform recorded in one chinchilla (chin12-1-17) in open field testing and (B) the pressure waveform recorded from another chinchilla (chin12-3-12) in shielded testing.

Table 1
List of TM rupture thresholds measured from a group of chinchillas tested in open field.

Animal	Chin-1	Chin-2	Chin-3	Chin-4	Chin-5	Chin-6	Chin-7	Chin-8	Chin-9	Mean ± S.D.
Positive peak (psi)	10.7	6.9	9.8	11.3	10.2	9.8	9.1	9.0	5.5	9.1 ± 1.7
Positive peak (dB SPL)	191.3	187.5	190.6	191.8	190.9	190.6	189.9	189.8	185.6	189.8 ± 1.9

Table 2
List of TM rupture thresholds measured from a group of chinchillas tested with a shield.

Animal	Chin-1s	Chin-2s	Chin-3s	Chin-4s	Chin-5s	Chin-6s	Chin-7s	Chin-8s	Chin-9s	Mean ± S.D.
Positive-peak (psi)	1.5	2.2	1.5	1.5	2.3	2.3	1.8	1.4	1.1	1.7 ± 0.4
Negative-peak (psi)	2.6	2.7	1.5	1.3	1.3	1.2	1.6	1.4	1.6	1.7 ± 0.5
Peak-to-peak (psi)	4.1	4.9	3.0	2.8	3.6	3.5	3.4	2.8	2.7	3.4 ± 0.7
Peak-to-peak (dB SPL)	183.0	184.6	180.3	179.7	181.9	181.6	181.4	179.7	179.4	181.3 ± 1.6

Figure 30 displays the distribution of energy flux (normalized) over 10 frequency bands. Under the open field condition, most of the energy flux is presented at lower frequencies below 500 Hz. However, under shielded condition, the energy flux is mainly involved at 500 and 1000 Hz. The impulse pressure energy spectra analysis of waveforms demonstrates that the shielded waveforms include greater energy at high frequencies than that of the open field waves. In addition to animal experiments, a 3D FE model of the chinchilla ear was developed and used to compute the distributions of stress in the TM and the TM displacement with impulse pressure waves. The FE model-derived change of stress in response to pressure loading in the shielded case was substantially faster than that in the open case. This finding provides the biomechanical mechanisms for blast induced TM damage in relation to overpressure waveforms. Details will be reported in Aim 3 for chinchilla FE model of the ear.

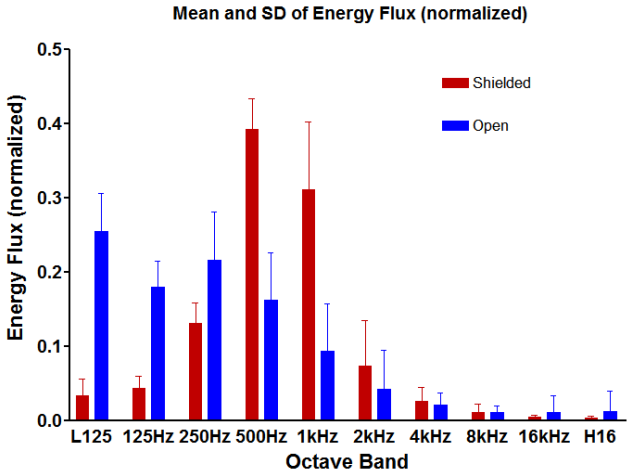


Figure 30. Comparison of normalized energy flux over 10 frequency bands from below 125 Hz to above 16 kHz between the waveforms recorded in the open and shielded groups of chinchillas.

We have investigated hearing damage induced by blast overpressure in open field at relatively mild TBI level (103-138 kPa or 15-20 psi) including the extent of hearing loss in relation to blast number and time course of post-blast. Figure 31 is an overview of the experimental procedures for the two experimental groups of chinchillas (n=7 each): to expose 2 blasts and 3 blasts on Day 1, respectively, and named as 2-Blast group and 3-Blast group, accordingly. Figure 32A is a schematic of animal experimental setup inside blast test chamber in our lab. The animal was fixed in an animal holder with the body up straight toward the blast source and a pressure sensor was placed at the ear canal entrance. Note that both ears of the animal involved in this study were inserted the standard foam earplugs to protect damage in the TM caused by blast pressure. Figure 32B shows the waveform of BOP measured at the entrance of the ear canal. This study has resulted in a journal article published in *Military Medicine*, Vol. 185 (Smith et al., 2020).

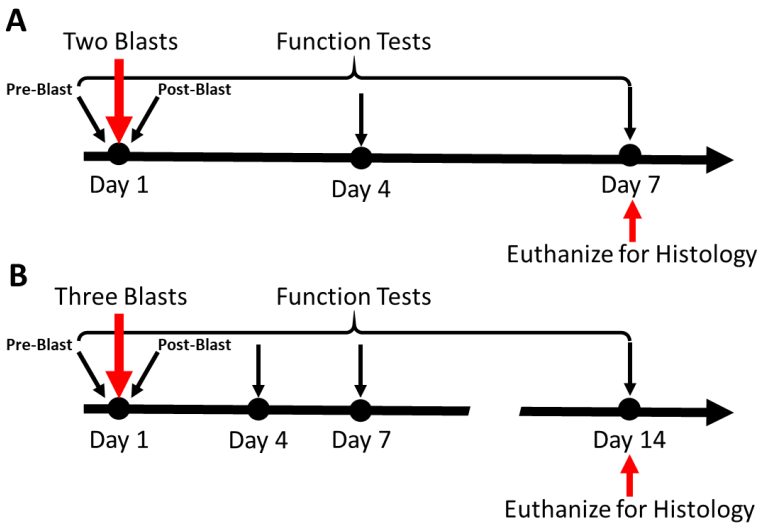


Figure 31. Diagram showing the time course and experimental procedure. (A) 2-Blast animals over 7-day experiment; (B) 3-Blast animals over 14-day experiment.

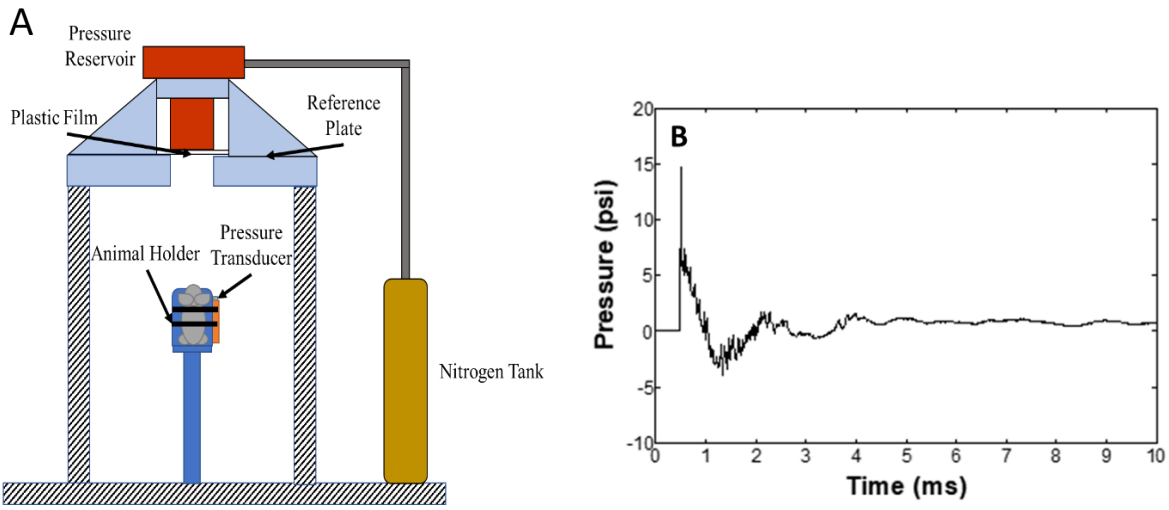


Figure 32. (A) Schematic of animal experimental setup with blast apparatus. (B) A recorded BOP waveform from an animal test in 3-Blast group with a peak pressure of 15 psi.

Results obtained from hearing function tests including the ABR threshold shift (increase) and DPOAE level (reduction) from two groups of animals are displayed in Fig. 33. The top two panels present the ABR threshold shifts and the bottom two panels present the DPOAE level shift. Results indicate that the ABR threshold and DPOAE level shifts in 2-blast animals were recovered after 7 days. In 3-blast animals, the ABR and DPOAE shifts remained at 26 and 23 dB, respectively after 14 days. Figure 34 shows in immunofluorescence staining of PI3K and DAPI images in auditory cortex (AC). In conclusion, two blasts were not sufficient to cause permanent hearing damage in ears protected with earplugs and three blasts caused permanent hearing damage reflected in ABR and DPOAE measurements and the damage in the AC. The results indicate that the foam earplug tested in this study could not provide adequate protection against permanent hearing damage when exposed to 3 blasts at the mTBI level.

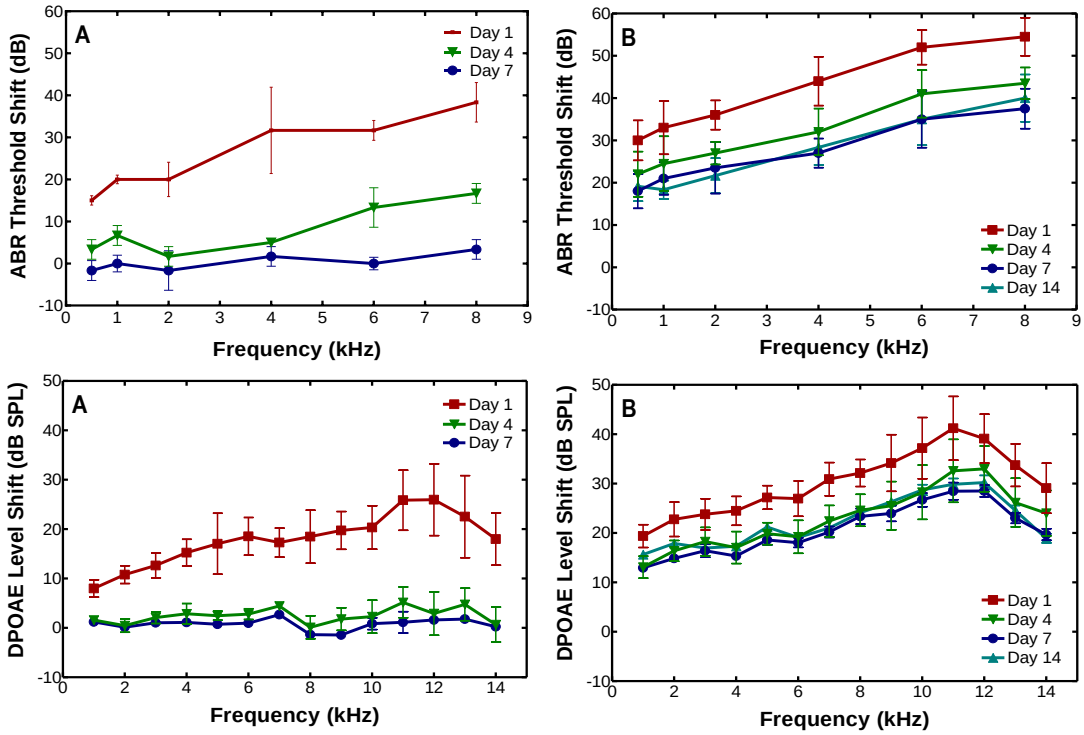


Figure 33. Top **(**A): ABR threshold shifts (mean ± SD) measured from 2-Blast group; and (B): ABR threshold shifts from 3-Blast group. Bottom (A): DPOAE level shifts (mean ± SD) measured from 2-Blast group; and (B): DPOAE level shifts from 3-Blast group. For each group, n=10 ears.

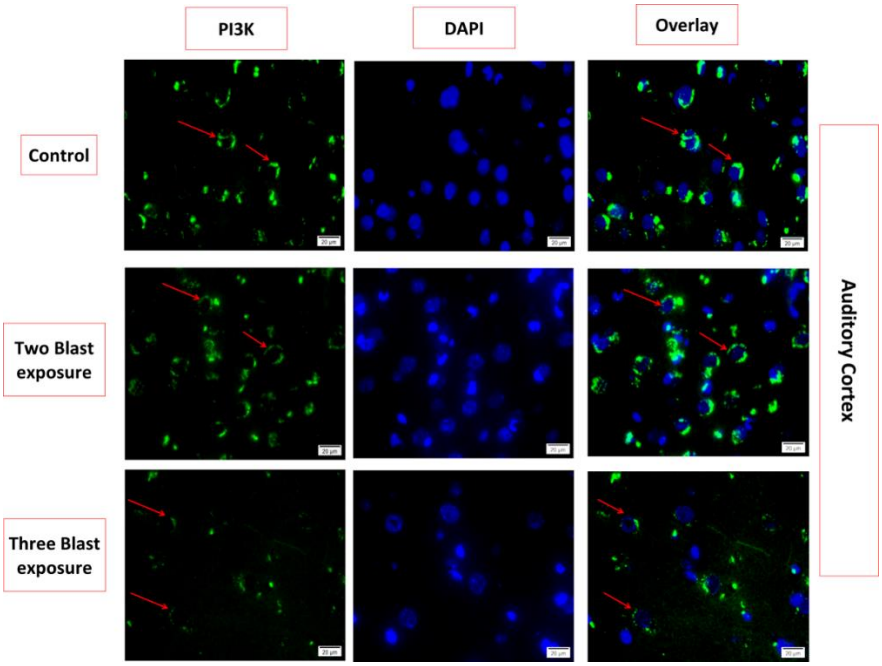


Figure 34. The immunofluorescence staining of PI3K in chinchilla auditory cortex (AC) in control, 2-Blast, and 3-Blast animals. The top three figures were from the AC in control animals; the middle three figures from the AC in 2-Blast animals on Day 7; the bottom three figures from the AC in 3-Blast animals on Day 14. Images were taken at a magnification of 400×. Arrows marked the p85α expression in the auditory cortex. The nuclear counter stain was DAPI (blue).

(2-3) Effect of the number of blast exposures at the low BOP intensity level on hearing damage in chinchillas over the recovery time course

We have utilized the chinchilla blast model to conduct studies on repetitive exposures at low blast overpressure of 3-5 psi or 21-35 kPa, named as G1 BOP level, below mild TBI pressure level. The goal is to determine hearing damage in relation to the number of blast exposures in acute and progressive injuries and the HPDs' protective mechanisms.

The first study included two groups of chinchillas (N=7 each): Group 1 was for an acute study with 2 blasts and Group 2 for progressive study with 3 blasts on Day 1 and observed for 7 days. Animals in both groups were exposed to G1 BOP level at which the eardrum was usually not ruptured. One ear was left open while another ear was protected with an earplug. Figure 35 shows the typical waveforms of BOPs measured at the entrance of the ear canal (P0) from two groups. The results were published in *Hearing Research*, Vol. 378 (Chen et al., 2019).

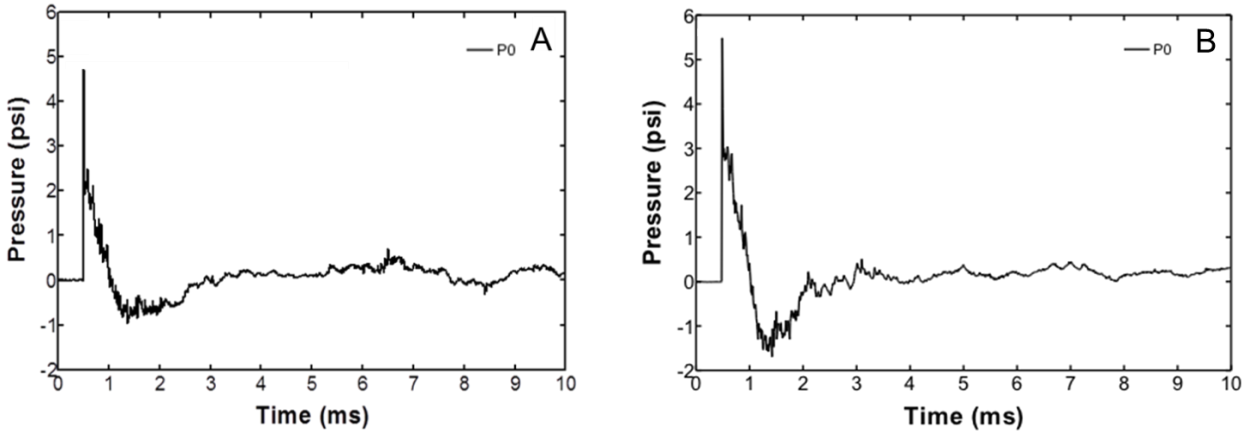


Figure 35. (A) A recorded BOP waveform at the entrance of the ear canal from an animal test in Group 1 with a peak pressure of 4.7 psi. (B) A recorded BOP waveform from an animal test in Group 2 with a peak pressure of 5.2 psi.

ABR thresholds, DPOAEs, and middle latency responses (MLRs) were measured after each blast series in the acute group and on Days 1, 4, and 7 in the progressive group. The acute results from Group 1 with 2 blasts are shown in Fig. 36. The ABR threshold shifts (elevations) obtained from seven animals before and after each blast exposure in open and plugged ears are presented in Fig. 36A and the DPOAE level shifts (reductions) are shown in Fig. 36B. Results indicated that the acute hearing damage immediately following blast exposures was characterized in relation to the number of blast exposures in both open and protected ears. The shifts in open ears were greater than that in plugged ears over the entire frequency range. The damage to cochlear outer hair cells became more severe from blast 1 to blast 2 as shown in Fig. 36B. With the protection of earplugs, the dysfunction of cochlear outer hair cells induced by blast exposure was reduced but still observed from the DPOAE results.

Figure 37 shows the ABR threshold shifts (elevations) measured from animals in Group 2 with 3 blasts over a 7-day period after blast exposures: (A) in ears with earplugs, (B) open ears, and (C) comparison of ABR threshold shift (elevation) on Days 1, 4, and 7 in both open and protected ears. Results indicated that 3 blasts were able to induce permanent hearing damage in open ears while only temporary damage occurred in protected ears.

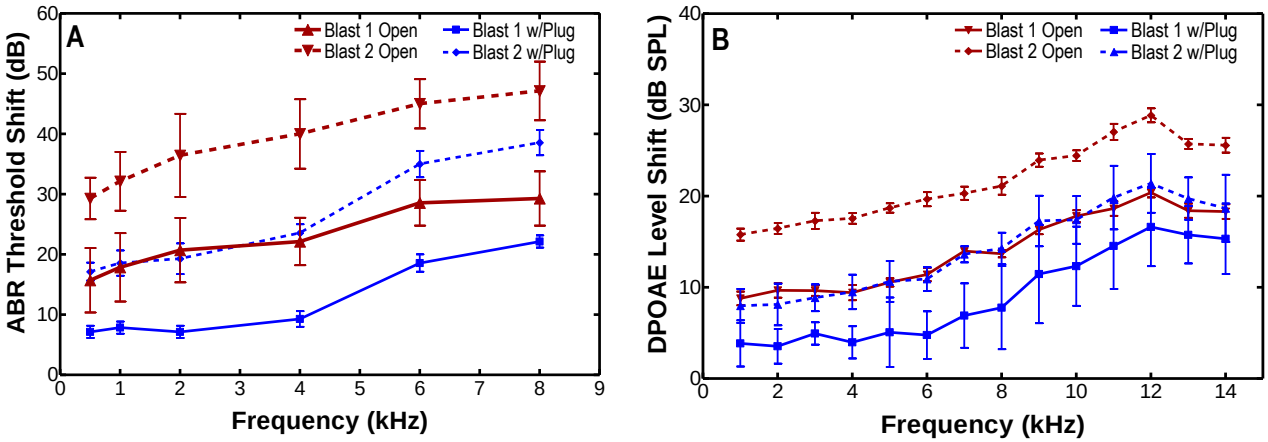


Figure 36. (A) ABR threshold shifts (mean ± SD, n=7) measured after each blast in open and plugged ears of the Group 1 animals. (B) DPOAE level shifts (mean ± SD, n=7) measured after each blast in open and plugged ears of the Group 1 animals.

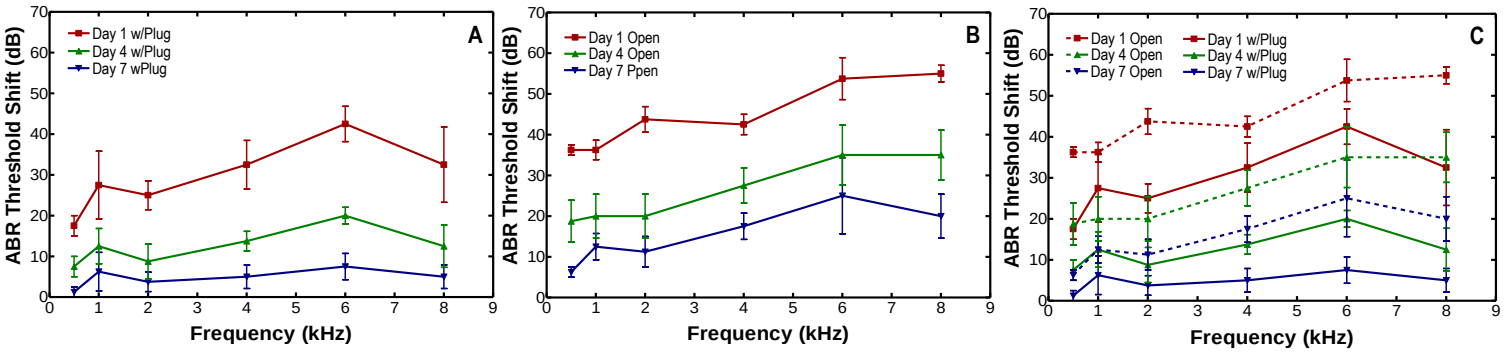


Figure 37. (A) ABR threshold shifts (mean ± SD, n=7) measured in plugged ears after 3 blasts on Day 1, Day 4, and Day 7 of the Group 2 animals. (B) ABR threshold shifts (mean ± SD, n=7) measured in open ears on Days 1, 4, and 7 of the Group 2 animals. (C) Comparison of ABR threshold shifts in plugged and open ears on Days 1, 4, and 7.

In conclusion, hearing damage was observed in both the peripheral and central auditory systems as reflected by the ABR, DPOAE and MLR results. Using this chinchilla blast model, acute and progressive hearing damages were quantified in both open and protected ears under repeated low-intensity blast exposures.

The 2nd study to determine hearing damage in relation to the number of blast exposures and the intensity of BOP level over the recovery time course and to evaluate the protective mechanism of HPDs (e.g. earplugs) for multiple exposures at low BOP level was conducted in 28 chinchillas. The animals were divided into two groups (14 for each group) under two conditions: open ear without earplug and protected ear with earplug over the course of 14 days. Animals were blasted 6 times on Day 1 with 10-minute interval between blasts at the G1 BOP level of 3-5 psi (21-35 kPa) monitored by a pressure sensor (P0) at the entrance of the ear canal. Function tests including ABR, DPOAE, and MLR level were conducted prior to blast, immediately post blast on Day 1, and Days 4, 7, and 14. The results from this study have been reported in Paige Welch's MS thesis published in May, 2020 and submitted to *Hearing Research*.

Figure 38 displays the ABR threshold shift for both protected and open ears. The results show that hearing damage of ABR threshold shift (elevation) was observed in both open and protected ears after blast exposure on Day 1. After 4 days, the protected ears regained most of their hearing function, shown in the decrease of ABR shift to 20-25 dB, and on Day 14 the threshold shift was further decreased to 8-12 dB. However, after 14 days in the open ears, the ABR threshold was still elevated by 15-31 dB from 1 to 8 kHz, which indicated the possible permanent hearing damage.

Figure 39 displays the comparison of ABR threshold shifts measured from the open ears (solid lines) and the protected ears (broken lines) on Days 1, 4, and 14. There was no significant difference between open and protected ears on D1, but the significant difference was observed on D4 and D14 at frequencies 4-8 kHz. The results demonstrated that the earplug provided a protective function during blast, facilitating hearing recovery.

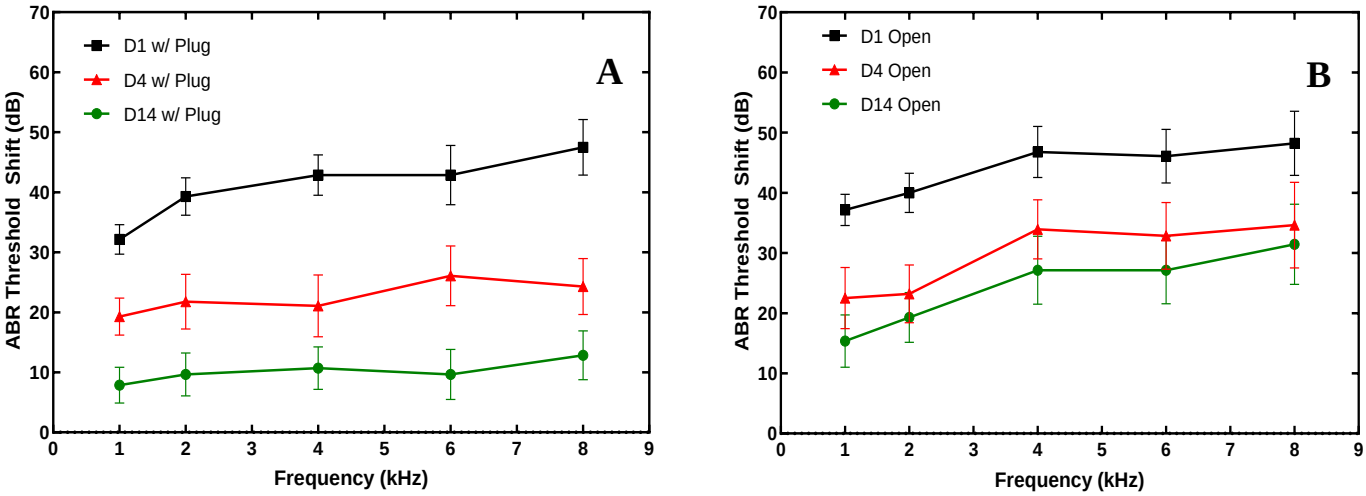


Figure 38. (A) ABR threshold shifts (mean ± SEM, n = 14) measured in plugged ears after 6 blasts on Days 1, 4, and 14. (B) ABR threshold shifts (mean ± SEM, n = 14) measured in open ears after 6 blasts on Days 1, 4, and 14.

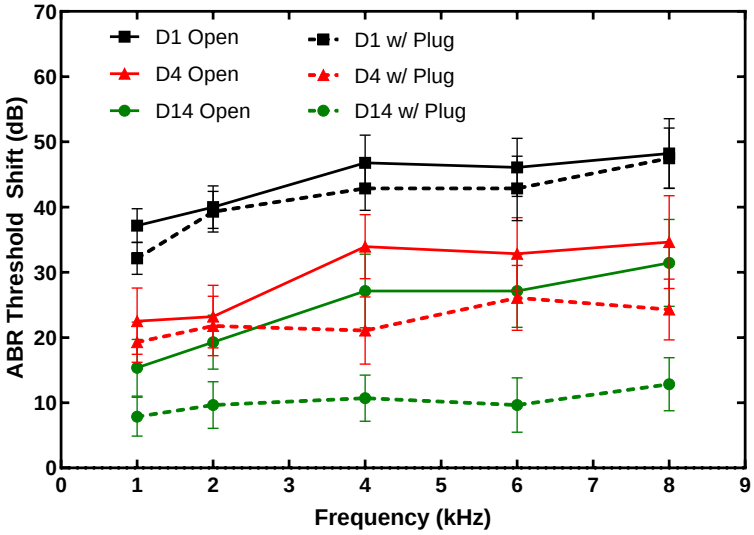


Figure 39. Comparison of ABR threshold shifts in protected and open ears on Days 1, 4, and 14.

The ABR wave I amplitudes measured from chinchillas with and without earplugs on D1 (pre and post-blast), D4, and D14 at frequencies 2 and 8 kHz are shown in Fig. 40. The wave I

amplitudes were plotted against the acoustic stimulus from 60 to 100 dB SPL measured in the ear canal. The results from protected ears show little difference between pre-blast and post-blast values and no difference between D4 and D14 values. This suggests that earplugs prevented acute and progressive damage to the auditory pathway. In contrast, the results from open ears show a substantial reduction in wave I amplitude immediately post-blast. Furthermore, the pre-blast amplitude is higher than those measured on D4 and D14, indicating possible permanent damage.

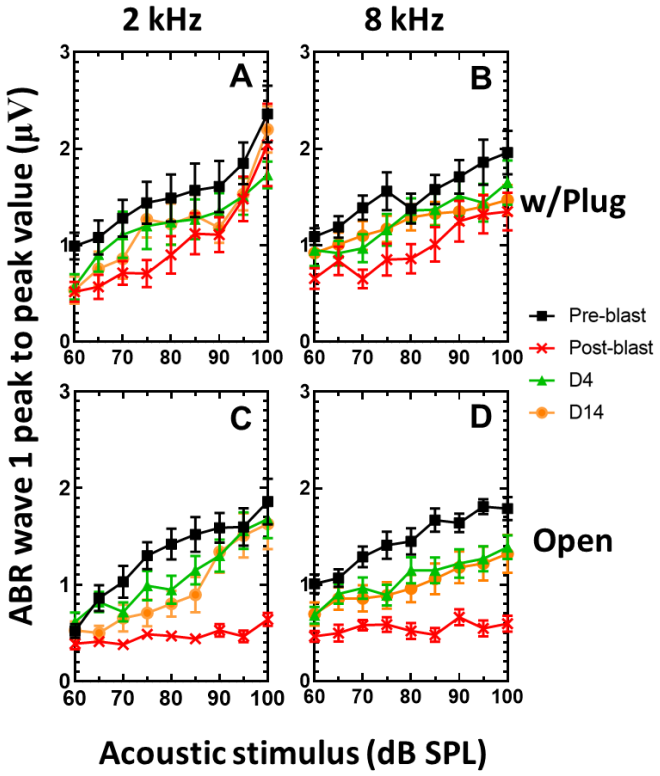


Figure 40. ABR wave I amplitude (mean ± SEM, n = 14) in response to stimulus level from 60 to 100 dB SPL measured from protected ears (top row) and open ears (bottom row). Measurements were taken at frequencies of 2 and 8 kHz.

The DPOAE results obtained in protected ears are summarized in Fig. 41. As shown in this figure there was a huge DPOAE shift (reduction) on Day 1, representing the acute cochlear damage. After 14 days, the protected ears regained most of their hearing function and the DPOAE level shifts had decreased to about 5 dB. In conclusion, the earplug likely prevented the permanent loss of outer hair cells, contributing to hearing recovery shown in both the DPOAE and ABR shifts.

The MLR signal is generated by the thalamus and primary cortical structures in brain. Representative curves of MLRs in open ears are shown in Fig. 42. MLR traces were recorded 100 ms after the acoustic stimulus at a level of 80 dB SPL and a frequency of 0.5 kHz. The latencies and amplitudes of the first Pa (positive) and Na (negative) peaks reflect the neural conduction velocity from the peripheral auditory nerve to the central auditory nervous system. In general, increased latency and reduced Na-Pa amplitude reflect that possible damage occurred at locations along the ascending auditory pathway. Figure 43 shows the peak-to-peak amplitude (mean ± SEM) measured from Na to Pa, Na latency, and Pa latency plotted against the time point of measurement for the protected and open ears. The shifts of MLRs' amplitude and latency were observed in both protected and open ears on Day 1 after repeated blast exposures, indicating the damage in auditory

thalamocortical pathway occurred post-blast in both plugged and open ears, but the MLR latencies appeared to have recovered by Day 14. However, the Na and Pa amplitudes need more studies.

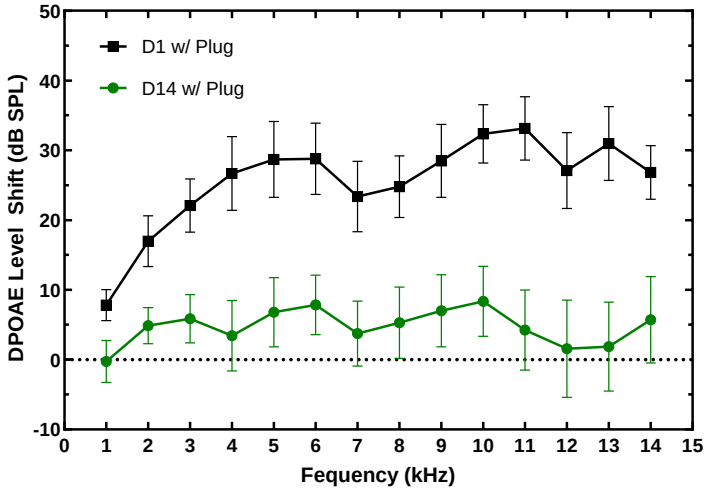


Figure 41. DPOAE level shifts (mean ± SEM, n = 14) measured from protected ears on Days 1 and 14.

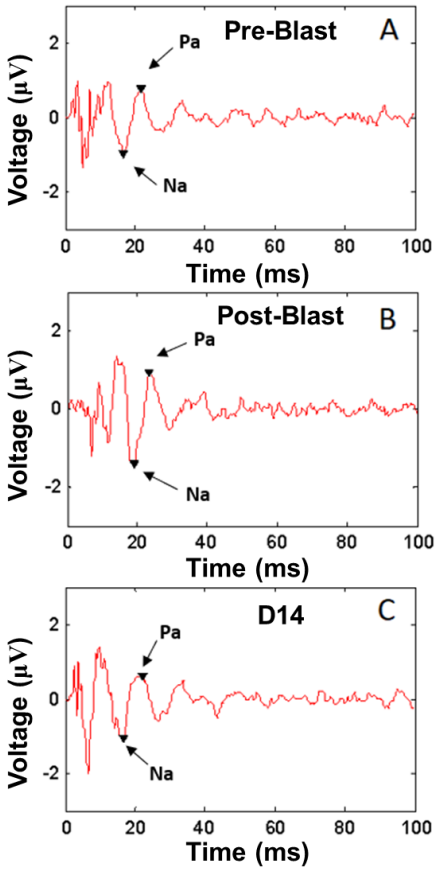


Figure 42. Representative MLR traces over 100 ms recorded at stimulus of 80 dB SPL from an open ear. (A) Pre-blast on Day 1, (B) post-blast on Day 1, and (C) Day 14. The Na peak and Pa peak are indicated by arrows.

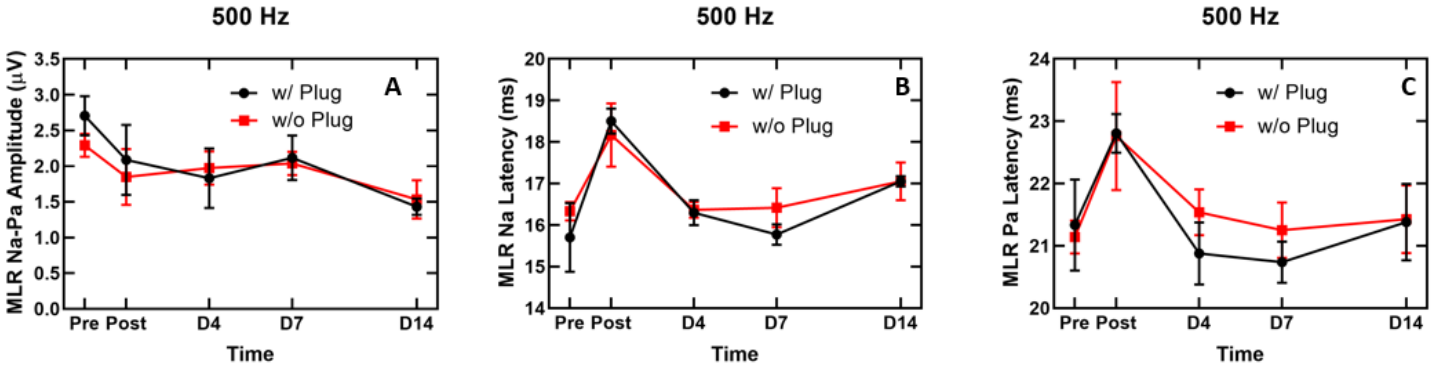


Figure 43. MLR amplitude (peak-to-peak) from Na to Pa and the latency of Na and Pa obtained at 500 Hz with 80 dB SPL stimulus in open ears (mean ± SEM, n=6) and protected ears (mean ± SEM, n=4) over the time point of measurement. (A) Peak-to-peak amplitudes, (B) Na latencies, and (C) Pa latencies.

(2-4) TM microstructure change and cochlear chair cell or stereocilia damage after blast exposure (SEM images)

TM is a complex tri-laminar membrane. Its middle layer, the lamina propia has a composite structure consisting of radially and circumferentially oriented collagen fibers embedded in the ground substance. To evaluate the microstructural changes of the TM after exposure to blast, the SEM images were obtained for both pre- and post-blast human and chinchilla TMs and examined with electron microscopes in the Samuel Roberts Noble Microscopy Laboratory at the University of Oklahoma.

Figure 44 shows the SEM image obtained from a post-blast human TM (left panel) and a normal TM (right panel) as reported by Engles et al. in *Annals of Biomedical Engineering*, Vol. 45, 2017. The images were viewed from the lateral side and focused on areas where the epithelial layer separated from the TM during SEM preparation. The effect of blast waves on the fiber bundles can be observed from Fig. 44 as shown by the radial orientation of the post-blast TM tears, which was a result of the circumferential fibers fractures. The normal TM shows a generally smoother appearance, reflecting the normal state of the TM. The SEM images suggested that the human TM damage along the radial direction may be more severe than that along the circumferential direction after blast exposure.

Figure 45 shows the SEM images of chinchilla TMs in the control case and post-blast case reported by Liang et al. in *Hearing Research*, Vol. 354, 2017. The surface layers of post-blast TM are much rougher than the control counterpart. While the blast was not severe enough to perforate the entire TM structure, it clearly induced damage in the surface of the TM as well as induced micro-cracks in the fiber layers. Damaged epidermis is also clearly observed all over the post-blast TM surface. The SEM images showed the damage formation in the post-blast TM indicating that the TM damage along the radial direction was more severe than that along the circumferential direction after blast exposure.

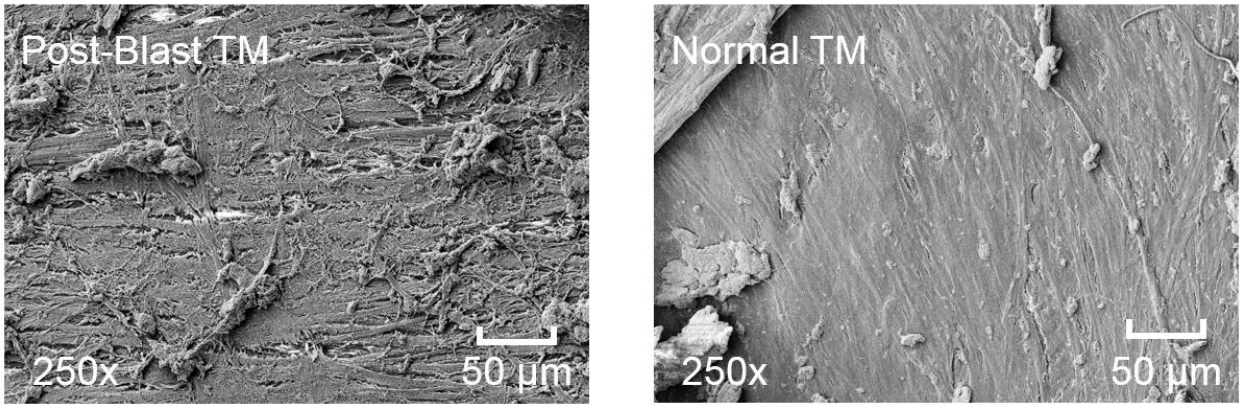


Figure 44. SEM images of the human TM surface. The left image shows the damage of the post-blast TM. The right panel shows the SEM image of the normal TM surface.

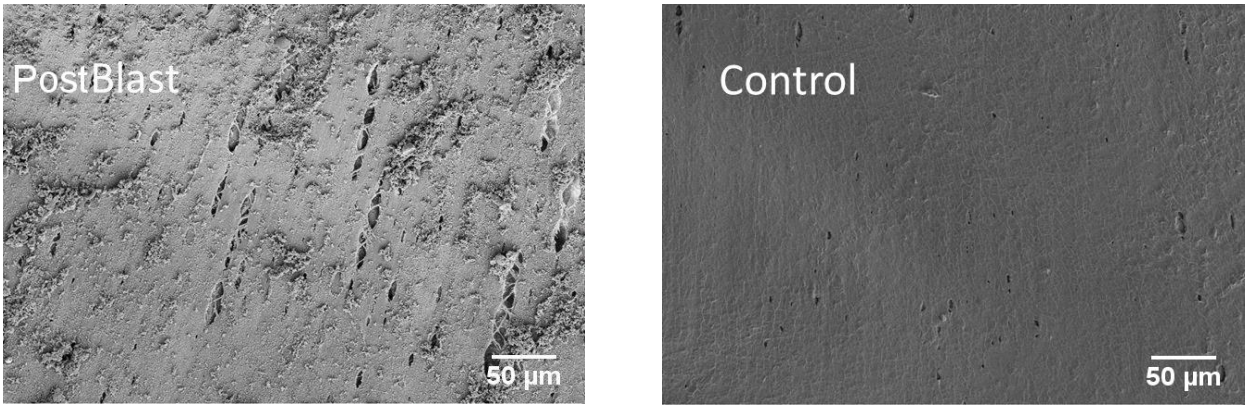


Figure 45. Typical SEM images for post-blast (left panel) and control (right panel) chinchilla TMs.

Exposure to blast overpressure causes hearing loss by applying intense sound pressure to the ear, which can damage the TM microstructure or rupture the TM and disrupt or reduce the number of viable cochlear hair cells. We have utilized SEM methods to observe the damage to the chinchilla's hair cell stereocilia after the animal was exposed to multiple blasts at a G2 BOP level that causes mild TBI. Figure 46 shows the SEM images of a control sample (17-2-8L) at the basal turn. As shown, most of the hair cells' stereocilia remain undisturbed. Some of the stereocilia experience a curling effect, mainly on the outer row of the outer hair cells.

Figures 47 and 48 show some sample SEM images of the damaged hair cells or stereocilia which were presented at the *ARO 41st Annual Midwinter Meeting* in 2018 (Brown et al., 2018). The loss of hair cells and formation of scars in the Organ of Corti occurred more often in the 3-blast group (Fig. 48) than in the 2-blast group (Fig. 47). The difference was far more prevailing in the middle turn closer to the basal turn (~2 – 8 kHz regions). In conclusion, multiple blast exposures at the level ranging from 15-20 psi damaged hair cells and caused the stereocilia to be disrupted even after 14 days of post-exposure. The damage was more prevalent and longer lasting in the animals that were exposed to 3 blasts when compared to the animals exposed to two.

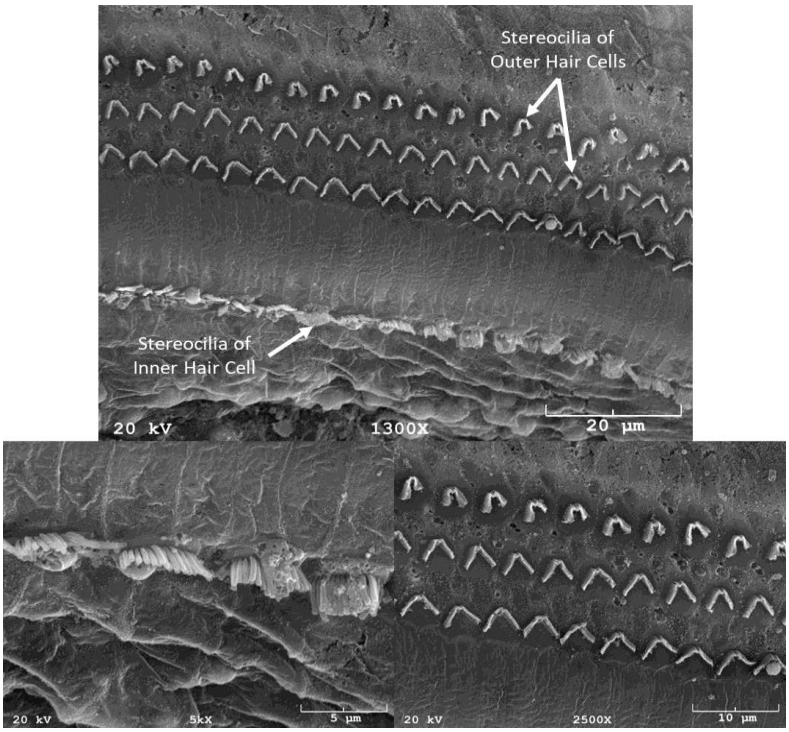


Figure 46. SEM images of the hair cells' stereocilia from the basal turn of a chinchilla from the control group (17-2-8L). Bottom left image is a close view of the inner hair cells (IHCs) and the bottom right is a close view of the outer hair cells (OHCs).

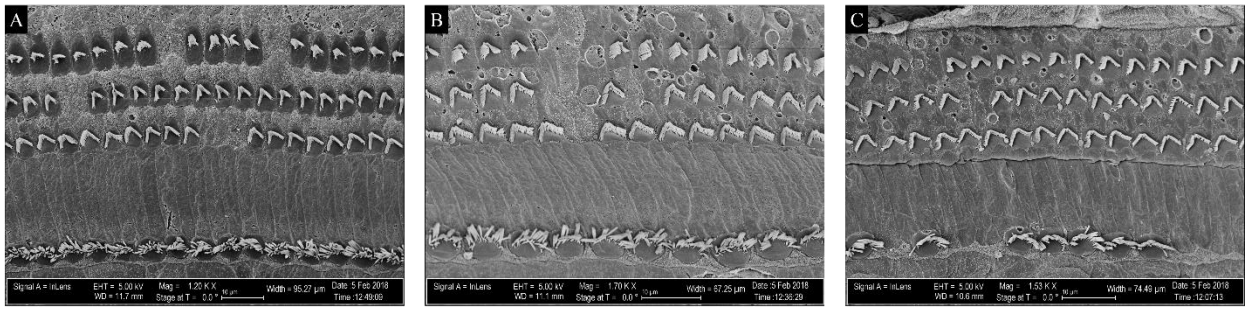


Figure 47. SEM images of outer and inner hair cells 7 days after being exposed to 2 blasts. (A) Apical turn (~0.5 kHz), (B) middle turn (~4 kHz), and (C) basal turn (~6 kHz). (#17-5-6R)

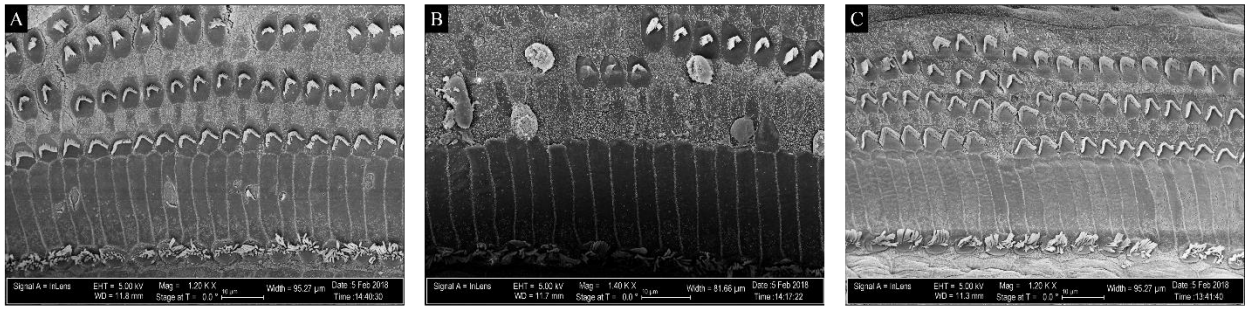


Figure 48. SEM images of outer and inner hair cells 14 days after being exposed to 3 blasts. (A) Apical turn (~0.5 kHz), (B) middle turn (~4 kHz), and (C) basal turn (~6 kHz). (#17-5-21R)

(2-5) Mechanical property changes of middle ear tissues after blast exposure identified with advanced techniques in both experimental measurement and modeling approaches

We have developed a series of techniques for measuring mechanical properties of ear tissues:
(1) Dynamic properties over the frequency domain using the dynamic mechanical analyzer with the frequency-temperature superposition principle – human incudostapedial joint
(2) Dynamic properties over the frequency domain using acoustic loading and LDV measurement with the inverse-problem solving method – human TM
(3) Quasi-static measurement using pressure load and micro-fringe protection with the inverse-problem solving method – human and chinchilla TMs and human round window membrane
(4) Dynamic properties at high strain rate or over the time domain using the split Hopkinson tension bar – human TM and Incudostapedial joint

Incudostapedial joint (ISJ) is a synovial joint connecting the incus and stapes in the middle ear. Mechanical properties of the ISJ directly affect sound transmission from the TM to the cochlea. To measure the mechanical properties of human ISJ in the auditable frequencies, we used a dynamic mechanical analyzer (DMA) with frequency-temperature superposition (FTS) principle in eight human ISJ samples. The FTS principle is an empirical method which relates the effect of temperature change on dynamic properties of some materials (e.g. polymers) to that of frequency change. ISJ samples were measured in the frequency range of 1-80 Hz at three different temperatures (5, 25 and 37°C). The FTS principle was used to extrapolate the results to 8 kHz. The average complex modulus of the joints was obtained directly from the experiments. Results from this study was published in *Medical Engineering and Physics*, Vol. 54, 2018 (Jiang and Gan, 2018).

Figure 49 is a schematic diagram of the experimental setup. The ISJ specimen was fixed onto a sample holder and the load cell of the DMA (ElectroForce 3200, Bose, Eden Prairie, MN) was placed between the sample holder and the X-Y translational stage.

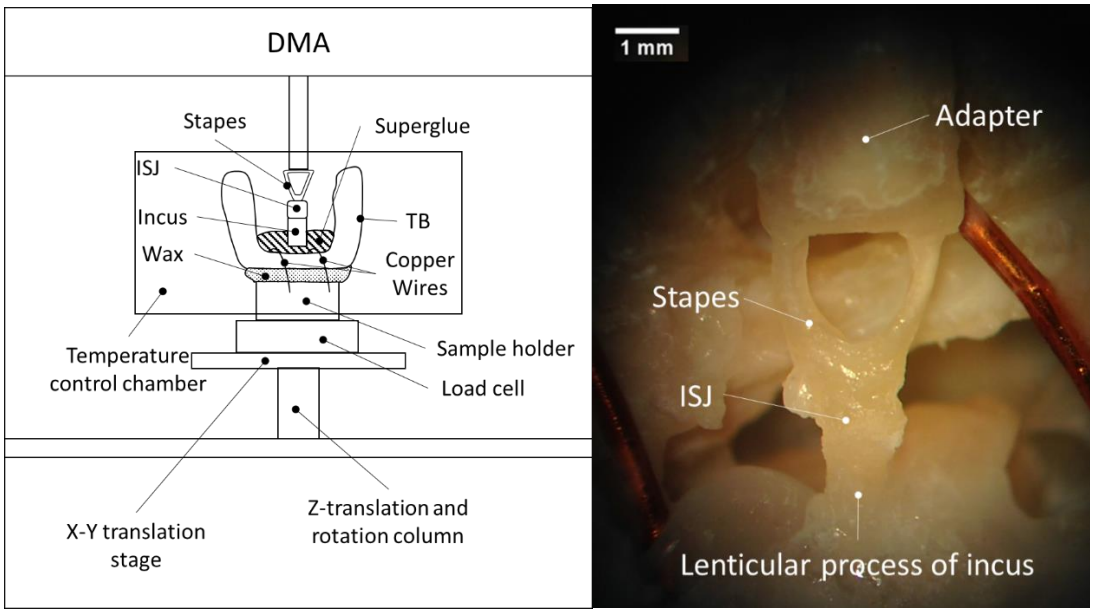


Figure 49. (A) Schematic diagram of the experiment setup. (B) ISJ specimen mounted on the machine observed under a microscope.

As a synovial joint, ISJ has a complex inner structure. The relationship between the measured mechanical properties of the joint as an isotropic body and the mechanical properties of the components inside the joint requires further investigation. We created a 3D FE model of the ISJ to identify the properties of the joint component as shown in Fig. 50. Figure 51 shows the master curves of the complex modulus of all eight ISJ samples. Results indicated that the complex modulus of ISJ was measured with a mean storage modulus of 1.14 MPa at 1 Hz that increased to 3.01 MPa at 8 kHz, and a loss modulus that increased from 0.07 to 0.47 MPa. FE modeling results showed that mechanical properties of the joint capsule and synovial fluid affected the dynamic behavior of the joint. The results from this study provide useful data for improving the accuracy of FE models of the human middle ear and contribute to a better understanding of the structure-function relationship of the ISJ.

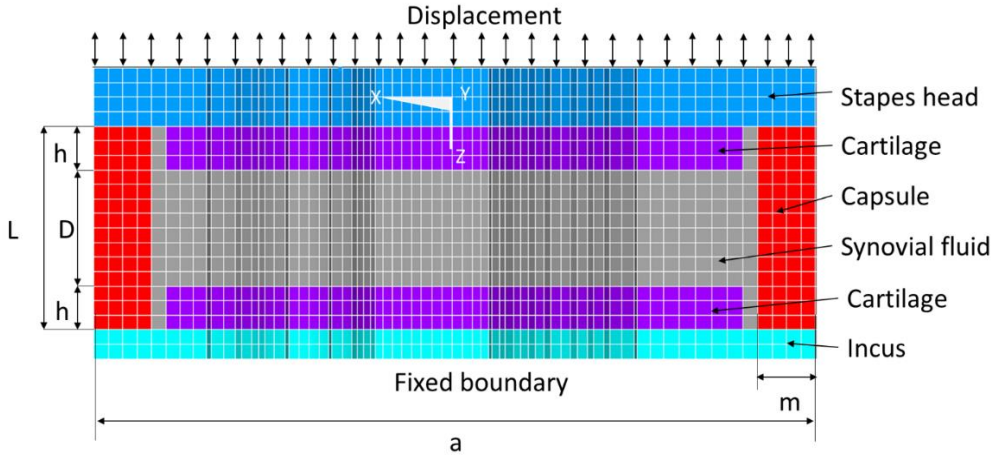


Figure 50. Axial cross section (X-Z plane) of the 3D FE model of the ISJ with boundary conditions.

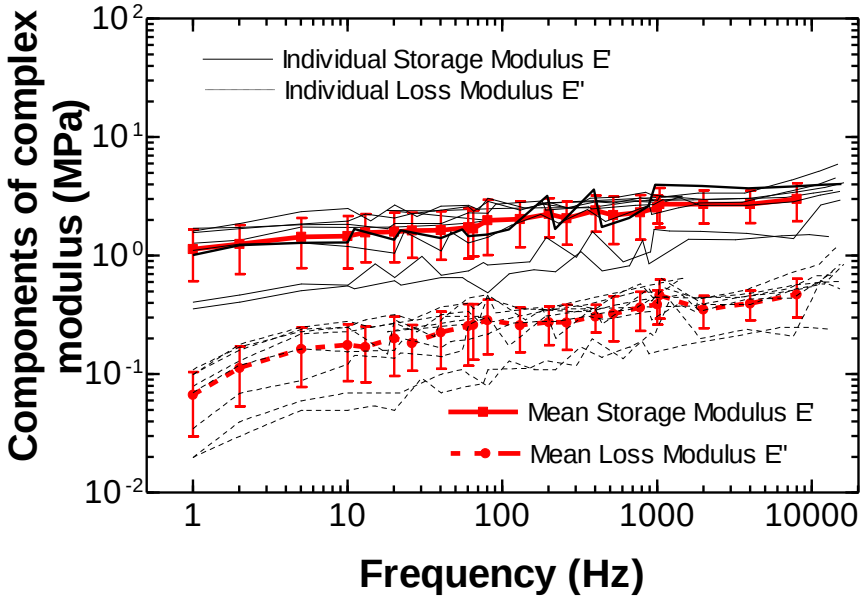


Figure 51. The master curves of the components of complex modulus at 37 °C from 8 ISJ samples and the mean master curves of the storage and loss modulus with SD.

Mechanical properties of human TM after exposure to blast waves were measured in our lab using acoustic loading and LDV measurement and the results were published by Engles et al. in *Annals of Biomedical Engineering*, Vol. 45, 2017. The TM specimens were prepared from human TBs following exposures to the TM rupture threshold ranged from 7.6 to 9.0 psi (52.4-62.1 kPa). Figure 52 is a schematic diagram of the experimental setup with LDV. The TM specimen for mechanical test was the rectangular strip (6 x 2 mm) cut from either the posterior or anterior site of the pars tensa with the tympanic annulus attached. The specimen was then mounted to the material testing system (MTS). The deformation or vibration of the sample induced by acoustic force applied to the TM was measured by LDV over the frequency range. Then, the material properties of the TM were determined by the inverse problem-solving method with FE modeling of dynamic experiment on the TM samples as shown in Fig. 53. FE models were generated to simulate the experiments of all TM samples. As an example, Fig. 54 shows the experimental results of the amplitude-frequency curve from two TM samples 47L and 41L (solid lines), compared with the FE model-derived curves (dashed lines).

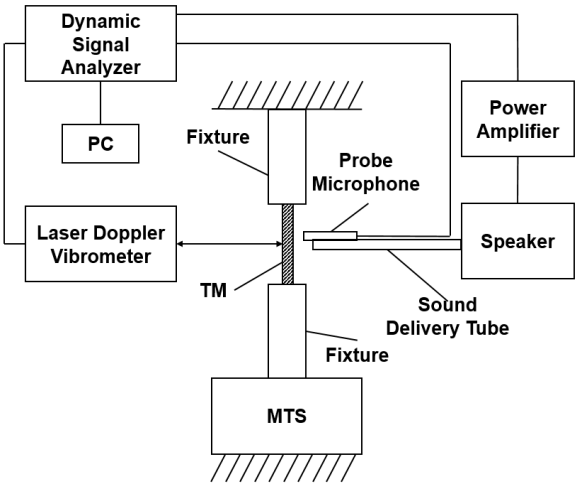


Figure 52. The schematic of the experimental setup for dynamic testing of TM specimens.

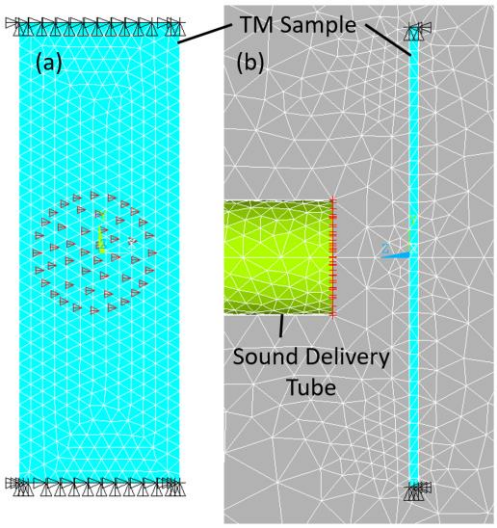


Figure 53. The FE model of dynamic experiment on the TM specimen. (a) Plane view of the FE model with fixed boundary condition (triangles) at both ends of the TM specimen and the acoustic pressure applied at the central area of the specimen. (b) Lateral view of the FE model including the TM specimen, sound delivery tube, and surrounding acoustic elements.

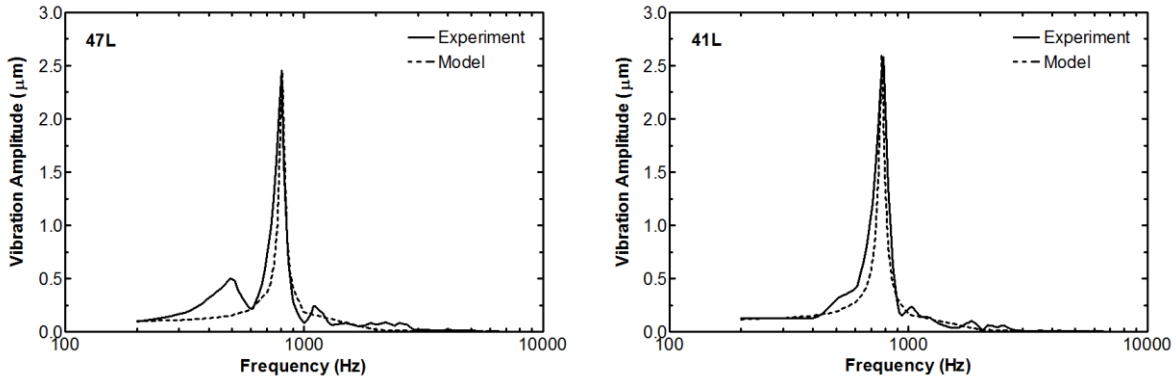


Figure 54. The FE fitting results obtained from two typical specimens in comparison with the corresponding experimental curves.

To determine the effect of blast waves on mechanical properties of the TM, the complex modulus for post-blast TMs was plotted against normal TMs published by Zhang and Gan (IJECB. Vol. 1, 2010) using acoustic stimulation and LDV in Fig. 55. Results indicated that the blast exposure caused the storage modulus and loss modulus of TM to become significantly reduced across the frequency range. These data reveal that the blast overpressure causes a frequency-dependent stiffness reduction of the TM.

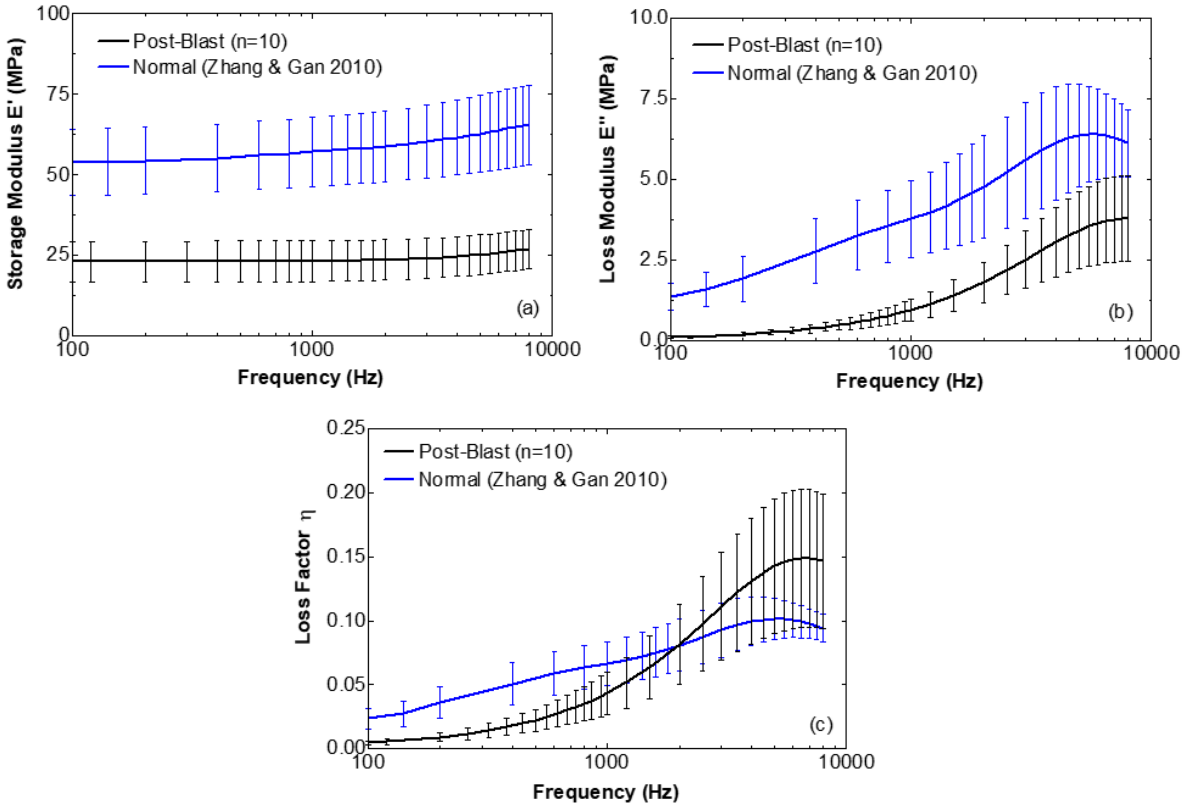


Figure 55. Comparison of complex modulus between blast-exposed and normal TMs over the frequency range of 100 – 8000 Hz. (a) Storage modulus, (b) loss modulus, and (c) loss factor.

Quasi-static properties of the chinchilla and human TMs and the human round window membrane (RWM) were measured using pressure loading on the entire TM and the micro-fringe projection with the inverse-problem solving method. This methodology was developed in our lab and used to measure mechanical properties of the TM with a series of publications. At first, the quasi-static mechanical properties of normal chinchilla TM (N=10) was reported in 2016 by Liang et al. in *Hearing Research*, Vol. 339. Then, the effect of blast overpressure on mechanical properties of chinchilla TM (N=8) was published in *Hearing Research*, Vol. 354 (Liang et al., 2017). Recently, the effect of BOP on human TM mechanical properties (N=16) using the micro-fringe protection with inverse-problem solving method was published in *J. Mechanical Behavior of Biomedical Materials*, Vol. 100 (Liang et al., 2019) and mechanical properties of human RWM was published in *Otology & Neurotology* by Liang et al., 2020 (In Press).

Figure 56 shows the experimental setup in a schematic diagram (a) and actual setup (b). The chinchilla bulla specimen was positioned on a gimbal sample holder. A self-developed projection system was used to project the parallel line pattern of a grating with a pitch of 20 cycles/mm to form micro-fringes onto the TM surface. The image of distorted fringes on the TM surface containing the topography information of the TM was captured by a digital camera. The acquired images were analyzed for 3D reconstruction of the TM surface using a five phase-shifting algorithm.

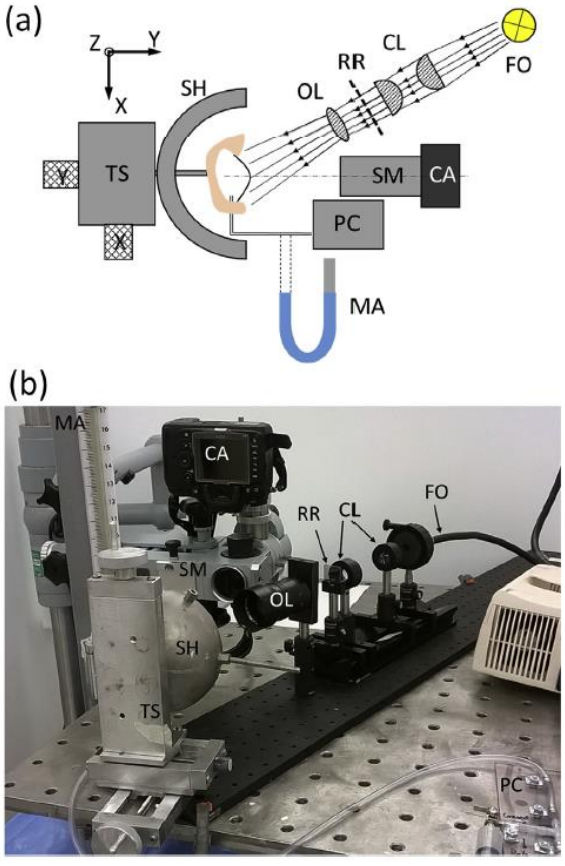


Figure 56. The experimental setup of the micro-fringe projection system and the pressure loading and monitoring system. (a) Schematic diagram; (b) Actual setup. The components include: manometer (MA), camera (CA), surgical microscope (SM), sample holder (SH), XYZ-translation stage (TS), objective lens (OL), Ronchi rulings (RR), condenser lenses (CL), fiber optics illuminator (FO) and pressure control (PC). (Liang et al., 2016)

Figure 57(a) shows the normal TM image under projected micro-fringes. The four sections of TM, namely superior, posterior, inferior, anterior, and umbo are shown and marked as S, P, I, A and U, respectively. Figure 57(b) shows a typical surface height color contours of TM under the zero-pressure from the reconstruction and Figs. 57(c) and (d) show the corresponding *z*-displacement, U_3 contours under -1.0 kPa and 1.0 kPa pressures.

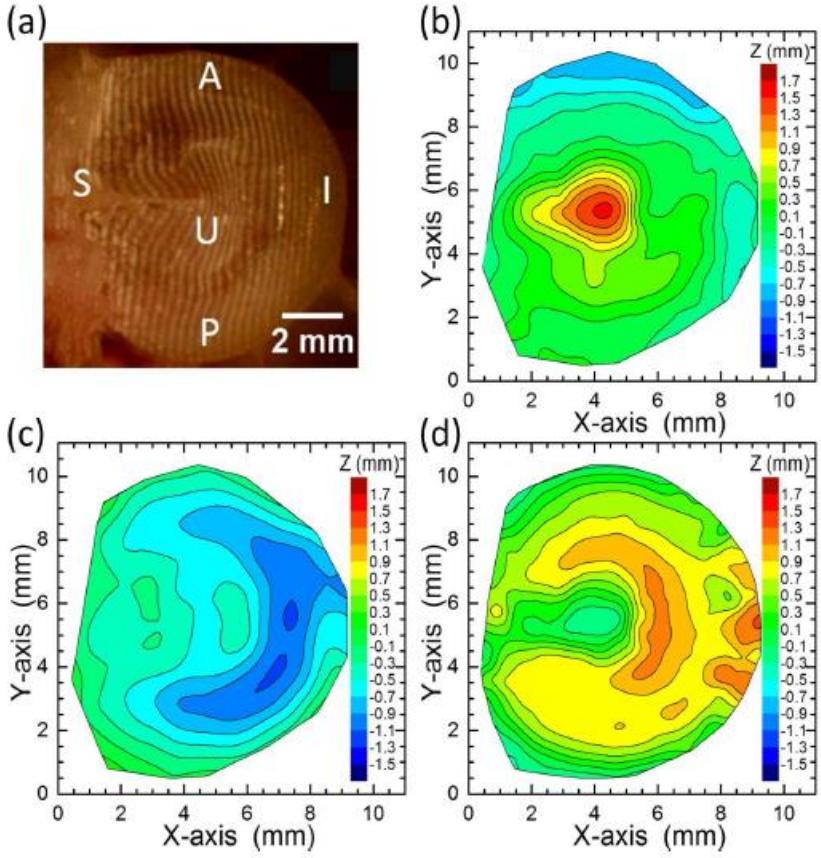


Figure 57. Projected micro-fringes and measured surface topography for chinchilla TM. (a). Micro-projected fringes on a chinchilla TM; (b). Height profile z(x, y) under zero pressure; (c). Z-displacement U_3 under -1.0 kPa pressure (TM's medial side pressure is higher than lateral side pressure); (d). Z-displacement U_3 under 1.0 kPa pressure (lateral side pressure is higher than medial side pressure). (Liang et al., 2016)

To determine the mechanical properties of the TM, the inverse solving method was employed by creating the FE model of the chinchilla TM based on the surface typography of a TM at zero-pressure state. Figure 58(a) shows the pressure as a function of the volume displacement, plotted in terms of the curves from the experimental results of ten normal chinchilla TMs and Fig. 58(b) shows a curve-fitting of the average pressure-volume displacement curve between FE modeling results and experimental data for ten TMs.

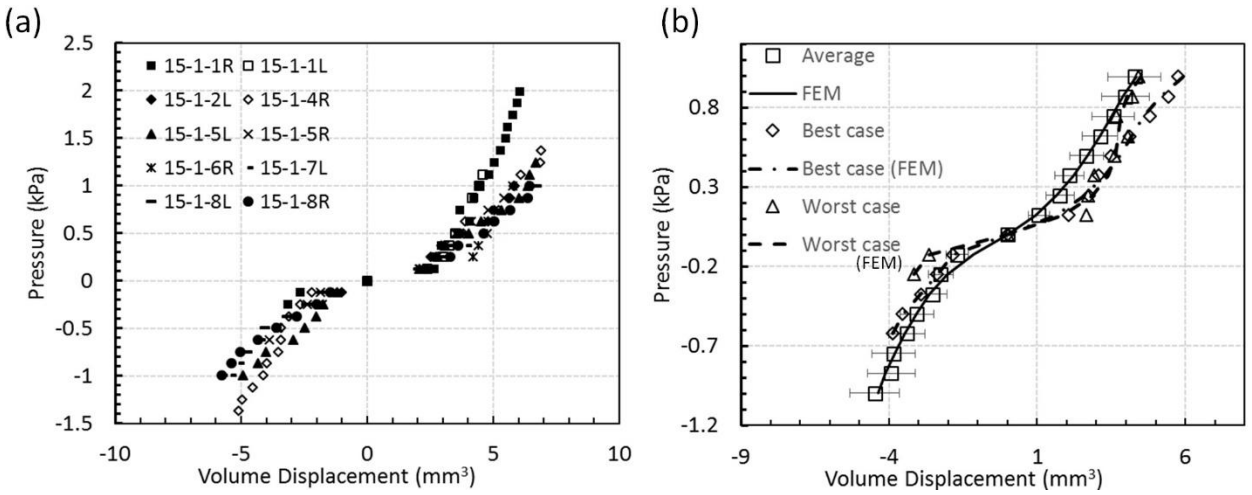


Figure 58. Pressure-volume displacement relationships for ten chinchilla TMs measured with the micro-fringe projection system. (a). Experimental results for 10 specimens; (b). A comparison between FE simulation results and experimental data. The error bar represents the standard deviation from the experiments. Both best and worst fitting results are given in (b). (Liang et al., 2016)

Following the same methods for the normal TMs, eight ears from chinchillas after multiple exposures to BOP level at 21-48 kPa were tested in lab and the results were published in *Hearing Research*, Vol. 354 (Liang et al., 2017). The pressure-volume displacement relationships of eight post-blast chinchilla TMs were calculated from the topographies reconstructed with micro-fringe projection. The applied pressures were plotted against the volume displacements as shown in Fig. 59. The volume displacements were calculated from the TM surface profiles during the pressure ramping-up phase. The strong nonlinearity exhibited in the pressure-volume displacement curves is similar to the results obtained in normal chinchilla TMs (Fig. 58).

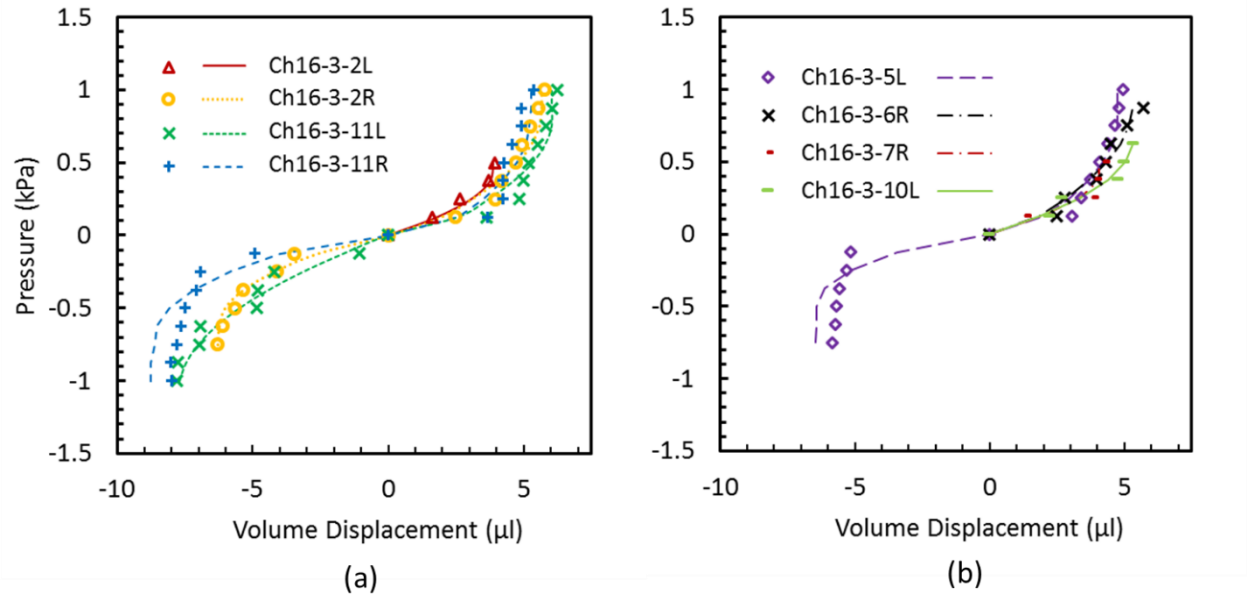


Figure 59. Pressure-volume displacement relationships for eight post-blast chinchilla TMs. The makers show the experimental results during of ramping up of the pressure and the smooth curves show the FE simulation results. Data were plotted in two figures for the convenience of reading.

A comparison between the mechanical properties of normal/control and post-blast chinchilla TMs was given in Fig. 60. To investigate the effect of the blast on the chinchilla TM, the average value of pressure-volume displacement relationships, stress-strain relationships and tangential modulus of TMs of two groups of animals (control and post-blast chinchilla) are shown in Figs. 60-62 respectively. The results are based on the average values for eight post-blast TMs and ten control samples respectively. When comparing the pressure-volume displacement relationship between the post-blast and the control TM (Fig. 60), an independent two sample t-test at each pressure level shows that there is a significant difference between these two groups of data ($p<0.05$) except at the pressure of 1.0 kPa ($p=0.123$). The notable rise of volume displacement of the post-blast TMs at the low-pressure level indicates the decrease of the stiffness of the structure.

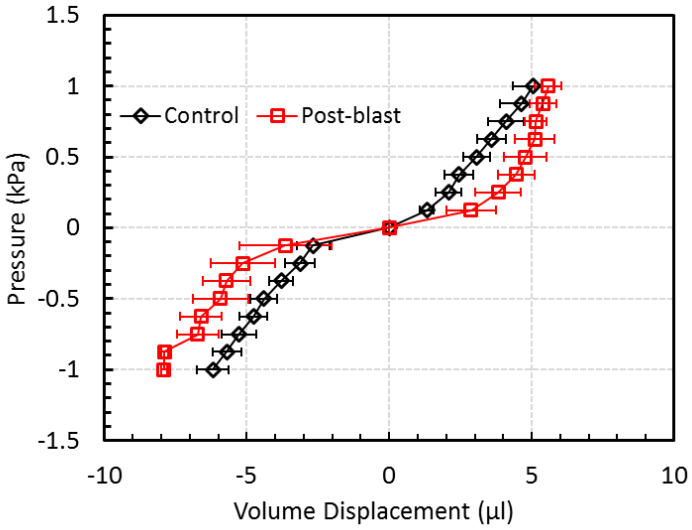


Figure 60. Pressure-volume displacement relationships for post-blast and control chinchilla TMs (n=10 for the control group and n=8 for the post-blast group). The error bar in the figure shows the standard deviation.

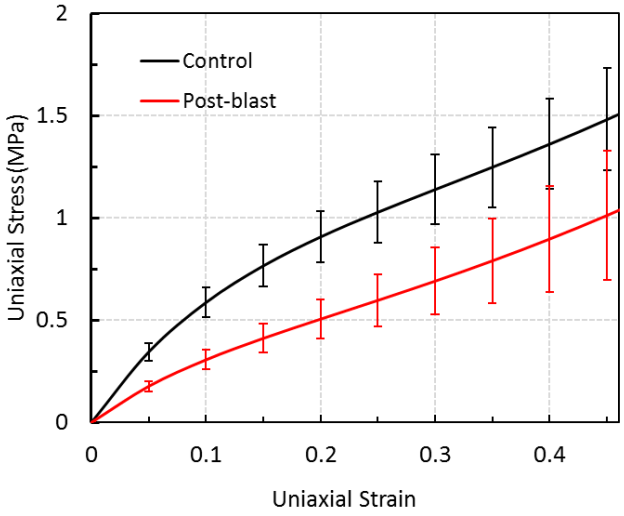


Figure 61. Uniaxial tensile stress-strain relationships for post-blast and control chinchilla TMs (n=10 for the control group and n=8 for the post-blast group. The error bar in the figure shows the standard deviation.)

A comparison of the stress-strain curves of post-blast and control TMs determined from the inverse method is shown in Fig. 61 which indicates the TM becomes softer after experiencing multiple blasts because the stress is lower in post-blast samples when compared to the control samples at the same strain. The difference in stresses between normal and post-blast TMs at strain levels above 20% is generally identical. Figure 62 shows that the tangent modulus has a pronounced decrease after the TM has experienced multiple blasts especially below 20% strain. Above 20% strain, the difference in modulus gradually decreases, which also agrees with the pattern of the difference in volume displacement between control and post-blast TMs. Note that the decrease of the stiffness of the structure and the weakening of the TM are believed to be related to the microscopic damages that were caused by the multiple blasts. Figure 45 shows the SEM images of the chinchilla TMs in the control case and post-blast case.

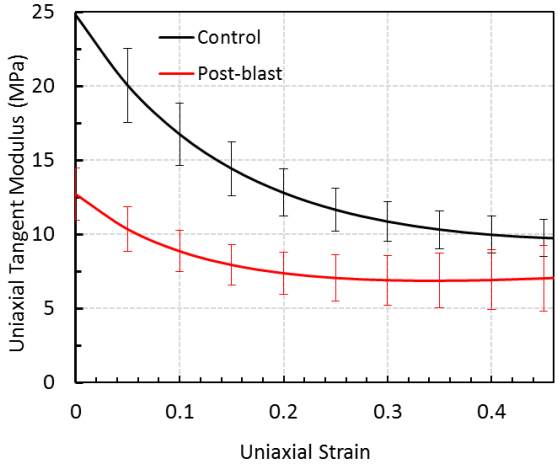


Figure 62. Tangential modulus for post-blast and control chinchilla TMs (n=10 for the control group and n=8 for the post-blast group. The error bar in the figure shows the standard deviation.)

We have applied the micro-fringe projection technique on human TMs to evaluate the change of the mechanical properties of the human TM after its exposure to the blast overpressure. This approach eliminates the effect of preparation using strip specimens. A total of 16 fresh human TBs were included in this study after exposed to 3 times of blast with an average peak pressure of 50 kPa below the rupture threshold (~70 kPa) of the human TM. Five TBs were used as controls without blast exposure. We measured the mechanical properties of TMs in-situ with their normal bony support. Results from this study were published in *J. Mechanical Behavior of Biomedical Materials,* Vol. 100 (Liang et al., 2019).

The volume displacements are plotted against the pressure for both control and post-blast TMs as shown in Fig. 63. It is noted that, for soft tissues such as TM, the volume displacement depends highly on the state of the loading or unloading. The curves shown in Fig. 63 are in general asymmetric with respect to the point at zero-pressure and zero-volume displacement. For the control TMs, the average volume displacement under positive pressure is about 40% higher than the corresponding value under negative pressure with the same magnitude. For post-blast TMs, the average volume displacement under a positive pressure is also higher, about 25% higher than the corresponding values under a negative pressure of the same magnitude. This asymmetry of the deformation of the TM is due to its nearly conical geometry.

Figure 64 shows the tangent modulus plotted against the uniaxial strain. The nonlinearity of the tangent modulus is easier to observe: as the strain increases, the tangent modulus decreases at strains below 20%, and it then gradually increases at strains above 20%. From Figs. 63 and 64, it is seen that the mechanical properties of the human TM changed after the TM is exposed to the blast overpressure. The reduction of the stiffness in the intact TM experiment is smaller than what is reported by Engles et al. (2017) on post-blast human TM strips. In that study, the storage modulus of the post-blast human TMs exhibits a reduction of more than 50% in comparison with that of control TMs. One possible reason for such a large magnitude in the change of storage modulus is that the small transverse vibration loading is applied to the TM strip. Such a loading condition is different from what is used in the intact TM.

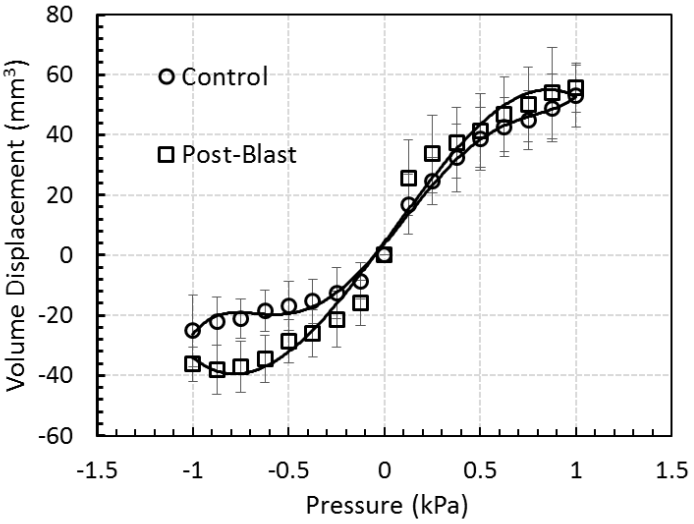


Figure 63. Pressure-volume displacement relationships for control (n=5) shown in (a) and post-blast human (n=16) TM shown in (b). Comparison between the two groups of TMs is also plotted with standard deviation as error bar shown in (c).

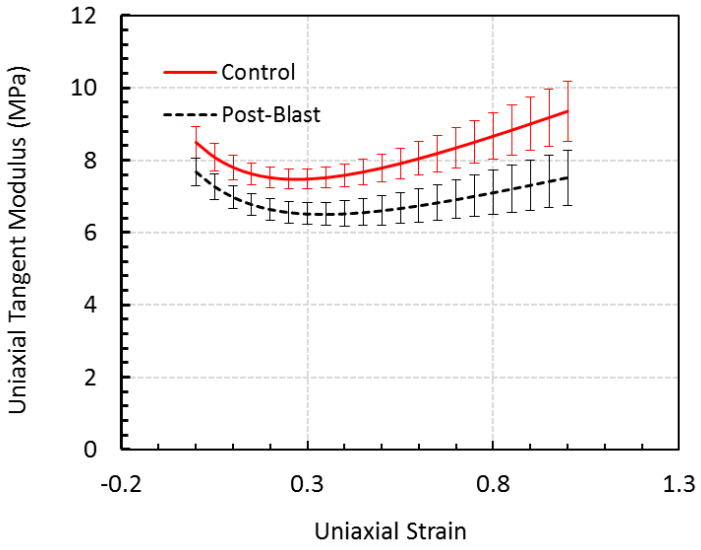


Figure 64. Comparison of tangential modulus data for control (n=5) and post-blast groups (n=16). The error bars show the standard deviation.

One of the important tasks for characterizing mechanical properties of ear soft tissues in response to blast exposure is to measure the mechanical behavior of tissues at high strain rate. We have used a highly sensitive miniature split Hopkinson tension bar (SHTB) to measure the mechanical properties of human TM after exposure to blasts at high strain rates. Two control TMs and 9 blast-exposed TMs were involved in this study and the results were published in *J. Dynamic Behavior of Materials*, Vol. 2 (Luo et al., 2016).

The TM strip specimens were prepared either along the radial or circumferential direction and tested in the SHTB to determine the Young's modulus at high strain rates. Figure 65 shows the TM strip-specimen orientations for ruptured TMs after four times of exposure at BOP level of 66.5 kPa (9.5 psi) and Fig. 66 shows the specimen orientations for un-ruptured TMs after four times of exposure at BOP level of 33 kPa (4.8 psi). A schematic diagram for the SHTB setup is shown in Fig. 67 including the incident bar, the transmission bar, two semiconductor strain gauges, and a striker bar or momentum trap bar to make impact to the incident bar. Figure 68 shows typical broken TM strip specimens after tensile experiments on SHTB: failure patterns for control TMs in the circumferential direction (a), control TMs in the radial direction (b), blast-exposed TMs in the circumferential direction (c), and blast-exposed TM in the radial direction (d). The control TMs show ductile fracture pattern in both the radial and the circumferential directions. However, blast-exposed strip TM specimens with length in the radial direction still show ductile failure mode (Fig. 68c) with the fracture surface in a 45 degree inclined with respect to the loading direction, but the blast-exposed TM strip specimens with length along the circumferential direction show a brittle failure pattern (Fig. 68d).

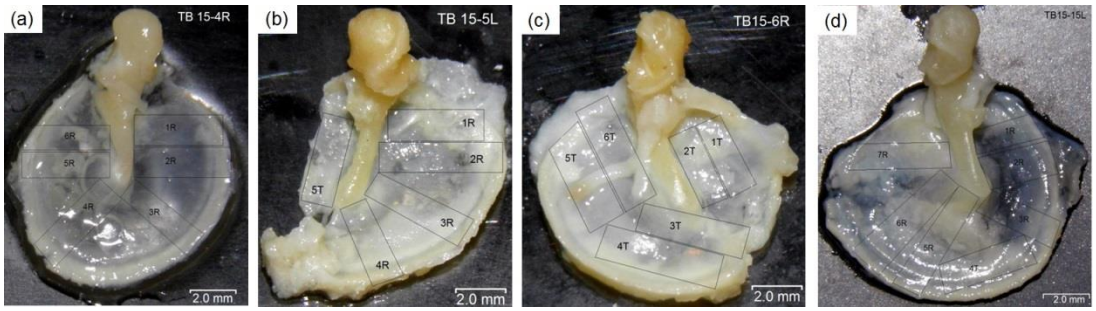


Figure 65. Blast-exposed TMs (ruptured) that would be cut into strip specimens as marked. (a) TB15-4R; (b). TB 15-5L; (c) TB15-6R; (d) TB 15-15L. Note, the TMs ruptured due to exposure to the blast waves.

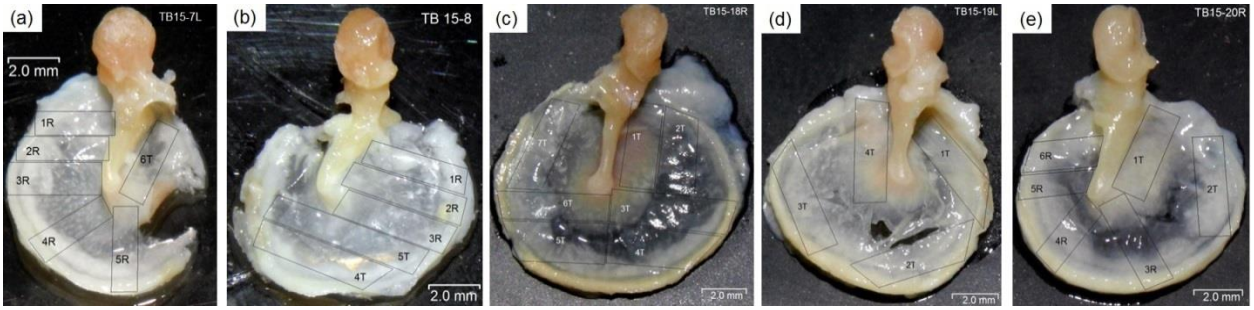


Figure 66. Blast-exposed TMs (non-ruptured) which would be cut into strip specimens as marked. (a). TB15-7L; (b). TB 15-8R; (c) TB15-18R; (d) TB 15-19L; (e) TB15-20R. Note, the TMs were damaged during the harvesting procedures, rather than due to the blast waves.

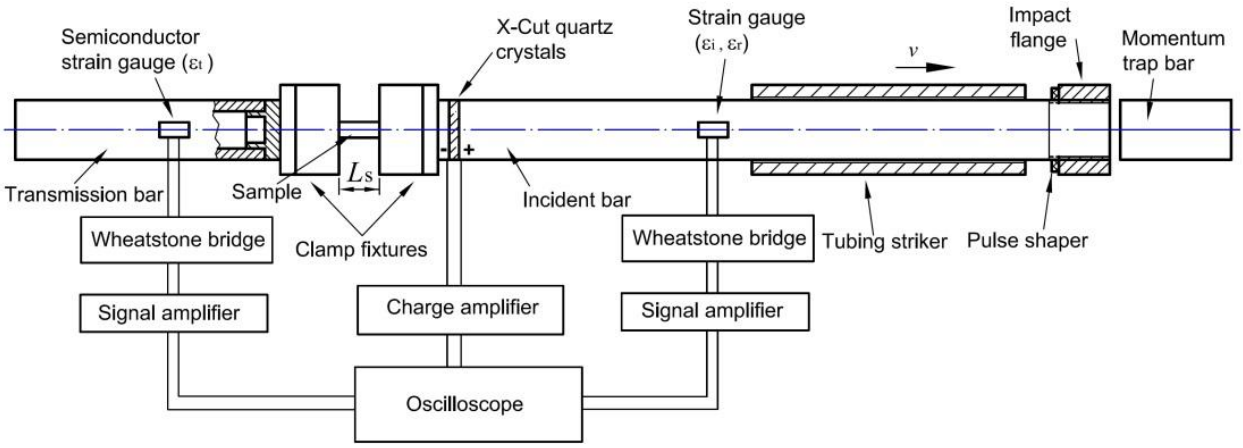


Figure 67. Schematic diagram of a miniature split Hopkinson tension bar setup.

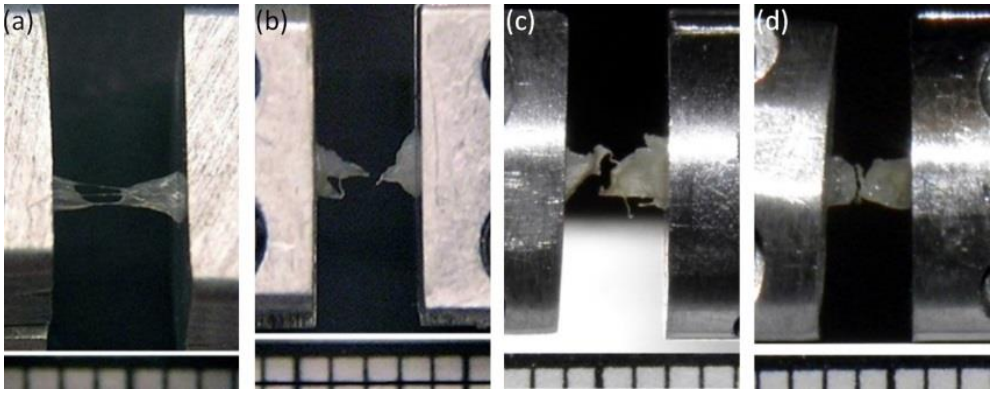


Figure 68. Typical failed TM strip specimens after SHTB test. (a). A control TM in the circumferential direction; (b). A control TM in the radial direction (c). TM (TB15-18R-7T) in the circumferential direction after blast wave; (d). TM (TB15-16L-3R) in the radial direction after blast wave.

The experimentally measured data were processed to determine the stress-strain relationships and the typical stress-strain curves are shown in Fig. 69 for blast-exposed TM specimens in the radial and circumferential directions at high strain rates. The curves are mostly linear until fracture. Note that TM specimens did not necessarily break at these strain rates. The maximum strain experienced in each experiment was limited by the loading duration time of the miniature SHTB. The results obtained for blast-exposed TMs indicate that the Young's modulus values of these TMs depend on the strain rate within high strain rate range. Since data for the Young's modulus have been obtained within three ranges of high strain rates (300-2000 s^{-1}), the mechanical behavior of the TM was described as a standard linear solid with three undetermined parameters: spring constants E_∞, E_1, and a dashpot with viscosity η. Figure 70A shows the best-fit Young's modulus plotted as a function of strain rate (10^2~2×10^4 s^{-1}) for TM in either radial or circumferential direction. The Young's relaxation modulus was obtained for TM strip specimens in both the radial and the circumferential directions as shown in Fig. 70B. In conclusion, the blast waves have different effects on the mechanical properties in the radial and circumferential directions. After exposure to the BOP waves, the mechanical behavior in the radial direction in general becomes stiffened, while it is weakened in the circumferential direction. Note that the STB techniques were also employed to measure human IS joint mechanical properties at high strain rates and reported by Shangyuan Jiang in his Ph.D. Dissertation at the University of Oklahoma, May 2018.

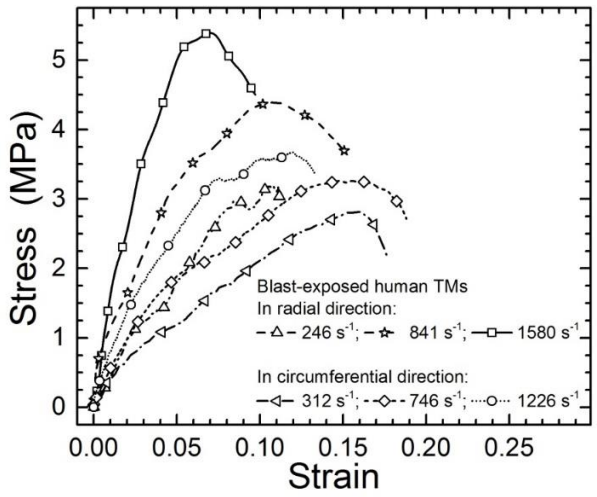


Figure 69. Typical stress-strain curves of blast-exposed TM strip specimens in the radial and circumferential directions at high strain rates. Note that the TM specimens did not break at strain rates less than 500 s^{-1}. The strain rates of 246 s^{-1}, 841 s^{-1}, 1580 s^{-1}, 312 s^{-1}, 746 s^{-1} and 1226 s^{-1} were used for testing TM specimens TB15-20R-3R, TB15-7L-2R, TB15-15L-1R, TB15-18R-2T, TB15-18R-3T, and TB15-6R-5T, respectively.

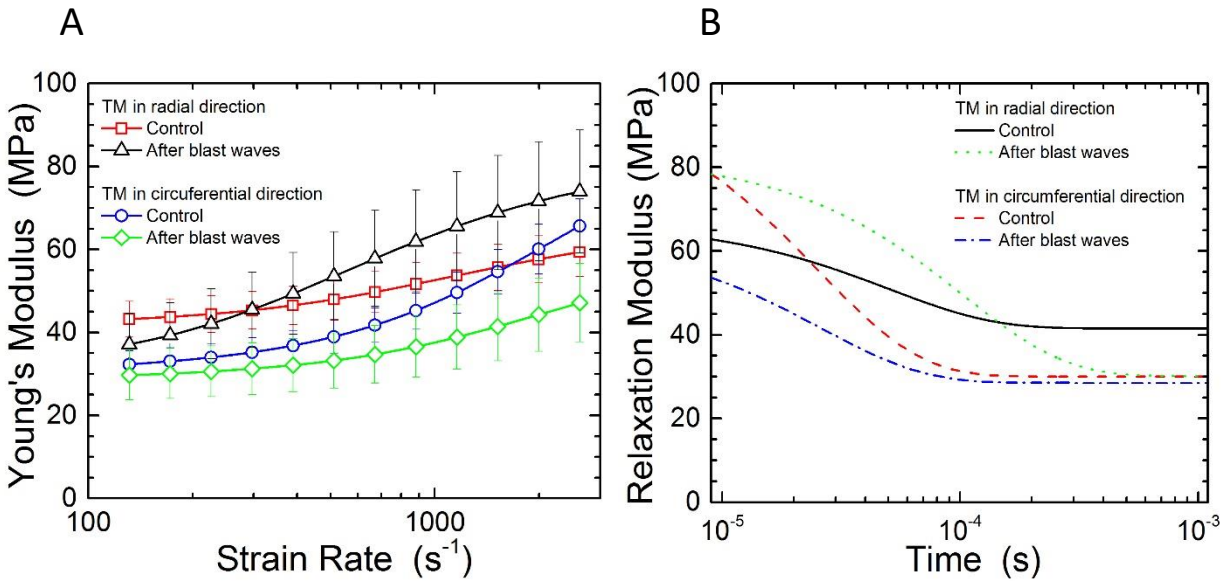


Figure 70. (A) Summary of fitted curves for the Young's modulus of control and blast-exposed TMs as a function of strain rate. (B) Comparison of Young's relaxation modulus between control and blast-exposed TMs in the time domain.

(2-6) Initiative chinchilla helmet study associated with HPDs to separate the hearing damage in peripheral auditory system and central auditory system

Repeated blast exposures result in structural damage to the peripheral auditory system (PAS) and the central auditory system (CAS). However, it is difficult to differentiate injuries between two distinct pathways: the mechanical damage in the PAS caused by blast pressure waves transmitted through the ear and the damage in the CAS caused by blast wave impacts on the head or TBI. We have initiated a novel study by using a 3D printed chinchilla "helmet" as a head

protection device associated with the hearing protection devices (HPDs, e.g. earplugs) to isolate the CAS damage from the PAS injuries under repeated blast exposures. This study was reported in several conferences and a journal paper was accepted to publish in *Military Medicine*, Vol. 186 (Jiang et al., 2020).

An FE model of the chinchilla helmet was created based on micro-computed tomography (micro-CT) images of a chinchilla skull and inputted into ANSYS for FE analysis on the helmet's protection against BOP. Figure 71A shows a cross-sectional view of FE model with chinchilla skull (grey), brain (blue), and intracranial tissue (red). The brain model was comprised of 1,055 tetrahedral elements and assumed as a viscoelastic solid due to the tissue response behavior to an applied pressure load. The helmet dimensions were designed from the skull FE model to fit and cover the skull but leave the ears exposed. The helmet was made in three sections as shown in Fig. 71B: the front, middle, and back covers with two side panels. The middle cover protects the majority of the chinchilla's head from the forehead to the ears. The whole helmet covers 75 – 80% of the chinchilla's head.

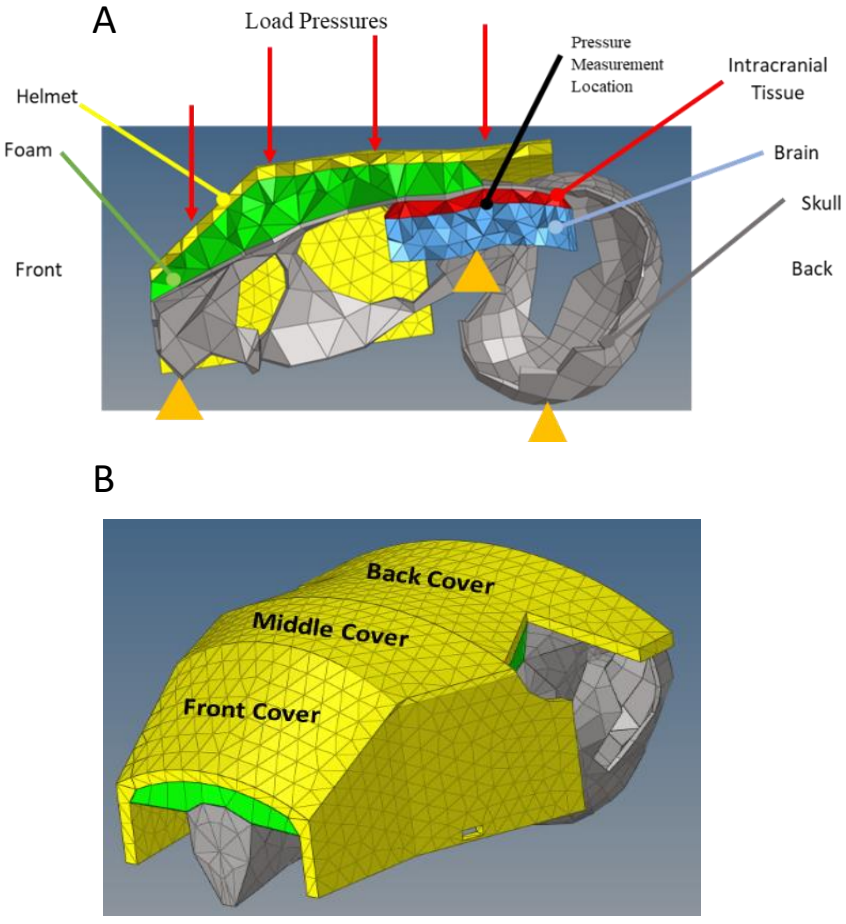


Figure 71. (A) Cross-sectional view of FE model simulation in ANSYS with chinchilla skull (grey), brain (blue), and intracranial tissue (red). (B) FE model of the chinchilla skull with helmet. The grey elements are the mesh of the skull. The green elements are the mesh of the foam and the yellow elements are the mesh of the helmet. The helmet was printed in our 3D system (Objet350 Connex3, Stratasys).

The Von Mises stresses on the top surface of the brain obtained from the FE model simulation are shown in Fig. 72A with the blue line representing without helmet and the red line representing with helmet. Figure 72B displays the measured BOP applied on the chinchilla skull or helmet model. As shown in Fig. 72A, the ratio of the peak pressure within the brain for the "with helmet" with respect to that of "without helmet" is 31.2%, a significant reduction in intracranial stress with the helmet. The modeling results suggested that the protective function of the helmet on the CAS was significant which provided the theoretical basis for the animal study.

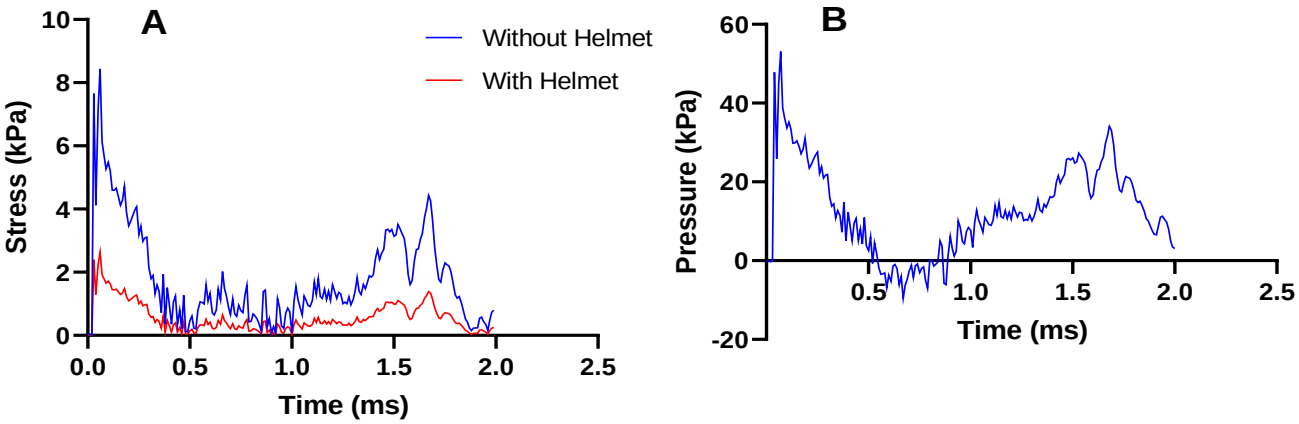


Figure 72. (A) Von Mises stress in the intracranial tissue over time calculated from the finite element model with and without helmet covered the chinchilla skull. (B) Measured blast pressure applied on the chinchilla skull and helmet model.

Thirty-two chinchillas were included in this study and equally divided into 4 groups or cases with 8 animals for each case. Standard foam earplugs were inserted into the chinchilla ear canals to protect their PAS, and the 3D printed helmet was fixed on the chinchilla head to protect the CAS against BOP exposures. Figure 73 illustrates the experimental design: **Case 1** - ears open without earplug and helmet; **Case 2** - ears protected with earplug, but without helmet; **Case 3** - ears protected with earplugs and with helmet; **Case 4** - ears open and with helmet.

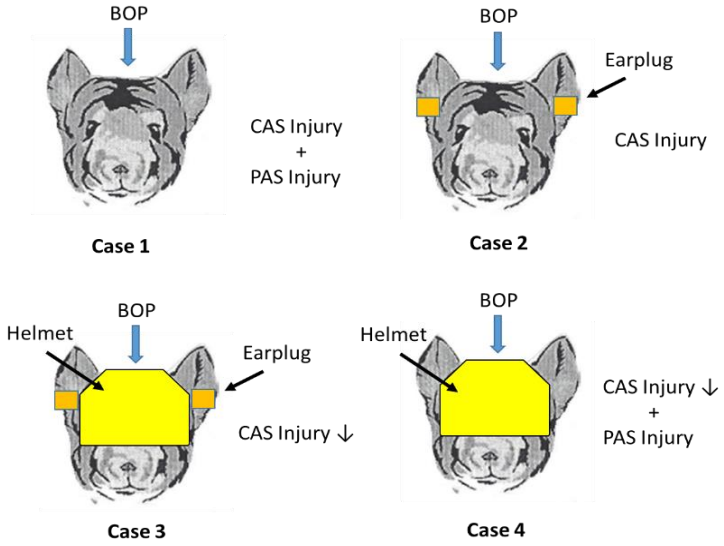


Figure 73. Illustration of 4 cases of chinchilla experiments attempting to isolate the traumatic brain injury damage to the central auditory system (CAS) from the injuries in peripheral auditory system (PAS). (BOP = blast over pressure).

The BOP level measured at the ear canal entrance was around 103-138 kPa or 15-20 psi. Each chinchilla was exposed to 3 blasts with a time interval of approximately 5 minutes between consecutive blasts on Day 1 and observed for 7 days. Figure 74 summarizes the ABR threshold shifts measured on Day 1 post-blast, Day 4, and Day 7 and were colored in red, green and blue, respectively.

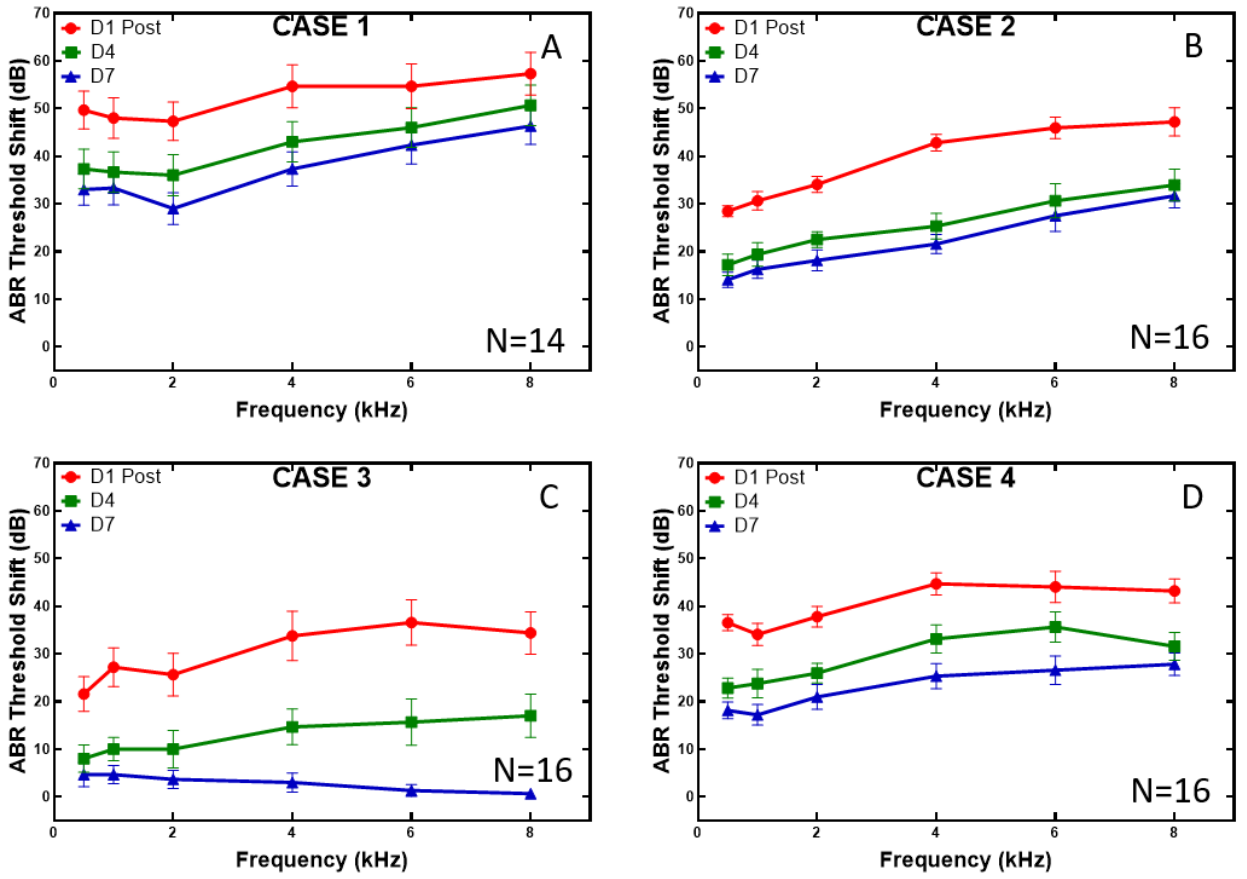


Figure 74. Mean and standard error of the ABR threshold shift results measured on post-blast of Day 1 (red), Day 4 (green), and Day 7 (blue) from animals in 4 Cases: (A) Case 1 (N=14 ears), without helmet protection and HPD (e.g. earplug) protection; (B) Case 2 (N=16 ears), with HPD protection only; (C) Case 3 (N=16 ears), with helmet protection and HPD protection. (D) Case 4 (N=16 ears), with helmet protection only.

Results in Fig. 74 suggested that chinchillas in Case 4 showed better post-blast hearing than in Case 1, and the Case 3 showed even better hearing than Case 2. Those data indicated that the chinchilla helmet invented in this study did protect the auditory function against the BOP exposures either with or without the assistant of HPDs (earplugs). Particularly, Fig. 74C or Case 3 indicated that the combination of earplug and helmet can completely eliminate the permanent hearing damage which was not observed in chinchilla ears protected by the earplugs only under the BOP exposure. In conclusion, the biomechanical modeling and animal experiments demonstrated that this 4-case study in chinchillas with helmet and HPDs provides a novel methodology to investigate the blast-induced damage in the PAS and CAS.

Aim 3:

(3-1) <u>First 3D FE model of the human ear for simulation of blast overpressure transmission through the ear and the model applications</u>

The first FE model of the human ear including the external ear, TM, middle ear, and middle ear cavity with cochlear load was developed within the ANSYS Workbench and conducting the FE analyses on BOP transmission through the ear using two strongly coupled Fluid-Structure Interactions (FSIs) as calculated by Fluent and ANSYS Mechanical. The model consists of the ear canal, TM (pars flaccida and pars tensa), TM annulus (TMA), manubrium, ossicles and associated suspensory ligaments, incudo-malleolar joint (IMJ), incudostapedial joint (ISJ), and stapedial annular ligament (SAL). The cochlea was not included in this model, but the cochlear load was modeled by a mass block-dashpot system to reflect the cochlear input impedance. This model was published in *Military Medicine*, Vol. 183 (Leckness et al., 2018) and Kegan Leckness' MS thesis at the University of Oklahoma, August 2016. The model was used to predict human TM injury in relation to blast wave direction (Gan et al., 2018), protection mechanisms of HPDs (Gan et al., 2019), and the TM motion under blast exposure (Jiang et al., 2019). Figure 75 shows the first FE model for computing the transmission of BOP (P0) at the ear canal entrance through the canal to the TM (P1) and inside the middle ear cavity (P2).

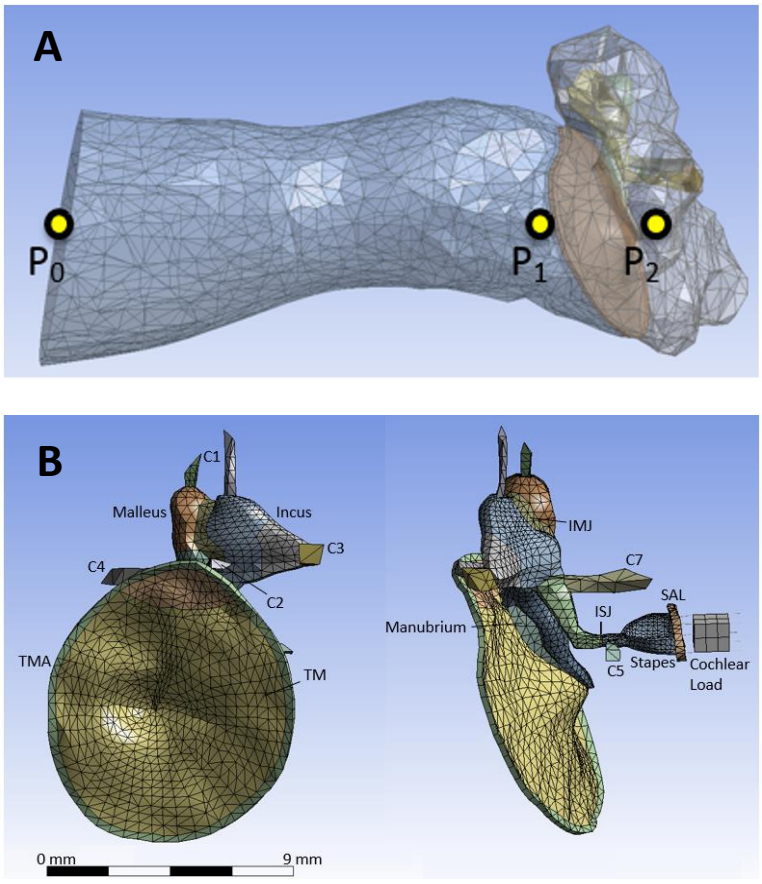


Figure 75. (A) FE model of the human ear comprised of the ear canal, TM, middle ear ossicles, and middle ear cavity. The locations for pressure monitoring points are designated as P0, P1, and P2. (B) Structural mesh of the model, showing the TM, TMA, middle ear ossicles, IMJ, ISJ, suspensory ligaments/muscle tendons (all Cs and SAL), and cochlear load.

The FE model was validated with the experimental results measured in human TBs. The P0 waveform recorded from blast tests along the incident wave directions of vertical, horizontal, and front was applied at the entrance of the ear canal in the model, respectively. The FE model-derived P1 waveform was compared with the measured P1 waveform along the vertical, horizontal, and front tests, respectively. Figure 76 shows the results: (A) experimental data; (B) model-derived data; (C) P1 waveform comparison between the model and experiments; (D) P2 waveform comparison between the model and experiments.

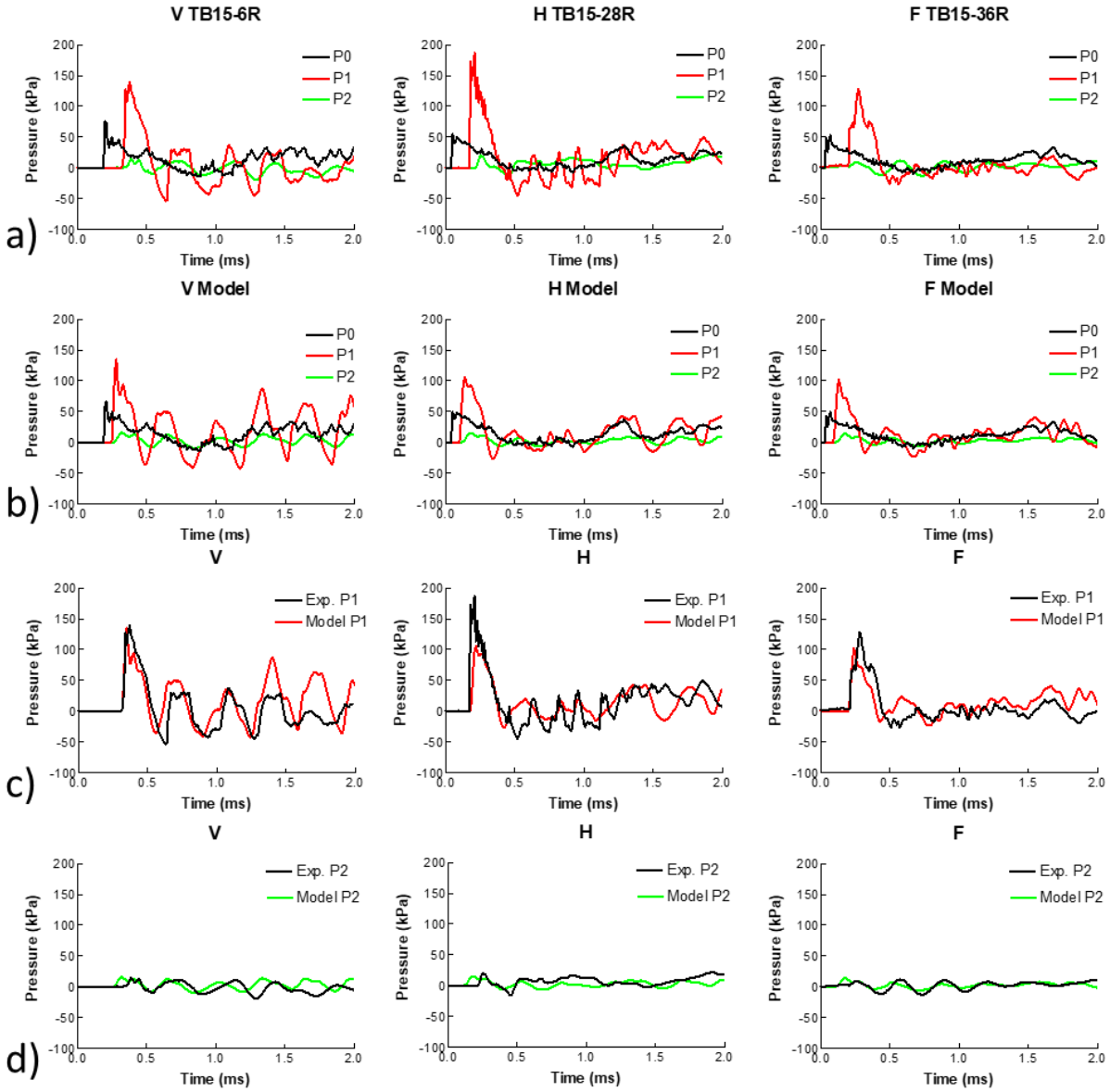


Figure 76. a) Experimental recordings of the P0, P1, and P2 waveforms from vertical, horizontal, and front blast exposures. b) Predicted P1 and P2 waveforms induced by experimental P0 waveforms from each blast direction. c) Comparison of experimental and model-predicted P1 waveforms from each blast direction. d) Comparison of experimental and model-predicted P2 waveforms from each blast direction. (Leckness et al., 2018)

Three metrics of the P1 waveforms in the time domain were considered for comparison: peak pressure level, A-duration, and Kurtosis. Results indicated that the model-derived P1 waveforms were in an agreement with the experimentally recorded waveforms with statistic Kurtosis analysis.

Figure 77 displays the displacement (a) and stress distributions (b) plotted onto the TM at the time maximum displacement or maximum stress occurred, for the vertical exposure. The maximum TM deformation of 1.4 mm occurs approximately 2 mm inferior and anterior to the umbo. The stress contours indicate maximum stresses at three locations on the TM (the anterior TMA, inferior to the umbo, and posterior to the manubrium) and may indicate possible locations prone to TM rupture.

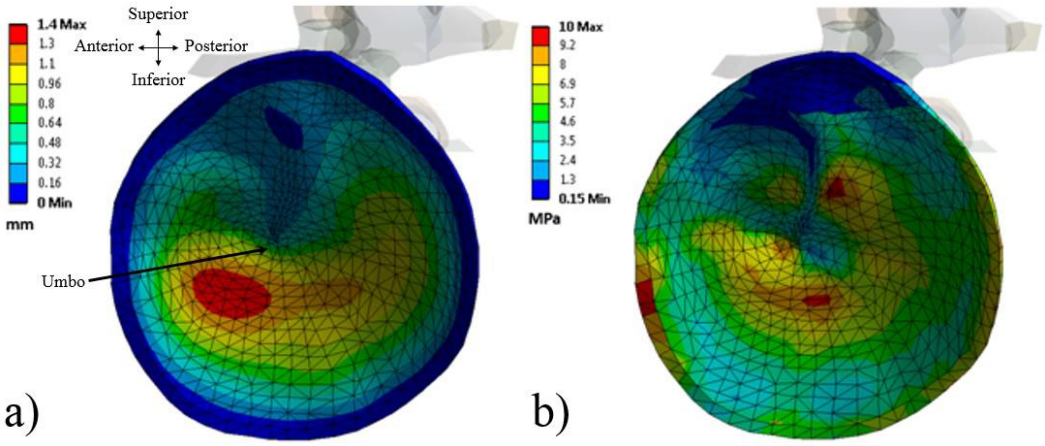


Figure 77. a) TM displacement distribution at time of maximum displacement for vertical exposure. TM is fixed to the bony wall along its annulus and experiences a maximum displacement of 1.4 mm approximately 2 mm inferior and anterior to the umbo. b) TM stress distribution at time of maximum stress. Displays three stress concentrations indicating possible locations for TM rupture. (Leckness et al., 2018)

The validated FE model was used for predicting human TM injury in relation to blast wave direction reported by Gan et al. (2018) in *Military Medicine*, Vol. 183. To investigate the mechanisms of TM injury in relation to blast wave direction, the recorded P1 waveforms were applied onto the surface of the TM in the 3D FE model of the human ear and distributions of the stress in TM were calculated.

Modeling results indicated that the average maximum stresses induced by the P1 rupture threshold waveforms were 16.2 ± 3.0 MPa, 16.3 ± 2.4 MPa, and 14.3 ± 2.5 MPa for the vertical, horizontal, and front wave directions, respectively. The average maximum stresses induced by the P1 waveforms that caused visible TM damage were 20.3 ± 1.2 MPa, 18.8 ± 2.0 MPa, and 15.5 ± 3.5 MPa for the vertical, horizontal, and front directions, respectively.

An example of TM stress distribution at the time of maximum stress due to an applied P1 waveform of 134 kPa maximum pressure is displayed in Figure 78. As shown in this figure, the maximum stress reached 16 MPa and the regions of highest stress were along the anterior portion of the TMA, the posterior to the center of the manubrium, and the inferior to the bottom of the manubrium. These locations may indicate potential sites for TM rupture. Modeling results indicated that the sensitivity of TM stress change with respect to P1 pressure ($d\sigma/dP_1$) may characterize mechanical damage of the TM in relation to blast waves.

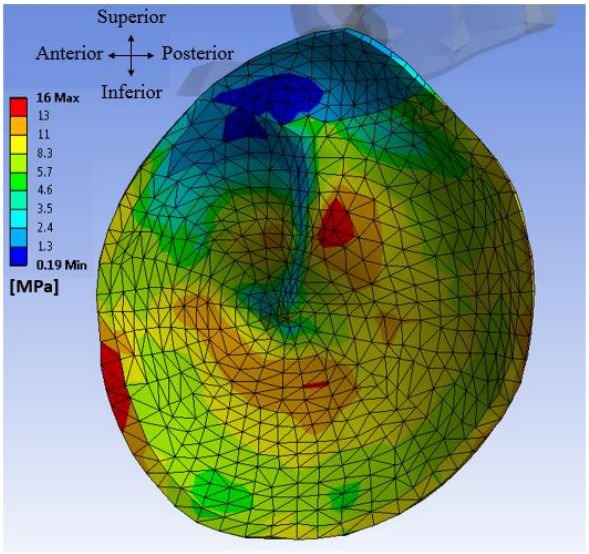
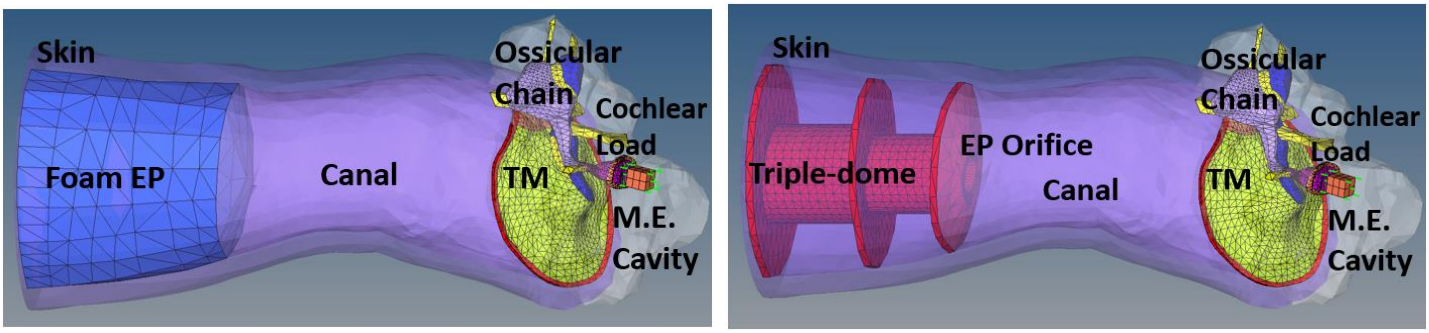


Figure 78. FE model-derived distribution of the equivalent (von Mises) stress in the TM when the maximum stress was reached under the vertical wave direction.

The validated FE model of the human ear was further developed to include the ear canal skin in order to simulate blast overpressure transduction through the ear canal with the earplug inserted. As shown in Fig. 79, two types of earplugs (EPs) were simulated in the FE model of the human ear: the classic foam EP and the Combat Arms earplug (CAE) or trip-dome occlusion which featured a variable orifice and silicon triple-dome structure. The FE model was used to predict the P1 and P2 pressures in ears with earplugs. This modeling study was published with the evaluation of various earplugs on human TBs in *Military Medicine*, Vol. 184 (Gan et al., 2019).



(A) **(B)**

Figure 79. FE modeling of earplugs in the ear canal. (A) The foam earplug simulated in the ear canal. (B) Combat Arms earplug named as "Triple-Dome" simulated in the ear canal. The ear canal, canal skin, earplug (EP), EP orifice, TM, middle ear ossicular chain, middle ear (M.E.) cavity, and cochlear load are displayed in the figure.

The model-predicted results were compared with the experimental data obtained from human cadaver ears in Fig. 80. Column (A) in Fig. 80 displays the results from the foam earplug in TB experiment (top panel) and human ear model (HEM, bottom panel). The P0 pressure wave used for the model was the same as that recorded from the experiments (15 kPa). Columns (B) and (C) show the results from experiments and HEM with the CAE at two P0 pressure levels: 14 kPa and

46 kPa, respectively. Both experiments and FE modeling resulted in the P1 reduction which represents the effective protection function of the earplug. Different earplugs showed variations in pressure waveforms transmitted to the eardrum, which determine the protection level of earplugs. The comparisons of model-derived P1 and P2 waveforms and the peak P1 pressure reduction (insertion loss) induced by the foam and CAE are promising for FE model's future applications. It is expected that the material properties, structural designs, and insertion depths can be evaluated in the FE model.

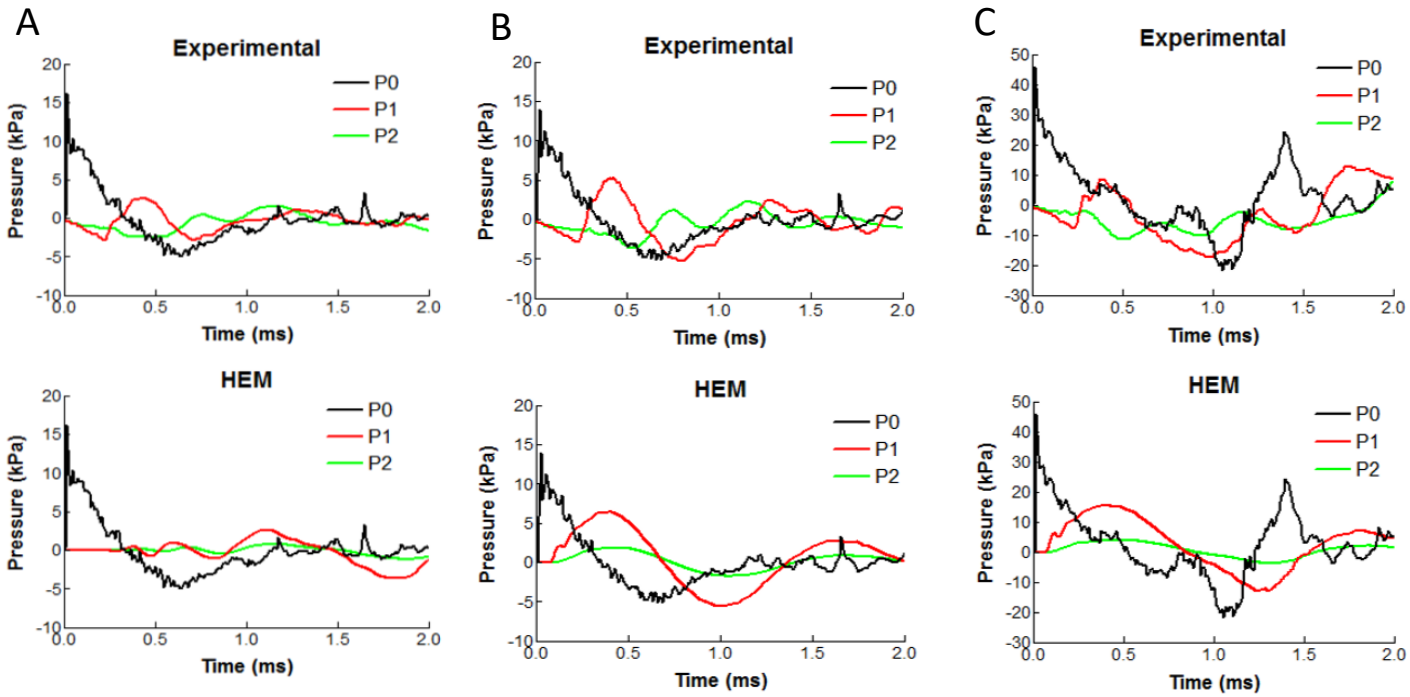


Figure 80. Waveform/Attenuation comparison between FE model and experimental data. Column (A) shows the results with foam earplug and columns (B) and (C) show the results with the Combat Arms or Triple-Dome earplug at two different input overpressure P0 levels: (B) 14 kPa and (C) 46 kPa. The top panels display the experimentally recorded waveforms of P0, P1 and P2 from TB15-35L (foam earplug) and TB15-36R (Combat Arms). The bottom panels display the human ear model (HEM)-derived waveforms.

Finally, as an example of the possible utility of the FE model to aid in nonlinear earplug design, Fig. 81 shows the velocity streamlines through the orifice of the CAE or triple-dome and into the ear canal and middle ear. Snapshots of the streamlines are taken at times 0.02, 0.08, 0.24, and 0.96 ms simulation time. As the flow develops, a swirling effect manifests in the ear canal, especially near the bottom of the canal near the TM. Although the current FE model does not include the hard plastic core of the CAE, it is possible that such information regarding the flow pattern throughout the EP and ear canal may be utilized to design orifice geometries capable of efficiently dissipating impulse energy, saving the ear from overpressure magnitudes that are currently deemed dangerous. Figure 81 was published in Kegan Leckness' MS thesis at University of Oklahoma, August 2016 and reported by Gan et al. at the *Military Health System Research Symposium (MHSRS)*, August 2017.

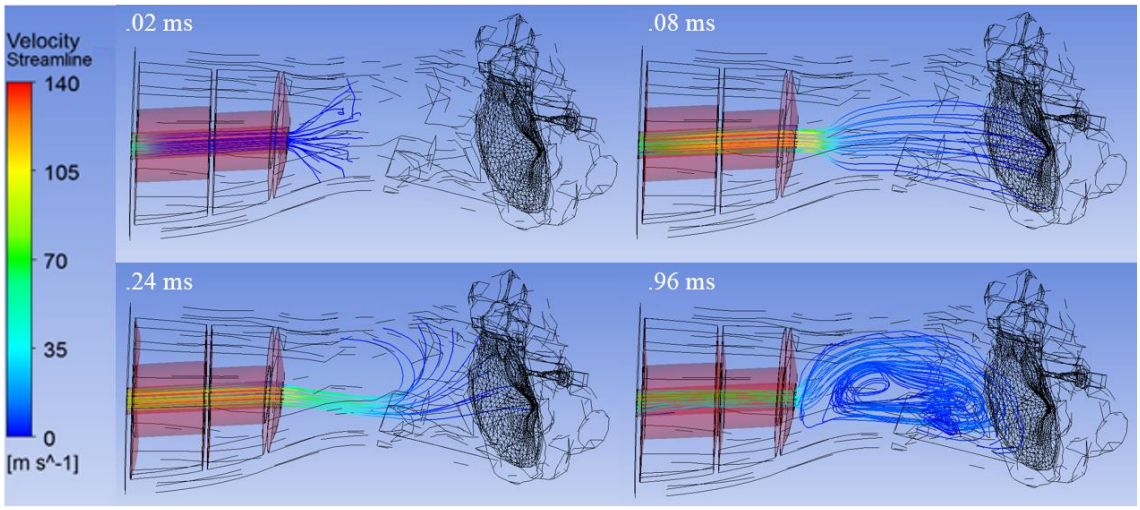


Figure 81. Time history of velocity streamlines through the ear with Combat Arms earplug or Triple-Dome earplug.

(3-2) 3D FE model of the entire human ear including the ear canal, middle ear, middle ear cavity, and cochlea for simulation of blast wave transmission from the ear canal to cochlea

To develop the 3D FE model of the entire human ear for modeling the transmission of BOP from the ear canal through the middle ear and into the cochlea, we have two steps to reach the goal:

Step 1. Create an uncoiled two-chambered cochlea model to replace the cochlear load with connections to middle ear at the stapes footplate (SFP) and round window membrane.
Step 2. Develop a spiral cochlea model of three cochlear chambers separated by the basilar membrane (BM) and Reissner's membrane (RM). We have completed Step 1 with several conference papers and a journal article published in *Annals of Biomedical Engineering* (2020) by Brown et al. Step 2 will be reported in Section (3-5).

The FE model of the entire human ear was created based on the models reported in above Section 3-1. Figure 82A illustrates the entire ear model consisting of the ear canal, middle ear, and cochlea. The middle ear model (Fig. 82B) consists of the ossicles and their suspensory ligaments and muscle tendons, pars flaccida and pars tensa of the TM, TM annulus, manubrium, incudomallear and incudostapedial joints (IMJ and ISJ respectively), stapedial annular ligament (SAL), and middle ear cavity. The two-chambered cochlea model shown in Figs. 82A and C includes the cochlear fluid in the scala vestibuli (SV) above the BM and the scala tympani (ST) below the BM connected by a helicotrema at the apex of the cochlea. The BM was supported with two supports (spiral lamina and spiral ligament) and a bony ledge at the helicotrema or apex separating the SV and ST fluid chambers (Fig. 82C).

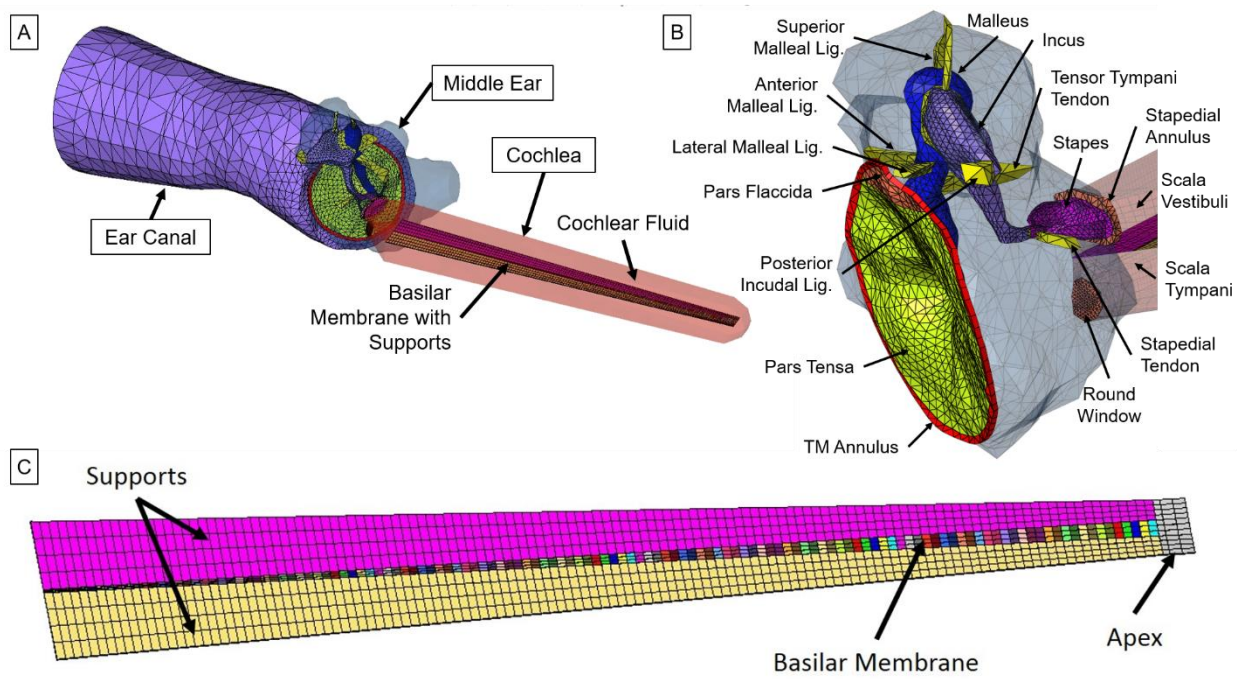


Figure 82. (A) FE model of the human ear with the ear canal, middle ear, and two-chambered cochlea. (B) Structural mesh of the middle ear with the TM, TMA, middle ear ossicles, SAL, round window membrane, and suspensory ligaments and muscle tendons. (C) The cochlea's BM mesh surrounded by two supports and the cochlea's bony apex.

The pressure waveforms, collected from human TB blast tests, were used as the input BOP waveform at the entrance of the ear canal (P0). Figure 83A shows the first 2 ms of the experimentally measured P0 pressure waveform used as input for the FE model with a peak pressure of 30.7 kPa (4.45 psi). Various locations throughout the model were calculated for pressure to track the blast wave transmission in the ear as shown in Fig. 83B.

The P1 pressure waveforms derived from the model were compared with that recorded from the experiments to validate the FE model as shown in Fig. 84: (a) the pressure waveforms recorded in a TB blast test; (b) P1 and P2 pressures calculated from the FE model; (c) comparison of P1 between FE model and experiment. Both model and experimental P1 pressure waveforms exhibited similar peak pressures and A-durations as shown in Fig. 84c.

The TM movement from the model (blue line) was compared with the experimental (red line) from Jiang et al. (2019) in Fig. 85. The P0 pressure waveform with peak pressure of 30.2 kPa or 4.4 psi (black line) from Jiang et al. was used as input to the model. These results indicated that the FE model was validated with experimentally measured blast pressure transduction in human TBs and the blast-induced TM movement.

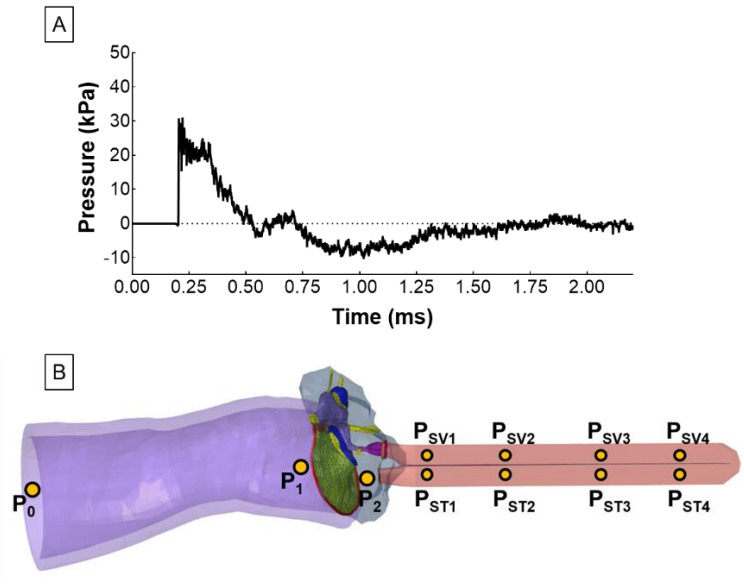


Figure 83. (A) Experimentally measured BOP used as input for the FE model at P0. (B) Input location for BOP at entrance of ear canal, P0, and locations in FE model monitored for pressure during simulations: P1, P2, P_{SV1} - P_{SV4}, and P_{ST1} - P_{ST4}.

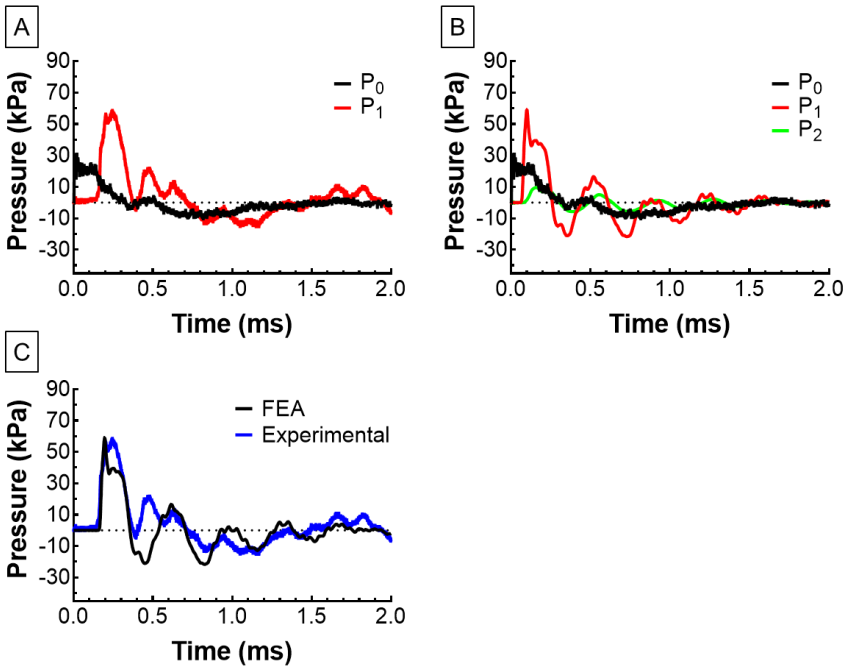


Figure 84. (A) Experimental measures of P0 and P1 during BOP. (B) The FE model's simulated pressures for P1 and P2 with P0 as input. (C) Comparison between FE model and experimental pressures of P1.

Figure 86 shows the cochlear pressures derived from the model in the SV and ST at 4 locations from the base to apex: 0.25, 7.5, 20.0, and 28.75 mm. The pressures in ST were all lower than the corresponding pressure at the SV, but the pressures in the SV and ST trended closer together as the pressure waves transmitted to the apex.

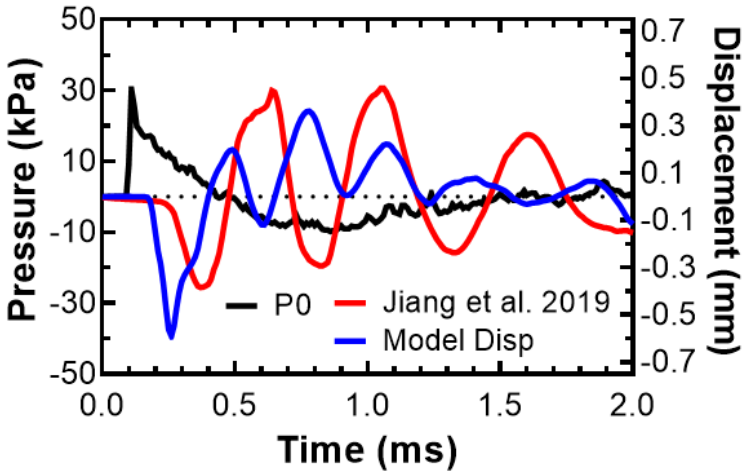


Figure 85. Comparison of the TM movement between the FE model (blue) and Jiang et al.'s (2019) experimental data (red). The simulation used the BOP waveform from the published data as the input pressure at P0 (black).

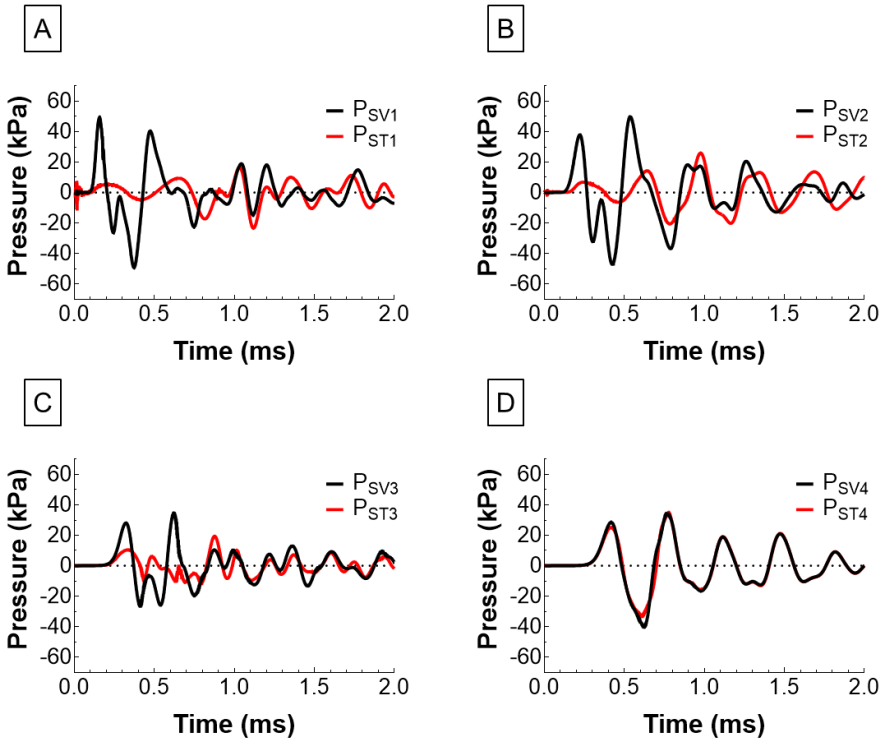


Figure 86. Pressures along the cochlea from base to apex during blast exposure. Pressures monitored in the scala vestibuli (P_{SV}) and scala tympani (P_{ST}) at 0.25, 7.5, 20.0, and 28.75 mm from the base of the cochlea (A, B, C, and D, respectively).

The model-derived displacement of the BM over time at various points: 4.3 to 29.3 mm from the base of the cochlea is shown in Fig. 87A. The BOP at the ear canal entrance resulted in an initial traveling wave in the BM that began displacing into the ST (negatively) and grew as the wave traveled toward the apex. Figure 87B shows the maximum upward displacement (towards the SV) over the BM from the base to the apex. The upward movement of the BM, or Organ of

Corti, is considered to cause greater damage to the cochlea's hair cells since the extreme displacements of the BM injure the stereocilia of the hair cells as they collide with the tectorial membrane above the Organ of Corti. From Fig. 87B, it can be seen that the middle to apex region of the cochlea experiences the greatest displacement during blast exposure.

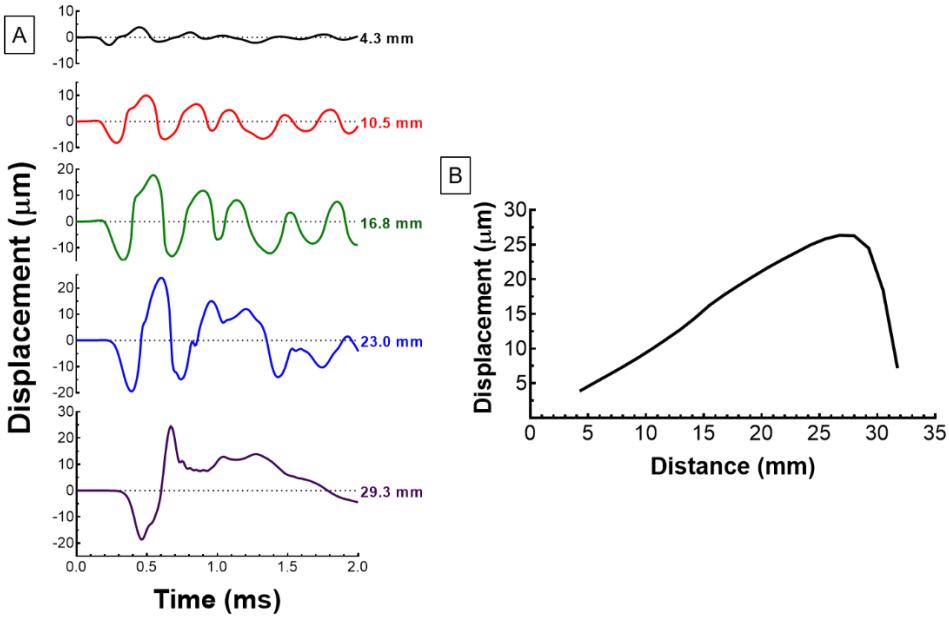


Figure 87. (A) Model-derived displacements of the BM at 4.3, 10.5, 16.8, 23.0, and 29.3 mm from the base of the cochlea. (B) Maximum displacement of the calculated BM along its length. Only the displacement upwards into the scala vestibuli normal to the plane of the BM is included in (B).

Compared with other models for predicting high intensity noise or blast induced hearing injury, such as the AHAAH model, a numerical method to perform the function of sound transmission through the ear of animal models, the 3D FE model of the human ear developed in this project has the capability to predict the biomechanical changes of ear components from BOP exposure which directly relates to dysfunction of the middle ear and cochlea resulting in hearing damage. We have proposed to use **auditory risk units** (ARUs) to predict if an exposure to a BOP waveform will incur inner ear or cochlea injury. ARU is a summation of the squared upward displacement over time at various points along the length of the BM during blast exposure. For each location along the basilar membrane, the number of ARUs can be presented as:

$$\text{ARU}=\sum d_i^2, \quad [\mu\text{m}^2] \tag{1}$$

where d_i is the displacement of the BM at the i^{th} location. Table 1 in Brown et al.'s paper (2020) lists the ARUs for the first 5 ms of our FE model's simulation at 23 points along the BM when the BOP waveform shown in Fig. 83A was applied at the entrance of the ear canal. With the maximum ARU of 13,452 occurring at 29.25 mm from the base (~0.52 kHz region of cochlea), the ARU values follow the same trend from Fig. 87B where highest values occur from the middle to near the apex of the cochlea. One contribution of this project is to extend the human ear FE model's predictive power to determine the resulting hearing impairment from blast-induced damage in the cochlea.

(3-3) Simulation of middle ear muscle active function in the FE model of the human ear

Two muscles in the human middle ear: the stapedius muscle and tensor tympani muscle are included in our 3D FE model and denoted as C5 and C7, respectively (see Fig. 82B). The movement of the ossicles is stiffened by the muscle contraction in response to high intensity sound so that the sound energy transmitted into the cochlea would be reduced.

In the FE model, the middle ear reflex was implemented by increasing the stiffness of the muscle (e.g. stapedius muscle C5). We first created the middle ear impedance change as a function of muscle stiffness change. Then, using the function of impedance change vs sound intensity published by A. R. MØller (1962), we created a function of stiffness change of the muscle vs sound intensity. The middle ear reflex is indirectly implemented by associating the stiffness change of the muscle with sound intensity.

As an example, Fig. 88 shows the FE model-derived the middle ear impedance change with respect to the stapedius muscle stiffness change or the relationship between the stapedius stiffness and middle ear impedance. E/E_0 is the ratio of active C5 stiffness to normal (passive) C5 stiffness. Figure 89 displays the comparison of stapes footplate displacement in warned or with active C5 muscle and the unwarned with passive or normal C5 muscle. Figure 90 displays the warned vs unwarned stapes movement caused by stapedius muscle C5 contraction. With an unwarned response (e.g. low stiffness), the maximum stapes displacement was about 140 microns with a blast of 5 psi. A warned response, however, reduces this maximum displacement by an order of magnitude.

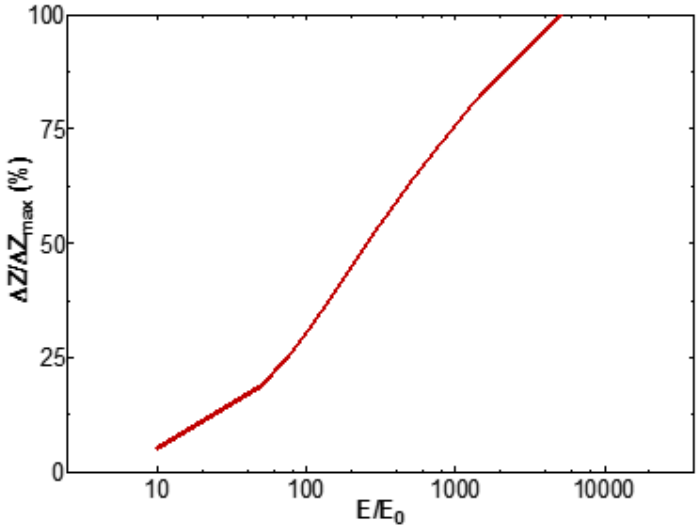


Figure 88. FE model-derived the middle ear impedance change with respect to the stapedius muscle (C5) stiffness. E/E_0 is the ratio of active C5 stiffness to normal (passive) C5 stiffness.

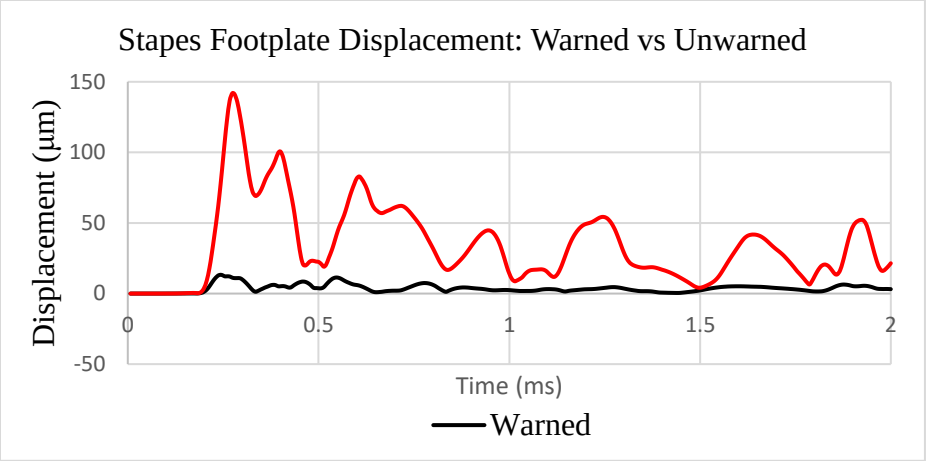


Figure 89. Stapes displacement calculated from the model with stapedius muscle contraction: warned vs. unwarned.

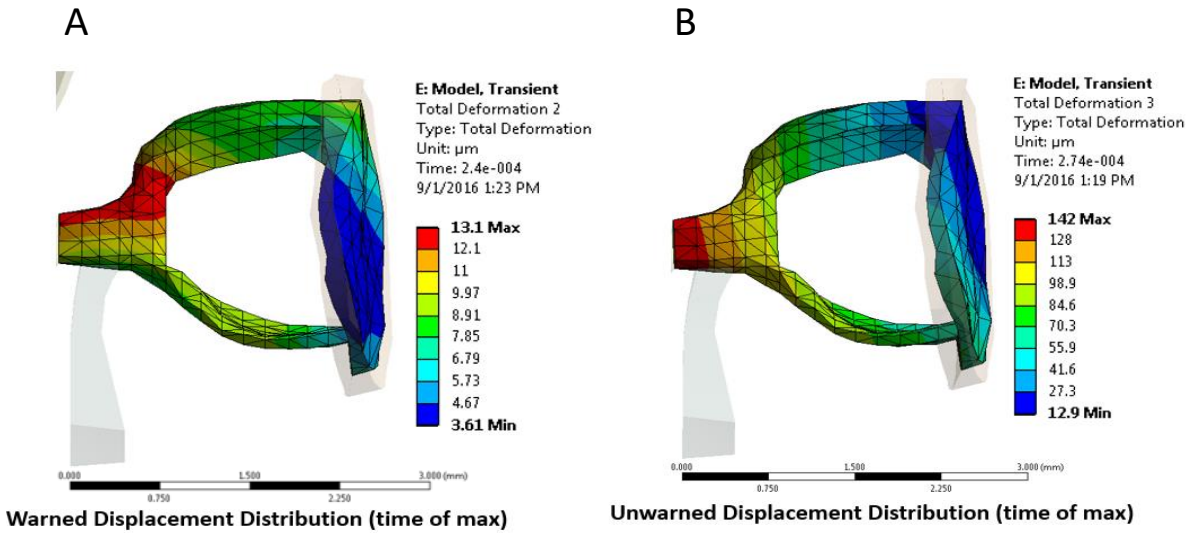


Figure 90. (A) Stapes displacement derived from the FE model in warned case with stapedius muscle contraction. (B) Stapes displacement from the model in unwarned case.

To further simulate the effect of MEMC on the TM and stapes footplate movement which reflect the energy transmitted into the cochlea, we changed the stiffness of the stapedius muscle C5 and tensor tympany muscle C7 and calculated the TM movement at the umbo and the stapes footplate movement when the BOP (P0) of 7 psi (or 50 kPa) was applied at the ear canal entrance in the FE model shown in Fig. 82. Figure 91A shows the TM displacement induced by BOP at three cases: normal ear, both C5 and C7 stiffness increased by 10 times, and C5 stiffness increased by 10 times over the time of 2 ms. Figure 91B displays the displacement of the stapes footplate induced by BOP at the same three cases: normal ear, both C5 and C7 stiffness increased by 10 times, and C5 stiffness increased by 10 times. Note that the displacement data shown in the figures are the value along piston direction of the stapes.

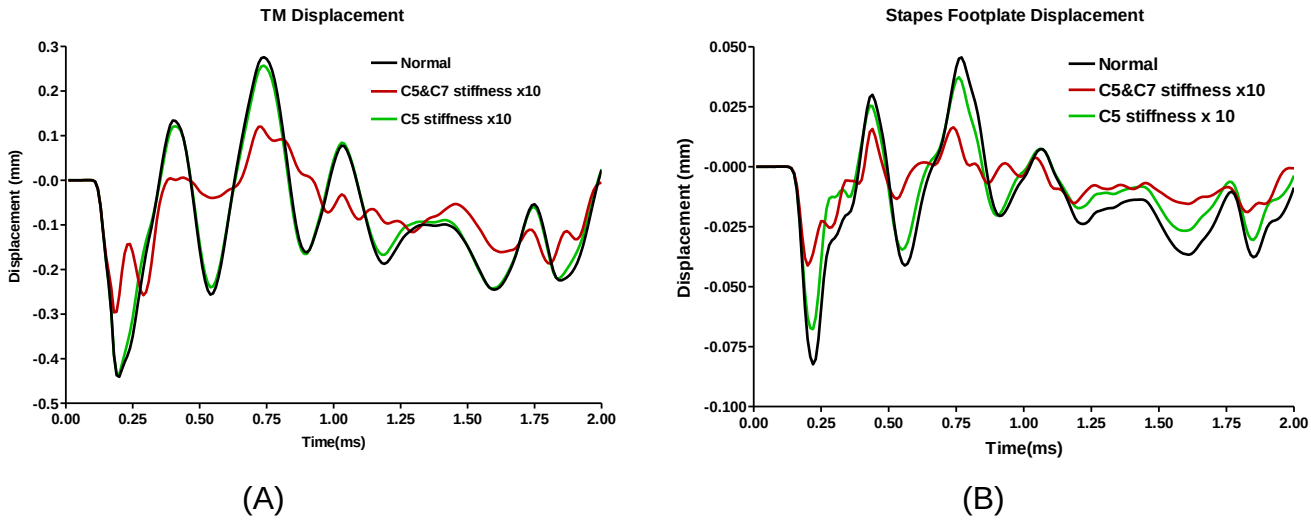


Figure 91. Model-derived displacement of the TM at the umbo (A) and the stapes footplate (B) in normal and MEMC cases.

These modeling results suggest that: 1) the C5 or stapedius muscle contraction may not affect the TM motion much but affect the stapes motion obviously; 2) the contraction of both C5 and C7 muscles may have more effects on the TM and stapes footplate movement than the single C5 muscle active function. It is also realized that the ratio of active C5 stiffness to normal C5 stiffness at 10 causes 5% middle ear impedance change, which may not be large enough to induce the changes of TM and stapes movement. Future studies are needed to quantify the C5 and C7 muscle active functions in relation to the motion changes of the TM and stapes under blast exposure.

(3-4) Multi-layer FE model of human TM to investigate microstructural damage of the TM after blast exposure

To simulate the TM damaged by blast waves as measured the TM surface motion in human TBs reported by Gan and Jiang (2019), an FE model of human TM with multilayer microstructure and orthogonal fiber network was created. The TM model was based on the entire ear model published by Zhang and Gan (2011). Figure 92a shows the ear model which consists of the ear canal, TM, middle ear ossicles, middle ear suspensory ligaments and muscle tendons, middle ear cavity, and the spiral cochlea with two and half turns. The TM in this published human ear model is a single layer of membrane with thickness of 75 μm. In the current project, the pars tensa part of the TM was modeled as a membrane consisting of five layers: epidermal layer, radial layer, middle layer, circumferential layer and the mucosal layer from the lateral to the medial side as shown in Fig. 92b, a schematic diagram illustrates the cross-section of the TM along the circumferential direction. The fiber orientations in radial and middle layers were following the directions of two major types of collagen fibers observed from experiments: the radial fibers originated from the manubrium and ended at the annulus; the circumferential fibers started and ended at the manubrium, parallel to the TM annulus and orthogonal to the radial fibers as shown in Fig. 92c. The pars flaccida was modeled as a non-fiber matrix.

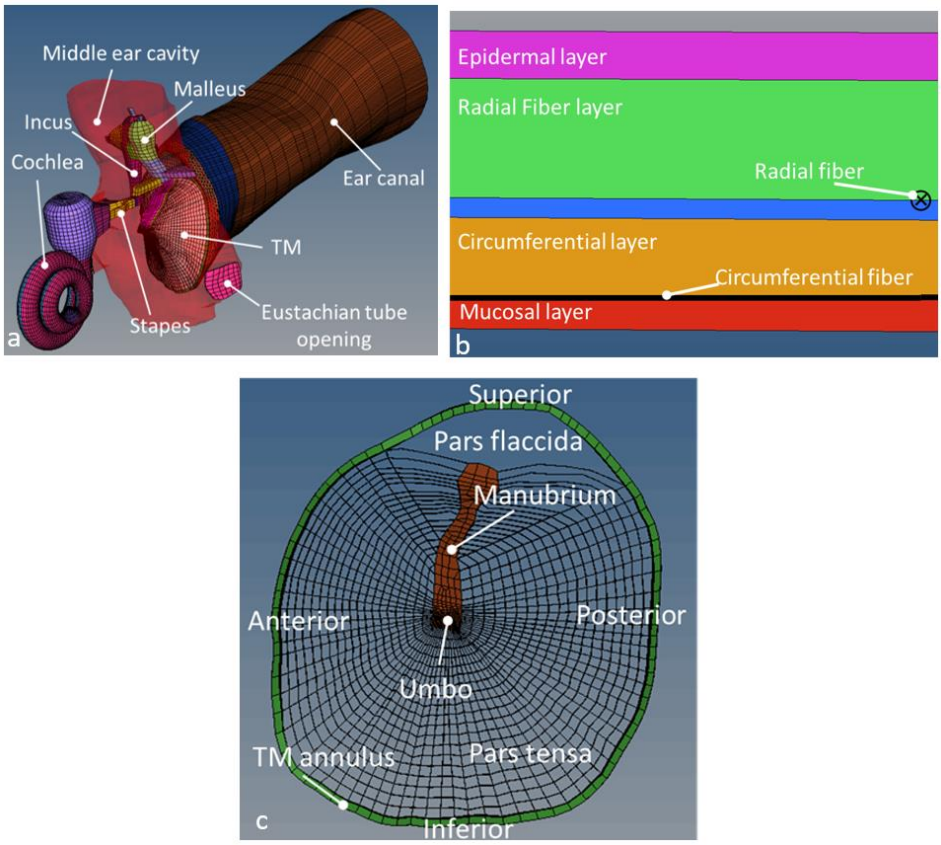


Figure 92. **(a)** 3D FE model of the entire ear reported by Zhang and Gan (2011) including the ear canal, middle ear, middle ear cavity, and spiral cochlea. The TM in this published model was replaced by the multilayer FE model of the TM with fibrous structure in this study. **(b)** Schematic of the cross-section of the TM model along the circumferential direction, showing the location where the fibers are inserted between the respective layers. **(c)** Alignment of radial and circumferential fiber elements in the pars tensa of the TM.

To investigate the relationship between the changes of the microstructure and mechanical properties of the TM and its surface motion, the blast-induced damage was simulated in the FE model of the TM using three approaches: 1) uniformly reduce the elastic modulus of fibers to simulate the mechanical properties of the fibers being altered by blast waves; 2) reduce the volume fraction of fibers to simulate the loss of fibers; 3) remove part of fibers in certain quadrant of the TM to simulate the regional loss of fibers. Following these three approaches, a damaged TM model to mimic the blast-induced changes in TM microstructure and mechanical properties was created as shown in Fig. 93. The deflection shapes of damaged TMs derived from FE model with reduced elastic modulus of the fibers, reduced fiber volume fraction, and partially removed local fibers generally followed the same trend of the experimental data with some minor discrepancies in Fig. 94.

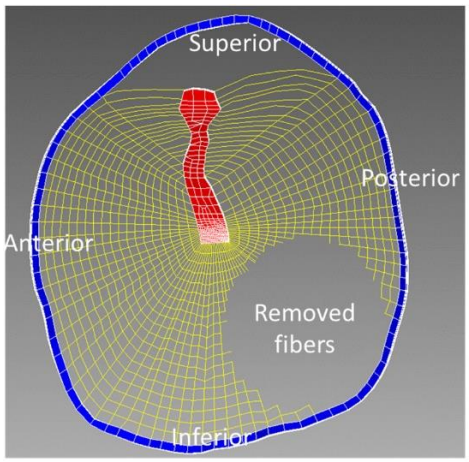


Figure 93. Fibrous structure of the TM model simulating the partial loss of fibers in the high-mobility region induced by blast exposure. The high-mobility region on TM was observed in the posterior-anterior region where the major displacement peak appeared at frequencies below 4 kHz.

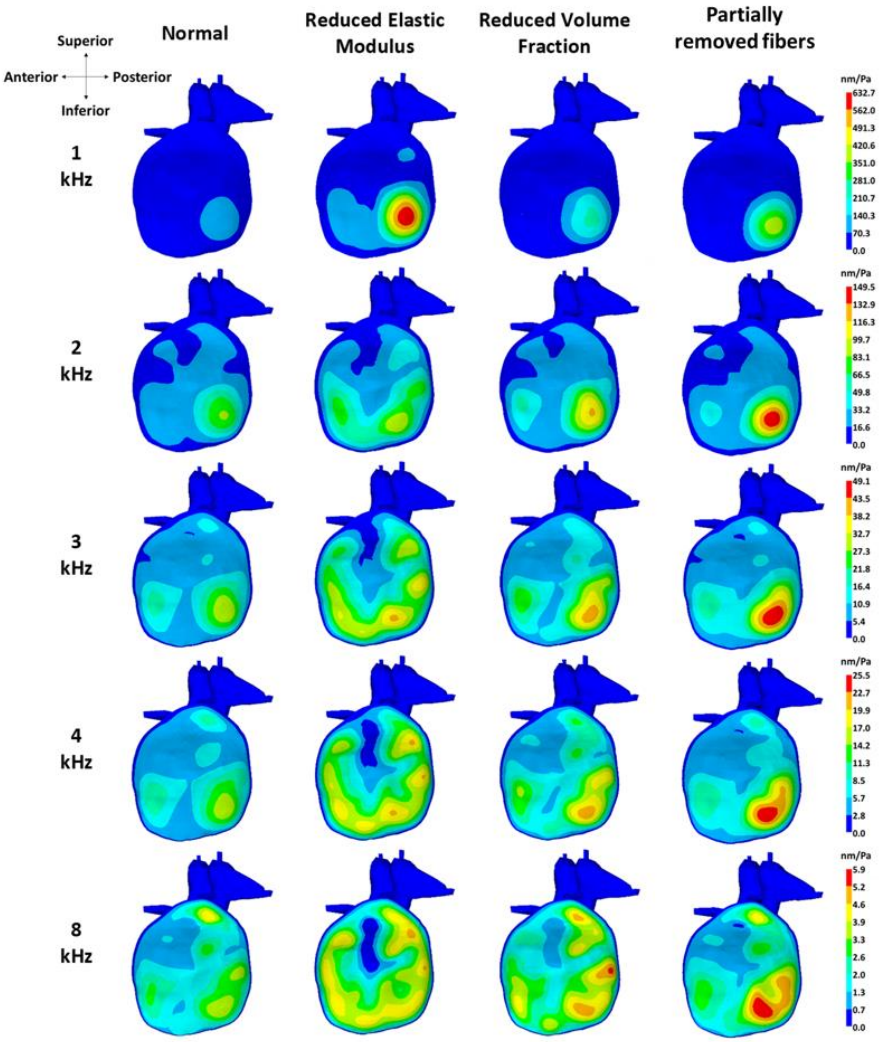


Figure 94. Deflection shapes of TM surface motion derived from 3D FE model of the human ear with the normal TM or damaged TM at five selected frequencies (1, 2, 3, 4, and 8 kHz). From the left to right, the 1st column shows normal TM; the 2nd column shows the TM with reduced elastic modulus; the 3rd column shows the TM with reduced volume fraction of fibers; and the 4th column shows TMs with partially removed fibers.

In conclusion, the full-field surface motion of human TM before and after blast exposures was measured by SLDV (see Section (1-5)) over a frequency range from 1-8 kHz. An FE model of human TM with multilayer fiber network was created to simulate the normal and blast-damaged TMs. The model-derived data successfully characterized the features of the TM surface motion measured from the normal and damaged ears. Results suggested that the blast-induced TM damage might be a combination of global and regional loss or mechanical property changes of the fibers. The technology developed in this study can detect and simulate the blast-induced microstructural damage in the TM and improve our understanding of post-blast injuries in the auditory system. The multilayer TM model created in this study provides a practical tool for microstructural biomechanical analysis of TM damage.

(3-5) 3D FE model of entire human ear with spiral cochlea

To reach the final goal of this project for FE modeling of the entire ear, we have replaced the straight cochlear model by a spiral cochlea for simulation of the blast overpressure or high intensity sound transmission through the ear as shown in Figs. 95 and 96.

As shown in Fig. 95, the spiral cochlea of two and a half turns is connected to the middle ear at the stapes footplate and the round window membrane (RWM). The scala tympani (ST) and scala vestibuli (SV), connected at the helicotrema, comprises of the perilymph fluid. This fluid is separated by the scala media (SM), or endolymph, with the basilar membrane (BM) and Reissner's membrane (RM) as the bottom and top barriers, respectively (Fig. 96). The length of the BM or RM was approximately 34 mm. The width of the BM varied from 116 μm at the base to 497 μm at the apex. The thickness of the BM varied from 7.8 μm at the base to 2.5 μm at the apex, while the thickness of the RM varied from 8.5 μm at the base to 4.5 μm at the apex.

The middle ear and ear canal model are the same as those of the uncoiled two-chambered cochlea model shown in Fig. 82, consisting of the ear canal, TM, TMA, manubrium, ossicles and associated suspensory ligaments, IMJ, ISJ, and SAL.

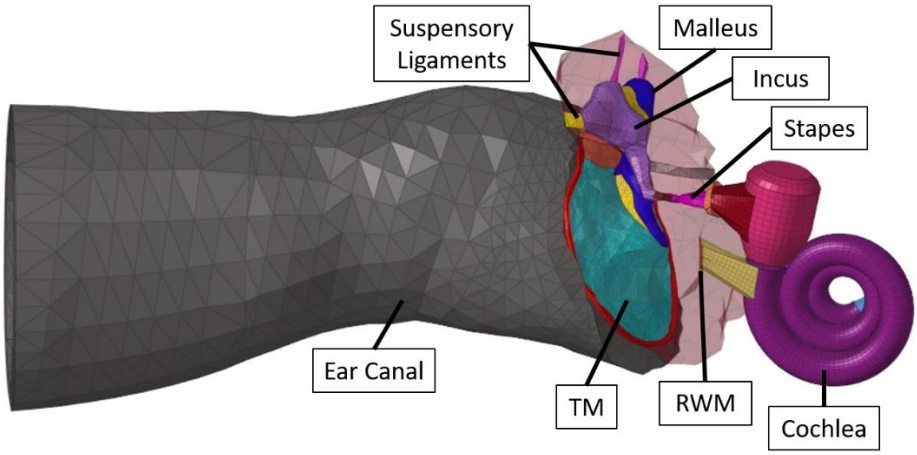


Figure 95. 3D FE model of the human ear with spiral cochlea (posterior view).

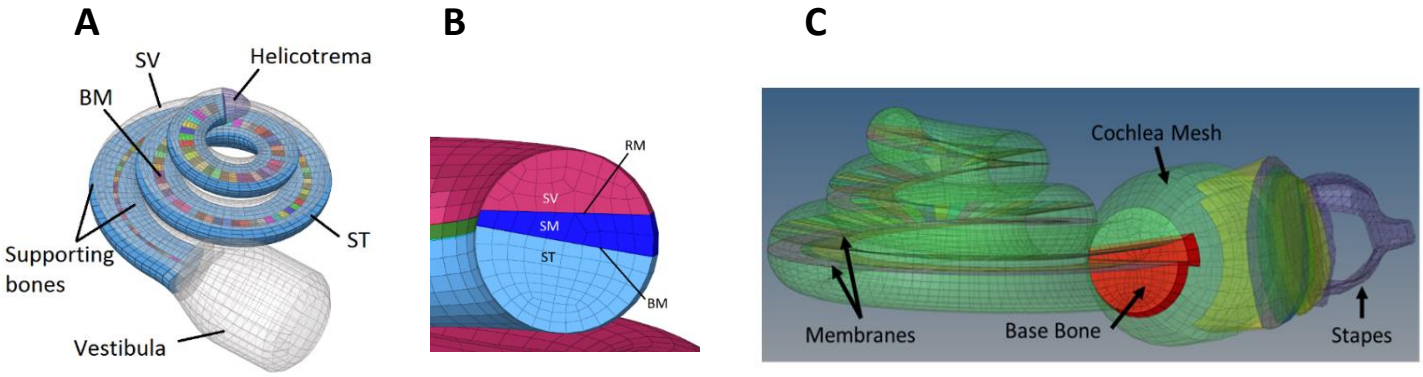


Figure 96. (A) FE model of spiral cochlea with BM (SV, SM and RM are transparent here). (B) Cross section of the cochlea model displaying the three chambers (SV, SM, and ST) and two membranes (RM and BM). (C) Image of the three chambers' connection at the base.

For simulating blast wave transmission through this three-chambered spiral cochlear model, we have faced challenges in running the FSI coupling between the fluid and structure using Fluent and Mechanical in ANSYS. Figure 97 displays the meshed cochlear fluids: perilymph and endolymph (A) and structural mesh of entire ear model (B). The spiral cochlea model was uploaded to Fluent (fluid) and Mechanical (structure) through the ANSYS Workbench, and the parameters and material properties of the cochlea were set to similar values as those used in the straight cochlea model for the initial simulations. The conditions for the middle ear portion of the model were set identical to the published ear model with uncoiled cochlea. Simulations are currently ongoing to evaluate the initial performance of the model. It is expected that the spiral cochlea model with 3 chambers will allow us to investigate the more advanced fluid mechanics from the addition of the SM chamber and Reissner's membrane.

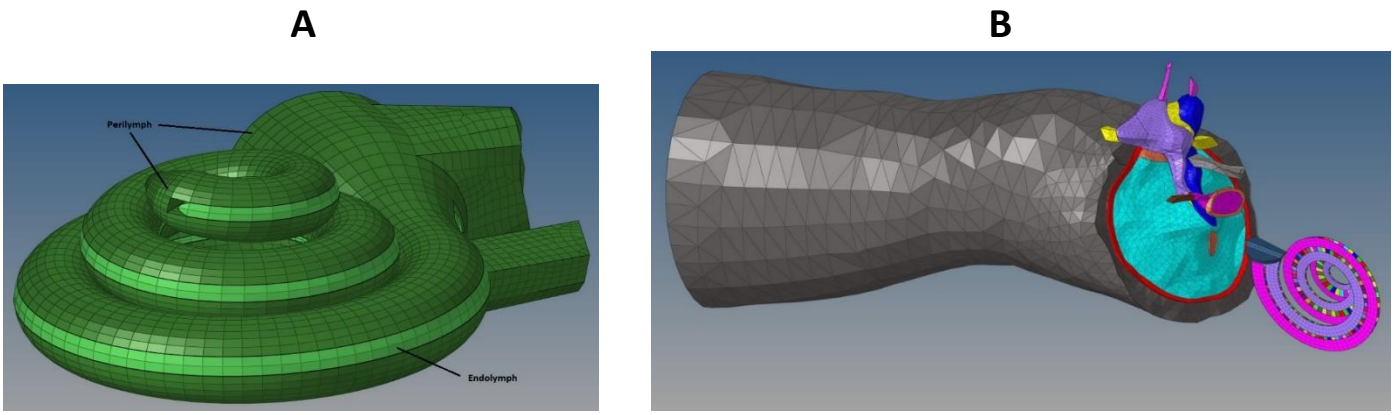


Figure 97. (A) Meshed fluid volumes of the cochlea showing the perilymph (dark green) and endolymph (light green). (B) Structural mesh of the ear canal, middle ear, and cochlea to be uploaded to ANSYS.

In addition to the 3-chambered spiral cochlea model, we have created the 2-chambered spiral cochlea model based on the uncoiled or straight cochlear model of Fig. 82. Figure 98A displays the cochlear structure consisting of SV and ST separated by BM and Fig. 98B shows cross-sectional view of the spiral cochlea near the apex. This model will allow us to analyze how the cochlea's anatomy affects the blast transmission within the cochlea.

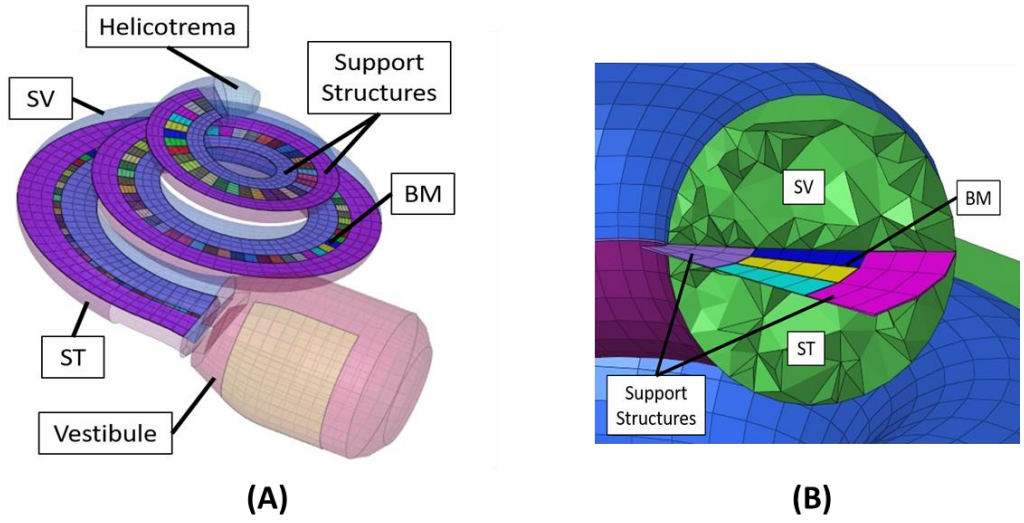


Figure 98. (A) FE model of spiral cochlea with BM (SV, ST, Vestibule, and Helicotrema are transparent here). (B) Cross-section of the spiral cochlea near the apex. Shows the two chambers (SV and ST), support structures, and BM.

(3-6) 3D FE model of chinchilla entire ear for simulation of acoustic or blast overpressure transmission through the ear

The 3D FE model of the human ear and the experimental measurements in cadaver ears provide important biomechanical date about the ear response to blast overpressure. However, there is a gap to connect those results to actual hearing damage because of the study limitation for human subjects. Therefore, the animal model becomes a necessary and very important research component for investigating the hearing damage and protection mechanisms.

To correlate the animal hearing test results with the human hearing damage, we have created a 3D FE model of the chinchilla ear or bulla based on X-ray (μCT) images of an adult chinchilla bulla. The model is consisted of the external ear canal and middle ear and published in *Biomechanics and Modeling in Mechanobiology*, Vol. 15 by Wang and Gan (2016). Figure 99A displays the medial view of the chinchilla left bulla reconstructed on a total of 519 μCT images that contained the entire middle ear cavity and cochlea in Amira software with the surface triangulation meshes. Figure 99B shows the FE model of chinchilla ear consisting of the bony ear canal, TM, ossicular chain, middle ear ligaments and tendons, septa, and middle ear cavity from medial view. At the first step, we did not include the cochlea in the model as shown in Fig. 99B and focused on chinchilla middle ear function in response to acoustic stimulation.

The air chambers and boundary conditions of the middle ear cavity in chinchilla may contribute fundamental features to the acoustic coupling of the ear and it is a challenge to accurately identify and simulate the acoustic boundary conditions of the middle ear cavity for chinchilla. In this study, we created two boundary conditions, or two types of fluid-structure interactions, defined in the acoustic elements of the ear canal and middle ear: Acoustic Boundary Condition 1 (BC1) representing the natural or sealed middle ear cavity wall as a rigid structure and BC2 representing the middle ear cavity wall as a partially flexible structure.

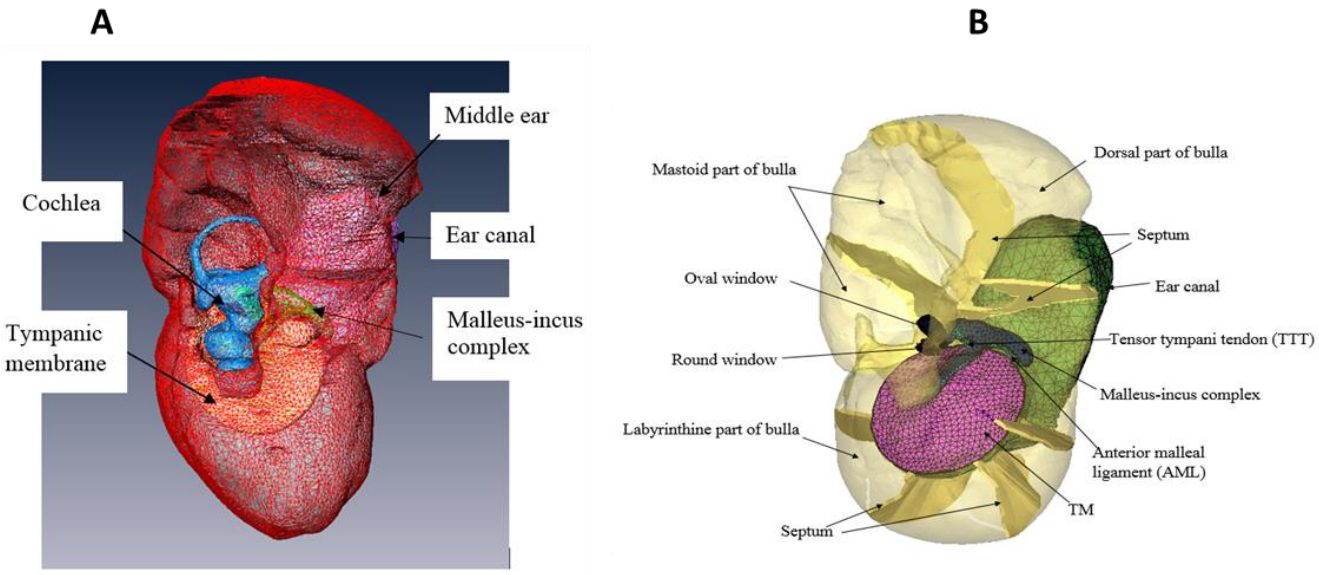


Figure 99. (A) The 3D geometrical model of a chinchilla left ear (medial view) reconstructed from μCT images. (B) FE model of the chinchilla ear with the external ear canal and middle ear inside the bulla from medial view of the model. The middle ear cavity was rendered transparently, and the septa were displayed as 3D solid.

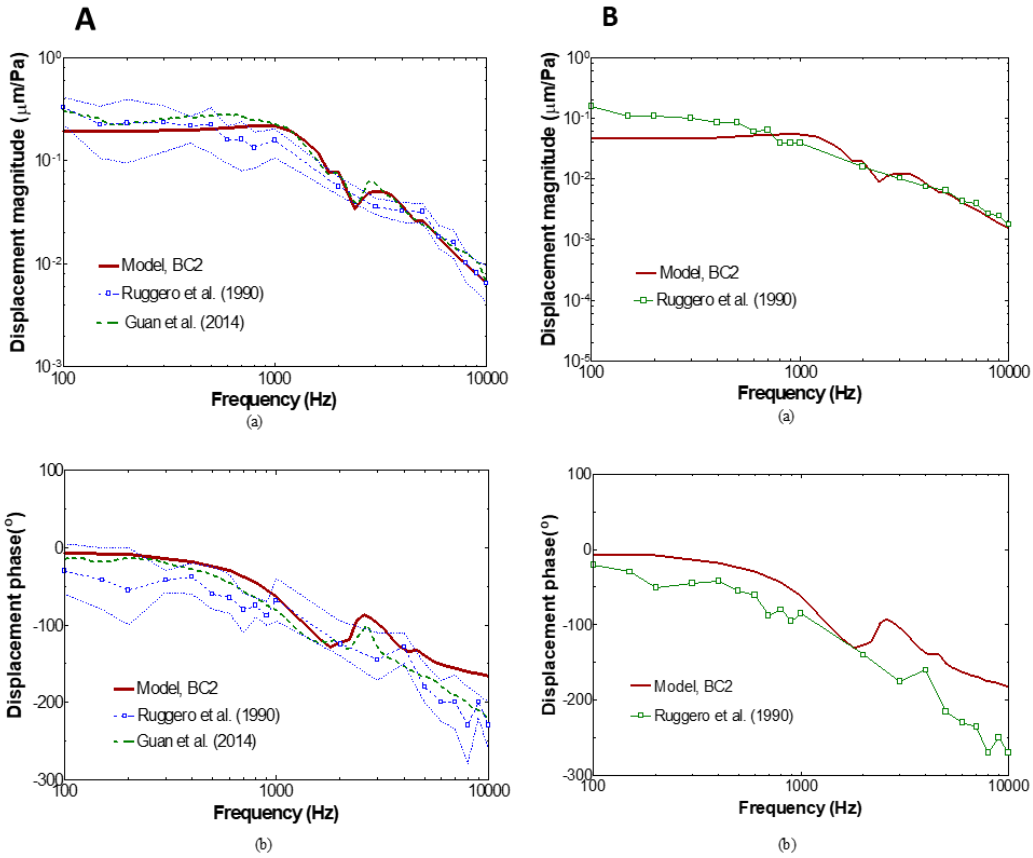


Figure 100. Comparison of the FE model-derived TM displacement with BC2 boundary condition (left panel A) and the stapes footplate displacement (right panel B) with the published experimental data measured in chinchillas.

The acoustic-mechanical coupled analysis was conducted with these two BCs to characterize the middle ear function. Figure 100 shows the frequency response curve of the TM displacement at umbo (Panel A, left)) and the stapes footplate displacement (Panel B, right) derived from the FE model with BC2 boundary condition (solid lines) in comparison with the published measurements in chinchillas: (a) magnitude and (b) phase. This study provides the first 3D FE model of the chinchilla ear for characterizing the middle ear functions through the acoustic-mechanical coupled FE analysis.

At the second step to develop the FE model of chinchilla ear, we have added the cochlear model to the middle ear as shown in Fig. 101. The basilar membrane is approximately 16 mm in length and has an elastic modulus that is 30 MPa at the base and 5 MPa at the apex. The damping coefficient is assumed as 0 s at the base and 7.5 x 10^{-4} s at the apex. Figure 102 displays the cochlear model with the scala vestibule and scala tympani (A), the basilar membrane structure and associated bony supports of the chinchilla cochlear model (B), and basilar membrane and associated bony supports surrounded by cochlear fluid (transparent) (C). Note that the basilar membrane separates the scala tympani and scala vestibuli. This FE model of entire chinchilla ear and the results for acoustic and blast wave transmissions were published in Paige Welch's MS thesis at University of Oklahoma, May 2020.

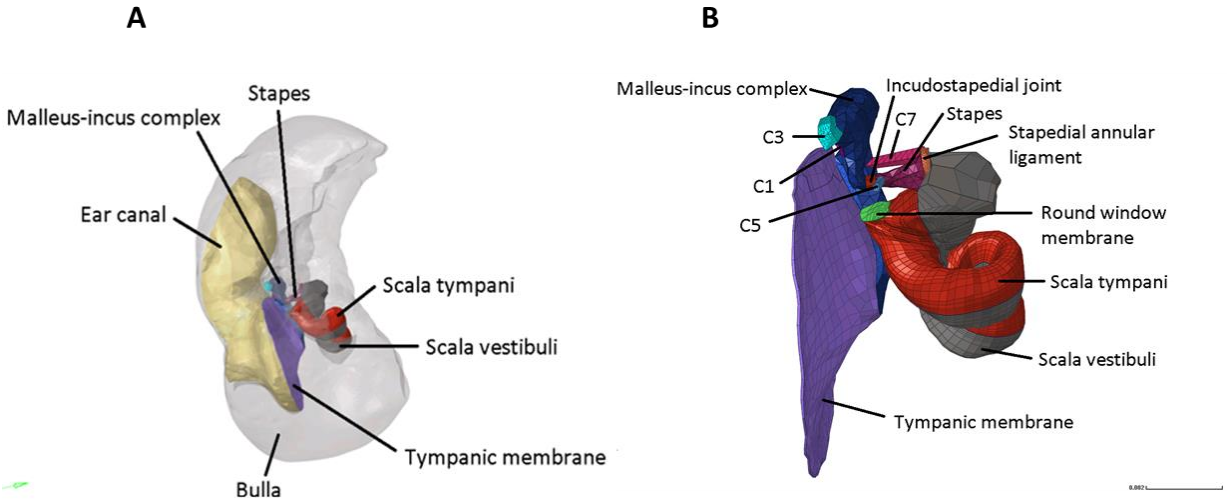


Figure 103. (A) Posterior view of the 3D FE model of the chinchilla ear including the external ear canal. Note that the bulla is rendered transparent for ease of viewing. (B) Posterior view of the middle ear structures and cochlea. The connection between the TM and cochlea through the ossicular chain is prominently displayed. All Cs are suspensory ligaments.

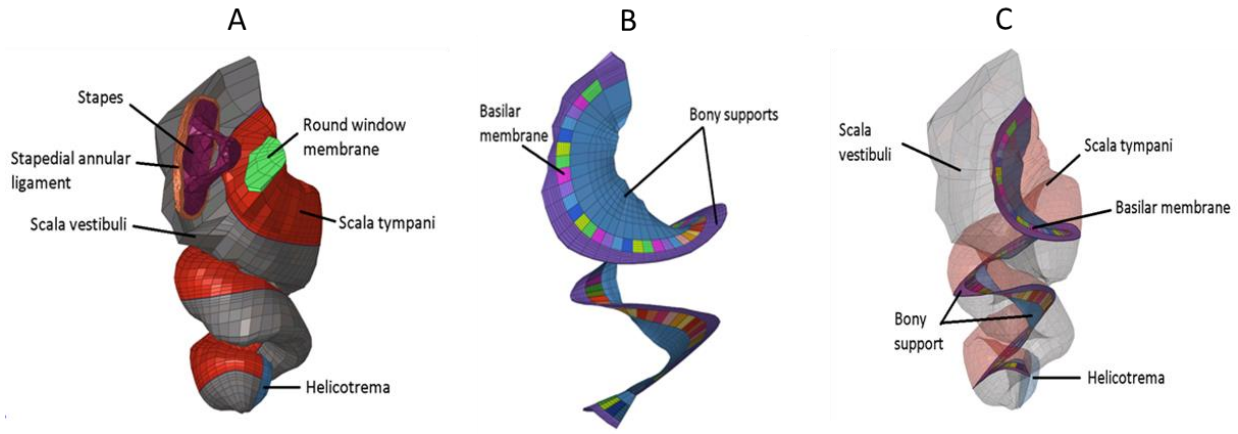


Figure 102. (A) FE model the chinchilla cochlea with middle ear components (stapes, stapedial annular ligament, and round window membrane) to illustrate connection points to the middle ear model. (B) Basilar membrane structure and associated bony supports of the FE model of the chinchilla cochlea. The basilar membrane was approximately 16 mm in length. (C) Basilar membrane and associated bony supports surrounded by cochlear fluid (transparent). Note that the basilar membrane separates the scala tympani and scala vestibuli. These two fluids filled chambers connect at the helicotrema.

The FE model of the entire chinchilla ear was validated for normal sound transmission (e.g., 90 dB SPL) from the ear canal to cochlea first. Figure 103 shows the FE model-derived magnitude of the TM and stapes footplate (FP) displacement in the direction normal to the FP per unit sound pressure (normalized by the input sound pressure 90 dB or 0.632 Pa) in comparison with published experimental data measured in chinchillas. The displacement of the basilar membrane from the base to the apex over frequencies ranging from 200 Hz to 15 kHz was derived (d_{BM}) and normalized by the stapes FP displacement (d_{FP}) across the frequency range as shown in Fig. 104. The BM data was compared to the frequency versus position map created from published chinchilla experimental data by Eldredge et al. (1981) in Greenwood (1990) in Fig. 105.

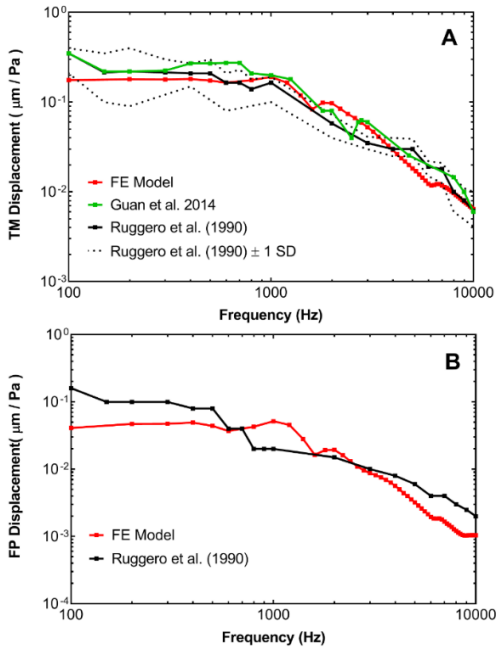


Figure 103. FE model-derived displacements of the (A) TM at the umbo and (B) stapes FP in comparison to published experimental data in chinchilla.

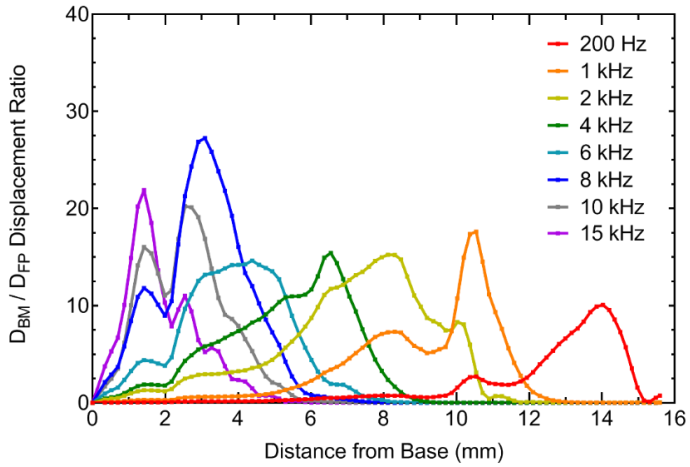


Figure 104. BM displacement normalized with respect to the footplate displacement (d_{BM} / d_{FP}) at frequencies of 200 Hz – 15 kHz from the base to apex.

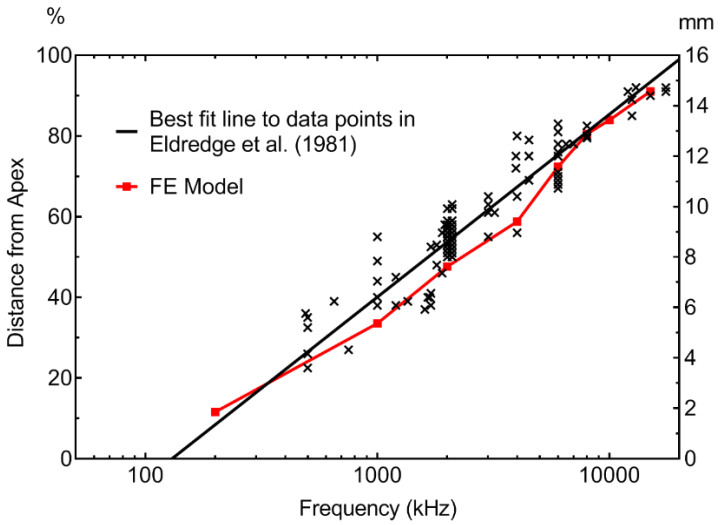


Figure 105. FE model-derived frequency versus position map in comparison to published chinchilla experimental data. The black line represents the line of best fit to data points (Eldredge et al., 1981).

The 3D FE model of the chinchilla bulla with the entire ear was further employed for analysis of blast wave transmission from the ear canal to the cochlea. As shown in Fig. 106, a recorded blast overpressure waveform P0 from a chinchilla test was applied as an input at the entrance of the ear canal. The pressure at the ear canal entrance (P0), pressure near the TM in the ear canal (P1), pressure behind the TM in the middle ear cavity (P2), and cochlear pressures P_{SV} and P_{ST} at three locations along its spiral length from the base to apex within the scala vestibule (SV) and scala tympani (ST) were derived from the model. The locations of those pressures, P0, P1, P2, and cochlear pressures, are shown in Fig. 107. The SV-1 was located approximately 0.6 mm below the stapes FP, while SV-2 and SV-3 were located about 5 mm and 13 mm from the base, respectively. ST-1 was located roughly 0.9 mm below the RWM, while ST-2 and ST-3 were located approximately 6 mm and 13 mm from the base, respectively.

Figure 108 shows the results of model-predicted cochlear pressures at 3 locations from base to apex within the scala vestibule (SV-1, SV-2, and SV-3) and scala tympani (ST-1, ST-2, and ST-3). The pressure closest to the stapes (SV-1) was the greatest, with a maximum peak pressure of approximately 1,500 Pa. As the location moved closer to the helicotrema, the pressure in the SV decreased. SV-2 and SV-3 had maximum peak pressures of 3.7 Pa and 0.04 Pa, respectively. In the scala tympani, the model-predicted pressure was greatest near the RWM (ST-1), with a maximum peak pressure of about 113 Pa, much lower than the pressure at SV-1. Similar to the trend observed in the scala vestibuli, as the location moved closer to the helicotrema the pressure in the ST decreased. ST-2 and ST-3 had peak pressures of 3.4 Pa and 0.06 Pa. These results indicated that the pressure wave in the cochlea did not distribute to the apex but had decreased substantially less than halfway down the cochlea.

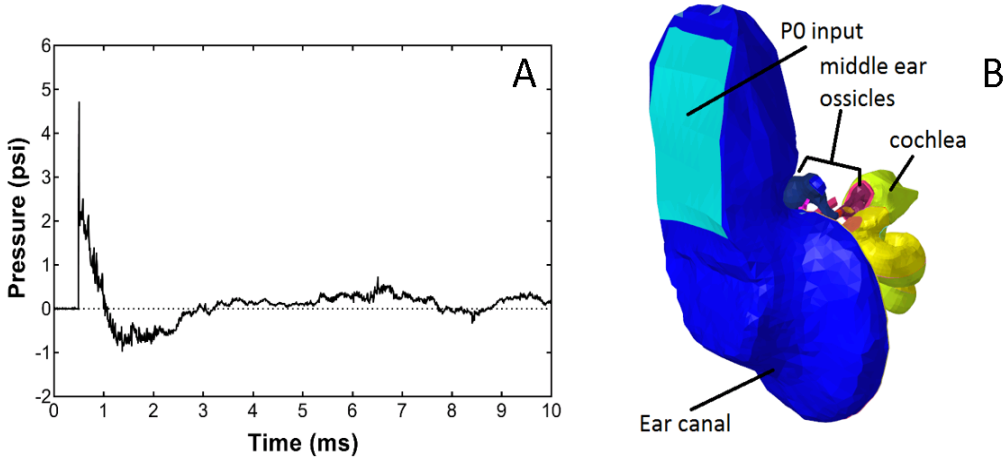
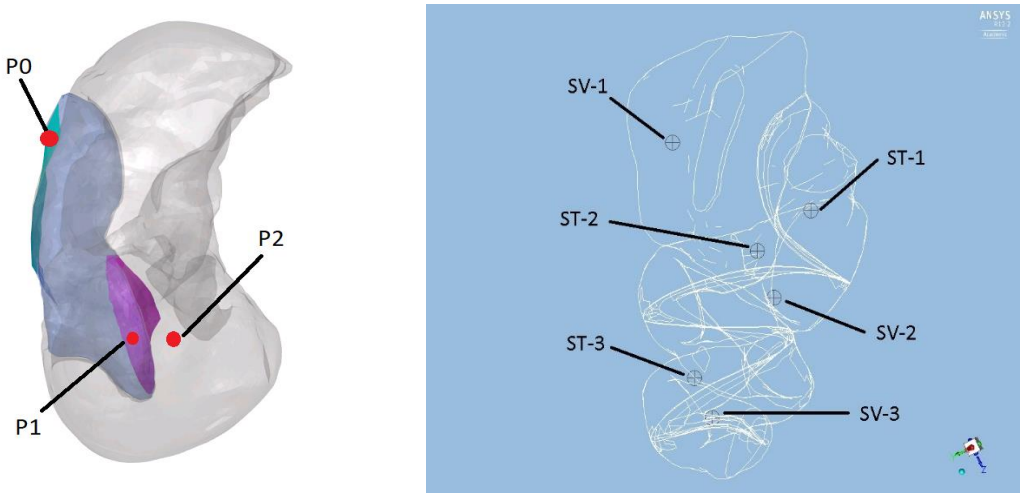


Figure 106. (A) Recorded BOP waveform P0 at the entrance of the ear canal. (B) The 3D FE model of the chinchilla ear with the middle ear cavity removed for a better view, showing the location of P0 input, middle ear ossicles, and cochlea.



(A) (B)

Figure 107. (A) Locations of the P1 and P2 pressures calculated from the model with the input pressure P0 applied at the chinchilla ear canal entrance. (B) Three locations of cochlear pressure calculated along the SV and ST from the base to apex, respectively.

The FE model-predicted displacements of the basilar membrane (BM) at 17 points from the base to the apex are shown in Fig. 109. The displacements were calculated in the direction normal to the BM. Positive displacement was the movement into the scala tympani, while negative displacement reflected the movement into the scala vestibuli. As seen in these figures, the greatest BM displacement occurred 2.17 mm from the base with a maximum positive displacement of 53 nm. The BM displayed an oscillating pattern of movement along the first 5.84 mm of length and the displacement decreased from base to apex. After the first 5.84 mm, the BM movement showed displacement only in the negative direction or in the direction into the scala vestibuli.

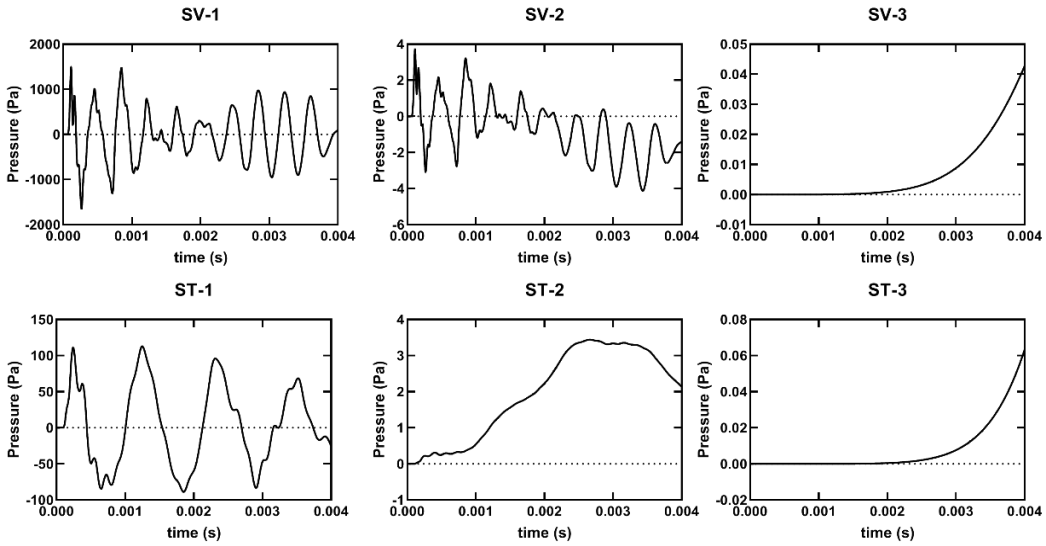


Figure 108. FE model-derived cochlear pressure distribution from the base to apex. The top row shows the pressure in the SV and the bottom row shows the pressure in the ST.

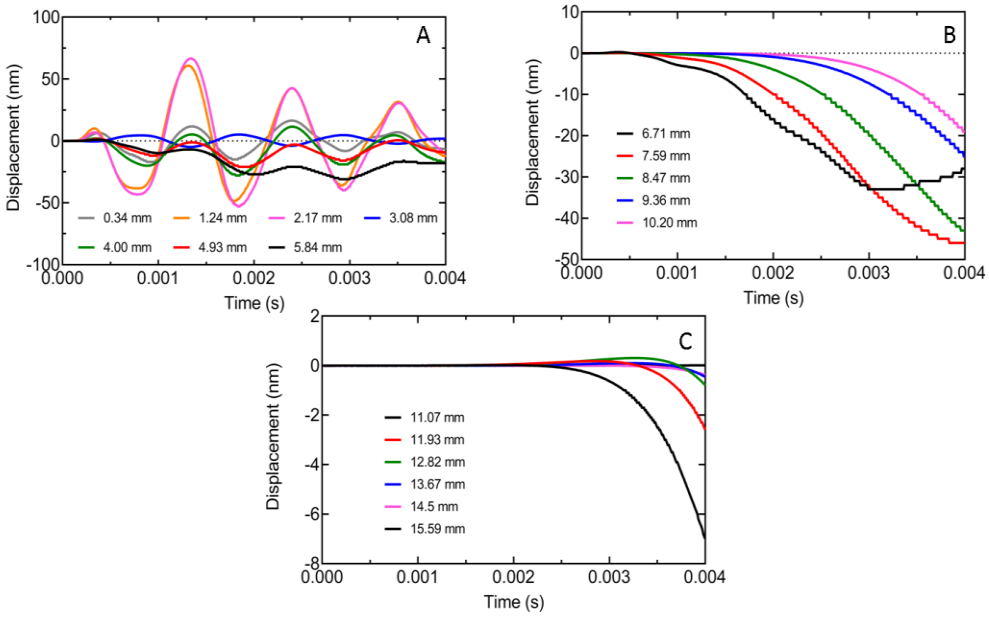


Figure 109. FE model-derived BM displacement from base to apex in response to BOP in the time domain. (A) Displacements of the basilar membrane up to 5.84 mm from the base. (B) Displacements of the BM from 6.71 mm to 10.20 mm from the base. (C) Displacements of the BM from 11.07 mm to 15.59 mm from the base.

(3-7) **Improvement of 3D printed human temporal bone or human ear for applications**

The 3D printing system (Object350, Stratasys) with multiple materials was used to print human TB or human ear consisting of the ear canal, TM, middle ear ossicular chain, and middle ear cavity based on an FE model of the human ear as shown in Figs. 8 and 9. The cochlear load was added to the stapes footplate through liquid pressure. A finished print of the 3D printed TB's unassembled middle ear can be seen in Figs. 110a-d where rigid materials were printed in either white or yellow (hard tissues) and flexible materials were printed in shades of gray or black (soft tissues). The lateral surface of the TM can be seen through the ear canal in Fig. 110a while Fig. 110b shows the medial-inferior side of the TM within the middle ear cavity. The ossicular chain was freely suspended after removal of the support material. The top and back seals (Fig. 110c) were affixed to the middle ear portion to form the middle ear cavity. For clarity, the TM, ossicular chain and their attached ligaments and tendons were 3D printed separately and are shown in Fig. 110d. The ossicular chain was printed at a 1:1 scale from the human ear or FE model and retained its shape throughout the 3D printed TB's fabrication. Figures 110e and 110f shows the fully assembled 3D printed TB. This study has been included in Marcus Brown's Ph.D. dissertation at the university of Oklahoma, May 2021.

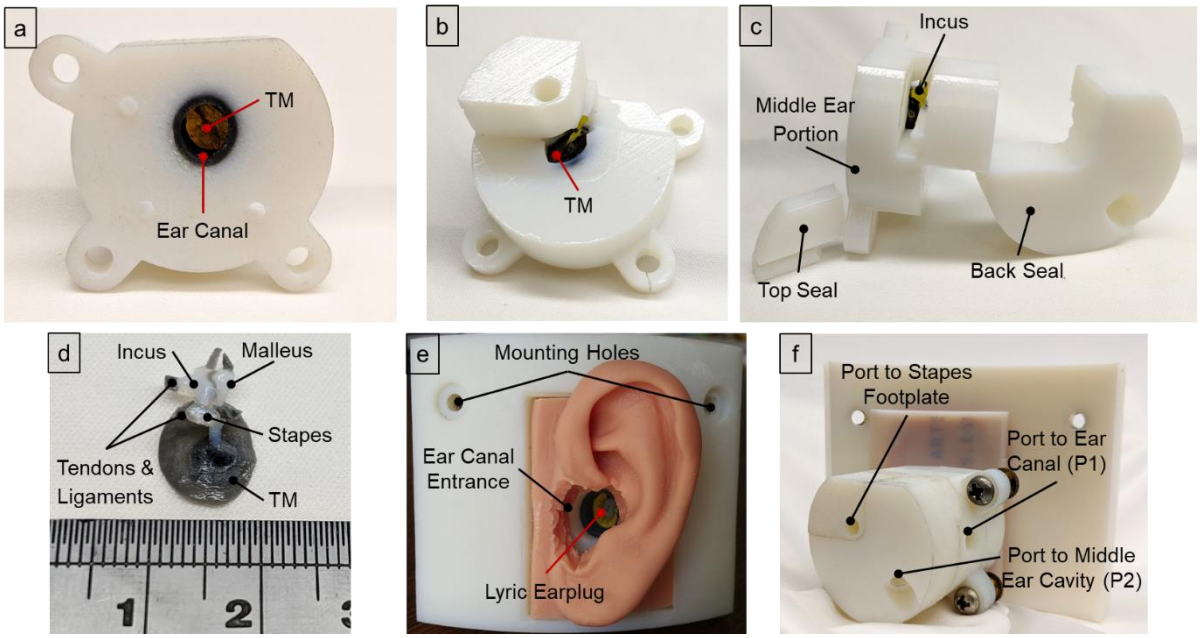


Figure 110. Images of a finished print of the 3D printed TB's unassembled middle ear portion. (a) Lateral view of the middle ear portion showing the ear canal and TM within. (b) Medial view of the middle ear portion of the 3D printed TB showing the opening used for cleaning. (c) Posterior view of the 3D printed TB's middle portion with the seals. (d) A 3D print of the ossicles, TM, and ligaments and tendons from within the middle ear cavity of the 3D printed TB. The ossicles were imaged without the surrounding material and with a scale to highlight the detail and size of the middle ear tissues. (e) Lateral view of the assembled 3D printed TB with a Lyric earplug inserted into the ear canal. A silicone mold of the pinna was adhered to the 3D printed TB to simulate the outer ear. (f) Medial view of the assembled 3D printed TB showing the ports to measure the pressures at the TM and in the middle ear cavity and to access the stapes footplate.

To validate the function capability of the 3D printed TB for sound transmission through the ear, the movement of the TM was measured using laser Doppler vibrometry under acoustic stimulation, and the data were compared with published human TM's displacement in the literature as shown in Fig. 111A. The LDV measurements performed in the 3D printed TB were similar to those measured in human cadaver TBs by Gan and Wang; however, only the TM velocity was recorded. The pressures measured during BOP exposure for the 3D printed TB and human TB are shown in Fig. 111B. Specifically, the plot compares the pressures recorded at P0 (entrance of the ear canal) and P1 (in ear canal near TM) for the printed TB and a human ear.

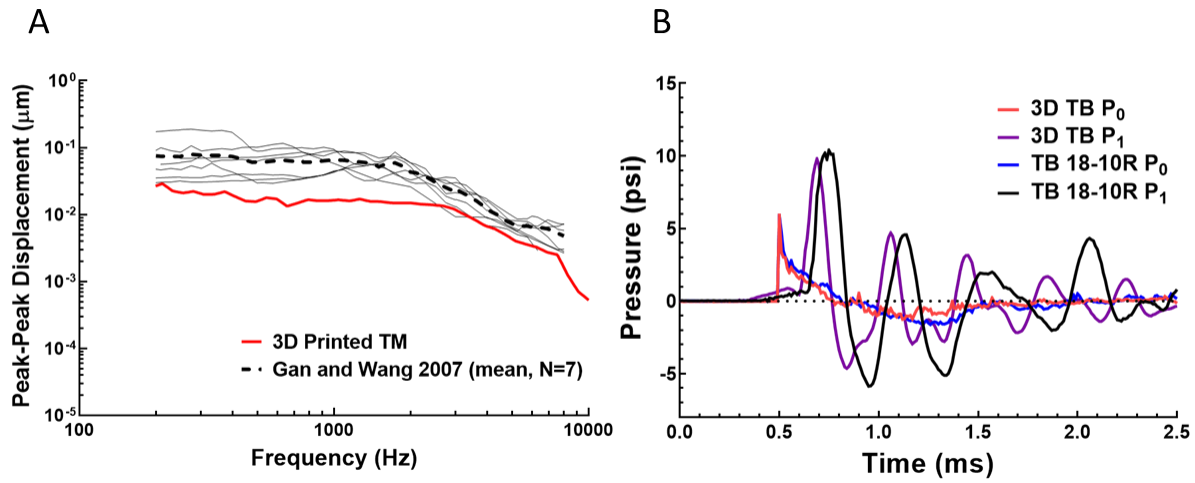


Figure 111. (A) Plot of the peak-to-peak displacement of the TM over the frequency range of 200 – 10,000 Hz for the 3D printed TB's TM (red line) and seven human TB samples (solid black lines) from Gan and Wang (2007). The average of the seven samples is plotted in the black dotted line. (B) Plot of the P0 (ear canal entrance) and P1 (in the ear canal near the TM) pressures measured in blast tests of the 3D printed TB (red line for P0 and green line for P1) and a human cadaveric TB (blue line for P0 and black line for P1) without hearing protection.

In conclusion, a 3D printed TB was created for the purpose of providing standardized testing of HPDs to blast exposure. Two HPDs (standard foam earplug and Lyric hearing aid) were included for testing the protective function with the 3D printed TB during blast (see Section (1-3)). Results show that the pressure measurements in the 3D printed TB were well within the mean and standard deviation of the published data from tests performed in human cadaveric TBs demonstrating that our 3D printed TB is a valid model for testing HPD designs. The 3D printed TB developed in this study provides an accurate and cost-effective evaluation for HPDs' protective function against BOP exposure with the potential to perform as a TB model for research in ear biomechanics for acoustic transmission.

- **What opportunities for training and professional development has the project provided?**

Nothing to Report

- **How were the results disseminated to communities of interest?**

Nothing to Report

- **What do you plan to do during the next reporting period to accomplish the goals?**

Nothing to Report

4. IMPACT

- **What was the impact on the development of the principal discipline(s) of the project?**

The accomplishments of this project for biomechanical modeling and measurement of blast injury have great impacts to understanding the hearing damage induced by blast exposure at various aspects in relation to the blast overpressure and the protection mechanisms of HPDs to blast-induced hearing injury. The major impacts are listed below:

1) The relationships between the ear injury and the intensity or direction of blast waves, the transfer functions of the ear canal and middle ear to blast overpressure, the middle ear muscle reflex to blast exposure, and the changes of ear tissues' mechanical properties caused by blast have been identified through the experiments in human ears and the animal model of chinchilla.

2) It is the first time that the movements of the TM and stapes footplate under blast exposure are measured by the dual-laser setup. The stapes footplate movement data can be directly used to determine the blast energy entering the cochlea, a significant step toward quantifying the cochlear hair cell damage or PAS injury in relation to blast exposure. The TM and stapes footplate movement data are also critical for validating the FE model of the human ear and understanding the middle ear damage induced by blast.

3) The 4-Case study in chinchillas is a novel investigation to separate the blast-induced damage in the PAS and CAS with the corresponding protective device to the PAS and CAS, respectively. Comparison between Case 2 and Case 3 reflects the CAS damage or the helmet protection; comparison between Case 3 and Case 4 indicates the PAS damage or the earplug protection on hearing threshold.

4) Hearing damage in relation to the number of blast exposures at an equivalent level to the mild TBI and the hearing damage after repetitive exposure to the low BOP level measured in chinchillas provide important information about permanent hearing damage in relation to the intensity of BOP, number of blast exposures, and time course after exposure. Our results demonstrate that HPDs can mitigate the hearing damage and help the recovery, but the effectiveness depends on the BOP intensity or TBI severity and the number of blast exposures.

5) The 3D FE model or 3D Biomechanical model of the entire human ear has been developed and validated. The model can predict the blast overpressure transmission from the ear canal to the middle ear and cochlea. The distributions of stress and strain or deformation of the TM and middle ear ossicular chain, the TM rupture in relation to blast waveform, the cochlear pressure distribution from the base to apex, and the cochlear basilar membrane movement can be derived from the model under blast exposure condition. It has also been demonstrated that the 3D FE model can be used for assisting the HPD design and function evaluation.

6) Characterization of HPDs' protective function to blast exposure through experiments in human cadaver ears, animal ears, and the 3D printed human ear or temporal bone, and the simulation in FE model is a major outcome from this research project. The standard criteria for HPDs design and evaluation based on nonlinear FE model of the human ear and biomechanics of tissue injury after blast exposure can be delivered.

- **What was the impact on other disciplines?**

Nothing to Report

- **What was the impact on technology transfer?**

The animal blast model (chinchilla) has resulted in the patent application entitled: "Uses of glucagon-like peptide-1 receptor agonists for treating trauma-induced hearing loss". The Final DD882, "Report of Inventions and Subcontracts", has been submitted.

- **What was the impact on society beyond science and technology?**

Nothing to Report

5. CHANGES/PROBLEMS

- **Changes in approach and reasons for change**

No significant changes in approach.

- **Actual or anticipated problems or delays and actions or plans to resolve them**

No significant problems and delays.

- **Changes that had a significant impact on expenditures**

No changes in expenditures.

- **Significant changes in use or care of human subjects, vertebrate animals, biohazards, and/or select agents**

Animal study protocol R17-015 at OU was renewed on March 4, 2020 as protocol R20-006. This new protocol R20-006 was submitted to USAMRMC ACURO on March 4, 2020 and approved by ACURO on April 23, 2020.

6. PRODUCTS

• publications, conference papers, and presentations;
• website(s) or other Internet site(s);
• technologies or techniques;
• inventions, patent applications, and/or licenses; and
• other products.

- **Publications, conference papers, and presentations**

A. <u>Peer-Reviewed Journal Papers</u> (Acknowledgement of Federal/DoD Grant Support – Yes for all)

1. Brown, M., Jiang, S. and **Gan, R. Z.** A 3D printed human ear model for standardized testing of hearing protection devices to blast exposure (In Submission)

2. Jiang, S., Dai, C. and **Gan, R. Z.** Dual-laser measurement of human stapes footplate motion under blast exposure. *Hearing Research*, 2020A (Under 2nd Review)

3. Jiang, S. Welch, P., Smith, K., and **Gan, R. Z.** Auditory dysfunction induced by repeated low intensity blast exposures in a chinchilla model. *Hearing Research*, 2020B (In Resubmission)

4. Shao, N., Jiang, S., Younger, D., Chen, T., Brown, M., Rama Rao, K. V., Skotak, M., **Gan, R. Z.**, and Chandra, N. Central and Peripheral Auditory Abnormalities in Chinchilla Animal Model of Blast-Injury. *Hearing Research*, 2020 (Under Review)

5. Brown, M., Ji, X. D. and **Gan, R. Z.** 3D finite element modeling of blast wave transmission from the external ear to cochlea. *Annals of Biomedical Engineering*, 2020 (In Press) DOI: 10.1007/s10439-020-02612-y

6. Jiang, S., Gannon, A., Smith, K., Liang, J., Brown, M., and **Gan, R. Z.** Prevention of blast-induced auditory injury using 3D printed helmet and hearing protection device – A preliminary study on biomechanical modeling and animal. *Military Medicine*, 2020C (In Press)

7. Liang, J., Nakmali, D., **Gan, R. Z.**, Lu, H., and Dai, C. Investigating the geometry and mechanical properties of human round window membranes using micro-fringe projection. *Otology & Neurotology*, 2020 (In Press)

8. Smith, K., Chen, T., and **Gan, R. Z.** Hearing damage induced by blast overpressure at the mild TBI level in a chinchilla model. *Military Medicine*, Vol. 185: 248-255, 2020. https://doi.org/10.1093/milmed/usz309

9. Liang, J., Smith, K., **Gan, R. Z.**, and Lu, H. Effect of blast overpressure on mechanical properties of human tympanic membrane. *J. Mech. Behavior Biomed Materials*, Vol. 100 (103368): pp. 1-9, 2019.

10. **Gan, R. Z.** and Jiang, S. Surface motion change of tympanic membrane damaged by blast waves. *J. Biomechanical Engineering*, Vol. 141: 091009-1 to -11, 2019A.

11. Luo, H., Wang, F., Cheng, C., Nakmali, D., Dai, C., Wei, L., **Gan, R. Z.**, and Lu, H. Measurement of the through-thickness Young's modulus of a human tympanic membrane by nanoindentation. *Hearing Research*, Vol. 378: 75-91, 2019.

12. Chen, T., Smith, K., Jiang, S., Zhang, T., and **Gan, R. Z.** Progressive hearing damage after repeated exposure to low level of blast overpressure in chinchillas. *Hearing Research*, Vol. 378: 33-42, 2019.

13. Jiang, S., Smith, K., and **Gan, R. Z.** Dual-laser measurement and finite element modeling of human tympanic membrane motion under blast exposure. *Hearing Research*, Vol. 378: 43-52, 2019.

14. **Gan, R. Z.**, Leckness, K., Smith, K., and Ji, X. D. Characterization of protection mechanisms to blast overpressure for personal hearing protection devices – Biomechanical measurement and computational modeling. *Military Medicine*, Vol. 184, 3/4: 251-260, 2019B.

15. Jiang S., and **Gan, R. Z.** Dynamic properties of human incudostapedial joint measured with frequency-temperature superposition. *Medical Engineering & Physics*, Vol. 54: 14-21, 2018.

16. **Gan, R. Z.**, Leckness, K., Nakmali, D., and Ji, X. D. Biomechanical measurement and modeling of human eardrum injury in relation to blast wave direction. *Military Medicine*, Vol. 183, 3/4: 245-251, 2018A.

17. Leckness, K., Nakmali, D., and **Gan, R. Z.** Computational modeling of blast wave transmission through human ear. *Military Medicine*, Vol. 183, 3/4: 262-268, 2018.

18. **Gan, R. Z.** Biomechanical changes of tympanic membrane to blast waves. In: Molecular, Cellular and Tissue Engineering of the Vascular System. Bingmei Fu and Neil Wright (Eds). Springer, pp. 321-334, 2018B.

19. Liang, J., Yokell, Z., Nakmali, D., **Gan, R. Z.**, and Lu, H. The effect of blast overpressure on the mechanical properties of a chinchilla tympanic membrane. *Hearing Research*, Vol. 354: 48-55, 2017.

20. Engles, W. G., Wang, X., and **Gan, R. Z.** Dynamic properties of human tympanic membrane after exposure to blast waves. *Annals of Biomedical Engineering*, Vol. 45 (10): 2383–2394, 2017.

21. Hu, X., Xu, T., Luo, H., **Gan, R. Z.**, and Lu, H. Measurement of thickness and profile of a transparent material using fluorescent stereo microscopy. *Optics Express*, Vol. 24 (26): 29822-29829, 2016.

22. **Gan, R. Z.**, Nakmali, D., Ji, X. D., Leckness, K., and Yokell, Z. Mechanical damage of tympanic membrane in relation to impulse pressure waveform – A study in chinchillas. *Hearing Research*, Vol. 340: 25-34, 2016.

23. Liang, J., Luo, H., Yokell, Z., Nakmali, D., **Gan, R. Z.**, and Lu, H. Characterization of the nonlinear elastic behavior of chinchilla tympanic membrane using micro-fringe projection and finite element simulation. *Hearing Research*, Vol. 339: 1-11, 2016.

24. Wang, X. and **Gan, R. Z.** 3D finite element model of the chinchilla ear for characterizing middle ear functions. *Biomechanics and Modeling in Mechanobiology*, Vol. 15 (5): 1263-1277, 2016.

25. Luo, H., Jiang, S., Nakmali, D., **Gan, R. Z.**, and Lu, H. Mechanical properties of a human eardrum at high strain rates after exposure to blast waves. *J. Dynamic Behavior of Materials*, Vol. 2: 59-73, 2016.

26. Hawa, T. and **Gan, R. Z.** Pressure distribution in a simplified human ear model for the high intensity sound transmission. *ASME J. Fluids Engineering*, Vol. 136: 111108-1 to -6, 2014.

B. <u>Dissertations/Theses</u> (Acknowledgement of Federal/DoD Grant Support – Yes for all)

<u>Ph.D. Dissertations and M.S. Theses</u>:

1. **Marcus Brow**: 3D Computational Modeling of Blast Wave Transmission through the Ear and Protection Mechanism. **Ph.D.** Dissertation at University of Oklahoma, May 2021.

2. **Zachary Yokell**: Electromyographic Measurement of the Chinchilla Middle Ear Muscle Reflex Elicited by Acoustic or Blast Stimuli. **Ph.D.** Dissertation at University of Oklahoma, May 2019.

3. **Shangyuan Jiang**: Mechanical Properties of Human Incudostapedial Joint and Tympanic Membrane in Normal and Blast-damaged Ears. **Ph.D.** Dissertation at University of Oklahoma, May 2018.

4. **Paige Welch**: Measurement and 3D Finite Element Modeling of Blast Wave Transmission through Chinchilla Ear. **M.S.** Thesis at University of Oklahoma, May 2020.

5. **Warren Engles**: Changes of Mechanical Properties of Tympanic Membrane after Blast Exposure. **M.S.** Thesis at University of Oklahoma, May 2017.

6. **Leckness Kegan**: Novel finite element method to predict blast wave transmission through human ear. **M.S.** Thesis at University of Oklahoma, August 2016.

C. <u>Conference Papers (National and International Conferences)</u> (Acknowledgement of Federal/DoD Grant Support – Yes for all)

1. **Gan, R. Z.**, Sanders, S., Welch, P., and Jiang, S. Mitigation of hearing damage after blast exposure in animal model of chinchilla. *Association for Research in Otolaryngology (ARO) - Midwinter Meeting (Virtual)*, February 20-24, 2021.
2. Jiang, S., Welch, P., Sanders, S., Smith, K., and **Gan, R. Z.** Liraglutide, a glucagon-like peptide-1 receptor agonist, mitigates the blast-induced hearing damage in chinchillas. *Association for Research in Otolaryngology (ARO) - Midwinter Meeting (Virtual)*, February 20-24, 2021.
3. Brown, M., Bradshaw, J. J., and **Gan, R. Z.** 3D finite element modeling of blast wave transmission from the external ear to a spiral cochlea. *Association for Research in Otolaryngology (ARO) - Midwinter Meeting (Virtual)*, February 20-24, 2021.
4. **Gan, R. Z.**, Welch, P., Sanders, S., and Jiang, S. Therapeutic function of liraglutide for mitigation of hearing damage after blast exposures in animal model of chinchilla with or without hearing protection devices. *Proceedings of the Biomedical Engineering Society 2020 Annual Meeting*, San Diego, CA, October 14-17, 2020. (Virtual Meeting due to COVID-19 pandemic)
5. **Gan, R. Z.**, Welch, P., Sanders, S., and Jiang, S. Hearing function restoration with liraglutide treatment after repeated low-intensity blast exposures in an animal model of chinchilla. *DoD 2020 Military Health System Research Symposium (MHSRS)*, Kissimmee, FL, August 2020. (Meeting was canceled due to COVID-19, but the abstract was posted online)
6. **Gan, R. Z.**, Jiang, S., Smith, K., and Dai, C. Dual-laser measurement of stapes footplate movement in human ears with and without hearing protection device (HPD) under blast exposure. *Association for Research in Otolaryngology (ARO) - Midwinter Meeting*, San Jose, CA, January 25-29, 2020.
7. Jiang, S., Smith, K. Liang, J., Wang, X., Gannon, A., Brown, M., and **Gan, R. Z.** A novel chinchilla model of blast-induced auditory injury for hearing damage prediction and prevention using 3D printed "helmet" and earplug. *Association for Research in Otolaryngology (ARO) - Midwinter Meeting*, San Jose, CA, January 25-29, 2020.
8. **Gan, R. Z.**, Jiang, S., Smith, K. and Dai, C. Measurement of middle ear ossicular motion under blast exposure with laser Doppler vibrometry. *Proceedings of the Biomedical Engineering Society 2019 Annual Meeting*, Philadelphia, PA, October 16-19, 2019.
9. Brown, M. and **Gan, R. Z.** Modeling the auditory nerve response during blast exposure. *Proceedings of the Biomedical Engineering Society 2019 Annual Meeting*, Philadelphia, PA, October 16-19, 2019.
10. Welch, P., Brown, M., Wang, X. and **Gan, R. Z.** 3D Finite element modeling of blast wave transmission through chinchilla ear. *Proceedings of the Biomedical Engineering Society 2019 Annual Meeting*, Philadelphia, PA, October 16-19, 2019.
11. **Gan, R. Z.**, Smith, K., Liang, J., Gannon, A., Brown, M., and Jiang, S. Prediction and prevention of blast-induced auditory injury using 3D-printed chinchilla "helmet" and hearing protection devices**.** *DoD 2019 Military Health System Research Symposium (MHSRS)*, Kissimmee, FL, August 17-22, 2019.
12. **Gan, R. Z.**, Smith, K., Chen, T., and Jiang, S. Mitigation of auditory damage after blast exposure with glucagon-like peptide-1 (GLP-1) – A study in chinchilla. *Association for*

Research in Otolaryngology (ARO) - Midwinter Meeting, Baltimore, MD, February 9-13, 2019.

13. Brown, M., Ji, X., and **Gan, R. Z. 3D finite element modeling of blast wave transmission from the external ear to the cochlea**. *Association for Research in Otolaryngology (ARO) - Midwinter Meeting*, Baltimore, MD, February 9-13, 2019.
14. Welch, P., Smith, K., Brown, M., and **Gan, R. Z. 3-D finite element model of the chinchilla ear for modeling sound transmission from ear canal to cochlea.** *Association for Research in Otolaryngology (ARO) - Midwinter Meeting*, Baltimore, MD, February 9-13, 2019.
15. **Gan, R. Z.**, Chen, T., Smith, K., and Jiang, S. Therapeutic function of glucagon-like peptide-1 (GLP-1) for hearing restoration after blast exposure. *Proceedings of the Biomedical Engineering Society 2018 Annual Meeting*, Atlanta, Georgia, October 17-20, 2018.
16. Brown, M., Jiang, S., and **Gan, R. Z.** A 3D printed ear model for standardized testing of hearing protection devices to blast exposure. *Proceedings of the Biomedical Engineering Society 2018 Annual Meeting*, Atlanta, Georgia, October 17-20, 2018.
17. **Gan, R. Z.**, Chen, T., and Smith, K. Hearing damage induced by blast Overpressure at the mild TBI level in a chinchilla model. *DoD 2018 Military Health System Research Symposium (MHSRS)*, Kissimmee, FL, August 20-23, 2018.
18. Chandra, N., Shao, N., Rama Rao, K. V., Jiang, S., Chen, T., Brown, M., and **Gan, R. Z.** Central and peripheral auditory abnormalities in animal models of blast-injury. *DoD 2018 Military Health System Research Symposium (MHSRS)*, Kissimmee, FL, August 20-23, 2018.
19. **Gan, R. Z.**, Jiang, S., and Smith, K. Dual-laser measurement and finite element modeling of human tympanic membrane motion under blast exposure. *8th International Symposium on Middle Ear Mechanics in Research and Otology (MEMRO)*, Shanghai, China, July 5 – 9, 2018.
20. Chandra, N., Shao, N., Rama Rao, K. V., Jiang, S., Chen, T., Brown, M., and **Gan, R. Z.** Central and peripheral auditory injuries in animal models after blast exposure. *8th International Symposium on Middle Ear Mechanics in Research and Otology (MEMRO)*, Shanghai, China, July 5 – 9, 2018.
21. Chen, T., Smith, K., Jiang, S., Zhang, T., and **Gan, R. Z.** Progressive Hearing Damage after Repeated Exposure to Low Level of Blast Overpressure in Chinchillas. *8th International Symposium on Middle Ear Mechanics in Research and Otology (MEMRO)*, Shanghai, China, July 5 – 9, 2018.
22. Lu, H., Lou, H., Wang, F., Cheng, Chen, Nakmali, D., Dai, C., Wei, Li, and **Gan, R. Z.** Measurement of the through-thickness Young's modulus of a human tympanic membrane by nanoindentation. *8th International Symposium on Middle Ear Mechanics in Research and Otology (MEMRO)*, Shanghai, China, July 5 – 9, 2018.
23. **Gan, R. Z.**, Chen, T., Smith, K., Jiang, S., Yokell, Z., Tsai Do, B., and Jyung, R. An animal model of cholesteatoma for improvement of middle ear surgical reconstruction. *Association for Research in Otolaryngology (ARO) - Midwinter Meeting*, San Diego, CA, February 10-14, 2018.
24. Brown, M., Chen, T., and **Gan, R. Z.** SEM Imaging of Cochlear Hair Cell Damage Caused by Blast Exposure. *Association for Research in Otolaryngology (ARO) - Midwinter Meeting*, San Diego, CA, February 10-14, 2018.

25. Chen, T., Smith, K., and **Gan, R. Z.** Progressive Hearing Damage after Exposure to Multiple Blasts in Chinchillas. *Association for Research in Otolaryngology (ARO) - Midwinter Meeting*, San Diego, CA, February 10-14, 2018.
26. Liang, J., **Gan, R. Z.**, and Lu, H. Measurement of the viscoelastic properties of the chinchilla tympanic membrane. Soc. Exp. Mech., IMAC Conference, Greenville, South Carolina, February 2018.
27. **Gan, R. Z.**, Chen, T., Smith, K., and Yokell, Z. Hearing damage caused by multiple blast exposure – A study on middle ear and cochlea function changes in chinchillas. *Proceedings of the Biomedical Engineering Society 2017 Annual Meeting*, Phoenix, Arizona, October 11-14, 2017.
28. Jiang, S., Smith, K., and **Gan, R. Z.** Movement of human tympanic membrane under blast exposure measured by laser Doppler vibrometer. *Proceedings of the Biomedical Engineering Society 2017 Annual Meeting*, Phoenix, Arizona, October 11-14, 2017.
29. Brown, M., Ji, X., and **Gan, R. Z.** 3D Finite element modeling of blast wave transmission from the external ear to the cochlea. *Proceedings of the Biomedical Engineering Society 2017 Annual Meeting*, Phoenix, Arizona, October 11-14, 2017.
30. **Gan, R. Z.**, Leckness, K., Smith, K., and Ji, X. D. Characterization of protection mechanisms to blast overpressure for personal hearing protection devices – Biomechanical measurement and computational modeling. *DoD 2017 Military Health System Research Symposium (MHSRS)*, Kissimmee, FL, August 27-30, 2017.
31. **Gan, R. Z.**, Jiang, S., and Pineda, M. Age-dependent full-field motion of baboon tympanic membrane. *The 13th International Workshop on the Mechanics of Hearing*, Brock University, Ontario, Canada, June 19-24, 2017.
32. **Gan, R. Z.**, Leckness, K., and Nakmali, D. 3D computational modeling of blast wave transmission through the ear. *Association for Research in Otolaryngology (ARO) - Midwinter Meeting*, Baltimore, MD, February 11-15, 2017.
33. Yokell, Z., Nakmali, D., and **Gan, R. Z.** Switch of MEMR and ABR thresholds after high intensity sound exposure in chinchillas. *Association for Research in Otolaryngology (ARO) - Midwinter Meeting*, Baltimore, MD, February 11-15, 2017.
34. Jiang, S., Wang, X., Nakmali, D., and **Gan, R. Z.** Measurement of surface motion of human tympanic membrane after blast exposure. *Association for Research in Otolaryngology (ARO) - Midwinter Meeting*, Baltimore, MD, February 11-15, 2017.
35. Hu, Z., Liang, J., **Gan, R. Z.**, and Lu, H. Characterization of the mechanical behavior of tympanic membranes after exposure to blast waves using fluorescent micro-stereo digital image correlation (#68645). *Int. Mechanical Engineering Congress & Exposition (IMECE)*, Phoenix, AZ, Nov. 11-17, 2016.
36. Lu, H., Liang, J., Nakmali, D., **Gan, R. Z.**, and Luo, H. High-speed deformation of chinchilla tympanic membrane under blast wave. Paper #145, *17th International Conference on Experimental Mechanics (ICEM17)*, Rhodes, Greece, July 3-7, 2016.
37. **Gan, R. Z.**, Nakmali, D., and Leckness, K. Evaluation of hearing protection devices to blast exposure using human temporal bone and 3D ear model. *Proceedings of the Biomedical Engineering Society 2016 Annual Meeting*, Minneapolis, MN, October 5-8, 2016.
38. Engles, W., Nakmali, D., Smith, K., and **Gan, R. Z.** Mechanical properties of baboon tympanic membrane measured with DMA system. *Proceedings of the Biomedical Engineering Society 2016 Annual Meeting*, Minneapolis, MN, October 5-8, 2016.

39. Jiang, S., Luo, H., Lu, H., and **Gan, R. Z.** Mechanical properties of incudostapedial joint at high strain rate measured by SHTB. *Proceedings of the Biomedical Engineering Society 2016 Annual Meeting*, Minneapolis, MN, October 5-8, 2016.
40. Yokell, Z., Nakmali, D., and **Gan, R. Z.** Impact of high intensity noise exposure on stapedius muscle function in chinchillas. *Proceedings of the Biomedical Engineering Society 2016 Annual Meeting*, Minneapolis, MN, October 5-8, 2016.
41. **Gan, R. Z.**, Nakmali, D., and Leckness, K. Biomechanical measurement and modeling of human eardrum injury in relation to blast wave direction. *DoD 2016 Military Health System Research Symposium (MHSRS)*, Kissimmee, FL, August 15-18, 2016.
42. **Gan, R. Z.**, Nakmali, D., Smith, K., Leckness, K., and Yokell Z. Tympanic membrane damage induced by blast overpressure – A study in head block attached with human temporal bones. *Association for Research in Otolaryngology (ARO) - Midwinter Meeting*, Vol. 39: PD 154, San Diego, CA, February 20-24, 2016.
43. Wang, X., Hitt, B., and **Gan, R. Z.** Correlation of ABR, TM displacement and wideband energy absorbance in otitis media model of chinchilla. *Association for Research in Otolaryngology (ARO) - Midwinter Meeting*, Vol. 39: PS 602, San Diego, CA, February 20-24, 2016.
44. Jiang, S., Nakmali, D., and **Gan, R. Z.** Dynamic properties of human incudostapedial joint measured with frequency-temperature superposition. *Proceedings of the Biomedical Engineering Society 2015 Annual Meeting*, Tampa, FL, October 7-10, 2015.
45. Wang, X., and **Gan, R. Z.** Finite element modeling of the middle ear muscle effect on sound transmission from the ear canal to cochlea. *Proceedings of the Biomedical Engineering Society 2015 Annual Meeting*, Tampa, FL, October 7-10, 2015.
46. Yokell, Z., Nakmali, D., and **Gan, R. Z.** Electromyography (EMG) measurement of blast-induced chinchilla middle ear muscle reflex. *Proceedings of the Biomedical Engineering Society 2015 Annual Meeting*, Tampa, FL, October 7-10, 2015.
47. Leckness, K., Wang, X., and **Gan, R. Z.** Simulation of high intensity pressure transduction in human ear model. *Proceedings of the Biomedical Engineering Society 2015 Annual Meeting*, Tampa, FL, October 7-10, 2015.
48. **Gan, R. Z.**, Nakmali, D., Ji, X. D., and Yokell Z. Mechanical damage of tympanic membrane in relation to impulse pressure waveform – A study in chinchillas. *7th International Symposium on Middle Ear Mechanics in Research and Otology (MEMRO)*, Aalborg, Denmark, July 1 – 5, 2015.

D. <u>Unpublished Conference Papers and Presentations</u> (Acknowledgement of Federal/DoD Grant Support – Yes for all)

<u>Conference Papers/Presentations</u>:

1. Brown, M., Jiang, S., and **Gan, R. Z.** A 3D printed ear model for standardized testing of hearing protection devices to blast exposure. *39st Oklahoma AIAA/ASME Symposium*, April 6, 2019.

2. Gannon, A., Smith, K., Jiang, S., Brown, M., and **Gan, R. Z.** Helmet design for chinchilla head towards reduction of brain damage to blast overpressure. *39st Oklahoma AIAA/ASME Symposium*, April 6, 2019.
3. Jiang, S., Wang, X., and **Gan, R. Z.** Experimental measurement and finite element simulation on surface motion of human tympanic membrane after blast exposure. *39st Oklahoma AIAA/ASME Symposium*, April 6, 2019.
4. Engles, W., Wang, X., and **Gan, R. Z.** Dynamic properties of human tympanic membrane exposed to high intensity sound exposure. *36st Oklahoma AIAA/ASME Symposium*, April 16, 2016.
5. Leckness, K., Nakmali, D., and **Gan, R. Z.** High intensity pressure transduction in human ear model. *36st Oklahoma AIAA/ASME Symposium*, April 16, 2016.
6. Smith, K., Wang, X., and **Gan, R. Z.** Development of a 3-dimensional finite element model of chinchilla cochlea. *36st Oklahoma AIAA/ASME Symposium*, April 16, 2016.
7. Yokell, Z., Nakmali, D., and **Gan, R. Z.** Impact of high intensity noise exposure on chinchilla hearing. *36st Oklahoma AIAA/ASME Symposium*, April 16, 2016.

Invited Seminar or Keynote Speech:

1. **Gan, R. Z.,** Invited Speaker at The City College of New York, BME Department on October 28, 2020. Title of the seminar: "Biomechanical Measurement and Modeling of Blast Wave Transmission through the Ear".
2. **Gan, R. Z.,** Invited Speaker at Columbia University BME Breaks on July 24, 2020. Title of the seminar: "Measurement and Modeling of Blast-Induced Auditory Injury in Animal Model of Chinchilla".
3. **Gan, R. Z.,** Invited Keynote Speaker at 2019 International Conference on Biomedical Technology (ICBT), Hannover, Germany, November 18, 2019. Title of the keynote: "Computational Modeling and Biomechanical Measurement of Blast Wave Transmission through the Ear".

PARTICIPANTS & OTHER COLLABORATING ORGANIZATIONS

- **What individuals have worked on the project?**

Provide the name and identify the role the person played in the project. Indicate the nearest whole person month (Calendar, Academic, Summer) that the individual worked on the project. Show the most senior role in which the person worked on the project for any significant length of time. For example, if an undergraduate student graduated, entered graduate school, and continued to work on the project, show that person as a graduate student, preferably explaining the change in involvement.
Describe how this person contributed to the project and with what funding support. If information is unchanged from a previous submission, provide the name only and indicate "no change".

Name: Rong Gan, Ph.D.
Project Role: PI
Researcher Identifier (OU ID): 112129499

Nearest person month worked: 3
Contribution to Project: No change

Name: Xiao Ji, Ph.D.
Project Role: Research Associate
Researcher Identifier (OU ID): 112902618
Nearest person month worked: 3
Contribution to Project: No change

Name: Shangyuan Jiang, Ph.D.
Project Role: Research Scientist
Researcher Identifier (OU ID): 112979369
Nearest person month worked: 3
Contribution to Project: No change

Name: Marcus Brown
Project Role: Ph.D. Student
Researcher Identifier (OU ID): 113383397
Nearest person month worked: 2
Contribution to Project: No change

Name: Kyle Smith
Project Role: Research Technician
Researcher Identifier (OU ID): 112831425
Nearest person month worked: 2
Contribution to Project: No change

Name: Chenkai Dai, M.D., Ph.D.
Project Role: Associate Professor
Researcher Identifier (OU ID): 112148756
Nearest person month worked: 1
Contribution to Project: Dr. Dai has worked on surgery and experiment in human temporal bones with dual-laser setup for blast test.

Name: Junfeng Liang, Ph.D.
Project Role: Research Associate
Researcher Identifier (OU ID): 112792782
Nearest person month worked: 1
Contribution to Project: Dr. Liang has worked on Micro-fringe projection measurement on ear tissue testing.

Name: Paige Welch
Project Role: MS Student
Researcher Identifier (OU ID):

Nearest person month worked: 2
Contribution to Project: Paige has worked on the 3D FE model of the chinchilla ear and chinchilla experiment

Name: Ariana Gannon
Project Role: Undergraduate Student
Researcher Identifier (OU ID):
Nearest person month worked: 2
Contribution to Project: Ariana has worked on chinchilla helmet design and FE modeling

Name: Sarah Sanders
Project Role: Senior/MS Student
Researcher Identifier (OU ID):
Nearest person month worked: 2
Contribution to Project: Sarah has worked on the chinchilla experiment and data analysis.

Name: Jackson Bradshaw
Project Role: Undergraduate Student
Researcher Identifier (OU ID):
Nearest person month worked: 2
Contribution to Project: Jackson has worked on FE modeling of the spiral cochlea.

Name: Hongbing Lu, Ph.D.
Project Role: PI at UTD (subcontract)
Researcher Identifier (UTD ID): 2011733939
Nearest person month worked: 2
Contribution to Project: No change

- **Has there been a change in the active other support of the PD/PI(s) or senior/key personnel since the last reporting period?**

Nothing to Report.

- **What other organizations were involved as partners?**

Nothing to Report.

7. SPECIAL REPORTING REQUIREMENTS

QUAD CHARTS: The Quad Chart (available on https://www.usamraa.army.mil) shall be updated and submitted as an appendix.

A Quad Chart is submitted as an appendix.

8. APPENDICES

- **Quad Chart**
- **Copies of 21 Published Journal Articles**

Biomechanical Modeling and Measurement of Blast Injury and Hearing Protection Mechanisms

ERMS# 13063031 Task Title: Measuring and modeling of blast wave transduction through the ear canal

Award Number: W81XWH-14-1-0228

PI: Rong Z. Gan, Ph.D. **Org:** University of Oklahoma **Award Amount:** $2,521,486

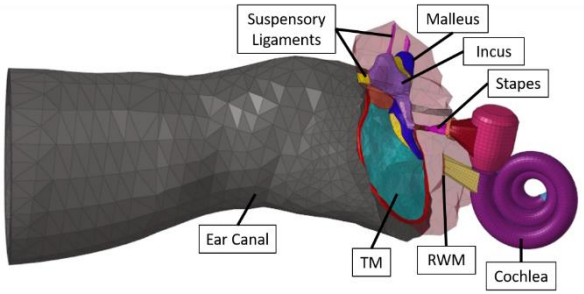
Study/Product Aim(s)

- Quantify middle ear injury in relation to blast pressure level and wave direction and overpressure transduction through the ear
- Identify middle ear protection mechanisms by detecting middle ear muscle reflex and measuring mechanical changes of ear tissues
- Develop the FE model of human ear to predict unwarned and warned responses of the middle ear to blast exposure

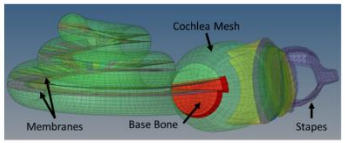
Approach

- Identify blast-induced eardrum and middle ear damage and the blast pressure transmission through the ear with multiple sensors inserted in cadaver ears
- Detect the acoustic reflex on EMG of middle ear stapedius muscle
- Measure mechanical properties of ear tissues after blast exposure
- Conduct nonlinear FE analysis on 3D FE model of the human ear – passive and active ear models in CFX/ANSYS
- Simulate the HPDs in FE model to derive prevention mechanisms

3D FE model of human ear: ear canal, middle ear, and spiral cochlea



Cochlea with 3 chambers



Accomplishment: 1) Dual-laser measurement of eardrum and stapes footplate motion during blast exposure; 2) changes of ear tissues in microstructure and mechanical properties after blast exposure; 3) chinchilla blast model for measuring middle ear muscle active function and hearing damage in relation to blast number and intensity; 4) protection mechanisms of HPDs identified in human ears, chinchillas, and FE models; 5) 3D FE model of the entire ear with spiral cochlea for modeling blast wave transduction through the ear and injury prediction.

Timeline and Cost

Activities / CY	15	16	17	18
Tasks 1-1 and 1-2 (Blast injury)				
Task 2-1 (Acoustic reflex-EMG)				
Task 2-2 (Tissue mechanics)				
Tasks 3-1, 3-2, and 3-3 (FE modeling of blast injury)				
Estimated Budget ($K)	**$619**	**$623**	**$641**	**$638**

Updated: December 28, 2020

Goals/Milestones

CY15 Goals – Establish measurement and modeling of blast overpressure

- ☑ Identify eardrum/middle ear damage thresholds and setup EMG measurement and tissue mechanical testing
- ☑ Building passive FE model of the ear for analysis of blast wave

CY16 Goals – Characterization of middle ear function

- ☐ Investigate ear canal/middle ear transfer function and muscle function
- ☐ Continue tissue mechanical testing and validate the passive FE model

CY17 Goals – Middle ear protection mechanisms and active model

- ☐ Complete muscle function test and continue tissue mechanical tests
- ☐ Develop active FE model of the model for blast wave analysis

CY18 Goals – Validate active FE model with applications

- ☐ Complete nonlinear active model and ear tissue testing
- ☐ Evaluate HPDs in FE model of the ear for hearing protection

Comments/Challenges/Issues/Concerns

- EMG measurement in animals and blast test in cadaver ears began.

Budget Expenditure to Date

Projected Expenditure: $2,521,486.30

Actual Expenditure: $2,521,486.30

3D Finite Element Modeling of Blast Wave Transmission from the External Ear to Cochlea

Marcus A. Brown, Xiao D. Ji & Rong Z. Gan



Annals of Biomedical Engineering
The Journal of the Biomedical Engineering Society

ISSN 0090-6964

Ann Biomed Eng
DOI 10.1007/s10439-020-02612-y

Springer

Your article is protected by copyright and all rights are held exclusively by Biomedical Engineering Society. This e-offprint is for personal use only and shall not be self-archived in electronic repositories. If you wish to self-archive your article, please use the accepted manuscript version for posting on your own website. You may further deposit the accepted manuscript version in any repository, provided it is only made publicly available 12 months after official publication or later and provided acknowledgement is given to the original source of publication and a link is inserted to the published article on Springer's website. The link must be accompanied by the following text: "The final publication is available at link.springer.com".



Author's personal copy

Annals of Biomedical Engineering (© 2020)
https://doi.org/10.1007/s10439-020-02612-y

BMES BIOMEDICAL ENGINEERING SOCIETY

Original Article

3D Finite Element Modeling of Blast Wave Transmission from the External Ear to Cochlea

MARCUS A. BROWN,[1] XIAO D. JI,[1] and RONG Z. GAN[1,2]

[1]School of Aerospace and Mechanical Engineering, University of Oklahoma, Norman, OK, USA; and [2]School of Aerospace and Mechanical Engineering, University of Oklahoma, 865 Asp Avenue, Room 200, Norman, OK 73019, USA

(*Received 3 June 2020; accepted 2 September 2020*)

Associate Editor Estefanía Peña oversaw the review of this article.

Abstract—As an organ that is sensitive to pressure changes, the ear is often damaged when a person is subjected to blast exposures resulting in hearing loss due to tissue damage in the middle ear and cochlea. While observation of middle ear damage is non-invasive, examining the damage to the cochlea is difficult to quantify. Previous works have modeled the cochlear response often when subjected to an acoustic pressure input, but the inner ear mechanics have rarely been studied when the ear is exposed to a blast wave. In this study we aim to develop a finite element (FE) model of the entire ear, particularly the cochlea, for predicting the blast wave transmission from the ear canal to cochlea. We utilized a FE model of the ear, which includes the ear canal, middle ear, and uncoiled two-chambered cochlea, to simulate the cochlear response to blast overpressure (BOP) at the entrance of the ear canal with ANSYS Mechanical and Fluent in a fluid–structure interface coupled analysis in the time domain. This model was developed based on previous middle and inner ear models, and the cochlea was remeshed to improve BOP simulation performance. The FE model was validated using experimentally measured blast pressure transduction from the ear canal to the middle ear and cochlea in human cadaveric temporal bones. Results from the FE model showed significant displacements of the tympanic membrane, middle ear ossicles, and basilar membrane (BM). The stapes footplate displacement was observed to be as high as 60 μm, far exceeding the displacement during normal acoustic stimulation, when the 30 kPa (4.35 psi, 183 dB (SPL), Sound Pressure Level) of BOP was applied at the ear canal entrance. The large stapes movement caused pressures in the cochlea to exceed the physiological pressure level [$<$ 10 Pa, 120 dB (SPL)] at a peak of 49.9 kPa, and the BM displacement was on the order of microns with a maximum displacement of 26.4 μm. The FE model of the entire human ear developed in this study provides a computational tool for prediction of blast wave transmission from the ear canal to cochlea and the future applications for assisting the prevention, diagnosis, and treatment of blast-induced hearing loss.

Keywords—Finite element model, Ear, Blast overpressure, Cochlear pressure, Basilar membrane.

INTRODUCTION

Blast-induced injuries affect the health and quality of life for veterans in the US.[18,22] Due to its exceptional sensitivity to air pressure changes, the ear is susceptible to damage during blast exposure, and consequently, an increasing number of veterans experience hearing loss after suffering blasts during deployment to recent conflicts.[1,4,21] Exposure to blast overpressure (BOP) can cause perforations in the tympanic membrane (TM) and dislocation of the ossicular chain, which are simply diagnosed through otoscopic examination.[4,9] Being far more difficult to observe, blast damage to the inner ear results in cochlear synaptopathy and hair cell loss.[1,17]

Experimental studies in human cadaveric temporal bones (TBs) have shown that exposure to BOP results in complex responses, but fewer experiments have analyzed the response of the ear during blast.[10,13,15] Blast exposure produces high pressures within a very short period of time in the ear canal and results in large movements of the TM, middle ear ossicles, and cochlea basilar membrane (BM) at values exceeding their displacements during normal sound stimulation.[12,13,15] Gan *et al.*[9] observed amplifications of blast pressure as the BOP wave travels through the ear canal to the TM and analyzed the resulting perforations and stresses in the TM. Similar results were repeated in a later study

Address correspondence to Rong Z. Gan, School of Aerospace and Mechanical Engineering, University of Oklahoma, 865 Asp Avenue, Room 200, Norman, OK 73019, USA. Electronic mail: rgan@ou.edu

© 2020 Biomedical Engineering Society

Published online: 14 September 2020

Author's personal copy

by Greene *et al.*[13] where they further studied the elevated pressures in the cochlea during blast wave exposure. Such high pressures applied to the TM would undoubtedly cause damage to the TM during its intense movement, and recent research has shown that the TM does displace substantial more during blast exposure and its surface motion was altered from the suffered damage.[8,15] While the ossicular chain's movement has yet to be reported during blast, elevated stapes displacement and cochlear pressure have been reported during exposure to intense low frequency tones as high as 170 dB SPL.[14] Extreme stapes movement and intracochlear pressure would damage the BM within the cochlea, however neither experimental results nor measurement methods have been reported for the BM motion during blast exposure.[14] Accurately detecting BM motion during stimulation requires sensitive measurements in a well-controlled environment, and for this reason, observing the BM during blast exposure is not yet possible and alternative approaches must be utilized.[20]

Models of the ear have been utilized to investigate the response of the ear to sound and more recently, to analyze blast wave transmission throughout the ear.[2,11,16,19] Leckness *et al.*[16] developed a three-dimensional (3D) finite element (FE) model of the human ear to simulate the transmission of a BOP from the ear canal to the middle ear based on a previous FE model for normal sound transmission by Gan *et al.*[7] Using experimentally measured blast waveforms in human TBs, the results from Leckness *et al.*'s FE model reflected the pressures observed throughout the ear, and the stress distribution within the TM was calculated from the model and was comparable to blast damage seen in otoscopic examination of the TM.[9,16] Other numerical models of the ear have been developed to analyze the response of the ear during blast exposure, such as the Auditory Hazard Assessment Algorithm for Humans (AHAAH) model by Price,[19] that attempts to quantify a threshold for sustained hearing loss based on an input pressure wave and BM displacement.[2] Despite the recent advancements in blast modelling of the ear, current models either lack the ability to model the cochlea and the BM or cannot analyze the ear's 3D response to BOPs limiting the available results and utility.[2]

In the present article, we report a recent study on development of a 3D FE model of the entire human ear to simulate the transmission of BOP from the ear canal through the middle ear and into the cochlea overcoming the one-dimensional and knowledge limitations of previous models. This model was based on the FE model created by Gan *et al.*,[11] consisting of the external ear, middle ear, and uncoiled two-chambered cochlea. The middle ear model was extended by Leckness *et al.*[16] for simulation of blast wave transduction from the ear canal to middle ear with the cochlear load applied at the stapes footplate. In the present study, the cochlea model was added to the middle ear and FE modeling of the BOP wave transduction through the entire ear, outer ear, middle ear, and cochlea, was completed.

The FE model was validated with the experimental data obtained in human TBs which includes the pressure near the TM in the ear canal and the displacement of the TM when the experimentally measured blast pressure was applied at the ear canal entrance in the model. The displacements of the middle ear ossicles (e.g., stapes footplate) and cochlea BM and the intracochlear pressures were derived from the model. With this newly developed FE model of the entire human ear we aim to provide a computational tool for prediction of blast wave transmission from the ear canal to the cochlea and for future applications for assisting the prevention, diagnosis, and treatment of blast-induced hearing loss.

MATERIALS AND METHODS

FE Model of the Human Ear

The FE model of the entire human ear was created based on the models reported by Leckness *et al.*[16] and Gan *et al.*[11] for the middle ear and the cochlea, respectively. Both middle ear and cochlear models were originally built from histological cross-sectional images of a human TB (left ear, 55 year-old, male),[7] and the resulting geometries were originally meshed in Hypermesh 13 (Altair Engineering, Inc., Troy, MI). In this study, the ear canal and middle ear from Leckness *et al.*[16] was connected to the cochlea at the stapes footplate (SFP) and round window membrane (RWM) from Gan *et al.*[11] The cochlea was remeshed in tetrahedral elements with Hypermesh 13 to improve the performance of the elements for transient, high deformation analysis in the time domain.

Figure 1a illustrates the entire ear model consisting of the meshed ear canal, middle ear, and cochlea. The middle ear model (Fig. 1b) consists of the ossicles and their suspensory ligaments and tendons, pars flaccida and pars tensa of the TM, TM annulus (TMA), manubrium, incudomallear and incudostapedial joints (IMJ and ISJ respectively), stapedial annular ligament (SAL), and middle ear cavity. The two-chambered cochlea model shown in Figs. 1a and 1c includes the cochlear fluid in the scala vestibuli (SV) above the BM and the scala tympani (ST) below the BM connected by a helicotrema at the apex of the cochlea. The BM was supported with two supports (spiral lamina and

Author's personal copy

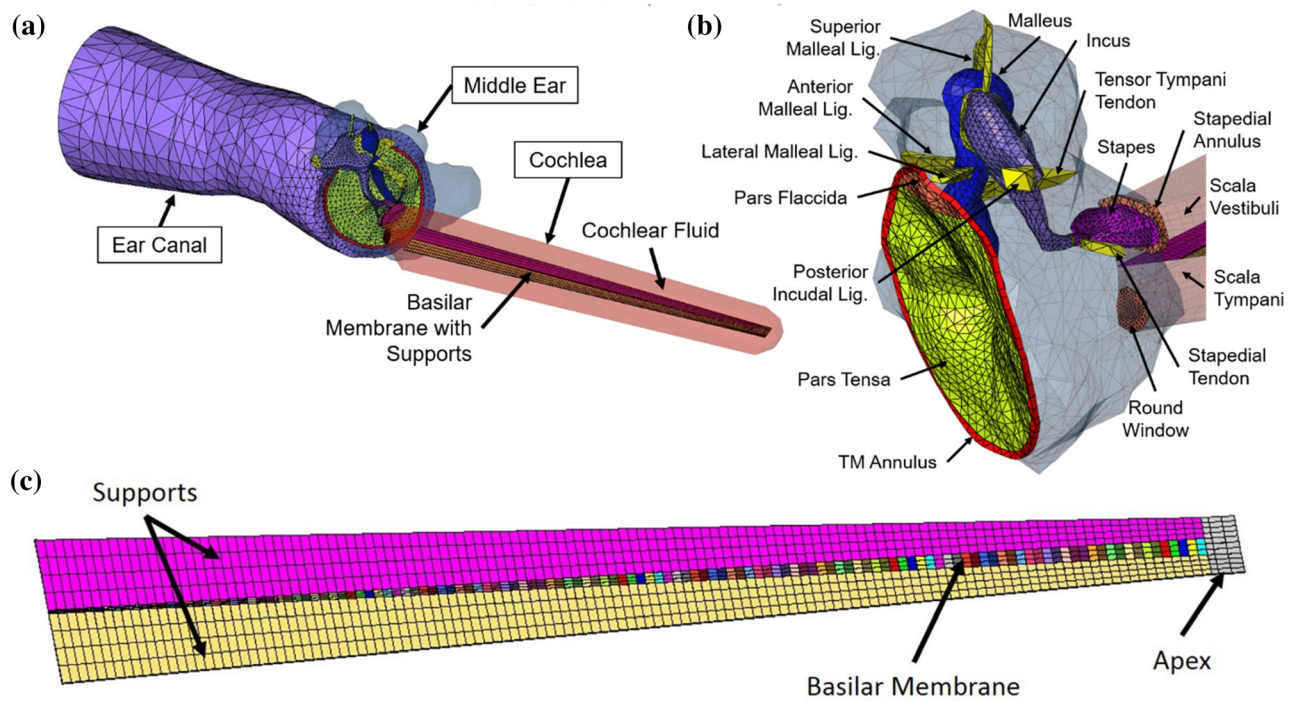


FIGURE 1. (a) FE model of the human ear with the ear canal, middle ear, and two-chambered cochlea. (b) Structural mesh of the middle ear with the TM, TMA, middle ear ossicles, SAL, round window membrane, and suspensory ligaments and muscle tendons. (c) The cochlea's BM mesh surrounded by two supports and the cochlea's bony apex

spiral ligament) and a bony ledge at the helicotrema or apex separating the SV and ST fluid chambers (Fig. 1c). The BM was 32 mm in length and separated into 128 portions with varying material properties. The resulting meshes for the ear canal, middle ear, and cochlea contained 16,482, 20,139, and 182,484 elements, respectively.

Material Properties of Structural Components and Boundary Conditions

The material properties and boundary conditions used for the structural components of the ear canal and middle ear were similar to those stated by Leckness *et al.*[16] In short, the standard linear viscoelastic model[6] in ANSYS (ANSYS Inc., Canonsburg, PA) was assigned to the TM, TMA, IMJ, ISJ, SAL, and RWM of all middle ear soft tissues with the Prony shear relaxation modulus:

$$G(t) = G_0\left[\alpha_\infty^{\mathrm{G}} + \alpha_1^{\mathrm{G}} e^{-t/\tau_1}\right], \ [\mathrm{MPa}], \qquad (1)$$

where G_0 is the shear relaxation modulus at $t = 0$, $\alpha_\infty^{\mathrm{G}}$ is the relative long-term modulus, α_1^G and τ_1 are the first-order relative modulus and relaxation time, respectively. The material properties reported in Table 1 of Zhang and Gan[23] were used to determine the values in Eq. (1) by converting the stated Young's modulus (E) into shear modulus (G):

$$E = 2G(1 + \nu), \ [\mathrm{MPa}] \qquad (2)$$

where ν is the Poisson's ratio of the material. The ossicles, suspensory ligaments and tendons, and manubrium were modeled as isotropic elastic materials as reported by Gan *et al.*,[11] and the ear canal skin (shown in Fig. 1a) was modeled as an isotropic elastic material with a Young's modulus of 0.42 MPa, density of 1050 kg/m^3, and a Poisson's ratio of 0.43. The skin of the ear canal, TMA, RWM, SAL, and suspensory ligaments and tendons that meet the bony wall of the ear were set to fixed boundary conditions.

Material properties of the structural components of the cochlea, including the BM, two supports (spiral lamina and spiral ligament), and a bony support at the apex (Fig. 1c), and their boundary conditions were assigned the same values as those reported by Gan *et al.*[11] With a length of 32 mm, the BM was separated into 128 sections along its length with the material properties varying per section. As in Gan *et al.*,[11] the Young's modulus changed linearly per section along the BM's length from 50 MPa at the base to 15 MPa in the middle to 3 MPa at the apex with a density and Poisson's ratio of 1200 kg/m^3 and 0.3, respectively. The β damping of the BM changed linearly from

Author's personal copy

2.0×10^{-3} s at the base to 1.0×10^{-2} s at the apex. The width and thickness of the BM elements changed linearly from 100 and 7.5 μm, respectively, at the base to 500 and 2.5 μm, respectively, at the apex, and the BM's mesh included 384 eight-node hexahedral elements, three elements per section. The spiral lamina and apex bony supports were assumed to have a Young's modulus of 14.1 GPa, density of 1200 kg/m^3, Poisson's ratio of 0.3, and β damping of 1.0×10^{-4} s, and the spiral ligament was assigned similar properties except with a Young's modulus of 5 MPa and a density of 1000 kg/m^3. All the BM support structures were fixed in place to give the BM a fixed boundary condition along its edges.

Fluid Properties and Boundary Conditions

The fluid properties and boundary conditions of the fluid domains in the human FE model were similar to the assigned properties in Leckness *et al.*[16] and Gan *et al.*[11]; however, the cochlea fluid domain was modeled in the ANSYS Fluent rather than ANSYS Mechanical APDL as in Gan *et al.*[11] The air fluid domains of the model (ear canal and middle ear cavity) were assigned as a compressible, ideal gas at sea level, and the ambient air pressure was set to that of sea level (101,325 Pa). The perilymphatic fluid inside the cochlea was assigned an initial density of 998.2 kg/m^3 and a viscosity of 1.003×10^{-3} kg/m-s. Fluid–structure interfaces (FSIs) were designated to the inner surface of the ear canal, medial and lateral surfaces of the TM, SFP, cochlea and middle ear cavity facing surfaces of the RWM, and SV and ST facing surfaces of the BM. All remaining walls were assigned as stationary, rigid walls. All walls of the fluid domains were defined with a no-slip boundary condition.

FE Analysis

The FE analysis for the model was setup within ANSYS Workbench v19.1 where ANSYS Mechanical and Fluent calculated the structural and fluid dynamics, respectively, and transferred the forces and displacements of the FSIs through a coupled analysis. The blast simulation was performed as a nonlinear, transient simulation with a time step size of 1 μs at a total signal length of 20 ms. Both ANSYS Mechanical and Fluent were set to calculate the large deformations of the FSIs that occur during blast exposure. Furthermore, the deforming fluid domains implemented a remeshing and smoothing function to ensure high mesh quality during simulations.

Experimental pressure waveforms, collected from cadaveric TB blast tests,[15] were used as the input BOP waveform at the entrance of the ear canal (P0). Figure 2a shows the first 2 ms of the experimentally measured P0 pressure waveform used as input for the FE model with a peak pressure of 30.7 kPa (4.45 psi),

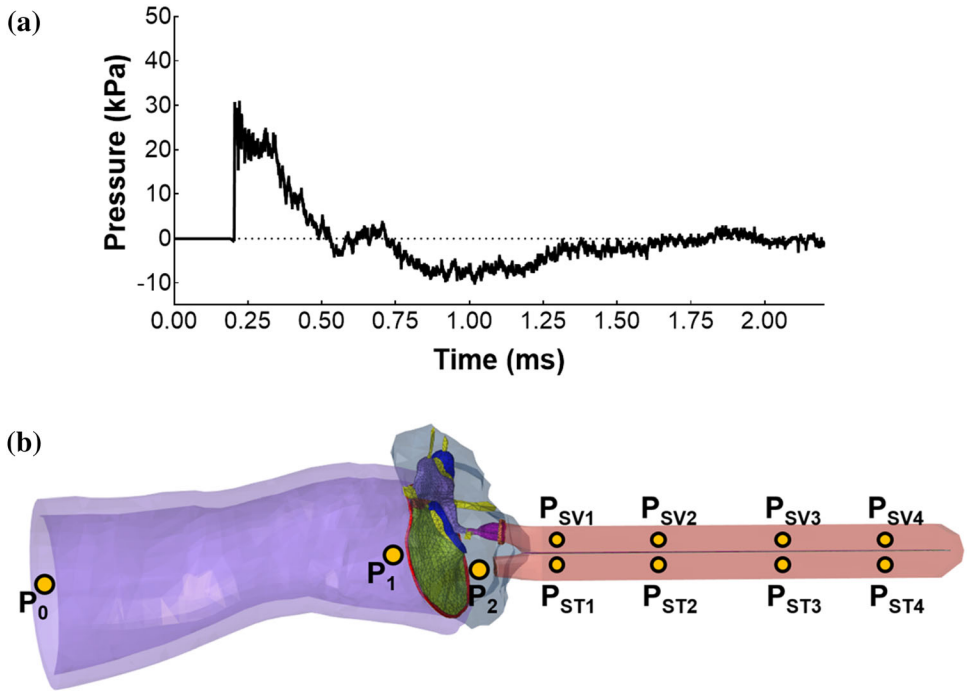


FIGURE 2. (a) Experimentally measured BOP used as input for the FE model at P0. (b) Input location for BOP at entrance of ear canal, P0, and locations in FE model monitored for pressure during simulations: P1, P2, P_{SV1}–P_{SV4}, and P_{ST1}–P_{ST4}

Author's personal copy

and Fig. 2b illustrates the location of P0 where the model's input was applied and the locations of other pressures being experimentally measured or calculated from the model. Various locations throughout the model were calculated for pressure to track the blast wave transmission in the ear. As shown in Fig. 2b, these locations were near the TM in the ear canal P1, behind the TM in the middle ear cavity P2, and four points in both the SV and ST along the BM from the base to the apex labeled as P_{SV1}–P_{SV4} and P_{ST1}–P_{ST4}, respectively. Additional model derived results include the displacements of the TM, SFP and BM.

Experimental Blast Test with Cadaveric Temporal Bones

The methods used for collecting experimental pressure waveforms in this study were extensively described by Jiang *et al.*[15] and Leckness *et al.*[16] In short, fresh human cadaver TB with no observable ear damage had a pressure sensor (Model 105C002, PCB Piezotronics, Depew, NY) surgically inserted into the ear canal near the TM (P1). The TB was mounted to a "head block" and placed under the blast apparatus designed for open-field blasts within an anechoic chamber. The P0 pressure sensor (Model 102B16, PCB Piezotronics, Depew, NY) was mounted 1 cm lateral to the entrance of the ear canal. The BOP was generated by bursting a polycarbonate film (McMaster-Carr, Atlanta, GA) with compressed nitrogen gas. Diagram and detailed description of the experimental setup can be viewed in Jiang *et al.*[15] The pressure sensor measurements were recorded and synchronized by a data acquisition system using a cDAQ 7194, A/D converter 9215 (National Instruments Inc., Austin, TX), and LabVIEW Signal Express software (National Instruments Inc., Austin, TX).

Model Validation with Experimental Results

The P1 pressure waveforms derived from the model were compared with that recorded from the experiments to validate the FE model. Similar to Leckness *et al.*,[16] the peak pressure level, P1:P0 peak pressure ratio, and A-duration were used to analyze and compare the P1 waveform's intensity and peak wave shape. The A-duration is defined as the measure of time (in ms) the positive portion of the peak pressure is sustained, and the B-duration is the time interval between the BOP peak pressure and the last value within 20 dB of the peak. The percent error was used to compare the P1:P0 ratio and P1 A-duration between the experiment and model data. Following an FFT analysis of the monitored pressures, the power density spectra normalized to the sampling frequency of 1 MHz and pressure gain (referenced to P0) of the experimental and model-derived pressure waveforms were calculated to observe their frequency behavior. A pressure waveform duration of 20 ms, sampled at 1 MHz, was used for these calculations. The model's TM movement was compared to experimental data recorded by Jiang *et al.*[15] during blast, and other results were compared to published data where available.

We propose to use *auditory risk units* (ARUs) to predict if an exposure to a BOP waveform will incur inner ear or cochlea injury. ARU is a summation of the squared upward displacement over time at various points along the length of the BM during blast exposure. For each location along the basilar membrane, the number of ARUs can be presented as:

$$\mathrm{ARU} = \sum d_i^2, \left[\mu\mathrm{m}^2\right], \tag{3}$$

where d_i is the displacement of the BM at the ith location.

RESULTS

Figures 3a and 3b present the pressure waveforms recorded in a TB blast test and calculated from the FE model, respectively. The P0 waveform had an A-duration of 0.307 ms and a B-duration of 9.792 ms. With a peak pressure of 30.7 kPa for P0, the peak pressures for P1 were 59.0 and 58.6 kPa for the model and TB blast test, respectively, resulting in very close peak pressure ratios, P1:P0, of 1.92 from the model and 1.91 from the experiment with an extremely low percent error of 0.7%. Both model and experimental P1 pressure waveforms exhibited similar A-durations of 0.16 and 0.175 ms (8.6% error), respectively as shown in Fig. 3c. It should be noted that P0 was measured at 1 cm from the ear canal entrance, while the FE model applied the P0 input pressure on the inlet face of the ear canal. While sound pressure travels at the speed of sound, the air velocity and pressure generated from blasts delay with increased distance.[3] Our blast chamber is designed for open-field blast tests which is subject to this phenomenon. This gave the model a faster time of arrival for the peak pressure at P1 than that shown in experimental blast tests. Despite the different time of arrival, the model-predicted P1 waveform agrees well with the experimental waveform. P2 (in the middle ear cavity) was not measured during the blast tests as conducted in Jiang *et al.*[15] so only the model-derived P2 pressure is shown in Fig. 3b. The model derived P2 waveform in Fig. 3b exhibits a reduction of peak pressure and has a peak pressure of 9.7 kPa much lower than P1 peak pressure of 59.0 kPa. Furthermore, the addition of the cochlea in

Author's personal copy

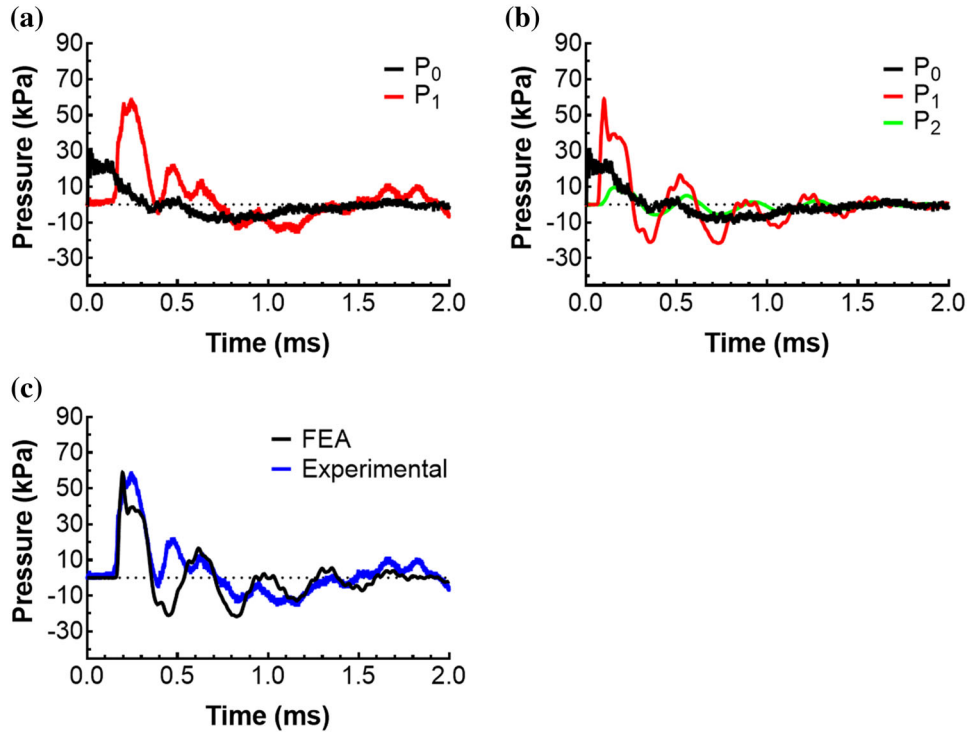


FIGURE 3. (a) Experimental measures of P0 and P1 during BOP. (b) The FE model's simulated pressures for P1 and P2 with P0 as input. (c) Comparison between FE model and experimental pressures of P1

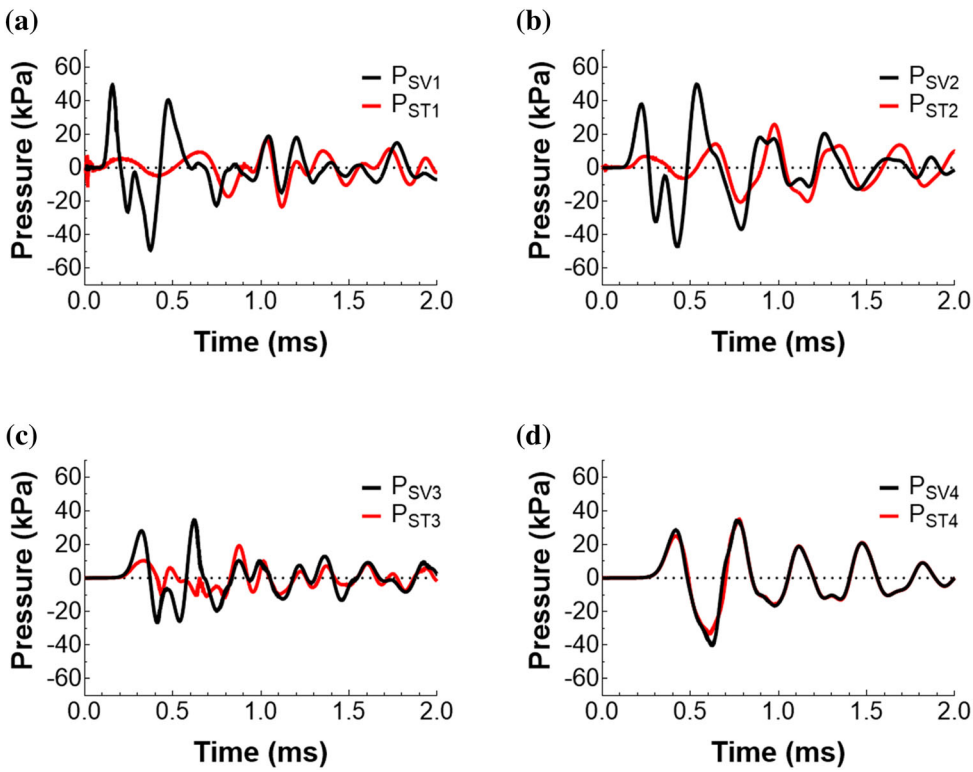


FIGURE 4. Pressures along the cochlea from base to apex during blast exposure. Pressures monitored in the scala vestibuli (P_{SV}) and scala tympani (P_{ST}) at 0.25, 7.5, 20.0, and 28.75 mm from the base of the cochlea (a, b, c, and d, respectively)

Author's personal copy

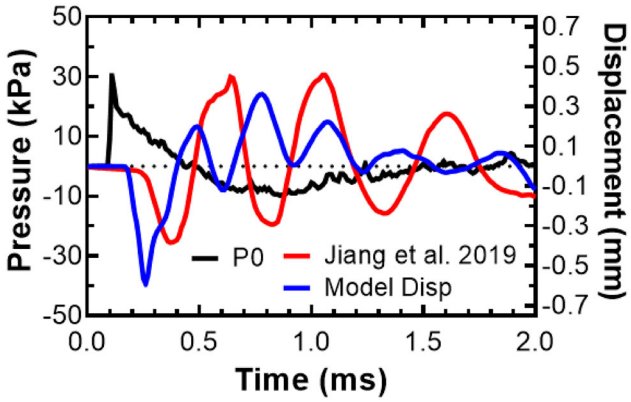


FIGURE 5. Comparison of the TM movement between the FE model (blue) and Jiang *et al.*'s[15] experimental data (red). The simulation used the BOP waveform from the published data as the input pressure at P0 (black)

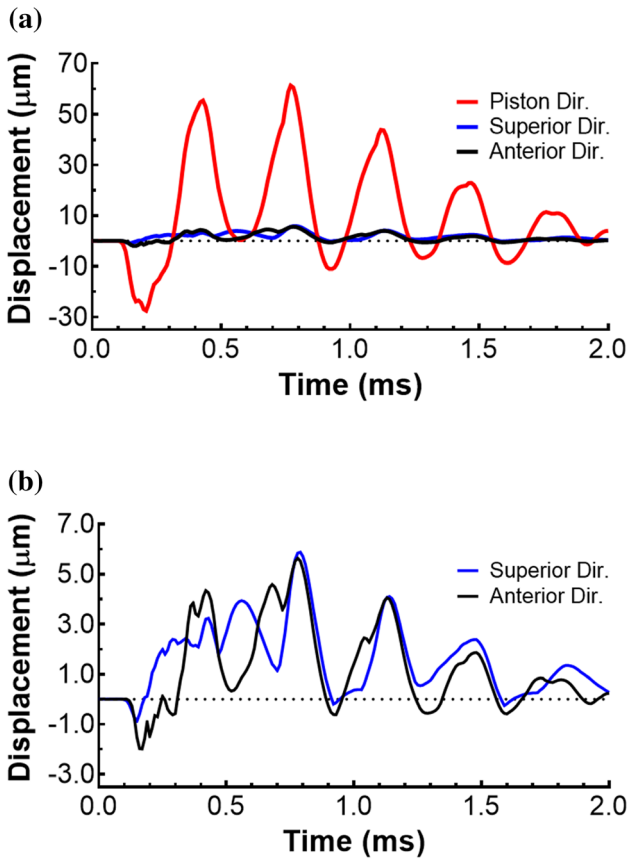


FIGURE 6. (a) Model-derived stapes displacement in the piston, superior/inferior, and anterior/posterior directions from BOP exposure. (b) Model-derived stapes displacement in the superior/inferior, and anterior/posterior directions, emphasizing the difference in magnitude between the stapes' piston and rocking movements

the current model did not exhibit an obvious change to middle ear pressure when compared to previous models.[10,16]

The cochlear pressures derived from the model in the SV and ST at 4 locations from the base to apex: 0.25, 7.5, 20.0, and 28.75 mm, are shown in Fig. 4. A maximum peak pressure of P_{SV1}, P_{SV2}, P_{SV3}, and P_{SV4} were observed to be 49.5, 49.9, 34.4, and 40.1 kPa from the base to apex (black lines), respectively. In the ST (red lines), there was an increase in the maximum pressures from P_{ST1} to P_{ST2}, a decrease at P_{ST3}, and an increase at P_{ST4} with values of 16.6, 26.0, 19.4, and

Author's personal copy

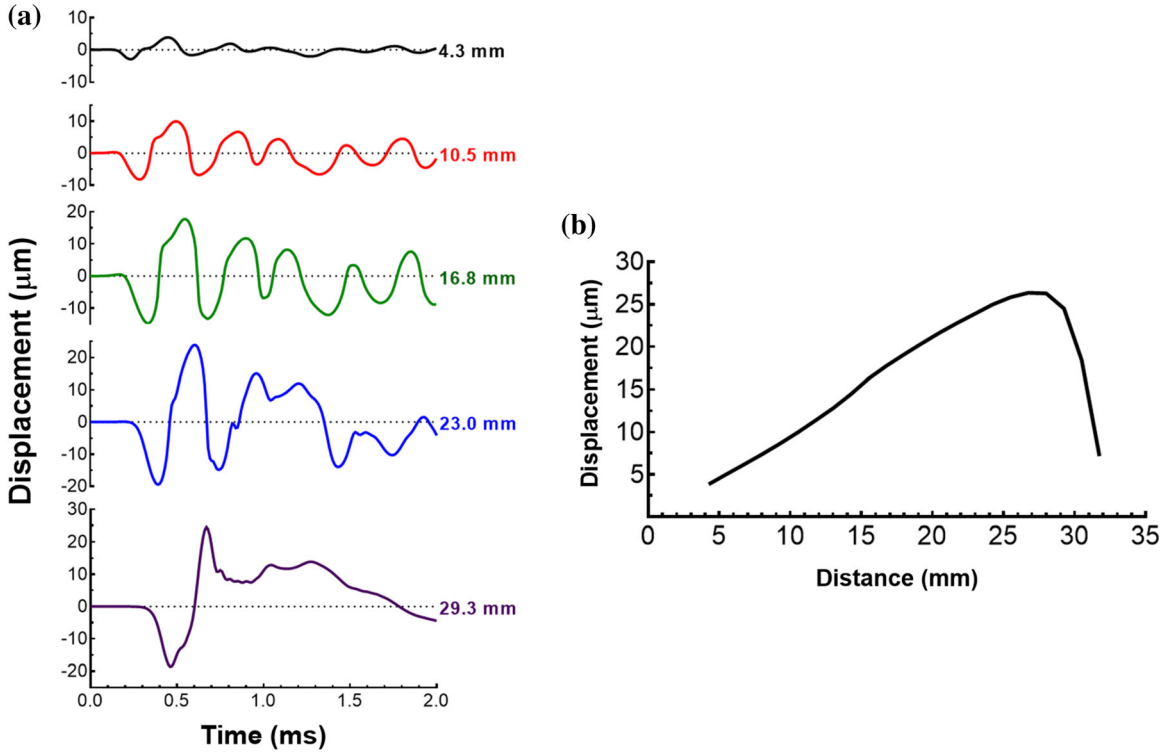


FIGURE 7. (a) Model-derived displacements of the BM at 4.3, 10.5, 16.8, 23.0, and 29.3 mm from the base of the cochlea. (b) Maximum displacement of the calculated BM along its length. Only the displacement upwards into the scala vestibuli normal to the plane of the BM is included in (b)

35.0 kPa, respectively, which were all lower than the corresponding pressure at the SV. The highest positive pressure in the cochlea of 49.9 kPa was observed at P_{SV2} (Fig. 4b) at 0.436 ms after the peak pressure occurred at P1 (0.101 ms). The greatest negative pressure occurred at the base (P_{SV1}) with a value of − 49.2 kPa at time point 0.374 ms (Fig. 4a, P_{SV1}), 0.273 ms after P1 peak pressure. It was also observed that the pressures in the SV and ST trended closer together as the pressure waves transmitted to the apex where the SV and ST pressures differed as much as 50.1 kPa closer to the base (Fig. 4b) then exhibited an insignificant pressure difference at the apex (Fig. 4d).

The TM movement from the FE model over 2 ms is shown in Fig. 5 (blue line) with the experimental data of the TM movement during blast from Jiang *et al.*[15] (red line). The P0 pressure waveform with peak pressure of 30.2 kPa or 4.4 psi (black line) from Jiang *et al.* was used as input to the model. From Fig. 5, the TM peak-to-peak displacement predicted from the model was 0.79 mm and the experimental data measured from a TB was 0.84 mm. The FE model stayed within 10% of the measured peak-to-peak displacement. With P0 peak pressure occurring at 0.11 ms, the model-derived and experimental TM peak displacements happened at 0.26 and 0.37 ms, respectively, resulting in a difference of 0.11 ms between the model and experimental TM displacement delays after the P0 peak pressure. This was expected since the model's time of arrival for the peak pressure at P1 consistently occurs before the experimental P1 peak pressure.

Figure 6 displays the model-derived displacement of the SFP over 2 ms along three directions: the piston, anterior, and superior directions. The piston direction is defined as perpendicular to the footplate plane. As shown in Fig. 6a, the SFP movement in the piston direction dominated the motion with the minimum displacement of − 27.5 μm and a maximum displacement of 61.3 μm, representing the movement directed into and out of the cochlea at the oval window with displacement into the cochlea being negative. The displacements along the superior and anterior directions were extremely small which relate to the rocking motion of the SFP in the planes normal to the piston direction. Despite the second maximum peak displacement having the largest value (Fig. 6a), the first maximum (55.5 μm) peak displacement had the greatest influence on the pressure fluctuations in the cochlea. The second peak occurred at 0.77 ms, but pressure magnitudes within the cochlea were subsequently lower after this time than before it (Fig. 4). As shown in Fig. 6b, the displacements in the superior and

Author's personal copy

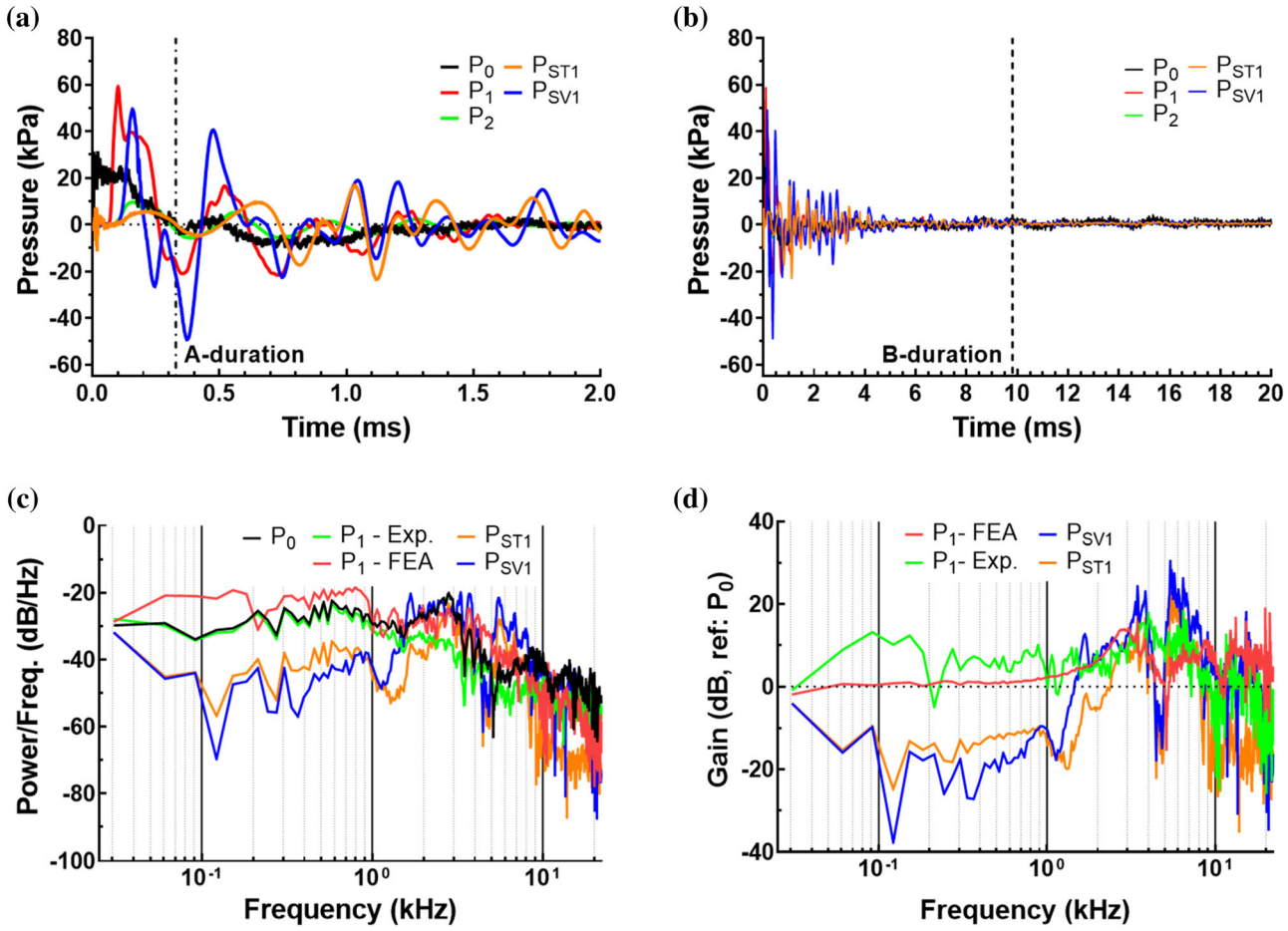


FIGURE 8. (a) The simulated pressures of P0, P1, P2, P_{SV1}, and P_{ST1} over 2 ms. The A-duration of the input pressure, P0, is marked at time 0.33 ms. (b) The simulated pressures of P0, P1, P2, P_{SV1}, and P_{ST1} over 20 ms. The B-duration of the input pressure, P0, is marked at time 9.81 ms. (c) The pressure frequency spectra of the P0, P1, P2, P_{SV1}, and P_{ST1} pressure waveforms over 20 ms. (d) Gain of P1, P2, P_{SV1}, and P_{ST1} over the frequency range with respect to P0

anterior directions were at least a magnitude lower than that in the piston direction, and despite these displacements being much lower, displacements in all directions were far greater than the maximum displacement of the SFP under normal conditions [typically < 0.1 μm at 90 dB (SPL)].[12]

Figure 7a shows the model-derived displacement of the BM over time at various points: 4.3 to 29.3 mm from the base of the cochlea. The BOP at the ear canal entrance resulted in an initial traveling wave in the BM that began displacing into the ST (negatively) and grew as the wave traveled toward the apex. The greatest displacement into the ST was 20.7 μm at 26.75 mm from the base (not shown in the figure). Figure 7b shows the maximum upward displacement (towards the SV) over the BM from the base to the apex, and the maximum displacement of the BM was 26.4 μm at 26.75 mm from the base. While the negative displacement of the BM had a significant magnitude, the upward movement of the BM, or Organ of Corti, is considered to cause greater damage to the cochlea's hair cells since the extreme displacements of the BM injure the hair cells' stereocilia as they collide with the tectorial membrane above the Organ of Corti overstretching their tip links.[19] From Fig. 7b, it can be seen that the middle to apex region of the cochlea experiences the greatest displacement during blast exposure.

To further illustrate how the BOP at the ear canal entrance (P0) transmitted to the TM (P1), middle ear (P2), and cochlea (P_{SV1} and P_{ST1}), all these pressure waveforms were collected in Fig. 8a over 2 ms and Fig. 8b over 20 ms. The A-duration and B-duration of input P0 waveform was marked in Figs. 8a and 8b at 0.307 and 9.792 ms, respectively. The pressure peaks for P0, P1, and P_{SV1} occurred at 0.021, 0.101, and 0.154 ms, respectively, showing the rapid transmission of the BOP through the ear. With such a short B-duration, P0 quickly dissipated and P1, P2, P_{SV1}, and P_{ST1} quickly followed that trend after 3 ms as shown in Fig. 8b. Figure 8c is the power spectral density of P0,

Author's personal copy

P1–FEA (P1 from FE analysis), P1–Exp. (P1 from experiment), P_{SV1}, and P_{ST1} normalized to the sampling frequency (1 MHz) from 0.01 to 22 kHz, and Fig. 8d plots the gain of P1-FEA, P1–Exp., P_{SV1}, and P_{ST1} with respect to P0. It was observed that most of the largest components of the pressure occurred at frequencies less than 4 kHz for P0, P1-FEA, and P1–Exp., and conversely, P_{SV1} and P_{ST1} have a much lower spectra values at low frequencies (Fig. 8c). A similar trend was seen for the gain of P_{SV1} and P_{ST1} where their gain was lower than those of P_{SV1} and P_{ST1} at frequencies less than 2 kHz; however, there were peaks in the gains of the cochlear pressures at about 3.4 kHz and 5.4 kHz that were significantly higher than the gains of the P1 pressures (Fig. 8d).

DISCUSSION

Model Comparison and Application for Predicting Blast-Induced Auditory Injuries

The ultimate goal of blast models of the human body is to accurately predict the sustained damage to the victim in order to better understand the exposure risk and to develop improved protective measures for future potential victims.[2] With this goal in mind, models have been developed to attempt a prediction of the potential hearing damage from BOP exposure.[1,2,5,16,19] The more widely known models for predicting high intensity noise or blast induced hearing injury, such as the AHAAH model, developed numerical methods to perform the function of sound transmission through the ear of animal models,[19] correlated the hearing loss observed from noise and intense pressure exposure in animal experiments to the response of the model to the same stimuli, then extrapolated the results to a human model with conversion factors.[5,19] While said models continue to improve through validation from patient data and field advancement,[19] the intrinsic nature of these models limit their versatility and the amount of provided information. The 3D FE model of the human ear developed in this study has the capability to predict the biomechanical changes of ear components from BOP exposure which directly relates to dysfunction of the middle ear and cochlea resulting in hearing damage.

The inherent properties of FE analysis allowed our model to simulate various middle ear ailments,[23] analyze the protective function of hearing protection devices,[10] and investigate the blast-induced stress and deformation responses of the ear.[9,16] An example of this model's versatility has been shown by Gan *et al.*[10] where earplug structures were added to the human ear FE model relatively easily and tested under blast condition. Furthermore, stress distribution in the TM caused by blast exposure has been reported for this model which gave insight into potential TM damage and perforation locations.[9,16]

One contribution of this study was to extend the human ear FE model's predictive power to determine the resulting hearing impairment from blast-induced damage in the cochlea. The calculated ARUs describe the cumulative property of the BM movement at each location along the BM from the base to the apex in response to high sound pressure waveforms and represent the cochlea injury criteria of our biomechanical model or FE model of the human ear. Table 1 lists the ARUs for the first 5 ms of our FE model's simulation at 23 points along the BM when the BOP waveform shown in Fig. 2a was applied at the entrance of the ear canal. With the maximum ARU of 13,452 occurring at 29.25 mm from the base (~ 0.52 kHz region of cochlea), the ARU values follow the same trend from Fig. 7b where highest values occur from the middle to near the apex of the cochlea. The ARU values together with blast exposure conditions and patient data could provide a predictive measure for sustained hearing damage when exposed to a certain BOP level.

Limitations and Future Work

There are still limitations to the FE model presented in this study. For example, the viscoelastic tissues of

TABLE 1. ARU values calculated from the FE model at various distances or frequency regions on basilar membrane from the base turn to apex of the cochlea

Distance from cochlea base (mm)	4.25	5.5	6.75	8	9.25	10.5	11.75	13	14.25	15.5	16.75	
Frequency (kHz)	11.76	10.06	8.6	7.36	6.29	5.38	4.6	3.94	3.37	2.88	2.46	
ARU	219	436	798	1347	2121	3134	4351	5745	7310	9046	10,179	
Distance from cochlea base (mm)	18	19.25	20.5	21.75	23	24.25	25.5	26.75	28	29.25	30.5	31.75
Frequency (kHz)	2.11	1.8	1.54	1.32	1.13	0.97	0.83	0.71	0.6	0.52	0.44	0.38
ARU	10,921	11,450	11,687	12,283	12,509	12,875	13,113	13,109	13,286	**13,452**	10,804	1262

Bold value indicates the max ARU value along the cochlea.

Author's personal copy

the middle ear, such as the TM, need improved material property models for high strain rate behavior which may account for the discrepancies between experimental and simulated data. For instance, Fig. 5 did show similar TM displacement peak values between the experimental and model data, but the motion of the TM after the peak pressure significantly differed thereafter. Improvement of the FE model includes developing an enhanced material model for the BM and a three-chamber spiral cochlea model. The present FE model's cochlea is a simplified, two-chambered cochlea whose BM material properties closely follow those used by Gan *et al.*[11] who modulated the material properties to have the BM function properly during acoustic stimuli.

The lack of stapes movement data and proven intracochlear pressure data during blast hinders the accuracy of the model's inner ear simulation. These two parameters are essential for determining the energy input into the cochlea. As previously mentioned, the SFP movement during blast has not been published; however, preliminary studies are ongoing to obtain this metric in human cadaveric TB, and the data will be used to improve the accuracy of the human ear FE model.

Comparing the FE model's results with a recent study by Greene *et al.*[13] shows the potential for validating the model with experimental intracochlear pressure measurements during blast. Specifically, in Fig. 8d, the gain of the SV and ST pressures were consistently lower than the gain of P1 showing a negative gain between the pressures at the TM and in the cochlea for frequencies lower than 1.4 kHz. This effect was observed experimentally by Greene *et al.*[13] as the intracochlear pressure gain diminished and was often negative as blast peak pressures increased at levels above 7 kPa; however, the gains of P_{SV} and P_{ST} were much lower in the FE model than those observed experimentally in the input peak pressure range of about 30 kPa.[13] The discrepancies between the model and published data could be due to numerous factors. The researchers used the complete head of the donor allowing bone conduction of the blast wave to the cochlea as hypothesized by the researchers.[13] The FE model only considers the blast energy transmission through the ear canal. Furthermore, the standard deviations of the intracochlear pressures measured by Greene *et al.* were quite large[13] (6.2 dB and 6.5 dB with respect to free field) for the SV and ST, respectively) revealing that more published data are still needed to further validate the current model as well as experiments whose setup resembles the modeling environment of the human ear FE model.

CONCLUSIONS

In summary, a 3D FE model of the entire human ear was developed and successfully simulated the BOP waves from the entrance of the ear canal to the cochlea. Results from the FE model showed significant displacements of the TM, middle ear ossicles, and cochlea BM. The stapes footplate displacement was observed to be as high as 60 μm, far exceeding the displacement during normal acoustic stimulation. The large stapes movement caused pressures in the cochlea to exceed the physiological pressure level (< 10 Pa) at a peak of 49.9 kPa, and the BM displacement was on the order of microns with a maximum displacement of 26.4 μm which would suggest substantial damage to the Organ of Corti during blast exposure. This study developed a tool for analyzing the pressure and BM movement within the cochlea which sets the stage for a model that predicts the potential auditory injury induced by the blast exposed victims.

ACKNOWLEDGMENTS

We would like to acknowledge Kegan Leckness for his early input into the development of the FE model. The study was supported by the Department of Defense (DOD) grant W81XWH-14-1-0228.

REFERENCES

[1]Cho, S.-I., S. S. Gao, A. Xia, R. Wang, F. T. Salles, P. D. Raphael, H. Abaya, J. Wachtel, J. Baek, D. Jacobs, M. N. Rasband, and J. S. Oghalai. Mechanisms of hearing loss after blast injury to the ear. *PLoS ONE* 8:e67618, 2013.

[2]De Paolis, A., M. Bikson, J. T. Nelson, J. A. de Ru, M. Packer, and L. Cardoso. Analytical and numerical modeling of the hearing system: advances towards the assessment of hearing damage. *Hear. Res.* 349:111–128, 2017.

[3]Dewey, J. M. The air velocity in blast waves from T.N.T. explosions. *Proc. R. Soc. London. Ser. A. Math. Phys. Sci.* 279:366–385, 1964.

[4]Dougherty, A. L., A. J. MacGregor, P. P. Han, E. Viirre, K. J. Heltemes, and M. R. Galarneau. Blast-related ear injuries among U.S. military personnel. *J. Rehabil. Res. Dev.* 50:893–904, 2013.

[5]Fedele, P. D., M. S. Binseel, J. T. Kalb, and G. R. Price. Using the Auditory Hazard Assessment Algorithm for Humans (AHAAH) With Hearing Protection Software, Release MIL-STD-1474E, 2013. http://www.arl.army.mil/arlreports/2013/ARL-TR-6748.pdf.

[6]Fung, Y. Biomechanics, 568 pp. New York, NY: Springer, 1993. https://doi.org/10.1007/978-1-4757-2257-4.

[7]Gan, R. Z., B. Feng, and Q. Sun. Three-dimensional finite element modeling of human ear for sound transmission. *Ann. Biomed. Eng.* 32:847–859, 2004.

Author's personal copy

[8]Gan, R. Z., and S. Jiang. Surface motion changes of tympanic membrane damaged by blast waves. *J. Biomech. Eng*. 2019. https://doi.org/10.1115/1.4044052.
[9]Gan, R. Z., K. Leckness, D. Nakmali, and X. D. Ji. Biomechanical measurement and modeling of human eardrum injury in relation to blast wave direction. *Mil. Med.* 183:245–251, 2018.
[10]Gan, R. Z., K. Leckness, K. Smith, and X. D. Ji. Characterization of protection mechanisms to blast overpressure for personal hearing protection devices—biomechanical measurement and computational modeling. *Mil. Med.* 184:251–260, 2019.
[11]Gan, R. Z., B. P. Reeves, and X. Wang. Modeling of sound transmission from ear canal to cochlea. *Ann. Biomed. Eng*. 35:2180–2195, 2007.
[12]Gan, R. Z., M. W. Wood, and K. J. Dormer. Human middle ear transfer function measured by double laser interferometry system. *Otol. Neurotol*. 25:423–435, 2004.
[13]Greene, N. T., M. A. Alhussaini, J. R. Easter, T. F. Argo, T. Walilko, and D. J. Tollin. Intracochlear pressure measurements during acoustic shock wave exposure. *Hear. Res*. 365:149–164, 2018.
[14]Greene, N. T., H. A. Jenkins, D. J. Tollin, and J. R. Easter. Stapes displacement and intracochlear pressure in response to very high level, low frequency sounds. *Hear. Res*. 348:16–30, 2017.
[15]Jiang, S., K. Smith, and R. Z. Gan. Dual-laser measurement and finite element modeling of human tympanic membrane motion under blast exposure. *Hear. Res*. 378:43–52, 2019.
[16]Leckness, K., D. Nakmali, and R. Z. Gan. Computational modeling of blast wave transmission through human ear. *Mil. Med.* 183:262–268, 2018.
[17]Liberman, M. C., and S. G. Kujawa. Cochlear synaptopathy in acquired sensorineural hearing loss: manifestations and mechanisms. *Hear. Res*. 349:138–147, 2017.
[18]Mathews, Z. R., and A. Koyfman. Blast injuries. *J. Emerg. Med.* 49:573–587, 2015.
[19]Price, G. R. Validation of the auditory hazard assessment algorithm for the human with impulse noise data. *J. Acoust. Soc. Am*. 122:2786, 2007.
[20]Ruggero, M. A., S. S. Narayan, A. N. Temchin, and A. Recio. Mechanical bases of frequency tuning and neural excitation at the base of the cochlea: comparison of basilar-membrane vibrations and auditory-nerve-fiber responses in chinchilla. *Proc. Natl. Acad. Sci. U. S. A*. 97:11744–11750, 2000.
[21]Tepe, V., C. Smalt, J. Nelson, T. Quatieri, and K. Pitts. Hidden hearing injury: the emerging science and military relevance of cochlear synaptopathy. *Mil. Med.* 182:e1785–e1795, 2017.
[22]Yeh, D. D., and W. P. Schecter. Primary blast injuries—an updated concise review. *World J. Surg*. 36:966–972, 2012.
[23]Zhang, X., and R. Z. Gan. Finite element modeling of energy absorbance in normal and disordered human ears. *Hear. Res*. 301:146–155, 2013.

Publisher's Note Springer Nature remains neutral with regard to jurisdictional claims in published maps and institutional affiliations.

PROOF FOR CHECKING PURPOSES ONLY

Prevention of Blast-induced Auditory Injury Using 3D Printed Helmet and Hearing Protection Device – A Preliminary Study on Biomechanical Modeling and Animal

Shangyuan Jiang PhD[*]; *Ariana N Gannon BS*[*]; *Kyle D. Smith MS*[*]; *Marcus Brown MS*[*]; *Junfeng Liang PhD*[*]; *Rong Z. Gan PhD*[*]

ABSTRACT

Introduction:

Repeated blast exposures result in structural damage to the peripheral auditory system (PAS) and the central auditory system (CAS). However, it is difficult to differentiate injuries between two distinct pathways: the mechanical damage in the PAS caused by blast pressure waves transmitted through the ear and the damage in the CAS caused by blast wave impacts on the head or traumatic brain injury. This article reports a preliminary study using a 3D printed chinchilla "helmet" as a head protection device associated with the hearing protection devices (e.g., earplugs) to isolate the CAS damage from the PAS injuries under repeated blast exposures.

Materials and Methods:

A finite element (FE) model of the chinchilla helmet was created based on micro-computed tomography images of a chinchilla skull and inputted into ANSYS for FE analysis on the helmet's protection against blast over pressure. The helmet was then 3D printed and used for animal experiments. Chinchillas were divided into four cases (ears open, with earplug only, with both earplug and helmet, and with helmet only) and exposed to three blasts at blast over pressure of 15 to 20 psi. Hearing function tests (e.g., auditory brainstem response) were performed before and after blast on Day 1 and Days 4 and 7 after blasts.

Results:

The FE model simulation showed a significant reduction in intracranial stress with the helmet, and the animal results indicated that both earplug and helmet reduced the severity of blast-induced auditory injuries by approximately 20 dB but with different mechanisms.

Conclusions:

The biomechanical modeling and animal experiments demonstrated that this four-case study in chinchillas with helmet and hearing protection devices provides a novel methodology to investigate the blast-induced damage in the PAS and CAS.

INTRODUCTION

Hearing loss and tinnitus are the top two types of occupational disabilities among military personnel which have been proved to be primarily caused by exposures to blasts during combat and military training by a series of epidemiologic studies.[1,2] Both the peripheral auditory system (PAS) and central auditory system (CAS) are vulnerable to blast injuries, and the intensities of blast overpressures (BOPs) are at mild traumatic brain injury (TBI) pressure levels.[3] However, blast-induced damage in the CAS and PAS has not been isolated and studied separately.[1,4] This gap of knowledge affects the development of hearing protection devices (HPD; e.g., earplugs), which are designed to attenuate the blast pressure reaching the tympanic membrane (TM) and protect the PAS but have questionable efficacy in protecting the CAS.[5–7]

Blast overpressure induces acoustic trauma through two distinct pathways: mechanical damage in the PAS caused by blast wave transmission through the ear including TM perforation, ossicular chain disruption, loss of hair cells, and tearing of the basilar membrane, and damage in the CAS caused by blast wave impacts on the head, or TBI, including blast-induced abnormally intense shearing and stretching of the auditory-related areas in the brain, e.g., the inferior colliculus in the midbrain and auditory cortex in the temporal lobe.[1,8–11] Clinical and laboratory studies indicate the blast-induced PAS damage can induce a significant and permanent increase of the hearing threshold. The CAS damage, however, tends to induce relatively small and temporary threshold shifts with other lasting auditory and perceptual deficits, which are new and still not well understood.[10–12] Acoustic trauma induced through these two pathways contribute to auditory dysfunction and result in complicated symptoms, which are difficult to clearly investigate and assess with clinical observations.[8,11,12] Therefore, development of an

[*]School of Aerospace and Mechanical Engineering, University of Oklahoma, Norman, OK 73019

AQ6

Presented as a poster at the 2019 Military Health System Research Symposium, Kissimmee, FL; MHSRS-19-00434.

doi:10.1093/milmed/usaa317

© The Association of Military Surgeons of the United States 2020. All rights reserved. For permissions, please e-mail: journals.permissions@oup.com.

PROOF FOR CHECKING PURPOSES ONLY

animal model that allows quantitative investigation on the two damage-formation pathways would greatly facilitate understanding of blast-induced auditory injuries and strategies for prediction and prevention of hearing loss.

Chinchilla is a well-developed animal model for hearing research on continuous and impulse noise exposures and has been recently developed for the field of blast-induced hearing damage with promising output.[13,14] Our laboratory has used electrophysiological measurement to quantify the acute and progressive effects of repetitive exposure to low BOP levels (3-5 psi or 21-35 kPa) and the effects of the number of blast exposures at high BOP levels (15-20 psi or 103-138 kPa), equivalent to mild TBI, on the hearing function in chinchillas.[15,16] Hearing protection devices (earplugs) were also included in those studies to assess the degree of protection from HPDs when animals were exposed to multiple blasts.

This article reports our recent and novel study that used the 3D printed chinchilla "helmet" as a head protection device to isolate the CAS damage from the PAS injuries and assessed the protective functions of the helmet and earplug. The design and evaluation of the chinchilla helmet using finite element (FE) modeling and 3D printing were described first. The protective function of the helmet associated with HPDs was assessed by studies in the chinchilla animal model. Chinchillas were divided into four groups, or cases, (ears open, with earplug only, with both earplug and helmet, or with helmet only) to repetitively expose blasts at a BOP level that causes mild TBI. The hearing sensitivity of the animals was observed for seven days by measuring the thresholds of auditory brainstem response (ABR). As a preliminary study, the biomechanical modeling and animal experiments demonstrated that the four-case study in chinchillas with helmet and HPDs provides a novel methodology to investigate the blast-induced damage in the PAS and CAS.

MATERIALS AND METHODS

3D Finite Element Modeling

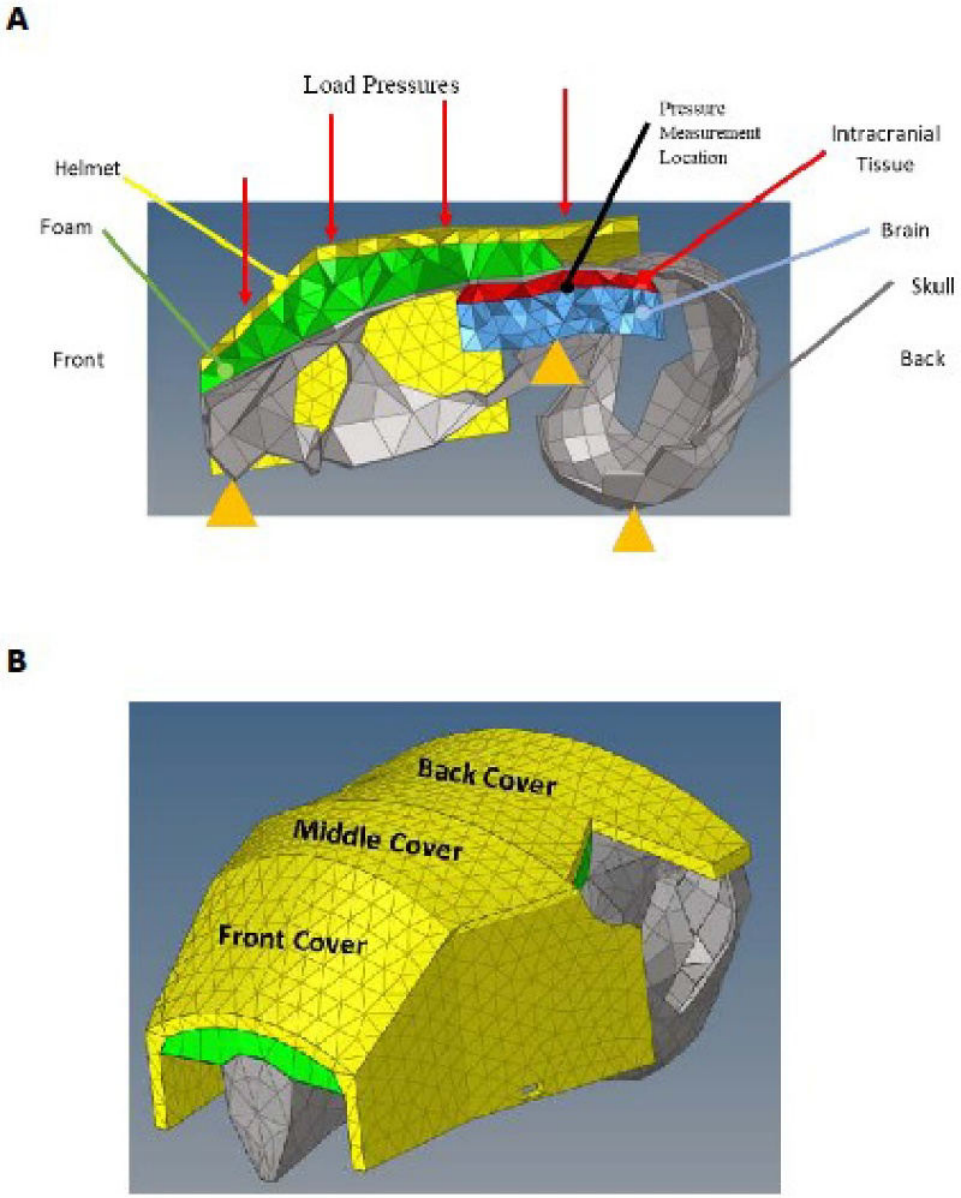
• Chinchilla skull model. The 3D structure of the chinchilla skull was created from a series of micro-CT images of a chinchilla skull specimen using the reconstruction software AMIRA (FEI Houston Inc., Hillsboro, OR). The solid model was then meshed in HyperMesh (HyperWorks, Altair Engineering, Troy, MI). The chinchilla brain's geometry and location within the chinchilla skull were obtained through measurements of a chinchilla brain specimen fixed in 4% paraformaldehyde in phosphate buffer solution. The 3D FE model was then established in ANSYS Workbench (ANSYS Inc., Canonsburg, PA) for FE analysis. Fig. 1A shows a cross-sectional view of FE model with chinchilla skull (grey), brain (blue), and intracranial tissue (red). The brain model was comprised of 1,055 tetrahedral elements and assumed as a viscoelastic solid because of the tissue response behavior to an applied pressure load. The Prony shear response material model with a relaxation time of 1.75 s and a shear modulus of 575 Pa was used for mechanical properties of the brain.[17] The intracranial tissue was modeled as a first-order Ogden hyperelastic solid and consisted of 401 tetrahedral elements.[18] The skull consisted of 741 tetrahedral linear elastic solid elements with a Young's modulus of 10 GPa and a Poisson's ratio of 0.3.[19]

• Chinchilla helmet model. The 3D FE model of the chinchilla helmet was then created as a blast wave shield that could provide two protective barriers to the brain. The helmet dimensions were designed from the skull FE model to fit and cover the skull but leave the ears exposed. The helmet was made in three sections as shown in Fig. 1B: the front, middle, and back covers with two side panels. The middle cover protects the majority of the chinchilla's head from the forehead to the ears. The back cover shields the back side of the head where the brain is located, and the front cover is an extension of the main body to protect the nasal and incisive bones. The whole helmet covers 75% to 80% of the chinchilla's head.

The helmet's design included two layers: a hard outer shell and a shock-absorbent inner layer to deflect the blast waves and reduce the energy transmitted to the brain, respectively (Fig. 1A). The structure of the helmet was designed in Solidworks (Solidworks Corp., Waltham, MA) and uploaded into HyperMesh. The helmet and chinchilla skull were connected by a foam layer and implemented as the interior helmet foam. The foam layer was modeled as 2,448 linear elastic tetrahedral solid elements with a Young's modulus of 130 MPa and a Poisson's ratio of 0.3.[20] The helmet consisted of 3,362 tetrahedral linear elastic elements with a Young's modulus of 2.5 GPa and Poisson's ratio of 0.3. The material properties of the helmet were provided by our datasheet of 3D printing materials.

• FE analysis. Once the full model was completed, two model cases of with and without helmet were uploaded into ANSYS for simulation of blast wave transduction (Fig. 1). A transient analysis was conducted by step-loading over the 2 ms of blast exposure time. The first test simulated Case 1 where the helmet was not present, and the second test simulated Case 2 where the helmet was on the skull. The BOP waveform used for FE simulation was originally measured with a pressure sensor at the ear canal entrance from an animal experiment and was applied on the top surface of the helmet or chinchilla skull (Fig. 1A).[15,16] The peak pressure level used in FE simulation (50 kPa) was lower than the pressure level measured in the animal experiment (103-138 kPa). The fixed boundary conditions applied on the base of the snout, bulla, and brain are illustrated as yellow triangles in Fig. 1A to simulate the status of the chinchilla head during blast exposure. The output data were presented as the Von Mises stress calculated at the point on the surface between the top of the brain and the bottom of the intracranial tissue as shown in Fig. 1A.

PROOF FOR CHECKING PURPOSES ONLY



AQ8 **FIGURE 1.** (A) Cross-sectional view of finite element (FE) model simulation in ANSYS with chinchilla skull (grey), brain (blue), and intracranial tissue (red). (B) FE model of the chinchilla skull with helmet. The grey elements are the mesh of the skull. The green elements are the mesh of the foam and the yellow elements are the mesh of the helmet.

3D Printing of Chinchilla Helmet

The geometric design of the FE model from Solidworks was used as the model for 3D printing. The geometry was further optimized for 3D printing in GrabCAD Print (GrabCAD, Cambridge, MA, USA) and printed in our 3D printing system (Objet350 Connex3, Stratasys). Once helmet was printed and cleaned, a thin layer of liquid foam was sprayed in the helmet and left to dry. The foam was designed to serve as the buffer layer between the helmet and the chinchilla head.

Animal Blast Experiment Protocol

Thirty-two healthy chinchillas (*Chinchilla laniger*), weighing between 600 and 800 g were included in this study. The study protocol was approved by the Institutional Animal Care and Use Committee of the University of Oklahoma. Animals were equally divided into four groups or cases with eight animals for each case. Standard foam earplugs (3M, Inc. St. Paul, MN) were inserted into the chinchilla ear canals to protect their PAS, and the 3D printed helmet was fixed on the chinchilla head using

PROOF FOR CHECKING PURPOSES ONLY

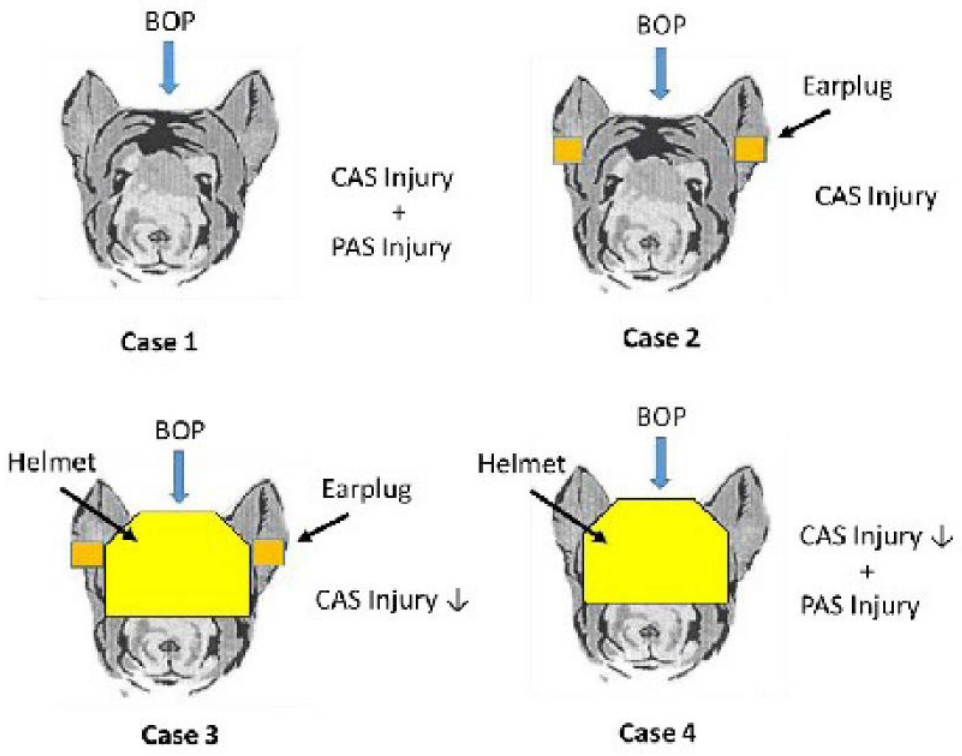


FIGURE 2. Illustration of four cases of chinchilla experiments attempting to isolate the traumatic brain injury damage to the central auditory system (CAS) from the injuries in peripheral auditory system (PAS); BOP, blast over pressure.

rubber bands to protect the CAS against BOP exposures. Fig. 2 illustrates the experimental design: Case 1—ears open without HPDs and helmet; Case 2—ears protected with earplug, but without helmet; Case 3—ears protected with earplugs and with helmet; and Case 4—ears open and with helmet.

On the day of blast experiment (Day 1), animals were first anesthetized with 35-mg/mL ketamine and 7-mg/mL xylazine. Each ear was examined using a surgical endoscope (Straight Endoscope, Stryker, MI) to ensure that the TM and middle ear were normal. The blast exposure followed the same protocol used in our previous studies.[15,16] Briefly, the chinchilla was placed in a specially designed L-shape animal holder and fixed using strips to maintain the body up straight towards the blast source after preblast hearing function tests. A pressure sensor (P0) (Model 102B16, PCB, Depew, NY) was placed at the entrance of the ear canal to monitor the blast pressure. The BOP was generated by a well-controlled compressed nitrogen-driven blast apparatus located inside an anechoic chamber.[21,22] Polycarbonate films (McMaster-Carr, Atlanta, GA) were ruptured to generate BOPs. In this study, the BOP level measured from P0 was around 103 to 138 kPa or 15 to 20 psi. Each chinchilla was exposed to 3 blasts, and there was a time interval of approximately 5 minutes between consecutive blasts. The P0 pressure signals were processed by cDAQ 7194 and A/D converter 9215 (National Instruments Inc., Austin, TX) with a sampling rate of 100k/s at a length of 10 ms after the trigger. The LabVIEW software package (NI Inc.) was used for data acquisition and analysis.

Upon the completion of blast exposures, the chinchilla TM was examined using the endoscope and hearing function tests were performed. Each chinchilla was observed for 7 days after the blast exposure.

Hearing Function Measurements

Hearing function measurements were conducted before and after blasts for animals on Day 1 and on Days 4 and 7 after the blast. The animals were anesthetized during the test following the same protocol in the section above. As a preliminary study, hearing level changes after BOP exposures in chinchillas were represented by ABR threshold variation in this article as a fundamental indicator of hearing function. Blast-induced injuries in the PAS and CAS both contributed to the change of ABR threshold.

The ABR was measured using Tucker Davis Technologies system III (Alachua, FL) following our previous protocol.[15,16] Briefly, under anesthesia, stainless steel needle electrodes were placed subcutaneously at the vertex of the skull, ventrolateral surfaces of the ear, and in the muscle rear leg, which served as the ground. Tone burst stimuli of 1-ms rise/fall time at frequencies of 0.5, 1, 2, 4, 6, and 8 kHz were delivered to and monitored by a microphone in the ear canal.[16,17,21] The ABR waveforms were recorded in descending 5-dB sound pressure level (SPL) intervals from the maximum stimulus

PROOF FOR CHECKING PURPOSES ONLY

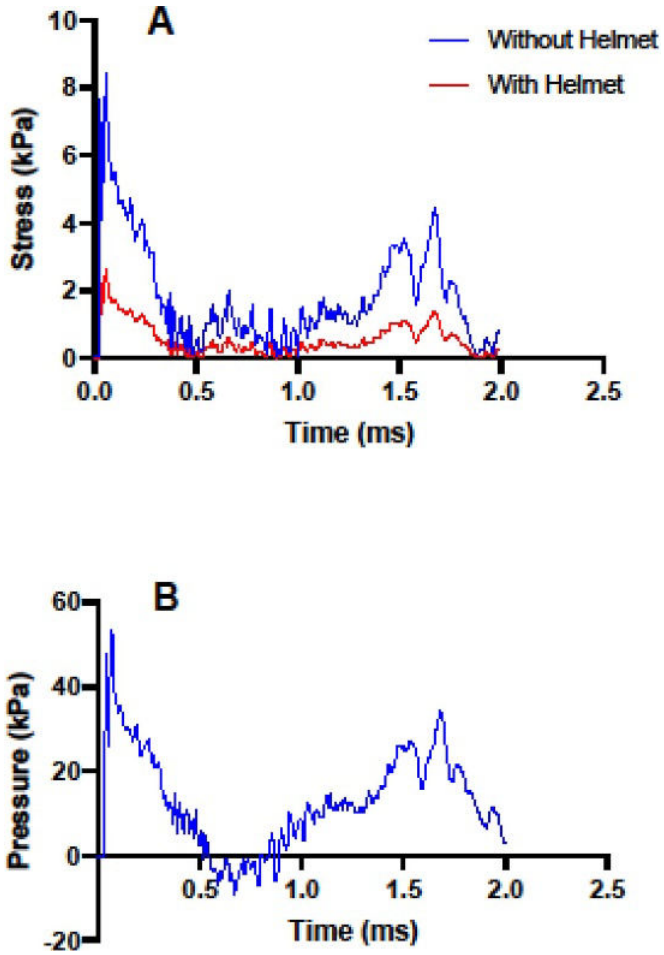


FIGURE 3. (A) Von Mises stress in the intracranial tissue over time calculated from the finite element model with and without helmet covered the chinchilla skull. (B) Measured blast pressure applied on the chinchilla skull and helmet model.

of 100-dB SPL until no significant signal could be identified from the background noise. If an ABR response was not detected at the maximum acoustic stimulation, the threshold was set to 100 dB. The ABR threshold shift point was calculated by subtracting the threshold levels measured from the preblast test from the levels measured at each following time point of measurement at each frequency, respectively.

RESULTS

Evaluation of Chinchilla Helmet Using FE Modeling

The Von Mises stresses on the top surface of the brain obtained from the FE model simulation are shown in Fig. 3A with the blue line representing without helmet and the red line representing with helmet. Fig. 3B displays the input BOP over the 2-ms duration.

The presence of the helmet between the two trials was used to compare the ability of the helmet's attenuation on the BOP. Higher shock absorption of the helmet reduced the pressure in the brain and lowered the magnitude of the pressure waveform that would translate through the skull. The blue curve in Fig. 3A has a larger magnitude but similar waveform shape to that of the red. The presence of the helmet resulted in a reduction of stress generated on the brain top surface. The ratio of the peak pressure within the brain for the "with helmet" with respect to that of "without helmet" is 31.2% as shown in Fig. 3A. These results suggested that the protective function of the helmet on the CAS was significant as evaluated by the FE model and provided the theoretical basis for the following animal study.

ABR Threshold Shifts in Four Cases of Animals

The mean and standard error of the mean of the ABR threshold shifts measured from four cases of chinchillas over a 7-day period after blast exposures at the frequencies of 0.5, 1, 2, 4, 6, and 8 kHz are shown in Fig. 4. The panels A, B, C, and D represent results measured from Cases 1, 2, 3, and 4, respectively. Each case includes 16 ears from 8 chinchillas, whereas Case 1 has 1 less animal because of the unexpected death before completing the experiment. The preblast thresholds of animals in four cases were measured to provide the

PROOF FOR CHECKING PURPOSES ONLY

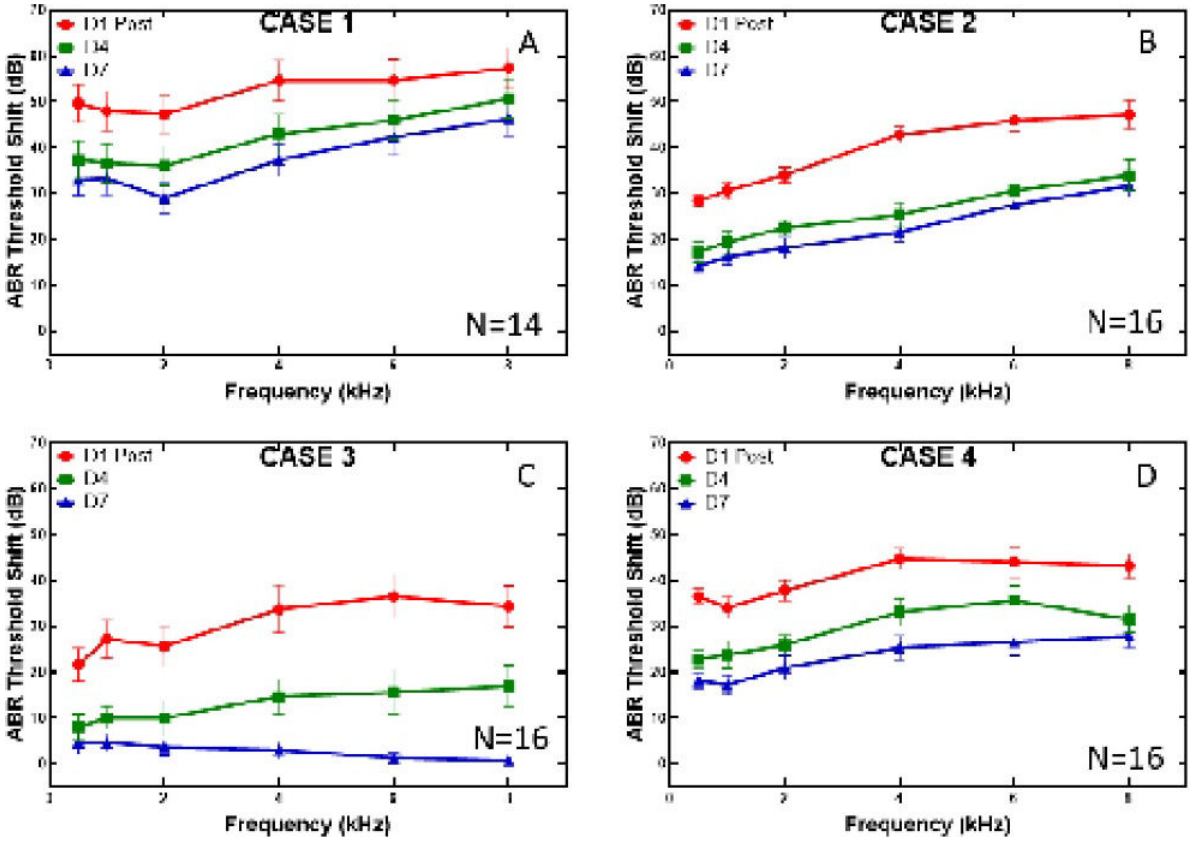


FIGURE 4. Mean and standard error of the auditory brainstem response (ABR) threshold shift results measured on postblast of Day 1 (red), Day 4 (green), and Day 7 (blue) from animals in four cases: (A) Case 1 (N = 14 ears), without helmet protection and hearing protection device (HPD; e.g., earplug) protection; (B) Case 2 (N = 16 ears), with HPD protection only; (C) Case 3 (N = 16 ears), with helmet protection and HPD protection. (D) Case 4 (N = 16 ears), with helmet protection only.

baseline data, and no significant difference between cases was observed. This indicated that the baseline of hearing threshold for all animals was similar without prior hearing damage. The threshold shifts measured on Day 1 postblast, Day 4, and Day 7 were colored in red, green, and blue, respectively. The higher threshold shift indicated more severe hearing loss.

Results shown in Fig. 4 demonstrated that the hearing damage was most severe immediately after the blast and gradually recovered to certain levels over the 7-day period after blast exposures. The greatest damage recovery was on Day 4 as reflected by the distances between the curves. All four cases indicated the damage induced by blasts was more severe at higher frequencies (>2 kHz) than at the low frequencies, but the recovery over 7 days was approximately 20 dB for all cases without showing strong dependency on frequencies. In this study, the ABR threshold shift immediately after the blast (D1 postblast) represented the acute damage induced by the blast and the D7 results represented the permanent damage.

Figure 4A indicated that chinchillas in Case 1 experienced the most severe hearing loss at all three time points of measurement. The postblast threshold shift was around 50 dB at frequencies below 2 kHz and increased approximately 10 dB at 8 kHz. The threshold shift decreased about 15 to 20 dB after 7 days of recovery over the frequencies. The postblast threshold shifts of Case 2 shown in Fig. 4B increased from 30 dB at 0.5 kHz to 50 dB at 8 kHz which was lower than Case 1 over the entire frequency range. With the protection of earplugs, Case 2 showed less damage at lower frequencies. Chinchillas in Case 3 show the least damage among all four cases with the protection of both earplug and helmet (Fig. 4C). The threshold shift was between 20 and 40 dB immediately after the blast. The ABR threshold shift was less than 5 dB and close to 0 on the Day 7, which indicated the nonexistence of permanent damage under the combined protection of the helmet and earplug. Case 4 results shown in Fig. 4D present the protective function of the helmet when compared with the Case 1. The helmet by itself reduced the threshold shift approximately 10 dB both acutely (postblast) and permanently (D7) over the entire frequency range. The postblast threshold shift ranged from 30 to 45 dB in Case 4. ABR threshold shift measured from four cases indicated the different protective functions of the helmets and earplugs.

PROOF FOR CHECKING PURPOSES ONLY

DISCUSSION

Protective Function of the Earplug and Helmet

Helmet and earplug are both widely accepted, traditional personal protection devices for military personnel. The protective function of various types of earplugs against blast-induced hearing damage was reported from measurements in human subjects, human cadaveric temporal bones, and animal studies.[5–7,15,16] However, helmets were usually used for protection against concussive TBI rather than the blast-induced TBI.[23] The study on protective function of the helmet to blast-induced TBI was limited.[23–25] During the blast, the helmet protects the head by reflecting and absorbing the energy carried by blast waves, which could create abnormally high intracranial pressure and damage the brain tissues.[24] Since the CAS includes inferior colliculus in the midbrain and auditory cortex in the temporal lobe, it is reasonable to hypothesize that the helmet should protect the CAS against BOP-induced damage by reducing the pressure directly applied on the brain. However, our previous study suggested that the helmet may increase the PAS damage by changing pressure waveforms reaching the TM.[21] Published data also indicated that the underwash effect caused by the gap between the helmet and head could impair the protective function of the helmet.[26] The unclear intertwined relationship of blast-induced PAS and CAS damage intrigued the need to correctly assess the hearing protective function of the helmet. Therefore, the first step of this study is to develop a new methodology to determine whether the helmet can protect the auditory system against BOP.

As the first step of this study, we established an FE model of the chinchilla head covered by the specially designed helmet. The helmet design focused on creating a close-fitting helmet to protect the top of the chinchilla skull and exposing of the pinna to avoid echoing between the head and the helmet which could increase the severity of the blast-induced damage.[21] The reduced intracranial stress after the involvement of the helmet indicated that the helmet could reduce the mechanical damage to the CAS (Fig. 3).

As the second step of this study, we confirmed the protective function of the helmet in animal experiments. Results in Fig. 4 suggested that chinchillas in Case 4 showed better postblast hearing than in Case 1, and the Case 3 showed even better hearing than Case 2. Those data indicated that the chinchilla helmet invented in this study did protect the auditory function against the BOP exposures either with or without the assistant of HPDs (earplugs). Particularly, Case 3 (Fig. 4C) indicated that the combination of earplug and helmet can completely eliminate the permanent hearing damage which was not observed in chinchilla ears protected by the earplugs only under the BOP level.[15,16]

Animal Model—Chinchilla to Differentiate the CAS and PAS Damage

Animal models have been playing critical roles in understanding the mechanism of formation, prevention, and postdamage restoration of blast-induced TBI.[13,27–29] However, there is a limited number of animal studies focusing on repetitive mild TBI-induced auditory injuries. One major challenge is how to select the appropriate animal species, blast level, and techniques of measurement. Unlike the traditional method to quantify the blast-induced mechanical damage in the ear or TBI injury such as the TM rupture, hair cell loss, and hemorrhage,[8,27,30,31] the damage induced by repetitive, low-level BOPs in the CAS and PAS are subtle and difficult to detect in either the CAS or PAS. Current methodologies of damage detection include diffusion tensor magnetic resonance imaging and electrophysiological measurements on auditory evoked potentials (AEPs) in addition to the behavior and histopathological examinations.[15,16,29,32–34]

Current experimental animals for TBI-related research are mostly rat or mice, except for Hickman et al., who used chinchillas to investigate the BOP-induced damage on cochlear function.[14] Therefore, as a preliminary study reported here, we selected chinchilla as our experimental animal because of its hearing function similar to human and good behavior as a noise damage animal model.[13] On the technique side, we choose the ABR, the most typical AEP signal as the primary damage index. The significant difference among four cases shown in Fig. 4 of this preliminary study indicates the great potential of current experimental design to investigate the damage-formation mechanism in the PAS and CAS. Since the function of helmet and earplug can be clearly differentiated from the 4-case results, we proposed a hypothesis: the helmet protects the CAS and the earplugs protect the PAS in animal model of chinchilla. This hypothesis will be confirmed in our future studies.

As the continuation of this preliminary study, we will introduce more sophisticated AEP measurements including ABR waveform analysis, distortion product otoacoustic emissions, and middle latency responses to determine the location of the damage in the CAS or PAS. The histopathological analysis will be conducted on the PAS and CAS tissues to further confirm the location of the injury. By confirming the hypothesis that the helmet and earplug protect the CAS and PAS separately, we attempt to develop a novel methodology and investigate the blast-induced damage in the PAS and CAS separately with the corresponding protective device to the PAS and CAS. With the establishment of this novel methodology, effects of multiple factors such as the blast-head orientations, the intensity of the blast, and the number of blasts on the severity of blast-induced damage will be investigated using the combination of animal and FE model of the chinchilla.[22,35] Moreover, the FE model of chinchilla skull will be further

PROOF FOR CHECKING PURPOSES ONLY

improved by refining mesh and boundary conditions based on current conceptual model. It is possible to use FE simulation for analysis of blast wave transmission through chinchilla ear with and without earplug to further correlate simulation and experimental data in chinchillas.

CONCLUSION

This article reports a novel study using the 3D printed chinchilla "helmet" as a head protection device against blast-induced auditory damage. As a preliminary study, the helmet was prototyped in 3D design software, and the protective function was assessed by FE modeling first. After confirming that the helmet can reduce the stress in the brain under blast exposure, a helmet was produced using 3D printing and applied to animal experiments. Chinchillas were divided into four groups or four cases (ears open, with earplug only, with both earplug and helmet, or with helmet only) and repetitively exposed to three blasts at BOP level of 15 to 20 psi or causing mild TBI. The hearing function tests were conducted on each animal, and the ABR thresholds were measured pre- and postblast on Day 1 and on Days 4 and 7 after blast exposures. The ABR threshold shifts were compared among four cases to determine the protective function of the helmet and earplugs. Both earplug and helmet reduced the severity of the blast-induced hearing loss at a value of approximately 20 dB, but the earplug and helmet altered the hearing function differently over the frequencies. The preliminary results are encouraging, and the advanced metrics analyses for the measurement data will be further conducted in future studies.

FUNDING

This study was supported by a grant from the U.S. Army Medical Research and Material Command (W81XWH-14-1-0228).

CONFLICT OF INTEREST STATEMENT

None declared.

REFERENCES

1. Gallun FJ, Lewis MS, Folmer RL, et al: Implications of blast exposure for central auditory function: a review. Bull Prosthet Res 2012; 49: 1059-74.
2. Oleksiak M, Smith BM, St Andre JR, Caughlan CM, Steiner M: Audiological issues and hearing loss among Veterans with mild traumatic brain injury. J Rehabil Res Dev 2012; 49: 995-1004.
3. Hoge CW, McGurk D, Thomas JL, Cox AL, Engel CC, Castro CA: Mild traumatic brain injury in U.S. soldiers returning from Iraq. NEJM 2008; 358: 453-63.
4. Theodoroff SM, Lewis MS, Folmer RL, Henry JA, Carlson KF: Hearing Impairment and tinnitus: prevalence, risk factors, and outcomes in US Service Members and Veterans deployed to the Iraq and Afghanistan Wars. Epidemiol Rev 2015; 37: 71-85.
5. Carr W, Stone JR, Walilko T, et al: Repeated low-level blast exposure: a descriptive human subjects study. J Mil Med 2016; 181: 28-39.
6. Murphy WJ, Flamme GA, Meinke DK, et al: Measurement of impulse peak insertion loss for four hearing protection devices in field conditions. Int J Audiol 2012; 51: S31-42.
7. Gan RZ, Leckness K, Smith K, Ji XD: Characterization of protection mechanisms to blast overpressure for personal hearing protection devices – biomechanical measurement and computational modeling. J Mil Med 2019; 184: 251-60.
8. Cho S-I, Gao SS, Xia A, et al: Mechanisms of hearing loss after blast injury to the ear. Plos One 2013; 8: e67618.
9. Dougherty AL, MacGregor AJ, Han PP, Viirre E, Heltemes KJ, Galarneau MR: Blast-related ear injuries among U.S. military personnel. J Rehabil Res Dev 2013; 50: 893-904.
10. Fausti SA, Wilmington DJ, Gallun FJ, Myers PJ, Henry JA: Auditory and vestibular dysfunction associated with blast-related traumatic brain injury. J Rehabil Res Deve 2009; 46: 797-810.
11. Gallun FJ, Papesh MA, Lewis MS: Hearing complaints among veterans following traumatic brain injury. Brain Injury 2017; 31: 1183-7.
12. Theodoroff SM, Reavis KM, Griest SE, Carlson KF, Hammill TL, Henry JA: Decreased sound tolerance associated with blast exposure. Sci Rep 2019; 9: 1-8.
13. Trevino M, Lobarinas E, Maulden AC, Heinz MG: The chinchilla animal model for hearing science and noise-induced hearing loss. J Acoust Soc Am 2019; 146: 3710-32.
14. Hickman TT, Smalt C, Bobrow J, Quatieri T, Liberman MC: Blast-induced cochlear synaptopathy in chinchillas. Sci Rep 2018; 8: 1-12.
15. Chen T, Smith K, Jiang S, Zhang T, Gan RZ: Progressive hearing damage after exposure to repeated low-intensity blasts in chinchillas. Hear Res 2019; 378: 33-42.
16. Smith K, Chen T, Gan RZ: Hearing damage induced by blast overpressure at the mild TBI level in a chinchilla model. J Mil Med 2020; 185(Suppl 1): 248-55.
17. Finan JD, Elkin BS, Pearson EM, Kalbian IL, Morrison B: Viscoelastic properties of the rat brain in the sagittal plane: effects of anatomical structure and age. Ann Biomed Eng 2012; 40: 70-8.
18. Elkin BS, Ilankovan A, Morrison B: Age-dependent regional mechanical properties of the rat hippocampus and cortex. J Biomech Eng 2010; 132: 011010.
19. Liang J, Luo H, Yokell Z, Nakmali DU, Gan RZ, Lu H: Characterization of the nonlinear elastic behavior of chinchilla tympanic membrane using micro-fringe projection. Hear Res 2016; 339: 1-11.
20. Zhang S, Dulieu-Barton JM, Fruehmann RK, Thomsen OT: A methodology for obtaining material properties of polymeric foam at elevated temperatures. Exp Mech 2012; 52: 3-15.
21. Gan RZ, Nakmali D, Ji XD, Leckness K, Yokell Z: Mechanical damage of tympanic membrane in relation to impulse pressure waveform – a study in chinchillas. Hear Res 2016; 340: 25-34.
22. Gan RZ, Leckness K, Nakmali D, Ji XD: Biomechanical measurement and modeling of human eardrum injury in relation to blast wave direction. Mil Med 2018; 183: 245-51.
23. Sone JY, Kondziolka D, Huang JH, Samadani U: Helmet efficacy against concussion and traumatic brain injury: a review. J Neurosurg 2017; 126: 768-81.
24. Sarvghad-Moghaddam H, Jazi MS, Rezaei A, Karami G, Ziejewski M: Examination of the protective roles of helmet/faceshield and directionality for human head under blast waves. Comput Methods Biomech Biomed Engin 2015; 18: 1846-55.
25. Sarvghad-Moghaddam H, Rezaei A, Ziejewski M, Karami G: Evaluation of brain tissue responses because of the underwash overpressure of helmet and faceshield under blast loading. Int J Numer Method Biomed Eng 2017; 33: e02782.
26. Leonardi ADC, Keane NJ, Hay K, Ryan AG, Bir CA, VandeVord PJ: Methodology and evaluation of intracranial pressure response in rats exposed to complex shock waves. Ann Biomed Eng 2013; 41: 2488-500.
27. Saunders RN, Tan XG, Qidwai SM, Bagchi A: Towards identification of correspondence rules to relate traumatic brain injury in different species. Ann Biomed Eng 2019; 47: 2005-18.

PROOF FOR CHECKING PURPOSES ONLY

28. Xiong Y, Mahmood A, Chopp M: Animal models of traumatic brain injury. Nat Rev Neurosci 2013; 14: 128-42.
29. Race N, Lai J, Shi R, Bartlett EL: Differences in post-injury auditory system pathophysiology after mild blast and non-blast acute acoustic trauma. J Neurophysiol 2017; 118: 782-99.
30. Pun PBL, Lu J: Experimental models of blast-induced neurotrauma. In: Animal Models of Neurotrauma. Edited by M Risling, J Davidsson. New York, NY, Springer, 2019; 77-92.
31. Patterson JH, Hamernik RP: Blast overpressure induced structural and functional changes in the auditory system. Toxicology 1997; 121: 29-40.
32. Mao JC, Pace E, Pierozynski P, et al: Blast-induced tinnitus and hearing loss in rats: behavioral and imaging assays. J Neurotrauma 2012; 29: 430-44.
33. Masri S, Zhang LS, Luo H, Pace E, Zhang J, Bao S: Blast exposure disrupts the tonotopic frequency map in the primary auditory cortex. Neuroscience 2018; 379: 428-34.
34. Luo H, Pace E, Zhang X, Zhang J: Blast-induced tinnitus and spontaneous activity changes in the rat inferior colliculus. Neurosci Lett 2014; 580: 47-51.
35. Wang X, Gan RZ: 3D finite element model of the chinchilla ear for characterizing middle ear functions. Biomech Model Mechanobiol 2016; 15: 1263-77.

AQ7

Hearing Damage Induced by Blast Overpressure at Mild TBI Level in a Chinchilla Model

Kyle D. Smith, MS; Tao Chen, MD*; Rong Z. Gan, PhD**

ABSTRACT Introduction: The peripheral auditory system and various structures within the central auditory system are vulnerable to blast injuries, and even blast overpressure is at relatively mild traumatic brain injury (TBI) level. However, the extent of hearing loss in relation to blast number and time course of post-blast is not well understood. This study reports the progressive hearing damage measured in chinchillas after multiple blast exposures at mild TBI levels (103–138 kPa or 15–20 psi). Materials and Methods: Sixteen animals (two controls) were exposed to two blasts and three blasts, respectively, in two groups with both ears plugged with foam earplugs to prevent the eardrum from rupturing. Auditory brainstem response (ABR) and distortion product otoacoustic emission (DPOAE) were measured in pre- and post-blasts. Immunohistochemical study of chinchilla brains were performed at the end of experiment. Results: Results show that the ABR threshold and DPOAE level shifts in 2-blast animals were recovered after 7 days. In 3-blast animals, the ABR and DPOAE shifts remained at 26 and 23 dB, respectively after 14 days. Variation of auditory cortex damage between 2-blast and 3-blast was also observed in immunofluorescence images. Conclusions: This study demonstrates that the number of blasts causing mild TBI critically affects hearing damage.

INTRODUCTION

Hearing damage is one of the most prevalent injuries in service members in the battle field. Both the peripheral auditory system (PAS) and various structures within the central auditory system (CAS) are vulnerable to blast injuries, even when blast overpressure (BOP) is at relatively mild traumatic brain injury (TBI) level. A 63% increased risk of hearing loss was found for personnel with combat experience and greater chance of sustaining hearing damage when exposed to blasts.[1] These injuries could cause long-term hearing disabilities and affect the quality of life of active service members and veterans.[2] However, the extent of hearing loss in relation to the number of blast exposure and the time course after blasts, and the protective mechanisms of hearing protection devices (eg, earplug) are not well understood.

BOP causes acoustic trauma through different mechanisms. Damage could be sustained in the form of tympanic membrane (TM) perforation, ossicular disjunction, overstimulation to the cochlea, or damage to the round window membrane, and in the forms of damage, all related to the PAS.[3,4] The hair cell loss in the cochlea and excitotoxicity of the spiral ganglion neurons further induces the sensorineural hearing loss.[4,5] A potential mechanism of blast-induced CAS damage similar to the TBI is the shearing and stretching forces applied on the brain tissue including brainstem and auditory cortex.[6–8] These injuries could cause long-term hearing disabilities depending on the intensity of the blast.[4,9,10]

Results from studies on blast-induced TBI in rats indicated that the pressure levels to induce mild, moderate, and severe TBI are 90–150, 150–230, and 230–350 kPa, respectively.[11] Damage caused by severe and moderate BOP levels had more attention than that of mild and low BOP levels.[12,13] Recently, Chen et al.[14] investigated the acute and progressive effects of repetitive exposures to low BOP level (21–35 kPa) in chinchillas at which the TM is usually not ruptured.[14] Chen et al.'s study quantified the effect of repeated low-intensity blasts with different number of blasts and time course after blasts on hearing damage. Their results indicated that three blasts were able to induce permanent hearing damage in open ears without hearing protection while only temporary damage occurred in protected ears with earplugs. However, there is no animal study reported in the literature about whether the repetitive exposures to a relatively high BOP level (eg, mild TBI [mTBI]) will result in permanent hearing damage under the protection of the TM from rupture.

This article reports the current study in chinchillas to investigate the progressive hearing damage after exposure to repeated BOPs at the level causing mTBI and the protective mechanism of the earplug for mTBI. Animals were exposed to the BOP at 103–138 kPa or 15–20 psi with both ears protected with earplugs. BOP levels were chosen based on evidence in literature that mTBIs can be caused at pressures ranging from 103–138 kPa or 15–20 psi.[15–17] Auditory brainstem response (ABR) threshold that provides general hearing sensitivity over the frequencies and distortion product otoacoustic emission (DPOAE) signals that reflect the function of the outer hair cells in the cochlea were measured in pre- and post-blasts as well as over the time course after blasts.[3,18–20] In addition to hearing function tests, immunohistochemistry or immunofluorescence images of the brain sections before and after blast

*School of Aerospace and Mechanical Engineering, University of Oklahoma, 865 Asp Avenue, Norman, OK 73019

Guarantor: Rong Z. Gan, Ph.D.

Presented in Poster Session I: "Medical Advancements in Operational & Clinical Hearing Protection & Treatment" at the 2018 Military Health System Research Symposium (Abstract number: MHSRS-18-0837).

doi:10.1093/milmed/usz309

© Association of Military Surgeons of the United States 2020. All rights reserved. For permissions, please e-mail: journals.permissions@oup.com.

Downloaded from https://academic.oup.com/milmed/article-abstract/185/Supplement_1/248/5740813 by University of Oklahoma user on 20 February 2020

exposures were performed to examine the neural damage sustained in the auditory cortex (AC) of the chinchilla. The goal of this study is to determine whether the number of repeated blast exposures at the mTBI level is the main cause of progressive hearing damage and how the permanent hearing damage is related to the number of blast exposures at this BOP level when ears are protected with hearing protections devices (eg, earplugs). The results can be used to guide clinical evaluation, rehabilitation, and future research in blast-induced auditory dysfunction.

MATERIALS AND METHODS

Animal Protocol

Sixteen healthy chinchillas (*Chinchilla lanigera*), weighing between 600 and 800 g, were included in this study. Chinchilla is a commonly used animal model for auditory research because its range of hearing is similar to that of humans.[3,21] The study protocol was approved by the Institutional Animal Care and Use Committee of the University of Oklahoma and met the guidelines of the National Institutes of Health and the U.S. Department of Agriculture. All animals were checked to be clear of disease in the ear.

Animals were divided into two experimental groups ($n = 7$ each) to expose 2-blasts and 3-blasts on day 1, respectively, and named as 2-blast group and 3-blast group, accordingly. Another two animals were used as controls for immunohistochemistry study. Figure 1 is an overview of the experimental procedures for two groups. Initially, animals received two blasts at mTBI level, and function tests were conducted before and after the two blasts, on day 4 and day 7. By day 7, hearing function levels had returned to normal or near normal for all animals, and animals were sacrificed to observe any neurological defects histologically. To determine if increasing the blast number had an effect on the permanency of hearing loss over time, the second group of animals was tested at mTBI level, receiving three consecutive blast exposures. Function tests were again conducted before and after the blasts, on day 4 and day 7. By day 7, hearing function levels had not returned to normal or near normal, and hence, animals were observed for an additional week. On day 14, hearing function was assessed and animals were sacrificed to observe possible neurological defects histologically.

Animals were anesthetized with 35 mg/mL ketamine and 7 mg/mL xylazine during the experiment. Each ear was examined using a surgical endoscope (Straight Endoscope, Stryker, MI) to ensure nonexistence of the TM and middle ear abnormalities. After initial function tests (pre-blast), the animal was placed in a specially designed L-shape animal holder and was fixed using straps to maintain the body up straight toward the blast source (Fig. 2). A pressure sensor (Model 102B16, PicoCoulomB Piezotronics, Depew, NY) was placed at the canal entrance and fixed on the animal holder to monitor the blast pressure at the entrance of the ear canal (P0). A

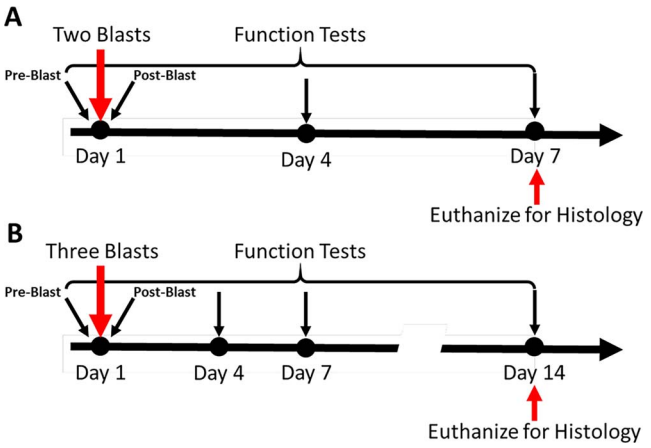


FIGURE 1. Diagram showing the time course and experimental procedure. (A) 2-Blast animals over 7-day experiment; (B) 3-Blast animals over 14-day experiment.

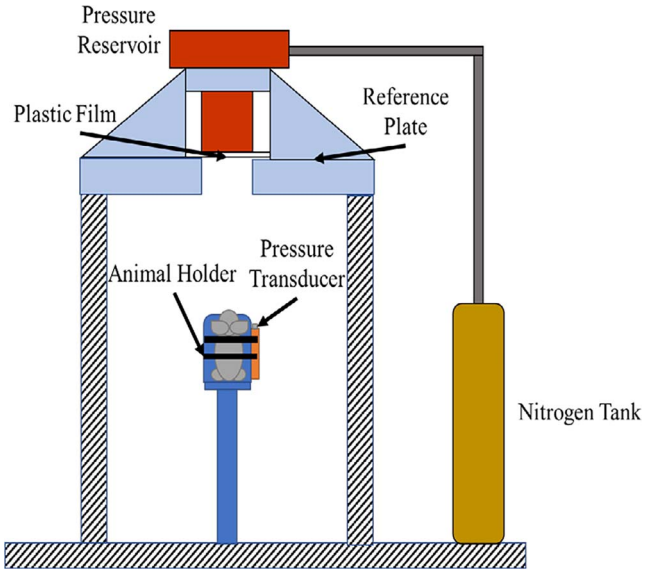


FIGURE 2. Schematic of animal experimental setup with blast apparatus.

standard foam earplug (3M, Inc. St. Paul, MN) was then inserted into both ears to protect damage in the TM caused by blast pressure. Once, all the function measurements were completed (7 days for 2-blast animals and 14 days for 3-blast animals), the animals were perfused intracardially with saline solution, followed by fixative (4% paraformaldehyde in phosphate buffer saline [PBS]) to harvest the brain tissues for histology study.

Blast Exposure Test

A well-controlled compressed air (nitrogen)-driven blast apparatus located inside an anechoic chamber in the Biomedical Engineering Laboratory at the University of Oklahoma (Fig. 2) was used to create BOPs in this study.[3,22] Polycarbonate films (McMaster-Carr, Atlanta, GA) of varying thickness (eg, 0.26 and 0.5 mm) were employed to generate

Downloaded from https://academic.oup.com/milmed/article-abstract/185/Supplement_1/248/5740813 by University of Oklahoma user on 20 February 2020

the various BOP levels. In this study, animals in both groups were exposed to BOP level around 103–138 kPa or 15–20 psi. There was a time interval of approximately 10 minutes between consecutive blasts in both groups of animals.

The pressure sensor signals were collected by cDAQ 7194 and A/D converter 9215 (National Instruments Inc., Austin, TX) with the sampling rate of 100 k/s (10 ms dwell time). The LabVIEW software package (NI Inc) was used for data acquisition. Note that the sampling rate is sufficient for the waveform recorded in this study. Upon the completion of blast exposure, the status of the chinchilla TM was examined using a surgical endoscope, and the auditory function tests were conducted.

Hearing Function Measurements

The ABR measurements were conducted in both ears using a Tucker Davis Technologies (TDT) system III (Alachua, FL) following our previous studies.[3] Briefly, under anesthesia, stainless steel needle electrodes were positioned subcutaneously at the vertex of the skull and ventrolateral surfaces of the ear, with a ground electrode placed in the rear leg. Tone burst stimuli of 1 ms rise/fall time at frequencies of 0.5, 1, 2, 4, 6, and 8 kHz were generated, which is a widely accepted frequency range for chinchilla studies.[3,23,24] The ABR waveforms were recorded in descending 5 dB sound pressure level (SPL) intervals from the maximum amplitude of 120 dB SPL until no waveform could be visualized. If an ABR response was not detected at the maximum acoustic stimulation, the threshold was set to 120 dB.

The DPOAE was measured using the TDT System III as described by Chen et al.[14] Briefly, a probe-tipped microphone (ER-10B, Etymotic Research) was sealed in the animal's external ear canal, and cubic 2f1-f2 DPOAE levels were recorded using two primary tones, f1 and f2, presented at primary tone levels of L1 = 70 dB SPL and L2 = 65 dB SPL. The DPOAE levels were defined as the single/noise ratio of the 2f1–f2 distortion product for the 70 and 65 dB SPL of f1 and f2 primaries, respectively, and were calculated by subtracting the 2f1–f2 distortion product from the surrounding noise. The DPOAE level shifts were derived by subtracting post-exposure from pre-exposure values.

AC Immunofluorescence Staining and Hoechst Staining

After intracardial fixation on day 7 or day 14, the chinchilla brains were excised, and then washed and fixed in 4% paraformaldehyde in 0.1 M PBS for 48 hours at 4°C. Following a standard histology protocol, the brains were dehydrated in ethanol, decolored in xylene, and embedded in paraffin.[25] Each specimen was sectioned along the central axis of the brain along the front-posterior direction using a rotatory microtome (Leitz 1512, Leitz, German) with a thickness of 8 μm. The sections were dewaxed and hydrated in xylene and ethanol with gradient concentration. An antigen retrieval was conducted by immersing the slides in 95–100°C 0.1 M sodium citrate buffer for 4–5 minutes. The slides were then processed by 3% H_2O_2 solution for 15 minutes. The tissue sections were blocked with 10% goat serum at room temperature for 1 hour in PBS containing 0.03% Triton X-100. Tissues were incubated overnight at 4°C with the PI3K mouse monoclonal primary antibody (1:100, sc-376112 Santa Cruz Biotechnology Inc, Dallas, TX) and immunofluorescence was performed using goat anti-mouse IgG secondary antibody (1:250, Alexafluor 488, #A32723, Thermo Fisher Scientific, Rockford, IL). Nuclei was stained by 4′,6-diamidino-2-phenylindole (DAPI) (D9542, Sigma-Aldrich, Saint Louis, MO). The immunofluorescence images were collected by an inverted microscope (IX73, OLYMPUS center Valley, PA). Fluorescence from two channels were collected for each section. Blue: 405 nm (DAPI) and green: 488 nm (PI3K).

Statistical Analysis

ABR and DPOAE measurement data were expressed as mean ± standard deviation (SD) and plotted in GraphPad Prism with SPSS 16.0 for statistical analysis. The paired *t*-tests were used to compare ABR thresholds and DPOAE levels at preblast and day 7 function tests in both blast groups, and at day 7 and 14 in the 3-blast group. *P* values of <0.05, 0.01, and 0.001 were considered statistically significant, very significant, and extremely significant. The paired *t*-test was also used to compare the function test results between the 2-blast and 3-blast groups at each point of measurement (days 1, 4, and 7). All results were compared at each frequency point independently.

RESULTS

BOP Waveforms

Figure 3 shows the typical waveforms of BOP in a unit of psi (1 psi = 6.9 kPa) over a time of 10 ms measured at the entrance of the ear canal (P0). Figure 3A shows the representative BOP waveform of a chinchilla in 2-blast group and Figure 3B shows the P0 waveform measured from a chinchilla in 3-blast group. Both waveforms illustrate a single positive overpressure peak at a level of 13 or 15 psi. After reaching the sharp positive peak, the pressure quickly decreased to a level of −2 psi and then leveled out to the baseline with a duration about 2 ms. The BOP waveforms were repeatable for each blast test.

ABR Threshold Shifts in 2-Blast and 3-Blast Animals

The mean and SD of ABR threshold shifts measured from animals in 2-blast group over 7 days (days 1, 4, and 7) after blast exposures are shown in Figure 4A. The greatest threshold shift occurred on day 1 and the shift value decreased with the time course. On day 1, the ABR threshold shift

Downloaded from https://academic.oup.com/milmed/article-abstract/185/Supplement_1/248/5740813 by University of Oklahoma user on 20 February 2020

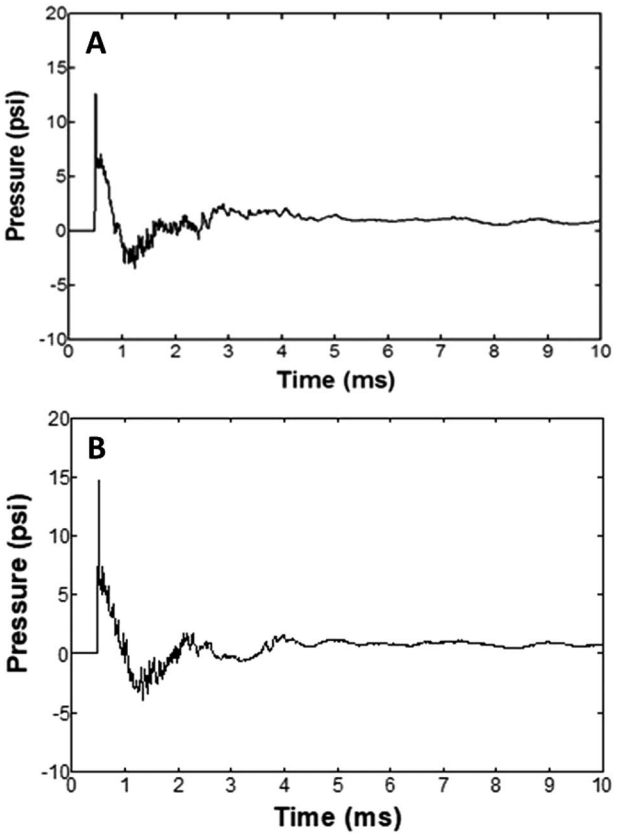


FIGURE 3. (A) A recorded BOP waveform at the entrance of the ear canal from an animal test in 2-Blast group with a peak pressure of 13 psi. (B) A recorded BOP waveform from an animal test in 3-Blast group with a peak pressure of 15 psi.

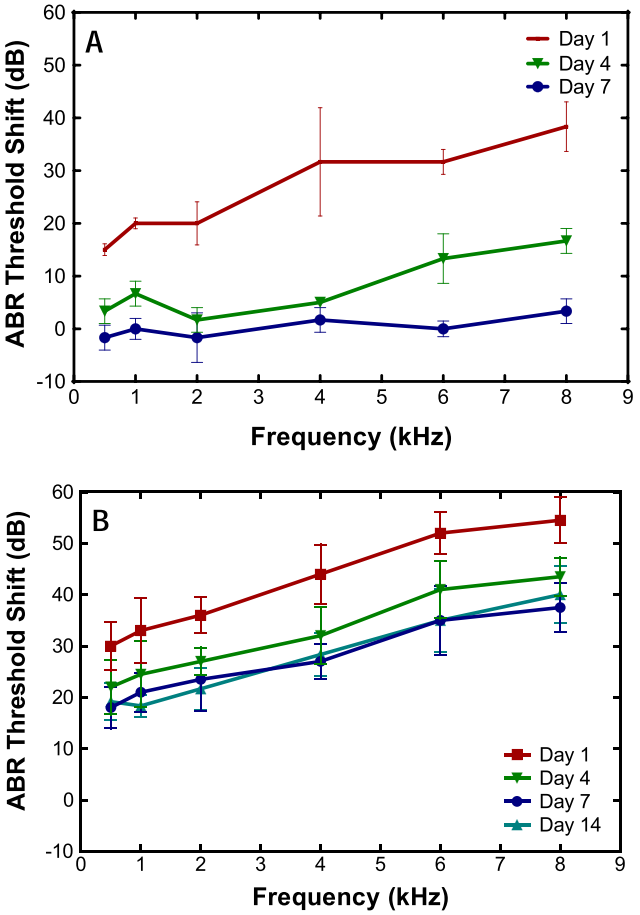


FIGURE 4. ABR threshold shifts (Mean ± SD) measured from 2-Blast group (A) and 3-Blast group (B). For each group, $n = 10$ ears.

increased almost linearly at all frequencies from 15 dB at 0.5 kHz to 38 dB at 8 kHz. On day 4, the shift decreased to 7 dB at 0.5 kHz and 16 dB at 8 kHz or about 8–22 dB decreasing over the frequencies. By day 7, the ABR threshold shift at all frequencies decreased to original levels at all frequencies, which indicates that the hearing damage was recovered to the pre-blast level after 7 days in the ears with earplugs ($P > 0.05$).

The mean and SD of the ABR threshold shifts measured from animals in 3-blast group over 14 days (days 1, 4, 7, and 14) after blast exposures are shown in Figure 4B. On day 1, the threshold shift increased almost linearly from 30 dB at 0.5 kHz to 55 dB at 8 kHz. Compared with the day 1 line in Figure 4A, there was a substantial increase of the ABR threshold shift in 3-blast animals from the 2-blast animals. On day 4, the threshold shift decreased from the day 1 about 8–11 dB over the frequencies, which were less than that observed in Figure 4A, 4 days after 2 blasts, particularly at higher frequencies. Moreover, on days 7 and 14, the ABR shifts reached the similar values over the frequencies from 18 dB at 0.5 kHz to 40 dB at 8 kHz, and a 4-dB decrease compared with that on day 4. These results indicate that no further recovery of the ABR threshold shift after 7 or 14 days was observed and the permanent hearing loss was demonstrated in chinchillas after three blasts at the BOP level of mTBI even with hearing protection devices (earplugs). Results of days 7 and 14 were compared to pre-exposure thresholds and were extremely significant at all frequencies in the 3-blast group ($P < 0.001$).

Additionally, statistical analysis comparing ABR threshold level shifts between the 2-blast and 3-blast groups after equivalent intervals after the blast indicated that the differences were extremely significant for post-blast, day 4, and day 7 over the frequency range ($P < 0.001$).

DPOAE Level Shifts in 2-Blast and 3-Blast Animals

Figure 5 shows the mean and SD of DPOAE level shifts (reductions) measured from animals in both groups at frequencies of 1–14 kHz. The results of 2-blast ears are shown in Figure 5A on days 1, 4, and 7. The mean value of the DPOAE level shift ($n = 10$ ears) increased from about 8 dB at 1 kHz to the peak of 35 dB at 11–12 kHz on day 1 after blasts. The shift decreased significantly on day 4 to a level lower than 5 dB and further decreased to around zero on day 7 over the entire frequency range. Results indicate that the damage induced

Downloaded from https://academic.oup.com/milmed/article-abstract/185/Supplement_1/248/5740813 by University of Oklahoma user on 20 February 2020

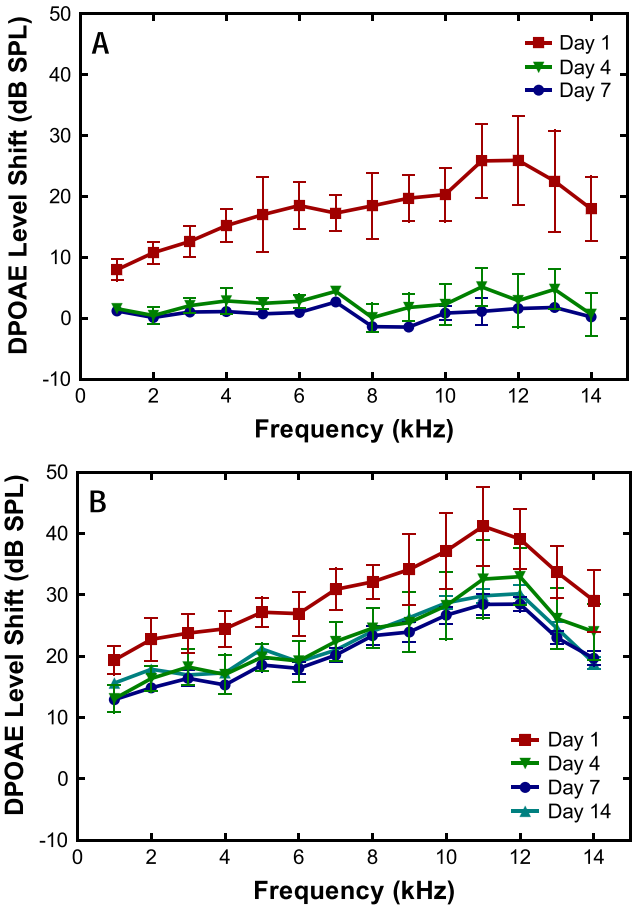


FIGURE 5. DPOAE level shifts (Mean ± SD) measured from 2-Blast Group (A) and 3-Blast group (B). For each group, $n = 10$ ears.

in cochlear outer hair cells was recovered after 7 days of post-blast in the ears with earplugs, with no significant difference when compared to pre-exposure levels ($P > 0.05$).

The DPOAE level shifts from 3-blast animals ($n = 10$ ears) are shown in Figure 5B. The DPOAE reduction increased from about 20 dB at 1 kHz to a peak of 40 dB at 11 kHz on day 1. This level shift increased by 12–15 dB across the frequency range compared with the shift after two blasts. On day 4, the DPOAE level shift decreased by 8 dB across the frequencies, which reflected the recovery of the cochlear function after 4 days of post-blast. On day 7 and day 14, there was no further change of the DPOAE level except at frequencies over 11 kHz with 5 dB decreasing. Results indicate that 3-blast at the intensity causing mTBI resulted in permanent cochlear damage with the DPOAE level reduction at the minimum of 13 dB at 1 kHz and the maximum of 28 dB at 11 kHz. Day 7 and day 14 results were compared to pre-exposure levels, and the results were extremely significant with $P < 0.001$.

Statistical tests comparing DPOAE threshold level shifts between the 2-blast and 3-blast groups were conducted in the same manner as the ABR. The statistical results indicate that differences between the DPOAE levels after equivalent time intervals were extremely significant for post-blast, day 4, and day 7 ($P < 0.001$).

Immunofluorescence Staining: PI3K and DAPI Imaging

Figure 6 is a comparison of immunofluorescence staining of phosphatidylinositol-4,5-bisphosphate 3-kinase (PI3K; green) and 4′,6-diamidino-2-phenylindole (DAPI; blue), the nuclear counter stain in the chinchilla AC. Images in the top row are stains of the AC taken from a control animal, with PI3K staining in the left column, DAPI staining in the center column, and the overlay in the right column. The second and third rows are similarly organized, with the second row showing staining results for a 2-blast animal on day 7 and the third row showing results for a 3-blast animal on day 14. The red arrows indicate the PI3K expression in the AC.

A strong PI3K response is shown in the control animal in Figure 6 (first row, left column). Immunofluorescence of the PI3K revealed the concentrated regions of the protein and the DAPI staining for the nuclear counter revealed tight, uniform groupings for each counter stain. The overlay shows that the PI3K protein was located similarly to the nucleus. The 2-blast animal (second row) showed a strong PI3K response as well (left) and each of the stains was concentrated and large. The DAPI counter stains (center) also demonstrated a strong nuclear response and the images overlaid well (right) showing integrity of the AC. Finally, the third row of Figure 6 displays the response from a 3-blast animal on day 14. The PI3K imaging (left) shows a declined response with regard to the control and 2-blast animal.

Hoechst Staining

Figure 7 is the Hoechst staining in the chinchilla AC for control (left), 2-blast (center), and 3-blast (right). The control image of the AC reveals dense, uniformly colored nuclei, showing the neurons were not damaged. The center image from a 2-blast animal shows similar nuclear distribution in the AC. The existence of uniform distribution suggests that two blasts were insufficient to cause observable neural damage in the AC after 7 days of post-blast. The right image of Figure 7 from a 3-blast animal shows nonuniform nuclear distribution, pointed out with red arrows. The density of the nuclear fragments suggests nuclear fragmentation, even after 14 days of post-blast exposure. Three blasts were sufficient to cause observable neural damage to the AC, which was either displayed or remained on day 14.

DISCUSSION

Temporary and Permanent Hearing Damage: 2-Blast vs. 3-Blast

mTBI induced by blast exposures can result in debilitating conditions such as posttraumatic stress disorder.[2] Hearing

Downloaded from https://academic.oup.com/milmed/article-abstract/185/Supplement_1/248/5740813 by University of Oklahoma user on 20 February 2020

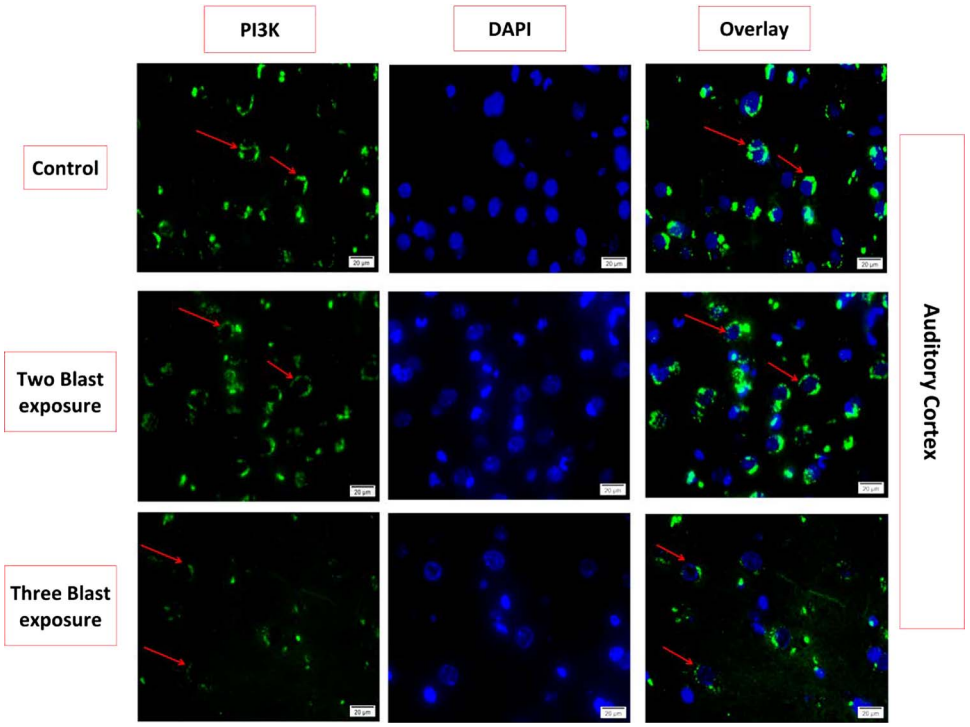


FIGURE 6. The immunofluorescence staining of PI3K in chinchilla AC in control, 2-Blast, and 3-Blast animals. The top three figures were from the AC in control animals; the middle three figures from the AC in 2-Blast animals on day 7; the bottom three figures from the AC in 3-Blast animals on day 14. Images were taken at a magnification of 400×. *Arrows* marked the p85α expression in the ac. The nuclear counter stain was DAPI (*Blue*).

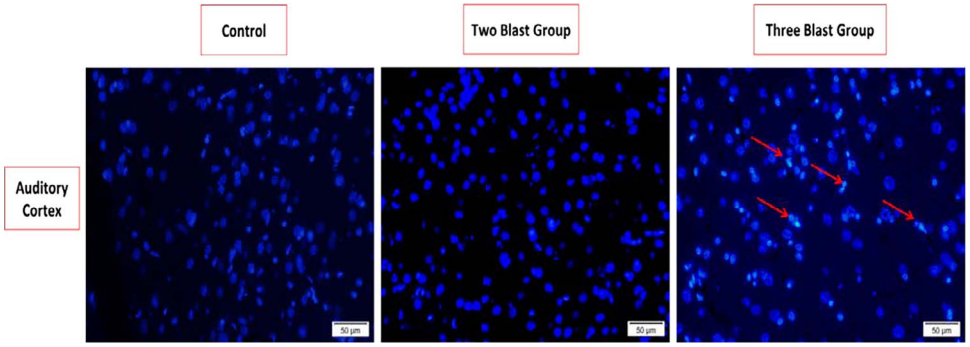


FIGURE 7. The hoechst staining in chinchilla AC in control (*Left*), 2-Blast (*Middle*), and 3-Blast (*Right*) animals. Images were taken at a magnification of 100×. *Arrows* marked the apoptotic cells for representing nuclear condensation/fragmentation.

damage also accompanies blast exposures as a consequence of either temporary hearing loss or permanent hearing loss, depending on the number of blast exposures and the time course after blasts. It is unclear if hearing protection devices (eg, earplugs) can provide adequate protection against hearing damage at the BOP level causing mTBI. Using the blast animal model of chinchilla, this study has provided some answers to those questions through the 2-blast and 3-blast animals over different time courses following exposures. Ears without protection were not tested in this study because the BOP level is higher than the threshold of TM rupture as reported by Gan et al.[3]

ABR threshold shift and DPOAE level change were increased after blasts in both 2-blast and 3-blast animals as shown in Figures 4 and 5, which reflected the acute or temporary hearing loss following the blasts. The severity of damage is significantly related to the number of blasts as the comparison between two day 1 curves in Figure 4A and B ($P < 0.001$). DPOAE level shifts further indicate immediate impairment of cochlear outer hair cells. These results parallel with that reported by Chen et al.[14] who observed an accumulative factor in severity of hearing damage when comparing the 2- and 3-blasts at low-level overpressures. Results from the present study support their conclusion that

Downloaded from https://academic.oup.com/milmed/article-abstract/185/Supplement_1/248/5740813 by University of Oklahoma user on 20 February 2020

while the blast pressure level is important, the additive effect from number of blasts is also a critical factor.

Effect of BOP Level on Protected Ears

Similar experimental methods were used by Chen et al.[14] in chinchilla blast model. In their study, chinchillas with foam earplugs in left ears were exposed to two blasts at low-intensity BOP levels, 21–35 kPa. Their results for acute hearing damage in protected ears were comparable to day 1 hearing damage found in this mTBI study, and the similarities were observed in ABR and DPOAE function tests over the measured frequencies. Though the progressive response from two blasts of low-intensity BOPs was not reported in Chen et al.'s work, we expect that the recovery of hearing function in those groups would match the observations of this study 7 days after blasts. This relationship will be investigated in future studies.

Chen et al. examined the progressive effect of blasts at low-intensity BOP levels on hearing damage over 7 days in chinchillas.[14] Animals with foam earplugs were exposed to three blasts at low-intensity BOPs levels (21–35 kPa) and hearing function was measured 7 days after blasts. The ABR and DPOAE results indicated some permanent hearing damage remained on day 7. The results of 3-blast animals 7 days after blasts in this study also demonstrate permanent hearing damage indicated by ABR threshold shifts and DPOAE level shifts. Overall, hearing function tests in chinchillas after blasts at the low-intensity and the mTBI BOP levels indicate that the protective function of earplugs is limited when exposed to more than two blasts. The limitation of the protective function of earplugs, especially when exposed to multiple blasts, is a fascinating and relatively uncharted research area and will be further investigated in future studies.

Cellular Evidences of mTBI-Induced Hearing Loss

PI3K is the second messenger in the PI3K/protein kinase B (AKT) intracellular signaling pathway, important in regulating the cell cycle. It is the major signaling axis that predominantly regulates downstream cellular events such as cell proliferation, apoptosis, mitochondrial biogenesis, or other protein synthesis.[26] The activation of this pathway promotes cell proliferation and viability, and inhibits apoptosis in neurodegenerative diseases.[27] Therefore, as a preliminary study, we expected to investigate the effect of the number of blasts on the regulation of the PI3K/AKT pathway by monitoring the expression level of PI3K in the CAS.

The results shown in Figure 6 indicate that the expression level of PI3K is inversely correlated with the hearing function, which can be explained by 3-blast exposures that are likely to damage the AC through downregulating the PI3K/AKT pathway. However, the downstream cellular events in the PI3K/AKT pathway are very complicated, which suggests the expression level of PI3K may not be an ideal biomarker for the actual cellular event such as cell proliferation or apoptosis in this situation. Moreover, the number of animals involved in this immunofluorescence study was very limited and the post-blast time for two groups of animals was different. Therefore, the results reported in Figures 6 and 7 are immature. We will increase the sample size, use consistent experimental time length, and choose more reasonable target protein such as Caspase-3 or NeuN for future studies on neural damage.

CONCLUSION

This study aimed at investigating the progressive hearing damage in chinchillas when exposed to two or three repeated mTBI level blasts. Animals were exposed to blasts at BOP levels of 103–138 kPa or 15–20 psi (mTBI level) with both ears plugged with foam earplugs. The ABR and DPOAE were measured before and after exposures on day 1 and over a time course of 7 or 14 days after two or three blasts, respectively, for the progressive study. Major findings from this study include: (1) the hearing damage following blast exposures on day 1 for 3-blast animals was greater than that for 2-blast animals; (2) two blasts were not sufficient to cause permanent hearing damage in ears protected with earplugs; (3) three blasts caused permanent hearing damage reflected in ABR and DPOAE measurements and the damage in the AC shown in immunofluorescence staining of PI3K and DAPI images. The results indicate that the foam earplug tested in this study could not provide adequate protection against permanent hearing damage when exposed to three blasts at the mTBI level. Future studies on the correlation between the CAS and PAS damages are needed to provide more inside of lights on the mechanisms of hearing protection devices to repetitive blast exposure at the mTBI level.

FUNDING

This work was supported by U.S. Army Medical Research and Material Command (USAMRMC) Military Operational Medicine Research Program, Contract No. W81XWH-14-1-0228.

REFERENCES

1. Wells TS, Seelig AD, Ryan MAK, et al: Hearing loss associated with US military combat deployment. Noise Health 2015; 17(74): 34–42.
2. Hoge CW, McGurk D, Thomas JL, et al: Mild traumatic brain injury in US soldiers returning from Iraq. N Engl J Med 2008; 358(5): 453–63.
3. Gan RZ, Nakmali D, Ji XD, Leckness K, Yokell Z: Mechanical damage of tympanic membrane in relation to impulse pressure waveform–a study in chinchillas. Hear Res 2016; 340: 25–34.
4. Cho S, Gao SS, Xia A, et al: Mechanisms of hearing loss after blast injury to the ear. PLoS One 2013; 8(7): 1–15.
5. Liberman MC, Kujawa SG: Cochlear synaptopathy in acquired sensorineural hearing loss: manifestations and mechanisms. Hear Res 2017; 349: 138–47.
6. Munjal SK, Panda NK, Pathak A: Dynamics of hearing status in closed head injury. J Neurotrauma 2010; 27: 309–16.

Downloaded from https://academic.oup.com/milmed/article-abstract/185/Supplement_1/248/5740813 by University of Oklahoma user on 20 February 2020

7. Song H, Konan LM, Cui J, et al: Ultrastructural brain abnormalities and associated behavioral changes in mice after low-intensity blast exposure. Behav Brain Res 2018; 347: 148–57.
8. Hall AA, Mendoza MI, Zhou H: Repeated low intensity blast exposure is associated with damaged endothelial glycocalyx and downstream behavior deficits. Front Behav Neurosci 2017; 11(104): 1–10.
9. Saunders GH, Griest SE: Hearing loss in veterans and the need for hearing loss prevention programs. Noise Health 2009; 11(42): 14.
10. Fausti SA, Wilmington DJ, Gallun FJ, Myers PJ, Henry JA: Auditory and vestibular dysfunction associated with blast-related traumatic brain injury. J Rehabil Res Dev 2009; 46(6): 797–810.
11. Abdul-Muneer PM, Schuetz H, Wang F, et al: Induction of oxidative and nitrosative damage leads to cerebrovascular inflammation in animal model of mild traumatic brain injury induced by primary blast. Free Radic Biol Med 2013; 60: 283–91.
12. DeKosky ST, Ikonomovic MD, Gandy S: Traumatic brain injury—football, warfare, and long-term effects. N Engl J Med 2010; 363(14): 1293–6.
13. DePalma RG, Hoffman SW: Combat blast related traumatic brain injury (TBI): decade of recognition; promise of progress. Behav Brain Res 2018; 340: 102–5.
14. Chen T, Smith K, Jiang S, Zhang T, Gan RZ: Progressive hearing damage after exposure to repeated low-intensity blasts in chinchillas. Hear Res 2019; 378: 33–42.
15. Perez-Polo JR, Rea HC, Johnson KM, et al: Inflammatory consequences in a rodent model of mild traumatic brain injury. J Neurotrauma 2013; 30: 727–40.
16. Race N, Lai J, Shi R, Bartlett EL: Differences in postinjury auditory system pathophysiology after mild blast and nonblast acute acoustic trauma. J Neurophysiol 2017; 118: 782–99.
17. Gallun FJ, Papesh MA, Lewis MS: Hearing complaints among veterans following traumatic brain injury. Brain Inj 2016; 31(9): 1183–7.
18. Guan X, Gan RZ: Effect of middle ear fluid on sound transmission and auditory brainstem response in Guinea pigs. Hear Res 2011; 277: 96–106.
19. Daniel SJ, Duval M, Sahmkow S, Akache F: Ototoxicity of topical moxifloxacin in a chinchilla animal model. Laryngoscope 2007; 117(12): 2201–5.
20. Hickman TT, Smalt C, Bobrow J, Quatieri T, Liberman MC: Blast-induced cochlear synaptopathy in chinchillas. Sci Rep 2018; 8(10740): 1–12.
21. Guan X, Seale TW, Gan RZ: Factors affecting sound energy absorbance in acute otitis media model of chinchilla. Hear Res 2017; 350: 22–31.
22. Engles WG, Wang X, Gan RZ: Dynamic properties of human tympanic membrane after exposure to blast waves. Ann Biomed Eng 2017; 45(10): 2383–94.
23. Henry KS, Kale S, Scheidt RE, Heinz MG: Auditory brainstem responses predict auditory nerve fiber thresholds and frequency selectivity in hearing impaired chinchillas. Hear Res 2011; 280: 236–44.
24. Zhong Z, Henry KS, Heinz MG: Sensorineural hearing loss amplifies neural coding of envelope information in the central auditory system of chinchillas. Hear Res 2014; 309: 55–62.
25. Jiang S, Seale TW, Gan RZ: Morphological changes in the round window membrane associated with Haemophilus influenzae-induced acute otitis media in the chinchilla. Int J Pediatr Otorhinolaryngol 2016; 88: 74–81.
26. Yang J-L, Chen W-Y, Chen S-D, Yang J-L, Chen W-Y, Chen S-D: The emerging role of GLP-1 receptors in DNA repair: implications in neurological disorders. Int J Mol Sci 2017; 18: 1861.
27. Athauda D, Foltynie T: The glucagon-like peptide 1 (GLP) receptor as a therapeutic target in Parkinson's disease: mechanisms of action. Drug Discov Today 2016; 21: 802–18.

Downloaded from https://academic.oup.com/milmed/article-abstract/185/Supplement_1/248/5740813 by University of Oklahoma user on 20 February 2020

Journal of the Mechanical Behavior of Biomedical Materials 100 (2019) 103368

Contents lists available at ScienceDirect

Journal of the Mechanical Behavior of Biomedical Materials

journal homepage: www.elsevier.com/locate/jmbbm

The effect of blast overpressure on the mechanical properties of the human tympanic membrane

Junfeng Liang[a,b], Kyle D. Smith[b], Rong Z. Gan[b], Hongbing Lu[a,*]

[a] Department of Mechanical Engineering, The University of Texas at Dallas, Richardson, TX, 75080, USA
[b] School of Aerospace and Mechanical Engineering, University of Oklahoma, Norman, OK, 73019, USA

ARTICLE INFO

Keywords:
Hearing damage
Blast overpressure
Tympanic membrane
Micro-fringe projection
Mechanical properties

ABSTRACT

The rupture of the tympanic membrane (TM) is one of the major indicators for blast injuries due to the vulnerability of TM under exposure to blast overpressure. The mechanical properties of the human TM exhibit a significant change after it is exposed to such a high intensity blast. To date, the published data were obtained from measurement on TM strips cut from a TM following an exposure to blast overpressure. The dissection of a TM for preparation of strip samples can induce secondary damage to the TM and thus potentially lead to data not representative of the blast damage. In this paper, we conduct mechanical testing on the full TM in a human temporal bone. A bulging experiment on the entire TM is carried out on each sample prepared from a temporal bone following the exposure to blast three times at a pressure level slightly below the TM rupture threshold. Using a micro-fringe projection method, the volume displacement is obtained as a function of pressure, and their relationship is modeled in the finite element analysis to determine the mechanical properties of the post-blast human TMs, the results of which are compared with the control TMs without an exposure to the blast. It is found that Young's modulus of human TM decreases by approximately 20% after exposure to multiple blast waves. The results can be used in the human ear simulation models to assist the understanding of the effect of blast overpressure on hearing loss.

1. Introduction

Blast-induced injuries commonly occur under such situations as accidents on construction sites and during terrorist attacks and military conflicts where the explosion takes place (Owens et al., 2008; Wolf et al., 2009). In explosion, the massive explosive energy released often leads to four types of injuries: primary, secondary, tertiary, and quaternary blast injuries. The primary injury is caused by the direct impact of the over-pressurized wave, in the form of rupture of gas-filled organs including lungs, middle ear, and eyes. The secondary injury results from flying debris and bomb fragments and occurs on the surface of a victim. The tertiary injury includes limb fracture, brain injury, and body part injury caused by blunt impact when an individual is thrown away by the blast wind. All the other explosion-related injuries especially those illnesses and diseases exacerbated by the blast are referred to as the quaternary injuries; they may include the exacerbation of asthma from toxic smoke and hyperglycemia from the trauma. The primary blast injury is often given the greatest concern (Mathews and Koyfman, 2015; Nakagawa et al., 2011).

Hearing loss or auditory system damage is one of the most critical sequelae among the primary blast injuries. As an air-filled organ, the ear is one of the most vulnerable organs to blast overpressure. Blast-induced hearing injury is categorized into tympanic membrane (TM) perforation or rupture, middle ear ossicular disruption, cochlear hair cell loss, and rupture of round window (Yeh and Schecter, 2012). The TMs have the lowest pressure threshold for injury in the auditory system; hence rupture of the human TM is one of the most common primary blast injuries. As an example, in the 2013 Boston blast, 90% of the hospitalized patients experienced TM perforation (Remenschneider et al., 2014). Because the lesion of the TM is strongly associated with hearing loss and tinnitus, the rupture of TM is usually a marker or an indicator for primary blast injury (Dougherty et al., 2013). The TM is a viscoelastic material with mechanical properties changing significantly at high frequencies or high strain rates (Luo et al., 2009). Even before the overpressure reaches the rupture threshold, it may have already experienced loading pressure at a high strain rate. This overpressure can potentially induce sub-microscopic damage to the fiber layers of the TM, which is difficult to observe directly, but can be severe enough to

* Corresponding author. Department of Mechanical Engineering, University of Texas at Dallas, 800 W Campbell Rd, ECSN 2.528, Richardson, TX, 75080-3021, USA.
E-mail address: hongbing.lu@utdallas.edu (H. Lu).

https://doi.org/10.1016/j.jmbbm.2019.07.026
Received 21 March 2019; Received in revised form 14 June 2019; Accepted 22 July 2019
Available online 07 August 2019
1751-6161/ © 2019 Published by Elsevier Ltd.

alter the overall mechanical properties of the TM (Engles et al., 2017; Liang et al., 2017).

Recently, using a miniature split Hopkinson tension bar, Luo et al. (2016) determined that the Young's modulus of the human TM at different strain rates changes significantly after its exposure to blast overpressure. Engles et al. (2017) measured the dynamic properties of the strips cut from blast-exposed TMs using acoustic loading and a laser Doppler vibrometer (LDV). They also found that both storage and loss moduli of the TM exhibit pronounced decrease over a frequency range of 200–8000 Hz. However, in those studies, strip specimens cut from the TM were used; cutting a TM into strips may alter the physiological condition of the TM (O'Connor et al., 2008). To circumvent this issue, a micro-fringe projection technique was used for characterization of the mechanical properties for chinchilla TMs (Liang et al., 2017). In this bulging experiment, fringes with sub-millimeter pitch are projected onto the TM, and quasi-static air pressure is applied to the TM. A comparison between control and post-blast chinchilla TMs shows that there is about a 50% reduction in Young's modulus for the post-blast chinchilla TM. The decrease is larger than that of a human TM observed by Engles et al. (2017) and Luo et al. (2016).

In this paper, we apply the micro-fringe projection technique on the human TMs to evaluate the change of the mechanical properties of the human TM after its exposure to the blast overpressure. The intact, full-size TMs in human cadaver temporal bones are used directly without sectioning in bulging experiments. They are subjected to multiple exposures of blast waves with a pressure slightly lower than the rupture threshold (~70 kPa) of the human TM (Gan et al., 2018). Results are compared between the control (normal) and post-blast TMs to evaluate the role of blast over-pressure on the mechanical property change of the human TMs.

2. Methods

2.1. Exposure of the human TMs to blast waves

Fresh human cadaveric temporal bones (n = 16) containing the intact auditory system from the Life Legacy Foundation, a certified human tissue supplier for military research, are used in this study. The protocol has been approved by the U.S. Army Medical Research and Material Command (USAMRMC) Office of Research Protections (ORP). To prepare the post-blast TM sample, the temporal bone is mounted to a head block placed inside a blast chamber where it is exposed to blast overpressure. The experiment is conducted in the Biomedical Engineering Laboratory at the University of Oklahoma (Fig. 1). The blast overpressure is generated using a comporessed-nitrogen-driven blast apparatus. A 130-μm thick polycarbonate film is used as a diaphragm sealing the outlet of the blast apparatus, the rupture of which releases blast overpressure between 45 and 55 kPa. The magnitude of overpressure applied on a TM is controlled by varying the distance between the blast outlet and the TM, and monitored by a pressure sensor (Model 102B16, PCB Piezotronics, Depew, NY) located at the entrance of the ear canal (approximately 1 cm from the ear canal opening). A data acquisition system using a LabVIEW interface on a PC (cDAQ 7194 and A/D converter 9215, National Instruments Inc., Austin, TX) with a sampling rate of 100 kS/s (10-μs interval) is used to acquire the pressure data. For the purpose of comparison, five control TMs (which are not exposed to blast waves) are harvested as the control TM samples prior to the TM blast experiments. The TM sample information is shown in Table 1. The remaining temporal bones are exposed to three times of blast with an average peak pressure of 50 kPa (equivalent to a sine wave of 188 dB SPL), which is below the rupture threshold of the human TM (~70 kPa). The information for this group of TM samples is listed in Table 2.

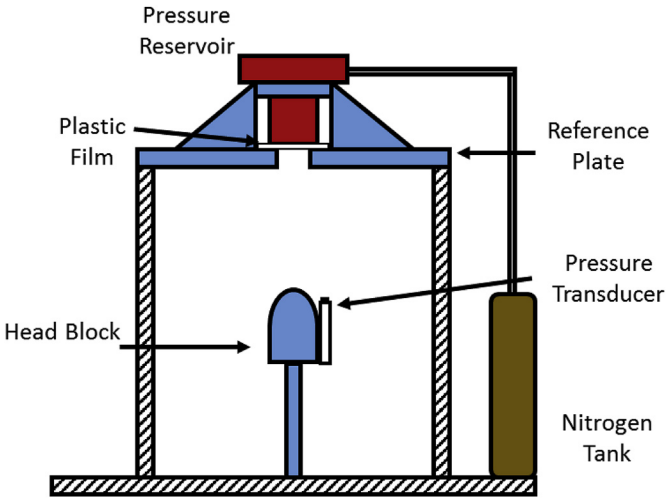


Fig. 1. Schematic of the blast testing chamber and the sample setup. For demonstration purposes, the components are not drawn to scale.

2.2. Sample preparation

To prepare a sample for the micro-fringe projection measurement, each temporal bone is first trimmed to a small bony block containing the entire TM and the entire middle ear. Then the ear canal is carefully ground until the TM is fully exposed. A 3-mm diameter hole is drilled in the posterior-superior area of the middle ear and a polyvinyl chloride (PVC) tubing (1.5 mm inner diameter, 3 mm outer diameter, 75 mm long) is inserted into the hole and sealed on the bony block with “two-part epoxy” (Devcon and 5 Minute, Illinois Tool Works Inc). The outer surface of the entire bony block is further sealed with paraffin to keep the middle ear cavity in an airtight condition. After the epoxy is fully cured, the outer end of the tubing is connected to a pressure monitoring system that consists of a syringe pump and a pressure gauge to apply static pressure to the TM from the medial side (Fig. 2). The time it takes to prepare a temporal bone before the measurement is approximately 45 min. To protect the TM from dehydration, a droplet of 0.9% saline solution is applied to the TM at 5-min intervals during the measurement. Meanwhile, the TM is covered with paper saturated with saline solution during the curing of the epoxy. To produce high-quality TM fringe images, the lateral surface of the TM is coated with a thin layer of titanium oxide (100 mg/ml) in saline to provide a diffused reflective surface. Titanium oxide has been widely used in Moiré techniques to measure the TM motion. A thin layer of titanium oxide coating is not anticipated to affect the mechanical response of the TM (Liang et al., 2015, 2016, 2017; Dirckx and Decraemer, 1997).

2.3. Micro-fringe projection experiments

A micro-fringe projection system is used to measure the volume displacement of the TM under different static pressures coupled with a 3-dimensional surface reconstruction algorithm. The system consists of a micro-fringe projector, a surgical microscope (Zeiss, model 50881) and a digital camera (Nikon D7000) as shown in the schematic diagram in Fig. 3. The micro-fringe projector projects the shadow of a fine Ronchi ruling grating with pitch density of 20 cycles/mm (Edmund Optics) onto the TM surface using a fiber optic illuminator (Techniquip Corp. model R150-A2). Stepwise pressures with increments of ± 0.125 kPa up to ± 1.0 kPa are applied through a PVC tube onto the middle ear side of the bony block and monitored with a pressure gauge. Images of the fringe patterns on the TM under different pressures are acquired with the Nikon digital camera connected to the surgical microscope. Before each test, the TM is preconditioned by applying a small pressure with a magnitude of 100 Pa for five cycles. This allows the tissue material to reach a steady state (Liang et al., 2016; Gaihede, 1996). Virtual interferometry is formed by digitally combining the

Table 1
Dimensions and parameters of the Ogden model for each control human TM.

Sample Number	Superior-Inferior Diameter (mm)	Anterior-Posterior Diameter (mm)	μ_1 (MPa)	α_1	μ_2 (MPa)	α_2
TB15-51	8.94	9.62	4.2	3.0	-1.3	0.8
TB15-52	7.81	8.89	3.7	3.2	-1.2	0.8
TB16-11	7.09	9.12	4.3	2.7	-1.0	0.8
TB16-12	8.53	8.91	3.8	2.6	-1.3	0.9
TB16-19L	7.95	8.12	4.1	2.6	-1.1	0.9
Average ± Standard Deviation	8.06 ± 0.63	8.93 ± 0.48	4.0 ± 0.2	2.8 ± 0.2	-1.2 ± 0.1	0.8 ± 0.1

Table 2
Dimensions, average pressure for the blast wave and parameters of the Ogden model for each post-blast human TM.

Sample Number	Superior-Inferior Diameter (mm)	Anterior-Posterior Diameter (mm)	Average Blast Pressure (kPa)	μ_1 (MPa)	α_1	μ_2 (MPa)	α_2
TB15-59	8.57	7.90	48	3.8	3.1	-1.5	1.0
TB15-60	8.83	7.77	48	3.7	3.0	-1.1	1.0
TB15-63	7.54	7.90	48	3.5	2.8	-1.5	1.0
TB15-64	7.43	7.04	48	3.6	2.9	-1.5	0.9
TB16-47	8.55	6.91	46	3.4	2.7	-1.2	0.9
TB16-48	8.24	7.15	46	3.5	3.0	-1.5	1.2
TB16-1L	10.0	7.12	61	4.0	2.4	-1.5	0.9
TB16-2R	8.53	6.95	61	3.3	2.8	-1.5	0.9
TB14-19	8.11	8.10	52	3.5	2.5	-1.1	1.0
TB14-20	8.55	7.89	45	3.9	2.6	-1.4	1.0
TB17-2R	10.7	10.3	26	2.4	-1	0.9	3.8
TB17-7L	8.5	8.3	28	2.1	-1.1	0.8	4.0
TB17-8R	9.6	7.2	25	2.4	-1.4	0.9	3.6
TB17-9L	9.9	7.8	21	2.7	-1.4	1.1	3.1
TB17-10R	7.7	7.7	26	2.8	-1.4	0.9	3.7
TB17-2R	8.3	7.2	26	2.4	-1	0.9	3.8
Average ± Standard Deviation	8.69 ± 0.89	7.68 ± 0.80	32 ± 13	3.6 ± 0.6	2.8 ± 1.9	-1.4 ± 1.1	1.0 ± 1.3

fringe pattern projected onto the TM with a reference fringe pattern projected onto a flat plane. Topography of the human TM that contains the height information of the TM surface is reconstructed from the interferometry using software Joshua (developed by Manuel Heredia at University of Sheffield) based on a five-step phase-shifted algorithm (Ortiz and Patterson, 2005). The resolution of the topography depends on the fringe density and the camera resolution. For the system used in this study, the height resolution is ~15 μm (Liang, 2009). To quantify the deformation of the TM under different static pressures, volume displacements are calculated by subtracting the reconstructed surface topography of the TM under pressure with that of the TM at the zero-pressure state. Details on the calculation of the surface topography and volume displacement calculations are described in previous publications (Liang et al., 2015, 2016, 2017).

2.4. Finite element method analysis

A finite element method (FEM) model for the human TM is established based on the surface topography of a human TM at the zero-pressure state reconstructed from the micro-fringe projection. The surface topography is converted to a three-dimensional solid model by computer-aided design (CAD) software (SolidWorks, 2014) and then further meshed into a FEM model for simulations in ANSYS15.0. Because the TM thickness is small compared to its major or minor axis, the TM is modeled as a shell with a thickness of 80 μm according to the average thickness of the human TMs used in this study. To match the model results with the experimental data, the dimensions of the TM FEM model are modified to appropriately reflect those of each individual TM sample. The dimensions of the TM samples used for

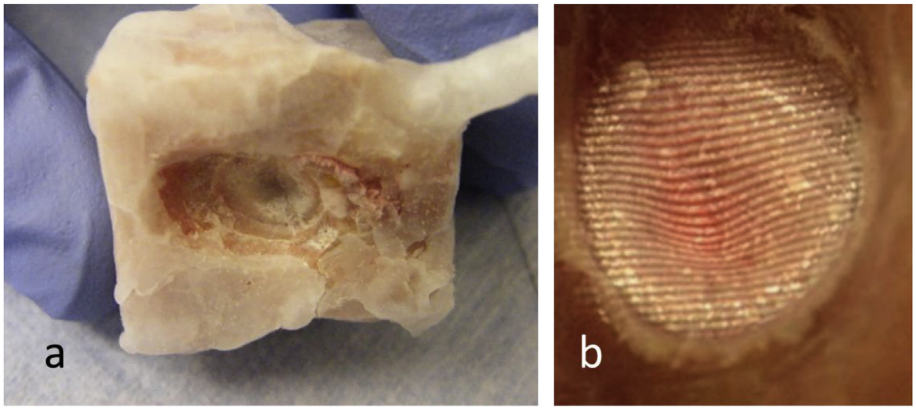


Fig. 2. Sample preparation: a) the bony block containing the entire middle and inner ear sealed with paraffin b) the human TM painted with titanium oxide.

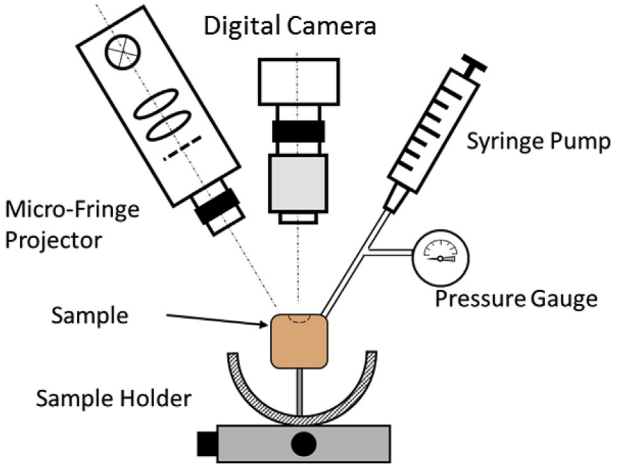


Fig. 3. Schematic view of the micro-fringe projection system and the pressure monitoring system utilized in this study.

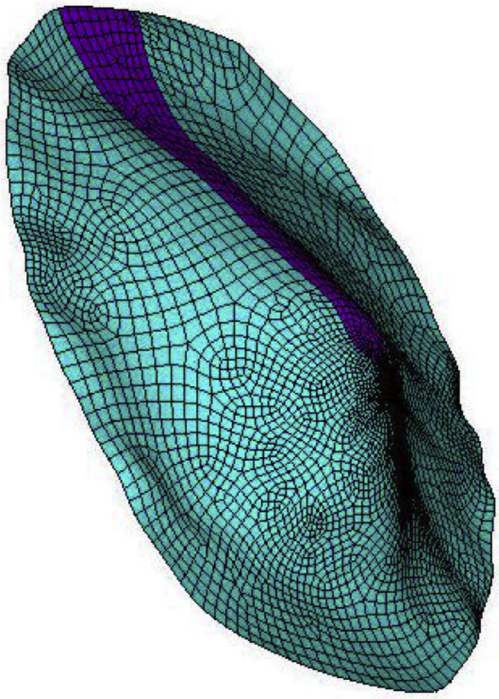


Fig. 4. Finite element mesh for TB15-51. The purple area is the simplified manubrium.

adjusting the FEM models are listed in Tables 1 and 2. To simplify the model, the manubrium of the malleus attached to the TM is also simulated as a section of the shell model of the TM using the properties of bone (10 GPa Young's modulus and 0.2 Poisson's ratio). The annulus of the TM is fixed for all degrees of freedom (no translation or rotation). The entire model (including the membrane and the manubrium) contains ~10,000 4-node tetrahedral shell elements (shell-181). Uniform pressures with an increment of ± 0.125 kPa up to ± 1.0 kPa are applied on the medial side of the TM. The boundary conditions, loading, and meshes of the TM FEM model are shown in Fig. 4. For each individual TM sample, the simulated volume displacement is calculated under each static pressure. It is noted that the actual connection between manubrium and TM is complicated and varies among individuals. Between the umbo and the lateral process of the malleus, the TM and the manubrium are connected through a layer of soft tissue (De Greef et al., 2016). To evaluate the effect of the coupling of the TM and the manubrium on the TM displacement in our model, a testing simulation is conducted. According to the results from De Greef et al., 25% of the length of the manubrium around the umbo and 12.5% of the length of the manubrium around the lateral process are set to have the properties of the bone. The remaining part of the manubrium is set to have the mechanical properties of the TM. The simulation results under 1 kPa show that the volume displacement changes only by 3.8%. Thus the variation of the TM-manubrium connection does not have a significant effect on our simulation results.

Similar to the studies on guinea pigs and chinchillas (Liang et al., 2015, 2016, 2017), the 2nd-order Ogden model is used in this study to describe the mechanical behavior of human TM under large deformations. The uniaxial form of the 2nd-order Ogden model is given as (Aernouts et al., 2010; Wang et al., 2002).

$$T_U = \sum_{i=1}^{2} \frac{2\mu_i}{\alpha_i}\left(\lambda_U^{\alpha_i - 1} - \lambda_U^{-0.5\alpha_i - 1}\right) \tag{1}$$

where T_U is the uniaxial stress; λ_U is the uniaxial stretch ratio, and $\lambda_U = 1 + \varepsilon_U$, with ε_U being the uniaxial strain. The parameters μ_i and α_i are constants representing the material hyperelastic properties. Under uniaxial stretch, assuming incompressibility of the TM, the principal stretch ratios λ_i (i = 1, 2, 3) are given as $\lambda_1 = \lambda_U$, $\lambda_2 = \lambda_3 = \lambda_U^{-\frac{1}{2}}$.

The slope of the stress-strain curve at any given stress or strain is the tangent modulus, which is calculated by taking the derivative of stress with respect to strain from Eq. (1),

$$\frac{dT_U}{d\varepsilon_U} = \sum_{i=1}^{2} \frac{2\mu_i}{\alpha_i}\left[(\alpha_i - 1)(1 + \varepsilon_U)^{\alpha_i - 2} + (0.5\alpha_i + 1)(1 + \varepsilon_U)^{-0.5\alpha_i - 2}\right] \tag{2}$$

The tangent modulus at the initial linear portion of the stress-strain curve under small deformations is Young's modulus. The Young's modulus of the TM is determined by linear regression of the tangent modulus data up to a strain of 0.25.

2.5. Inverse method

For each sample, the values of μ_i and α_i, are determined by minimizing a cost function, $C(\mu_i, \alpha_i)$ with respect to μ_i and α_i. The cost function is defined such that a minimal value achieves when the volume displacements calculated using the FEM model for a particular sample matches the corresponding values measured from the experiment:

$$C = \sum_{i=1}^{M} (\Delta V_i^{exp} - \Delta V_i^{FEM})^2 \tag{3}$$

where ΔV_i^{exp} is the volume displacement obtained in experiment under a given pressure, ΔV_i^{FEM} is the corresponding FEM simulated volume displacement, M is the number of pressurized states.

In the iterative solving process, the values of μ_i and α_i are first set to be identical to the parameters for a human TM (Cheng et al., 2007). Uniform pressures in the range of 0 kPa–1.0 kPa with an increment of 0.125 kPa are applied on the medial side and the lateral side, corresponding to the pressure used in the experiments. The volume displacement under each static pressure is calculated by summing the volume displacements of all the elements. An iterative procedure is used to modify μ_i and α_i until the volume displacements calculated by the FEM model match well with the corresponding experimental data, similar to the procedure documented in our previous work (Liang et al., 2015).

3. Results

3.1. Surface topography

A typical reconstruction of the human TM in Fig. 5 shows the surface height topography of the TM under 0 kPa, +1.0 kPa and −1.0 kPa

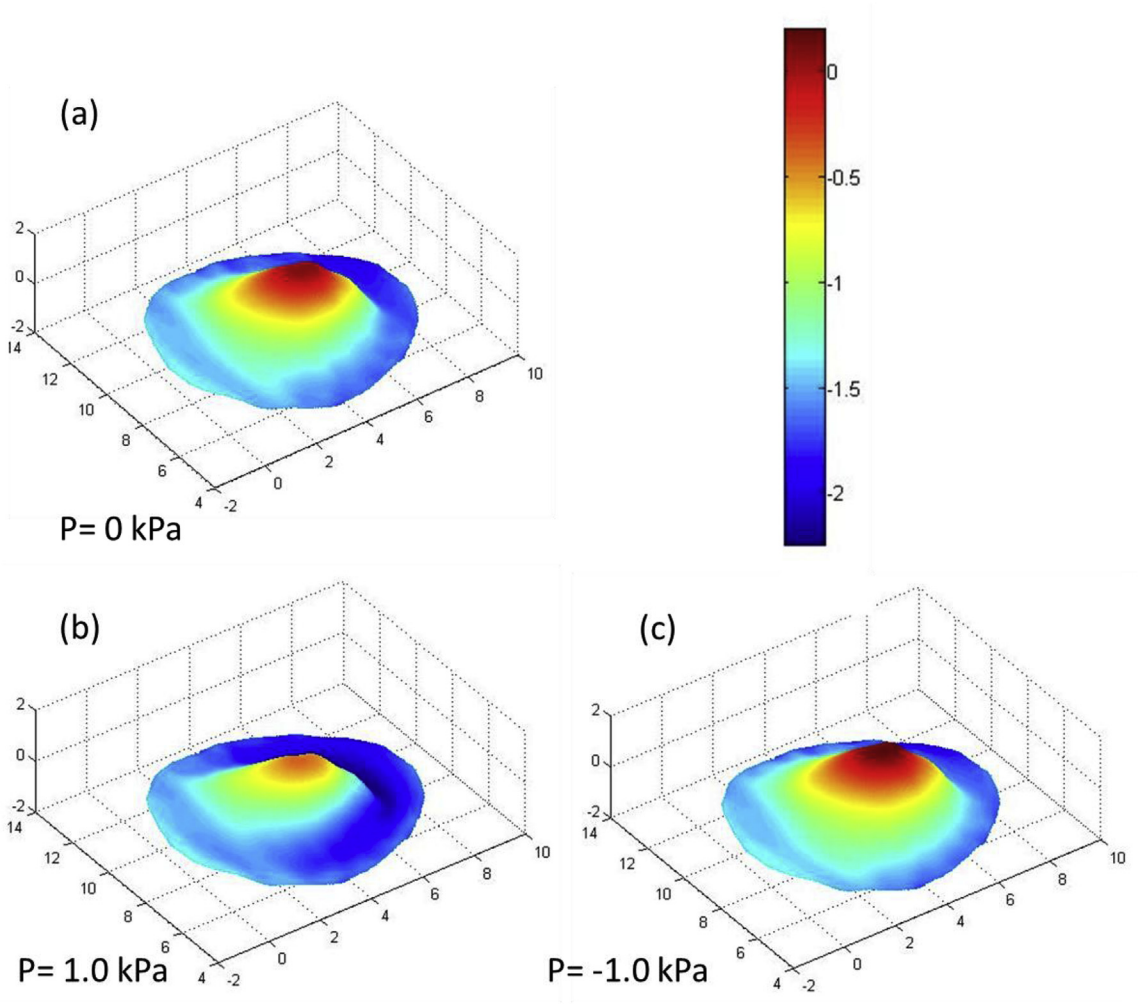


Fig. 5. Typical 3D reconstructed tomogram of a human TM surface (TB16-19). The unit in the figure is mm.

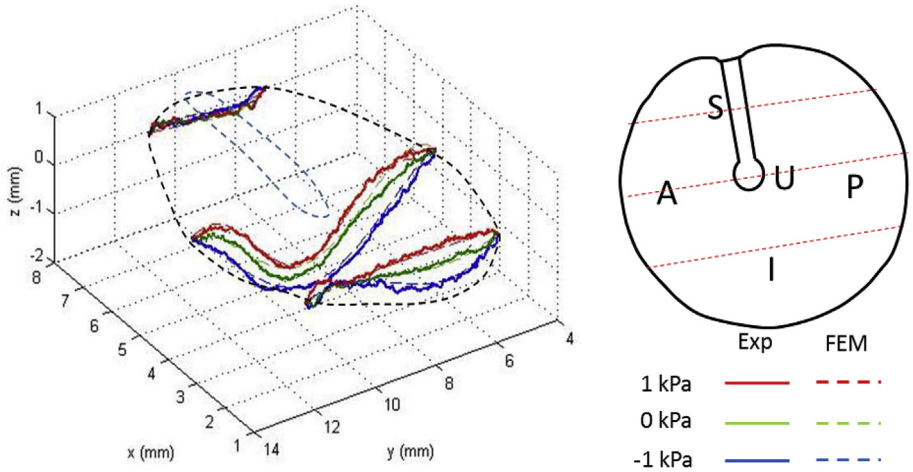


Fig. 6. Comparison of the surface profile of a typical TM between experimental (Exp) results and FEM simulation under −1.0 kPa, 0 kPa and +1.0 kPa pressures. The three dash-dot lines along the anterior-posterior direction in the schematic in the right figure show the cross-sections for comparison in the figure on the left. The labels in the schematics are: A (anterior quadrant), P (posterior quadrant), S (superior quadrant), I (inferior quadrant), and U (umbo).

pressures. For the purpose of validation, the height topographic profile of a typical human TM sample is compared between experiment and simulation in three cross-sections at each of the three different pressure levels (−1.0 kPa, 0 kPa and +1.0 kPa) (Fig. 6). Simulation height profiles are reasonably close to the experimental results, with errors less than 10%.

Fig. 7 shows the contour of displacement along the z-direction perpendicular to the imaging plane of the TM, obtained by subtracting the surface profile at 0 kPa pressure from the corresponding profiles at ± 1.0 kPa pressure. Although the magnitudes of the displacement are different under the application of positive and negative pressures, the profile of the displacement distribution is generally similar between them. The displacement is close to zero at the superior and gradually increases along the superior-inferior direction and along the radial direction from the manubrium. The maximum displacement is found in the inferior area, forming a U-shape plateau surrounding the umbo at

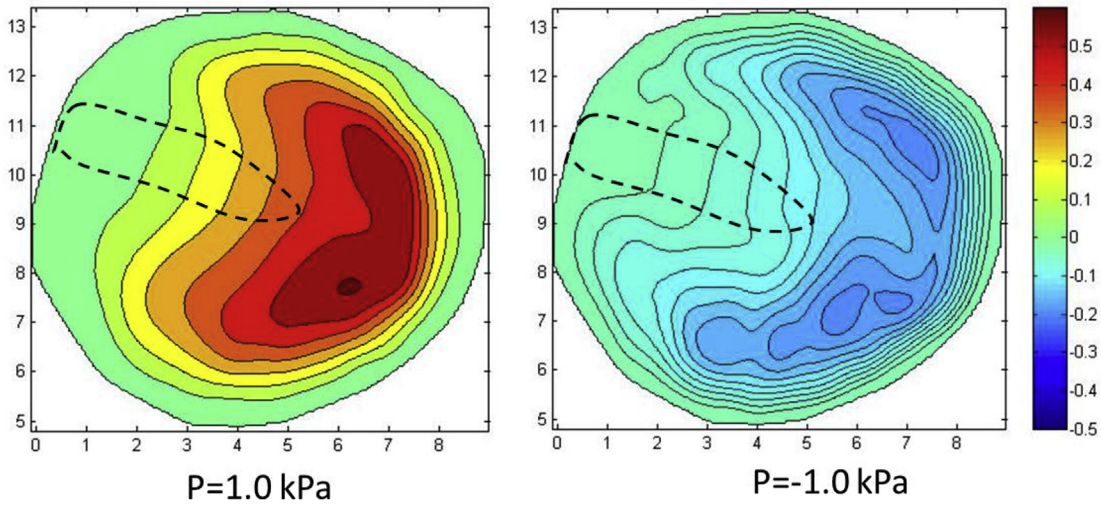


Fig. 7. Displacement maps calculated from the data in Fig. 6. The dash line shows the boundary of the manubrium. The step distance between the height line is 0.05 mm.

approximately midway between the malleus and the annulus ring under both positive and negative pressure cases. In the case of negative pressure, the area with the peak displacement is separated into two sections between the anterior and posterior. This could be caused by the uneven distribution of the thickness of the human TM along the radial direction from the malleus to the edge of the annulus ring. The deformation pattern is in general similar to what is seen for cat, guinea pig, and chinchilla TMs due to the similarity of the geometries of the TMs in these species (Liang et al., 2015, 2016; Ladak et al., 2004) and is consistent with what has been reported on the human TMs (Dirckx and Decraemer, 1991).

3.2. Volume displacement-pressure relationship

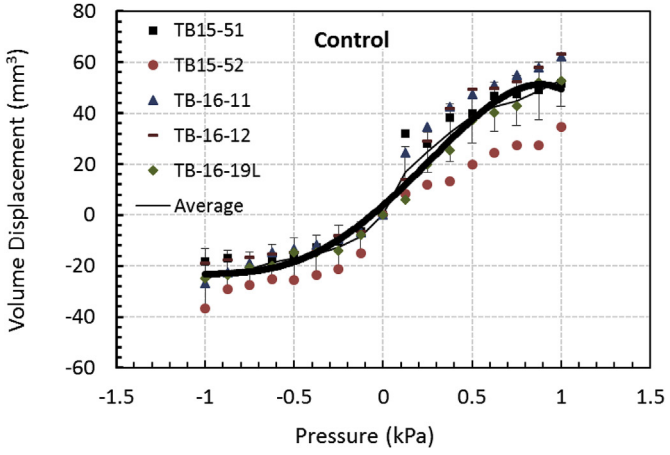
The volume displacements are plotted against the pressure for both control and post-blast TMs as shown in Fig. 8. It is noted that, for soft tissues such as TM, the volume displacement-pressure relationship depends highly on the state of the loading or unloading. When pre-conditioning is conducted, the hysteresis of the TM samples is reduced to a negligible level. Therefore the volume displacements are only computed under the loading stage in this study. The curves shown in Fig. 8 are in general asymmetric with respect to the point at zero-pressure and zero-volume displacement. For the control TMs, the average volume displacement under positive pressure is about 40% higher than the corresponding value under negative pressure with the same magnitude. For post-blast TMs, the average volume displacement under a positive pressure is also higher, about 25% higher than the corresponding values under a negative pressure of the same magnitude. This asymmetry of the deformation of the TM is due to its nearly conical geometry. The fact that the manubrium structure crosses the apex of the TM also contributes to its uneven deformation under positive and negative pressure. The malleus on the medial side of the TM is held in tension with ossicular chains connecting to it, which reduces the TM deformation as pressure increases in the negative direction (Kartush et al., 2006). The asymmetrical volume displacement is consistent with our previous findings (Liang et al., 2016) and others' findings on TMs of mammals such as gerbils (Gea et al., 2010), cats (Funnell and Decraemer, 1996), and humans (Gaihede et al., 2007).

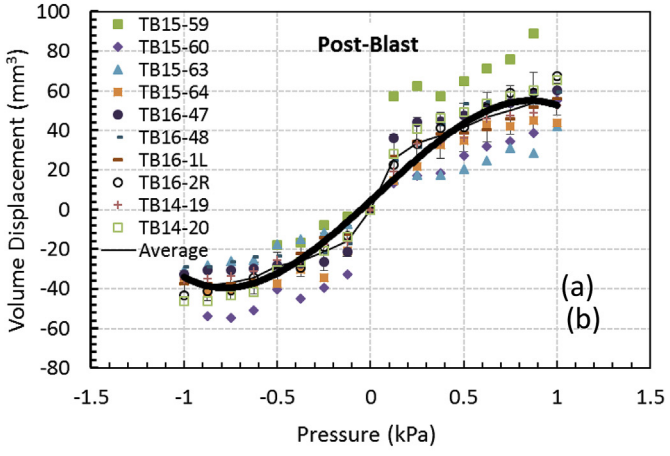
3.3. Mechanical properties of control and post-blast TMs

Tables 1 and 2 list the dimensions and the material property parameters in the Ogden model for each TM. The model parameters are determined from the entire loading cycle for each TM sample. The stress-strain relationships of the control and post-blast TMs determined using Eqn. (1) and the parameters in Tables 1 and 2 are plotted in Fig. 9. The curves shown in Fig. 9 demonstrate hyperelastic behavior of the human TM: the TM becomes stiffer as the strain increases. In Fig. 10, the tangent modulus is also plotted against the uniaxial strain. The nonlinearity of the tangent modulus is easier to observe: as the strain increases, the tangent modulus decreases at strains below 20%, and it then gradually increases at strains above 20%. At a strain near zero, the tangent modulus is 8.5 MPa for the control TMs and 6.7 MPa for the post-blast TMs. At 30% strain, which is the maximum strain on the TM determined by FEM analysis, the tangent modulus is slightly lower: 7.5 MPa for the control TM and 6.1 MPa for the post-blast TM. The average Young's modulus is calculated based on the results obtained from 8 TMs using Eqn. (2). In this study, the average tangent modulus, at strains less than 25%, is defined as the representative Young's modulus for comparison. The average values of Young's modulus for the control TMs and post-blast TMs are ~7.8 MPa and ~6.3 MPa respectively. The average Young's modulus of the control TMs is lower than that measured by Luo et al. using split Hopkinson tension bar (Luo et al., 2016) and higher than that measured by Rohani et al. using a pressurization method (Rohani et al., 2017). This is probably because of the difference in the measurement methods applied.

4. Discussion

The TM is a complex tissue that consists of an epidermis layer, a connective layer (lamina propria), and a mucosal epithelial layer (Lim, 1995). The core of the structural layer, the lamina propria, is a fibrous layer made up of outer radial fibers and inner circular (circumferential) fibers in addition to parabolic fibers. The fracture strength of the radial fibrous layer is higher than that of the circumferential fibrous layer. On exposure to blast waves, the TM is prone to break in the circumferential direction rather than in the radial direction. To evaluate the effect of blast wave on the microstructures of the TM, a post-blast TM sample is observed with scanning electronic microscopy (SEM) and compared with an SEM image of a control TM (Fig. 11). In this study the intensity of the blast wave used is not enough to induce perforation across the entire TM thickness, it has induced damage on the TM as micro-ruptures in the fibrous layer. In contrast to the well-aligned circumferential fibers in the control TM, some fibers are randomly aligned over the circumferential fibrous layer of the post-blast TM. It is noticed that, although it is beneficial to investigate the radial fibrous layers further by removing or dissecting the circumferential layer, such a process can induce secondary damage to the radial fibrous layers. Thus, we are





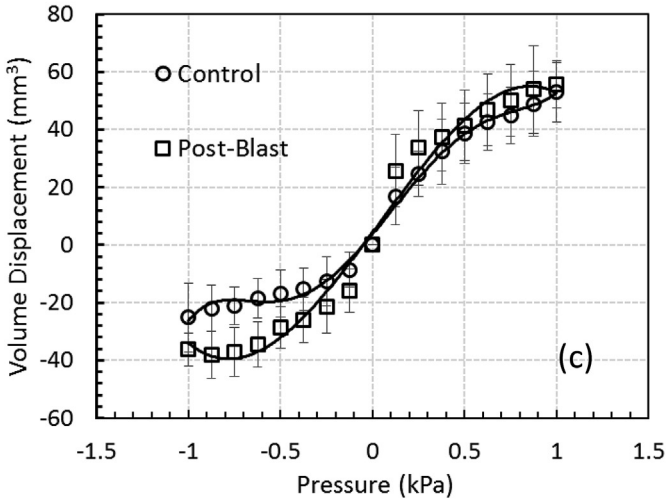
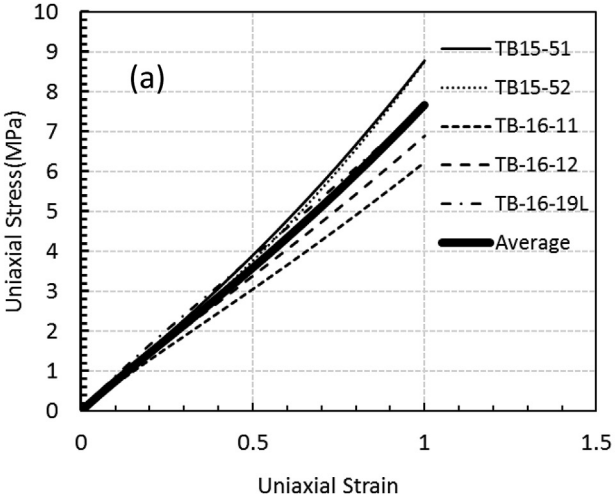


Fig. 8. Volume displacement – pressure relationships for control (n = 5) shown in (a) and post-blast human (n = 16) TM shown in (b). Comparison between the two groups of TMs is also plotted with the standard deviation as the error bar shown in (c).

unable to observe the blast damage to the radial fibers using SEM. The damage in the post-blast TM is likely responsible for the reduction of mechanical properties in comparison with the control TM.

From Figs. 8 and 10, it is seen that the mechanical properties of the human TM changed after the TM is exposed to the blast overpressure. In the volume displacement-pressure relationship, the alternation of the



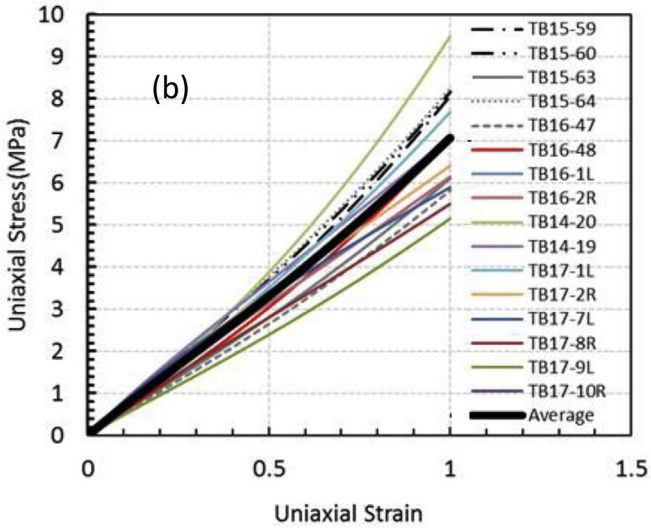


Fig. 9. Stress-strain relationships for the control (n = 5) shown in (a) and post-blast (n = 16) human TMs shown in (b).

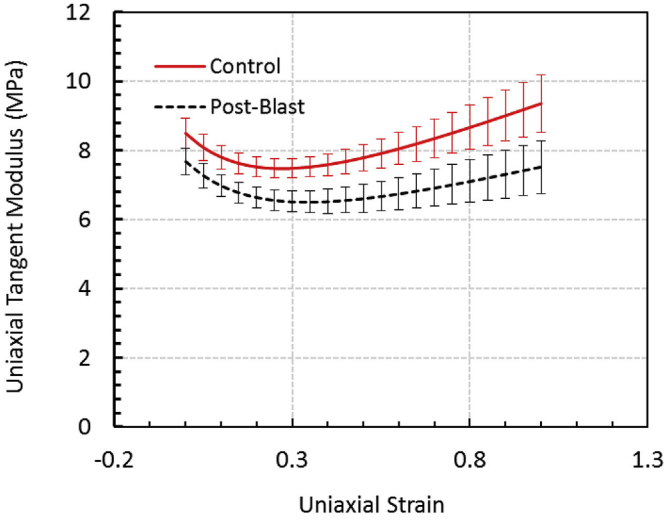


Fig. 10. Comparison of tangential modulus data for control (n = 5) and post-blast groups (n = 16). The error bars show the standard deviation.

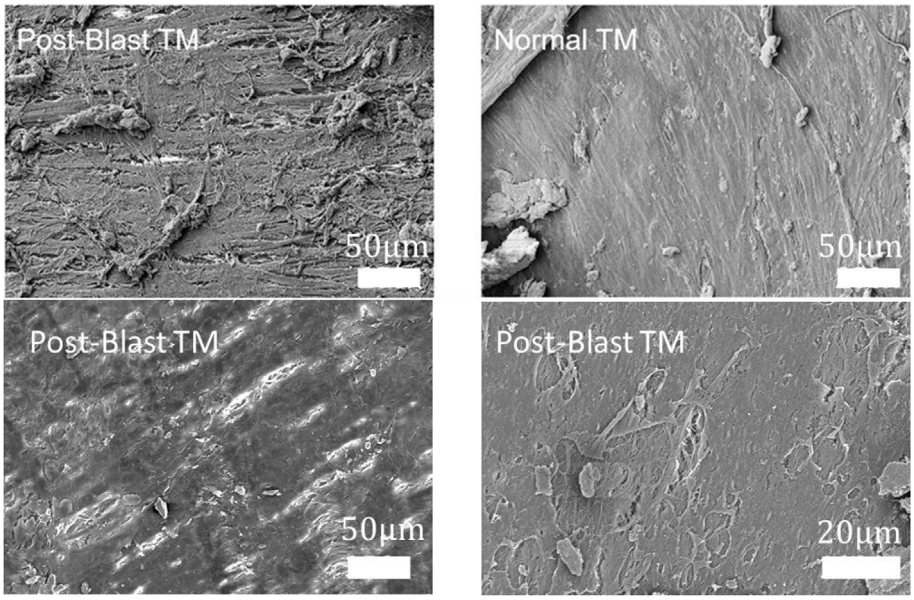


Fig. 11. Typical SEM micrographs for post-blast and control human TMs.

mechanical response exhibits asymmetry between positive pressure and negative pressure. In the positive direction, the volume displacement of the post-blast TM is nearly identical to that of the control TM. This is different from the observation of chinchilla TM (Liang et al., 2016). This could be due to the different ways of sample preparation for the fringe projection measurement. For the chinchilla, the entire cochlea and the stapes were removed and the positive pressure was applied from the lateral side of the TM, therefore the TM did not have constraint for motion under both the positive and negative pressure. The ruptures can form and propagate in both directions. For the human TM samples used in this work, the entire cochlea and the ossicular chain are kept intact and the positive pressure is applied from the medial side of the TM. When a positive pressure is applied to the human TM, the ossicular chain is stretched and restricts the deformation from distorting the conical geometry of the TM, thus the ruptures cannot propagate along this direction. As a result, the volume displacement in the positive direction does not show a significant increase as in the case under negative pressure.

The tangent modulus of the TM, however, which is independent of the structure of the system, shows clearly the weakening of the TM after its exposure to blast overpressure. The Young's modulus, which is identical to the linear section of the tangent modulus, decreases by about 20%. This reduction is much lower than the 50% reduction in Young's modulus for the chinchilla TM in our previous work (Liang et al., 2017). It is reasoned that the thickness of the human TM plays an important role to mitigate the damage in comparison with the thinner TM of the chinchilla: the thickness of the human TM is about 80 μm, while it is 20 μm for a chinchilla TM. The value of the reduction in Young's modulus in this study is consistent with what is reported in the work of Luo et al. (2016). In that study, it is found that at a low strain rate, the TM exhibits 22% reduction in Young's modulus in the radial direction and about 8% reduction in the modulus in the circumferential direction. Although it is still unable to quantify the damage induced by the sample preparation of cutting the TM into strips, the comparison between our data and Luo's data implies that the fibers in the radial direction dominate the performance of the TM at least at low strain rates. The reduction of the stiffness in the intact TM is smaller than what is reported by Engles et al. on post-blast human TM strips (2017). In that study, the storage modulus of the post-blast human TMs exhibits a reduction of more than 50% in comparison with that of control TMs. The reason for such a large magnitude in the change of storage modulus is still unclear. One possible reason is that the small transverse vibration loading is applied to the TM strip. Such a loading condition is different from what is used in our work.

In this work, the micro-fringe projection technique allows investigation of the blast damage on the TM without dissecting the TM sample. This approach eliminates the effect of possible damage and alteration of collagen fibers in the preparation of strip specimens. The direct measurement of the mechanical properties of a human TM rather than a chinchilla TM eliminates the need to factor the species difference between human and chinchilla. However, this method depends on the ability to apply pressure to the confined middle ear, consequently this technique cannot be applied for a ruptured TM. In addition, in the calculation of the mechanical properties using the inverse method, the TM is considered as an isotropic and homogenous material. Thus, the mechanical properties reported herein represent the overall effective isotropic properties and cannot identify the potentially extremely localized damage. This study provides results on the change of the effective mechanical property the TM under overpressure, which can be used in FEM simulations to evaluate the effect of TM damage on the sound transmission in the middle ear. In the work in the future, orthotropic and inhomogeneous characteristics of the TM need to be considered so that a realistic model of the blast-damaged TM model can be established.

The results obtained in this work indicates that repetitively exposed to low pressure level blast induces mechanical damages to the TM. However, the threshold of the overpressure inducing microstructural damage was not determined; in addition, how the damage is accumulated and when a cumulative damage reaches a detrimental level on the TM were not determined. These are areas that require further investigation.

5. Conclusion

The effect of blast overpressure on the mechanical property change of the TM in humans is evaluated using a micro-fringe projection system with pressure loading applied on the entire TM suspended on an annulus. FEM models for human TMs are developed to determine the mechanical properties of the TMs. It is shown that the Young's modulus of the post-blast human TMs decreased by about 20% in comparison with control TMs. The measurement technique used in this work is in-situ and does not induce potential damage to the TM in preparation.

The technique thus allows a more accurate evaluation of the blast effect on the human TM mechanical properties change.

Acknowledgement

We acknowledge the support of DOD W81XWH-13-MOMJPC5-IPPEHA, NSF CMMI-1636306, CMMI-1661246 and CMMI-1726435. We thank Mr. Warren Engles for the SEM imaging and Mr. Don U. Nakmali for preparation of TM samples. Lu acknowledges the Luis A. Beecherl Jr. endowed chair for additional support.

References

Aernouts, J., Soons, J.A.M., Dirckx, J.J.J., 2010. Quantification of tympanic membrane elasticity parameters from in situ point indentation measurements: validation and preliminary study. Hear. Res. 263 (1–2), 177–182.

Cheng, T., Dai, C.K., Gan, R.Z., 2007. Viscoelastic properties of human tympanic membrane. Ann. Biomed. Eng. 35 (2), 305–314.

De Greef, D., Goyens, J., Pintelon, I., Bogers, J.P., Van Rompaey, V., Hamans, E., Van de Heyning, P., Dirckx, J.J.J., 2016. On the connection between the tympanic membrane and the malleus. Hear. Res. 340, 50–59.

Dirckx, J.J., Decraemer, W.F., 1991. Human tympanic membrane deformation under static pressure. Hear. Res. 51 (1), 93–105.

Dirckx, J.J.J., Decraemer, W.F., 1997. Coating techniques in optical interferometric metrology. Appl. Opt. 36 (13), 2776–2782.

Dougherty, A.L., MacGregor, A.J., Han, P.P., Viirre, E., Heltemes, K.J., Galarneau, M.R., 2013. Blast-related ear injuries among U.S. military personnel. J. Rehabil. Res. Dev. 50 (6), 893–904.

Engles, W.G., Wang, X., Gan, R.Z., 2017. Dynamic properties of human tympanic membrane after exposure to blast waves. Ann. Biomed. Eng. 45 (10), 2383–2394.

Funnell, W.R.J., Decraemer, W.F., 1996. On the incorporation of moire shape measurements in finite-element models of the cat eardrum. J. Acoust. Soc. Am. 100 (2), 925–932.

Gaihede, M., 1996. Tympanometric preconditioning of the tympanic membrane. Hear. Res. 102 (1–2), 28–34.

Gaihede, M., Liao, D.H., Gregersen, H., 2007. In vivo areal modulus of elasticity estimation of the human tympanic membrane system: modelling of middle ear mechanical function in normal young and aged ears. Phys. Med. Biol. 52 (3), 803–814.

Gan, R.Z., Leckness, K., Nakmali, D., Ji, X.D., 2018. Biomechanical measurement and modeling of human eardrum injury in relation to blast wave direction. Mil. Med. 183 (1), 245–251.

Gea, S.L.R., Decraemer, W.F., Funnell, W.R.J., Dirckx, J.J.J., Maier, H., 2010. Tympanic membrane boundary deformations derived from static displacements observed with computerized tomography in human and gerbil (vol 11, pg 1, 2010). JARO J. Assoc. Res. Otolaryngol. 11 (3) 525-525.

Kartush, J.M., Babu, S.C., 2006. "Ossicular Chain Reconstruction: Maximizing Success and Minimizing Errors," Ear and Temporal Bone Surgery. In: Wiet, R.J. (Ed.), Thieme Clinical Collections, pp. 90–92.

Ladak, H.M., Decraemer, W.F., Dirckx, J.J., Funnell, W.R., 2004. Response of the cat eardrum to static pressures: mobile versus immobile malleus. J. Acoust. Soc. Am. 116 (5), 3008–3021.

Liang, J., 2009. Determination of the Mechanical Properties of guinea Pig Tympanic Membrane Using Combined Fringe Projection and Simulations. Oklahoma State University.

Liang, J., Fu, B., Luo, H., Nakmali, D., Gan, R.Z., Lu, H., 2015. Characterization the nonlinear elastic behavior of Guinea pig tympanic membrane using micro-fringe projection. Int. J. Exp. Comput. Biomech. 3, 319–344.

Liang, J.F., Luo, H.Y., Yokell, Z., Nakmali, D.U., Gan, R.Z., Lu, H.B., 2016. Characterization of the nonlinear elastic behavior of chinchilla tympanic membrane using micro-fringe projection. Hear. Res. 339, 1–11.

Liang, J., Yokell, Z.A., Nakmaili, D.U., Gan, R.Z., Lu, H., 2017. The effect of blast overpressure on the mechanical properties of a chinchilla tympanic membrane. Hear. Res. 354, 48–55.

Lim, D.J., 1995. Structure and function of the tympanic membrane: a review. Acta Oto-Rhino-Laryngol. Belg. 49 (2), 101–115.

Luo, H., Dai, C., Gan, R.Z., Lu, H., 2009. Measurement of young's modulus of human tympanic membrane at high strain rates. J. Biomech. Eng. 131 (6), 064501.

Luo, H., Jiang, S., Nakmali, D.U., Gan, R.Z., Lu, H., 2016. Mechanical properties of a human eardrum at high strain rates after exposure to blast waves. J. Dyn. Behav. Mater. 2, 59–73.

Mathews, Z.R., Koyfman, A., 2015. Blast injuries. J. Emerg. Med. 49 (4), 573–587.

Nakagawa, A., Manley, G.T., Gean, A.D., Ohtani, K., Armonda, R., Tsukamoto, A., Yamamoto, H., Takayama, K., Tominaga, T., 2011. Mechanisms of primary blast-induced traumatic brain injury: insights from shock-wave research. J. Neurotrauma 28 (6), 1101–1119.

O'Connor, K.N., Tam, M., Blevins, N.H., Puria, S., 2008. Tympanic membrane collagen fibers: a key to high-frequency sound conduction. The Laryngoscope 118 (3), 483–490.

Ortiz, M.H., Patterson, E.A., 2005. Location and shape measurement using a portable fringe projection system. Exp. Mech. 45 (3), 197–204.

Owens, B.D., Kragh, J.F., Wenke, J.C., Macaitis, J., Wade, C.E., Holcomb, J.B., 2008. Combat wounds in operation Iraqi freedom and operation enduring freedom. J. Trauma 64 (2), 295–299.

Remenschneider, A.K., Lookabaugh, S., Aliphas, A., Brodsky, J.R., Devaiah, A.K., Dagher, W., Grundfast, K.M., Heman-Ackah, S.E., Rubin, S., Sillman, J., Tsai, A.C., Vecchiotti, M., Kujawa, S.G., Lee, D.J., Quesnel, A.M., 2014. Otologic outcomes after blast injury: the Boston marathon experience. Otol. Neurotol. 35 (10), 1825–1834.

Rohani, S.A., Ghomashchi, S., Agrawal, S.K., Ladak, H.M., 2017. Estimation of the Young's modulus of the human pars tensa using in-situ pressurization and inverse finite-element analysis. Hear. Res. 345, 69–78.

Wang, B., Lu, H.B., Kim, G.H., 2002. A damage model for the fatigue life of elastomeric materials. Mech. Mater. 34 (8), 475–483.

Wolf, S.J., Bebarta, V.S., Bonnett, C.J., Pons, P.T., Cantrill, S.V., 2009. Blast injuries. Lancet 374 (9687), 405–415.

Yeh, D.D., Schecter, W.P., 2012. Primary blast injuries-an updated concise review. World J. Surg. 36 (5), 966–972.

Surface Motion Changes of Tympanic Membrane Damaged by Blast Waves

Rong Z. Gan[1]
Biomedical Engineering Laboratory,
School of Aerospace and
Mechanical Engineering,
University of Oklahoma,
865 Asp Avenue,
Norman, OK 73019
e-mail: rgan@ou.edu

Shangyuan Jiang
Biomedical Engineering Laboratory,
School of Aerospace and
Mechanical Engineering,
University of Oklahoma,
865 Asp Avenue,
Norman, OK 73019

Eardrum or tympanic membrane (TM) is a multilayer soft tissue membrane located at the end of the ear canal to receive sound pressure and transport the sound into the middle ear and cochlea. Recent studies reported that the TM microstructure and mechanical properties varied after the ear was exposed to blast overpressure. However, the impact of such biomechanical changes of the TM on its movement for sound transmission has not been investigated. This paper reports the full-field surface motion of the human TM using the scanning laser Doppler vibrometry in human temporal bones under normal and post-blast conditions. An increase of the TM displacement after blast exposure was observed in the posterior region of the TM in four temporal bone samples at the frequencies between 3 and 4 kHz. A finite element model of human TM with multilayer microstructure and orthogonal fiber network was created to simulate the TM damaged by blast waves. The consistency between the experimental data and the model-derived TM surface motion suggests that the tissue injuries were resulted from a combination of mechanical property change and regional discontinuity of collagen fibers. This study provides the evidences of surface motion changes of the TM damaged by blast waves and possible fiber damage locations. [DOI: 10.1115/1.4044052]

Keywords: ear biomechanics, tympanic membrane, scanning laser Doppler vibrometry, finite element model, tissue microstructure

1 Introduction

Eardrum or tympanic membrane is a multilayer soft tissue membrane separating the ear canal from the middle ear. The tympanic membrane (TM) plays an important role in the transmission of sound pressure from the environment into mechanical vibration of the ossicular chain in the middle ear, which is transported into the inner ear or cochlea and then to the brain for hearing. Exposure to high intensity sound or blast overpressure waves causes injuries to auditory system and results in acute hearing loss in military service members and the long-term hearing disabilities in veterans [1,2]. The primary blast injury to the ear is induced by the direct effect of blast waves upon the TM and middle ear ossicular chain. Rupture of the TM is one of the most frequent injuries of the ear and has been investigated in animals and humans with wide variability [3–5].

The human TM is composed of three distinct layers. The lateral side is an epidermal layer and the medial side is a mucosal layer. The middle layer is composed of collagen fibers which are embedded in a matrix of ground substance, aligning primarily along the radial and circumferential directions [6]. A major part of the TM is the pars tensa, which is within the tympanic annulus ring located at the boundary; the malleus manubrium bone is attached in the central portion at the medial side [6–8].

Recent studies reported that the TM microstructure and mechanical properties varied after the ear was exposed to blast waves [9,10]. The postblast TM tears were oriented in the radial direction observed under the scanning electron microscope by Engles et al. [10]. They also measured the complex modulus of the human TM samples by using acoustic loading and laser Doppler vibrometry and found that the storage and loss modulus of the TM decreased significantly after the blast over a frequency range of 200–8000 Hz. In a study performed by Luo et al. [8], the results indicated that Young's modulus is higher in the radial direction than in the circumferential direction, and the fracture strength in the radial direction is also higher than that in the circumferential direction under the condition of the same strain rate. Moreover, the recent study by Luo et al. [9] showed that blast waves cause significant changes on mechanical properties of the TM mainly due to the damage induced in the circumferential fibers and the stiffening in the radial fibers. However, the impact of such biomechanical changes of the TM on its movement for sound transmission has not been investigated.

Full-field motion measurement of the TM can provide simultaneous vibration data from a large number of points on the membrane surface, which has the benefit of showing both the spatial and temporal behaviors of the TM vibration in response to sound stimuli. The term "full-field" herein means that the measurement is performed over the entire visible area of the TM. Measurement of the entire TM surface motion has been used to explore the relationships between the structure and the acoustic function of the middle ear in animals and human cadaveric temporal bones [11–14]. To analyze middle ear mechanics in diseased and reconstructed ears, Zhang et al. [15] investigated the effects of middle ear fluid on TM surface motion in human cadaver ears by using scanning laser Doppler vibrometry (SLDV). Recently, the TM surface motion was determined using SLDV in a chinchilla model of acute otitis media by Wang and Gan [16].

This paper reports the full-field surface motion of human TM measured by SLDV over a frequency range of 1–8 kHz in human temporal bones before (or normal) and after blast exposure. In addition to experimental measurement, a three-dimensional (3D) multilayer finite element (FE) model to mimic the fibrous microstructure of the human TM was developed to replace the TM in our previously published FE model of the entire ear [17]. The new TM model was composed of multilayer matrix embedded with radial and circumferential fibers, which was used to simulate the damaged TM by altering the mechanical properties and microstructure of the fiber network after blast exposure. The purpose of this study is to investigate how the TM motion is altered after

[1]Corresponding author.

Manuscript received February 19, 2019; final manuscript received June 14, 2019; published online August 2, 2019. Assoc. Editor: X. Edward Guo.

 Copyright © 2019 by ASME

Downloaded from https://asmedigitalcollection.asme.org/biomechanical/article-pdf/141/9/091009/5193736/bio_141_09_091009.pdf by University Of Oklahoma user on 22 September 2019

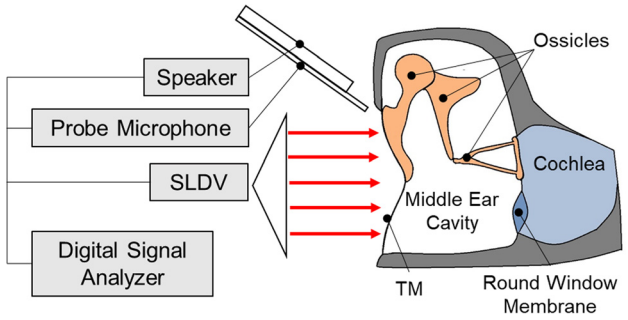


Fig. 1 Schematic diagram of the experimental setup showing the scanning SLDV and a human temporal bone

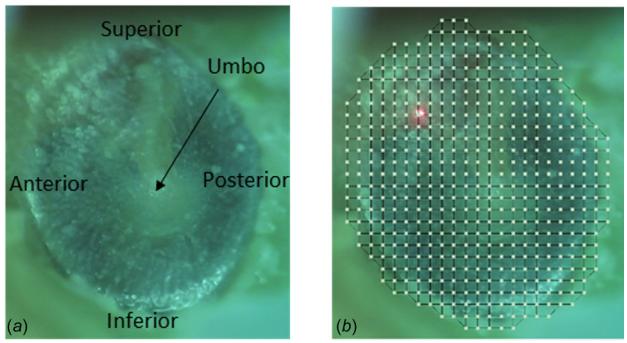


Fig. 2 (*a*) One exposed TM sample image (left ear) captured by the SLDV and (*b*) the typical scanning points defined on the TM surface with a laser spot shown

blast exposure and what is the possible relation between the TM movement variation and its microstructure damage induced by blast waves.

2 Methods

2.1 Sample Preparation. Two pairs of fresh human temporal bones (TBs) from two donors of age 67 and 71 yr old were involved in this study. TB samples were packed in dry ice and shipped from LifeLegacy Foundation, a certified human tissue supplier for military-related research. The study protocol was approved by the U.S. Army Medical Research and Material Command (USAMRMC), Office of Research Protections (ORP). The experiments were conducted within one week after the temporal bones arrived. The samples were processed with a solution of 0.9% saline and 15% povidone at 5 °C to maintain the physiological condition before the experiment. Each sample was examined under an operating microscope (OPMI-1, Zeiss, Thornwood, NY) to confirm a normal ear canal and an intact TM.

The surgery to expose the TM was conducted under the microscope by separating the pinna and soft tissues from the lateral bony wall of the TB with a #10 scalpel and removing the bony part of the ear canal for the SLDV measurement. After the test in a normal TB sample was completed, the removed pinna and soft tissues were reattached to the TB by suture and the TB sample was exposed to blast tests. The pinna and soft tissues were then removed again to expose TM for the SLDV measurement after blast tests.

2.2 Experimental Protocol

2.2.1 Surface Motion of the Tympanic Membrane Measured With Scanning Laser Doppler Vibrometry. The schematic diagram of the experimental setup with SLDV to measure the motion of the TM surface is shown in Fig. 1. The TB was fixed in a temporal bone holder and placed on a vibration isolation table. The experiment was conducted following the protocol reported by Zhang et al. [15]. Briefly, a chirp stimulus at 80 dB sound pressure level with a frequency range of 1–8 kHz was produced by a function generator (Polytec Ethernet Generator, Polytec, Inc., Irvine, CA), an amplifier (RCA SA-155, Radio Shack, Fort Worth, TX), and a speaker (CF1, Tucker-Davis Technologies, Alachua, FL). The sound was delivered through a tube with an inner diameter of 1 mm. A probe microphone (Model ER-7, Etymotic Research) used for monitoring the input sound pressure level was secured parallel to the sound delivery tube and placed about 2 mm away from the TM.

A SLDV (PSV-500, Polytec, Inc., Irvine, CA) with a software package (PSV 9.2, Polytec, Inc., Irvine, CA) was used to measure the full-field vibration of the TM. The orientation of the plane of the tympanic annulus was set perpendicular to the laser beam. Figure 2(*a*) shows a typical view of a TM sample captured by the SLDV. Scanning grids of 400–500 measurement points were distributed evenly over the entire surface of the TM and aligned by drawing them onto the TM live video image using the PSV 9.2 software (see Fig. 2(*b*)). The vibration velocity of each measurement point along with the sound pressure was recorded simultaneously by PSV 9.2 over the frequency range from 1 to 8 kHz. The displacement amplitudes at different frequencies were simply calculated from the velocity and normalized by the input sound pressure.

2.2.2 Exposure of Temporal Bone Samples to Blast Waves. Upon completing the surface motion measurement of a normal TM, the previously removed pinna and soft tissue around the ear canal were reattached to the TB by suture. The TB was then mounted to a "head block" inside an anechoic test chamber in our lab at the University of Oklahoma as shown in Fig. 3. Following the previously established methodologies, a compressed nitrogen-driven blast apparatus was utilized to produce blast overpressure by rupturing a polycarbonate film (McMaster-Carr, Atlanta, GA) [9,10,18]. Blast overpressure level was controlled by changing the thickness of the film or the distance from the blast reference plane. The blast pressure at the entrance of the ear canal was monitored by a pressure sensor (Model 102B16, PCB Piezotronics, Depew, NY) mounted on a column approximately 1 cm away from the head block (Fig. 3). The data acquisition system consisted of the cDAQ 7194, A/D converter 9215 (National Instruments, Inc., Austin, TX), and a software package LabVIEW (National Instruments, Inc., Austin, TX). The sampling rate of the acquisition system was 100 k/s, which was proved to be appropriate in the previous studies [4,9,10,18].

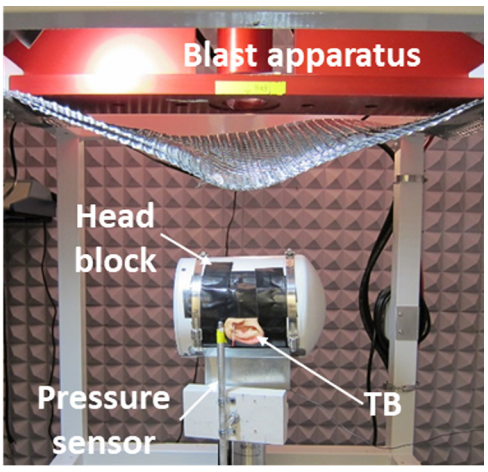


Fig. 3 Picture of the experimental setup with the head block attached with human temporal bone in front setup (blast wave from the front of the face) inside the blast chamber

Downloaded from https://asmedigitalcollection.asme.org/biomechanical/article-pdf/141/9/091009/5193736/bio_141_09_091009.pdf by University Of Oklahoma user on 22 September 2019

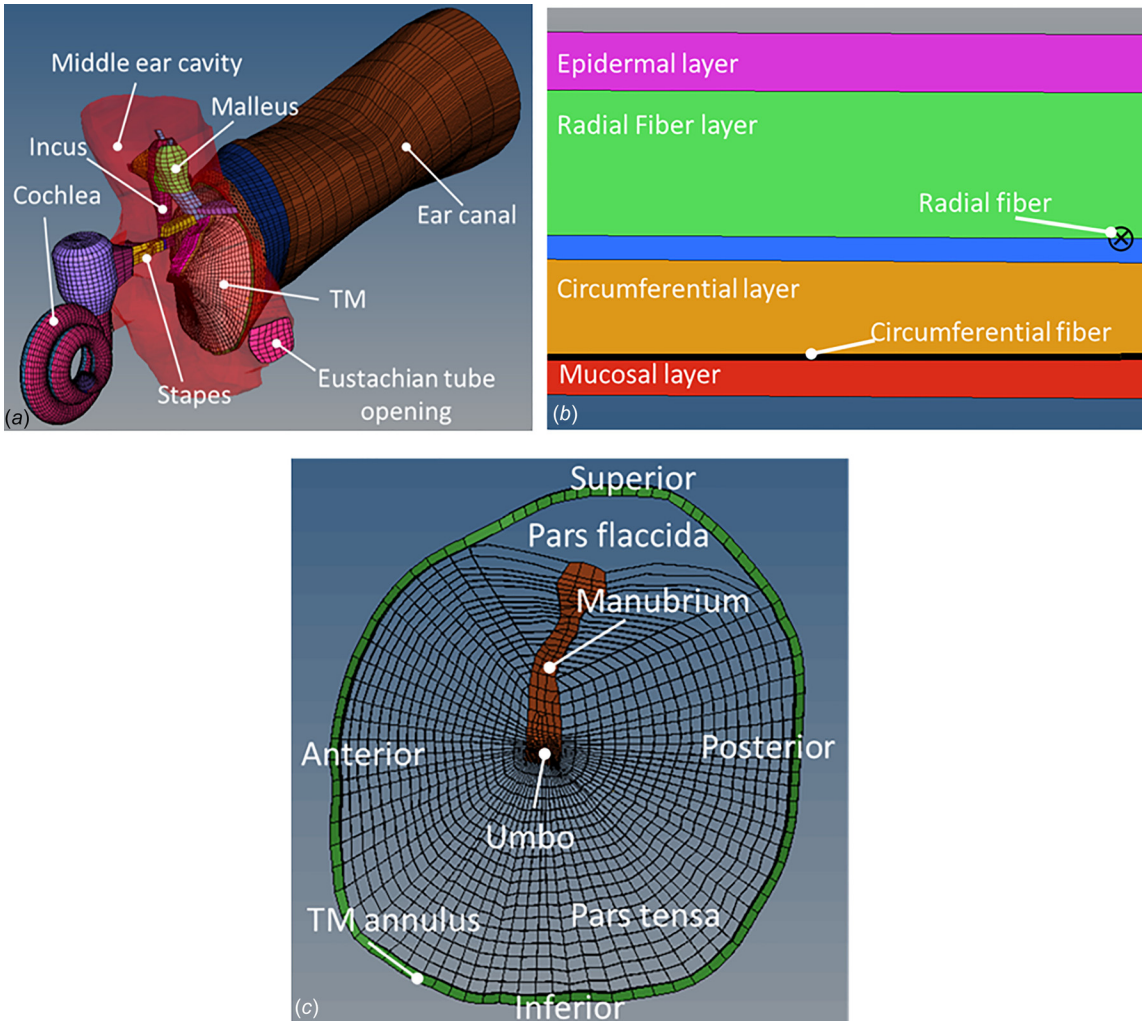


Fig. 4 (*a*) Three-dimensional FE model of the entire ear reported by Zhang and Gan [17] including the ear canal, middle ear, middle ear cavity, and spiral cochlea. The TM in this published model was replaced by the multilayer FE model of the TM with fibrous structure in this study. (*b*) Schematic of the cross section of the TM model along the circumferential direction, showing the location where the fibers are inserted between the respective layers. (*c*) Alignment of radial and circumferential fiber elements in the pars tensa of the TM.

The pressure waveform of each blast had a single positive overpressure peak, and the peak pressure was used to assess the pressure level of blast. Each TB specimen experienced four repeated blasts at a level of 38–54 kPa (or 5.5–7.5 psi). Note that the rupture threshold of human TM was 52.4–62.1 kPa [10,19], and thus, the repeated blasts in this study can induce discernable tissue damage in the TM without rupturing it. After the completion of blast exposure, a microscopic examination was applied to each TM to ensure the nonexistence of the rupture. The surface motion measurement was conducted again immediately after the completion of blast tests, following the same protocol described in Sec. 2.2.1 and the results were compared with the preblast data obtained in each TB.

2.3 Finite Element Modeling Normal and Damaged Human Tympanic Membrane

2.3.1 Multilayer Finite Element Model of Normal Tympanic Membrane—Structure. A multilayer FE model of the human TM with fibers was created in ANSYS (ANSYS, Inc., Canonsburg, PA) based on the entire ear model published by Gan et al. [20] and Zhang et al. [15]. Figure 4(*a*) shows the ear model which consists of the ear canal, TM, middle ear ossicles, middle ear suspensory ligaments and muscle tendons, middle ear cavity, and the spiral cochlea with two and half turns. The TM in this published human ear model is a single layer of membrane with thickness of 75 μm. In this study, the pars tensa part of the TM was modeled as a membrane consisting of five layers: epidermal layer, radial layer, middle layer, circumferential layer, and the mucosal layer from the lateral to the medial side as shown in Fig. 4(*b*) schematically. The thickness of each layer was assumed to be 10, 30, 5, 20, and 10 μm, respectively [21]. The total thickness was 75 μm, the same value as that used in the published ear model [15,20,22]. Note that the middle layer was a virtual layer designed to allow the relative motion between the circumferential and radial layers. Figure 4(*b*) is a diagram showing the cross section of the TM along the circumferential direction. The radial fibers were embedded between the radial and middle layers, while the circumferential fibers were between the circumferential and mucosal layers [23].

The fiber orientations in the radial and middle layers were following the directions of two major types of collagen fibers observed from experiments: the radial fibers originated from the manubrium and ended at the annulus; the circumferential fibers started and ended at the manubrium, parallel to the TM annulus and orthogonal to the radial fibers [7,8,21,24]. The fibers in the radial and circumferential layers simulated in the TM model are

Downloaded from https://asmedigitalcollection.asme.org/biomechanical/article-pdf/141/9/091009/5193736/bio_141_09_091009.pdf by University Of Oklahoma user on 22 September 2019

shown in Fig. 4(*c*). The pars flaccida was modeled as a nonfiber matrix. Note that this method of multiscale modeling of fiber-embedded tissues was reported by Shirazi and Shirazi-Adl [25] and Tiburtius et al. [26].

2.3.2 Multilayer Finite Element Model of Normal Tympanic Membrane—Materials. The matrix of five layers of pars tensa was assumed as solid elements in ANSYS (Solid 185) and the pars flaccida of the TM was modeled as the matrix of solid elements (Solid 185) without fibers. The radial and circumferential fibers were modeled using beam elements (Beam 188) with a rectangular cross section. The fibers, matrix, pars flaccida, and tissues attached to the TM including the TM annulus and manubrium were all modeled as linear elastic materials. The elastic modulus of the TM annulus, manubrium, and pars flaccida was 0.6 MPa, 4.7 GPa, and 10 MPa, respectively [22]. The elastic modulus for matrix of the pars tensa or five layers was the same as that used for pars flaccida (10 MPa).

In TM model, the length of the radial fiber and the radial side length of the matrix element were equal, as well as the equal length of circumferential fiber and the circumferential side matrix. The thickness of the fiber element equaled to its layer so that the volume fraction of fibers was controlled by fiber's width. The volume fraction of fibers in a certain direction at a node of the TM was assumed to be the ratio of the fiber volume to the matrix which could be simplified as the width of the fiber at the node divided by the distance between the current and next adjacent nodes in the given direction within the layer of the fiber [25,26]. For the volume fraction of fibers in human TM, Fay et al. [21] suggested a value around 30–50%, and thus, the width of the radial or circumferential fiber elements was selected at 90 μm in this study which resulted in an approximately volume fraction of 20–40% in either radial or circumferential direction in the boundary area of the TM. Note that the volume fraction would increase from the edge to center because of the width of the fiber element remaining constant, while the size of the matrix element gradually decreased from the edge to center.

Volume fraction and elastic modulus of the fibers are critical parameters affecting the TM stiffness. The equivalent elastic moduli of the TM in the radial and circumferential directions are calculated by the empirical method derived from composite material mechanics as shown in the following equation [27]:

$$E_{\text{ave}} = E_f V + E_m(1 - V) \tag{1}$$

where E_{ave} is the equivalent elastic modulus of the composite, which is the TM with fibers embedded in the matrix in this study; E_f and E_m are elastic modulus of the fiber and matrix, respectively; and V is the volume fraction of the fibers. The fibers in human TM mostly consist of collagen types I and II fibrils whose elastic modulus varied from 1 to 10 GPa [21,28] and the average elastic modulus in the radial direction was about 1.5–2 times of that in the circumferential direction [8,9,22]. After a cross-calibration process to match the model-derived TM surface motion to the experimental data, the elastic modulus of radial fiber was determined to be 10 GPa while 6 GPa for the circumferential fiber.

2.3.3 Multilayer Finite Element Model of Damaged Tympanic Membrane. Mechanical tests on TM samples indicated that the exposure to blast overpressure resulted in changes of mechanical properties of the TM [9,10]. Microstructural variations of the TM were detected by scanning electron microscope images, which provide an insight into the structural aspects of the injury on the surface of the TM [10]. To investigate the relationship between the changes of the microstructure and mechanical properties of the TM and its surface motion, the blast-induced damage was simulated in the FE model of the TM using three approaches.

The first approach was to uniformly reduce the elastic modulus of fibers to simulate the mechanical properties of the fibers that were altered by blast waves. The elastic modulus of the radial and circumferential fibers was set to be 1 and 0.6 MPa, respectively, much lower than the normal fibers. The second approach was to reduce the volume fraction of fibers to simulate the loss of fibers. The width of fibers was reduced to 9 μm which resulted in the volume fraction of fibers to 1/10 of the original value. The third approach was to remove the part of fibers in certain quadrant of the TM to simulate the regional loss of fibers. This simulation of blast-induced damage was conducted following the SLDV measurement in TB samples. We hypothesized that the regions in the TM where the high displacement peak appears during the surface motion measurement may represent more severely damaged fiber network than the other regions. The model-predicted TM surface motion was compared with the experimental data over the frequency range from 1 to 8 kHz.

3 Results

3.1 Full-Field Surface Motion of the Tympanic Membrane Measured by Scanning Laser Doppler Vibrometry. Figure 5 shows the full-field surface motion of specimen TB-60 (right ear) at five frequencies of 1, 2, 3, 4, and 8 kHz before and after four repeated blasts at the level of 53 kPa. The color bars on the right side of images represent the displacement amplitude normalized by the input sound pressure in nm/Pa. The orientation of the right ear TM is shown in the upper left-hand corner of the figure. Note that the scale of the color bar varies from 1 kHz to 8 kHz to provide better illustration of images.

For normal ear at 1 kHz, the deflection shape of the TM motion showed a major vibration peak in the posterior region of the membrane. The maximum displacement amplitude was close to 180 nm/Pa. For the ear after blast exposure, the location of the maximum displacement stayed in the posterior region of the membrane, but the maximum displacement decreased to around 100 nm/Pa. A low-displacement region located around the manubrium separated the membrane into the posterior region with higher displacement and the anterior region with less mobility in both pre- and postblast TMs. The blast exposure did not alter the shape of deflection and the location of the maximum movement at 1 kHz.

The high vibration peak areas were still in the posterior region of the TM before blast at 2 kHz, and multiple peaks emerged around 80 nm/Pa. After blast exposure, a major peak with a maximum displacement of 200 nm/Pa appeared in the posterior region of the TM and a fusion of minor peaks into one major peak was similar to what was observed at 1 kHz, but the significant increase of the displacement amplitude in the posterior region was different. The low-mobility area around the manubrium separated the TM into the high-mobility posterior and low-mobility anterior quadrants unsymmetrically, which was clearer in the TM experienced blasts. The blast exposure induced changes in displacement magnitude instead of the location of the vibration peaks.

Distribution of the deflection shape of the TM motion at 3 kHz of both normal and blasted TMs showed no conspicuous difference compared to the deflection shape at 2 kHz. The displacement amplitude was almost uniformly decreased over the entire surface when the frequency increased from 2 to 3 kHz. The maximum displacement in normal TM before blast exposure was 70 nm/Pa and increased to 180 nm/Pa in blasted TM. The high-mobility area still located in the posterior region which was consistent with the results at 2 kHz.

Shapes of the TM deflection at 4 kHz started to change. In preblast TM, although the high-displacement area still existed in the posterior, another high-vibration area appeared in the anterior region. In postblast TM, multiple peaks emerged at the posterior, anterior, and inferior regions. The posterior and anterior peaks shared a maximum displacement of 60 nm/Pa. The postblast TM at 4 kHz still illustrated the deflection shape similar to the normal TM, which had high-mobility peaks in the posterior region. The changes induced by blast exposure at 4 kHz include the increased

Downloaded from https://asmedigitalcollection.asme.org/biomechanical/article-pdf/141/9/091009/5193736/bio_141_09_091009.pdf by University Of Oklahoma user on 22 September 2019

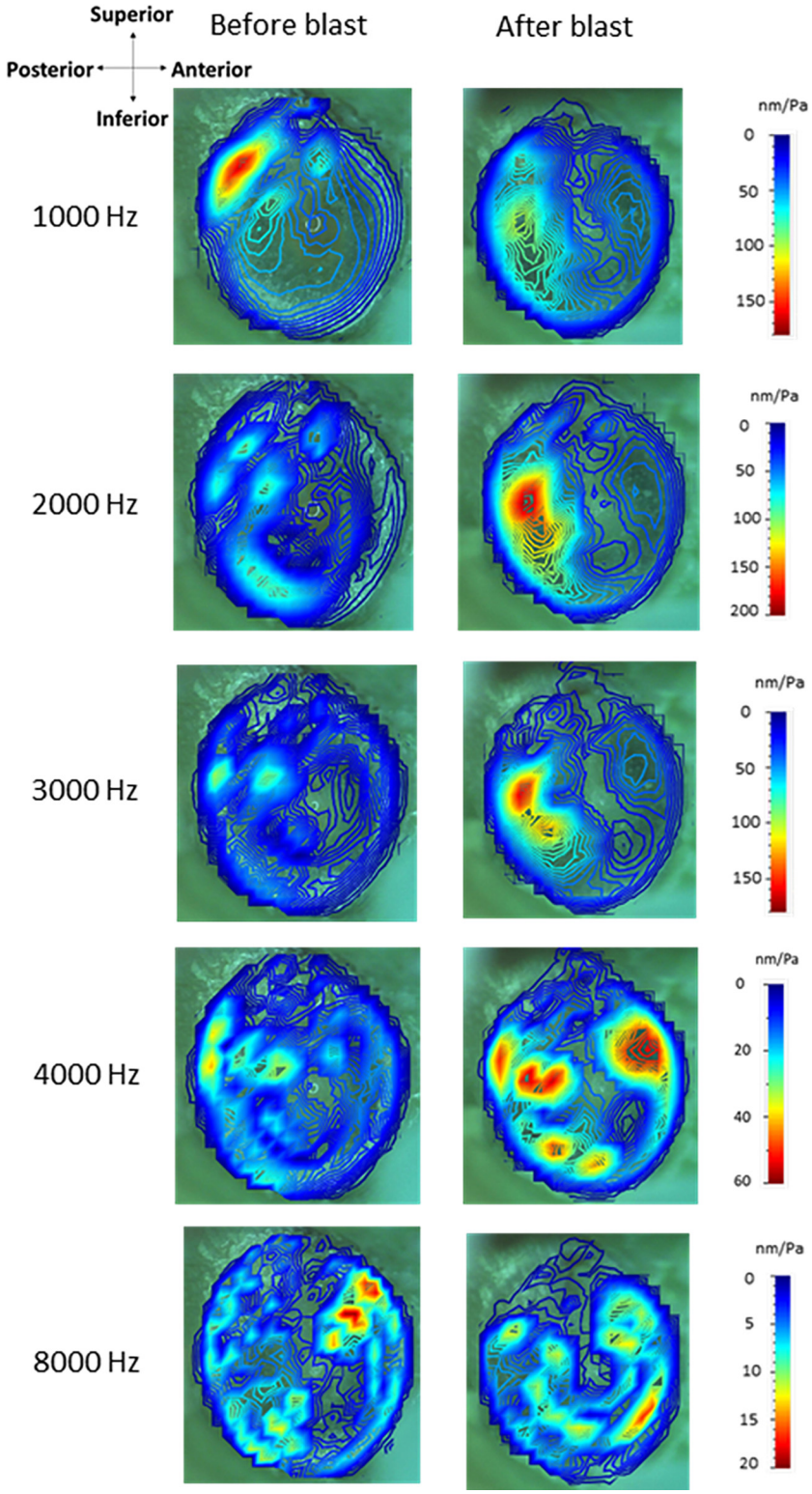


Fig. 5 Deflection shapes of TM surface motion measured by SLDV on specimen TB-60 (right ear) at five frequencies of 1, 2, 3, 4, and 8 kHz before and after four repeated blasts at the level of 53 kPa

maximum displacement peaks and a new peak appeared in the anterior region.

When frequency increased to 8 kHz, no prominent major peaks were observed on the TM before and after blast exposure due to the complexity of the deflection shape and the decrease of the vibration amplitude. The whole TM surface was vibrating below 20 nm/Pa. The superior quadrant including the manubrium showed that the lowest mobility and multiple minor peaks were observed in the anterior region. Neither displacement magnitude nor the distribution of the contours showed discernable difference before and after the blast exposure. In summary, the results obtained from the TM of TB-60 indicate that at the middle

Downloaded from https://asmedigitalcollection.asme.org/biomechanical/article-pdf/141/9/091009/5193736/bio_141_09_091009.pdf by University Of Oklahoma user on 22 September 2019

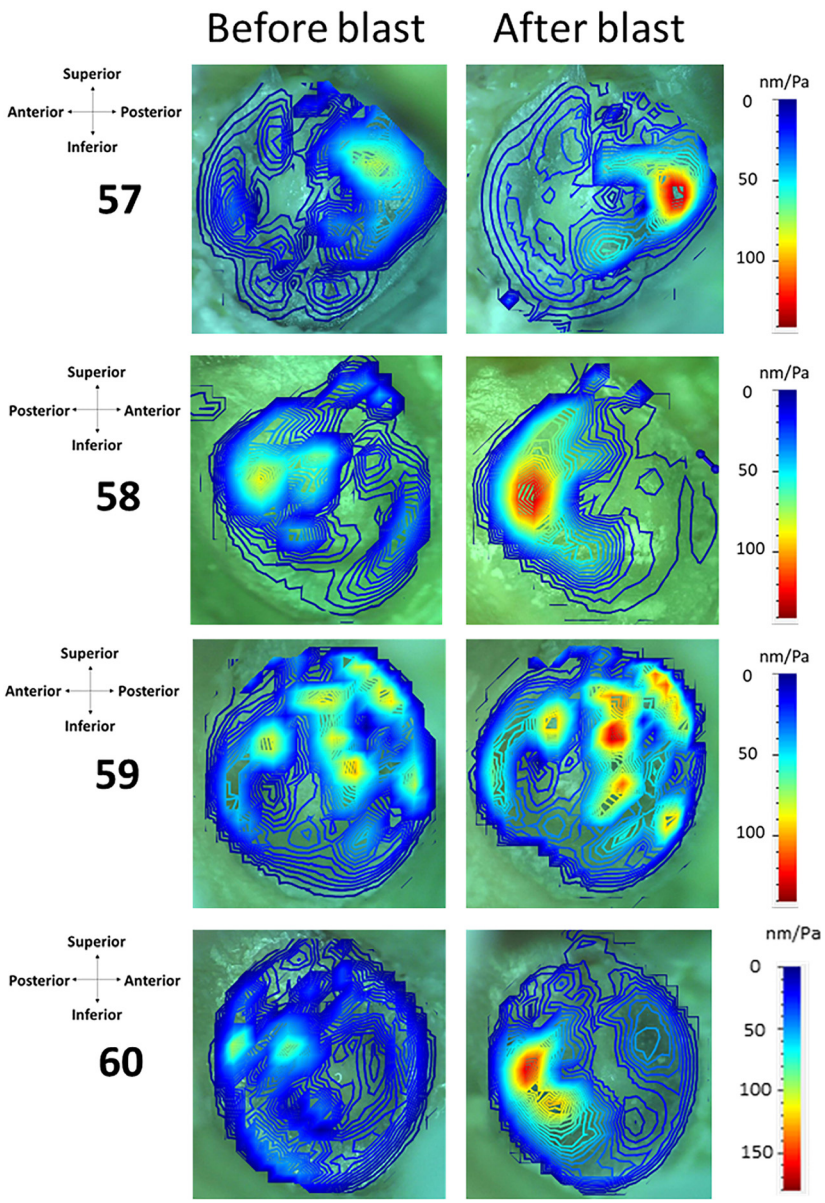


Fig. 6 Deflection shapes of TM surface motion measured by SLDV on all TBs at 3 kHz

frequencies (2–4 kHz), the areas with high mobility concentrated in the posterior region of the membrane and the blast damage mainly increased the TM movement in that region without changing the peak distribution pattern.

The deflection shapes of four TMs from all TBs at 3 kHz are presented in Fig. 6 to investigate whether this phenomenon exists in all TM samples. The left column of Fig. 6 displays the shapes of TM deflection before blast exposure, and the right column shows the TM deflection shapes after blast exposure. The TM surface motion of four TBs are displayed from top to bottom in Fig. 6. Similar to Fig. 5, the color bars on the right side of images represent the displacement amplitude normalized by the input sound pressure in nm/Pa. The orientation of each TB's TM is shown in the upper left-hand corner of each image (TB-57: left ear, TB-58: right ear, TB-59: left ear, and TB-60: right ear). A major peak of displacement in the posterior region of the TM was observed in all four TM samples. The maximum displacement of the TM increased from 80 to 140 nm/Pa in TB-57, 58, and 59 and from 70 to 180 nm/Pa in TB-60 after blast exposure. The shapes of the TM deflection or displacement contours remained unchanged after the blast exposure. A single major peak of the TM was observed in the central posterior region of TBs 57, 58, and 60, but TB-59 showed a more complicated shape of deflection. However, the maximum displacement still located in the posterior region and the blast-induced damage increased the displacement amplitude at the same level compared to the other three specimens.

Displacement contours of all four TMs before and after blast exposure at 4 kHz are shown in Fig. 7. Like Fig. 6, the TM displacement after blast exposure increased in the posterior region of the membrane at 4 kHz, and the peak distribution pattern was similar to that observed at 3 kHz. However, the displacement amplitude was lower than that at 3 kHz. The maximum TM displacement of TB-57 in the posterior region increased from 40 to 100 nm/Pa after the blast, but in TB-58, the peak vibration area of the TM increased due to the blast. In TB-59, the maximum displacement increased from 50 to 80 nm/Pa, while from 30 to 60 nm/Pa in TB-60. Note that at 4 kHz, high-vibration areas emerged in the anterior region of the TM after the blast exposure. Moreover, the long and narrow high-displacement area appeared

Downloaded from https://asmedigitalcollection.asme.org/biomechanical/article-pdf/141/9/091009/5193736/bio_141_09_091009.pdf by University Of Oklahoma user on 22 September 2019

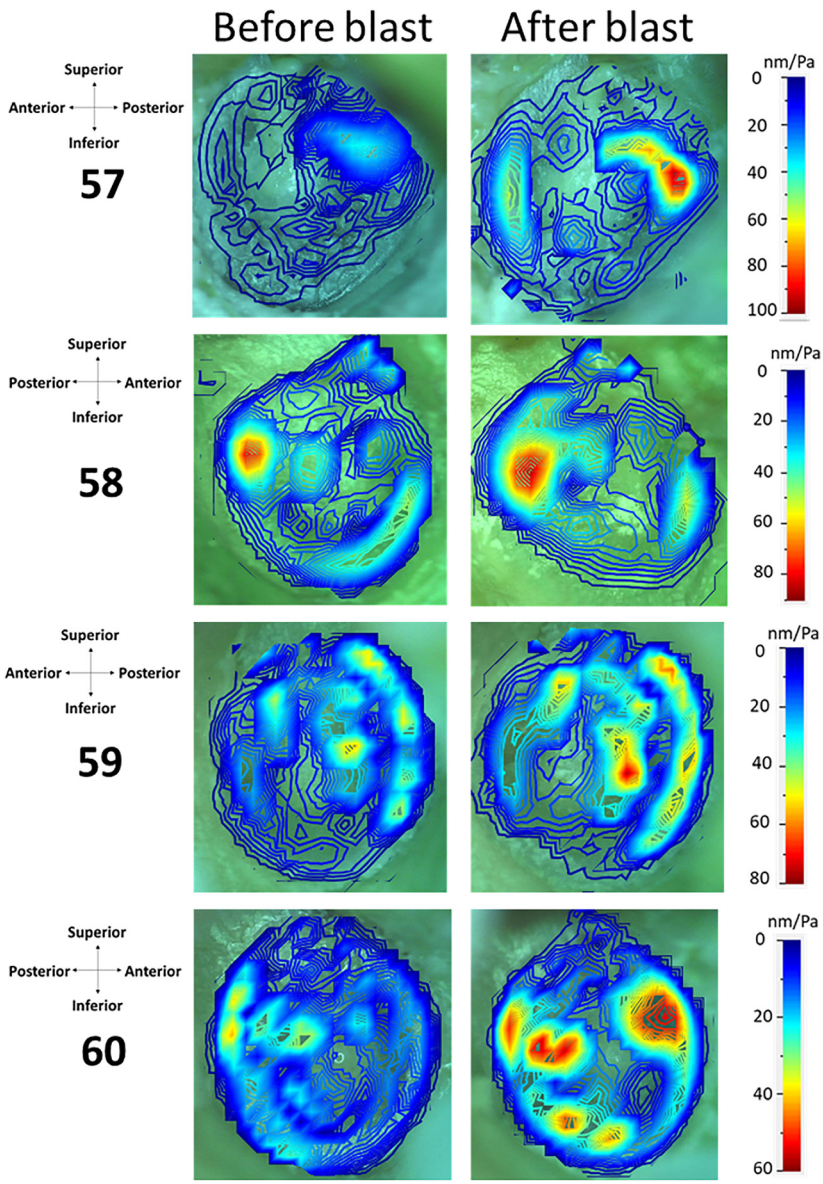


Fig. 7 Deflection shapes of TM surface motion measured by SLDV on all TBs at 4 kHz

in the anterior region of the TM after blast in TB-57. In TB-59 and TB-60, the displacement in the anterior high-vibration area increased after the blast. This phenomenon indicated that the vibration mode of single posterior peak domination changed to a two-peak formation starting at 4 kHz.

3.2 Tympanic Membrane Surface Motion Simulated by Finite Element Model. Following the three approaches described in Sec. 2.3.3, a damaged TM model to mimic the blast-induced changes in TM microstructure and mechanical properties was created as shown in Fig. 8. In addition to reducing the elastic modulus and the volume fraction of fibers in the model, part of the fibers in the posterior–inferior quadrant of the TM was removed to simulate the local damage or loss of fibers based on observations from the surface motion measurements from experiments (Figs. 5–7). This was also designed to test the hypothesis that the regions in the TM where the highest displacement peak appears during the surface motion measurement may represent more severely damaged fiber network than the other regions. As shown in Fig. 8, a round-shape nonfiber area with a diameter of approximately 4 mm was created by deleting the fiber elements in the posterior–inferior quadrant. The location, size, and shape of the nonfiber area were simulated based on the high-displacement area of the TM in Fig. 5 at 1, 2, and 3 kHz.

The deflection shapes of the TM along the direction perpendicular to the plane of the tympanic annulus were calculated from the FE model of the entire ear shown in Fig. 4 (left ear) with the normal TM or damaged TM at five selected frequencies (1, 2, 3, 4, and 8 kHz) and plotted in Fig. 9. The orientation of the left ear is shown in the upper left-hand corner of the figure. Scale bars in unit nm/Pa are shown in the right column for each group of images obtained at the same frequency. From the left to right, the images in the first column show the deflection or displacement shapes of normal TM derived from the FE model of the ear over the frequencies of 1–8 kHz from the top to bottom. The images in the second column show the deflection shapes of damaged TM simulated by reducing elastic modulus of the fibers. Images in columns 3 and 4 represent the deflection shapes of damaged TM simulated by reducing fiber volume fraction and partially removing local fibers, respectively.

In normal TM, a prominent major peak was observed in the posterior–inferior region at all frequencies and the dominance of a single peak decreased with the frequency increasing. A secondary

Downloaded from https://asmedigitalcollection.asme.org/biomechanical/article-pdf/141/9/091009/5193736/bio_141_09_091009.pdf by University Of Oklahoma user on 22 September 2019

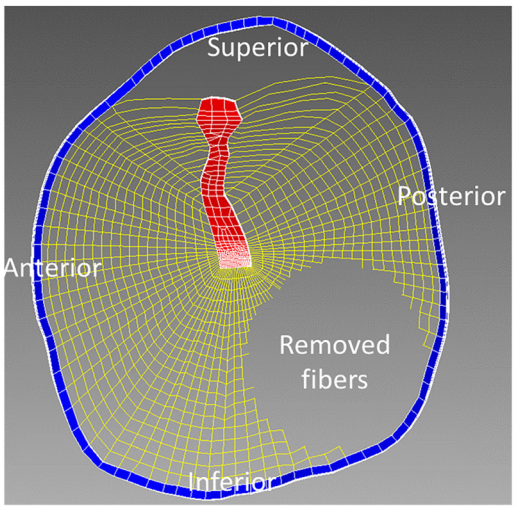


Fig. 8 Fibrous structure of the TM model simulating the partial loss of fibers in the high-mobility region induced by blast exposure. The high-mobility region on TM was observed in the posterior–anterior region where the major displacement peak appeared at frequencies below 4 kHz.

peak emerged in the anterior region at 3 kHz or higher frequencies and the multiple minor peaks formed a complicated shape of deflection at 8 kHz. The maximum displacement gradually decreased as frequency increasing from 118 nm/Pa at 1 kHz to 4.5 nm/Pa at 8 kHz. The normal TM showed the lowest surface mobility over the frequencies.

For damaged TM simulated in the model, the major peak in the posterior region was discernable at the frequencies below 3 kHz. The location of the major peak was consistent with what was observed in the normal TM and the maximum displacement value was greater in the damaged TMs. At 1 kHz, there was only one major displacement peak in all TMs, and the TM with reduced elastic modulus showed the highest maximum displacement of 632.7 nm/Pa among three damaged TM models. At 2 kHz, the second peak in the anterior region emerged in the TM with a reduced elastic modulus, but the other two damaged TMs kept the similar deflection shape as the normal TM. The highest displacement at a value of 149.5 nm/Pa emerged in the TM of partially removed fibers. At 3 kHz, multiple peaks appeared to form a half-ring-shaped high displacement area in the TM with reduced elastic modulus. The TMs with reduced volume fraction and removed fibers showed deflection shape close to the normal TM, but with increased mobility. The highest maximum displacement decreased to 49.1 nm/Pa in the removed fibers. At 4 and 8 kHz, the trend continued in all four TMs. A ring-shaped high-displacement area emerged on the surface of the TM with reduced elastic modulus. The behavior of the TM with reduced volume fraction at high frequencies was similar to what was observed in the reduced modulus TM. The TM of partially removed fibers was unique, whose deflection shape remained unchanged over the entire frequency range. The high-displacement area remained at the same location, but the maximum displacement gradually decreased from 400 nm/Pa at 1 kHz to 5.9 nm/Pa at 8 kHz. The FE model-derived TM surface motion was generally consistent with those observed from the experimental results measured by SLDV (Figs. 5–7).

4 Discussion

4.1 Comparison of Scanning Laser Doppler Vibrometry Measured Tympanic Membrane Surface Motion With Published Data—Normal Tympanic Membrane. In this study, the full-field surface motion of human TM under a chirp stimulus of 1–8 kHz was measured by SLDV before and after blast exposures. As an important indicator to evaluate the sound transmission function of the TM and middle ear, the surface motion of the TM has been measured on human and animal ears using SLDV [15,16,29] and stroboscopic holography [30–32]. The maximum displacements on the human TM surface were 400, 80, and 16 nm/Pa at 1, 4, and 8 kHz, respectively, reported by Zhang et al. [15]. The values measured by stroboscopic holography in two different human cadaveric TMs reported by Cheng et al. [31] were 200/200, 30/35, and 16/8 nm/Pa at 1, 4, and 10 kHz, respectively. In this study, the maximum displacements on the TM surface of TB 60 before blast exposures (normal ear) were 180, 30, and 20 nm/Pa at 1, 4, and 8 kHz, respectively. Although there were some variations, the values of the TM maximum displacement measured in this study were generally consistent with the published data over the frequency range of 1–8 kHz.

The shape of the TM deflection is another parameter to evaluate the mobility of the TM. At 1 kHz, a single prominent peak was observed in the posterior–superior area of the TM (Fig. 5), which was close to what was reported by Cheng et al. [31] and to that the peak displacement emerged in the posterior–inferior region of the TM by Zhang et al. [15]. The peak area appearing in the posterior region in the previous and current studies was also observed in the surface motion of animals at the low frequencies [11,29,33]. At 4 kHz, a half-ring-shaped or ring-shaped high displacement area covered most of the TM surface except the superior region observed in this study and previous studies. At 8 kHz, multiple high displacement areas were in shape of concentric circles centered at the umbo and spread out to the TM annulus, which was also observed in Cheng et al. [31] and Zhang et al. [15]. Overall, the full-field surface motion of the normal human TM measured in this study agreed with the published data, which confirmed that the experimental setup is reliable.

4.2 Comparison of Finite Element Model-Predicted Tympanic Membrane Surface Motion With the Experimental Data—Normal and Blast-Damaged Tympanic Membrane. The full-field TM motion was measured experimentally (Figs. 5–7) and simulated by the FE model (Fig. 9). The maximum displacement in the posterior–inferior region of the normal TM predicted by the FE model was 118, 16.3, and 4.5 nm/Pa at 1, 4, and 8 kHz, respectively, which is consistent with the experimental data of 105, 25, and 10 nm/Pa in TB 60 at 1, 4, and 8 kHz, respectively. The major peak in the posterior–inferior region of the TM was observed in the normal TM at frequencies below 4 kHz in Figs. 5 and 9. Multiple peaks emerged on the TM surface including the superior were observed at 8 kHz in both experimental and model-derived results. Therefore, the multilayer fibrous model of TM was capable to simulate the behavior of normal TM over the frequency range.

The key application of the FE model for damaged TM was to investigate how the TM motion is altered after blast exposure and what is the possible relation between the TM movement variation and its microstructure damage induced by blast waves. Figures 6 and 7 demonstrated a typical feature of the change in full-field surface motion of the TM after blast exposures: an increase of the maximum displacement with a major peak in the posterior region at the frequencies between 3 and 4 kHz. As shown in Figs. 6 and 7, the increased displacement of the major peak was observed in all four samples at 3 and 4 kHz. The deflection shapes of damaged TMs derived from FE model with reduced elastic modulus of the fibers, reduced fiber volume fraction, and partially removed local fibers generally followed the same trend of the experimental data with some minor discrepancies in Fig. 9.

The damage simulation with reduced elastic modulus captured the increased magnitude of the major displacement peak at low frequencies but shared the least similarity with the experimental results among three damage models. The expansion of the major peak area and the increase of the magnitude were minimum at frequencies above 2 kHz. In contrast, the TM with reduced fiber

Downloaded from https://asmedigitalcollection.asme.org/biomechanical/article-pdf/141/9/091009/5193736/bio_141_09_091009.pdf by University Of Oklahoma user on 22 September 2019

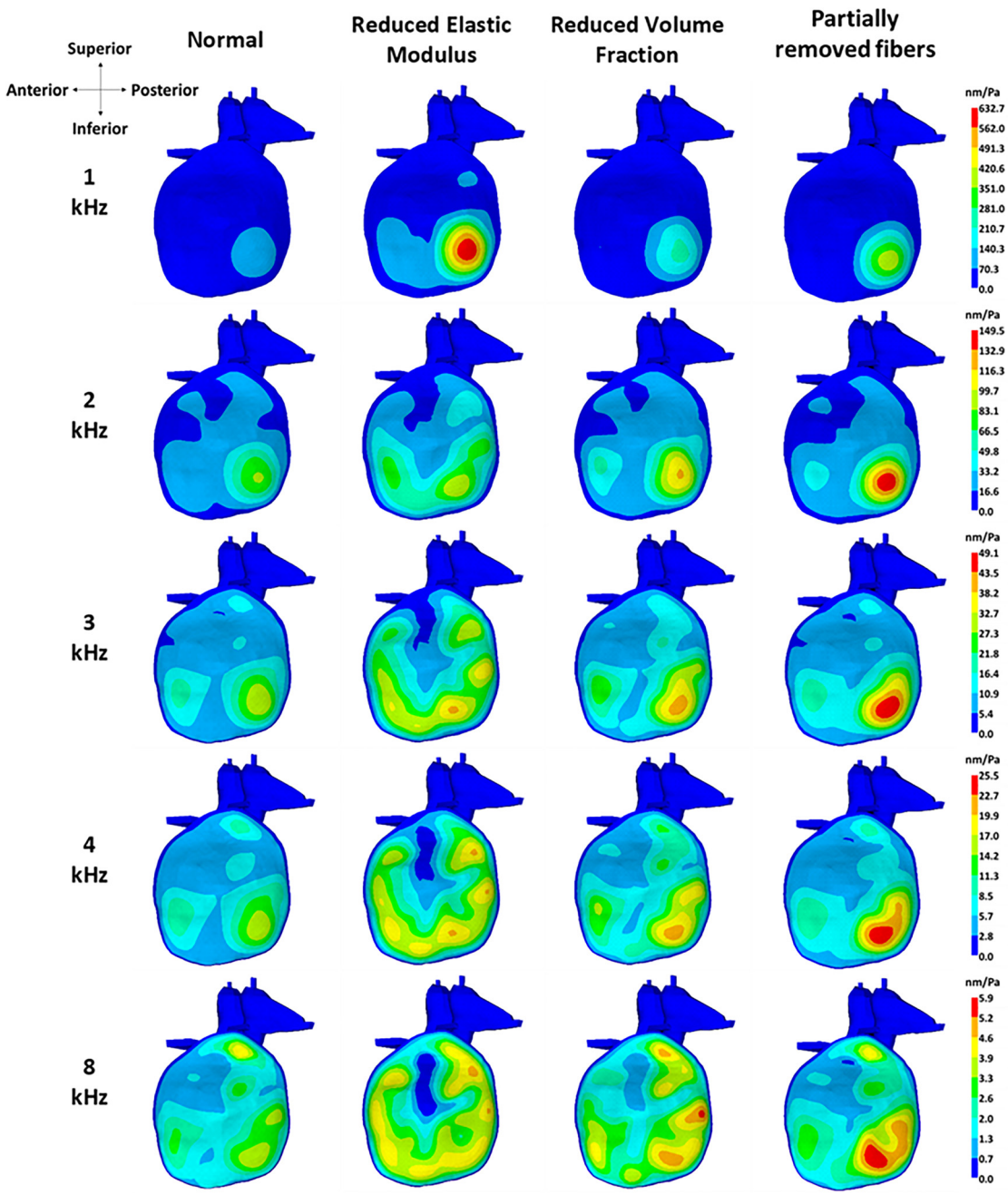


Fig. 9 Deflection shapes of TM surface motion derived from 3D FE model of the human ear (Fig. 4(*a*)) with the normal TM or damaged TM at five selected frequencies (1, 2, 3, 4, and 8 kHz). From the left to right, the first column shows normal TM, the second column shows the TM with reduced elastic modulus, the third column shows the TM with reduced volume fraction of fibers, and the fourth column shows TMs with partially removed fibers.

volume fraction followed the trend of the experimental data better than that of reduced elastic modulus over the frequency range. The typical feature of the major displacement peak was observed at frequencies below 4 kHz, but the multiple peaks or the expansion of the high-displacement area over the entire surface of TM were only observed at 8 kHz in both normal and damaged TMs. The increase of the peak displacement from the normal to the reduced volume fraction TM was significant as shown from the scale bars. In the TM with partially removed fibers, the deflection shape of a major peak in the nonfiber area stayed unchanged but the amplitude decreased with the frequency. In summary, the FE simulation indicated that the pattern of the TM surface motion was significantly affected by the microstructure or fiber damage of the tissue. The consistency between the simulation and the experimental data revealed that the postblast TM motion change could be resulted by the alteration of the fiber mechanical properties or the loss of fibers.

4.3 Contribution and Limitation of This Study. Rupture of the TM is a typical injury caused by blast exposure which can result in severe hearing loss and pain [1,4,34]. However, recent biomechanical measurement on the TM after blast indicated the microstructural damage and mechanical property changes of the TM even there was no discernable existence of the rupture [9,10,35]. These permanent alterations in TM tissues would affect

Downloaded from https://asmedigitalcollection.asme.org/biomechanical/article-pdf/141/9/091009/5193736/bio_141_09_091009.pdf by University Of Oklahoma user on 22 September 2019

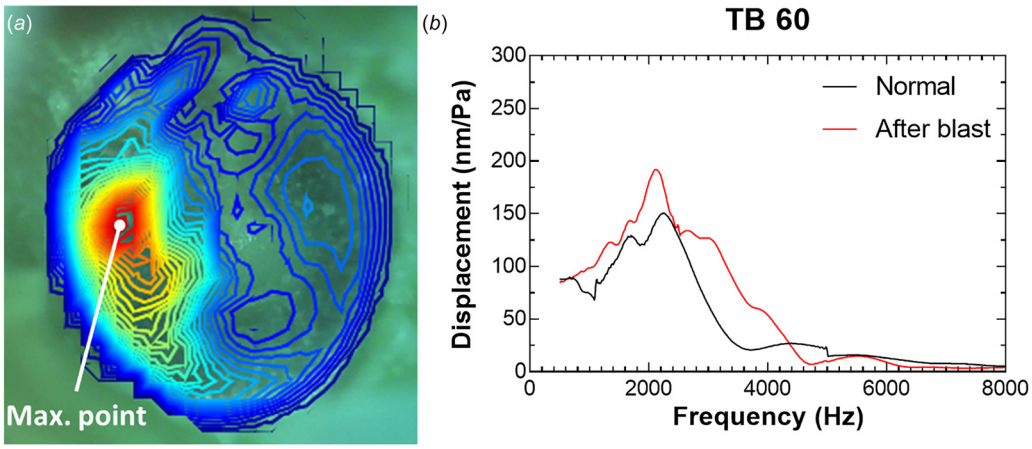


Fig. 10 (*a*) Deflection shapes or displacement contours of TB-60 at 3 kHz showing the location of the maximum displacement point. (*b*) Maximum displacement measured from TB-60 before and after the blast exposure.

the progressive hearing loss after blast exposure [36,37], but the role of the TM damage in the progressive hearing loss or recovery process remains unclear. This study on measurement of the full-field surface motion of the TM damaged by blast waves may provide needed information for characterization of the postblast sound transmission function of the middle ear.

The experimental data obtained in this study demonstrate that the major peak of the TM motion located in the posterior region of the TM and an increase in maximum displacement at 3–4 kHz in that region were discovered in all TBs after the blast exposure. For a more detailed analysis of the maximum displacement on TM, Fig. 10(*b*) shows the displacement–frequency curves of a point selected at the center of the major peak at 3 kHz in TB 60 (see Fig. 10(*a*)) before and after the blast exposure. The frequencies of reaching maximum displacement for normal and postblast ears were almost the same, while the peak value of the curve after blast was approximately 50 nm/Pa higher than the normal curve or the curve before blast to reach a value of 180 nm/Pa. At frequencies from 1 to 4 kHz, the displacement at this selected point increased significantly after the blast exposure. These results together with those shown in Figs. 5–7 suggest that the increase of the TM mobility in postblast human ears is both frequency and location dependent.

In this study, the multilayer model of the TM including the radial and circumferential fiber network was successfully constructed. The consistency between the model-derived and the experimental data indicates that the model is capable to characterize the structure–function relationship of the normal and damaged TMs over the frequency range. The multilayer TM model generates a connection between the microstructure and mechanical properties of the TM with the TM surface motion which improves biomechanical analysis on the TM with higher complexity. For example, using this model, we will predict the stress distribution in the TM to understand the mechanism of TM rupturing process in future studies. The evaluation on the TM graft of fibrous structure [36] and the simulation of interlayer edema in TM resulted by otitis media [38] are also clinical-relevant applications of this model in future studies.

There are some limitations in this study. In Fig. 5, the results at 1 kHz show a higher displacement in the TM before blast exposure. The reason behind this could be the surgical process to expose the TM in this TB. At the superior edge of the TB sample, the epidermal layer of the TM might be connected to the ear canal tissue which affected the TM motion at the low-frequencies. The mechanical properties of the TM model may require further adjustment. To simulate the damage and emphasize the effect of fibers, the average stiffness of the TM model was relatively high which resulted in a smaller displacement than the experimental data. The viscoelastic behavior of the collagen fibers will also need to be considered to improve the accuracy of the model, especially at high frequencies.

5 Conclusion

In this study, the full-field surface motion of human TM before and after blast exposures was measured by SLDV over a frequency range from 1 to 8 kHz. An FE model of human TM with multilayer fiber network was created to simulate the normal and blast-damaged TMs. The major displacement peaks whose magnitude increased after the blast exposure emerged in the posterior region of the TM were observed in all TBs at the frequencies of 3–4 kHz. The model-derived data successfully characterized the features of the TM surface motion measured from the normal and damaged ears. The results suggested that the blast-induced TM damage might be a combination of global and regional loss or mechanical property changes of the fibers. The technology developed in this study can detect and simulate the blast-induced microstructural damage in the TM and improve our understanding of postblast injuries in the auditory system. The multilayer TM model created in this study provides a practical tool for microstructural biomechanical analysis of TM damage.

Acknowledgment

The authors would like to express their deep appreciation for the guidance and vision offered by Professor Y. C. Fung to biomechanical measurement and modeling of human ear for sound transmission. For the first author (Rong Z. Gan), Professor Fung has personally mentored her research and career development in biomedical engineering for 40 years. Professor Fung introduced her to the biomechanics field in 1979. Following several milestones guided by Professor Fung, her major research direction shifted from lung biomechanics to hearing and ear biomechanics at the University of Oklahoma in 1999. Since then, a new research area, "Biomechanics for Restoration of Hearing," has been established with the great impacts on hearing research across the World in both measurement technologies and computational modeling. Professor Fung's influences on Rong Gan's research in hearing biomechanics will continue to be demonstrated through the past, present, and future research projects.

For the second author (Shangyuan Jiang), Professor Fung's Biomechanics textbooks have guided his studies for completing the Ph.D. research in mechanical properties of ear tissues. The quality and breath of Professor Fung's contributions to the field of

Downloaded from https://asmedigitalcollection.asme.org/biomechanical/article-pdf/141/9/091009/5193736/bio_141_09_091009.pdf by University Of Oklahoma user on 22 September 2019

biomechanics are motivating all younger generations of students and researchers.

We dedicate this innovative work with scanning laser Doppler vibrometry measurement and 3D multilayer modeling of damaged eardrum (tympanic membrane) induced by blast waves to honor Professor Fung's 100th birthday. This research was supported by grants from the U.S. Department of Defense (W81XWH-14-1-0228).

Funding Data

- U.S. Department of Defense (Grant No. W81XWH-14-1-0228, Funder ID: 10.13039/100000005).

References

[1] Cave, K. M., Cornish, E. M., and Chandler, D. W., 2007, "Blast Injury of the Ear: Clinical Update From the Global War on Terror," J. Mil. Med., **172**(7), pp. 726–730.

[2] Dougherty, A. L., MacGregor, A. J., Han, P. P., Viirre, E., Heltemes, K. J., and Galarneau, M. R., 2013, "Blast-Related Ear Injuries Among U.S. Military Personnel," J. Rehabil. Res. Dev., **50**(6), pp. 893–904.

[3] Cho, S.-I., Gao, S. S., Xia, A., Wang, R., Salles, F. T., Raphael, P. D., Abaya, H., Wachtel, J., Baek, J., Jacobs, D., Rasband, M. N., and Oghalai, J. S., 2013, "Mechanisms of Hearing Loss After Blast Injury to the Ear," PLoS One, **8**(7), p. e67618.

[4] Gan, R. Z., Nakmali, D., Ji, X. D., Leckness, K., and Yokell, Z., 2016, "Mechanical Damage of Tympanic Membrane in Relation to Impulse Pressure Waveform—A Study in Chinchillas," Hear. Res., **340**, pp. 25–34.

[5] Keller, M., Sload, R., Wilson, J., Greene, H., Han, P., and Wise, S., 2017, "Tympanoplasty Following Blast Injury," Otolaryngol. Head Neck Surg., **157**(6), pp. 1025–1033.

[6] Lim, D. J., 1995, "Structure and Function of the Tympanic Membrane: A Review," Acta Otorhinolaryngol., **49**(2), pp. 101–115.

[7] Volandri, G., Di Puccio, F., Forte, P., and Carmignani, C., 2011, "Biomechanics of the Tympanic Membrane," J. Biomech., **44**(7), pp. 1219–1236.

[8] Luo, H., Dai, C., Gan, R. Z., and Lu, H., 2009, "Measurement of Young's Modulus of Human Tympanic Membrane at High Strain Rates," ASME J. Biomech. Eng., **131**(6), p. 064501.

[9] Luo, H., Jiang, S., Nakmali, D. U., Gan, R. Z., and Lu, H., 2016, "Mechanical Properties of a Human Eardrum at High Strain Rates After Exposure to Blast Waves," J. Dyn. Behav. Mater., **2**(1), pp. 59–73.

[10] Engles, W. G., Wang, X., and Gan, R. Z., 2017, "Dynamic Properties of Human Tympanic Membrane After Exposure to Blast Waves," Ann. Biomed. Eng., **45**(10), pp. 2383–2394.

[11] Rosowski, J. J., Cheng, J. T., Ravicz, M. E., Hulli, N., Hernandez-Montes, M., Harrington, E., and Furlong, C., 2009, "Computer-Assisted Time-Averaged Holograms of the Motion of the Surface of the Mammalian Tympanic Membrane With Sound Stimuli of 0.4–25 KHz," Hear. Res., **253**(1–2), pp. 83–96.

[12] Wada, H., Ando, M., Takeuchi, M., Sugawara, H., Koike, T., Kobayashi, T., Hozawa, K., Gemma, T., and Nara, M., 2002, "Vibration Measurement of the Tympanic Membrane of Guinea Pig Temporal Bones Using Time-Averaged Speckle Pattern Interferometry," J. Acoust. Soc. Am., **111**(5), pp. 2189–2199.

[13] Cheng, J. T., Aarnisalo, A. A., Harrington, E., Hernandez-Montes, M. D. S., Furlong, C., Merchant, S. N., and Rosowski, J. J., 2010, "Motion of the Surface of the Human Tympanic Membrane Measured With Stroboscopic Holography," Hear. Res., **263**(1–2), pp. 66–77.

[14] Burkhardt, A., Kirsten, L., Bornitz, M., Zahnert, T., and Koch, E., 2014, "Investigation of the Human Tympanic Membrane Oscillation Ex Vivo by Doppler Optical Coherence Tomography," J. Biophotonics, **7**(6), pp. 434–441.

[15] Zhang, X., Guan, X., Nakmali, D., Palan, V., Pineda, M., and Gan, R. Z., 2014, "Experimental and Modeling Study of Human Tympanic Membrane Motion in the Presence of Middle Ear Liquid," J. Assoc. Res. Otolaryngol., **15**(6), pp. 867–881.

[16] Wang, X., and Gan, R. Z., 2018, "Surface Motion of Tympanic Membrane in a Chinchilla Model of Acute Otitis Media," J. Assoc. Res. Otolaryngol., **19**(6), pp. 619–635.

[17] Zhang, X., and Gan, R. Z., 2011, "A Comprehensive Model of Human Ear for Analysis of Implantable Hearing Devices," IEEE Trans. Biomed. Eng., **58**(10), pp. 3024–3027.

[18] Gan, R. Z., Leckness, K., Nakmali, D., and Ji, X. D., 2018, "Biomechanical Measurement and Modeling of Human Eardrum Injury in Relation to Blast Wave Direction," Mil. Med., **183**(Suppl. 1), pp. 245–251.

[19] Kingery, C. N., and Pannill, B. F., 1964, "Peak Overpressure Vs Scaled Distance for TNT Surface Bursts (Hemispherical Charges)," Army Ballistic Research Lab, Aberdeen Proving Ground, MD, Report No. BRL-MR-1518.

[20] Gan, R. Z., Zhang, X., and Guan, X., 2011, "Modeling Analysis of Biomechanical Changes of Middle Ear and Cochlea in Otitis Media," AIP Conf. Proc., **1403**, pp. 539–544.

[21] Fay, J., Puria, S., Decraemer, W. F., and Steele, C., 2005, "Three Approaches for Estimating the Elastic Modulus of the Tympanic Membrane," J. Biomech., **38**(9), pp. 1807–1815.

[22] Gan, R. Z., and Wang, X., 2007, "Multifield Coupled Finite Element Analysis for Sound Transmission in Otitis Media With Effusion," J. Acoust. Soc. Am., **122**(6), pp. 3527–3538.

[23] Gentil, F., Parente, M., Martins, P., Garbe, C., Santos, C., Areias, B., Branco, C., Paço, J., and Jorge, R. N., 2016, "Effects of the Fibers Distribution in the Human Eardrum: A Biomechanical Study," J. Biomech., **49**(9), pp. 1518–1523.

[24] Tuck-Lee, J. P., Pinsky, P. M., Steele, C. R., and Puria, S., 2008, "Finite Element Modeling of Acousto-Mechanical Coupling in the Cat Middle Ear," J. Acoust. Soc. Am., **124**(1), pp. 348–362.

[25] Shirazi, R., and Shirazi-Adl, A., 2005, "Analysis of Articular Cartilage as a Composite Using Nonlinear Membrane Elements for Collagen Fibrils," Med. Eng. Phys., **27**(10), pp. 827–835.

[26] Tiburtius, S., Schrof, S., Molnár, F., Varga, P., Peyrin, F., Grimal, Q., Raum, K., and Gerisch, A., 2014, "On the Elastic Properties of Mineralized Turkey Leg Tendon Tissue: Multiscale Model and Experiment," Biomech. Model. Mechanobiol., **13**(5), pp. 1003–1023.

[27] Gibson, R. F., 2011, *Principles of Composite Material Mechanics*, 3rd ed., CRC Press, Boca Raton, FL.

[28] Wenger, M. P. E., Bozec, L., Horton, M. A., and Mesquida, P., 2007, "Mechanical Properties of Collagen Fibrils," Biophys. J., **93**(4), pp. 1255–1263.

[29] Wang, X., Guan, X., Pineda, M., and Gan, R. Z., 2016, "Motion of Tympanic Membrane in Guinea Pig Otitis Media Model Measured by Scanning Laser Doppler Vibrometry," Hear. Res., **339**, pp. 184–194.

[30] Kozin, E. D., Black, N. L., Cheng, J. T., Cotler, M. J., McKenna, M. J., Lee, D. J., Lewis, J. A., Rosowski, J. J., and Remenschneider, A. K., 2016, "Design, Fabrication, and In Vivo Testing of Novel Three-Dimensionally Printed Tympanic Membrane Grafts," Hear. Res., **340**, pp. 191–203.

[31] Cheng, J. T., Hamade, M., Merchant, S. N., Rosowski, J. J., Harrington, E., and Furlong, C., 2013, "Wave Motion on the Surface of the Human Tympanic Membrane: Holographic Measurement and Modeling Analysis," J. Acoust. Soc. Am., **133**(2), pp. 918–937.

[32] Rosowski, J., Cheng, J., Merchant, S., Harrington, E., and Furlong, C., 2011, "New Data on the Motion of the Normal and Reconstructed Tympanic Membrane," Otol. Neurotol., **32**(9), pp. 1559–1567.

[33] Rosowski, J. J., Dobrev, I., Khaleghi, M., Lu, W., Cheng, J. T., Harrington, E., and Furlong, C., 2013, "Measurements of Three-Dimensional Shape and Sound-Induced Motion of the Chinchilla Tympanic Membrane," Hear. Res., **301**, pp. 44–52.

[34] Patterson, J. H., and Hamernik, R. P., 1997, "Blast Overpressure Induced Structural and Functional Changes in the Auditory System," Toxicology, **121**(1), pp. 29–40.

[35] Liang, J., Yokell, Z. A., Nakmaili, D. U., Gan, R. Z., and Lu, H., 2017, "The Effect of Blast Overpressure on the Mechanical Properties of a Chinchilla Tympanic Membrane," Hear. Res., **354**, pp. 48–55.

[36] Race, N., Lai, J., Shi, R., and Bartlett, E. L., 2017, "Differences in Post-Injury Auditory System Pathophysiology After Mild Blast and Non-Blast Acute Acoustic Trauma," J. Neurophysiol., **118**(2), pp. 782–799.

[37] Bohne, B. A., Kimlinger, M., and Harding, G. W., 2017, "Time Course of Organ of Corti Degeneration After Noise Exposure," Hear. Res., **344**, pp. 158–169.

[38] Guan, X., Jiang, S., Seale, T. W., Hitt, B. M., and Gan, R. Z., 2015, "Morphological Changes in the Tympanic Membrane Associated With Haemophilus Influenzae-Induced Acute Otitis Media in the Chinchilla," Int. J. Pediatr. Otorhinolaryngol., **79**(9), pp. 1462–1471.

Downloaded from https://asmedigitalcollection.asme.org/biomechanical/article-pdf/141/9/091009/5193736/bio_141_09_091009.pdf by University Of Oklahoma user on 22 September 2019

Hearing Research 378 (2019) 75–91

Contents lists available at ScienceDirect

Hearing Research

journal homepage: www.elsevier.com/locate/heares

Research Paper

Mapping the Young's modulus distribution of the human tympanic membrane by microindentation

Huiyang Luo [a, b], Fang Wang [a], Chen Cheng [a], Don U. Nakmali [c], Rong Z. Gan [c], Hongbing Lu [a, *]

[a] Department of Mechanical Engineering, The University of Texas at Dallas, Richardson, TX, 75080, USA
[b] Karagozian and Case, Inc., 700 N Brand Blvd., Suite 700, Glendale, CA, 91203, USA
[c] School of Aerospace and Mechanical Engineering, The University of Oklahoma, Norman, OK, 73019, USA

ARTICLE INFO

Article history:
Received 14 August 2018
Received in revised form
12 February 2019
Accepted 20 February 2019
Available online 23 February 2019

Keywords:
Human tympanic membrane
Viscoelastic
Microindentation
Young's modulus
Statistical analysis
Modulus map

ABSTRACT

The human tympanic membrane (TM, or eardrum) is composed primarily of layers of collagen fibers oriented in the radial and circumferential directions, as well as epidermal and mucosal layers at the lateral and medial surfaces. The mechanical properties of the TM depend on the microstructures of the collagen fibers, which vary with location, resulting in a spatial variation of Young's modulus. In this study, the Young's modulus of the human TM is measured using microindentation. A 10 μm diameter spherical nanoindenter tip is used to indent the TM at different locations in the lateral and medial surfaces. Through a viscoelastic contact analysis, the steady state out-of-plane (through thickness) Young's modulus at a constant strain rate for the TM is determined from the uniaxial relaxation modulus. The measured spatial distribution of Young's modulus is reported for the entire TM pars tensa on both lateral and medial surfaces. The Young's modulus, for the four TM quadrants, is analyzed statistically using a normal quantile-quantile (Q-Q) plot. The obtained S-shaped curve indicates a bi-modal Gaussian distribution in the Q-Q plot. The spatial distribution of the Young's modulus is modeled by a bivariate Gaussian function in the polar coordinates over the entire TM on both the lateral and medial surfaces. It is shown that the anterior-superior quadrant has the smallest value of Young's modulus. Differences are observed in the spatial distribution of the Young's modulus for both the lateral and medial surfaces. For the medial surface, Young's modulus varies mainly along the radial direction following a small-large-small trend, emanating from the umbo. For the lateral surface, the modulus at the anterior-superior quadrant shows the smallest modulus; the modulus decreases gradually along the radial directions. The quantitative results presented in this paper will help improve future simulation models of the middle ear by using spatial dependence of Young's modulus over the entire TM.

© 2019 Elsevier B.V. All rights reserved.

1. Introduction

The eardrum or tympanic membrane (TM) separates the middle ear from the outer ear, and the tympanic membrane converts sound waves into vibrations of ossicular bones. The foot of the stapes converts the bone movements (vibrations) into a hydrodynamic pressure wave within the inner ear that travels along the cochlea. These traveling waves then result in deflection of the stereocilia of the cochlear hair cells and ultimately to the sensation of hearing. However, alterations in the structures or mechanical properties of the TM due to diseases and trauma can affect the sound transmission and lead to conductive hearing loss (Gan et al., 2004, 2006 & 2010; Kochkin, 2005; Wang et al., 2007). To understand the sound transmission, it is necessary to understand the role of individual components in the middle ear in acoustic transmission (Eiber and Schidhlen, 1996; Ferris and Prendergast, 2000).

Measurements of the mechanical properties over the entire eardrum provide material input parameters for finite element method (FEM) simulation models of the middle ear. Values of Young's modulus for the TM, under different conditions reported in the literature, are summarized in Table 1. The first of these measurements in 1960 reported a Young's modulus of 20 MPa for the TM using a beam test (Von Békésy, 1960). At about the same time,

* Corresponding author. Department of Mechanical Engineering, The University of Texas at Dallas, 800 W. Campbell Rd, EC38, Richardson, TX, 75080, USA.
E-mail address: hongbing.lu@utdallas.edu (H. Lu).

https://doi.org/10.1016/j.heares.2019.02.009
0378-5955/© 2019 Elsevier B.V. All rights reserved.

Abbreviations

TM	Tympanic Membrane
Q-Q	Quantile-Quantile
CDF	Cumulative Distribution Function
PDF	Probability Density Function
FEM	Finite Element Methods
COD	Coefficient of Determination
R^2	R squared
LP	Lateral Process of the malleus
AS	Anterior-Superior quadrant
AI	Anterior-Inferior quadrant
PS	Posterior-Superior quadrant
PI	Posterior-Inferior quadrant
U	Umbo
M	Malleus
SP	Short Process of the malleus
TIR	Trigonum Interradiale
C	Circumferential fiber
R_1	radial fibers which attach straight into annular ring
R_2	a few radial fibers which diverge or crossover their terminals
T	Transverse fibers
P	Parabolic fibers
SMR	Submucous Fine Radial fibers

the Young's modulus of TM strip was measured as 40 MPa using a longitudinal dynamic tensile oscillator (Kirikae, 1960). Later, through uniaxial tension on a human TM, the Young's modulus was determined as 23 MPa at a relatively high strain of 60% (Decraemer et al., 1980). The areal modulus of elasticity of the human eardrum was also found to depend on the undeformed area of the eardrum (Gaihede et al., 2007). The in-plane Young's relaxation modulus was determined from tensile relaxation on human TM strip specimens, primarily along the circumferential direction (Cheng et al., 2007). A nanoindentation technique was used to measure the relaxation modulus of the TM in the out-of-plane (through-thickness) direction; measurement was conducted on a small sample for demonstration of the feasibility of the technique. The in-plane Young's modulus for four quadrants of the TM was determined to be 26–38 MPa from different individuals (Huang et al., 2008). The Young's modulus of a human TM in the out-of-plane direction was found in the range of 2–15 MPa over the entire TM on the medial surface without removing the mucosal layer (Daphalapurkar et al., 2009). A human TM was stretched at high strain rates, corresponding to high frequencies up to 2000 Hz (Luo et al., 2009a & 2009b), and the Young's modulus was reported as 45–59 MPa in the radial direction, and 34–57 MPa in the circumferential direction. Using a dynamic mechanical analyzer, the storage modulus of the human TM was determined as 15–28 MPa at 1–3800 Hz using frequency-temperature superposition (Zhang and Gan, 2013).

Young's modulus values for the TM under different conditions reported in the literature are summarized in Table 1. Dynamic properties of human tympanic membrane were also measured using an electromagnetic driver to actuate remotely a magnet attached to a TM strip sample under tension (Zhang and Gan, 2010). In that work, a laser Doppler vibrometor was used to measure the movement of the TM to determine the onset of resonance. FEM simulations were used to model the vibration of the TM strip and the dynamic stiffness at which resonance occurs. It was determined that the storage modulus was within 54–66 MPa at 200–8000 Hz. A laser holography technique was used to measure the surface profile, and motion of a tympanic membrane induced by sound (Puria, 2003; Rosowski et al., 2013; Beyea et al., 2013). A high-speed digital holography method was used to quantitatively characterize the transient dynamics of a TM (Dobrev et al., 2014). The stroboscopic holography yields maps of the amplitude and phase of the displacement of the entire membrane surface at selected frequencies (Greef et al., 2014). The measured stiffness of the TM was found to depend strongly on the fiber density in a particular portion of a TM. An indentation technique was developed to apply indentation at a particular location in an intact, full size TM, while the surface topography was measured by geometric moiré (Hesabgar et al., 2010; Aernouts et al., 2012). FEM analysis was conducted to analyze this indentation problem to determine the Young's modulus of the TM. Using this method, the Young's modulus of a rat eardrum was determined to be approximately 22 MPa, which is sensitive to the thickness of the pars tensa (Hesabgar et al., 2010). The Young's modulus of a human TM was determined through indentation; the value was found to be within 2–5 MPa (Aernouts et al., 2012). The mechanical properties of a guinea pig TM (Liang et al., 2015) and a chinchilla TM (Liang et al., 2016) were measured under pressure loading using a combined micro-fringe projection and the finite element simulation method; Young's moduli were determined as 15–28 MPa and 11–25 MPa for guinea pig and chinchilla, respectively. Since the calculation of the modulus in bulging experiments needs the thickness data as input and the thickness of a TM changes with location, using a high-

Table 1
Young's modulus values of TM reported in literature.

Literature	Young modulus (MPa) measured	Direction	Type	Methods
Von Békésy, 1960	20	Circumferential	Human	Qusai-static beam
Kirikae (1960)	40	Radial	Human	Dynamic tension
Decraemer et al. (1980)	23	Circumferential	Human	Uniaxial tension
Cheng et al. (2007).	13–22	Circumferential	Human	Tension
Huang et al. (2008)	26–38	Lateral surface	Human	Nanoindentation
Daphalapurkar et al. (2009)	2–15	Medial surface	Human	Nanoindentation
Luo et al. (2009a)	45–59	Radial	Human	SHTB
Luo et al. (2009b)	34–57	Circumferential	Human	SHTB
Zhang and Gan (2010)	54–66	Radial	Human	Dynamic tension
Zhang and Gan (2013)	15–28	Circumferential	Human	DMA
Liang et al. (2015)	15–28	Entire TM	Guinea pig	Bulging
Liang et al. (2016)	11–25	Entire TM	Chinchilla	Bulging
Hesabgar et al. (2010)	22	Local	Human	Indentation
Aernouts et al. (2012)	2–5	Entire TM	Human	Indentation

resolution optical coherence tomography apparatus, the thickness of human eardrum was found to vary between 79 and 97 μm (Kuypers et al., 2006; Jeught et al., 2013). The conventional methods for measurements of TM modulus utilize a strip or entire TM specimen; the average values for a TM are reported. However, a TM contains heterogeneous structures with possibly anisotropic behavior in the radial, circumferential, and through-thickness directions. The reported results focused on the in-plane properties; the out-of-plane properties, which could be different from the in-plane properties, were not reported for the TM. We investigate in this work the out-of-plane properties in the human TM.

In this paper, microindentation is used to probe the local indentation load-displacement response when a spherical indenter tip indents into the surface of a TM on a substrate. A viscoelastic indentation contact mechanics analysis is used to calculate the Young's relaxation modulus (Lu et al., 2003; Huang and Lu, 2006; Huang et al., 2008; Daphalapurkar et al., 2009). The measured Young's relaxation modulus is further converted into Young's modulus at a given strain rate. We report the results of Young's modulus measured on four different quadrants of a human TM, on both the lateral and medial surfaces of the human TM.

2. Materials and methods

2.1. TM structures, layout and quadrants

The human TM consists mainly of parsa tensa, surrounded by the annulus ring. A malleus bone is located in the upper half of the medial surface in the center of Fig. 1a. The parsa flaccida is located at the top. The parsa tensa contains posterior-superior (PS), anterior-superior (AS), posterior-inferior (PI), and anterior-inferior (AI) quadrants, as shown in Fig. 1a. The human TM consists of three membrane layers: the epidermal layer on the lateral surface, middle lamina propria layer, and mucosal layer on the medial surface. The lamina propria layer consists of two separate layers of bundled collagen fibers oriented in the radial and the circumferential directions (Lim, 1970 & 1995) on the lateral and medial surfaces, respectively. Fig. 1b shows a schematic diagram of these layers across the thickness (Lim, 1970; Fay et al., 2005). The mucosal layer is thin (1–2 μm, typically consists of 1–2 layers of cells) in a healthy TM. The epidermal layer is typically 8 μm thick. In order to investigate the properties of the collagen fibrous layer, both epidermal and mucosal layers were removed during the preparation of TM samples.

2.2. Tympanic membrane samples

All TM samples used in this study were harvested from fresh-frozen human temporal bones (cadaver ears) through the Willed Body Program at the University of Oklahoma Health Science Center. The study protocol was approved by both Institutional Animal Care and Use Committees (IACUC) at the University of Oklahoma and the University of Texas at Dallas, and met the guidelines of the National Institutes of Health. The tympanic annulus was separated from the bony ear canal, while the ossicular bone chain was removed at the joints with malleus. Then, the malleus bone was removed from the TM medial surface. Since the outer epidermal and mucosal layers are much softer than the collagen fiber layers, under observation through a surgical microscope a round wooden stick (with rounded-end) was used to slightly scratch both top surfaces of TM samples for 4–5 times until the lamina propria layer was exposed; the exposed layer had no visible damage. After the outer epidermal and mucosal layers were removed, the microindenter tip was placed in direct contact with the lamina propria layer consisting of collagen fibers.

Seven (7) TM samples were prepared for the measurement on the medial surface and eight (8) TM samples were used for the measurement on the lateral surface. The TM samples were transported in a thermally-insulated cooler filled with dry ice; then stored in a freezer at −30 to −40 °C before the experiments. Each TM was defrosted for approximately 20 min prior to sectioning using a scalpel for microindentation. The information and images of the seven TM samples used for the measurement of the medial surface and the eight TM samples for measurement on the lateral surface are shown in Tables 2 and 3, respectively. Information for age, gender, and orientation (left/right) is also shown in both tables for each TM.

2.3. Microindentation experiments

Since a TM is a nearly conical-shaped membrane with a cone angle within 132°–137° (Gaihede et al., 2007), it is not possible to

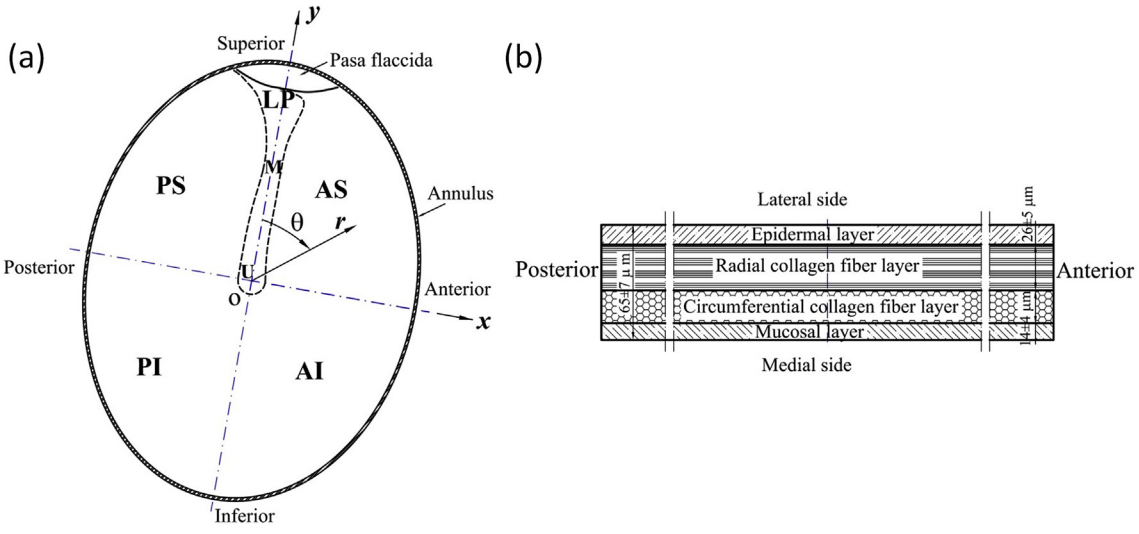
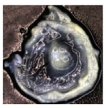
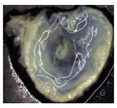
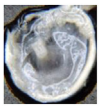


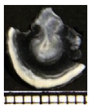
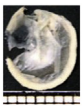
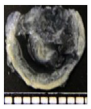
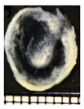
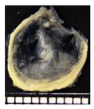
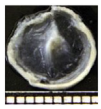
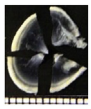
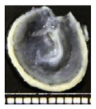
Fig. 1. Schematic diagram of human TM layout and structures.(a). Four quadrants of right ear TM at lateral view (Beyea et al., 2013). LP: lateral process of the malleus, AS: Anterior-Superior quadrant, AI: Anterior-Inferior quadrant, PS: Posterior-Superior quadrant, PI: Posterior-Inferior quadrant; U: Umbo, M: Malleus; (b). Schematic of TM layer structure (Fay et al., 2005; Daphalapurkar et al., 2009).

Table 2
Information on the 7 TMs for microindentation on the medial surface.

Sample	TB08-02	TB08-03	TB08-17	TB08-27	TB08-28	[a]TB09-05	TB09-08
Image							
Information	89/M/R	83/F/L	77/F/L	71/F/L	71/F/R	60/M/L	60/F/R
Data points	82	83	77	74	84	97	89

Notation: M – Male, F – Female, R – Right ear, L – Left ear.
Note:
[a] TB09-05 TM sample was dyed with biocompatible blue pigments for other testing. Since the pigments are ultramarine nanoparticle with diameters in tens of nanometers, soluble to water and dispersed in solution with less than 1% w/w concentration, the dye is not anticipated to significantly affect the TM mechanical properties such as modulus results. The total number of indentations made on these samples is 586.

Table 3
Information on the 8 TMs for microindentation on the lateral surface.

Sample	[a]TB09-19	TB09-20	TB10-01	TB10-02	TB10-03	TB10-22	[b]TB10-23	TB10-24
Image								
Information	66/M/L	66/M/R	59/F/L	59/F/R	80/M/L	87/F/R	74/F/L	74/F/R
Data points	41	73	78	108	98	77	113	110

Note.
[a] Only half of TB09-19 TM was harvested.
[b] TB10-23 TM was already cut into four quadrants for microindentation testing. The total number of indentations made was 698. The small grids at the bottom of each image show a scale bar with the side length of each grid at 1.0 mm.

lay down an entire TM flat on a substrate. Thus, to obtain a flat specimen for the microindentation experiments, a TM was cut into four quadrants, which were then laid down flat on an aluminum substrate. A quadrant of the TM sample was placed on the aluminum substrate. Before microindentation, each TM specimen was gently stretched by several cycles on a flat substrate for preconditioning and flattened gently before placing it on the aluminum substrate. This process is not anticipated to damage the collagen fiber network of the TM sample (Cheng et al., 2007; Daphalapurkar et al., 2009). The TM initially placed on the aluminum substrate was soaked in saline solution (0.9% NaCl, pH 5.6). Fingers covered with a silicone rubber glove gently pressed a quadrant against the hard substrate, to allow the TM quadrant to stay flat and rest on the substrate, to ensure that no air was entrapped between the TM sample and the substrate. The force applied was estimated to be in the neighborhood of 0.1 N, and was not anticipated to induce damage to the collagen fiber network of the TM sample. The saline solution allowed its meniscus to make contact with the TM periphery, so that the TM remained in the moisturized condition during microindentation. The same round wooden sticks were used to flip the TM sample, and to stretch and flatten the TM sample gently for 3–4 times for preconditioning.

A schematic diagram of a sample mounted on a specimen holder (island) for microindentation is shown in Fig. 2a. The circular groove surrounding the island was filled with saline solution to allow the saline solution to moisturize the TM sample during microindentation. An actual AI quadrant placed on an island substrate in the center is shown in Fig. 2b. An entire TM that was cut to four quadrants is shown in Fig. 2c, before placement on the aluminum island substrate. During microindentation, the saline level was monitored and the saline solution was added every 10 min, to ensure that the TM was maintained in a saline-soaked condition. Microindentation was made on either the medial surface or the lateral surface in all measurements. Within the TM, the collagen fibers are aligned either along the radial direction on the lateral surface or in the circumferential direction on the medial surface, as observed by high-magnification SEM images (Moller, 1981, 1984; Cheng, 2007; Mota et al., 2015).

The TM is a thin membrane of material in a rubbery state. Its lateral surface is in contact with air, and *in-vivo* its periphery has only the annulus ring connected to the ear canal tissue at the body temperature of 37 °C. Under this situation, the TM temperature is likely to be between room temperature and the body temperature. Therefore, it seemed feasible to conduct the microindentation experiments at approximately 23 °C.

The long time it took for microindentation on a TM quadrant made it difficult to perform testing on both sides of each sample. Specifically, one microindentation site was conducted in 30 min. This process includes identification of contact point (5 min), loading and unloading (10 min), and thermal drift correction for the nanoindenter system (15 min). Each TM quadrant had 20-30 microindentation sites and it took about 10–15 h to complete the microindentation experiments on one quadrant. After this long time on one surface, the same TM was no longer suitable for another 10–15 h of microindentation on the other surface. Therefore, microindentations were made on only one of the two surfaces of each sample.

Microindentation was made on each quadrant of TM, starting from the inner location close to the umbo towards the outer perimeter along radial directions. The umbo is set as the origin, and the indents close to umbo were nearly evenly distributed along the radial lines. For each quadrant, microindentation was made along 3–6 different radial lines; along each radial line, microindentation was made at about 10 locations. The microindentation point array is along the radial direction, with an angle of 20° of separation from a neighboring array. The first array of microindentation points form an angle of 10–15° from the cutting edge. The location of each microindentation point is controlled by a positioning stage with submicron resolution. The location of the umbo center was taken as

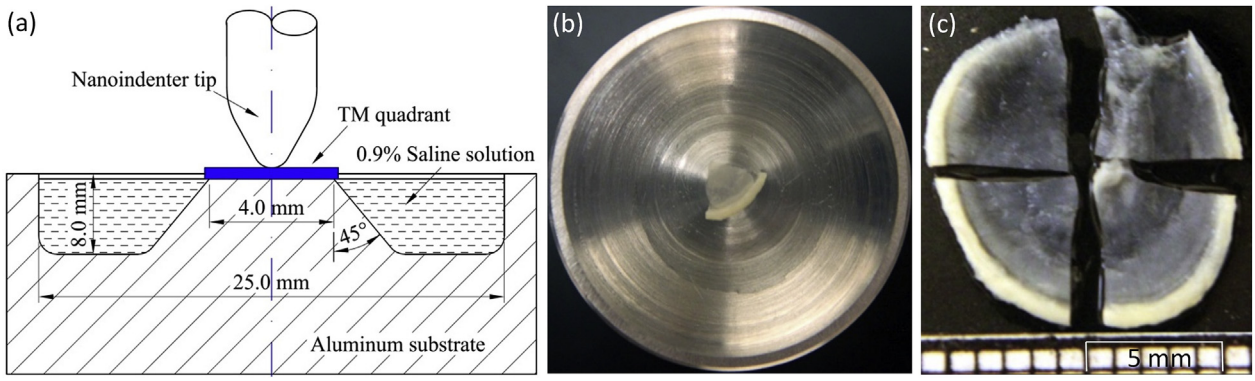


Fig. 2. Through-thickness microindentation experimental setup.(a). Schematic setup;(b). An actual top view of AI quadrant TM placed on an aluminum substrate;(c). Image of four cut TM quadrants (TB10-24).

the origin, and one cutting edge was selected as the *x*-direction. A small amount of shrinkage (5–10%) of collagen fibers in the cutting section (at the cutting edge) occurred and is considered to have negligible effect on the property measurements on locations far away from the edges, and microindentations were made at points far away from the cutting edge. In Tables 2 and 3, the total number of microindentation points is also given for each TM sample. The actual shapes of the manubrium of each TM are also shown in Tables 2 and 3 In total, 586 and 698 microindentations were made in the medial surface and the lateral surface, respectively. In Fig. 3a, a schematic drawing on these measurement points on the AI quadrant is shown as an example.

Microindentation was conducted on four quadrants of the TM and the Young's modulus results are reported. To determine the spatial distribution of Young's modulus, under the nanoindenter tip (10 μm radius), the indent impression would have a dimension on the order of 10 μm at an indentation depth of 1.2 μm; hence, there are many collagen fibers (each collagen fiber has approximately 10 nm diameter) within the indent impression. Thus, for analysis, the continuum assumption is made to determine the local effective properties.

2.4. Viscoelastic analysis

The microindentation depth is on the order of a few microns, which is less than 1/10 of the thickness of the TM (70 μm). Therefore, the spherical indentation into the TM sample is modeled as a contact mechanics problem in which a sphere indents into a viscoelastic half space (Lu et al., 2003, 2006; Huang and Lu, 2006; Huang et al., 2008). The diamond indenter tip has a modulus that is four orders of magnitde higher than that of the TM, so that the tip is modeled as rigid. From Hertzian contact mechanics analysis, with the consideration of a time-dependent viscoelastic boundary value problem (Lee and Radok, 1960), the viscoelastic microindentation depth, $h(t)$, is calculated from the microindentation load, $P(t)$, using the following equation (Lu et al., 2003):

$$h^{3/2}(t) = \frac{3(1-\nu)}{8\sqrt{R}} \int_{-\infty}^{t} D(t-\xi)\left[\frac{dP(\xi)}{d\xi}\right] d\xi \tag{1}$$

where ν is the Poisson's ratio, assumed to be constant, R is the radius of the spherical indenter, $D(t)$ is the uniaxial creep

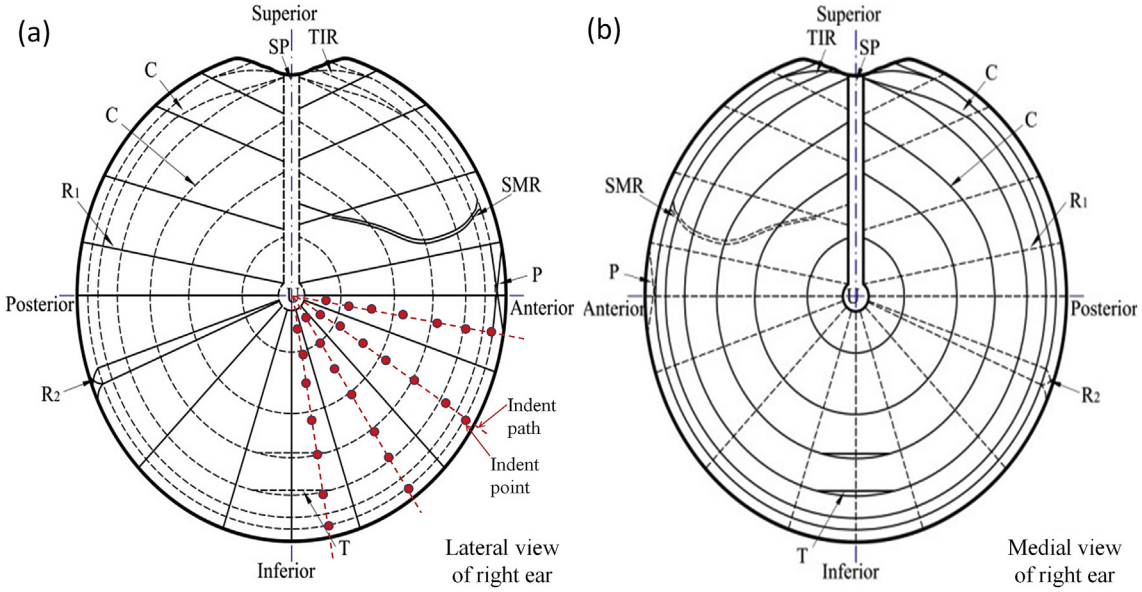


Fig. 3. A schematic diagram showing fiber orientations in a human tympanic membrane of right ear (adapted from Lim, 1995). (a). Lateral view; (b). Medial view. Note, in (a), a schematic of indent path (4 radial lines separated by about 20°) and indentation points (about 7 points) are marked in red dash-lines and dots in AI quadrant, respectively. SP: short process of the malleus; TIR: trigonum interradiale; C: circular fiber; R_1: radial fibers which attach straight into annular ring; R_2: a few radial fibers which diverge or crossover their terminals; T: transverse fiber; P: parabolic fibers; SMR: submucous fine radial fiber.

compliance. A curve fitting approach is used to determine the creep compliance. In this method, the uniaxial creep compliance is represented as a generalized Kelvin model,

$$D(t) = D_0 + \sum_{i=1}^{N} D_i\left(1 - e^{-t/\tau_i}\right) \tag{2}$$

where D_0 and D_i ($i = 1, \ldots, N$) are compliance coefficients, τ_i are retardation times, N is the number of terms in the Prony's series. For spherical microindentation under a constant rate loading history, $P(t) = \dot{P}_0 t H(t)$, where $\dot{P}_0$ is the constant loading rate, and $H(t)$ is the Heaviside unit step function, substituting Eqn. (2) into Eqn. (1) leads to:

$$h^{3/2}(t) = \frac{3(1-\nu)}{8\sqrt{R}}\left[\left(D_0 + \sum_{i=1}^{N} D_i\right)P(t) - \sum_{i=1}^{N} D_i(v_0\tau_i)\left(1 - e^{-\frac{P(t)}{v_0\tau_i}}\right)\right] \tag{3}$$

The loading rate $\dot{P}_0 = 8.83\ \mu N/s$ was applied in this study. This value is the same as that used in our previous microindentation measurements on TM (Huang et al., 2008; Daphalapurkar et al., 2009). Since the viscoelastic theory was used to convert the relaxation modulus to Young's modulus at a given strain rate, the effect of loading rate has been considered in the analysis. However, it does not play an additional role in the interpretation of the measurement results.

Using the least squares correlation to fit Eqn. (3) to the load-displacement curve measured from microindentation, all parameters, D_0, D_i, and τ_i are obtained. With the known parameters, the creep compliance in Eqn. (2) is determined. The relaxation modulus $E(t)$ is obtained from the uniaxial creep compliance (Knauss et al., 2008) by:

$$\int_0^t E(\tau)D(t-\tau)d\tau = t \tag{4}$$

Since TM is a soft tissue in its rubbery state, its Poisson's ratio is usually taken as 0.495 to avoid an ill-posed problem. The relaxation modulus was determined numerically from the uniaxial creep compliance using an inversion method (Luo et al., 2013). The discrete relaxation modulus data is subsequently fitted with a generalized Maxwell model:

$$E(t) = E_\infty + \sum_{i=0}^{N} E_i e^{-t/\tau_i} \tag{5}$$

where E_∞ is the steady-state relaxation modulus, E_i ($i = 0, \ldots N$) are relaxation coefficients.

Since the TM behaves as nearly linearly viscoelastic at small deformations (Luo et al., 2009a; 2009b), using a linearly viscoelastic analysis, the Young's relaxation modulus can be converted into Young's modulus at a given strain rate (Luo et al., 2010, 2013). For a linearly viscoelastic material under uniaxial stress state, the uniaxial stress $\sigma(t)$ is calculated from the applied strain history $\varepsilon(t)$, using the Boltzmann superposition principle:

$$\sigma(t) = \int_0^t E(t-\xi)\frac{d\varepsilon(\xi)}{d\xi}d\xi \tag{6}$$

where $E(t)$ is the Young's relaxation modulus. At a constant strain rate $\dot{\varepsilon}_0$, $\varepsilon(t) = \dot{\varepsilon}_0 t$, Eqn. (6) becomes:

$$\bar{E}(t) = \frac{\sigma(t)}{\varepsilon(t)} = \frac{1}{t_0}\int_0^{t_0} E(\xi)d\xi \tag{7}$$

where $\bar{E}(t)$ is the average uniaxial relaxation modulus from time 0 to t_0. Eqn. (7) indicates that the average Young's relaxation modulus (over time period 0 to t_0) is equal to the Young's modulus at a constant strain rate $\dot{\varepsilon}_0$ (Luo et al., 2009a; 2009b, 2010, 2013).

2.5. Young's modulus map

Since different TMs have different dimensions and shapes, the dimensions are normalized for comparison of modulus data obtained from different locations of individual TMs. Since most TMs have either round or elliptical shape, the locations are normalized by dividing the radial coordinate by the diameter (r_0 for round shape) or the length of the major axis (for elliptical shape). The actual Cartesian coordinates (x', y') are converted into the normalized Cartesian coordinates (x, y) through $x = x'/r_0$ and $y = y'/r_0$, with a range [-1,1], with the umbo center as the origin (0, 0). The normalized Cartesian coordinates x-y are further converted into polar coordinates (r,θ) through:

$$r = \sqrt{x^2 + y^2},\ \theta = \tan^{-1}\left(\frac{y}{x}\right) \tag{8}$$

where $-1 \le x, y \le 1$, $0 \le r \le 1$, $0° \le \theta \le 360°$. Fig. 1a shows the coordinate conversion. At the malleus, $\theta = 0°$, and θ is positive in the clockwise direction. After normalization into polar coordinates, all modulus data are combined and plotted as a Young's modulus map.

Since a TM has four views: lateral view at right ear, medial view at right ear, lateral view at left ear, and medial view at left ear, three views are transformed onto the lateral view in the right ear as shown in Fig. 3a. It has the same configuration as the medial view at the left ear. They are symmetric with respect to other two views (lateral surface at left ear, and medial surface at right ear) with respect to the malleus bone axis. Therefore, all other three views projected onto the lateral view in the right ear are unique for identification of the location for the comparison.

2.6. Statistical analysis

2.6.1. Q-Q plot

In this statistical analysis, the first step is to construct a histogram from the experimental data. A quantile-quantile (Q-Q) plot is used to evaluate visually the data set. The Q-Q plot (or probability plot) gives a quick graphical diagnostic on whether the experimental data follows the assumed distribution or not (Chambers et al., 1983). It is noted that the location information is not considered in this Q-Q plot analysis. Instead, the spatial dependence is considered in the modeling of the modulus distribution described in the next section.

The procedures to construct the Q-Q plot are given as follows (Chambers et al., 1983):

(a). Sorting data: The experimental data set $\{x_1, x_2, ..., x_i, \ldots, x_n\}$ for $i = 1, 2, ..., n$, is sorted from the lowest to the highest values. The sorted values are denoted by $\{x_{(1)}, x_{(2)}, ..., x_{(i)}, \ldots, x_{(n)}\}$, where $x_{(1)} < x_{(2)} < ... < x_{(i)} < ... < x_{(n)}$. The subscripts in parentheses represent the new resorted order for $(i) = (1), (2), ..., (n)$.

(b). Calculating the experimental accumulated probability q_i: The values at $x_{(i)}$ are used to calculate this value:

$$q_i = \frac{i - 0.5}{n} \ (i = 1, 2, \ldots, n) \tag{9}$$

(c). Calculating the theoretical quantile: Since the cumulative distribution function (CDF), $\Phi(z)$, has an integration relation with the probability density function (PDF) $\phi(z)$, $\Phi(z)$ is calculated as:

$$\Phi(z) = \int_0^z \phi(\xi) d\xi \tag{10}$$

The quantile notation is used. If z_i is the ith quantile of a distribution, then $\Phi(z_i) = q_i$. Thus, the theoretical quantile is defined by the inverse function of the CDF as

$$z_i = \Phi^{-1}(q_i) \tag{11}$$

(d). Q-Q plot: The sorted experimental quantile set of $\{x_{(i)}\}$ is plotted as the abscissa and the theoretical quantile set of $\{z_i\}$ is plotted as the ordinate, to form the Q-Q plot.

2.6.2. PDF and CDF plots

Through Q-Q plots, the Young's modulus data from human TM is tested to determine whether it follows a single-modal or multi-modal normal distribution. At the same time, the histogram and the empirical CDF figure are constructed. In the histogram, the sorted experimental quantile data set of $\{x_{(i)}\}$ ($i = 1, 2, ..., n$) is used as the abscissa. Then, the ordinate represents the empirical probability density $\phi'(x_i)$, calculated from the relative frequency f_i divided by the empirical quantile step:

$$\phi'(x_i) = f_i \,/[(x_{(n)} - x_{(1)})/n] \tag{12}$$

where the relative frequency f_i is defined as the ratio of counts occurring in the interval (x_i, x_{i+1}) to that of the total counts. Therefore, the bar figure with sorted data set $\{x_{(i)}\}$ and the empirical probability density are plotted as the histogram (PDF plot). For the empirical CDF figure, the abscissa is the sorted experimental quantile set of $\{x_{(i)}\}$ ($i = 1, 2, ..., n$), and the ordinate is the accumulated probability, or the calculated experimental accumulation $\{q_i\}$. The data set of $\{x_{(i)}, q_i\}$ is then plotted as the empirical CDF figure and is used for comparison between modeling results and the experimental data to determine the distribution parameters.

2.6.3. Modeling the modulus map

The Young's modulus of human TM changes with location as indicated by microindentation measurement; the modulus depends on the fiber arrangements. Fig. 3a shows the conceptual fiber arrangements for human tympanic membrane (adapted from Lim, 1995) of the right ear. In addition to the major radial and circumferential collagen fibers, R_1, R_2, T, P, and SMR, fibers also exist in a TM either on the medial or lateral surface. Fig. 3b for the medial surface shows a pattern, similar to the lateral surface, except with a different orientation. It is nearly a mirror image of Fig. 3a with respect to the malleus bone axis. The solid lines represent the fibers at the top, and the dashed lines refer to the hidden fibers below the surface layer. The other two views of TMs in the left ear have similar patterns to those of the right ear, at different orientations. With a projection onto the lateral view in the right ear, all modulus results are presented in the sequel for comparison. With all this data available, it is possible to model the statistical distribution of Young's modulus.

In general, for the multi-modal Gaussian distribution, the probability density function is the summation of individual Gaussian PDFs weighted by factors, given as:

$$g(E) = \sum_{i=1}^{N} \frac{\alpha_i}{\sigma_i \sqrt{2\pi}} e^{\left[-0.5\left(\frac{E-\mu_i}{\sigma_i}\right)^2\right]}, \tag{13}$$

where N is the order of multi-modes, α_i, σ_i, μ_i ($i = 1$ to N) are the weight factors ($\sum_{i=1}^{N} \alpha_i = 1$), the standard deviation and expectation (mean) values, respectively. The corresponding CDF is given as:

$$G(E) = 0.5 + 0.5 \sum_{i=1}^{N} \alpha_i * erf\left(\frac{E - \mu_i}{\sigma_i}\right), \tag{14}$$

where *erf* is the error function. When a bimodal Gaussian function is chosen, the order is $N = 2$. The best-fit parameters α_i, σ_i, μ_i ($i = 1$, 2) are determined using the nonlinear least squares Levenberg-Marquardt method (Luo et al., 2015; Xu et al., 2018). With these parameters known, the theoretical multi-Gaussian PDF curve was constructed, and compared with the experimental histogram.

3. Results and discussion

3.1. TM samples and microindentation

The information and images for the TM samples are shown in Tables 2 and 3 It is noted that portions of some annulus rings are damaged during preparation of the TM samples. Since microindentation is made on the pars tensa, the damage in the annulus ring does not affect the TM modulus measurement. The left/right ear orientation listed is important for projection of TMs at different surfaces and orientations onto the same lateral view in the right ear, so that the combined modulus data from different TMs can be analyzed for further comparison.

The mechanical properties determined represent those of the lamina propria. The maximum indentation depth used for viscoelastic analysis to determine viscoelastic properties (Lu et al., 2006) is restricted to 1.2 μm so that the effect of substrate can be neglected since the maximum indentation depth was less than 1/35 of the TM thickness. The microindentation load-displacement curve is very similar to previous work on the human TM (Huang et al., 2008; Daphalapurkar et al., 2009). A typical microindentation load-displacement curve is shown in Fig. 4, with labels indicating the loading and unloading paths. The Young's modulus is calculated from the loading curve.

In any quadrant of the TM, collagen fibers are largely oriented within a plane. The TM quadrant could be considered as a transversely isotropic material. The Young's modulus in the through-thickness direction can be different from the in-plane modulus. The relaxation functions were obtained based on the analysis of a homogeneous, isotropic, linearly viscoelastic material. The nanoindentation in the through-thickness direction invokes primarily the behavior of the material in the thickness direction (Daphalapurkar et al., 2009). The assumption of isotropy in this analysis is not anticipated to affect the measurement of the through-thickness Young's relaxation modulus significantly (Daphalapurkar et al., 2009).

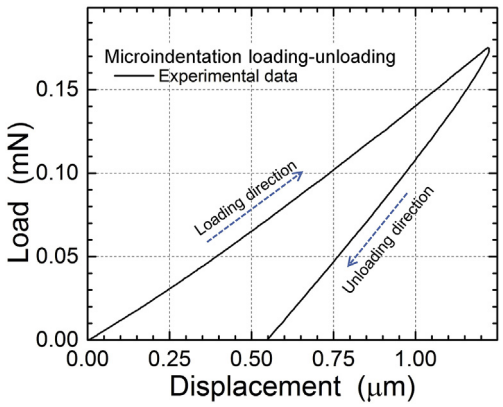


Fig. 4. Typical microindentation load-displacement curve for human TM.

3.2. Young's modulus map

A typical Young's modulus map at the medial surface in the normalized (x, y) coordinate system for the TM sample TB 08-02 is shown in Fig. 5a. It is noted that the original Young's modulus map in the actual (x', y') coordinate system has the same map as shown in Fig. 5a, the difference is in the coordinate scales used. After the rectilinear coordinates (x, y) are converted into the polar coordinates (r, θ), the Young's modulus map has a symmetric configuration with respect to the y-axis. For the right ear with microindentation at the medial surface, the medial view is shown in Fig. 5a and the lateral view is shown in Fig. 5b. The small black dots in the polar coordinates show the actual locations of microindentation. The original modulus maps (Fig. 5a) show an irregular boundary formed by piecewise lines connecting neighboring points at the actual boundary. The boundary is within the TM parsa tensa range, close to the annulus ring. The maps in the polar coordinates (Fig. 5b) show a smooth round boundary at $r = 1.0$, defined as the dimensionless radial coordinate, which is the ratio of the radius of a point to the radius of the annulus. The data at the boundary is interpolated. The Young's modulus maps for the other six TMs measured at the medial surface (TB08-03, TB08-17, TB08-27, TB 08–28, TB09-05 and TB09-08) are shown in the lateral view of Fig. 6a–f in the normalized polar coordinates.

Another typical Young's modulus map of TM at the lateral surface is shown in Fig. 7 for the TM sample labeled TB10-02. Fig. 7a is plotted with the same configuration as Fig. 7b at the same lateral view of right ear. Fig. 8a–f (the lateral view) show the Young's modulus maps for the lateral surface for six TMs: TB09-20, TB10-01, TB10-03, TB10-22, TB10-23 and TB10-24, except for TB09-19, which has results for only a half of the TM.

In Figs. 5–8, the Young's modulus data shows one or more peaks, where the locations and values vary with different TMs. In order to find common features, all modulus data from different TMs are combined into a single modulus map from all seven TM samples at the medial surface and all eight TMs at the lateral surface, respectively.

We define the coordinates of each point in Fig. 1a and convert the map of four quadrants into a combined map for each TM. Figs. 5b, 6 and 7b and 8 show the smooth interpolated 2D map in polar coordinates. Even though microindentation on each TM has low spatial resolution and different distribution, combining all data from different TMs, a trend and distribution are obtained through statistical analysis. The results are analyzed statistically in Section 3.3, and the modulus map is modeled based on the statistical analysis. These results show effective properties for the TMs used in this study.

3.3. Normal Q-Q plot

A normal Q-Q plot is used to test whether the modulus distribution follows a single-modal or multi-modal normal distribution. This plot compares the experimental quantiles against a corresponding theoretical fitted quantiles. The normal (Gaussian) distribution is assumed as the theoretical reference. It is represented as $N[\mu,\sigma]$, with mean μ and standard deviation σ. Consequently, the normal probability (or normal Q-Q) plot provides a quick test for the null hypothesis that the data follows a normal distribution (Filliben, 1975; Gnanadesikan, 1977). If the points in the Q-Q plot fall approximately on a straight line, the hypothesis is supported.

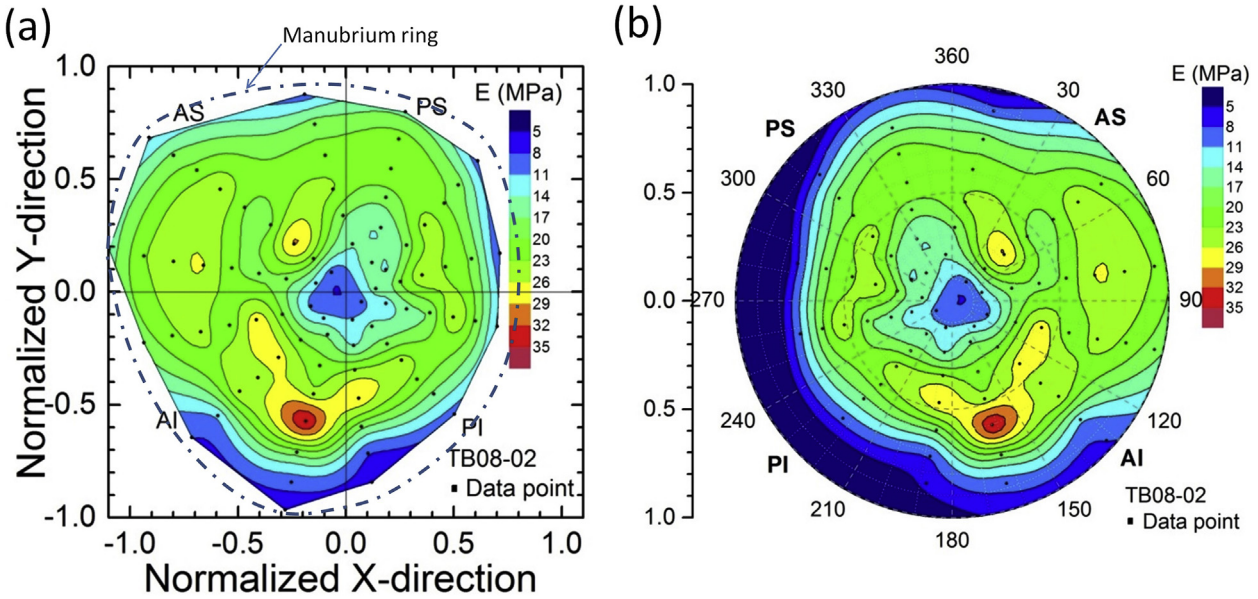


Fig. 5. Young's modulus distribution of TM (TB08-02) at the medial surface. An outline of the manubrium is plotted as a blue dot-dash curve in Fig. 5a. (a). Original Young's modulus map in normalized x-y coordinates; (b). Smoothed map in normalized polar coordinates. Note, the malleus is located at $x = 0$, $0 < y < 1$ in Fig. 5a, and $\theta = 0°$ or $360°$, $0 < r < 1$.

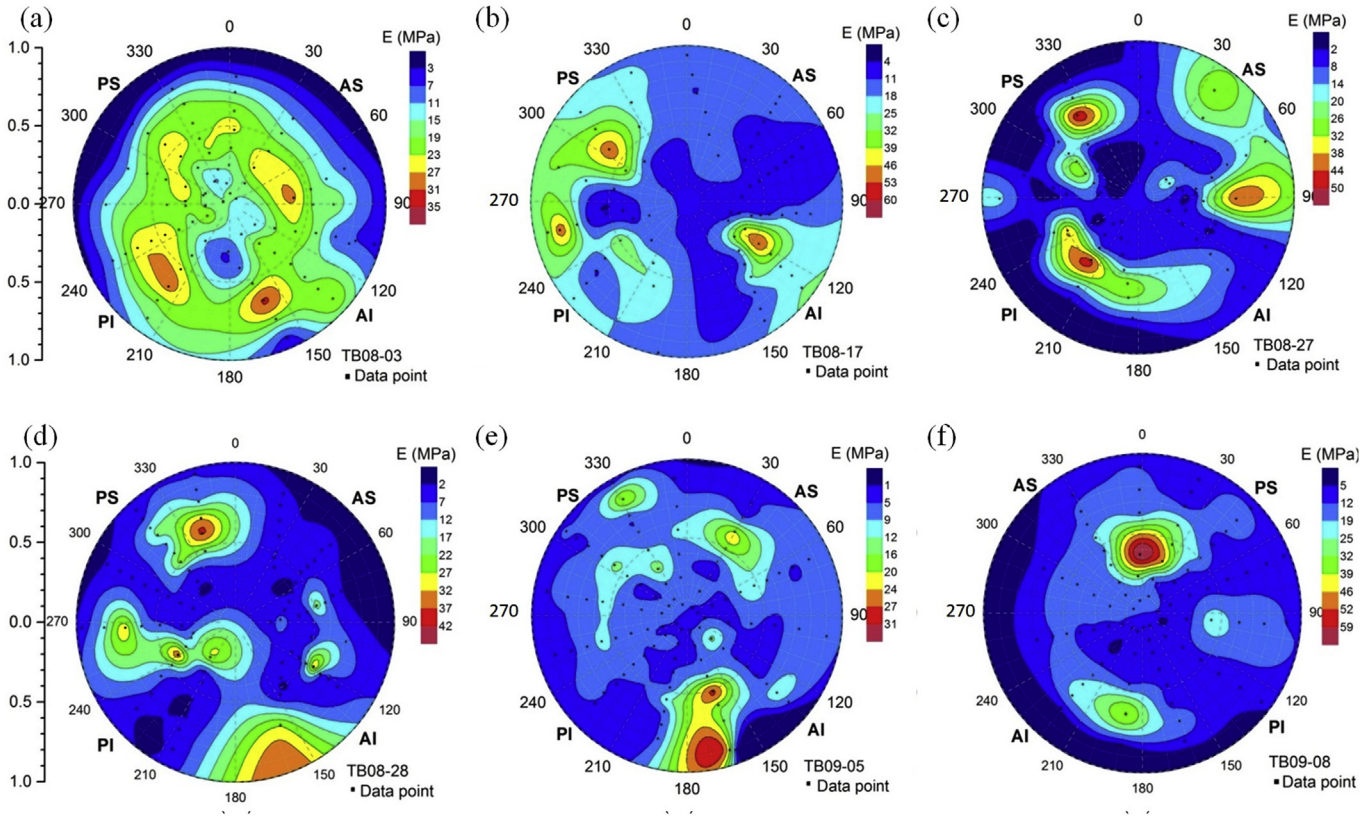


Fig. 6. Young's modulus map data at medial surface in normalized polar coordinates. (a). TB0803; (b). TB08-17; (c). TB08-27; (d). TB08-28; (e). TB 09-05; (f). TB09-08.

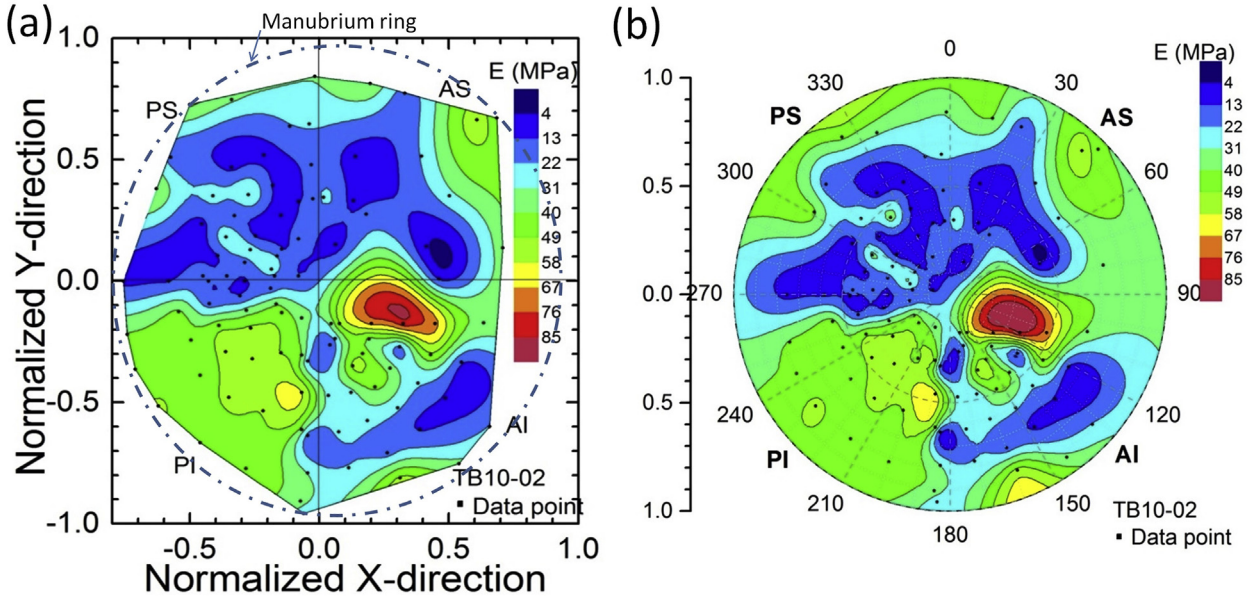


Fig. 7. Young's modulus distribution of TM (TB10-02) at the lateral surface. An outline of the manubrium is plotted as a blue dot-dash curve in Fig. 5a.(a). Original map in normalized *x-y* coordinates;(b). Smoothed map in normalized polar coordinates.

The Q-Q plot also provides an assessment of "goodness of fit" graphically. When a Q–Q plot shows an arc and "S" shape, it indicates that one of the distributions is more skewed relative to the other, indicating most likely the data follow a bimodal distribution (Kotz et al., 2005; Thode, 2002).

Figs. 9 and 10 show the normal Q-Q plot of the TM modulus data for each of the four quadrants measured from the medial surface and the lateral surface, respectively. The points do not form one straight line. Fig. 11a and b include all the data points from the four quadrants. The points do not form a straight line even though most data within the range of P_{80}– P_{20} are close to a straight line. P_{80} and P_{20} are defined as the modulus at which 80% and 20% of the data

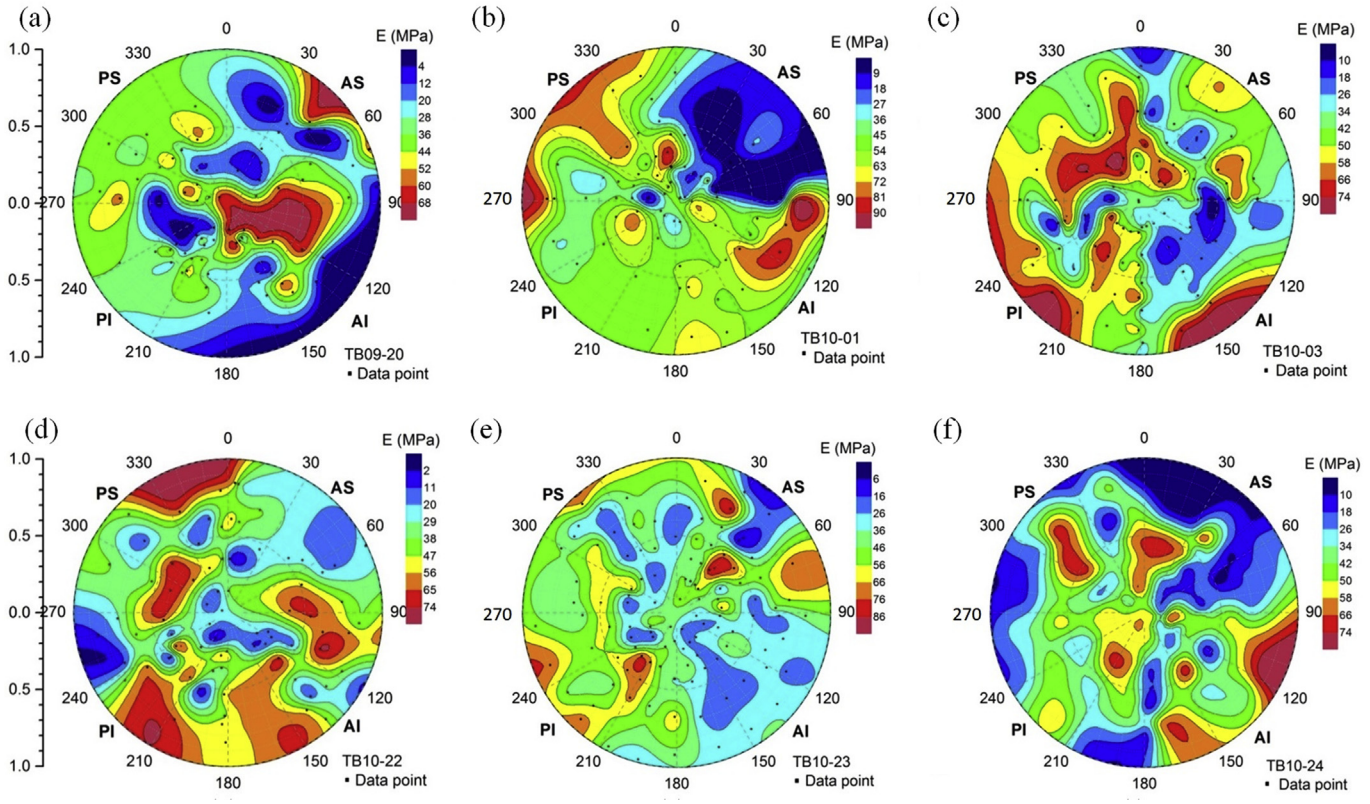


Fig. 8. Young's modulus map data of TMs at lateral surface in normalized polar coordinates. (a). TB09-20; (b). TB10-01; (c). TB10-03; (d). TB10-22; (e). Tb10-23; (f) TB10-24.

points have these values, respectively. Based on Figs. 9–11, the data is likely to follow a bimodal distribution.

3.4. Bi-modal Gaussian distribution

In addition to the CDF distribution, the PDF distribution is also included. The modulus data points are combined from different TMs for the same quadrant of PS, AS, PI and AI. They are plotted in Fig. 12 for the 7 TMs with microindentation at the medial surface. Similarly, for the 8 TMs with microindentation at the lateral surface, the modulus data points are also combined from different TMs for the same quadrant of PS, AS, PI and AI. They are plotted in Fig. 13. Modulus data are also combined for the four quadrants. Fig. 14a and b shows the PDF histogram of all modulus values for the entire TM at the medial and lateral surfaces, respectively.

In general, the Young's modulus values of the human eardrum vary within 1.5–50 MPa for the medial surface, with most data falling within 5–30 MPa. The modulus values vary within 2–90 MPa for the lateral surface, and most data points are within the range of 15–60 MPa. The data on the AS quadrant show in general the smallest values compared with the other three quadrants.

Next, a bi-modal Gaussian CDF is used to fit the distribution parameters. Fig. 15a and b shows the experimental CDF curves of TM modulus data for all quadrants measured from the medial surface and lateral surface, respectively, as well as the best-fit results. The confidence level of the fitting is noted as COD (R^2), which is bounded between 0.0 and 1.0, corresponding to poor to excellent fitting, respectively. The fitting parameters and confidence levels obtained in this study are listed in Tables 4 and 5 for the medial surface and the lateral surface, respectively. All COD (R^2) range from 0.99 to 1.00, indicating an excellent fit for statistical analysis. The standard deviations for all parameters are calculated through the Levenberg-Marquard algorithm, which are summarized in Tables 4 and 5 following the ± symbol. The relative standard deviation was mostly in the range of 2%–8%, up to 11%, which indicate excellent confidence levels and statistical reliability. It indicates that the Young's modulus can be well described using the bimodal Gaussian distribution and the Young's modulus maps can be most possibly modeled as a bi-bivariate Gaussian map. In Fig. 15, the bimodal Gaussian function fits the CDF well for TM modulus at both medial and lateral surfaces.

With these parameters known, the theoretical PDF curves, superimposed in Figs. 12–14, agree reasonably well with the corresponding histograms. In Fig. 12, two peaks are seen clearly that occur at 6–8 MPa and 19–20 MPa for all TM quadrants at the medial surface. The weight factor for two expectations is close to 50% for the PS, PI and AI quadrants while only 40% for the AS quadrant. For the entire TM at the medial surface, the two expectations are 6.6 MPa and 19.2 MPa with 0.5 wt ratio, as shown in Fig. 14a. Except for Fig. 13a, where two peaks overlap at 40 MPa, the other three quadrants (AS, PI, and AI) all show two peaks of modulus in the ranges of 12–24 MPa and 44–47 MPa as shown in Fig. 13. The weight factors for the PI and AI quadrants (0.22 and 0.37) are less than that of the AS quadrant (0.48). For the entire TM at the lateral surface, the modulus has two peaks at 16.3 MPa and 41.6 MPa with the weight ratio 18:82 as shown in Fig. 14b. This weight factor represents the ratio of two expectations. The differences in weight factors in different quadrants may be due to differences in the fiber distribution and density.

In the literature, the average values reported for the TM modulus are approximately 20 MPa (Von Békésy, 1960) and about 40 MPa (Kirikae, 1960) in the circumferential and radial directions, respectively. In this study, even smaller values of TM modulus were

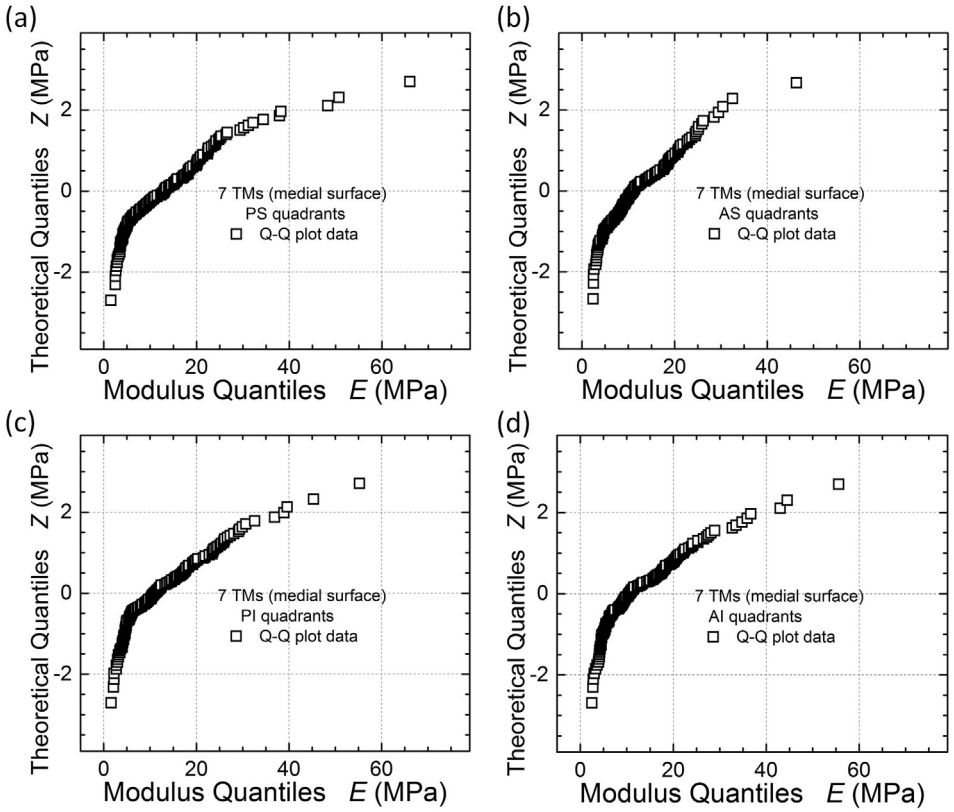


Fig. 9. Normal Q-Q plots of four quadrants for 7 TM at medial surfaces. (a). PS quadrant; (b). AS quadrant; (c). PI quadrant; (d). AI quadrant.

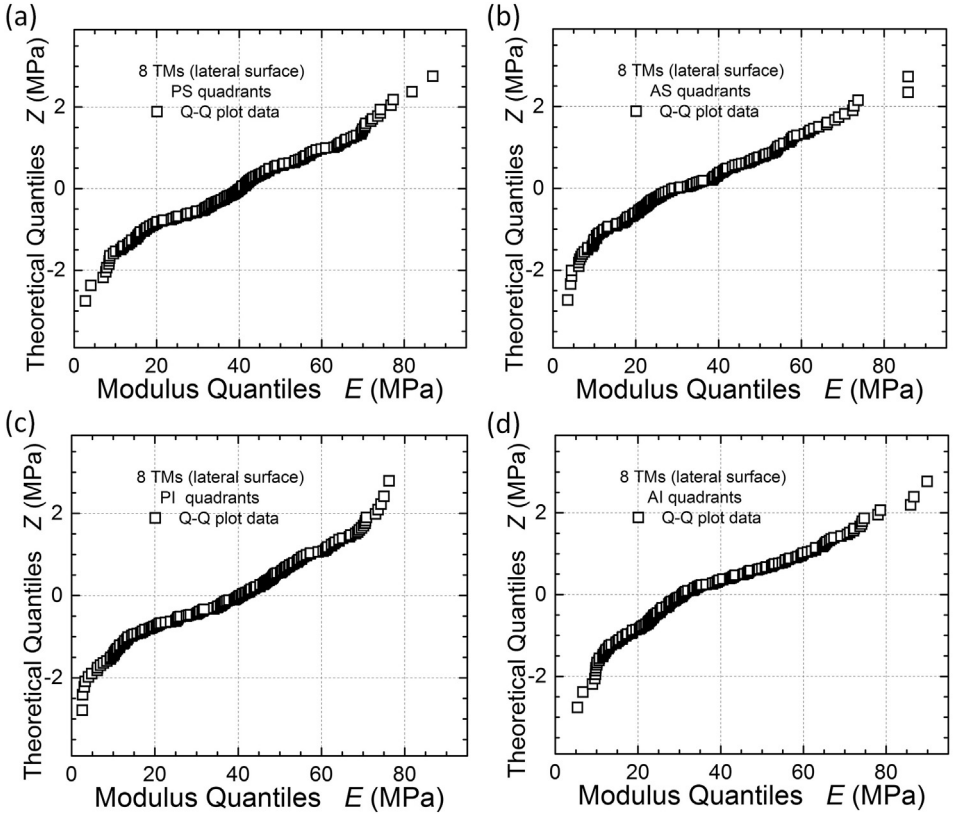


Fig. 10. Normal Q-Q plots of four quadrants of TM at the lateral surface. (a). PS quadrant; (b). AS quadrant; (c). PI quadrant; (d). AI quadrant.

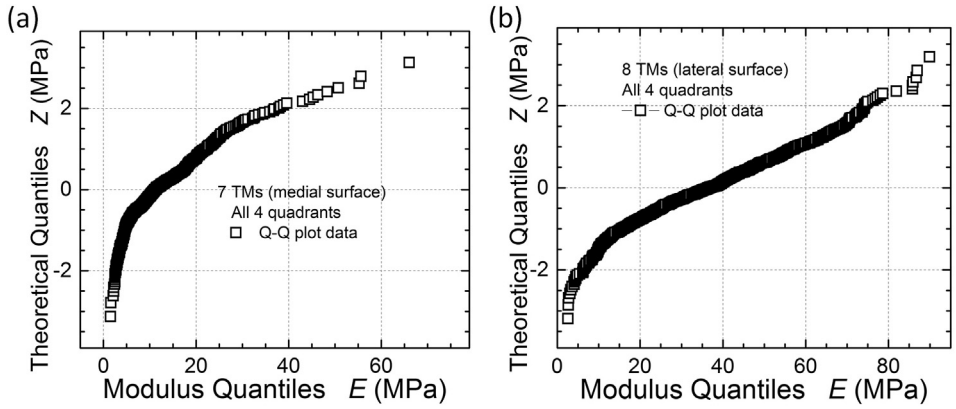


Fig. 11. Normal Q-Q plots for all quadrants.(a). 7 TM at the medial surface; (b). 8 TM at the lateral surface.

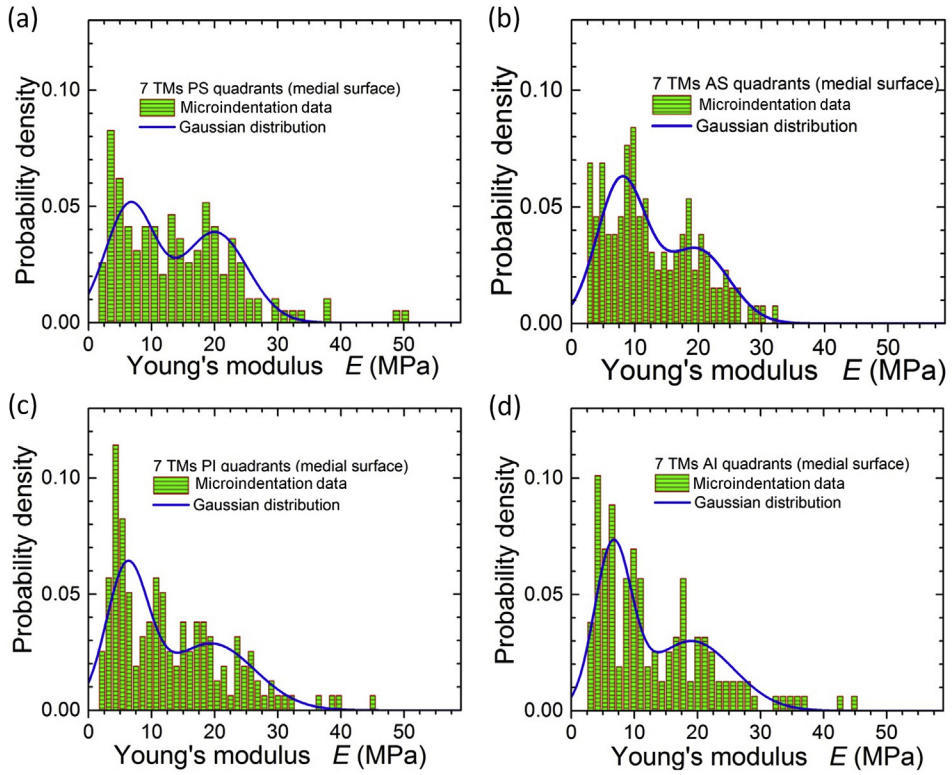


Fig. 12. Bi-modal Gaussian distribution of four quadrants for 7 TM at the medial surface.(a). PS quadrant; (b). AS quadrant; (c). PI quadrant; (d). AI quadrant.

obtained. They are 6.6 ± 3.5 MPa and 16.3 ± 7.1 MPa at both the medial and the lateral surfaces, respectively. The smaller TM modulus may be associated with lower density of collagen fibers. The larger modulus values measured as 19.2 ± 6.2 MPa and 41.6 ± 18.8 MPa for the circumferential and radial fiber layers, respectively, may be the consequence of difference in collagen fiber density. From Table 4, the two averages of the mean values (μ_{m1} and μ_{m2}) for the four quadrants at the medial surface are 19.6 ± 0.5 MPa and 6.8 ± 0.8 MPa, likely corresponding to the main circumferential fibers and the minor fibers such as transverse fibers, TIR (trigonum interradiale in Fig. 3) fibers and parabolic fibers (Fig. 3), respectively. The statistical average of the modulus of 19.6 MPa is very close to the value of 19.2 MPa obtained from all four quadrants. The value is consistent with the nearly 20 MPa reported for the TM in the circumferential direction (Table 1). From Table 5, the two averages of the mean values (μ_{L2} and μ_{L1}) for the four quadrants at the lateral surface are 44.3 ± 3.1 MPa and 23.6 ± 11.8 MPa, likely corresponding to the main radial fibers and the minor fibers such as R_1 radial fibers, R_2 radial fibers, and SMR submucous fine radial fibers (Fig. 3), respectively. The average of the larger mean values (μ_{m2}), quoted as a representative modulus, of 44.3 MPa is consistent with most reported data for the modulus in the radial direction (Table 1). It is noted that the modulus values at minor radial fibers have a higher standard deviation than the other fibers, which may be due to the huge difference in configurations among the three minor radial fibers. Another factor could be the effect of the thickness of the TM. The thinnest part of the TM is found in the central region between the annulus and the manubrium (Kuypers et al., 2006) where there were no modulus measurements. The TM thickness has a significant effect on measurement of modulus

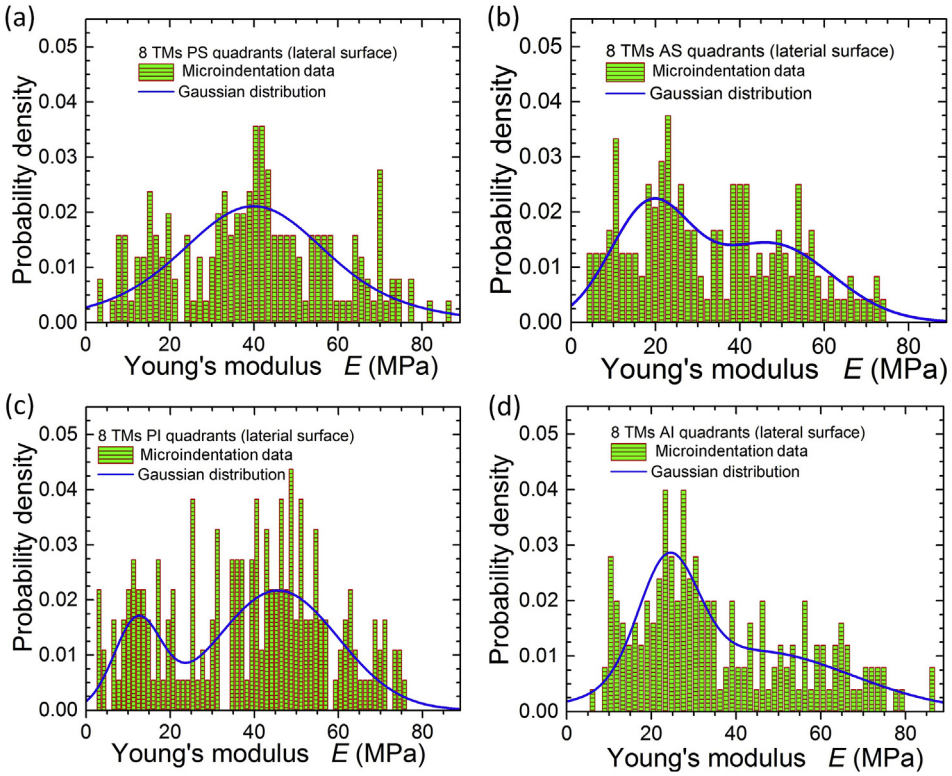


Fig. 13. Bi-modal Gaussian distribution of four quadrants for 8 TM at the lateral surface.(a). PS quadrant; (b). AS quadrant; (c). PI quadrant; (d). AI quadrant.

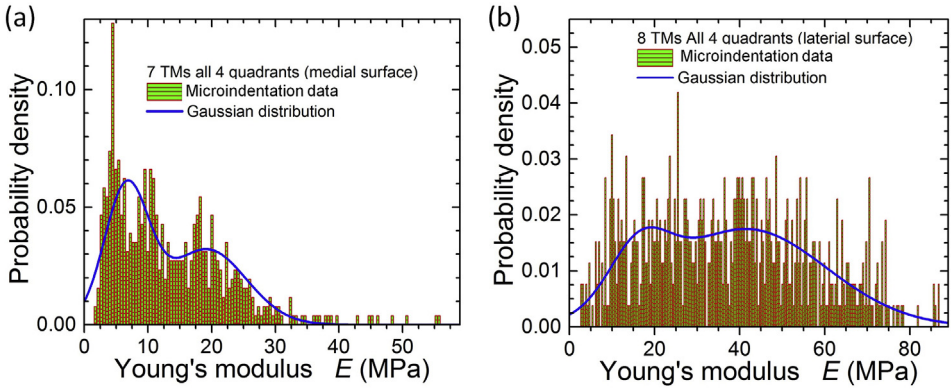


Fig. 14. Bi-modal Gaussian distribution of all quadrants.(a). 7 TM at the medial surface; (b). 8 TM at the lateral surface.

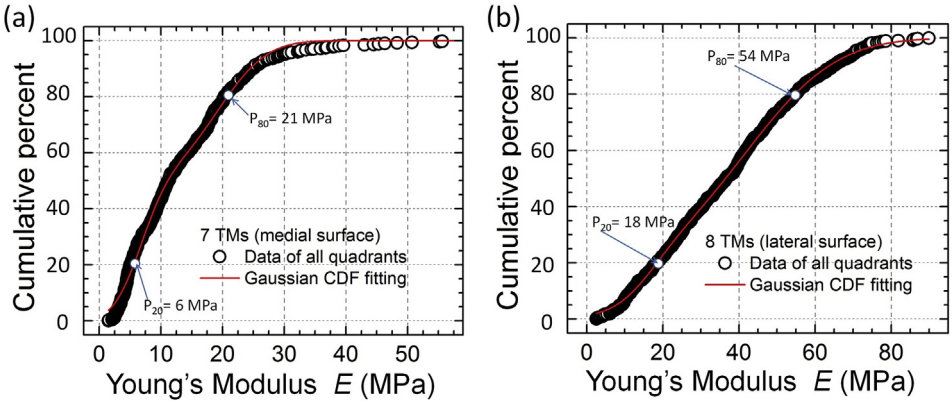


Fig. 15. Bi-modal Gaussian distribution CDF fitting of all quadrants. (a). 7 TM at the medial surface; (b). 8 TM at the lateral surface.

Table 4
Parameters for the bimodal Gaussian distribution at the medial surface.

Parameters	PS	AS	PI	AI	Whole
α_{m1}	0.50 ± 0.033	0.40 ± 0.035	0.50 ± 0.041	0.50 ± 0.038	0.50 ± 0.019
μ_{m1}	20.1 ± 0.479	19.8 ± 0.602	19.4 ± 0.998	19.0 ± 0.729	19.2 ± 0.329
σ_{m1}	5.13 ± 0.445	5.03 ± 0.465	6.93 ± 0.795	6.65 ± 0.063	6.22 ± 0.264
μ_{m2}	6.61 ± 0.332	7.85 ± 0.261	6.09 ± 0.264	6.56 ± 0.165	6.59 ± 0.117
σ_{m2}	3.94 ± 0.265	3.91 ± 0.163	3.34 ± 0.269	2.92 ± 0.177	3.49 ± 0.095
Data points	142	132	148	141	563
COD(R^2)	0.994	0.997	0.991	0.994	0.996

Note, the subscription "m" refers to the medial surface. α_{m1} is the weight factor of μ_{m1}.
The standard errors of the parameters through Levenberg-Marquard algorithm are shown following the ± symbol.

Table 5
Parameters for the bimodal Gaussian distribution at the lateral surface.

Parameters	PS	AS	PI	AI	Whole
α_{L1}	0.50 ± 0.057	0.482 ± 0.038	0.221 ± 0.006	0.368 ± 0.019	0.176 ± 0.011
μ_{L1}	39.8 ± 0.980	18.5 ± 0.636	12.2 ± 0.209	23.9 ± 0.199	16.3 ± 0.103
σ_{L1}	26.6 ± 1.96	9.47 ± 0.399	5.62 ± 0.286	6.95 ± 0.365	7.05 ± 0.287
μ_{L2}	40.0 ± 0.614	47.3 ± 1.430	45.7 ± 0.173	44.1 ± 0.758	41.6 ± 0.314
σ_{L2}	14.6 ± 1.49	14.5 ± 0.971	14.3 ± 0.181	23.2 ± 0.366	18.8 ± 0.188
Data points	171	158	189	177	695
COD(R^2)	0.994	0.998	0.999	0.998	0.999

Note, the subscription "L" refers to the lateral surface. α_{L1} is the weight factor of μ_{L1}.
The standard errors of the parameters through Levenberg-Marquard algorithm are shown following the ± symbol.

through tensile experiments and simulation (Liang et al., 2015, 2016). In the tension of a TM strip, the thinnest region of the TM shows the smallest Young's modulus when the TM is assumed to have the uniform thickness. The underlying reasons for the existence of the two peaks in the TM modulus need further investigation to examine possible correlations between the TM microstructures and the modulus data.

3.5. Modeling the distribution of Young's modulus

The Young's modulus curves (Figs. 12–14) show one or more peaks, and the locations and values vary in individual TMs (Figs. 5–8). Moreover, individual TMs show variation in the modulus map. The statistical analysis indicates that the Young's modulus follows the bimodal Gaussian distribution. From individual TM modulus maps, it appears that the bivariate Gaussian surface or the summation of several different bivariate Gaussian surfaces is appropriate to model the Young's modulus map. Thus, all modulus values from different TMs are plotted in a single map, as in Fig. 16a for the medial surface from all 7 TM samples, and Fig. 17a for the lateral surface from all 8 TMs, respectively.

The bivariate Gaussian curves show a bell shape with multi-peaks. Thus, we consider describing the spatial distribution of the Young's modulus as a series of bivariate Gaussian functions in polar coordinates by:

$$E(r,\theta) = \sum_{i=1}^{N} A_i * e^{\left(-0.5\left[\frac{(r-\mu_{ri})^2}{\sigma_{ri}^2}+\frac{(\theta-\mu_{\theta i})^2}{\sigma_{\theta i}^2}\right]\right)} + B \qquad (15)$$

where N is the number of terms; A_i is the peak modulus; B is the baseline modulus; μ and σ are the expectation (mean) and standard deviation, respectively; the subscripts r and θ represent radial and angular coordinates, respectively, as shown in Fig. 1a. The best-fit parameters A_i, B, σ_i, and μ_i ($i = 1, \ldots, N$) are determined using the nonlinear least squares Levenberg-Marquardt method.

It is seen in Figs. 16a and 17a that the combined modulus maps show numerous bell shapes. Under such a situation, it is appropriate to use a series of bivariate Gaussian functions to model the modulus map. Since the modulus has more bell shapes with different peaks, two types of mapping functions are used: single bivariate Gaussian and bi-bivariate Gaussian. The bivariate Gaussian is a normal distribution function for the radial and the angular coordinates. It has a baseline modulus value B, and several peak moduli A_i. The best-fit parameters A_i, B, μ_{ri}, $\sigma_{\theta i}$, $\mu_{\theta i}$, and $\sigma_{\theta i}$ ($i = 1, \ldots, N$) are listed in Table 6 for the two fitting approaches. The standard deviations for all parameters through the Levenberg-Marquard algorithm are also summarized in Table 6. The confidence levels of modeling is much lower than the statistical analysis in (Tables 4 and 5), which indicates poor statistical reliability. From Table 6, the bi-bivariate Gaussian maps show better modeling than the single-bivariate Gaussian map. It is noted that, in theory, there are many parameter sets which can be fitted through nonlinear Levenberg-Marquard algorithm. In practice, only one set of parameter is searched; the number of parameters depends on the initial values, the boundaries, and the parameter values. The parameters are 6 and 11 in the single- and bi-bivariate Gaussian functions, respectively. In addition to the initial values and the boundaries, more parameters result in difficulty in fitting through the nonlinear fitting algorithm. For a large number of parameters such as 21 parameters in the quad-bivariate Gaussian fitting, there are occasions when the algorithm does not lead to convergence even after 400 iterations. In consideration of a balance between accuracy and convergence in fitting, the bi-bivariate Gaussian function turns out to be the best option to describe the spatial distribution of Young's modulus.

As shown in Fig. 16b and c, the modulus distribution at the medial surface has a certain trend. At the perimeter of the eardrum close to the annulus ring, the Young's modulus is relatively small; it is considered to be the baseline modulus. This is reasonable since the TM tissue close to the annulus ring has a longer perimeter and is softer than the membrane in the central region. In the central region around the umbo, the Young's modulus is also smaller, possibly due to the fact that it is close to the umbo which provides support to the membrane. It is seen that, along a ray from the perimeter to the center, the Young's modulus follows a small-large-

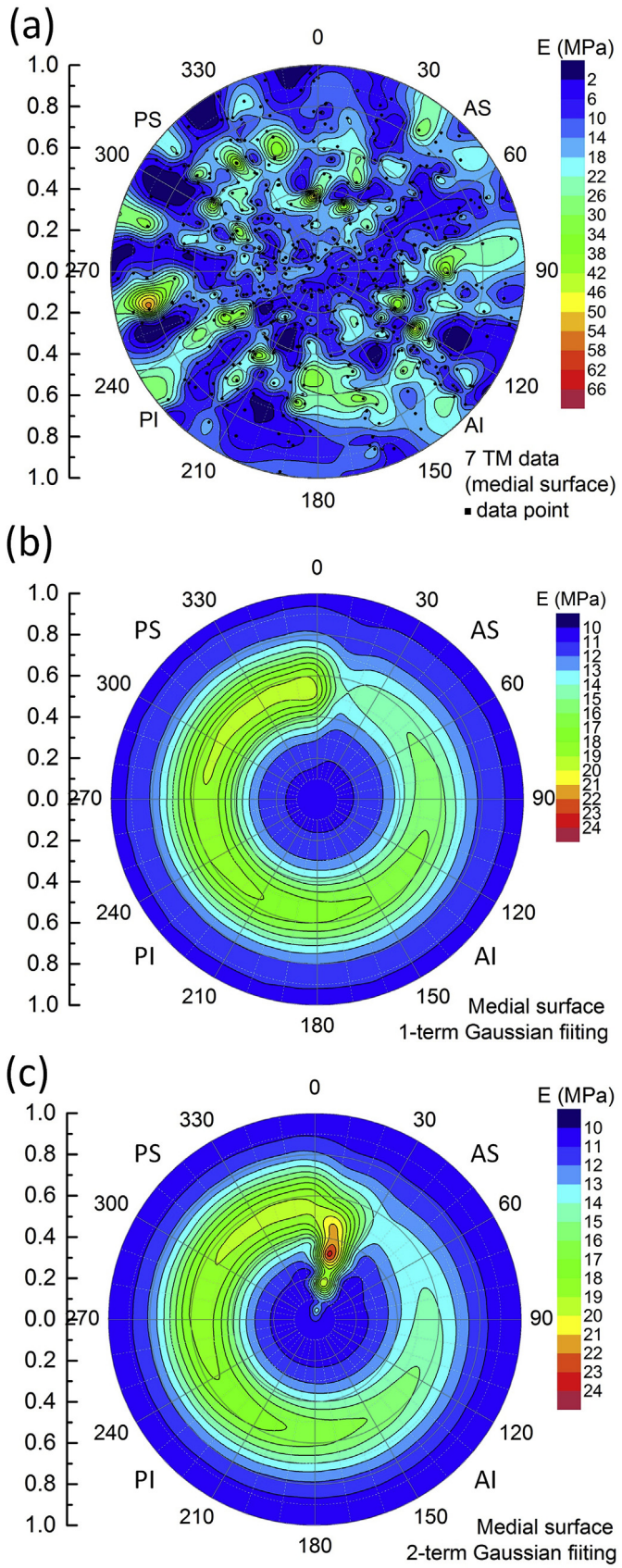


Fig. 16. Young's modulus map for 7 TM at the medial surface.(a). Combined experimental data from 7 TMs.(b). Single-bivariate Gaussian map.(c). Bi-bivariate Gaussian map.

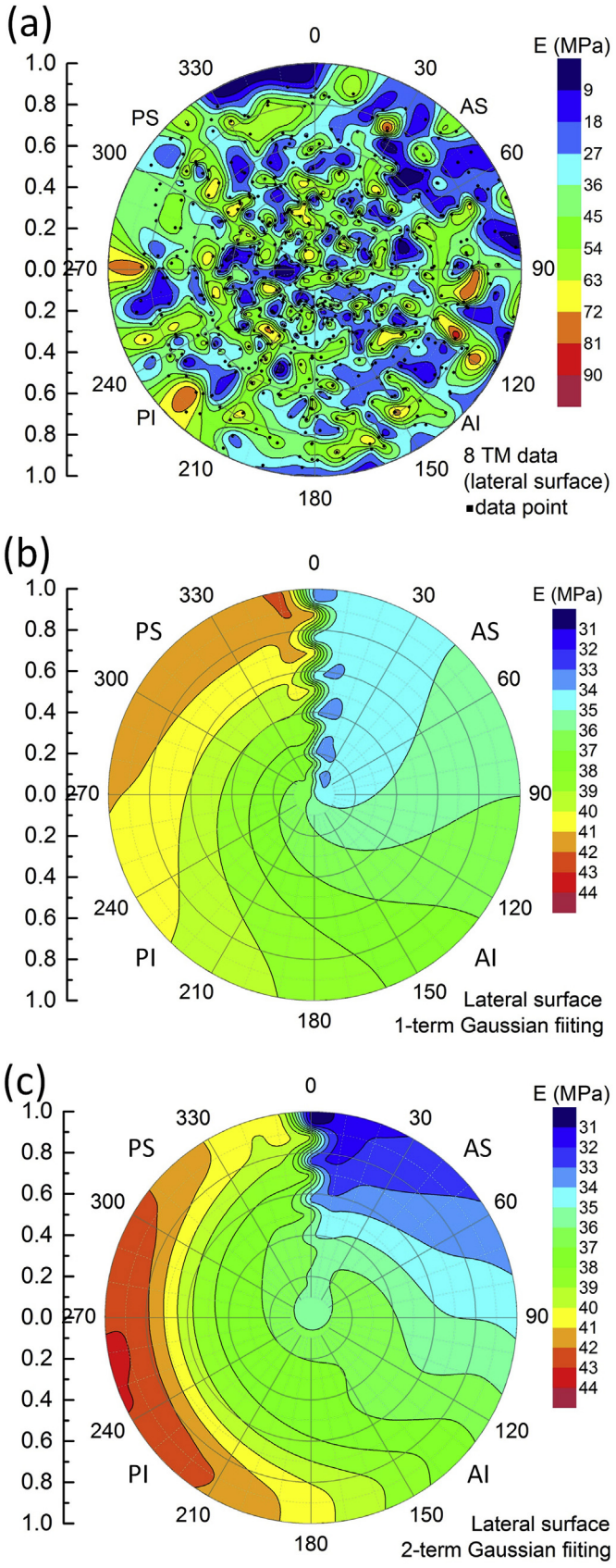


Fig. 17. Young's modulus map for 8 TM at the lateral surface(a). Combined experimental data from 8 TMs.(b). Single-bivariate Gaussian map.(c). Bi-bivariate Gaussian map.

Table 6
Parameters for the single- and bi-bivariate Gaussian maps.

Parameters	Single-bivariate Gaussian		Bi-bivariate Gaussian	
	Medial surface	Lateral surface	Medial surface	Lateral surface
A_1 (MPa)	8.66 ± 2.76	8.00 ± 4.05	12.8 ± 5.86	6.44 ± 5.10
A_2 (MPa)	N/A	N/A	8.96 ± 2.87	12.6 ± 7.70
B (MPa)	10.9 ± 0.782	33.6 ± 4.96	10.6 ± 0.832	30.1 ± 13.3
μ_{r1} (MPa)	0.546 ± 0.020	1.00 ± 0.49	0.300 ± 0.123	0.206 ± 0.108
μ_{r2} (MPa)	N/A	N/A	0.548 ± 0.021	0.956 ± 0.523
σ_{r1} (MPa)	0.130 ± 0.028	0.684 ± 0.340	0.192 ± 0.115	0.321 ± 0.182
σ_{r2} (MPa)	N/A	N/A	0.138 ± 0.030	0.306 ± 0.221
$\mu_{\theta1}$ (°)	360.0 ± 79.0	325.4 ± 72.7	12.0 ± 3.75	180.0 ± 32.9
$\mu_{\theta2}$ (°)	N/A	N/A	360.0 ± 51.3	258.8 ± 42.8
$\sigma_{\theta1}$ (°)	250.9 ± 121	151.9 ± 94.3	9.54 ± 4.62	360.0 ± 120.9
$\sigma_{\theta2}$ (°)	N/A	N/A	208.8 ± 107.9	115.6 ± 59.3
COD (R^2)	0.060	0.108	0.074	0.13

Note, N/A means that these parameters are not applicable for single-bivariate Gaussian fitting, they are for use in the bi-bivariate Gaussian fitting only. The standard deviations of the parameters through Levenberg-Marquard algorithm are shown following the ± symbol.

small trend at the medial surface for circumferential fibers. This lower modulus close to the perimeter may be due to the existence of the P and TIR fibers, which have lower densities than the circumferential fibers. The highest modulus close to the half of the radius may be due to T fibers which have possibly higher density than the circumferential fibers. The contour lines for the modulus are distributed along the circumferential fiber directions (Fig. 1c). In Fig. 16b and c for the two different terms, the difference appears only in the region close to the malleus bone at $\theta = 0–30°$. Since malleus bone exists in the top radial direction at the medial surface of the TM, these differences do not represent the modulus of the membrane and, therefore, should be ignored. Thus, the single-bivariate Gaussian function (Fig. 16b) is sufficiently accurate to describe the map of Young's modulus for circumferential fibers.

As shown in Fig. 17b and c, the modulus distribution at the lateral surface has a different trend. The AS quadrant shows the smallest modulus distribution and the AI quadrant shows the smallest modulus. The lower modulus in the AS quadrant may be due to the fact that if SMR fibers exist, they probably have lower fiber density than the other straight R_1 radial fibers. However, the highest modulus is distributed close to the annulus ring edge at the PS and PI quadrants ($\theta = 200–300°$); then the modulus decreases gradually along the radial direction to the origin at the umbo. The highest modulus at the edge between the PS and PI quadrant may be due to the presence of the R_2 fibers, which are radial fibers diverging or crossing over their annulus ring terminals, at which fibers have higher density than the other straight R_1 fibers in the radial direction. It appears that the modulus of the radial fibers is distributed in a strip shape along the radial fibers. The modulus increases gradually with the increase of polar angle, from the AS quadrant to AI quadrant. However, it changes the distribution along the circumferential direction. Around the region close to the malleus bone, the modulus has some perturbation since the malleus bone is attached to the other medial surface. Therefore, the bi-bivariate Gaussian (Fig. 17c) provides the best-fit to the modulus map of Young's modulus for the radial fibers.

It is noted that, for the modulus map, the confidence level for the coefficient of determination (COD) or R squared (R^2) is as low as 0.2–0.3. This value is not as high as 0.99 for the fitting of the CDF. Due to limited TM samples (7 TMs for the medial surface and 8 TMs for the lateral surface) and microindentation data points (about 600 and about 700 data points, respectively), the statistical analysis and the Young's modulus map may likely have some uncertainties and variation. However, the TM out-of-plane modulus distribution will perhaps improve the TM models for computational simulations of sound transmission. The results obtained in this study will enable input of TM mechanical properties in both the in-plane and the out-of-plane directions, necessary for simulation of TM vibrations under sound pressure. With the mechanical properties, data reported herein and other data reported in the literature for the TM, in the future, the two-layer collagen fibers of the TM can be assigned with different material properties, to account for anisotropy and viscoelastic behavior for the entire TM, for simulations of sound transmission with improved accuracy.

4. Conclusion

Measurement of the Young's modulus in the through-thickness direction was made by spherical microindentation on a human TM. The out-of-plane Young's modulus was measured for 7 TMs on the medial surface and 8 TMs on the lateral surface, respectively. The collagen fiber layers are in direct contact with the nanoindenter tip in saline condition. Viscoelastic microindentation analysis yields the Young's relaxation modulus data, which is converted to the Young's modulus at a given strain rate. The modulus data exhibit strong variation from one location to another. The Young's modulus varies over a wide range from 1.5 MPa to 50 MPa (mostly around 5–30 MPa) on the medial surface, and 2 MPa–90 MPa (mostly around 15–60 MPa) on the lateral surface.

The Q-Q plot, and the empirical CDF and PDF histograms are used for statistical analysis. Using the normal Q-Q plot, the S-shaped curves indicate a bimodal Gaussian distribution for both the radial fibers on the lateral surface and the circumferential fibers on the medial surface. The distribution parameters are determined from the best-fit CDF for each quadrant and for the entire TM. The PDF agrees well with the histograms. The two means of Young's modulus are determined as 6.6 MPa and 19.2 MPa for the medial surface, and 16.3 MPa and 41.6 MPa for the lateral surface, respectively. The lower modulus is likely due to lower fiber density, while the higher modulus is close to the values reported in the literature.

The Young's modulus maps were also modeled as a series of bivariate Gaussian functions in polar coordinates at both the medial and lateral surfaces over the entire TM. Two types of bivariate Gaussian functions were considered: single and double series. The parameters for the spatial distribution of modulus were also determined from the best-fit. For the medial surface, Young's modulus changed mainly along the radial direction, and followed a small-large-small trend from the perimeter to the center. For the lateral surface, Young's modulus showed a trend different from the medial surface. The AS quadrant showed the smallest modulus, then followed by the AI quadrant. The higher modulus was located close to the annulus ring edge at the PS and PI quadrants. The modulus gradually decreased along the radial direction to the origin, which is set at the umbo. Among the three types of models, single-bivariate and bi-bivariate Gaussians provided the best-fit to the spatial distribution of Young's modulus at the medial surface and the lateral surface, respectively. The local properties measured by microindentation can be used as input for future computer simulations of the middle ear using accurate two-layer structures with different modulus values over the TM to understand sound transmission.

Acknowledgments

We acknowledge the support of DOD W81XWH-14-1-0228, NIH R01DC011585, DOD W81XWH-13-MOMJPC5-IPPEHA, and NSF CMMI-1636306, CMMI-1661246, and CMMI-172043. Lu acknowledges the Louis A. Beecherl Jr. Chair for additional support. We also thank Dr. Chengkai Dai at University of Oklahoma, Dr. Wei Li at Hough Ear Institute for assistance on sample preparations, and Dr.

Xuelin Wang at Huazhong University of Science and Technology for helpful discussions. The authors thank Dr. Dani Fadda and one of the anonymous reviewers for editing the manuscript.

References

Aernouts, J., Aerts, J.R.M., Dirckx, J.J.J., 2012. Mechanical properties of human tympanic membrane in the quasi-static regime from in situ point indentation measurements. Hear. Res. 290, 45–54.

Beyea, J.A., Rohani, S.A., Ladak, H.M., Agrawa, S.K., 2013. Laser Doppler vibrometry measurements of human cadaveric tympanic membrane vibration. Otolaryngol. Head Neck Surg. 42, 17–26.

Chambers, J.M., Cleveland, W.S., Kleiner, B., Tukey, P.A., 1983. Graphical Methods for Data Analysis. Wadsworth International Group, Duxbury Press.

Cheng, T., 2007. Mechanical Properties of Human Middle Ear Tissues. PhD dissertation. University of Oklahoma.

Cheng, T., Dai, C., Gan, R.Z., 2007. Viscoelastic properties of human tympanic membrane. Ann. Biomed. Eng. 35, 305–314.

Daphalapurkar, N.P., Dai, C., Gan, R.Z., Lu, H., 2009. Characterization of the linearly viscoelastic behavior of human tympanic membrane by nanoindentation. J. Mech. Behav. Biomed. Mater. 2, 82–92.

Decraemer, W.F., Maes, M.A., Vanhuyse, V.J., 1980. An elastic stress-strain relation for soft biological tissues based on a structural model. J. Biomech. 13, 463–468.

Dobrev, I., Furlong, C., Cheng, J.T., Rosowski, J.J., 2014. Acousto-mechanical Response of the Human TM Characterized by High-Speed Digital Holographic Methods. Springer Berlin, pp. 657–660. Fringe 2013.

Eiber, A., Schidhlen, W., 1996. Reconstruction of hearing by mechatronical devices. Robot. Autonom. Syst. 19, 199–204.

Fay, J., Puria, S., Decraemer, W.F., Steele, C., 2005. Three approaches for estimating the elastic modulus of the tympanic membrane. J. Biomech. 38, 1807–1815.

Ferris, P., Prendergast, P.J., 2000. Middle-ear dynamics before and after ossicular replacement. J. Biomech. 33, 581–590.

Filliben, J.J., 1975. The probability plot correlation coefficient test for normality. Technometrics 17 (1), 111–117.

Gaihede, M., Liao, D., Gregersen, H., 2007. In vivo areal modulus of elasticity estimation of the human tympanic membrane system: modeling of middle ear mechanical function in normal young and aged ears. Phys. Med. Biol. 52, 803–814.

Gan, R.Z., Feng, B., Sun, Q., 2004. Three dimensional finite modeling of human ear for sound transmission. Ann. Biomed. Eng. 32, 847–859.

Gan, R.Z., Sun, Q., Feng, B., Wood, M.W., 2006. Acoustic-structural coupled finite element analysis for sound transmission in human ear-pressure distributions. Med. Eng. Phys. 28, 395–404.

Gan, R.Z., Dai, C., Wang, X., Nakmali, D., Wood, M.W., 2010. A totally implantable hearing system–Design and function characterization in 3D computational model and temporal bones. Hear. Res. 263, 138–144.

Gnanadesikan, R., 1977. Methods for Statistical Analysis of Multivariate Observations, second ed. John Wiley & Sons.

Greef, D.D., Aernouts, J., Aerts, J., Cheng, J.T., Horwitz, R., Rosowski, J.J., Dirckx, J.J.J., 2014. Viscoelastic properties of the human tympanic membrane studied with stroboscopic holography and finite element modeling. Hear. Res. 312, 69–80.

Hesabgar, S.M., Marshall, H., Agrawal, S.K., Samani, A., Ladak, H.M., 2010. Measuring the quasi-static Young's modulus of the eardrum using an indentation technique. Hear. Res. 263, 168–176.

Huang, G., Lu, H., 2006. Measurement of Young's relaxation modulus using nanoindentation. Mech. Time-Dependent Mater. 10, 229–243.

Huang, G., Daphalapurkar, N.P., Gan, R.Z., Lu, H., 2008. A method for measuring linearly viscoelastic properties of human tympanic membrane using nanoindentation. J. Biomech. Eng.-Trans. ASME 130, 014501.

Jeught, S.V.D., Dirckx, J.J.J., Aerts, J.R.M., Bradu, A., Podoleanu, A.G., Buytaert, J.A.N., 2013. Full-field thickness distribution of human tympanic membrane obtained with optical coherence tomography. J. Assoc. Res. Otolaryngol. 14, 483–494.

Kirikae, I., 1960. The Structure and Function of the Middle Ear. University of Tokyo Press, Tokyo.

Knauss, W.G., Emri, I., Lu, H., 2008. Mechanics of polymers: viscoelasticity. In: Sharpe, W.N. (Ed.), Handbook of Experimental Solid Mechanics. Springer, New York, pp. 49–95.

Kochkin, S., 2005. MarkeTrak VII: hearing loss population tops 31 million people. Hear. Rev. 12, 16–29.

Kotz, S., Read, C.B., Balakrishnan, N., Vidakovic, B., 2005. Encyclopedia of Statistical Sciences. John Wiley & Sons, Inc, Now York.

Kuypers, L.C., Decraemer, W.F., Dirckx, J.J.J., 2006. Thickness distribution of fresh and preserved human eardrums measured with confocal microscopy. Otol. Neurotol. 27, 256–264.

Lee, W.H., Radok, J.R.M., 1960. The contact problem for viscoelastic bodies. J. Appl. Mech. 27, 438–444.

Liang, J., Fu, B., Luo, H., Nakmali, D., Gan, R.Z., Lu, H., 2015. Characterisation of the nonlinear elastic behaviour of Guinea pig tympanic membrane using microfringe projection. Int. J. Exp. Comput. Biomech. 3 (4), 319–344.

Liang, J., Luo, H., Yokell, Z., Nakmali, D., Gan, R.Z., Lu, H., 2016. Characterization of the nonlinear elastic behavior of chinchilla tympanic membrane using microfringe projection. Hear. Res. 339, 1–11.

Lim, D.J., 1970. Human tympanic membrane: an ultrastructural observation. Acta Otolaryngol. 70 (3), 176–186.

Lim, D.J., 1995. Structure and function of the tympanic membrane: a review. Acta Oto-Rhino-Laryngol. Belg. 49, 101–115.

Lu, H., Wang, B., Ma, J., Huang, G., Viswanathan, H., 2003. Measurement of creep compliance of solid polymers by nanoindentation. Mech. Time-Dependent Mater. 7, 189–207.

Lu, H., Huang, G., Wang, B., Mamedov, A., Gupta, S., 2006. Characterization of the linear viscoelastic behavior of single-wall carbon nanotube/polyelectrolyte multilayer nanocomposite film using nanoindentation. Thin Solid Films 500, 197–202.

Luo, H., Lu, H., Dai, C., Gan, R.Z., 2009a. A comparison of Young's modulus for normal and diseased human eardrum at high strain rates. Int. J. Exp. Comput. Biomech. 1, 1–22.

Luo, H., Dai, C., Gan, R.Z., Lu, H., 2009b. Measurement of Young's modulus of human tympanic membrane at high strain rates. J. Biomech. Eng.- Trans. ASME 131, 064501.

Luo, H., Zhang, Y., Wang, B., Lu, H., 2010. Characterization of the compressive behavior of glass fiber reinforced polyurethane foam at different strain rates. J. Offshore Mech. Arct. Eng.- Trans. ASME. 132 (2), 021301.

Luo, H., Lu, G., Roy, S., Lu, H., 2013. Characterization of the viscoelastic behavior of bismaleimide resin before and after exposure to high temperatures. Mech. Time-Dependent Mater. 17 (3), 369–399.

Luo, H., Du, Y., Hu, Z., Cooper, W.L., Lu, H., 2015. High-strain rate compressive behavior of glass beads under confinement. Exp. Mech. 55, 935–950.

Moller, P., 1981. Tympanosclerosis of the ear drum: a scanning electron microscopic study. Acta Otolaryngol. 91, 215–221.

Moller, P., 1984. Tympanosclerosis of the ear drum in secretory otitis media. Acta Otolaryngol (Stockh) Suppl. 414, 171–177.

Mota, C., Danti, S., D'Alessandro, D., Trombi, L., Ricci, C., Puppi, D., Dinucci, D., Milazzo, M., Stefanini, C., Chiellini, F., Moroni, L., Berrettini, S., 2015. Multiscale fabrication of biomimetic scaffolds for tympanic membrane tissue engineering. Biofabrication 7, 025005.

Puria, S., 2003. Measurement of human middle ear forward and reverse acoustics: implications for otoacoustic emissions. J. Acoust. Soc. Am. 113, 2773–2789.

Rosowski, J.J., Dobrev, I., Khaleghi, M., Lu, W., Cheng, J.T., Harrington, E., Furlong, C., 2013. Measurements of three-dimensional shape and sound-induced motion of the chinchilla tympanic membrane. Hear. Res. 301, 44–52.

Thode, H.C., 2002. Testing for Normality. CRC Press.

Von Békésy, G., 1960. Experiments in Hearing. McGraw Hill, New York.

Wang, X., Cheng, T., Gan, R.Z., 2007. Finite-element analysis of middle-ear pressure effects on static and dynamic behavior of human ear. J. Acoust. Soc. Am. 122, 906–917.

Xu, T., Du, Y., Luo, H., Hu, Z., Wang, X., Guo, L., Lu, H., 2018. Characterization of the mechanical behavior of Colorado Mason sand at grain-level by nanoindentation. Exp. Mech. 58 (3), 449–463.

Zhang, X., Gan, R.Z., 2010. Dynamic properties of human tympanic membrane–experimental measurement and modelling analysis. Int. J. Exp. Comput. Biomech. 1, 252–270.

Zhang, X., Gan, R.Z., 2013. Dynamic properties of human tympanic membrane based on frequency-temperature superposition. Ann. Biomed. Eng. 41, 205–214.

Hearing Research 378 (2019) 33–42

Contents lists available at ScienceDirect

Hearing Research

journal homepage: www.elsevier.com/locate/heares

Research Paper

Progressive hearing damage after exposure to repeated low-intensity blasts in chinchillas

Tao Chen [a, b], Kyle Smith [a], Shangyuan Jiang [a], Tianyu Zhang [b], Rong Z. Gan [a, *]

[a] School of Aerospace and Mechanical Engineering, University of Oklahoma, Norman, OK, USA
[b] Department of Facial Plastic and Reconstructive Surgery, Eye & ENT Hospital of Fudan University, Shanghai, China

ARTICLE INFO

Article history:
Received 15 August 2018
Received in revised form
9 January 2019
Accepted 15 January 2019
Available online 17 January 2019

Keywords:
Repetitive low-intensity blast
Progressive hearing damage
Hearing protection devices

ABSTRACT

Hearing damage caused by blast waves is a frequent and common injury for Service members. However, most studies have focused on high-intensity blast exposures that are known to cause moderate to severe traumatic brain injury (TBI), and fewer studies have investigated the progressive hearing damage caused by low-intensity blast exposures (below mild TBI). In this paper, we report our recent study in chinchillas to investigate the auditory function changes over the time course after repetitive exposures to low-intensity blast. Two groups of chinchillas (N = 7 each) were used in this study. Group 1 was for an acute study with 2 blasts and Group 2 for progressive study with 3 blasts on Day 1 and observed for 7 days. Animals in both groups were exposed to blast overpressures of 21–35 kPa (3–5 psi or 180–185 dB SPL) at which the eardrum was usually not ruptured. One ear was left open while another ear was protected with an earplug. Blast overpressures were monitored at the entrance of the ear canal (P0) and near the eardrum in the canal (P1). Auditory brainstem responses (ABRs), distortion product otoacoustic emissions (DPOAEs), and middle latency responses (MLRs) were measured after each blast series in the acute group and on Days 1, 4, and 7 in the progressive group. Results show that hearing damage was induced in both ears after blast exposure on Day 1 and more damage was observed in open ears than plugged ears. Seven days after the three-blast series, the ABR threshold in open ears was still 7–20 dB higher on average than prior to the blasts. The MLR wave amplitude shifts were observed in both open and protected ears, which indicated central auditory damage. With the protection of an earplug, hearing thresholds had recovered to the pre-blast level by Day 7. Using this chinchilla blast model, acute and progressive hearing damages were quantified in both open and protected ears following repeated low-intensity blast exposures.

© 2019 Elsevier B.V. All rights reserved.

1. Introduction

Hearing damage caused by blast waves is a frequent and common injury for Service members. Blast overpressure (BOP) refers to a high-intensity disturbance in ambient air pressure (Stuhmiller et al., 1991). Recent clinical and animal studies have reported that both the peripheral (outer, middle, and inner ear) auditory system (PAS) and various structures within the central (brainstem and brain) auditory system (CAS) are vulnerable to blast injuries.

When blast waves propagate through the ear, the resulting acoustic trauma on the tympanic membrane and middle ear induces conductive hearing loss (Gan et al., 2016; Mayorga, 1997; Patterson and Hamernik, 1997). The hair cell loss in the cochlea and excitotoxicity in the spiral ganglion further induce sensorineural hearing loss (Cho et al., 2013; Liberman and Kujawa, 2017; Mao et al., 2012; Patterson and Hamernik, 1997). Similar to what is observed during traumatic brain injury (TBI), a potential mechanism of blast-induced damage to the CAS is the shearing and stretching forces applied on brain tissues including brainstem and auditory cortex (Gutierrez-Cadavid et al., 2005; Munjal et al., 2010a, 2010b; Song et al., 2018; Hall et al., 2017). These injuries could cause long-term hearing disabilities depending on the intensity of the blast (Saunders and Griest, 2009; Fausti et al., 2009; DePalma et al., 2005; Cho et al., 2013).

The severity of blast-induced TBI was first divided into three levels using the Glasgow Coma Scale: mild, moderate and severe (Teasdale and Jennett, 1974). Subsequently, there are several

* Corresponding author. School of Aerospace and Mechanical Engineering, University of Oklahoma, 865 Asp Avenue, Room 200, Norman, OK, 73019, USA.
E-mail address: rgan@ou.edu (R.Z. Gan).

https://doi.org/10.1016/j.heares.2019.01.010
0378-5955/© 2019 Elsevier B.V. All rights reserved.

commonly used classifications, all of which define the injury severity in relation to alteration of consciousness at the time of injury (Elder et al., 2014). Exposure to blasts below levels that cause such a loss of consciousness is defined as subclinical or a mild TBI (mTBI). To define the level of mTBI in animal models, a correlation between the BOP level and the respective post-blast symptoms of animals was built to establish a BOP-based system of TBI severity (Ahlers et al., 2012). Results from studies on blast-induced TBI in rats indicated that the pressure levels to induce mild, moderate, and severe TBI were 90–150, 150–230, and 230–350 kPa, respectively (Abdul-Muneer et al., 2013). Tympanic membrane (TM) perforation, cochlear damage, and long-term hearing loss were observed in rats after a single blast of 170 kPa (194 dB SPL) (Cho et al., 2013). TM rupture and hearing loss were observed in chinchillas after a blast of 63 kPa (190 dB SPL) (Gan et al., 2016). However, most studies have focused on outcomes from moderate to high BOP exposure (DePalma and Hoffman., 2018; DeKosky et al., 2010). Fewer animal studies have addressed the effects of repetitive exposure to low-level blasts that are comparable to those involved in human below the mTBI or subclinical blast. Particularly, there is no animal study reported in the literature to quantify the effect of repeated low-intensity blasts with different number of blasts on hearing function and the recovery over time after blasts. It is unclear if the repetitive exposures to low BOP level will result in permanent hearing damage after seven days.

Moreover, hearing protection devices (e.g. earplugs) have been used to protect against injuries to the peripheral auditory system. Sufficient attenuation of sound pressure level can be achieved with earmuffs, earplugs, or combination of those two to prevent hearing loss from operational noise. To understand the transduction of BOP through the ear canal to the TM and middle ear and to characterize the relationship between the TM rupture threshold and overpressure waveform, Gan et al. (2018) developed a “head block” attached with human cadaver ear and mounted with pressure sensors to monitor the BOP reaching the TM in the canal and inside the middle ear. Gan et al. demonstrated that the earplugs placed in the ear canal can dramatically reduce the pressure near the TM and inside the middle ear cavity. However, the mechanisms or effects of earplugs on hearing protection during blast exposure must be studied in animal models.

The mechanism and location of the blast-induced damage in auditory system can be reflected by various hearing function tests. Auditory brainstem response (ABR) provides general hearing sensitivity information by recording threshold values over a range of frequencies (Gan et al., 2016; Guan and Gan, 2011). Distortions of ABR waveforms (e.g. wave 1) indicate pathologies in specific regions of the auditory pathway (Henry et al., 2011; Liberman and Kujawa, 2017). Distortion product otoacoustic emission (DPOAE) signals reflect the function of the outer hair cells in the cochlea (Daniel et al., 2007; Hickman et al., 2018). Waveforms of middle latency responses (MLRs) capture thalamocortical transmissions and cortical activation impairments in the CAS (Phillips et al., 2011; Race et al., 2017). Collectively, abnormal ABR, DPOAE, and MLR measures strongly suggest BOP exposure compromises electrophysiological auditory function at all levels of the auditory pathway ranging from the organ of Corti to the auditory cortex (Shera and Guinan, 1999; Šuta et al., 2011; Norrix and Velenovsky, 2017).

In this paper, we report our recent study in chinchillas to investigate the progressive hearing damage after exposure to repeated low-intensity blasts and the protective mechanism of the earplug. Animals were exposed to low BOPs of 21–35 kPa (3–5 psi), below mTBI pressure levels, with one ear left open and another ear protected with an earplug. The pressure at the lateral side of the TM was measured in both ears. ABR, DPOAE, and MLR signals were measured before and after exposure and over seven-day time periods. The goal of this study was to determine whether repeated low-intensity blast exposures was the cause of progressive hearing damage and the protective mechanism of hearing protection devices. Knowledge of the hearing damage from the repetitive exposure to low-intensity blasts may be used to guide clinical evaluation and future research in blast-induced auditory injury.

2. Methods

2.1. Animal protocol

Healthy chinchillas (*Chinchilla laniger*), weighing between 500 and 800 g were included in this study. Chinchilla is a commonly used animal model for auditory research because of its large TM and middle ear space for an animal of its size, and the range of hearing is similar to that of humans (Heffner and Heffner, 1991; Jensen and Bonding, 1993; Richmond et al., 1989). The study's protocol was approved by the Institutional Animal Care and Use Committee of the University of Oklahoma and met the guidelines of the National Institutes of Health (NIH) and the US Department of Agriculture (USDA). All animals were checked for the existence of middle ear diseases by wideband tympanometry (Model AT235h, Interacoustics, MN).

Fourteen chinchillas were divided into two groups (N = 7 each): Group 1 for one-day acute study with two blasts (2-h interval between blasts) and Group 2 for progressive study over 7 days with three blasts (5–10 min intervals between blasts) on Day 1. The chinchilla's hearing damage induced by exposure to BOPs was related to the BOP level, the number of blast exposures, and the recovery time after blasts. The selection of 2 blasts for the acute study (1-day) and 3 blasts for the progressive study (7-days) was based on our preliminary study results: no permanent hearing damage was observed after one blast at the low BOP level, and the two blast-induced hearing loss in ears with an earplug generally recovered after 7 days (Smith et al., 2018).

The animals were anesthetized with 35 mg/kg Ketamine and 7 mg/kg Xylazine to ensure the chinchilla was sedated during the experiment. Each ear was examined using a surgical endoscope (Straight Endoscope, Stryker, MI) to ensure the nonexistence of TM and middle ear abnormalities. The ABR, DPOAE, and MLR tests were conducted to measure the baseline of the hearing function of each animal before blast exposure.

After initial function tests (pre-blast), the animal was placed in a specially designed L-shape animal holder to position its body so that the top of the animal's head faces the blast source and was then fixed using straps (Fig. 1A). Two identical pressure sensors (Model 102B16, PCB Piezotronics, Depew, NY) were installed to monitor the blast pressure at the entrance of the ear canal (P0) and near the TM in the canal (P1) as shown in Fig. 1B. P0 sensor was placed at the canal entrance and fixed on the animal holder. P1 sensor was inserted into the ear canal through a plastic guide tube. A small incision was made in the mastoid area of the chinchilla, and a 2 mm diameter hole was drilled at the inferior end of the ear canal bony wall to allow the insertion of the tube. Dental cement was applied to fix the guide tube outside of the bulla. A standard foam earplug (3M, Inc. St. Paul, MN) was then inserted into the left ear while the right ear was left open. Note that the P1 sensor was not in contact with the earplug in the canal.

A well-controlled compressed nitrogen-driven blast apparatus located inside an anechoic chamber in the Biomedical Engineering Laboratory at the University of Oklahoma was used to create a BOP in this study (Hawa and Gan, 2014; Gan et al., 2016; Engles et al., 2017). Polycarbonate films (McMaster-Carr, Atlanta, GA) of varying thickness (i.e. 0.25 mm and 0.5 mm) were employed to generate the BOP levels. In this study, animals in both groups were exposed

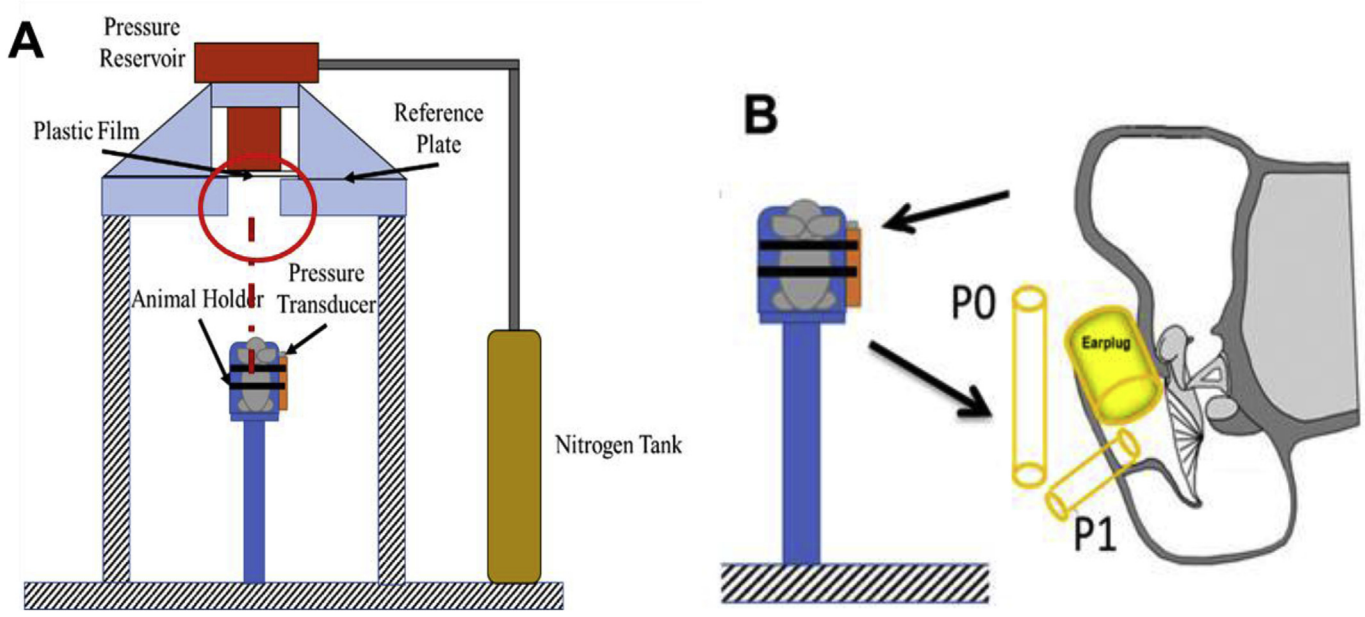


Fig. 1. (A) Schematic of animal experimental setup with blast apparatus. (B) Diagram showing the location of two pressure sensors installed into the ear: one was fixed at the entrance of the ear canal (P0) and another one fixed in the canal wall near the TM (P1).

to BOP levels of 21–35 kPa or 3–5 psi. Animals experienced two repeated blasts at time intervals of approximately 2 h in Group 1 while 3 repeated blasts at time intervals of approximately 10 min in Group 2.

The pressure sensor signals were collected by a cDAQ 7194 and A/D converter 9215 (National Instruments Inc., Austin, TX) with a sampling rate of 100k/s (10 ms dwell time). The LabVIEW software package (NI Inc) was used for data acquisition and analysis. The waveform of each blast test was saved to a PC for further analysis. Note that the sampling rate is sufficient for the waveform recorded in this study.

Upon the completion of blast exposure, the status of the chinchilla's TM was examined using a surgical endoscope and the auditory function tests were conducted. The animals in Group 1 were then euthanized for histology studies while Group 2 animals were observed for seven days.

2.2. Middle ear and cochlear function measurements

Auditory measurements including ABR, DPOAE, and MLR were conducted before and after each blast for animals in Group 1. For animals in Group 2, auditory function tests were performed before and after the three-blast series on Day 1 and then again on Days 4 and 7. The animals were anesthetized following the protocol in Section 2.1 during the function tests.

2.2.1. ABR and DPOAE measurements

Hearing level changes after blast exposure in chinchillas were measured by ABR threshold variation. The ABR measurements were conducted in both ears using a TDT system III (Tucker-Davis Technologies, Alachua, FL) following the procedure in our previous studies (Gan et al., 2016). Briefly, under anesthesia, stainless steel needle electrodes were positioned subcutaneously at the vertex of the skull and ventrolateral surfaces of the ear, with a ground electrode placed in the rear leg. Tone burst stimuli of 1 ms rise/fall time at frequencies of 0.5, 1, 2, 4, 6, and 8 kHz were generated which is a widely-accepted frequency range for chinchilla studies (Gan et al., 2016; Henry et al., 2011; Zhong et al., 2014). The ABR waveforms were recorded in descending 5 dB SPL intervals from the maximum amplitude of 120 dB SPL until no waveform could be observed. If an ABR response was not detected at the maximum acoustic stimulation, the threshold was set to 120 dB.

DPOAE measurement assesses the cochlear outer hair cell function. In this study, the DPOAE level shifts after blast exposure were measured in animals for pre- and post-series of exposures using the TDT system III. Cubic 2f1-f2 DPOAE levels were recorded using two primary tones, f1 and f2, presented at primary tone levels of L1 = 70 dB SPL and L2 = 65 dB SPL (Daniel et al., 2007). DPOAE recording at 2f1-f2 (f2 = 1.22xf1) was made with a microphone (ER-10B, Etymotic Research) sealed in the animal's external ear canal. The DPOAE levels were defined as the signal/noise ratio of the 2f1-f2 distortion product for the 70 dB and 65 dB SPL of f1 and f2 primaries, respectively, and were calculated by subtracting the 2f1-f2 distortion product from the surrounding noise. DPOAE level shifts were derived by subtracting post-exposure from pre-exposure values.

2.3. Central auditory function measurement

Part of the central auditory cortex function was measured by middle latency responses. MLR is useful in assessment of neurological function of the higher central auditory nervous system within several areas of the cerebral cortex (Torre and Fowler, 2000; Biessels et al., 1999). In acoustic MLR waveforms, there are four major components including two negative voltage waves (Na and Nb); and two positive voltage waves (Pa and Pb). The latency and amplitude of Pa (positive) and Na (negative) peak reflect the neural conduction velocity from the peripheral auditory nerve to the central auditory nervous system. The Pa component of the MLR arises from the inferior colliculus within the midbrain region, and the Na component is generated from the subcortical and cortical regions of the auditory system. Therefore, the acoustic MLR tests were used to estimate the impairment of the auditory central nerve pathway after blast exposure.

MLRs were recorded using short click and tone stimuli presented at a rate of 4/sec and with a 100 ms long recording window (TDT system III). As such, early components (<10 ms) of the waveform collected under the MLR acquisition settings correspond to

the responses from ABR generator regions, while later responses correspond to the aforementioned more central generators in the thalamus and cortex (Arnold, 2000). Chinchillas show an acoustic MLR wave with one negative peak (Na) with a high amplitude wave at 14–18 ms and one positive peak (Pa) with a high amplitude wave at 19–35 ms in response to the click sound. Only MLRs recorded from the interaural line (channel 2) were analyzed. Brief 0.5 kHz tones (2 ms in duration) of alternating polarity were used in MLR recording (Race et al., 2017; Phillips et al., 2011).

2.4. Statistical analysis

The ABR, DPOAE and MLR measurement data were expressed as the mean ± SD and plotted in GraphPad Prism with SPSS (Software Version 16.0) for statistical analysis. The paired *t*-test was used to compare the ABR threshold, DPOAE level, and MLR wave amplitude measured at pre- and post-exposures. A value of $P < 0.05$, 0.01 and 0.001 were considered statistically significant.

3. Results

3.1. BOP waveforms (P0 and P1)

Fig. 2 shows the typical waveforms of BOPs in units of psi (1 psi = 6.9 kPa) measured at the entrance of the ear canal (P0) over a time of 10 ms. Fig. 2A shows the representative BOP waveform of a chinchilla in Group 1, and Fig. 2B shows the P0 waveform measured from a chinchilla in Group 2. Both P0 waveforms illustrate a single positive overpressure peak at a level of 4.7 or 5.2 psi. After reaching the sharp positive peak, the pressure quickly decreased to a level of −1 psi and then returned to 0 psi.

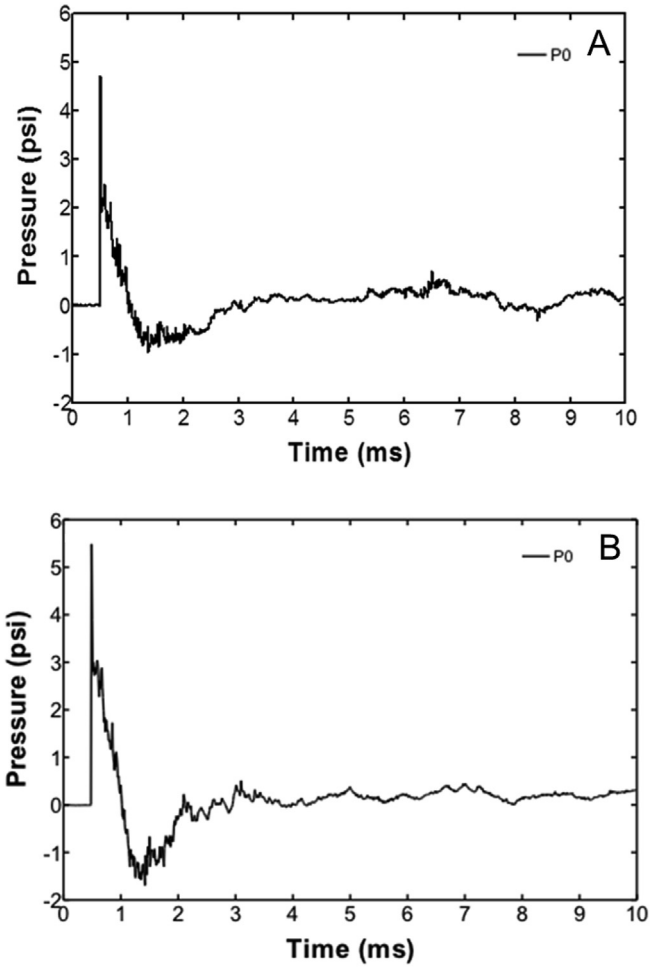


Fig. 2. (A) A recorded BOP waveform at the entrance of the ear canal from an animal test in Group 1 with a peak pressure of 4.7 psi. (B) A BOP waveform recorded from an animal test in Group 2 with a peak pressure of 5.2 psi.

Fig. 3 displays the P0 and P1 waveforms measured in a protected ear (Fig. 3A) and an open ear (Fig. 3B) from Group 1 chinchillas. The average value of the P1 peak pressure was 0.45 psi in plugged ears, which was much lower than the P0 due to the protection of the earplug. This indicates that the earplug greatly reduced the intensity of BOP reaching to the TM. In open ears, the mean of the P1 peak pressure increased to 6.5 psi with a P0 of 4.8 psi. The higher pressure near the TM was a result of the outer ear's amplification function.

3.2. ABR threshold and DPOAE level shifts in group 1 animals (acute study)

The ABR and DPOAE results measured from Group 1 chinchillas are summarized in Fig. 4. The mean and SD values of the ABR

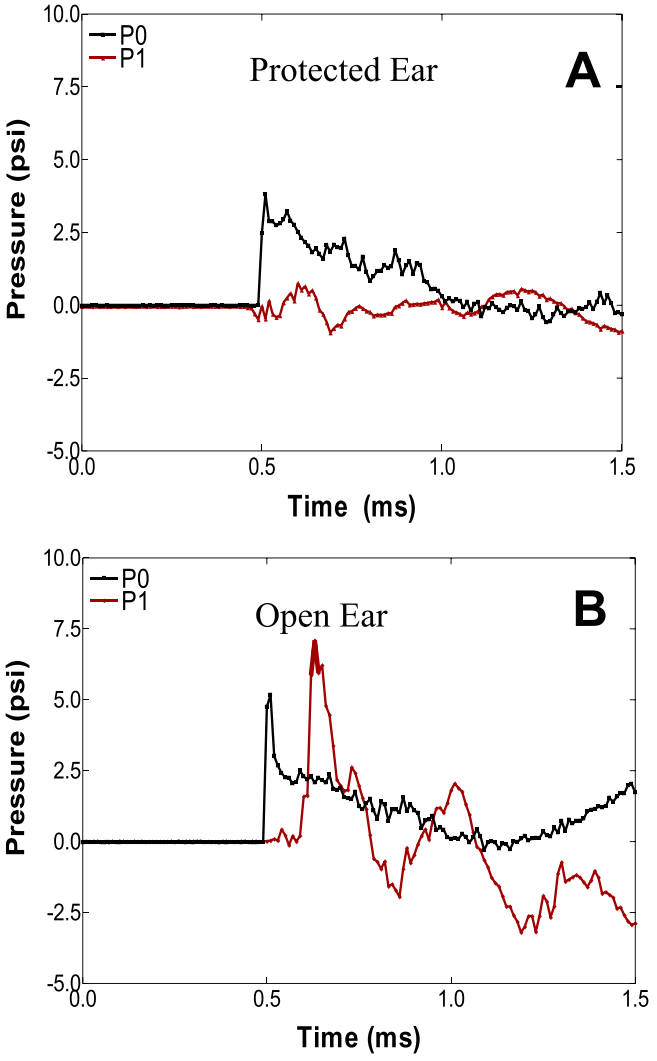


Fig. 3. (A) Representative BOP waveforms recorded at the entrance of the ear canal (P0) and near the TM in the canal (P1) from an animal test in Group 1 with plugged ear. (B) Representative BOP waveforms recorded at the entrance of the ear canal (P0) and near the TM in the canal (P1) from an animal test in Group 1 with open ear.

thresholds obtained from seven animals before and after each blast exposure are presented in Fig. 3A at the tested frequencies of 500 Hz - 8 kHz. Measurements were conducted in open and plugged ears before the blast exposure and after the completion of each blast (Blast 1 and Blast 2 as labeled in Fig. 4). An increase in ABR thresholds after the first blast was observed in open ears with values of approximately 16 dB at 500 Hz and 28 dB at 8 kHz, while the ABR thresholds were increased to 29 dB at 500 Hz and 46 dB at 8 kHz after the second blast. The threshold shifts generally increased with frequency for both Blast 1 and Blast 2 curves. In protected ears, the ABR threshold shifts were smaller than that of the open ears. The average threshold shifts increased from 7 dB at 500 Hz to 22 dB at 8 kHz after the first blast and from 17 dB to 37 dB after the second blast, respectively.

Fig. 4B shows the mean and SD of the DPOAE level shifts (reduction) measured from the animals in Group 1 at frequencies of 1 kHz–14 kHz. The value of the DPOAE level shifts increased from about 8 dB at 1 kHz to 20 dB at 12 kHz after blast 1 and from 16 dB to 28 dB after blast 2 in open ears. In protected ears, the DPOAE levels increased from about 4 dB at 1 kHz to 15 dB at 12 kHz after blast 1 and from 7 dB to 21 dB after blast 2, respectively. The shifts in open ears were greater than that in plugged ears over the entire frequency range. The damage to cochlear outer hair cells (OHCs) became more severe from blast 1 to blast 2. With the protection of earplugs, the dysfunction of cochlear OHCs induced by blast exposure was reduced but still observed from the DPOAE results.

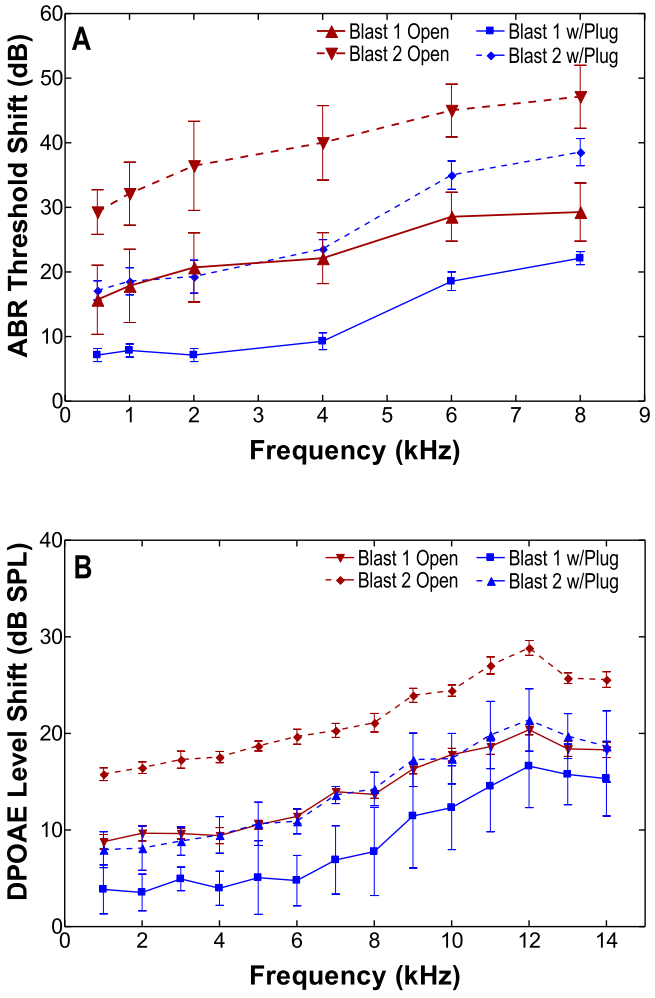


Fig. 4. (A) ABR threshold shifts (mean ± SD, n = 7) measured after each blast in open and plugged ears of the Group 1 animals. (B) DPOAE level shifts (mean ± SD, n = 7) measured after each blast in open and plugged ears of the Group 1 animals.

3.3. ABR threshold shifts in group 2 animals (progressive study)

The mean and SD of the ABR threshold shifts measured from seven animals in Group 2 over a 7-day period after blast exposures are shown in Fig. 5. Fig. 5A shows the ABR threshold shifts measured from plugged ears immediately after blasts on Day 1, those measured after 4 days (Day 4), and 7 days (Day 7) after blasts. The greatest threshold shifts occurred on Day 1 and the shift values decreased with the time. Fig. 5B shows the ABR threshold shifts obtained from open or unprotected ears at the same time points as those presented in Fig. 5A. On Day 1, Day 4, and Day 7, the open ears show greater damage than the plugged ears. Moreover, on Day 7, the mean ABR threshold shifts were still around 7–20 dB from 0.5 to 8 kHz respectively, while the shifts in the plugged ears were close to zero. On Day 7, the threshold shifts increased from about 6 dB at 500 Hz to 25 dB at 6 kHz in open ears, while the shifts were approximately 5 dB or less in plugged ears at all tested frequencies. The temporary threshold shifts were reflected by the results from Day 1 while the permanent shifts were reflected by Day 7 results. The data obtained from open and plugged ears on Days 1, 4, and 7 are compared in Fig. 5C. As shown in Fig. 5C, the ABR thresholds gradually recovered in the plugged ears after 4 days and 7 days (the bottom two solid curves). There was some recovery in open ears (the middle two broken curves), but the threshold shifts remained at 20–35 dB after 4 days and 10–20 dB after 7 days. This indicates that permanent damage occurred in the open ears, while the damage in plugged ears almost recovered (<5 dB shift) after 7 days.

3.4. ABR wave I amplitudes in group 2 animals (progressive study)

The ABR wave I amplitudes (peak to peak values) measured from seven animals in Group 2 on Day 1 (pre- and post-blast), Day 4, and Day 7 after blast exposures are presented in Fig. 6. The mean and SD values were plotted against the level of acoustic stimulus from 40 to 100 dB SPL measured in chinchilla ear canal. Data obtained at frequencies of 1, 2, 4, and 8 kHz from open and plugged ears were presented in different subplots. The top row of Fig. 6 for open ears demonstrated substantial wave I amplitude reduction after blasts at all frequencies. The curves on Day 4 and Day 7 almost overlap with the pre-blast at 1–4 kHz showing some recovery of damage over time. At 8 kHz, the pre-blast curve was slightly higher than those measured on Day 4 and Day 7 which may indicate some permanent change of the wave I amplitude. The results obtained from plugged ears (the bottom row) show no difference before and after blast exposure at all frequencies, which may indicate that the earplugs prevented both the temporary and permanent damage to cochlear ribbon synapses, spiral ganglion neurons, and auditory neural fibers when the chinchillas were exposed to low BOPs.

3.5. DPOAE level shifts in group 2 animals (progressive study)

Fig. 7 shows the mean and SD of DPOAE level shifts (reductions) measured from animals in Group 2 at frequencies of 1–14 kHz. The results from plugged ears are shown in Fig. 7A on Days 1, 4, and 7. The mean values of the DPOAE level shifts (n = 7) increased from about 5 dB at 1 kHz to a peak of 30 dB at 12 kHz on Day 1. The shifts decreased significantly on Day 4 and further decreased to a level lower than 10 dB on Day 7 over the entire frequency range. The DPOAE level shifts from open ears (n = 4) are shown in Fig. 7B. The DPOAE reductions increased from about 15 dB at 1 kHz to a peak of 35 dB at 10–11 kHz on Day 1. The shifts decreased over time to the level of 1 dB at 1 kHz with a peak of 25 dB at 11 kHz on Day 4.

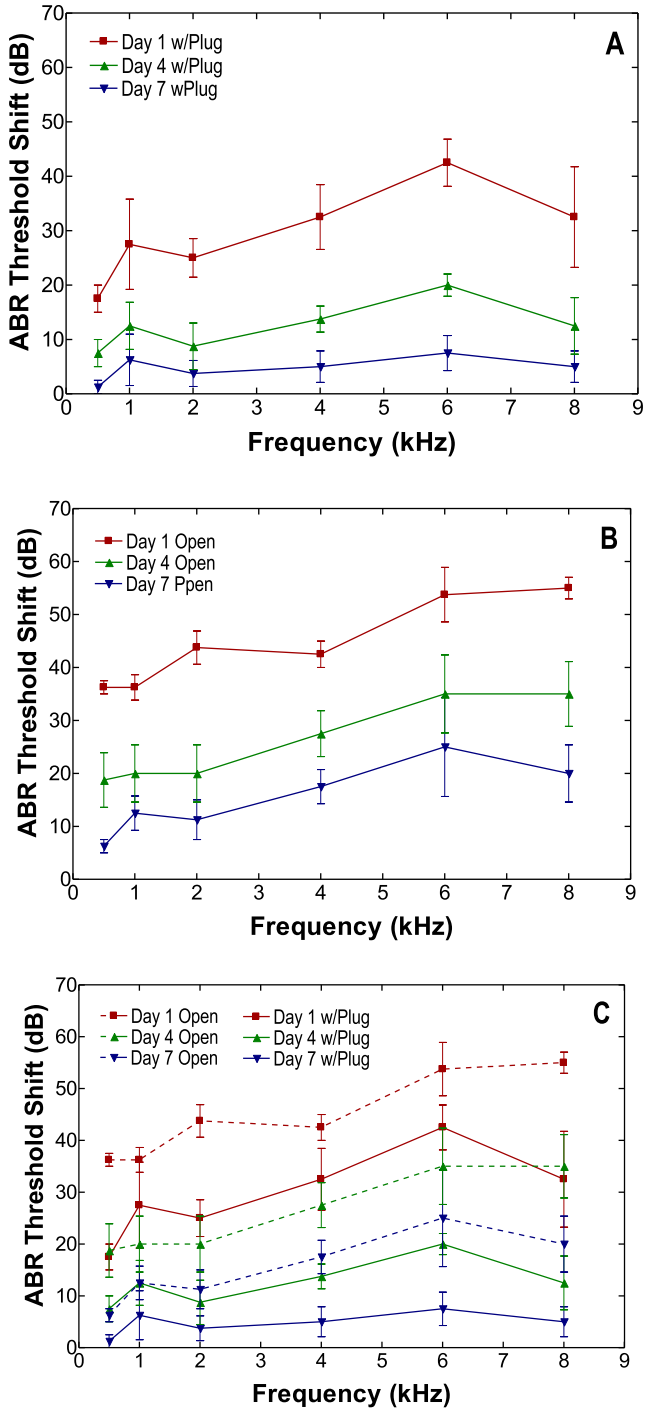


Fig. 5. (A) ABR threshold shifts (mean ± SD, n = 7) measured in plugged ears after 3 blasts on Day 1, Day 4, and Day 7 of the Group 2 animals. (B) ABR threshold shifts (mean ± SD, n = 7) measured in open ears on Days 1, 4, and 7 of the Group 2 animals. (C) Comparison of ABR threshold shifts in plugged and open ears on Days 1, 4, and 7.

Contrary to the plugged ears, no significant difference was observed between the results obtained from Day 4 and Day 7 and the DPOAE reductions remained at 10–20 dB at frequencies over 6 kHz.

Compared with Fig. 7A, the protection of earplug likely limited the temporary shift of the DOPAE levels, facilitated the recovery, and prevented the permanent loss of the OHCs. Note that the SD of the DPOAE data in Fig. 7B is larger than Fig. 7A even on Day 1. This might be caused by the microstructural damage in TM induced by the third blast which is not discernible under an endoscope (Engles et al., 2017; Liang et al., 2017). The accumulated damage which impaired the function of TM varied among ears and resulted in DPOAE results with large SD in addition to the lower ear number (4 ears vs 7 ears).

3.6. Assessment of central auditory system damage (MLRs)

Summary data and representative curves of MLR signals measured from Group 2 animals are listed in Tables 1 and 2 and shown in Fig. 8. The amplitude and time delay of the Pa and Na peaks reflect the vitality of the central auditory nervous system. Fig. 8 shows the representative MLR traces recorded in our experiments at 70 dB SPL with the stimulate frequency of 0.5 kHz. The response consists of negative peaks at l4-17 ms (Na peak) and a positive peak at 19–21 ms (Pa peak) in the pre-blast waveform. The post-blast waveforms in both ears were characterized by smaller response amplitudes and shorter latencies relative to the pre-blast response. The waveforms in open ears reveal a diminished amplitude response and an increased latency response. However, both responses return to pre-blast levels in the plugged ears 7 days after blast exposures.

The mean latency and amplitude of the Na and Pa peak for 7 animals are listed in Tables 1 and 2 for the open and protected ears, respectively. Table 1 shows the average Na and Pa peak latencies in open ears before blast exposure to be 15.01 ± 0.92 and 19.77 ± 0.72 ms, respectively. After the blast exposures, the average Na and Pa peak latencies increased to 17.85 ± 0.82 and 23.02 ± 1.24 ms, respectively. The shifts of the latencies in the Na and Pa peak were 2.84 and 3.25 ms, respectively. In protected ears (Table 2), the average Na and Pa peak latencies before the blast exposures were 14.73 ± 1.21 and 20.01 ± 2.16 ms, respectively. After the blast exposures, the average Na and Pa peak latencies increased to 17.15 ± 1.33 and 22.91 ± 1.77 ms, respectively. The shifts of the latencies in the Na and Pa peak were 2.42 and 2.9 ms, respectively. Seven days after the blast exposures, the time delays recovered to pre-blast exposure levels in both groups ($p > 0.05$).

The open and protected ears exhibited peak amplitude changes in Na and Pa peaks, as compared to pre-blast levels ($p < 0.01$), shown in Tables 1 and 2. The pre-blast Na and Pa peak amplitudes in open ears were -1.01 ± 0.11 and 1.19 ± 0.14 μV, respectively. After the blast exposures, the average Na and Pa peak amplitudes decreased to -0.52 ± 0.07 and 0.42 ± 0.05 μV, respectively. The shifts of the amplitudes in the Na and Pa peak were 0.49 and 0.77 μV, respectively. In protected ears, the average Na and Pa peak amplitudes before the blast exposures were -1.01 ± 0.21 and 1.02 ± 0.11 μV, respectively. After the blast exposures, the average Na and Pa peak amplitudes decreased to -0.72 ± 0.07 and 0.62 ± 0.08 μV, respectively. The shifts of the amplitudes in the Na and Pa peak were 0.29 and 0.4 μV, respectively. Seven days after the blast exposures, the peak amplitudes of Pa and Na recovered to the pre-blast levels in plugged ears, which was proved by non-significant differences between the pre-blast levels and levels measured 7 days after blast ($p > 0.05$). However, the shifts of the amplitudes of Pa and Na peaks in open ears were 0.32 and 0.58 μV, respectively, significantly different from the pre-blast results recorded 7 days after the blast exposures ($^{**}p < 0.01$).

4. Discussions

4.1. Hearing damage induced by repeated low-level blast overpressures

Repeated low-intensity blast overpressures can cause ultra-structural damage of animal brains, and a variety of anxiety-related

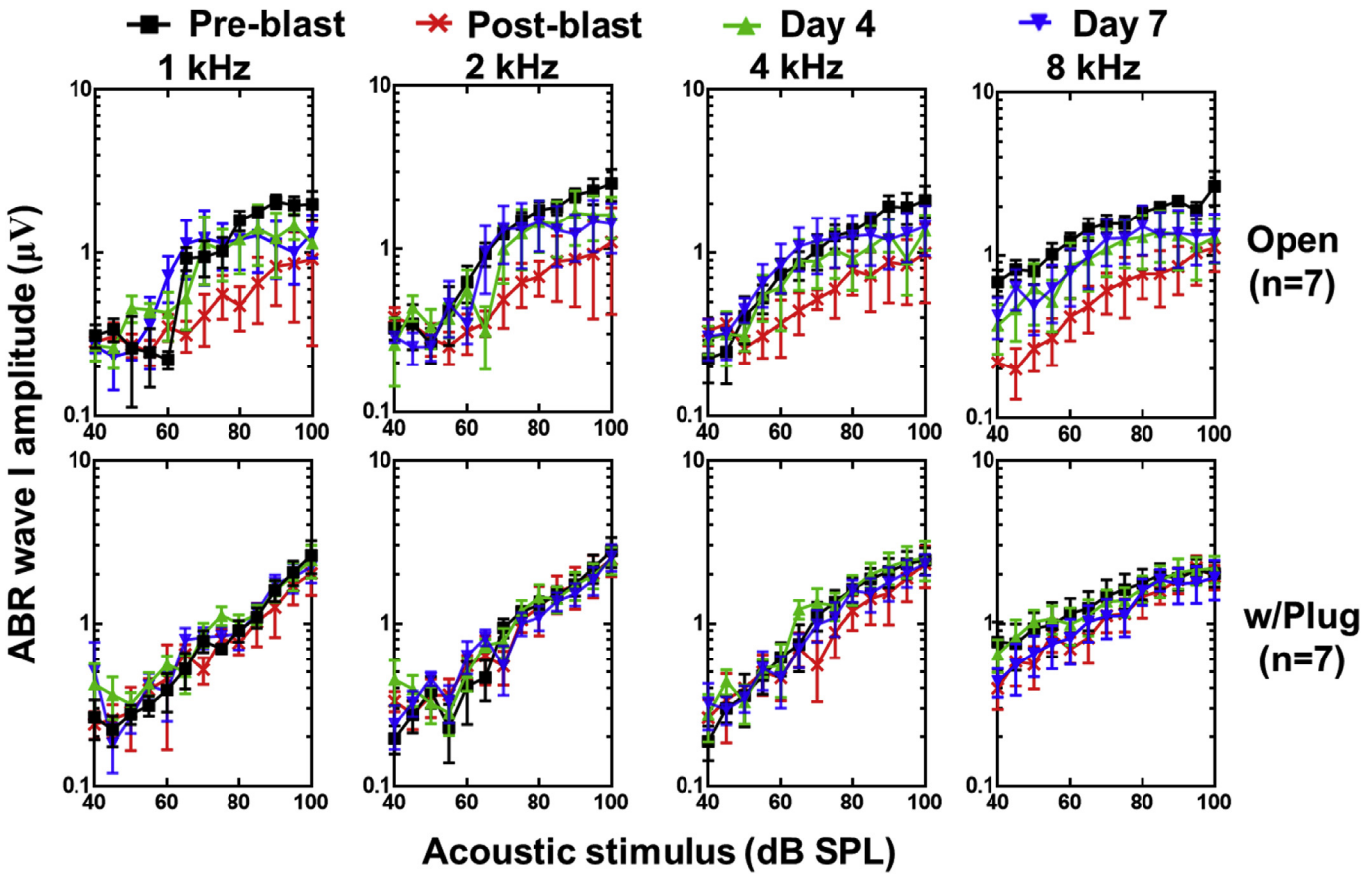


Fig. 6. ABR wave I amplitude (mean ± SD, n = 7) in response to stimulus level from 40 to 100 dB SPL measured from open and protected ears in chinchillas of Group 2. Measurements were taken at frequencies of 1, 2, 4, and 8 kHz.

behavioral traits including exaggerated fear responses have been reported (Song et al., 2018; Ahmed et al., 2015). However, hearing damage resulting from repeated low-level BOPs is still unclear. In this study, the ABR thresholds were significantly elevated after each blast exposure in the acute animal study of Group 1 as shown in Fig. 4A. Damage to cochlear OHCs was observed after the blast exposures as indicated by the increase in DPOAE level shifts shown in Fig. 4B. These results suggest that the repetitive blast exposures can aggravate and damage the auditory system immediately following blast exposures. Moreover, the severity of the damage increased with the number of blast exposures indicated by the increase in ABR and DPOAE shift shown in Fig. 4. This suggests an accumulative effect of acute hearing damage caused by repeated low-intensity blasts.

In both open and plugged ears from the progressive study with three blasts in Group 2, the ABR threshold shifts measured on Day 1 (Fig. 5) were greater than the respective results measured from animals in Group 1 (Fig. 4A). The DPOAE levels measured in Group 2 were slightly higher than Group 1, similar to the ABR results (Fig. 7 vs Fig. 4B). It further indicates that the severity of hearing damage increased with the number of exposures. The decreased amplitudes and increased latencies of Pa and Na peaks in MLR signals measured after blast exposures indicate the damage occurred in the central auditory system (Tables 1 and 2). These findings obtained from chinchilla blast model added quantitative information on acute hearing damage resulting from the repeated low-level blast exposures in relation to the number of exposures.

The progressive study of Group 2 animals over the 7-day time course after blasts demonstrates the ABR threshold shifts decreasing with time as shown in Fig. 5. The greatest shift was observed on Day 1, immediately following the blast exposures. Then the ABR shifts decreased with time over 7 days in both open and plugged ears, which indicate hearing recovery during this period. Particularly, the ABR threshold shifts of the plugged ears on Day 7 were under 5 dB which suggests the hearing was almost recovered to the levels before the blasts. The recovery process of the central auditory system after the blasts is reflected by the MLR data. The amplitudes and latencies of the Na and Pa peaks measured on Day 1 (post-blast), Day 4, and Day 7 showed a trend of returning to pre-blast levels with time, which may suggest that the blast-induced damage in the central auditory system is gradually recovered in protected ears. In contrast to the open ears on Day 7, the ABR threshold shifts remained 10–20 dB over the frequency range of 1–8 kHz, which may indicate permanent hearing damage.

Furthermore, the ABR wave I is a highly predictive indicator of the cochlear synaptopathy (Hickman et al., 2018; Liberman and Kujawa, 2017). The decreased wave I amplitudes in open ears after blast exposures were observed in Group 2 animals and are shown in Fig. 6. The results could be partially explained by acute cochlear synaptopathy induced by repeated low-level blasts, observed in similar studies on noise-induced acoustic trauma which suggested the repair of the ribbon synapses was predominated within 5 days after the injury and followed by a relative longer recovery process of the OHCs (Puel et al., 2002; Ruel et al., 2007). Here, damage was mostly recovered over 7 days at frequencies below 8 kHz. The progressive recovery of the OHCs, as reflected by the DPOAE shifts, decreases with time shown in Fig. 7, which also suggests some degree of recovery occurred in the PAS

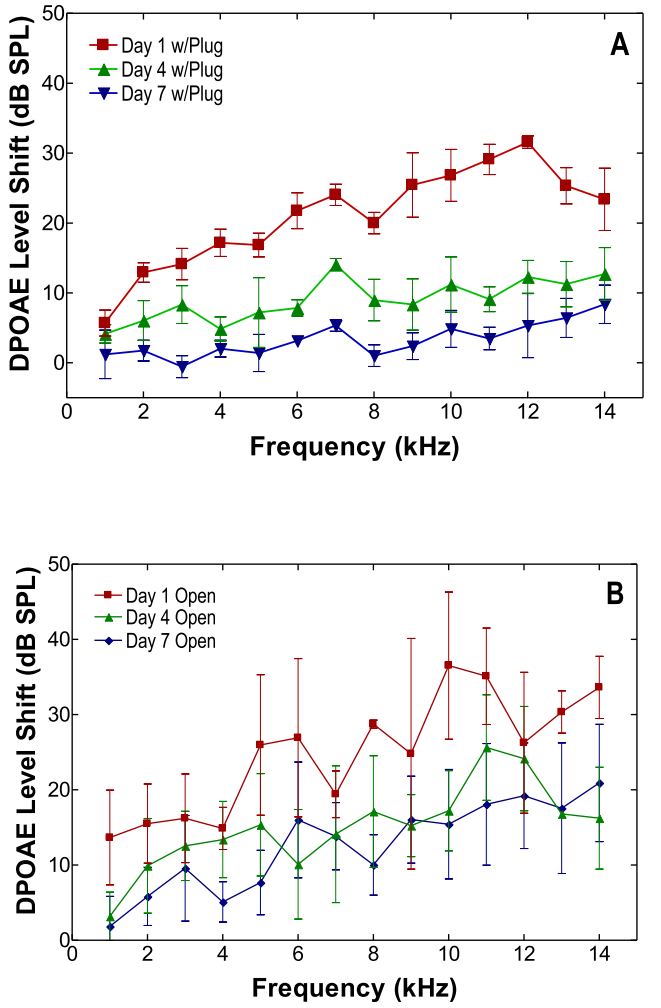


Fig. 7. DPOAE level shifts measured from the progressive group 2 on Days 1, 4, and 7. (A) The mean and SD of DPOAE shifts obtained from 7 ears protected with earplugs; (B) the mean and SD measured from 4 open ears with intact TM.

over a period of 7 days after blasts.

Overall, multiple blasts may introduce dysfunction of both the ribbon synapses and the OHCs followed by a recovery process. More detailed mechanisms of the damage and recovery processes in the PAS will require immunohistochemical studies in future (Hickman et al., 2018).

Note that the ABR threshold shifts induced by repetitive blast exposures are frequency-dependent with relatively greater shifts at high frequencies ($f > 4$ kHz) than low frequencies ($f < 4$ kHz) as shown in Figs. 4A and 5C for both groups of animals, except the situation when the shift was below 10 dB over the frequencies (Fig. 5C). Similar phenomena were observed in DPOAE level shifts, as shown in Figs. 4B and 7, even though the frequency range for DPOAE was wider. This tendency of hearing damage to increase at high frequencies is consistency with another recent study on the damage due to extremely low-intensity blasts in chinchillas (Hickman et al., 2018). It could be partially explained by the anatomy of the cochlea as the basal area or mid-cochlear region is closer to the oval window where the impact of the blast waves reaches first in the cochlea. More details on the mechanisms require further investigations and more evidence from the damage in the CAS.

4.2. Protective function of earplugs to BOP exposure

In this study, the animals had foam earplugs inserted into left ears. The TM in those ears showed no signs of damage after BOP exposures. It has been reported that earplugs have protective effects against blast exposures in a guinea pig study, including maintaining the integrity of the TM and reducing OHCs loss compared to open ears (Li et al., 2006). Our observations of the earplug's protective function to maintain the TM's integrity are consistent with those published, even with repeated blast exposures.

The comparison of ABR threshold shifts between the plugged ears and open ears in Group 1 and Group 2 are shown in Figs. 4 and 5. In protected ears, hearing damage after blast exposures was still observed, but at a much lower level compared to open ears after each blast in Group 1 animals (acute study). In Group 2 animals (progressive study) as shown in Fig. 5A, seven days after the repeated blasts, it could be observed that the hearing function recovered to the pre-blast levels (ABR shifts less than 5 dB), while the threshold shift still existed in the open ears on Day 7 (10–20 dB) as shown in Fig. 5B. The comparison between the open and protected ears suggests that the hearing protection device can prevent the repeated low intensity blast-induced auditory damage in a long-term observation.

Moreover, the sound attenuation of the earplug was investigated by Abel and Odell (2006), and they indicated that sufficient low-frequency attenuation may be achieved with an earmuff and earplug in combination to prevent hearing loss from operational noise. Our results are in agreement with Abel et al. and further demonstrate that the earplug can drastically attenuate the blast overpressure and protect the TM and hearing from blast-induced

Table 1
Latencies and amplitudes of the Na and Pa peak measures for animals of open ears (N = 7). Data are means ± SEM. *p < 0.05, **p < 0.01 for post-blast vs. pre-blast.

	Peak	Pre	Post	Day 4	Day 7
Latency (ms)	Na(ms)	15.01 ± 0.92	17.85 ± 0.82 **	15.41 ± 0.66	15.23 ± 1.02
	Pa(ms)	19.77 ± 0.72	23.02 ± 1.24**	21.19 ± 2.01*	20.45 ± 1.72
Amplitude (μV)	Na(μV)	−1.01 ± 0.11	−0.52 ± 0.07**	−0.65 ± 0.09**	−0.69 ± 0.08**
	Pa(μV)	1.19 ± 0.14	0.42 ± 0.05**	0.56 ± 0.04**	0.61 ± 0.08**

Table 2
Latencies and amplitudes of the Na and Pa peak measures for animals of plugged ears (N = 7). Data are means ± SEM. *p < 0.05, **p < 0.01 for post-blast vs. pre-blast.

	Peak	Pre	Post	Day 4	Day 7
Latency (ms)	Na(ms)	14.73 ± 1.21	17.15 ± 1.33**	15.22 ± 0.99	15.12 ± 0.91
	Pa(ms)	20.01 ± 2.16	22.91 ± 1.77**	21.35 ± 1.89*	20.22 ± 1.71
Amplitude (μV)	Na(μV)	−1.01 ± 0.21	−0.72 ± 0.07**	−0.88 ± 0.09*	−0.91 ± 0.14
	Pa(μV)	1.02 ± 0.11	0.62 ± 0.08**	0.86 ± 0.07*	0.89 ± 0.15

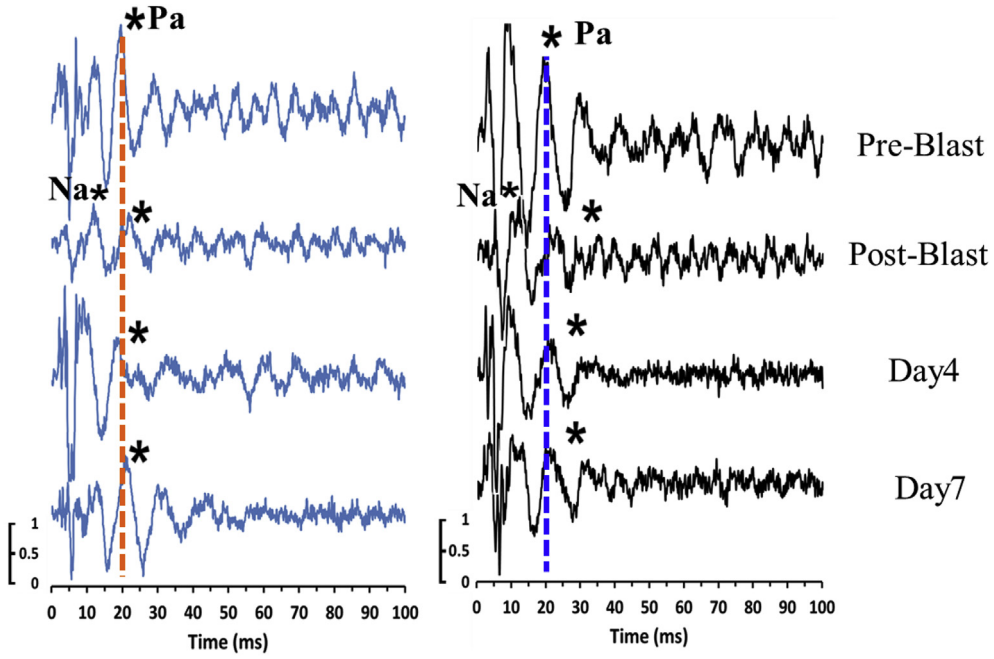


Fig. 8. Representative MLR traces at 80 dB SPL in the open ear (right panel) and plugged ear (left panel). The Pa and Na peak latency and amplitude on Days 1, 4, and 7 are marked by asterisk.

damage. In this study, the blast pressure of P0 at the ear canal entrance was around 4.6 psi, the P1 pressure near the TM was decreased to 0.45 psi with the earplug protection as shown in Fig. 3. However, the peak pressure level is not the only parameter to evaluate the possible damage that blast waves exert on the ear. A blast with an altered waveform can induce severe hearing damage even if the peak pressure is below the TM rupture threshold of 9.1 psi (Gan et al., 2016). Therefore, the distribution of energy flux of the blast wave that reaches the TM with and without the hearing protection devices should be further analyzed to improve our understanding on the protection mechanism of the hearing protection devices.

OHCs are one of the most easily damaged components in the inner ear, and Fig. 4B shows the DPOAE level shifts in protected ears after each blast exposure in Group 1 animals, and Fig. 7A shows the DPOAE shifts in protected ears of Group 2 animals. Even with the protection of the earplug, the DPOAE shift or reduction was enhanced after each blast exposure (acute study) or after three blasts on Day 1 (progressive study), especially at high frequencies (above 8 kHz). Since the TM and middle ear ossicles were not damaged in protected ears, the measured DPOAE shifts should reflect cochlea trauma or OHCs' damage. The cochlear damage induced by blast is more obvious at high frequencies ($f > 7$ kHz), which could be partially explained by that the base turn of cochlear basilar membrane is more vulnerable to blast. The blast-induced OHCs' morphological changes (e.g. hair cell distortion and hair cell loss) between the open and protected ears will be investigated in our future studies.

5. Conclusion

This study aimed at investigating the acute and progressive hearing damage in chinchillas after exposure to repeated low-intensity blasts and the protective mechanism of the hearing protection devices (e.g. earplug). Animals were exposed to low-level blast overpressure of 21–35 kPa (3–5 psi) with one ear left open and another ear protected with an earplug. ABRs, DPOAEs, and MLRs were measured before and after each exposure for the acute study and over a time period of 7 days after a series of multiple blasts for the progressive study. There are three major findings from this study: 1) the acute hearing damage immediately following blast exposures was characterized in relation to the number of blast exposures in both open and protected ears; 2) three blasts were able to induce permanent hearing damage in open ears while only temporary damage occurred in protected ears; 3) damage was observed in both the peripheral and central auditory systems as reflected by the ABR, DPOAE and MLR results. Using this chinchilla blast model, acute and progressive hearing damages were quantified in both open and protected ears under repeated low-intensity blast exposures.

Acknowledgments

The authors thank Dr. Junfeng Liang and Zachary Yokell in the Biomedical Engineering Lab at the University of Oklahoma for assistance in histology and animal studies. This work was supported by the US DoD W81XWH-14-1-0228 and NSF-China 81570934.

References

Abdul-Muneer, P.M., Schuetz, H., Wang, F., Skotak, M., Jones, J., Gorantla, S., Zimmerman, M.C., Chandra, N., Haorah, J., 2013. Induction of oxidative and nitrosative damage leads to cerebrovascular inflammation in an animal model of mild traumatic brain injury induced by primary blast. Free Radic. Biol. Med. 60, 282–291.

Abel, S.M., Odell, P., 2006. Sound attenuation from earmuffs and earplugs in combination: maximum benefits vs. missed information. Aviat. Space Environ. Med. 77 (9), 899–904.

Ahlers, S.T., Vasserman-Stokes, E., Shaughness, M.C., Hall, A.A., Shear, D.A., Chavko, M., McCarron, R.M., Stone, J.R., 2012. Assessment of the effects of acute and repeated exposure to blast overpressure in rodents: toward a greater understanding of blast and the potential ramifications for injury in humans exposed to blast. Front. Neurol. 3 (32), 1–12.

Ahmed, F., Plantman, S., Cernak, I., 2015. The temporal pattern of changes in serum biomarker levels reveals complex and dynamically changing pathologies after exposure to a single low-intensity blast in mice. Front. Neurol. 6, 114.

Arnold, S.A., 2000. The auditory brainstem response. Audiology: Diagnosis 1,

451–470.
Biessels, G.J., Cristino, N.A., Rutten, G.J., 1999. Neurophysiological changes in the central and peripheral nervous system of streptozotocin-diabetic rats: course of development and effects of insulin treatment. Brain 122 (4), 757–768.
Cho, S.I., Gao, S.S., Xia, A., Wang, R., Salles, F.T., Raphael, P.D., Abaya, H., Wachtel, J., Baek, J., Jacobs, D., Rasband, M.N., Oghalai, J.S., 2013. Mechanisms of hearing loss after blast injury to the ear. PLoS One 8 (7) e67618.
Daniel, S.J., Duval, M., Sahmkow, S., Akache, F., 2007. Ototoxicity of topical moxifloxacin in a chinchilla animal model. Laryngoscope 117 (12), 2201–2205.
DeKosky, S.T., Ikonomovic, M.D., Gandy, S., 2010. Traumatic brain injury—football, warfare, and long-term effects. N. Engl. J. Med. 363 (14), 1293–1296.
DePalma, R.G., Hoffman, Stuart W., 2018. Combat blast related traumatic brain injury (TBI): decade of recognition; promise of progress. Behav. Brain Res. 340, 102–105.
DePalma, R.G., Burris, D.G., Champion, H.R., Hodgson, M.J., 2005. Blast injuries. N. Engl. J. Med. 352 (13), 1335–1342.
Elder, G.A., Stone, J.R., Ahlers, S.T., 2014. Effects of low-level blast exposure on the nervous system: is there really a controversy? Front. Neurol. 5 (269), 1–22.
Engles, W.G., Wang, X., Gan, R.Z., 2017. Dynamic properties of human tympanic membrane after exposure to blast waves. Ann. Biomed. Eng. 45 (10), 2383–2394.
Fausti, S.A., Wilmington, D.J., Gallun, F.J., Myers, P.J., Henry, J.A., 2009. Auditory and vestibular dysfunction associated with blast-related traumatic brain injury. J. Rehabil. Res. Dev. 46 (6), 797–810.
Gan, R.Z., Leckness, K., Nakmali, D., Ji, X.D., 2018. Biomechanical measurement and modeling of human eardrum injury in relation to blast wave direction. Mil. Med. 183, 245–251.
Gan, R.Z., Nakmali, D., Ji, X.D., Leckness, K., Yokell, Z., 2016. Mechanical damage of tympanic membrane in relation to impulse pressure waveform–A study in chinchillas. Hear. Res. 340, 25–34.
Guan, X., Gan, R.Z., 2011. Effect of middle ear fluid on sound transmission and auditory brainstem response in Guinea pigs. Hear. Res. 277, 96–106.
Gutierrez-Cadavid, J.E., Latchaw, R.E., Kucharczyk, J., 2005. Imaging of head trauma. In: Latchaw, R.E., Kucharczyk, J., Moseley, M.E. (Eds.), Imaging of the Nervous System. Elsevier Mosby, Philadelphia, pp. 869–904.
Hall, A.A., Mendoza, M.I., Zhou, H., 2017. Repeated low intensity blast exposure is associated with damaged endothelial glycocalyx and downstream behavioral deficits. Front. Behav. Neurosci. 11, 104.
Hawa, T., Gan, R.Z., 2014. Pressure distribution in a simplified human ear model for high intensity sound transmission. J. Fluid Eng. 136 (11), 111108-1 to -6.
Heffner, R.S., Heffner, H.E., 1991. Behavioral hearing range of the chinchilla. Hear. Res. 52 (1), 13–16.
Henry, K.S., Kale, S., Scheidt, R.E., Heinz, M.G., 2011. Auditory brainstem responses predict auditory nerve fiber thresholds and frequency selectivity in hearing impaired chinchillas. Hear. Res. 280, 236–244.
Hickman, T.T., Smalt, C., Bobrow, J., Quatieri, T., Liberman, M.C., 2018. Blast-induced cochlear synaptopathy in chinchillas. Sci. Rep. 8, 10740.
Jensen, J.H., Bonding, P., 1993. Experimental pressure induced rupture of the tympanic membrane in man. Acta Otolaryngol. 113 (1), 62–67.
Li, C.J., Liu, Z.H., Zhu, P.F., 2006. Morphologic observation in the hair cell nucleus of the Guinea pig exposed to blast under pressure. Chongqing Med 5, 001.
Liang, J., Yokell, Z.A., Nakmaili, D.U., Gan, R.Z., Lu, H., 2017. The effect of blast overpressure on the mechanical properties of a chinchilla tympanic membrane. Hear. Res. 354, 48–55.
Liberman, M.C., Kujawa, S.G., 2017. Cochlear synaptopathy in acquired sensorineural hearing loss: manifestations and mechanisms. Hear. Res. 349, 138–147.
Mao, J.C., Pace, E., Pierozynski, P., 2012. Blast-induced tinnitus and hearing loss in rats: behavioral and imaging assays. J. Neurotrauma 29 (2), 430–444.
Mayorga, M.A., 1997. The pathology of primary blast overpressure injury. Toxicology 121, 17–28.
Munjal, S.K., Panda, N.K., Pathak, A., 2010a. Audiological deficits after closed head injury. J. Trauma Acute Care Surg. 68 (1), 13–18.
Munjal, S.K., Panda, N.K., Pathak, A., 2010b. Dynamics of hearing status in closed head injury. J. Neurotrauma 27, 309–316.
Norrix, L.W., Velenovsky, D., 2017. Unraveling the mystery of auditory brainstem response corrections: the need for universal standards. J. Am. Acad. Audiol. 27 (10), 950–960.
Patterson, J.H., Hamernik, R.P., 1997. Blast overpressure induced structural and functional changes in the auditory system. Toxicology 121, 29–40.
Phillips, D.J., Schei, J.L., Meighan, P.C., 2011. State-dependent changes in cortical gain control as measured by auditory evoked responses to varying intensity stimuli. Sleep 34 (11), 1527–1537.
Puel, J.-L., Ruel, J., Guitton, M., Wang, J., Pujol, R., 2002. The inner hair cell synaptic complex: physiology, pharmacology and new therapeutic strategies. AUD 7, 49–54.
Race, N., Lai, J., Shi, R., 2017. Differences in postinjury auditory system pathophysiology after mild blast and nonblast acute acoustic trauma. J. Neurophysiol. 118 (2), 782–799.
Richmond, D.R., Fletcher, E.R., Yelverton, J.T., Phillips, Y.Y., 1989. Physical correlates of eardrum rupture. Ann. Otol. Rhinol. Laryngol. 98 (5_Suppl. I), 35–41.
Ruel, J., Wang, J., Rebillard, G., Eybalin, M., Lloyd, R., Pujol, R., Puel, J.-L., 2007. Physiology, pharmacology and plasticity at the inner hair cell synaptic complex. Hear. Res. 227 (1), 19–27.
Saunders, G.H., Griest, S.E., 2009. Hearing loss in veterans and the need for hearing loss prevention programs. Noise Health 11, 14, 42.
Shera, C.A., Guinan, J.J., 1999. Evoked otoacoustic emissions arise by two fundamentally different mechanisms: a taxonomy for mammalian OAEs. J. Acoust. Soc. Am. 105, 782–798.
Smith, K., Chen, T., Gan, R.Z., 2018. Hearing damage induced by blast Overpressure at the mild TBI level in a chinchilla model. Presented at 2018 Military Health System Research Symposium (MHSRS) and submitted to. J. Mil. Med. (In review).
Song, H., Konan, L.M., Cui, J., 2018. Ultrastructural brain abnormalities and associated behavioral changes in mice after low-intensity blast exposure. Behav. Brain Res. 347, 148–157.
Stuhmiller, J.H., Phillips, Y.Y., Richmond, D.R., 1991. The Physics and Mechanisms of Primary Blast Injury. Conventional Warfare: Ballistic, Blast, and Burn Injuries. Department of the Army, Office of the Surgeon General, pp. 241–270.
Šuta, D., Rybalko, N., Pelánová, J., Popelář, J., Syka, J., 2011. Age-related changes in auditory temporal processing in the rat. Exp. Gerontol. 46, 739–746.
Teasdale, G., Jennett, B., 1974. Assessment of coma and impaired consciousness: a practical scale. Lancet 304 (7872), 81–84.
Torre III., P., Fowler, C.G., 2000. Age-related changes in auditory function of rhesus monkeys (Macaca mulatta). Hear. Res. 142 (1), 131–140.
Zhong, Z., Henry, K.S., Heinz, M.G., 2014. Sensorineural hearing loss amplifies neural coding of envelope information in the central auditory system of chinchillas. Hear. Res. 309, 55–62.

Hearing Research 378 (2019) 43–52

Contents lists available at ScienceDirect

Hearing Research

journal homepage: www.elsevier.com/locate/heares

Research Paper

Dual-laser measurement and finite element modeling of human tympanic membrane motion under blast exposure

Shangyuan Jiang, Kyle Smith, Rong Z. Gan*

School of Aerospace and Mechanical Engineering, University of Oklahoma, Norman, OK, USA

ARTICLE INFO

Article history:
Received 15 August 2018
Received in revised form
10 December 2018
Accepted 12 December 2018
Available online 14 December 2018

Keywords:
Tympanic membrane
Blast exposure
Middle ear
Finite element modeling
Laser Doppler vibrometry

ABSTRACT

Hearing damage is one of most prevalent injuries in military personnel and civilians exposed to a blast. However, the mechanism of how the blast overpressure interacts with the tympanic membrane (TM) and impairs the peripheral auditory system still remains unclear. A 3D finite element (FE) model of the human ear has been developed to predict the blast overpressure transmission through the ear (Leckness et al., 2018), but the model needs to be further validated in TM response to blast pressure. This paper reports the first-ever approach using two laser Doppler vibrometers (LDVs) to measure the motion of the TM when the ear was exposed to a blast.

Five fresh human temporal bones were used in this study with a pressure sensor inserted near the TM to measure the pressure reaching the TM (P1). The temporal bone was mounted in a "head block" and exposed to blast at the overpressure around 35 kPa measured at the entrance of the ear canal (P0). The movements of the TM at the umbo and the "head block" were measured simultaneously by two LDVs and the exact motion of the TM was determined by subtracting the head block motion from the TM data. Results include that the maximum TM velocity was 12.62 ± 3.63 m/s (mean $\pm$ SD) and the displacement was 0.78 ± 0.26 mm. The peak-to-peak displacement normalized by the P0 pressure was 22.9 ± 6.6 μm/kPa. The frequency domain analysis indicated that the spectrum peaks were located at frequencies below 3 kHz. The TM motion was then compared with that calculated from the FE model of the human ear with the measured P0 pressure wave applied at the ear canal entrance. The FE model-derived TM displacement under blast overpressure was consistent with the experimental results. This study provides a new methodology to determine the behavior of the middle ear in response to blast overpressure. The experimental data are critical for validating the FE model of the human ear for blast wave transduction and understanding the TM damage induced by blast exposure.

© 2018 Elsevier B.V. All rights reserved.

1. Introduction

Blast overpressure is a high intensity disturbance in the ambient air pressure which creates impulse over 170 dB sound pressure level (SPL). Blast overpressure waveform is characterized by high peak pressure over a short time duration as called the Friedlander curve or waveform (Sundaramurthy et al., 2012; Walter, 2004). When exposed to a blast, the human auditory system is vulnerable to both peripheral and central damage from overpressure. Exposure to blast overpressure at a level of 104 kPa can result in 50% rupture rate of the tympanic membrane (TM), while at levels of roughly 554 kPa, the damage can be lethal (Cho et al., 2013; Garner and Brett, 2007).

Blast-induced hearing loss occurs in a significant fraction of military personnel coming back from the battlefield (Breeze et al., 2011; Dougherty et al., 2013; Garth, 1994; Régloix et al., 2017; Sridhara et al., 2013). In past decades, the increasing number of civilians involved in terroristic bombing attacks have made the blast-induced hearing loss a public health issue (Champion et al., 2009; Mathews and Koyfman, 2015; Yeh and Schecter, 2012). The abnormally large deformation of the TM when blast overpressure propagates through the ear causes damages to the ear such as the rupture of the TM, disarticulation of ossicular chain, and hair cell loss in cochlea or vestibular system (Dougherty et al., 2013; Gan et al., 2016; Patterson and Hamernik, 1997). However, the detailed mechanism of how the blast overpressure interacts with the TM and impairs the peripheral auditory system remains unclear

* Corresponding author. School of Aerospace and Mechanical Engineering, University of Oklahoma, 865 Asp Avenue, Room 200, Norman, OK, 73019, USA.
E-mail address: rgan@ou.edu (R.Z. Gan).

https://doi.org/10.1016/j.heares.2018.12.003
0378-5955/© 2018 Elsevier B.V. All rights reserved.

due to the absence of the TM movement data under blast exposure.

The motion of the TM induced by acoustic stimulation represents the transfer function of the middle ear for sound transmission (Cheng et al., 2010; Gan et al., 2004). Laser Doppler vibrometry has been applied to measure the frequency response of the TM in human cadaveric temporal bones (TBs) and experimental animals under normal and diseased conditions to assess the function of the middle ear in relation to various factors such as species, age, existence of middle ear fluid, and bacterial infections (Gan et al., 2004, 2018a; Rosowski et al., 2009; Voss et al., 2000; Wang et al., 2016; Zhang et al., 2014). Most of the published measurements were conducted at sound pressure levels under 130 dB SPL, which is widely accepted as the linear range of the human middle ear (Gan et al., 2004; Goode et al., 1994; Voss et al., 2000). The TMs of the blast victims usually experienced disturbance of the pressure with peak values far beyond this linear range (Chandra et al., 2012; Gan et al., 2018b; Hawa and Gan, 2014; Patterson and Hamernik, 1997). The experimental measurement on TM movement under high-intensity stimulus beyond the linear acoustic range such as blast or noise exposure, however, is limited.

The nonlinear behavior of the middle ear has been characterized in gerbil, rabbit, and human cadaveric temporal bones by measuring the vibration of the TM and stapes under high-intensity noise using laser vibrometry (Aerts and Dirckx, 2010; Cheng et al., 2017; Greene et al., 2017; Peacock et al., 2015). Note that there is a limitation of using the concept of "transfer function" to describe the nonlinear behavior of the middle ear under high intensity sound or blast exposure (Aström and Murray, 2010). The intracochlear pressure during acoustic shock wave exposure has been measured recently, but the TM displacement has not been reported in human (Greene et al., 2018). Unlike the measurement conducted under normal acoustic or high-intensity sound stimuli during which the movement of the TM and ossicles can be isolated by the stable sample holder, the blast overpressure is strong enough to possibly result in drastic vibration of the sample holder and thus affect the experimental outcome. The design of a novel experimental setup based on laser Doppler vibrometers (LDVs) is required for measuring TM movement under blast exposure. The differential LDV is also capable to measure the relative velocity of two points in a structure (Castellini et al., 2006; Rothberg et al., 2017; Yang et al., 2013). However, the dual-laser setup with two LDVs for measuring the movement of the TM and head block is available in our lab and flexible with the blast test system. Even though the laser beams are emitted from two laser sources, the measurement output from two Polytec LDVs is reliable with high accuracy.

In addition to experimental measurement, a 3D finite elemental (FE) model of the human ear has been developed for simulation of blast overpressure transduction through the ear and the blast-induced auditory damage (Gan et al., 2018b; Leckness et al., 2018). As a critical parameter to validate the FE model, the response of the TM to blast overpressure, however, has not been measured experimentally. Therefore, there is an urgent need to provide the experimental data of the TM movement under blast to validate the FE model in addition to the pressure measurement inside the ear.

In this study, a novel dual-laser setup was first ever established in our laboratory based on a blast chamber and two LDVs to make the real-time measurement on the movement of TM under blast exposure. By measuring vibrations of the TM and the TB specimen or "head block" (Gan et al., 2018b) simultaneously using two LDVs under blast, the head block vibration can be eliminated from the movement of the TM. The blast waveform recorded at the entrance of the ear canal during blast was used as an input for the 3D FE model of the human ear to calculate the response of the TM. The experimental results were analyzed in time and frequency domain and compared with the FE model predictions.

2. Methods

2.1. Sample preparation and experimental setup

Five fresh human TBs from donors with an average age of 78, ranging from 64 to 87 years old (2 female and 3 male) were involved in this study. Note that the age of TB donors is higher than most of the military personnel although changes in mechanical properties and structure of the human middle ear after adulthood are limited (Keefe and Levi, 1996; Ruah et al., 1991). Temporal bones were packed in dry ice and shipped from the Life Legacy Foundation, a certified human tissue supplier for military health research. The study protocol was approved by the US Army Medical Research and Material Command (USAMRMC), Office of Research Protections (ORP). The samples were processed with a solution of 0.9% saline and 15% povidone at 5 °C to maintain the physiological conditions within 24 h of the arrival before the start of the experiment. Each sample was examined under a light microscope (OPMI-1, Zeiss, Thornwood, NY) to ensure the ear was free from middle ear diseases.

Upon the completion of the surgery of expanding the opening of the ear canal, the umbo of the TM was exposed by removing part of the tragus to allow the laser beam to reach the umbo. A reflective tape at a size of 1 mm × 1 mm was placed on the umbo as a laser target. Another piece of reflective tape was attached to the lateral surface of the "head block", an artificial human head with the TB specimen mounted in (Gan et al., 2018b). Fig. 1 is a schematic diagram of the experimental setup. The "head block" attached with human TB and mounted with two pressure sensors for measuring the response of the middle ear to the blast overpressure. The shaded square represents the location of the TB whose inner structure is shown in the block on the right. All TBs were covered by paper soaked in saline solution during the process of sample preparation for maintaining the moisture of TB specimens. The process of blast exposure was limited within 1 h to avoid any risk of drying of the specimen.

Two pressure sensors were simultaneously monitoring blast pressure at the entrance of the ear canal (P0) and near the TM in the canal (P1). The pressure sensor P1 (Model 105C02, PCB Piezotronics, Depew, NY) was surgically inserted into the ear canal near the TM (3 mm away). The pressure sensor P0 (Model 102B16, PCB Piezotronics, Depew, NY) was mounted on a column approximately

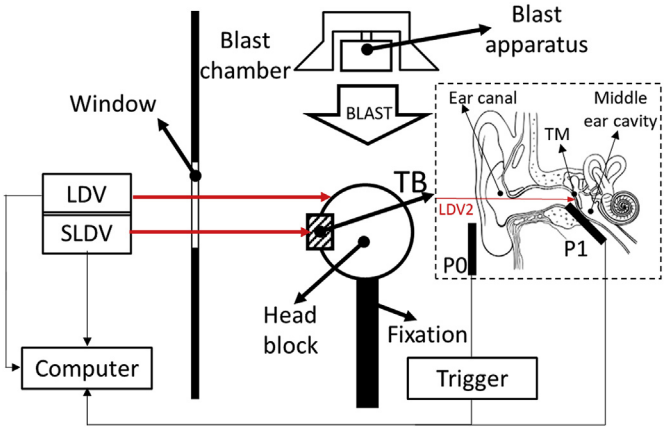


Fig. 1. Schematic of the experimental setup showing the blast chamber and LDVs. The inside structure of the TB specimen and the location of the pressure sensors are shown in the dashed square.

1 cm lateral to the ear canal opening with the sensing surface facing the blast. As shown in Fig. 1, the "head block" was fixed under the blasting apparatus and exposed to open-field blast inside an anechoic chamber following the previously established methodologies (Engles et al., 2017; Gan et al., 2018b; Leckness et al., 2018). Briefly, the blast overpressure was generated by rupturing polycarbonate film(s) (McMaster-Carr, Atlanta, GA) at a thickness of 0.26 mm using compressed nitrogen. The intensity of the blast was controlled by varying the distance from the blast reference plane. The blast wave was propagating towards the front side of the head block or in front of the face as shown in Fig. 2. The interior surface of the blast chamber was covered by acoustic foam except for a transparent window through which the laser beams can pass and reach the targets.

After completion of the sample-mounting process, the chamber was closed and the two LDVs were placed outside on a stable surface. The lower panel of Fig. 2 exhibits the experimental setup inside the blast chamber observed through the window. The laser beams emitted from the heads transmitted through the window to reach the targets placed on the TM and the head block, respectively, as shown in the upper panel of Fig. 2. LDV1 (Polytec CLV 2534, Tustin, CA) aimed at the target placed on the head block to measure the movement of the entire TB specimen while LDV2 (PSV-400, Polytec Inc., Irvine, CA) aimed at the umbo to measure the movement of the TM which includes both the TM and head block movements. Two laser beams were aligned parallel to each other and the high laser signal intensity shown in Fig. 2 indicated that two laser beams aimed at the correct target. Moreover, two LDVs were set to show negative velocity values when the target was moving in the direction away from the laser source or in the direction into the middle ear cavity.

The data acquisition system consisted of a cDAQ 7194, A/D

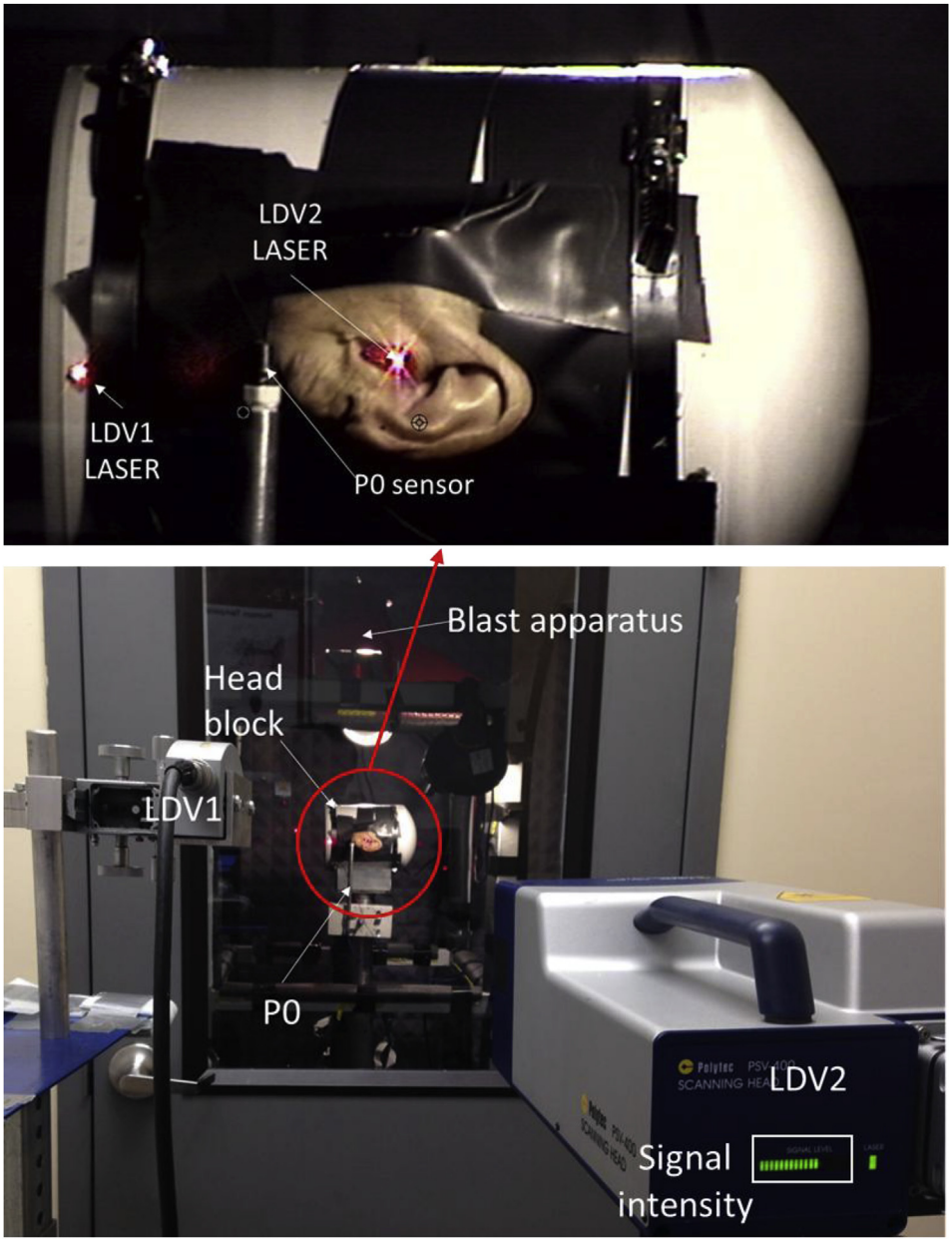


Fig. 2. Experimental setup: upper panel shows the zoomed-in view of the "head block" showing two lasers aiming at their targets; lower panel shows the blast chamber and two LDVs viewed from the outside of the blast room.

converter 9215 (National Instruments Inc., Austin, TX), and a software package LabVIEW (National Instruments Inc., Austin, TX) which collected and synchronized the signals from the pressure sensors and two LDVs. The sampling rate of the signals measured from P0, P1, LDV1, and LDV2 was 100 kHz. When the front of blast overpressure arrived at the P0 sensor, it triggered the P1 and two LDVs to start recording the signals at the length of 20 ms (2 ms prior and 18 ms post the trigger). The P0 level was designed to be around 35 kPa in this study to avoid TM perforation which has a threshold of 52.4–62.1 kPa (Engles et al., 2017). Upon the completion of the blast exposure, an otoscopic examination was conducted on each TB to ensure the TM is not ruptured.

2.2. Data processing

Due to the high-intensity energy carried by blast overpressure, the resulted vibration of the head block or TB may be high enough to interfere with the movement of the TM. Thus, the data acquired by LDV2 were a combination of the TM movement and the movement of the experimental setup including the head block and TB. To eliminate the effect of the background vibration, the velocity measured from LDV1 was subtracted from the velocity measured from LDV2. Since the velocities measured from two LDVs were synchronized and aligned in the same direction, the real-time velocity of the TM at the umbo equaled to velocity from LDV2 minus LDV1 based on the theory of relative motion.

Considering the fact that the dual-laser measurement for blast exposure-induced TM movement without previous experience, the repeatability of the TM velocity data measured from each TB was examined for 5 consistent tests or each TB experienced five repeated blasts at the same overpressure level with the identical experimental setup. The signal quality and intensity obtained from two LDVs were checked after each blast to ensure the laser beams aimed at the targets. After the reliability check, results obtained from the first test were used for time-domain analysis. The time-domain displacement signals were calculated in MATLAB using a trapezoidal approximation to the integral of the TM velocity after subtraction of the head block vibration. Then the velocity and displacement signals were converted to the frequency domain in MATLAB using fast Fourier transformation (FFT) over a frequency range of 100 Hz-50 kHz at an interval of 50 Hz.

2.3. Finite element modeling

A 3D FE model of the human ear was developed for transient analysis on the blast wave transmission through the middle ear as shown in Fig. 3 (Gan et al., 2018b; Leckness et al., 2018). The geometry and mesh of this model were based on the human ear model developed for TM perforations by Gan et al. (2009). The model consisted of the external ear canal, TM, ossicles, incudostapedial and incudomalleal joints, suspensory ligaments or muscle tendons, and simplified cochlear load. The air in the ear canal and middle ear cavity was included and modeled as fluid elements. The FE model was generated in ANSYS Workbench (ANSYS Inc., Canonsburg, PA, USA) where Fluent/ANSYS Mechanical coupled fluid-structure interaction analyses were employed to compute blast overpressure transduction through the ear canal to the middle ear. The P0, P1, and P2 were three checkpoints to check the pressure waveforms at the entrance of the ear canal, near the TM, and inside the middle ear cavity, respectively. The manubrium, ossicles, and suspensory ligaments in the middle ear cavity were modeled as elastic materials (Gan et al., 2007). The TM, TM annular ligament, joints, and stapedial annular ligament were modeled as linear viscoelastic materials (Leckness et al., 2018; Zhang and Gan, 2013). The cochlea was simplified as a mass block-dashpot system connected to the stapes footplate with parameters adjusted to reflect an input impedance of 20 GΩ. The detailed information about the geometry, FE mesh, material properties, boundary conditions, and validation of the model was reported by Leckness et al. (2018).

TM movement induced by blast overpressure was derived from the FE model by applying the experimentally recorded P0 waveform at the entrance of the ear canal in the model. The pressure in the ear canal near the TM and the displacement of the TM umbo were then calculated from ANSYS and compared with the experimental results. Considering that the displacement was measured along the stapes piston movement direction in the experiment, the model-derived displacement vector of the umbo was projected on to a vector along the piston direction for the comparison with the experimental data. The time step used for the FE simulation was 1 μs and the signal length was 2 ms.

3. Results

3.1. Measurement of TM movement under blast overpressure

The typical results obtained from the TB #5 are displayed in Fig. 4 including the pressure data of P0 and P1 and velocity data measured by LDV1 and LDV2 over 5 ms. Fig. 4a shows that the P0 (black line) displays a shape of typical Friedlander curve with a peak pressure of 30 kPa. The P1 curve (red line) shows a peak pressure of 69 kPa which is approximately twice as high as the P0 peak pressure. The pressure level increase from P0 to P1 demonstrated the amplification function of the pinna and ear canal for blast overpressure transmission from the outside of the ear to the TM. Both P0 and P1 peaks were attenuated within 1 ms and the P1 curve showed more fluctuations than the P0 curve following the first peak.

Fig. 4b exhibits the velocity data measured from LDV1 and LDV2 or the velocity of the head block and TM, respectively. The movement of the TM was significantly larger than that of the head block. Negative values of the velocity at the starting indicated that the initial movement of the TM was in the direction toward to the middle ear cavity. The velocity obtained after subtracting the head block vibration is shown in Fig. 4c. The TM velocity did not reach its maximum value immediately after the TM started moving, but reached its maximum positive and negative peak after the first negative peak. Displacement of the TM derived from integrating the velocity over time is plotted in Fig. 4d. The displacement curve indicated that the TM started to move into the middle ear cavity in response to the blast overpressure, then vibrated at an amplitude of 0.4 mm for approximately two cycles with a waveform similar to a sine wave at an almost constant amplitude. The amplitude then diminished after 2 ms.

The maximum values of the peak to peak velocity and displacement were recorded as ΔV and ΔD, respectively, as shown in Fig. 4c and d. The P0, P1, ΔV, ΔD, and the ΔD normalized by P0 obtained from five TBs are listed in Table 1 with the mean and standard deviation (SD). The ΔD/P0 value represents the TM motion induced by unit blast overpressure, a parameter relating to TM damage under blast exposure. The results in Table 1 showed that the blast overpressure at the entrance of the ear canal (P0) was 34.3 ± 5.2 kPa in this study and the pressure reaching the TM (P1) increased to 61.1 ± 23.0 kPa. The P1 pressure waves directly induced the motion of the TM and middle ear ossicular chain and resulted in a peak to peak velocity ΔV of 12.62 ± 3.63 m/s and a displacement ΔD of 0.78 ± 0.26 mm. The ΔD/P0 value was 22.9 ± 6.6 μm/kPa.

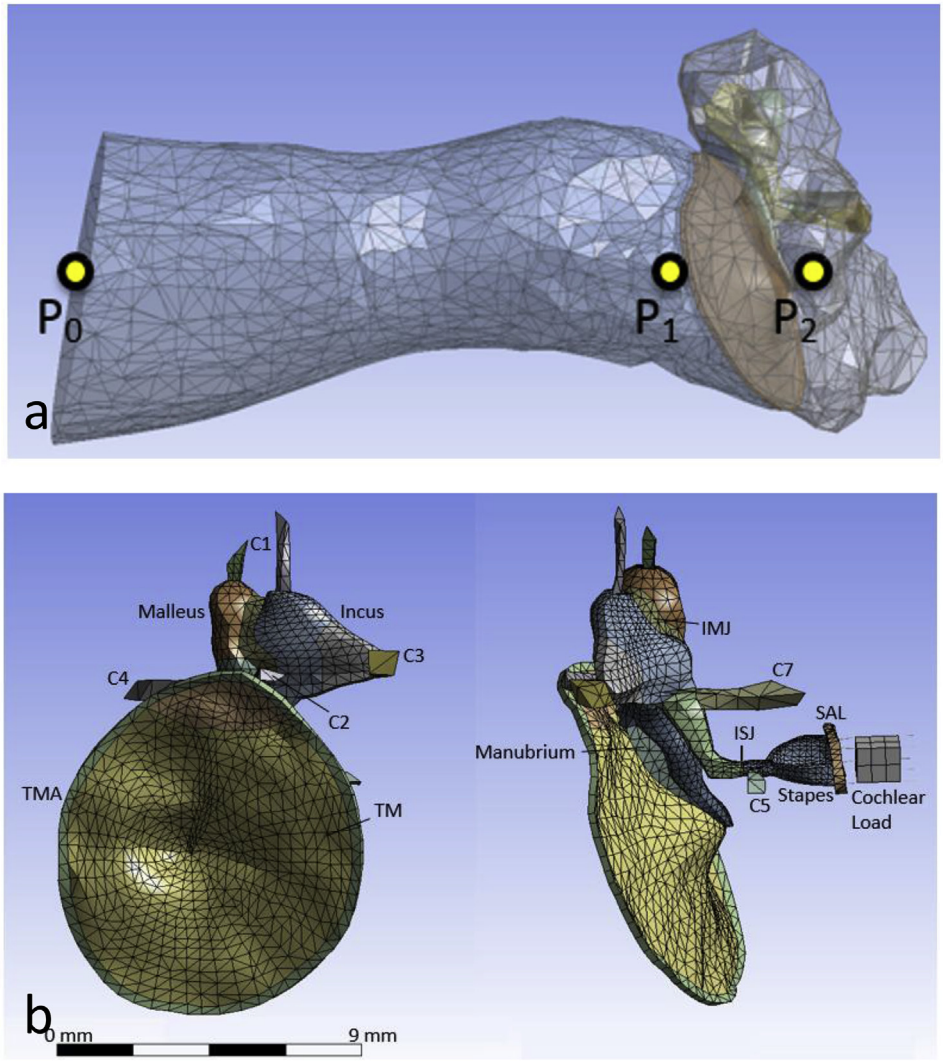


Fig. 3. FE model of the human ear developed by Gan et al. (2018b): (a) The FE model includes the ear canal, TM, and middle ear. The location of three points to monitor the pressure at the entrance of the ear canal, at the TM in the ear canal, and in the middle ear cavity are marked as P0, P1, and P2 respectively. (b) The structural mesh of the middle ear including TM, ossicles, incudomalleal joint (IMJ), incudostapedial joint (ISJ), and suspensory ligaments/muscle tendons (all Cs and SAL).

3.2. Repeatability of the experimental measurement

Fig. 5 illustrates the velocity-time curves of the TM measured from LDV2 in TB #1 during 5 repeated tests under the same blast overpressure level. The data recorded from each test were plotted in different color. It could be observed that curves obtained from five individual tests overlapped each other over the entire period of 20 ms with some fluctuations after 5 ms. Prominent positive and negative peaks could be observed at the time of 2 ms which indicated the large velocity initiated by the blast wave reached the TM. The major peaks and valleys generally remained unchanged in 5 tests while small-scale random vibrations were captured in signals after 5 ms. The other 4 TBs exhibited similar repeatable results as shown in Fig. 4 which suggested the experimental setup was reliable. Note that the recorded data shown in Fig. 5 exhibits a relatively high noise level because there was no filter applied on the LDV signals for capturing the peak value. The overlapping of multiple signals also made the noise level seems higher than it is the actual value. However, the noise did not affect the results and consistency of the data.

3.3. Time domain analysis

The P0, P1, and displacement signals measured from TB #5 were synchronized and plotted on the same time axis in Fig. 6. Note that the signals were trimmed into 1 ms-long to focus on the duration when the blast overpressure reached and started interacting with the TM. The left y-axis represents pressure while the right y-axis represents displacement. The time point at which P0 reaches its first peak was marked as t_1. Similarly, t_2 was the time point for P1 and t_3 was the time point for the TM displacement. The time delay between P0 and P1 was calculated as t_2-t_1, and the time delay between the first peaks of P1 and displacement was calculated as t_3-t_2. Fig. 6 demonstrates the delayed response of the ear when exposed to blast overpressure. The time delay between the t_1 and t_2 was 0.25 ms, which indicated that the front of the blast overpressure took 0.25 ms to propagate through the ear canal and reach the TM. The time delay between t2 and t3 was 0.02 ms, which suggested the TM reached its maximum deformation soon after the maximum pressure applied to its surface. Fig. 6 also indicated that the displacement and P1 were in opposite phase at the starting

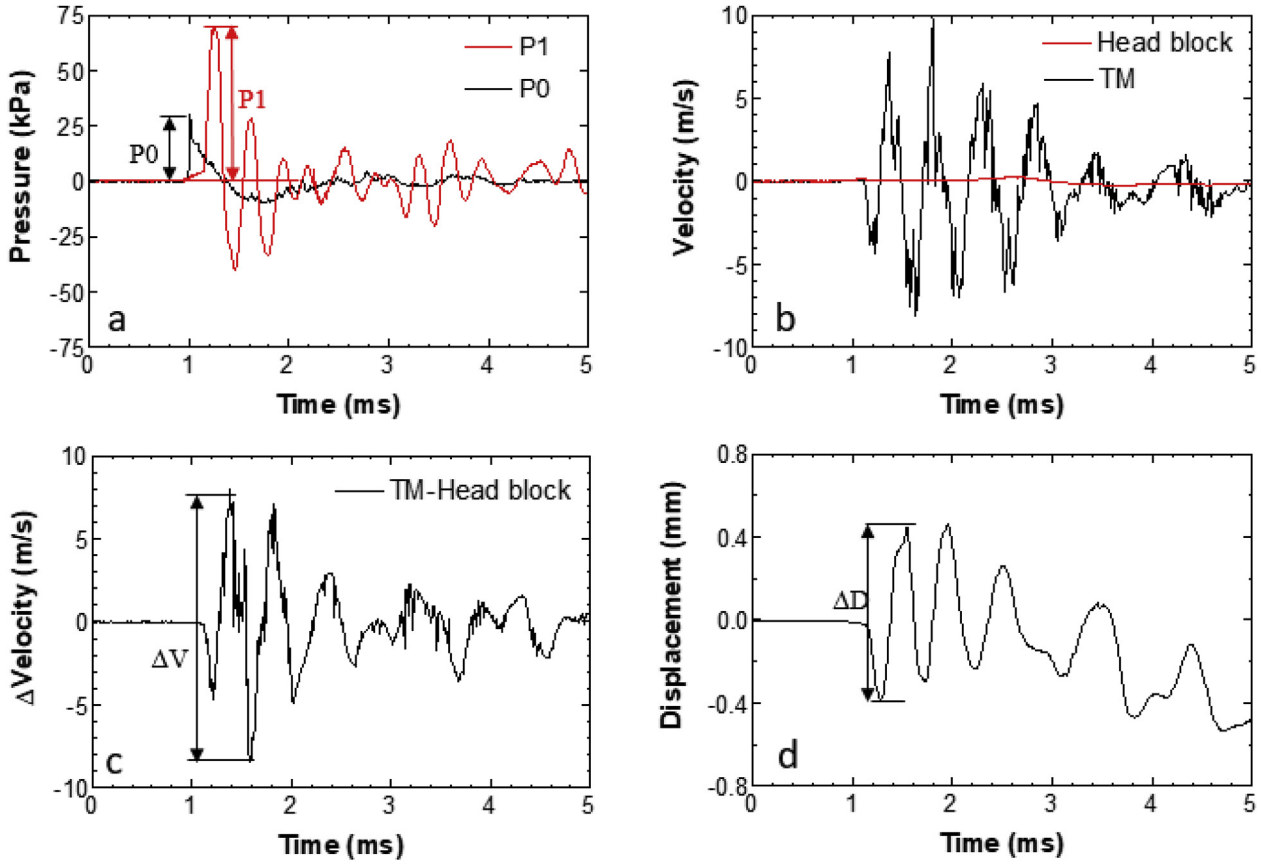


Fig. 4. Typical results from TB #5: (a) Pressure curves obtained from P0 and P1 sensor; (b) raw velocity data obtained from LDV1 and LDV2; (c) TM velocity after the subtracting head block velocity from the TM velocity; (d) TM displacement curves.

Table 1
Experimental data summary of five TBs.

Sample number	P0 (kPa)	P1 (kPa)	ΔV (m/s)	ΔD (mm)	ΔD/P0 (μm/kPa)
#1	31.0	35.9	8.44	0.55	17.6
#2	31.0	96.5	9.32	0.73	23.6
#3	40.0	53.1	13.20	0.59	14.8
#4	40.0	51.0	15.81	1.20	30.0
#5	30.0	69.0	16.32	0.84	28.4
Mean ± SD	34.3 ± 5.2	61.1 ± 23.0	12.62 ± 3.63	0.78 ± 0.26	22.9 ± 6.6

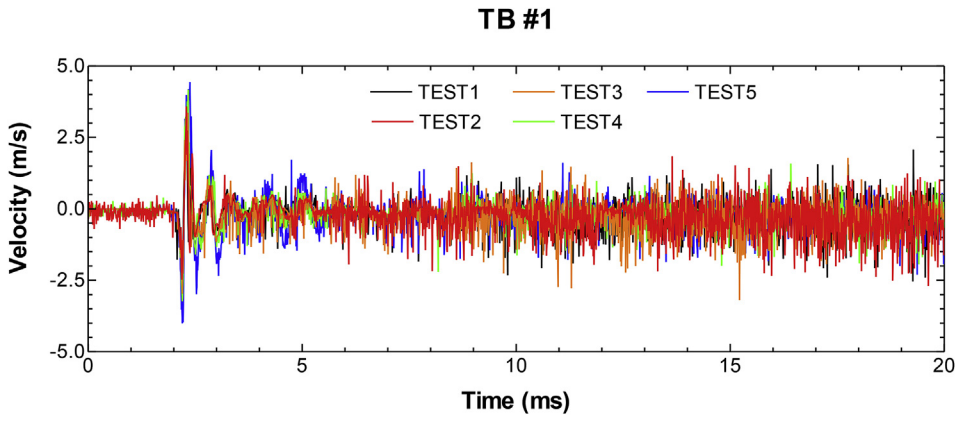


Fig. 5. Velocity-time curves obtained by 5 repeated blast tests on TB #1.

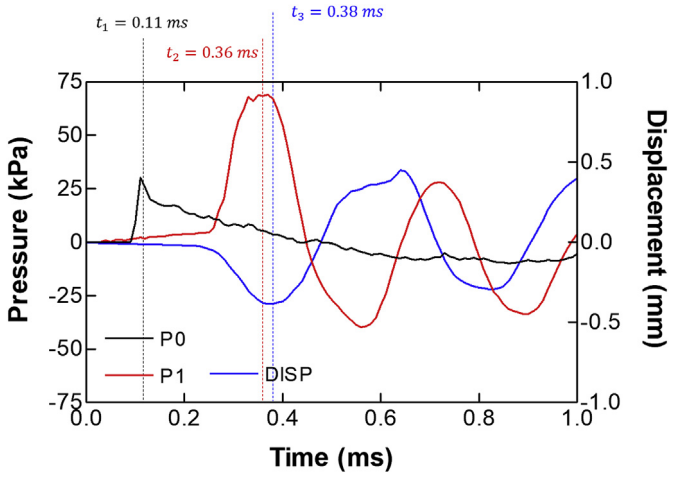


Fig. 6. Time domain waveforms showing the peak values and time delay between the P0, P1 and displacement signals measured in the experiment.

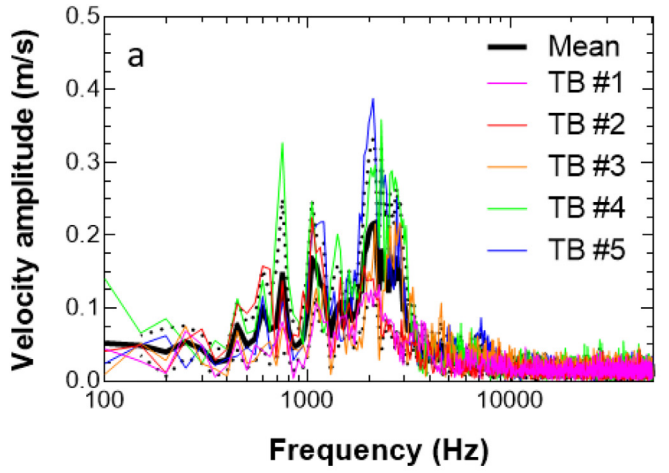
point and then the phase delay quickly decreased within 1 ms.

3.4. Frequency domain analysis

Fig. 7 illustrates the frequency spectra of velocity and displacement signals obtained from 5 TBs with the mean and SD. The velocity spectra of 5 TBs and their mean curves are plotted in Fig. 7a. Most of the frequency components concentrated between 700 Hz and 3 kHz. A prominent major peak could be observed around 2 kHz and the maximum point on the mean curve was located at 2.15 kHz with a value of 0.21 m/s. A secondary peak appeared around 700 Hz. The velocity amplitudes at the frequencies below 700 Hz or above 3 kHz were generally lower than 0.1 m/s. Fig. 7b exhibits the frequency spectra of the displacement signals obtained from 5 TBs with their mean values. The displacement amplitude decreased with the frequency exponentially over the entire frequency range from 100 Hz to 50 kHz. The mean values of the displacement were 490 μm at 100 Hz, 44 μm at 1 kHz, 4 μm at 10 kHz, and 0.7 μm at 50 kHz. The shape of the displacement curve of 5 TBs over the frequency range was similar to each other.

3.5. FE model analysis

The FE model-predicted blast pressure waveforms and the TM displacement are shown in Fig. 8 which shares the same layout as Fig. 6 with pressure on the left and displacement on the right. The input pressure P0 was obtained from the experimental data of TB #5 as it was shown in Fig. 6. The P1, ΔD, t_1, t_2, and t_3 values derived from the model were compared with the experimental results of TB #5 as listed in Table 2. The P1 predicted by the model was 52.4 kPa while the measured P1 was 69.0 kPa. The model-derived ΔD was 0.84 mm while 0.77 mm was obtained in the TB experiment. The difference between these two values was less than 10% of the experimental data. The model-predicted time delay between the P1 and P0 was 0.09 ms, which was shorter than the experimental data of 0.25 ms. The delay between the displacement and the P1 was 0.07 ms, which was very short but longer than the experimental. Comparing the waveforms in Figs. 6 and 8, the order of the first peak to appear in P1 and displacement and the peak values of the model-derived data were in agreement with the experimental data. However, the curves obtained from experiments were smoother while the model-predicted curves exhibited impulse-like sharp peaks. Fluctuations of the P1 curve after the initial peak were less



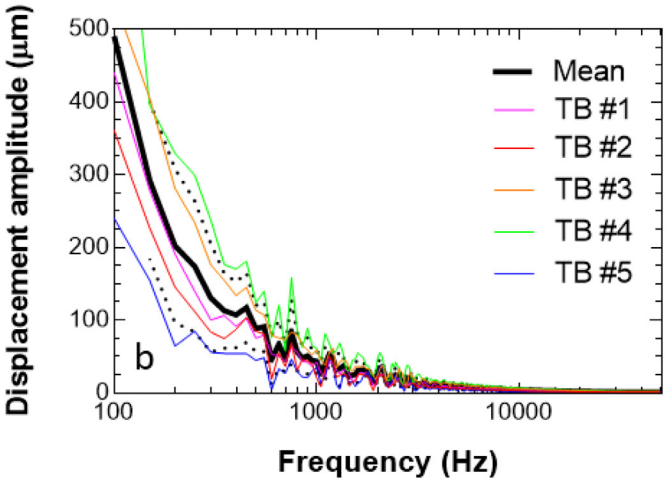


Fig. 7. Frequency domain analysis: (a) Amplitude spectrum of the umbo velocity after subtraction; (b) Amplitude spectrum of the umbo displacement. The mean and standard deviation are marked as black solid and dotted lines.

prominent in the model simulation than the experimental data. The decrease of the phase delay between the P1 and TM displacement was smaller in the model simulation than the experimental data.

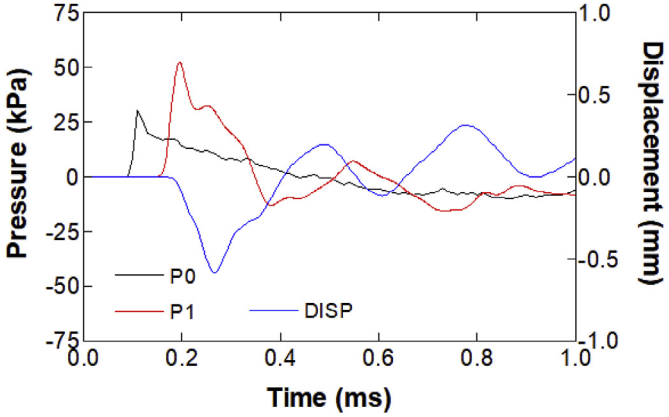


Fig. 8. Time domain waveforms showing the peak values and the time delay between the P0, P1, and displacement signals predicted by the FE model.

Table 2
Comparison between experimental data from TB #5 and model predictions.

	P0 (kPa)	P1 (kPa)	ΔD (mm)	t_1 (ms)	t_2 (ms)	t_3 (ms)
Experiment	29.7	69.0	0.84	0.11	0.36	0.38
Model	29.7	52.4	0.77	0.11	0.20	0.27

4. Discussion

4.1. Response of the middle ear under blast exposure

TM movement in response to acoustic stimulation has been used to describe the transfer function of the middle ear for sound transmission (Cheng et al., 2010; Gan et al., 2004; Rosowski et al., 2009). However, the TM motion under blast exposure has not been measured until the completion of this study. This is the first ever approach using two laser Doppler vibrometers to measure the real-time movement of the TM under blast exposure. The deformation of the TM in response to blast overpressure is identified through this study.

Blast-induced traumatic brain injury can be caused by blasts with peak pressure level as low as 20 kPa (Courtney and Courtney, 2011; Taber et al., 2006). Blast-induced hearing damage depends on the pressure entering the ear canal. As reported in the literature, the threshold of overpressure at the ear canal to rupture the human TM is 52.4–62.1 kPa (Cho et al., 2013; Engles et al., 2017; Garner and Brett, 2007), which is representative of an explosion of 0.45 kg of TNT at distance 3.35 m from the person (Kingery and Pannill, 1964). In this study, the P0 value at 30–40 kPa as listed in Table 1 may induce the damage in TM tissue, but will not rupture the TM.

The blast overpressure reaching the TM in the ear canal (P1) and the pressure transmitted into the middle ear cavity (P2) have been reported by Gan et al. (2018b) and Leckness et al. (2018) who used the same blast exposure system as that applied in this study. The reported peak values of P1 by Gan and Leckness are similar to those measured in this study as shown in Table 1, an approximately twice of the P0 value under the similar P0 input. Greene et al. (2018) reported the peak pressure in the ear canal about 1.7 times of the field pressure measured at 28 kPa, which is also consistent with our current results. For the TM displacement, Gan et al. (2004) reported that the peak to peak displacement of the human TM at the umbo was around 0.1 μm at the frequencies below 1 kHz with 90 dB SPL stimuli, which equaled to 0.16 μm/Pa. Since the velocity and displacement spectra in Fig. 7 show that most of the components located at low frequencies, the published TM displacement at low-frequencies may be able to use as a reference for comparison. However, the mean value of ΔD/P0 shown in Table 1(0.0229 μm/Pa) is much lower than those results measured under the acoustic load. Although the ratio of the peak values (ΔD/P0) measured under blast cannot represent the transfer function of the TM, it suggests that the deformation of the TM is not linearly related to input pressure when the P0 increases to a level of 35 kPa. The middle ear system, in addition, is no longer responding as a linear system to blast overpressure and the blast waveform entering the ear canal plays a critical role for energy transmission into the ear or peripheral auditory system as reported by Gan et al. (2016, 2018b) in chinchillas and human temporal bones and predicted in 3D FE model of the human ear by Leckness (2018).

Mechanical property change of the TM induced by blast exposure is another reason for the change of the blast wave transmission in the middle ear. As reported by Engles et al. (2017), the storage and loss moduli of human TM were reduced after blasts, which suggested a possible increased TM mobility after blast exposure due to the reduced stiffness of the membrane. However, further studies on the response of middle ear to blast exposure and the mechanisms of system response to blast are needed through both experiment measurement and modeling analysis.

4.2. FE simulation in comparison with experimental data

The comparison between Figs. 6 and 8 indicates that the experimental results and 3D model-predicted data are generally in an agreement. The FE model of the human ear is capable to predict the response of the TM in response to the blast. Given the same P0 input, the peak value of the TM displacement predicted by the model was about 92% of the experimental data and the P1 measured in TBs was slightly higher than the predicted by the model. The values of ΔD from experiments and model suggest that the middle ear structure of the FE model is appropriate to describe the deformation of TM under blast exposure. The viscoelastic properties of the soft tissues in FE model contribute to the nonlinear behavior of the TM and middle ear under blast exposure. For deformation at high-strain-rate, the viscoelastic material properties result in an increase of the stiffness of soft tissues which limit the deformation of the TM.

Table 2 and Fig. 8 also suggest some improvements are needed for the FE model. The P1 level predicted by the FE model is lower than the experimental data given the same P0 input. The geometry, mechanical properties, and boundary conditions of the ear canal and TM all affect the value of P1. Considering the relatively large variation of P1 listed in Table 1, the variation of experimental data may come from the difference of individual ear canal anatomy. The geometry of the ear canal in the model is also different from the TBs used in experiments. The t_2 in the model is shorter than the experimental value but the time difference between t_3 and t_2 are almost the same (0.05 ms). As shown in Fig. 3, the input pressure P0 was applied at the ear canal boundary in the model, but in TB experiments the P0 sensor was placed at 1 cm away from the entrance of the ear canal (See Fig. 2). The actual distance between locations of P0 and P1 sensors in experiments is longer than the model, which requires a longer time for the front of blast wave to propagate through. Secondly, the waveform of the experimental data is smoother than the model predicted even with similar peak values. The viscoelastic properties of the TM and middle ear soft tissues in the FE model require further optimization based on biomechanical measurements of the mechanical properties of tissues under high-strain-rate deformation.

4.3. Mechanism of blast-induced TM damage and future studies

Results shown in Fig. 4d and Table 1 indicate that the blast-induced high displacement can reach and remain at a level of 0.5–1.0 mm for 2 ms after the blast wave reaches the TM and is quickly attenuated. The maximum velocity or displacement of the TM may not appear at the very beginning but occur later within the first 2 ms. Based on the assumption that the pattern of TM movement reported in this study is similar to how the TM moves before its rupture, the damage is likely to occur in TM at a time point within the first 2 ms after the overpressure reaches the ear. The detailed mechanism of how the TM is ruptured during the blast exposure still requires further investigations to conduct experimental measurement or use the FE model to simulate the TM movement at different quadrants in additional to the umbo displacement. Tensile stress induced by the large deformation and shear stress resulted by the phase difference between different quadrants can both contribute to the rupture of the TM. It is also expected that the damage to the peripheral auditory system, such as the extremely high deformation of the ossicular chain, stapedial

annular ligament, and abruptly change of the intracochlear pressure, occur during the first 2 ms period of time following blast exposure. This is consistent with the 2–3 ms long A-duration of the intracochlear pressure resulted from the blast exposure reported by Greene et al. (2018). This is the first time the TM movement under blast exposure was measured experimentally and simulated in the FE model. As a novel investigation of the methodology with the dual-laser system on TM response to blast overpressure, the experiments were limited in 5 TBs under an overpressure level about 35 kPa. In future studies, different blast intensity levels may be tested to observe the nonlinear behavior of the TM under blast overpressure. The length and size of the external ear canal may vary among different temporal bones which contribute to the relatively large variation of P1 value listed in Table 1. The surgery to expand the entrance of the ear canal for laser beam passing through and the insertion of the P1 sensor may also add some variations between ears in this study. Moreover, to understand the detailed mechanism of blast-induced TM rupture, the next step of the experiment is to measure the movement at the center of each quadrant or the entire TM surface under blast exposure. To understand the nonlinear behavior of the middle ear under blast exposure, the real-time movement of the stapes is necessary in addition to the TM displacement.

5. Conclusion

This paper reports the first-ever approach using two laser Doppler vibrometers to measure the motion of the TM when the ear was exposed to blast at the overpressure around 35 kPa. The deformation of TM was measured with a result of 22.9 ± 6.6 μm/kPa. The frequency domain analysis on the velocity and displacement signals indicate the frequency components of the TM vibration were below 3 kHz. The delayed movement of the TM with respect to blast overpressure at the canal entrance was observed and the time for the blast wave to propagate through the ear canal to deform the TM was measured. The TM motion was then compared with that calculated from the FE model of the human ear with the measured P0 pressure wave applied at the ear canal entrance. The FE model-derived TM displacement under blast overpressure was consistent with the experimental results. This study provides a new methodology to determine the behavior of the middle ear in response to blast overpressure. The experimental data are critical for validating the FE model of the human ear for blast wave transduction and understanding the TM damage induced by blast exposure.

Acknowledgments

This study was supported by the US Department of Defense (DOD) grant W81XWH-14-1-0228.

References

Aerts, J.R.M., Dirckx, J.J.J., 2010. Nonlinearity in eardrum vibration as a function of frequency and sound pressure. Hear. Res. 263, 26–32. MEMRO 2009: Middle-Ear Science and Technology. https://doi.org/10.1016/j.heares.2009.12.022.

Aström, K.J., Murray, R.M., 2010. Feedback Systems: an Introduction for Scientists and Engineers. Princeton University Press, pp. 241–276 (Chapter 8).

Breeze, J., Cooper, H., Pearson, C.R., Henney, S., Reid, A., 2011. Ear injuries sustained by British service personnel subjected to blast trauma. J. Laryngol. Amp Otol. 125, 13–17. https://doi.org/10.1017/S0022215110002215.

Castellini, P., Martarelli, M., Tomasini, E.P., 2006. Laser Doppler Vibrometry: development of advanced solutions answering to technology's needs. Mech. Syst. Signal Process. 20, 1265–1285. Special Issue: Laser Doppler Vibrometry. https://doi.org/10.1016/j.ymssp.2005.11.015.

Champion, H.R., Holcomb, J.B., Young, L.A., 2009. Injuries from explosions: physics, biophysics, pathology, and required research focus. J. Trauma Inj. Infect. Crit. Care 66, 1468–1477. https://doi.org/10.1097/TA.0b013e3181a27e7f.

Chandra, N., Ganpule, S., Kleinschmit, N.N., Feng, R., Holmberg, A.D., Sundaramurthy, A., Selvan, V., Alai, A., 2012. Evolution of blast wave profiles in simulated air blasts: experiment and computational modeling. Shock Waves 22, 403–415. https://doi.org/10.1007/s00193-012-0399-2.

Cheng, J.T., Aarnisalo, A.A., Harrington, E., Hernandez-Montes, M., del, S., Furlong, C., Merchant, S.N., Rosowski, J.J., 2010. Motion of the surface of the human tympanic membrane measured with stroboscopic holography. Hear. Res. 263, 66–77. MEMRO 2009: Middle-Ear Science and Technology. https://doi.org/10.1016/j.heares.2009.12.024.

Cheng, J.T., Remenschneider, A., Kozin, E., Furlong, C., Rosowski, J.J., 2017. Nonlinear response of human middle ear to high level sound. J. Acoust. Soc. Am. 141, 3897–3898. https://doi.org/10.1121/1.4988760.

Cho, S.-I., Gao, S.S., Xia, A., Wang, R., Salles, F.T., Raphael, P.D., Abaya, H., Wachtel, J., Baek, J., Jacobs, D., Rasband, M.N., Oghalai, J.S., 2013. Mechanisms of hearing loss after blast injury to the ear. PLoS One 8, e67618. https://doi.org/10.1371/journal.pone.0067618.

Courtney, M.W., Courtney, A.C., 2011. Working toward exposure thresholds for blast-induced traumatic brain injury: thoracic and acceleration mechanisms. NeuroImage 54, S55–S61. International Brain Mapping & Intraoperative Surgical Planning Society (IBMISPS)2009 Supplement. https://doi.org/10.1016/j.neuroimage.2010.05.025.

Dougherty, A.L., MacGregor, A.J., Han, P.P., Viirre, E., Heltemes, K.J., Galarneau, M.R., 2013. Blast-related ear injuries among U.S. military personnel. J. Rehabil. Res. Dev. 50, 893–904. https://doi.org/10.1682/JRRD.2012.02.0024.

Engles, W.G., Wang, X., Gan, R.Z., 2017. Dynamic properties of human tympanic membrane after exposure to blast waves. Ann. Biomed. Eng. 45, 2383–2394. https://doi.org/10.1007/s10439-017-1870-0.

Gan, R.Z., Cheng, T., Dai, C., Yang, F., Wood, M.W., 2009. Finite element modeling of sound transmission with perforations of tympanic membrane. J. Acoust. Soc. Am. 126, 243–253. https://doi.org/10.1121/1.3129129.

Gan, R.Z., Jiang, S., Pineda, M., 2018a. Age-related full-field motion change in baboon tympanic membrane. In: AIP Conf. Proc. 1965, p. 110002. https://doi.org/10.1063/1.5038502.

Gan, R.Z., Leckness, K., Nakmali, D., Ji, X.D., 2018b. Biomechanical measurement and modeling of human eardrum injury in relation to blast wave direction. Mil. Med. 183, 245–251. https://doi.org/10.1093/milmed/usx149.

Gan, R.Z., Nakmali, D., Ji, X.D., Leckness, K., Yokell, Z., 2016. Mechanical damage of tympanic membrane in relation to impulse pressure waveform – a study in chinchillas. Hear. Res. 340, 25–34. MEMRO 2015 – Basic Science meets Clinical Otology. https://doi.org/10.1016/j.heares.2016.01.004.

Gan, R.Z., Reeves, B.P., Wang, X., 2007. Modeling of sound transmission from ear canal to cochlea. Ann. Biomed. Eng. 35, 2180–2195. https://doi.org/10.1007/s10439-007-9366-y.

Gan, R.Z., Wood, M.W., Dormer, K.J., 2004. Human middle ear transfer function measured by double laser interferometry system. Otol. Neurotol. Off. Publ. Am. Otol. Soc. Am. Neurotol. Soc. Eur. Acad. Otol. Neurotol. 25, 423–435.

Garner, M.J., Brett, S.J., 2007. Mechanisms of injury by explosive devices. Anesthesiol. Clin. Trauma 25, 147–160. https://doi.org/10.1016/j.anclin.2006.11.002.

Garth, R.J.N., 1994. Blast injury of the auditory system: a review of the mechanisms and pathology. J. Laryngol. Otol. 108, 925–929. https://doi.org/10.1017/S0022215100128555.

Goode, R.L., Killion, M., Nakamura, K., Nishihara, S., 1994. New knowledge about the function of the human middle ear: development of an improved analog model. Am. J. Otol. 15, 145–154.

Greene, N.T., Alhussaini, M.A., Easter, J.R., Argo, T.F., Walilko, T., Tollin, D.J., 2018. Intracochlear pressure measurements during acoustic shock wave exposure. Hear. Res. 365, 149–164. https://doi.org/10.1016/j.heares.2018.05.014.

Greene, N.T., Jenkins, H.A., Tollin, D.J., Easter, J.R., 2017. Stapes displacement and intracochlear pressure in response to very high level, low frequency sounds. Hear. Res. 348, 16–30. https://doi.org/10.1016/j.heares.2017.02.002.

Hawa, T., Gan, R.Z., 2014. Pressure distribution in a simplified human ear model for high intensity sound transmission. J. Fluid Eng. 136, 111108-111108–7. https://doi.org/10.1115/1.4027141.

Keefe, D.H., Levi, E., 1996. Maturation of the middle and external ears: acoustic power-based responses and reflectance tympanometry. Ear Hear. 17, 361.

Kingery, C.N., Pannill, B.F., 1964. Peak Overpressure Vs Scaled Distance for TNT Surface Bursts (Hemispherical Charges). Ballistics Research Laboratory. Report No. 1518.

Leckness, K., Nakmali, D., Gan, R.Z., 2018. Computational modeling of blast wave transmission through human ear. Mil. Med. 183, 262–268. https://doi.org/10.1093/milmed/usx226.

Mathews, Z.R., Koyfman, A., 2015. Blast injuries. J. Emerg. Med. 49, 573–587. https://doi.org/10.1016/j.jemermed.2015.03.013.

Patterson, J.H., Hamernik, R.P., 1997. Blast overpressure induced structural and functional changes in the auditory system. Toxicology 121, 29–40. The Molecular Mechanism(s) of Blast Overpressure-Induced Injury. https://doi.org/10.1016/S0300-483X(97)03653-6.

Peacock, J., Pintelon, R., Dirckx, J., 2015. Nonlinear vibration response measured at umbo and stapes in the rabbit middle ear. J. Assoc. Res. Otolaryngol. 16, 569–580. https://doi.org/10.1007/s10162-015-0535-7.

Régloix, S.B. de, Crambert, A., Maurin, O., Lisan, Q., Marty, S., Pons, Y., 2017. Blast injury of the ear by massive explosion: a review of 41 cases. J. Roy. Army Med. Corps 163, 333–338. https://doi.org/10.1136/jramc-2016-000733.

Rosowski, J.J., Cheng, J.T., Ravicz, M.E., Hulli, N., Hernandez-Montes, M., Harrington, E., Furlong, C., 2009. Computer-assisted time-averaged holograms

of the motion of the surface of the mammalian tympanic membrane with sound stimuli of 0.4–25 kHz. Hear. Res. 253, 83–96. https://doi.org/10.1016/j.heares.2009.03.010.

Rothberg, S.J., Allen, M.S., Castellini, P., Di Maio, D., Dirckx, J.J.J., Ewins, D.J., Halkon, B.J., Muyshondt, P., Paone, N., Ryan, T., Steger, H., Tomasini, E.P., Vanlanduit, S., Vignola, J.F., 2017. An international review of laser Doppler vibrometry: making light work of vibration measurement. Opt. Lasers Eng. 99, 11–22. Laser Doppler vibrometry. https://doi.org/10.1016/j.optlaseng.2016.10.023.

Ruah, C.B., Schachern, P.A., Zelterman, D., Paparella, M.M., Yoon, T.H., 1991. Age-related morphologic changes in the human tympanic membrane: a light and electron microscopic study. Arch. Otolaryngol. Neck Surg. 117, 627–634. https://doi.org/10.1001/archotol.1991.01870180063013.

Sridhara, S.K., Rivera, A., Littlefield, P., 2013. Tympanoplasty for blast-induced perforations ,the walter reed experience. Otolaryngol. Neck Surg. 148, 103–107. https://doi.org/10.1177/0194599812459326.

Sundaramurthy, A., Alai, A., Ganpule, S., Holmberg, A., Plougonven, E., Chandra, N., 2012. Blast-induced biomechanical loading of the rat: an experimental and anatomically accurate computational blast injury model. J. Neurotrauma 29, 2352–2364. https://doi.org/10.1089/neu.2012.2413.

Taber, K.H., Warden, D.L., Hurley, R.A., 2006. Blast-related traumatic brain injury: what is known? J. Neuropsychiatry Clin. Neurosci. 18, 141–145. https://doi.org/10.1176/jnp.2006.18.2.141.

Voss, S.E., Rosowski, J.J., Merchant, S.N., Peake, W.T., 2000. Acoustic responses of the human middle ear. Hear. Res. 150, 43–69. https://doi.org/10.1016/S0378-5955(00)00177-5.

Walter, P.L., 2004. Air-blast and the science of dynamic pressure measurements. Sound Vib. 38, 10–17.

Wang, X., Guan, X., Pineda, M., Gan, R.Z., 2016. Motion of tympanic membrane in Guinea pig otitis media model measured by scanning laser Doppler vibrometry. Hear. Res. 339, 184–194. https://doi.org/10.1016/j.heares.2016.07.015.

Yang, C., Guo, M., Liu, H., Yan, K., Xu, Y.J., Miao, H., Fu, Y., 2013. A multi-point laser Doppler vibrometer with fiber-based configuration. Rev. Sci. Instrum. 84, 121702. https://doi.org/10.1063/1.4845335.

Yeh, D.D., Schecter, W.P., 2012. Primary blast injuries—an updated concise review. World J. Surg. 36, 966–972. https://doi.org/10.1007/s00268-012-1500-9.

Zhang, X., Gan, R.Z., 2013. Finite element modeling of energy absorbance in normal and disordered human ears. Hear. Res. 301, 146–155. MEMRO 2012 – Middle-Ear Bridge between Science and Otology. https://doi.org/10.1016/j.heares.2012.12.005.

Zhang, X., Guan, X., Nakmali, D., Palan, V., Pineda, M., Gan, R.Z., 2014. Experimental and modeling study of human tympanic membrane motion in the presence of middle ear liquid. J. Assoc. Res. Otolaryngol. 15, 867–881. https://doi.org/10.1007/s10162-014-0482-8.

Characterization of Protection Mechanisms to Blast Overpressure for Personal Hearing Protection Devices – Biomechanical Measurement and Computational Modeling

Rong Z. Gan, PhD; Kegan Leckness, MS; Kyle Smith, MS; Xiao D. Ji, PhD

ABSTRACT Hearing damage induced by blast exposure is a common injury in military personnel involved in most operation activities. Personal hearing protection devices such as earplugs come as a standard issue for Service members; however, it is not clear how to accurately evaluate the protection mechanisms of different hearing protection devices for blast overpressures (BOP). This paper reports a recent study on characterization of earplugs' protective function to BOP using human cadaver ears and 3D finite element (FE) model of the human ear. The cadaver ear mounted with pressure sensors near the eardrum (P1) and inside the middle ear (P2) and with an earplug inserted was exposed to BOP in the blast test chamber. P1, P2, and BOP at the ear canal entrance (P0) were simultaneously recorded. The measured P0 waveform was then applied at the ear canal entrance in the FE model and the P1 and P2 pressures were derived from the model. Both experiments and FE modeling resulted in the P1 reduction which represents the effective protection function of the earplug. Different earplugs showed variations in pressure waveforms transmitted to the eardrum, which determine the protection level of earplugs.

INTRODUCTION

Blast overpressure is a high intensity disturbance in the ambient air pressure that is characterized by an intense impulse pressure wave of over 170 dB SPL. Exposure to high-intensity sound or blast overpressure waves is considered an intrinsic situation faced by military personnel. The direct consequence of blast injury to the auditory system is acute hearing loss. Personal hearing protection devices (HPDs) such as earplugs (EPs) come as a standard issue for Service members.

The protective function of different EPs to impulsive noises at peak sound pressure level below 168 dB (0.75 psi or 5.17 kPa) has been reported by using acoustic test fixtures (ATFs).[1,2] The ATF, an artificial head containing a human ear simulator, was used in their studies to evaluate the performance of different EPs. The impulse peak insertion loss of the EPs or HPDs were measured over the range of impulse levels at 134, 150, and 168 dB. However, the ear simulator inside the ATF cannot accurately represent the biomechanics of a real ear in response to blast overpressure because the anatomic structure of the individual ear and the tissue mechanical response to blast pressure such as the eardrum or tympanic membrane (TM) and the middle ear ossicular chain are not included in ATF, which may affect the accuracy of HPDs' evaluation.

A "head block" attached with human cadaver ear or temporal bone and mounted with two pressure sensors, one near the TM in the ear canal and one inside the middle ear cavity, was developed in our lab to measure the transmission of blast overpressure through the ear.[3] The head block provides an accurate experimental setup to test the transfer functions of the ear canal and middle ear in response to blast overpressure (BOP) and characterize the relationship between the TM rupture threshold and overpressure waveform with the anatomic structure of the human ear.[3–5] Using the head block with cadaver ears, the changes of human TM tissue mechanical properties after multiple blast exposures have been reported by Engles et al[4] and Lou et al[5] with microstructural variations of the TM.

In this paper, we report a recent study on characterization of EPs' protective function to BOP using the head block with human cadaver ears and the 3D finite element (FE) model of the human ear for blast wave transmission. Different EPs were inserted to cadaver ears and exposed to BOP level around 189 dB (8 psi or 57 kPa) using a compressed nitrogen-driven blast apparatus located inside the anechoic chamber in our lab.[3,6] The blast pressures at the entrance of the ear canal (P0), near the TM in the canal (P1), and behind the TM in the middle ear (P2) were simultaneously monitored during blast tests. The "effective protection" function of the earplug, defined as the P1 reduction in dB, was measured to represent the amount of pressure reaching on the TM reduced by inserting the earplug. The Combat Arms, Battle Plugs, the foam, and the Lyric EPs were included in the study. The established FE model of the human ear was further developed to have the EPs simulated in the ear canal and predict their protective function.[7] This study provides new methodologies for biomechanical characterization of military EPs' blast attenuation rating which is currently not available.

School of Aerospace and Mechanical Engineering, University of Oklahoma, 865 Asp Avenue, Norman, OK 73019.

doi: 10.1093/milmed/usy299

© Association of Military Surgeons of the United States 2019. All rights reserved. For permissions, please e-mail: journals.permissions@oup.com.

Downloaded from https://academic.oup.com/milmed/article-abstract/184/Supplement_1/251/5418722 by Johns Hopkins University user on 27 March 2019

METHODS

Experimental Setup and Protocol

Human Cadaver Ear Specimen Preparation

Fresh human cadaver ear or temporal bone which includes a complete normal organ of the ear was mounted with two pressure sensors and then assembled to the head block inside the blast chamber (Fig. 1A, set up for vertical exposure). A third sensor was placed at the entrance of the ear canal. The three pressure sensors simultaneously monitor the blast pressure at the entrance of the ear canal (P0), near the TM in the canal (P1), and behind the TM in the middle ear cavity (P2) as shown in the schematic of Figure 1B. P0 sensor (Model 102B16, PCB Piezotronics, Depew, NY, USA) was placed 1 cm lateral to the ear canal opening and P1 and P2 (Model 105C02, PCB Piezotronics) were placed 3 mm from the TM in the canal and inside the middle ear cavity through the Eustachian tube, respectively. The surgical approach for insertion of the P1 and P2 sensors was done carefully under a surgical microscope to assure the P1 sensor's surface was edged at the ear canal wall and the P2 sensor was behind the TM and extended from the Eustachian tube. It is important to make sure P1 sensor's position would not affect the transduction pathway. In the ear without earplug, the P0 and P1 difference shows the transfer function of the ear canal in response to blast wave; in the ear with an earplug inserted in the canal, the difference between P0 and P1 indicates the attenuation of the earplug to BOP.

HPDs or EPs Tested

Two types of military EPs, Combat Arms earplugs (CAEs, Aearo Technologies, Indianapolis, IN, USA) and Battle Plugs (Moldex Metrix Inc., Culver City, CA, USA), and the commonly used foam earplugs (3M Co., St. Paul, MN, USA) were selected for this study (Fig. 2A–C). Lyric hearing aid/earplug (Phonak, LLC, Warrenville, IL, USA) was also included in this study as a collaborative research with Walter Reed National Military Medical Center (PI: Douglas Brungart). As shown in Figure 2D, the Lyric earplug is deep in the canal with an insertion depth between 4 and 16 mm and the distance to the TM remaining 4 mm. Note that the Lyric was tested as an inactive (without battery) in deep canal position earplug like other HPDs in this study.

A total of 48 fresh human temporal bones (TBs) were used in this study for testing four types of EPs: 14 TBs for CAEs (donors' age 79.3 ± 7.7), 15 TBs for Battle Plugs (age 77.9 ± 8.7), 13 TBs for foam EPs (age 74.5 ± 7.6), and 6 TBs for Lyric EPs (age 79.7 ± 5.2). The TBs were obtained from Life Legacy Foundation, a certified human tissue supply source for military research. The study protocol was approved by the U.S. Army Medical Research and Material Command Office of Research Protections.

The CAEs, Battle Plug, and Foam EPs were inserted into the ear canal as shown in Figure 3A–C. There were two settings for CAE and Battle Plug: maximum (closed orifice) and minimum (open orifice) protection settings. Figure 3D shows the cadaver ear inserted with a Lyric earplug. Laser reflective tape was placed on the lateral solid surface for measuring the movement of Lyric earplug during blast exposure, which is not included in this paper. Note that the Lyric EPs were deeply inserted into the ear canal by an audiologist from Phonak, LLC and other EPs were inserted by a research technician in our lab. Figure 3E displays the experimental setup. The blast exposure in the front setup (blast wave from the front of the face) was used for all experiments in this study.

Blast Overpressure Testing Procedure

The "head block" was exposed to open-field blast inside an anechoic test chamber in Biomedical Engineering Laboratory at the University of Oklahoma. A compressed nitrogen-driven blast apparatus was utilized to produce blast overpressure by rupturing a polycarbonate film (McMaster-Carr, Atlanta, GA, USA). Blast overpressures level was controlled by changing the thickness of the film, or the distance from the blast reference plane. Overpressure level at the canal entrance (P0) was controlled by varying the distance of the head block from the blast reference plane and the blast wave direction was along the front of the face with respect to the head.

The pressure sensor signal was measured by cDAQ 7194 and A/D converter 9,215 (National Instruments Inc., Austin, TX, USA) with the sampling rate of 100k/s (10 μs dwell time). The LabVIEW software package (NI Inc.) was used for data acquisition and analysis. Note that the sampling rate is sufficient for the waveform recorded in this study.

Blast experiment with the TB without the earplug was performed first and the pressure waveforms P0, P1 and P2 were simultaneously recorded. Then, the earplug was inserted into the ear canal and the blast test was conducted again. Note that the P0 pressure level recorded at the entrance of the ear canal should be the same in the tests of with and without EPs. The BOP level was maintained around 189 dB or 8 psi or 57 kPa (188–190, 7–9, 56–58, respectively) below the TM rupture threshold.[3]

Waveform Analysis

Blast pressure energy spectra analysis on recorded waveforms (P0 and P1) in the time domain was conducted in MATLAB to determine the signal energy distribution over the frequencies without an earplug and with four different EPs. First, the recorded pressure waveforms were converted to pressure distributions over the frequencies of 0.2–20 kHz by using Fast Fourier Transform spectral analysis. Next, following the methods of impulse signal energy distribution theory reported by Gan et al[6] the total sound exposure was divided by the standard characteristic impedance of the air ρc as impulse energy flux (energy per unit area) and expressed as:

Downloaded from https://academic.oup.com/milmed/article-abstract/184/Supplement_1/251/5418722 by Johns Hopkins University user on 27 March 2019

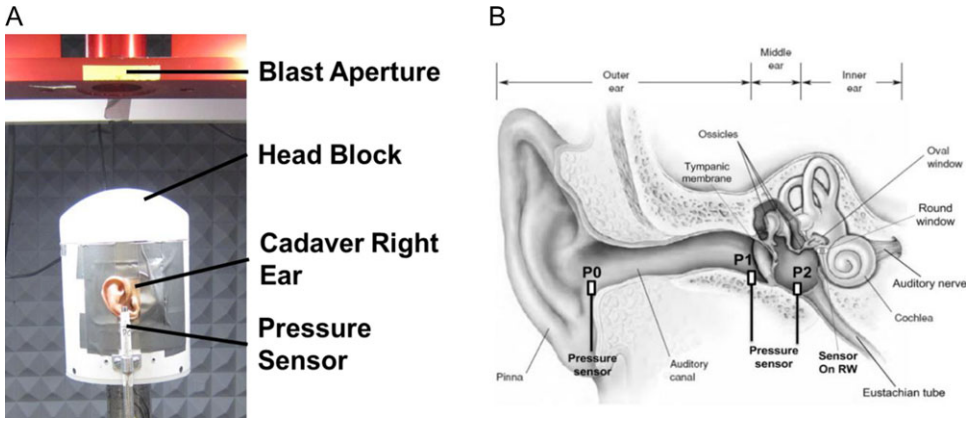


FIGURE 1. (A) Picture of experimental setup with the head block along the vertical blast wave direction inside the test chamber. (B) Schematic for simultaneously measuring blast overpressure transduction through the ear with three pressure sensors.

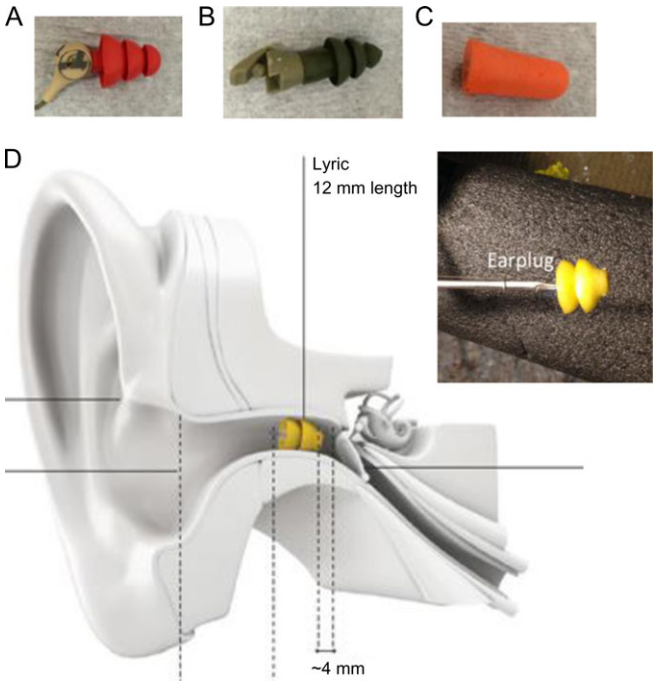


FIGURE 2. EPs tested with human cadaver ears. (A) Combat Arms earplug; (B) Battle Plug; (C) foam earplug; (D) lyric earplug.

$$E* = \frac{1}{\rho c}\int_0^T p^2(t)\,dt, \quad [\mathrm{J/m^2}] \qquad (1)$$

where $p(t)$ is the instantaneous value of acoustic pressure in Pa or N/m^2, dt is the time increment for scanning of acoustic pressure in seconds, T is the duration of P(t), and ρc = 406 mks rayls to produce a quantity with units of energy flux (i.e., J/m^2). Both ρ and c are pressure-dependent in the shock front. The duration of T = 6 ms was used for calculation in the present study.

Eight octave band-pass filters with center frequencies at 125 Hz, 250 Hz, 500 Hz, 1 kHz, 2 kHz, 4 kHz, 8 kHz, and 16 kHz were designed. To catch signals at frequencies lower than 125 Hz and higher than 16 kHz, additional low-pass (L125, cutoff at 88 Hz) and high-pass (H16k, cutoff at 22.627 kHz) filters were designed. The MATLAB SPTOOL was used to create all the filters (10 bands). The energy in each band was normalized with respect to the total sound energy in that band, and the resulting energy fluxes of the experimental and predicted waveforms were compared. Note that the energy analysis on P2 waveform was not reported here because the P1 pressure waveforms are more important than P2 due to their direct responsibility for TM damage and ossicular chain motion and reflecting the protective function of the earplug.

FE Modeling

3D FE Model of the Human Ear for Blast Wave Transduction

A 3D FE model of the human ear for simulating the blast wave transduction through the ear was recently developed in our lab.[3,7,8] The model consists of the ear canal, TM, TM annulus (TMA), three ossicles connected by two joints: incudomelleolar joint (IMJ) and incudostapedial joint (ISJ), middle ear suspensory ligaments/muscle tendons, stapedial annular ligament (SAL), and the middle ear cavity (Fig. 4). The cochlea was not included in this model, but a cochlear load was applied on the stapes footplate by a mass block-dashpot system with the cochlear input impedance of 20 GΩ.[9] The cochlear impedance was defined as the pressure per unit volume velocity of the stapes footplate.

This FE model of the human ear was generated in ANSYS Workbench (ANSYS Inc., Canonsburg, PA, USA) where Fluent/ANSYS Mechanical coupled fluid-structure interaction (FSI) analyses were employed to compute blast overpressure transduction from the environment to the TM and middle ear.[8] Viscoelastic material properties were assigned to soft tissues in the middle ear including the TM, TMA, IMJ, ISJ, and SAL. The experimentally recorded P0 waveforms from the head block with cadaver TBs were

Downloaded from https://academic.oup.com/milmed/article-abstract/184/Supplement_1/251/5418722 by Johns Hopkins University user on 27 March 2019

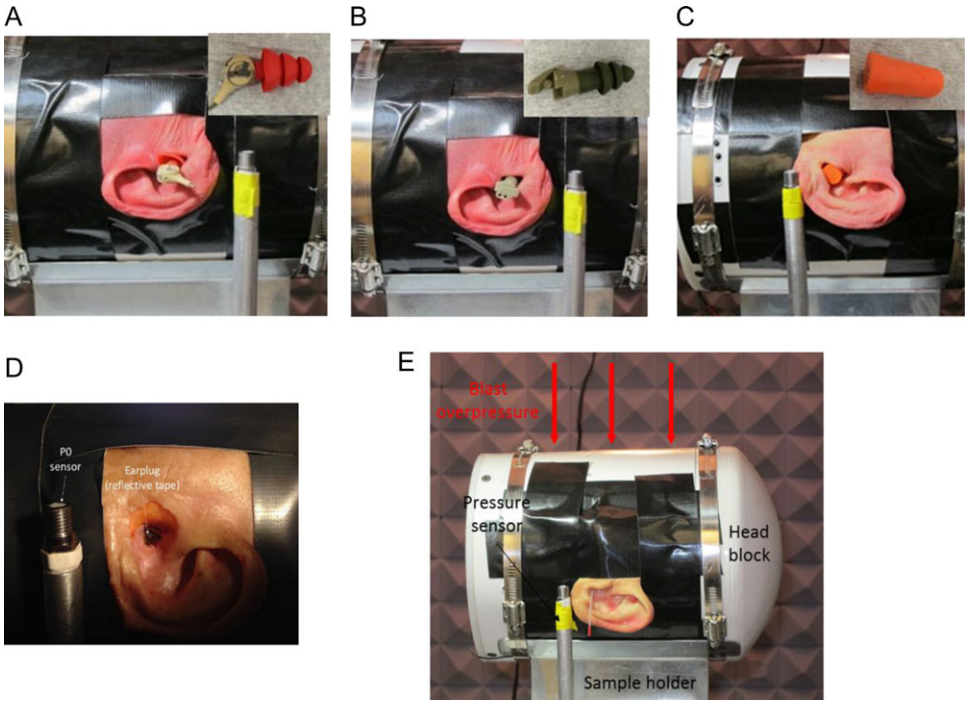


FIGURE 3. Pictures of the experimental setup with earplug in human cadaver ear attached to the head block in front setup (blast wave from the front of the face). (A) Combat Arms, (B) Battle Plug, (C) foam, (D) lyric earplug, (E) entire head block attached with the human ear inside the blast chamber. Note that the yellow taped pole was the P0 pressure sensor and the reflective tape pointed on the Lyric earplug was used for laser measurement of Lyric's movement under blast exposure, which is not included in this paper.

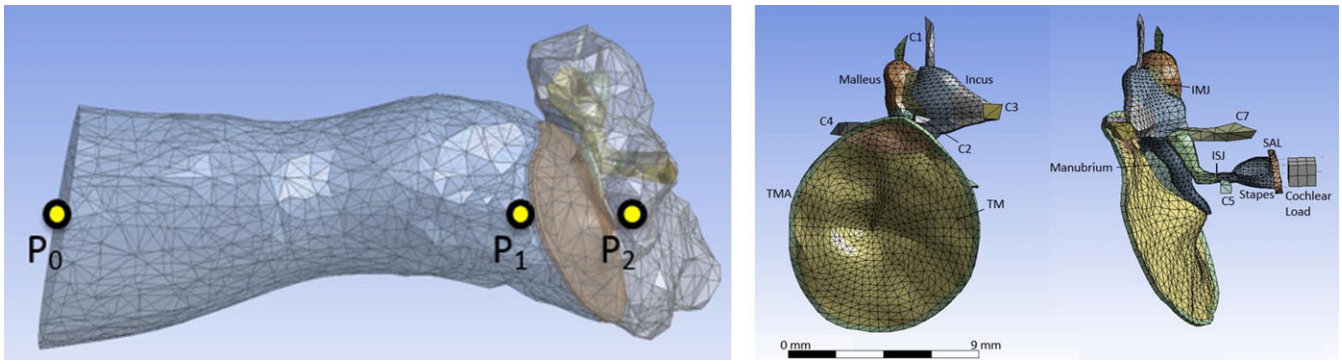


FIGURE 4. (Left) FE model of the human ear comprised of the ear canal, TM, middle ear ossicles, and middle ear cavity. The locations for pressure monitoring points are designated as P0, P1, and P2. (Right) Structural mesh of the model, showing the TM, TMA, middle ear ossicles, IMJ, ISJ, suspensory ligaments/muscle tendons (all Cs and SAL), and cochlear load.

applied onto the boundary at the entrance of the ear canal and the pressure waveforms P1 and P2 were then calculated.

FE Modeling of EPs for Blast Wave Transduction

The original FE model published by Gan et al[9] does not have the canal skin. However, to simulate blast overpressure transduction through the ear canal with the earplug inserted, the ear canal skin was added to the model (Fig. 5).[7] A layer of skin with an average thickness of 1.5 mm was added to the ear canal as an elastic isotropic solid with properties of: 0.42 MPa (Young's modulus), 1,050 kg/m^3 (density), 0.43 (Poisson's ratio), and 0.2 (loss factor). Material beta (β) damping was applied to the skin to introduce loss factor, a convenient value to represent viscoelastic behavior via following equation,

$$\beta = \frac{\eta}{\pi f} \tag{2}$$

where β is the material beta damping factor, η is the loss factor, and f is frequency. A complication arises when prescribing beta damping in a transient analysis due to the frequency component of the damping, thus, an average value was taken from 0 to 10 kHz. Fluid-structure interfaces were applied

Downloaded from https://academic.oup.com/milmed/article-abstract/184/Supplement_1/251/5418722 by Johns Hopkins University user on 27 March 2019

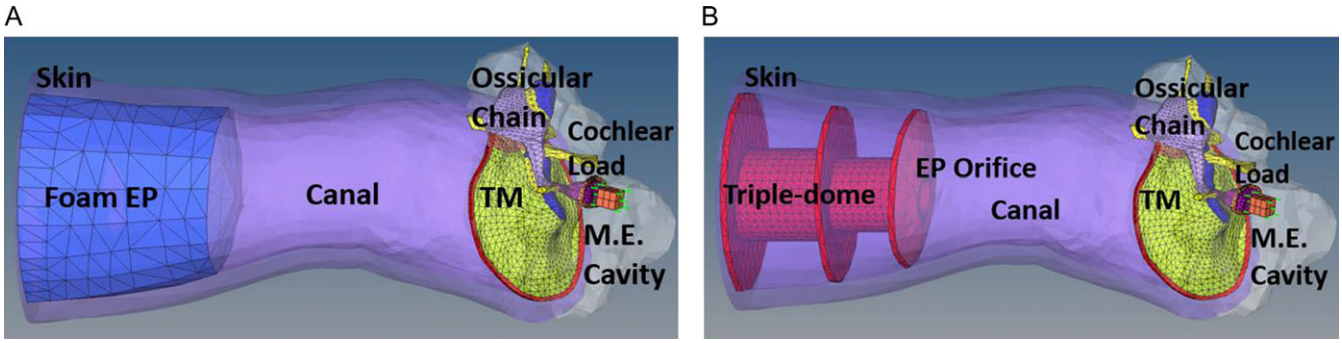


FIGURE 5. FE modeling of EPs in the ear canal. (A) The foam earplug simulated in the ear canal. (B) Combat Arms earplug named as "Triple-Dome" simulated in the ear canal. The ear canal, canal skin, earplug (EP), EP orifice, TM, middle ear ossicular chain, middle ear (M.E.) cavity, and cochlear load are displayed in the figure.

between the skin and fluid (air) of the ear canal in ANSYS Mechanical and Fluent, respectively.

Two types of EPs were simulated in the FE model of the human ear: the classic foam EP and the CAE which featured a variable orifice and silicon triple-dome structure (Fig. 5). To create the foam occlusion, the fluid domain of the ear canal was modified in addition to generating the structure of the foam EP to completely occlude the ear canal (Fig. 5A); i.e., no leaks were present, and the nodes of the foam EP and skin were coincident along the wall of the ear canal. The foam EP insertion depth as measured from the entrance of the canal to the EP's apex was 12 mm. The foam EP was assumed to be an elastic solid[10,11] with Young's modulus of 22.2 kPa and density of 228 kg/m^3 reported by Leckness.[7]

During experiments of the CAE, it was observed that only the first two domes were fully inserted into the ear canal. The primary function of the third dome was to obstruct the entrance to the ear canal and only the apex of the third dome was set inside (Fig. 5B). Note that as the hard-plastic core of the CAE terminates prior to the apex of the third dome, the hard-plastic core was not included in the FE model. There is truly no possible effect to the model nor its outcomes of not including the core. The CAE was generated within the human FE model with a total length of 11.4 mm, the diameter of EP orifice of 2.1 mm. The distances between the first dome and second dome flanges and that between the second and third dome flanges were 5 mm and 6 mm, respectively. The detailed model of CAE can be found in Leckness.[7]

Figure 5B shows the FE model of human ear with CAE triple-dome occlusion. The applied silicon material properties were adapted from Viallet et al.[12] The EP was defined as elastic isotropic solid with properties: 1.2 MPa (Young's modulus), 1,150 kg/m^3 (density), 0.48 (Poisson's ratio), and 0.12 (loss factor). The loss factor here was also represented as the average material beta damping factor from 0 to 10 kHz. Four FSIs were applied between the EP and air in the ear canal. Since the CAE model does not include the hard-plastic core, the CAE' maximum and minimum protection settings' exposure waveforms were not utilized in this study. Triple-dome-only P0 blast exposure waveforms obtained from one temporal bone (TB16-30R) were applied to the skin and triple-dome EP at the entrance of the canal in ANSYS Mechanical; in Fluent, the identical waveforms were applied to the entrance of the EP orifice.

RESULTS

Effects of HPDs (EPs) on Blast Wave Transmission

Figure 6 shows the typical overpressure waveforms of P0, P1, and P2 recorded from a cadaver ear or TB without the earplug (Fig. 6A) and a TB with the earplug (CAE, Fig. 3A) over 10 ms of time duration. The P0 or BOP waveforms recorded in all cases with or without EPs were verified to be consistent, serving as a baseline for comparison of different EPs. The peak P0 level was around 57 kPa (48–70 kPa) or 189 dB (187–190 dB) for all tests. The P1 peak pressure shows a substantial increase compared to the P0 pressure in all the ears without protection devices (Fig. 6A), reflecting the effect of the ear canal on enhancing the impulse pressure level near the TM. In ears with EPs, the peak P1 pressure is much lower than P0 (32 kPa reduction in Fig. 6B). P2 waves are different from P1 and P0 waves with a much lower peak pressure value than the P1 (Fig. 6).

Figure 7A displays the P1 waveforms recorded from ears without EPs and ears with different EPs or attenuation settings, including the Battle plugs, CAE, foam, and Lyric. The waveform variation indicates the different effects of EPs on the pressure wave reaching to the TM in the canal. To quantify the EPs' effects on Impulse Energy Flux (energy per unit area in unit J/m^2) over 10 octave frequency bands from below 125 Hz to above 16 kHz, the impulse energy spectra analyses on those waveforms were performed. Figure 7B and C illustrates the comparison of energy fluxes of P1 waves obtained from seven ear cases in bar curves and in line curves, respectively. The P1 energy distribution over octave bands was altered when the earplug was placed in the ear canal.

The peak P1 energy flux of the CAE (blue solid line) or Lyric (purple line) were expanded between 2 kHz to 500 Hz

Downloaded from https://academic.oup.com/milmed/article-abstract/184/Supplement_1/251/5418722 by Johns Hopkins University user on 27 March 2019

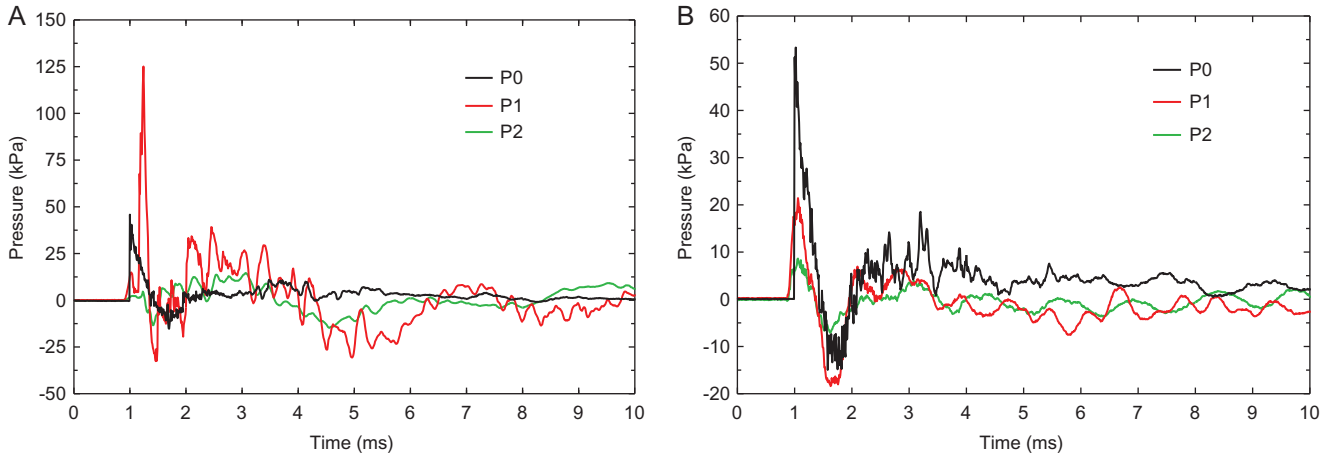


FIGURE 6. Waveforms of P0 (black line), P1 (red), and P2 (green) recorded in the cadaver ear (TB15-35L) in the front setup test. (B) Waveforms recorded from another cadaver ear (TB15-36R) inserted with Combat Arms earplug during the front test inside the blast chamber.

at 0.28 and 0.2 J/m^2, respectively, compared with a single peak of 0.4 J/m^2 at 2 kHz for no earplug case (black line). The peak P1 energy flux for the CAE Min (blue dashed line) even expanded to 250 Hz. However, the P1 energy resulted from Battle plugs in both Max. and Min. settings (red solid and dashed lines) was similar to the open ear (no earplug, black line) with peaks at 1 kHz. For foam earplug (green line), there was a clear shift to lower frequency at 250–500 Hz. The peak at f < 125 Hz for Lyric plug was also shown in Figures 7B and C. These observations depict how the EPs change energy distribution of pressure waves reaching the TM. Further analysis of P1 energy distribution over frequency bands is needed for understanding the protection mechanisms of different EPs under blast exposure.

Table I lists the mean and standard deviation of experimental data obtained from human cadaver ears with six earplug cases, including the peak values of P0, P1, and P0-P1 in ears with earplug, the peak P1 and the ratio of P1/P0 in ears without earplug, and the P1 reduction induced by the earplug. The P1/P0 was the ratio of the first peak pressure (amplitude) of P1 and P0. P1 reduction in dB, or insertion loss, is the P1 pressure level with earplug subtracted from P1 level in ears without EPs. P1 reduction represents the effective protection function, the pressure level prevented from reaching the TM by inserting the earplug. Table I shows that the average P0–P1 (dB) in ears with five standard EPs was 12–13 dB and that for Lyric earplug was 16 dB. The average P1 reduction for CAE, Battle, and foam was 17–18 dB and that for Lyric was 21 dB.

It should be noted that the variation of P1 measurement is usually greater than the P0 measurement because of the individual ear canal difference (size and length), the depth of insertion, the geometry of the earplug, and materials of the earplug. We have also observed that the insertion quality of the earplug in the ear canal affected the results of earplug's effective protection function. Thus, the extra care of fitting the earplug was taken through the study. We did check the consistency of P1 waveform for each blast test and one research technician did the insertion for all different EPs reported in this paper except the Lyric earplug which was inserted by an audiologist.

FE Modeling of HPDs (EPs) in Comparison With Experimental Data

The FE model of the human ear was used to predict the P1 and P2 pressures in ears with EPs: the foam and CAE as illustrated in Figure 5. The model-predicted results were compared with the experimental data obtained from human cadaver ears (Fig. 8). Column (A) in Figure 8 displays the resulting waveforms for P0, P1, and P2 from both experiments (top panel) and human ear model (HEM) with foam earplug (bottom panel). The P0 pressure wave used for the model was the same as that recorded from the experiments with a peak P0 level at 15 kPa (2.2 psi or 177 dB). The P1 reduction or insertion loss obtained from the cadaver ear and FE model was 18 dB and 19 dB, respectively, but the P1 and P2 waveforms from the experiments and FE model showed some inconsistency. Although the linear elastic representation of the foam earplug has been implemented successfully in other studies,[10,11] this material model may be unsuitable for the high pressure and high strain rate analyses inherent when modeling blast exposures. A more appropriate nonlinear material model is necessary to accurately predict the earplug attenuation of foam materials subjected to blast overpressures.

Columns (B) and (C) in Figure 8 show the results from experiments and HEM with the CAE at two P0 pressure levels: 14 kPa (2.0 psi or 177 dB) – mild-level blast exposure in column (B) and 46 kPa (6.7 psi or 187 dB) – high-level blast exposure in column (C). The top panels display the experimentally recorded waveforms of P0, P1 and P2 from TB15-36R and the bottom panels display the human ear model-derived waveforms. Note that to be consistent with the CAE simulated in the model, the blast experiment was

Downloaded from https://academic.oup.com/milmed/article-abstract/184/Supplement_1/251/5418722 by Johns Hopkins University user on 27 March 2019

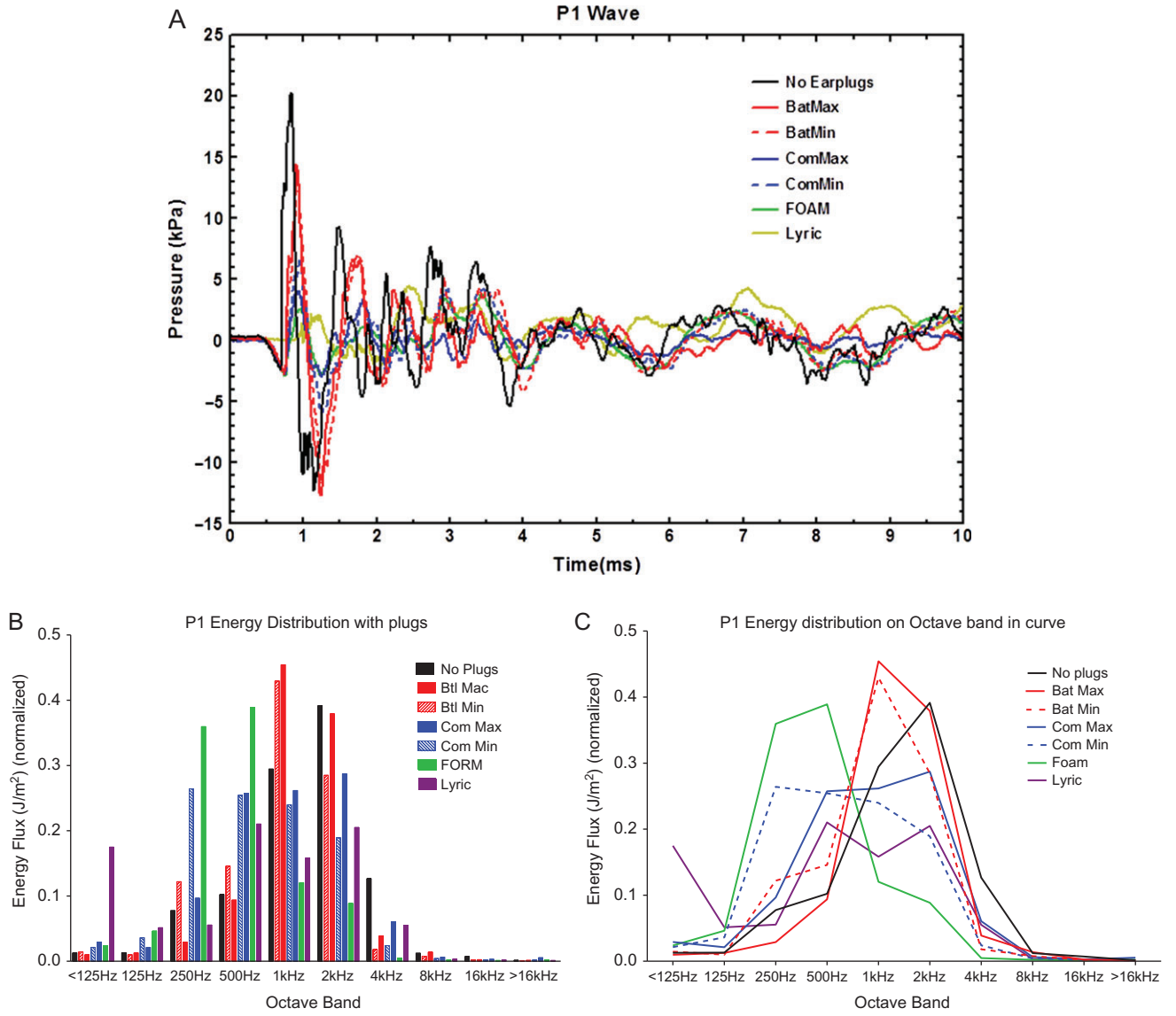


FIGURE 7. (A) Comparison of P1 waveforms measured in the ear without an earplug and the ears with EPs: Battle plug at Max and Min settings, Combat Arms at Max and Min settings, foam earplug, and Lyric earplug. (B) Normalized P1 wave energy flux distribution over 10 octave bands from below 125 Hz to above 16 kHz in bar curves. (C) Normalized P1 wave energy flux distribution over 10 octave bands from below 125 Hz to above 16 kHz in line curves.

TABLE I. Experimental Results of EPs Tested in Human Cadaver Ears During Blast Exposure

Earplug Type	P0 (dB) w/Earplug	P1(dB) w/Earplug	P0 – P1 (dB) w/Earplug	P1 (dB) w/Out earplug	P1/P0 ratio w/Out earplug	P1 (dB) Reduction
Battle maximum ($N = 15$)	188.9 ± 1.8	176.1 ± 7.5	12.8 ± 7.1	194.3 ± 2.9	1.7 ± 0.4	18.2 ± 6.9
Battle minimum ($N = 13$)	188.1 ± 1.4	175.7 ± 8.1	12.4 ± 8.4	193.8 ± 3.0	1.6 ± 0.4	18.1 ± 7.4
Combat Arms maximum ($N = 14$)	189.8 ± 1.3	176.5 ± 6.9	13.4 ± 6.7	194.5 ± 2.6	1.7 ± 0.4	18.0 ± 7.0
Combat Arms minimum ($N = 12$)	188.3 ± 1.8	176.3 ± 6.5	11.9 ± 5.7	193.6 ± 3.1	1.7 ± 0.4	17.3 ± 5.9
Foam ($N = 13$)	189.1 ± 1.7	176.8 ± 7.2	12.3 ± 6.4	194.2 ± 3.1	1.7 ± 0.4	17.3 ± 6.8
Lyric ($N = 6$)	189.1 ± 1.3	172.8 ± 2.1	16.3 ± 1.7	193.7 ± 3.2	1.8 ± 0.8	20.9 ± 5.3

Note that the P0-P1 without earplug can be derived from the P0 and P1/P0 ratio.

conducted in CAE-only occluded ears, with the hard-plastic core removed.

As displayed in columns (B) and (C), the predicted waveforms (P1) show that there is an obvious first peak pressure, which agrees with the shape of the experimental pressure profiles. However, the greatest discrepancy was in the duration of positive P1 overpressure when compared to the relatively short duration of initially positive overpressure observed in the

Downloaded from https://academic.oup.com/milmed/article-abstract/184/Supplement_1/251/5418722 by Johns Hopkins University user on 27 March 2019

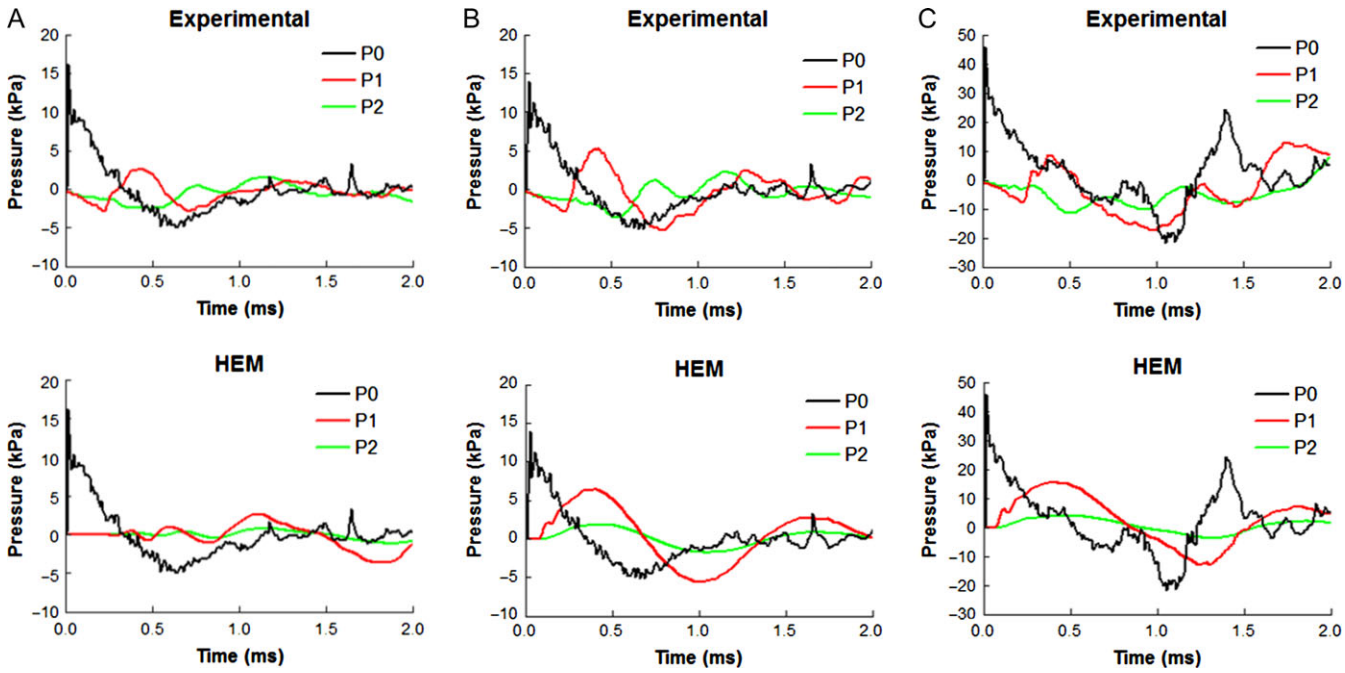


FIGURE 8. Waveform/Attenuation comparison between FE model and experimental data. The top panels display the experimentally recorded waveforms of P0, P1 and P2 from TB15-35L (foam earplug) and TB15-36R (CAE). The bottom panels display the human ear model (HEM)-derived waveforms. Column (A) shows the results with foam earplug and columns (B) and (C) show the results with the CAE at two different input overpressure P0 levels: (B) 14 kPa and (C) 46 kPa.

experiment (roughly 0.25 ms). A portion of this is explained by the initial drop in pressure level measured during experiment that is likely due to experimental setup. The experimental P1 waveform also contains a higher degree of undulation than was predicted, although this may be simply due to variations in canal geometry. For mild-level exposure, predicted versus measured P1 reduction or insertion loss was 11.4 dB versus 11.3 dB. Predicted versus measured P1 reduction for high-level exposure was 14 dB versus 12 dB.

DISCUSSION

Characterization of HPDs attenuation properties to blast overpressure was reported in this study with experiments in human cadaver ears and computational modeling in a 3D FE model of the human ear. Four EPs including CAE, Battle Plugs, foam, and Lyric earplug (inactive hearing aid) were tested in fresh human cadaver ears attached to the head block and exposed the BOP level of 189 dB (57 kPa or 8 psi) at the ear canal entrance. The pressure near the eardrum (P1) reduction or insertion loss of the earplug was used as a main parameter to describe the attenuation of HPDs. The impulse energy spectra of P1 waveforms provided the energy distribution over frequencies. The CAE and foam earplug were also simulated in the 3D FE model of the human ear with the measured P0 waveform applied at the canal entrance to calculate P1 and P2.

Biomechanical Characterization of HPDs in Human Ears

The protective function of four EPs was tested in human cadaver ears, which represent an ideal platform to characterize the attenuation provided by HPDs, as all nonlinearities and biomechanics of peripheral auditory system for the BOP wave transduction pathway are included. This contrasts with use of the ATF, which does not include biological components of the ear such as the TM, middle ear ossicular chain, and cochlea.

Using the new testing method for HPDs, we can evaluate the attenuation function of deeply inserted EPs, like Lyric. In comparison of the Lyric with three standard EPs in this study, 3 dB more P1 insertion loss for Lyric at BOP level of 189 ± 1.3 dB was. This result indicates that the Lyric earplug is 3 dB more protective than the other plugs. Thus, the earplug in deep canal position (4 to 16 mm insertion depth) may provide an optimal protection mechanism to BOP at the mild TBI level (69–138 kPa or 10–20 psi).

In addition to measurements of P1 peak insertion loss for HPDs in the time domain, the impulse energy spectra analyses on P1 waveforms recorded in open ears and the ears inserted with EPs were performed in this study. Results from all tested EPs shown in Figure 7 display the P1 energy distribution over 10 octave bands from below 125 Hz to above 16 kHz. The CAE and Lyric shared some common properties of the P1 energy distribution over 500 Hz to 2 kHz, and the

Downloaded from https://academic.oup.com/milmed/article-abstract/184/Supplement_1/251/5418722 by Johns Hopkins University user on 27 March 2019

Lyric had lower energy flux than that of CAE (Fig. 7C). These findings suggest that the P1 waveform induced by different EPs reflects not only the peak pressure attenuation, but also the impulse energy reaching to the TM over the frequency range. The waveform analysis provides a useful method to investigate the effects of EPs on P1 pressure reaching to the TM from the time-domain measures to the frequency-dependent protective behavior. However, the mechanism of earplug-induced P1 waveform change on energy transmission to the middle ear and cochlea needs further studies. The FE model simulation of the HPDs may serve as a promised approach for the research in this area.

Biomechanical Modeling of HPDs in Human Ears

The 3D FE model of the human ear has been developed and utilized to simulate the BOP transduction through the ear[8] and predict the TM injury in relation to blast wave direction.[3] In these previous studies, the model was validated with the experimental results obtained in human cadaver ears. The new application of the human ear model to simulate the HPDs, including the foam and CAE EPs in the canal, was conducted in the present study. The comparisons of model-derived P1 and P2 waveforms and the peak P1 pressure reduction (insertion loss) induced by the foam and CAE (Fig. 8) are promising for FE model's future applications. It is expected that the material properties, structural designs, and insertion depths can be evaluated in the FE model.

The nonlinear earplug design requires strong fluid-structure-interface coupling analyses conducted in Fluent/ANSYS Mechanical as performed with both foam and CAE in this study. However, improved modeling simulation is needed, including the porous viscoelastic material model for the foam and the involvement of hard plastic core for TripleDome. It should be noted that the model-derived ear response to the BOP applied at the ear canal entrance is not only the P1 and P2 pressure waves; the utility of the human ear model also includes the prediction of velocity streamlines through the orifice of the Combat Arms into the ear canal and the TM movement (results not shown here). The FE model of the human ear and computational method show great promise in providing enhanced means of designing and optimizing advanced HPDs.

CONCLUSIONS

The function of four different EPs, including the CAE, Battle, foam, and Lyric, to attenuate the blast overpressure reaching to the eardrum has been characterized in human cadaver ears or TB in this study. The CAE and foam earplug were also simulated in the ear canal of the 3D FE model of the human ear to predict blast overpressure transmission through the ear. Both experiments and FE modeling resulted in the reduction of P1 pressure (the pressure near the TM in the ear canal) which represents the effective protection function of the earplug. Different EPs showed variations in pressure waveforms transmitted to the TM, which determine the protection level of EPs.

This is the first time of using cadaver ears to evaluate HPDs' function and compare the measurements with the FE modeling results. The experimental measurements in the ears with and without EPs provide a valuable database for understanding of human ear response to blast waves. These data will be employed for further prediction of blast-induced hearing damage and protection methods in the FE model. Both experimental platform and FE model of the human ear reported in this study provide new biomechanical characterization methodologies for HPDs function evaluation and design improvement.

PRESENTATIONS

Presented in Poster Session II: "Medical Advancements in Operational & Clinical Hearing Protection & Treatment" at the 2017 Military Health System Research Symposium.

FUNDING

This work was supported by U.S. Army Medical Research and Material Command (USAMRMC) Military Operational Medicine Research Program, Contract No. W81XWH-14-1-0228. This supplement was sponsored by the Office of the Secretary of Defense for Health Affairs.

REFERENCES

1. Murphy WJ, Fackler CJ, Berger EH, Shaw PB, Stergar M: Measurement of impulse peak insertion loss from two acoustic test fixtures and four hearing protector conditions with an acoustic shock tube. Noise Health 2015; 17(78): 364–73.
2. Fackler CJ, Berger EH, Murphy WJ, Stergar ME: Spectral analysis of hearing protector impulsive insertion loss. Int J Audiology 2017; 56 (sup1): 13–21.
3. Gan RZ, Leckness K, Nakmali D, Ji XD: Biomechanical measurement and modeling of human eardrum injury in relation to blast wave direction. J Mil Med 2018; 183(Suppl 1): 245–51.
4. Engles WG, Wang X, Gan RZ: Dynamic properties of human tympanic membrane after exposure to blast waves. Ann Biomed Eng 2017; 45 (10): 2383–94.
5. Luo H, Jiang S, Nakmali D, Gan RZ, Lu H: Mechanical properties of a human eardrum at high strain rates after exposure to blast waves. J Dyn Behav Mater 2015; 2: 59–73.
6. Gan RZ, Nakmali D, Ji X, Leckness K, Yokell Z: Mechanical damage of tympanic membrane in relation to impulse pressure waveform - a study in chinchillas. Hear Res 2016; 340: 25–34.
7. Leckness K: Novel finite element method to predict blast wave transmission through human ear. MS thesis at University of Oklahoma. Available at https://shareok.org/bitstream/handle/11244/44932/2016_Leckness_Kegan_Thesis.pdf?sequence=2&isAllowed=y; accessed April 11, 2018.
8. Leckness K, Nakmali D, Gan RZ: Computational modeling of blast wave transmission through human ear. J Mil Med 2018; 183(Supp 1): 262–8.
9. Gan RZ, Cheng T, Dai C, Yang F, Wood MW: Finite element modeling of sound transmission with perforations of tympanic membrane. J Acoust Soc Am 2009; 126(1): 243–53.
10. Viallet G, Sgard F, Laville F, Boutin J: A finite element model to predict the sound attenuation of earplugs in an acoustical test fixture. J Acoust Soc Am 2014; 136: 1269–80.

Downloaded from https://academic.oup.com/milmed/article-abstract/184/Supplement_1/251/5418722 by Johns Hopkins University user on 27 March 2019

11. Brummund M, Sgard F, Petit Y, et al: Three-dimensional finite element modeling of the human external ear: Simulation study of the bone conduction occlusion effect. J Acoust Soc Am 2014; 135(3): 1433–44.

12. Viallet G, Sgard F, Laville F, Nelisse H: Investigation of the variability in earplugs sound attenuation measurements using a finte element method. Appl Acoust 2015; 89: 333–44.

Downloaded from https://academic.oup.com/milmed/article-abstract/184/Supplement_1/251/5418722 by Johns Hopkins University user on 27 March 2019

Medical Engineering and Physics 54 (2018) 14–21

Contents lists available at ScienceDirect

Medical Engineering and Physics

journal homepage: www.elsevier.com/locate/medengphy

Dynamic properties of human incudostapedial joint—Experimental measurement and finite element modeling

Shangyuan Jiang, Rong Z. Gan*

School of Aerospace and Mechanical Engineering, University of Oklahoma, 865 Asp Avenue, Room 200, Norman, OK 73019, USA

ARTICLE INFO

Article history:
Received 2 March 2017
Revised 31 December 2017
Accepted 11 February 2018

Keywords:
Incudostapedial joint
Dynamic properties
Dynamic mechanical analyzer
Frequency–temperature superposition
Finite element modeling

ABSTRACT

The incudostapedial joint (ISJ) is a synovial joint connecting the incus and stapes in the middle ear. Mechanical properties of the ISJ directly affect sound transmission from the tympanic membrane to the cochlea. However, how ISJ properties change with frequency has not been investigated. In this paper, we report the dynamic properties of the human ISJ measured in eight samples using a dynamic mechanical analyzer (DMA) for frequencies from 1 to 80 Hz at three temperatures of 5, 25 and 37 °C. The frequency–temperature superposition (FTS) principle was used to extrapolate the results to 8 kHz. The complex modulus of ISJ was measured with a mean storage modulus of 1.14 MPa at 1 Hz that increased to 3.01 MPa at 8 kHz, and a loss modulus that increased from 0.07 to 0.47 MPa. A 3-dimensional finite element (FE) model consisting of the articular cartilage, joint capsule and synovial fluid was then constructed to derive mechanical properties of ISJ components by matching the model results to experimental data. Modeling results showed that mechanical properties of the joint capsule and synovial fluid affected the dynamic behavior of the joint. This study contributes to a better understanding of the structure–function relationship of the ISJ for sound transmission.

© 2018 IPEM. Published by Elsevier Ltd. All rights reserved.

1. Introduction

The incudostapedial joint (ISJ) is a synovial joint connecting the incus and stapes in the middle ear. ISJ consists of the articular cartilage, meniscus, capsule, and synovial fluid [1–3]. The function of the ISJ is to transmit mechanical vibration of the tympanic membrane (TM) to the stapes and cochlea, and provide flexibility to the middle ear ossicular chain [4]. The sound transmission function of the middle ear is closely related to the mechanical properties of the ISJ [4,5]. Abnormalities of the joint have been shown to impose severe conductive hearing loss, which usually requires surgical reconstruction of the ossicular chain to restore the hearing [6–10]. Recent experimental studies suggested that the increased ISJ stiffness (ankyloses) reduced the mobility of the TM and stapes footplate at 0.5–1 kHz [11], while the reduced ISJ stiffness (separation) was related to the stapes mobility loss at high frequencies [12]. These experiments, however, were not specific enough to characterize the relationship between the ISJ stiffness and middle ear transfer function without providing the material properties of the joint quantitatively.

In addition to experimental studies, the lack of knowledge on dynamic properties of the ISJ affects the accuracy of finite element (FE) modeling of the human middle ear. The ISJ has been modeled as an isotropic elastic solid body [1,13–16], an isotropic viscoelastic solid body [17,18], and a synovial joint with viscoelastic capsule [4] in published FE models of the human middle ear. The material properties of the ISJ used in these models were determined through the cross-calibration process and had significant variation across the models [4,5,16].

Experimentally measured data on the mechanical properties of the ISJ is very limited. Zhang and Gan [19] conducted quasi-static uniaxial loading tests on human ISJ samples and this is the only published biomechanical measurement based on our knowledge. Their results demonstrated that the ISJ shows viscoelastic behavior with nonlinear stress–strain relationship under quasi-static loading. They used a FE model of ISJ to show that the behavior of the joint was closely related to the mechanical properties of the joint capsule, cartilage and synovial fluid. However, the human auditory frequency ranges from 20 Hz to 20 kHz which is the normal working frequency range of the ISJ. Thus, the dynamic properties of ISJ over the frequency range may provide a better understanding of the joint's transmission function and should be modeled more accurately to describe the joint behavior.

In this paper, we report the dynamic properties of human ISJ using a dynamic mechanical analyzer (DMA) with frequency–temperature superposition (FTS). DMA is a widely used system to measure dynamic properties of materials in the frequency domain.

* Corresponding author.
E-mail address: rgan@ou.edu (R.Z. Gan).

https://doi.org/10.1016/j.medengphy.2018.02.006
1350-4533/© 2018 IPEM. Published by Elsevier Ltd. All rights reserved.

However, the frequency range of current DMA has limited high frequency access and a method to expand the testing frequency to high frequency, the FTS principle, has been reported [20,21]. The FTS principle is an empirical method which relates the effect of temperature change on dynamic properties of some materials (e.g. polymers) to that of frequency change [22,23]. In the past two decades, researchers have applied FTS principle in dynamic tests of biological tissues such as the bovine brain and vocal-fold [24–26]. Recently, our lab has reported the mechanical properties of the human TM and stapedial annular ligament (SAL) and the chinchilla SAL measured using DMA with FTS to extend measured complex modulus data of tissues to higher frequencies [27–29].

In the present study, the DMA with FTS was used for measuring dynamic properties of the human ISJ. ISJ samples were measured in the frequency range of 1–80 Hz at three different temperatures (5, 25 and 37 °C). The average complex modulus of the joints was obtained directly from the experiments. A 3D FE model of the ISJ consisting of the articular cartilage, joint capsule and synovial fluid was then constructed to identify the mechanical properties of ISJ components by matching the modeling results to the experimental data. The model was used to investigate the effect of the mechanical properties of the ISJ (the capsule and synovial fluid) on the dynamic behavior of the joint.

2. Methods

2.1. Specimen preparation and experimental setup

Eight (four left and four right) fresh human temporal bones (TBs) with an average donor's age of 69 years were involved in this study. All TBs were provided by Life Legacy Foundation, a certified human tissue supply source for medical and military research. The experiments were conducted within one week after the TB samples were received. The TB samples were covered by wet paper soaked in a prepared solution made of 0.9% saline and 15% povidone at 5 °C to maintain the physiological condition before the experiment. Each TB was examined using a light microscope to ensure that the middle ear appeared normal. The middle ear ossicles were then accessed by opening the tegmen tympani and removing the TM together with the malleus. The scala vestibule of the cochlea was opened and the stapes footplate was exposed through the medial side. The TB was then trimmed to a cube with a size of 1.5 cm × 1.5 cm × 1.5 cm to expose the ISJ with incus and stapes. A #11 scalpel was used to cut along the SAL to separate the footplate from the oval window. Note that special care was applied to keep the ISJ unstretched during the separation of the footplate from the bony wall. Finally, the stapedial tendon was removed to assure the ISJ was the only stress-bearing soft tissue in the test.

The schematic diagram of the experimental setup is shown in Fig. 1A. The ISJ specimen was fixed onto a sample holder using copper wire and melted paraffin. The load cell (5 lb, WMC-5-455 Bose, Eden Prairie, MN) of the DMA (ElectroForce 3200, Bose, Eden Prairie, MN) was placed between the sample holder and the *X*–*Y* translational stage. The translational stage was used for aligning the ISJ with the load cell in the *Z* axis under a surgical microscope (Zeiss, OPMI 1-FC), viewing from the front and lateral directions. The long process of the incus was fixed to the middle ear bony wall using cyanoacrylate gel glue. This type of glue had been validated by previous studies to provide stable fixation on the surface of biological tissues [19,27]. After the glue dried, a sharp-tip tweezer was used to assure the incus was completely immovable. The specimen was then raised up to a position where the stapes footplate was directly in contact with the lower end of the adapter. Cyanoacrylate gel glue was applied between the stapes footplate and the wooden adapter connected to the upper grip of the DMA (Fig. 1B). During this process, the ISJ stayed straight as shown in Fig. 1B indicating the structure was intact before the experiment. After the glue dried, a preload of 0.02 N compression was applied on the ISJ specimen before the experiment was started to assure all samples were tested under the same initial conditions. The preload was zeroed out before the start of the dynamic tests. The specimen was placed in a temperature-controlled chamber with a size of 25 cm × 25 cm × 10 cm (Fig. 1A). The fluctuation of the temperature inside the chamber during the test was controlled within ±1 °C by a system consisting of a thermal couple, a negative feedback circuit and a fan delivering hot or cold air.

For the dynamic measurements, sinusoidal displacements with an amplitude of 0.1 mm at the frequencies of 1, 2, 5, 10, 20, 40, 60 and 80 Hz were applied on the stapes footplate, and the force was measured by the load cell. Each measurement was performed at three temperatures: 5, 25 and 37 °C. The moisture of the specimen was maintained by adding 0.9% saline solution every five minutes onto the specimen using a syringe. At each frequency and temperature, results recorded in the first five seconds of the test were abandoned to serve as the preconditioning process. Therefore, each dynamic test itself included the preconditioning process with exactly the same testing conditions.

2.2. Dimensions and viscoelastic material model of ISJ specimen

The ISJ was separated after the completion of the dynamic test. The lenticular process of the incus and the head of the stapes were examined under a microscope. Images of the lenticular process of the incus were captured by a digital camera through the microscope (Fig. 2). The stapes head was assumed to share the same geometry with the lenticular process of the incus based on the histological images provided by Zhang and Gan [19]. Under the assumption that the cross section of the ISJ was elliptical [19], the lengths of the long axis a and short axis b were measured by image analysis software (ImageJ). The measurement was based on calculation of the pixels with a scale calibrated by a standard 1 mm scale bar next to the specimen as shown in Fig. 2. The largest values of a and b in perpendicular directions were accepted and the cross-sectional area of the ISJ was calculated by $A = \pi ab/4$. Table 1 lists the geometry data from eight ISJ specimens with the mean and standard deviation. The length of the ISJ could not be measured by direct observation. Therefore, we used the value of 0.28 mm, which was the length of the ISJ capsule measured from a histology section reported by Zhang and Gan [19].

Based on the dimensions of each specimen, the ISJ was initially assumed as an isotropic viscoelastic body to derive its complex modulus. Even though the quasi-static test of the ISJ reported the nonlinear behavior of the ISJ, the material model of the joint can still be considered as linear viscoelastic in this study because the deformation is small. Both the displacement d applied on the stapes footplate and the force F measured with the load cell were sinusoid signals for each frequency f, defined as

$$d = d_0 e^{i2\pi ft} \tag{1}$$

$$F = F_0 e^{i(2\pi ft+\delta)} \tag{2}$$

where d_0 and F_0 are the amplitude of the displacement and force, respectively, and δ is the phase delay between the displacement and force. The complex modulus at frequency f is calculated by

$$|E^*| = \frac{\sigma_0}{E_0} = \frac{F_0/A}{d_0/L} \tag{3}$$

$$E' = |E^*|\cos\delta \tag{4}$$

$$E'' = |E^*|\sin\delta \tag{5}$$

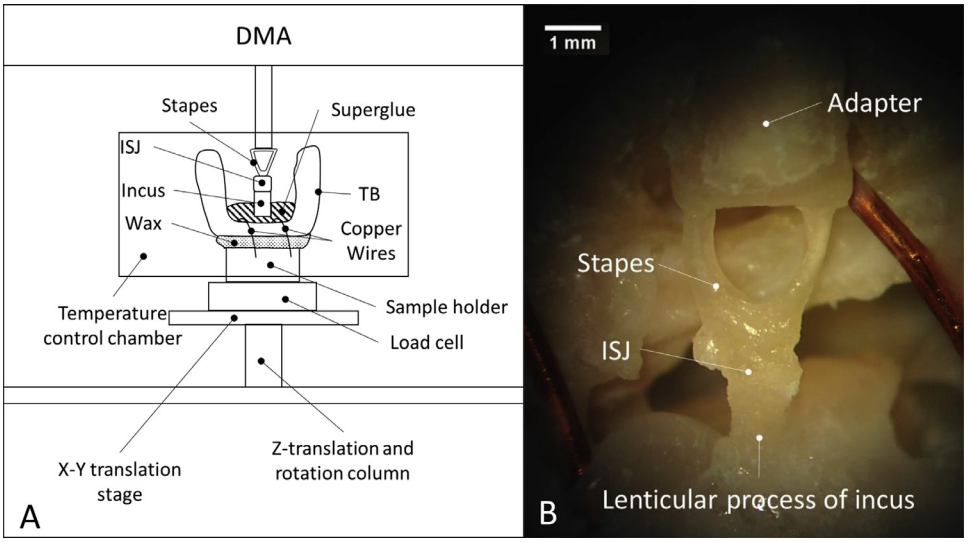


Fig. 1. (A) Schematic diagram of the experiment setup. (B) ISJ specimen mounted on the machine observed under a microscope.

Table 1
Dimensions of the ISJ specimens.

ISJ specimen ($N=8$)	ISJ-1	ISJ-2	ISJ-3	ISJ-4	ISJ-5	ISJ-6	ISJ-7	ISJ-8	Mean	SD
Length: a (mm)	0.95	0.80	0.87	0.86	1.01	0.93	0.91	1.02	0.92	0.07
Width: b (mm)	0.65	0.57	0.65	0.60	0.71	0.68	0.75	0.70	0.66	0.06
Cross sectional area: A (mm^2)	0.485	0.358	0.444	0.405	0.563	0.496	0.536	0.560	0.481	0.074

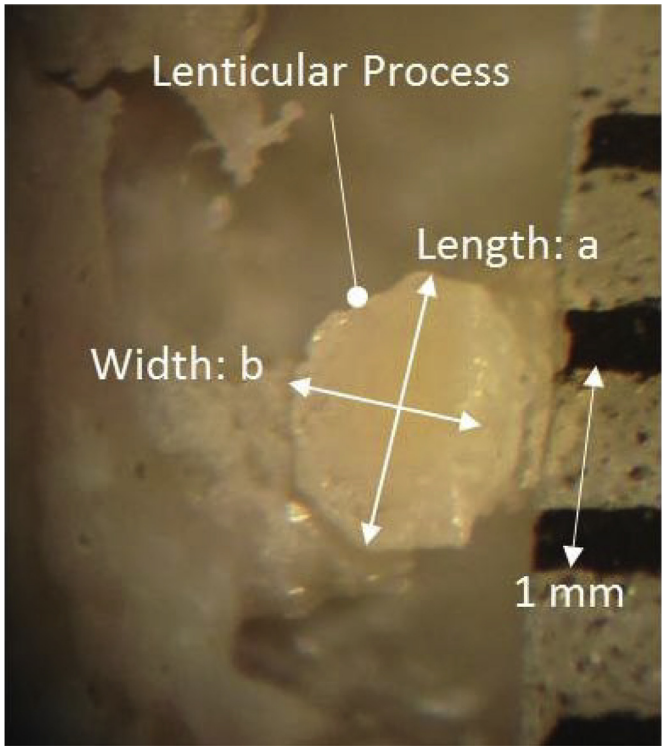


Fig. 2. Microscopic image of the lenticular process of the incus after the dynamic test for geometric measurement.

where σ_0, E_0, A, L, E^*, E' and E'' are the stress amplitude, strain amplitude, cross sectional area, length, complex modulus, storage modulus, and loss modulus of the ISJ, respectively. The inner structure and the mechanical properties of joint components were not taken into consideration at this step.

2.3. FTS principle

The FTS principle was employed to expand the frequency range of the experimental results. The FTS principle states that the curves of the complex modulus E^* obtained at a reference temperature T_0 (37 °C) can be expressed by

$$E^*(T_0,\ f) = E^*(T,\ f/\alpha_T) \tag{6}$$

where T is a lower temperature (5 or 25 °C), α_T is the shift factor quantifying the temperature's effect on a material's dynamic properties. The shift factor α_T must comply with the WLF equation which was first introduced by Williams et al. and widely used for the FTS principle [21,25]:

$$\log_{10}^{\alpha_T} = \frac{C_1(T-T_0)}{C_2+T-T_0} \tag{7}$$

where T and T_0 are the absolute temperatures in Kelvin. c_1 is a dimensionless constant and c_2 is a constant with a unit of Kelvin.

In order to use the FTS principle, the complex moduli measured from ISJ specimens at 5, 25 and 37 °C were first plotted as a function of frequency in a logarithmic coordinate system. Then the 25 °C curves were shifted together horizontally toward higher frequencies to align with the curves obtained from 37 °C (reference temperature). Subsequently, curves from 5 °C were shifted in the same way further horizontally to connect with the points belonging to the shifted 25 °C curves. In adjacent areas, the high-frequency results obtained from the higher temperature tests were connected with the low-frequency results obtained from the lower temperature tests. Note that the shapes of the curves were horizontally stretched (37 °C) and shrunken (25 °C) in the shifting process. Finally, the master curves of complex moduli at the reference temperature were obtained. The values of α_T, c_1 and c_2 could be determined by Eqs. (6) and (7). There are three requirements in this shifting process for the FTS principle to hold: (1) the shifted curves in adjacent areas have to be matched perfectly with the curves from the lower temperature; (2) the shift factors for both

Table 2
Components and mechanical parameters of the ISJ FE model.

Components	Young's modulus (Pa)	Poisson's ratio	Viscosity (cp)
Incus	1.41×10^{10}	0.3	
Stapes head	1.41×10^{10}	0.3	
Cartilage	1.00×10^{7}	0.3	
Capsule	$E_0 = 2.9$ MPa, $E_1 = 1.25$ MPa, $E_2 = 1.9$ MPa $E_3 = 0.12$ MPa, $\tau_1 = 2.6$ ms, $\tau_2 = 0.14$ ms $\tau_3 = 0.13$ ms	0.3	
Synovial fluid	2.20×10^{9} (Bulk modulus)		4×10^{2}

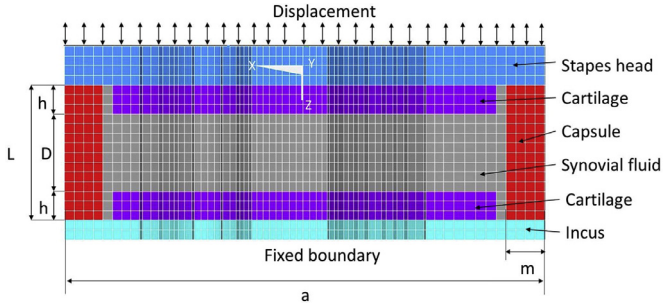


Fig. 3. Axial cross section (X–Z plane) of the 3D FE model of the ISJ with boundary conditions.

loss and storage modulus curves are the same; (3) the shift factors have to obey the WLF equation, or in other words, values of c_1 and c_2 should have a small standard deviation among all specimens [22,23,27–29].

2.4. Finite element modeling of ISJ

ISJ is a synovial joint with a complex inner structure. The relationship between the measured mechanical properties of the joint as an isotropic body and the mechanical properties of the components inside the joint requires further investigation. In this study, a 3D FE model of the ISJ was developed to attempt to identify the properties of the joint component. The structure of the FE model was similar to the one built in our previous study [19]. Fig. 3 shows the longitudinal cross sectional (X–Z plane) view of the model with boundary conditions. The X–Y plane cross section of the model was elliptical and X-axis represented the long axis. The length of the long and short axis was 0.92 and 0.66 mm, respectively, which were the mean values listed in Table 1. The thickness of the incus and stapes in this model were assumed to be 0.04 and 0.08 mm, respectively. The distance between the incus and stapes was $L = 0.28$ mm and the thickness of the capsule was $m = 0.08$ mm. The thickness of the cartilage covering the lenticular process and stapes head was set as $h = 0.08$ mm. The distance between the two cartilage layers was $D = 0.12$ mm. The FE model was meshed with hexahedral elements in ANSYS 15.0 (ANSYS Inc., Canonsburg, PA). The lenticular process, stapes, and cartilage were assigned as linear elastic Solid 45 elements. The capsule was modeled by nonlinear Solid 185 elements of viscoelastic material and the synovial fluid was modeled as Fluid 80 elements with a constant viscosity. The mechanical properties used in the model are listed in Table 2. The Young's modulus of 14.1 GPa was used for the bony structures, incus and stapes [16]. The cartilage was considered as a linear elastic material with Young's modulus of 10 MPa, the same value as that used by Funnell et al. [1] and Zhang and Gan [19]. The bulk modulus and the viscosity of the synovial fluid were obtained from Gan and Wang [16] and Zhang and Gan [19].

Our previous studies reported that the function of the ISJ largely depended on the properties of the joint capsule [19], and the viscoelastic properties of the joint capsule significantly affected the behavior of the ISJ over a frequency range of 600–6000 Hz [4]. Therefore, the capsule was assumed to be viscoelastic and the values listed in Table 2 were determined by fitting the FE model-derived force-displacement curves with the experimental results. The generalized Maxwell model was used to represent the viscoelastic behavior of the capsule as

$$E'(\omega) = E_0 + \sum_{i=1}^{n} E_i \tau_i^2 \omega^2 / \left[1 + \tau_i^2 \omega^2\right] \quad (8)$$

$$E''(\omega) = \sum_{i=1}^{n} E_i \tau_i \omega / \left[1 + \tau_i^2 \omega^2\right] \quad (9)$$

where ω is the circular frequency ($\omega = 2\pi f$) and n equals 3 (giving seven parameters E_0, E_1, E_2, E_3, τ_1, τ_2, τ_3) [27–30]. A harmonic analysis with the same boundary conditions and frequency was conducted to simulate the dynamic test. An iteration process was conducted to determine mechanical properties of the joint capsule by comparing the model-derived curves with the experimental data.

3. Results

3.1. Complex modulus obtained from dynamic tests

Dynamic tests were conducted on eight ISJ specimens to obtain their storage modulus E' and loss modulus E''. Two typical results obtained from specimens ISJ-6 and ISJ-8 are shown in Fig. 4. The storage and loss modulus measured at each frequency point at different temperatures were plotted in logarithmic coordinate system. Generally, the storage and loss modulus increased with increasing frequency or decreasing temperature. The loss modulus changed rapidly at frequencies below 5 Hz at 37 °C tests. Relatively large slopes were observed at high frequencies ($f > 10$ Hz) in both storage and loss modulus at all three temperatures. The complex modulus of other ISJ specimens showed similar curves to those in Fig. 4.

The curves of the complex moduli at 5 and 25 °C were shifted to high frequencies following the FTS principles. The master curves of samples ISJ-6 and ISJ-8 are displayed in Fig. 5A and B, respectively. For specimen ISJ-6, the storage modulus was 1.63 MPa at 1 Hz and increased to 5.97 MPa at 15 kHz, while the loss modulus increased from 0.10 MPa to 1.23 MPa. For specimen ISJ-8, the storage modulus was 1.58 MPa at 1 Hz and increased to 4.15 MPa at 15 kHz, while the loss modulus increased from 0.10 MPa to 0.85 MPa. In Fig. 5, the complex modulus-frequency curves were smoothly connected at the adjacent area without discernible discontinuities. Therefore, the master curves were generally well-matched which satisfied the first requirement of the FTS principle. Occasional fluctuations of the loss modulus curves were caused by the instability of the DMA machine at 80 Hz tests. Both storage and loss modulus were shifted by the same α_T for each specimen, which satisfied the second requirement of the FTS. The shift factors, maximum frequencies and constants c_1 and c_2 obtained from eight samples were listed in Table 3. The mean value with SD of the shift factor from 5 to 37 °C (α_5) was 183 ± 13.4. The mean value with SD of the shift factor from 25 to 37 °C (α_{25}) was 15.5 ± 4.0. The maximum frequency ranged from 12.8 to 16.0 kHz, which could cover most of the human hearing frequency range.

Table 3
The shift factors, c1 and c2 of WLF equation, and maximum frequency of human ISJ samples.

Specimen	ISJ-1	ISJ-2	ISJ-3	ISJ-4	ISJ-5	ISJ-6	ISJ-7	ISJ-8	Mean ± SD
α_{25}	12	15	23	11	18	14	18	13	15.5 ± 4.0
α_5	195	190	177	160	170	184	189	200	183 ± 13.4
ln α_5	5.27	5.24	5.17	5.07	5.13	5.21	5.24	5.29	5.20 ± 0.07
ln α_{25}	2.48	2.70	3.13	2.39	2.89	2.63	2.89	2.56	2.71 ± 0.24
c_1	16.1	11.9	8.4	15.3	9.6	12.5	10.2	14.6	12.4 ± 2.8
c_2 (K)	−65	−41	−20	−64	−27	−45	−30	−56	−44.1 ± 17.2
Maximum frequency (kHz)	15.6	15.2	14.1	12.8	13.6	14.7	15.1	16.0	14.6 ± 1.0

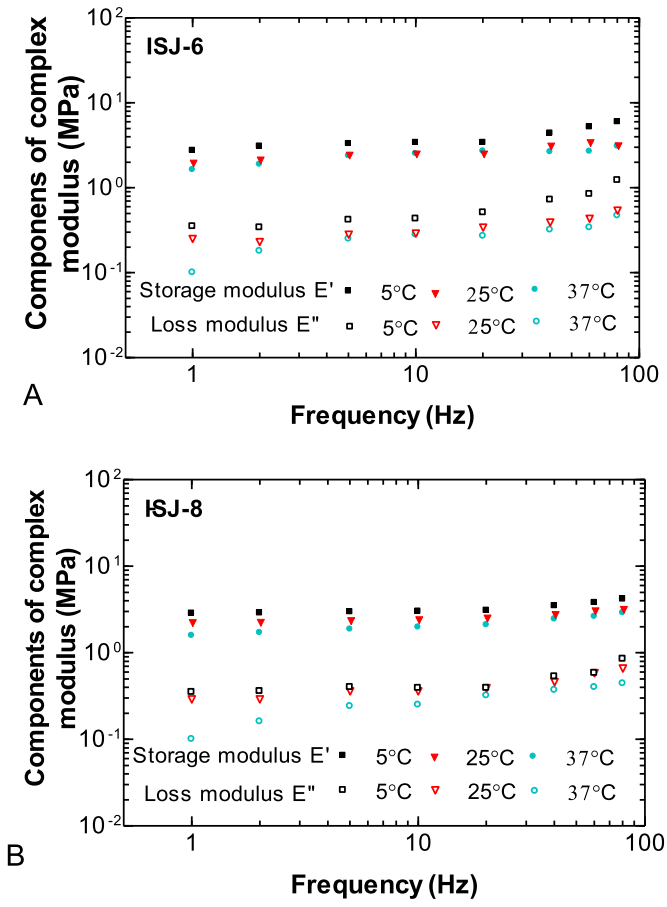


Fig. 4. The components of complex modulus curves obtained from the dynamic tests of ISJ specimens. (A) Data acquired from ISJ-6. (B) Data acquired from ISJ-8.

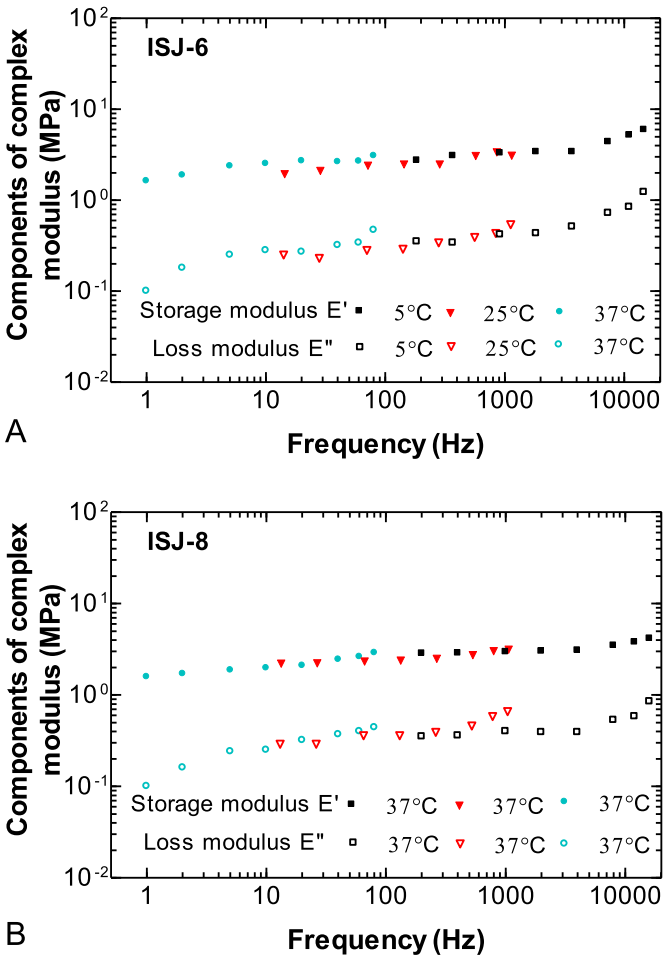


Fig. 5. Two representative master curves of the components of complex modulus at a reference temperature (37 °C) obtained by FTS principle. (A) Data acquired from specimen ISJ-6. (B) Data acquired from specimen ISJ-8.

The SD of c_1 and c_2 were 2.8 and 17.2 K, respectively, which were smaller than the values in published literature [28]. Therefore, the third requirement of the FTS is satisfied.

The master curves of the complex modulus of all eight ISJ samples were shown in Fig. 6. The mean complex modulus was calculated over the frequency range from 1 Hz to 8 kHz, the common frequency range for the eight ISJ samples. Frequencies below 8 kHz is a common range of interest in research on middle ear mechanics [4,5,14,16,17]. At 1 Hz, the mean storage modulus with SD was 1.14 ± 0.53 MPa and the loss modulus was 0.07 ± 0.04 MPa. At 8 kHz, the storage modulus was 3.01 ± 1.06 MPa, and the loss modulus was 0.47 ± 0.17 MPa. The mean curves in Fig. 6 indicate that the storage and loss modulus gradually increased with the frequency and the loss modulus had a larger slope than the storage modulus, especially at frequencies below 20 Hz. This trend shared some similarities with the viscoelastic behavior of other middle ear soft tissues reported in the previous studies [27,28].

3.2. FE model-derived data

The magnitude and phase of the force on the incus can be calculated by the complex modulus curves in Fig. 6 and the geometry data of the ISJ in Table 1 using Eqs. (1)–(5). By matching the FE model-predicted results to the experimental data, the mechanical properties of the joint capsule were determined and listed in Table 2. The seven viscoelastic parameters for the ISJ capsule solved from the FE model were $E_0 = 2.9$ MPa, $E_1 = 1.25$ MPa, $E_2 = 1.9$ MPa, $E_3 = 0.12$ MPa, $\tau_1 = 2.6$ ms, $\tau_2 = 0.14$ ms, and $\tau_3 = 0.13$ ms. The black solid line in Fig. 7A represents the mean (with SD) magnitude of force on the incus measured from eight ISJ samples and the red broken line represents the result obtained from the FE model. The black solid and red broken lines in Fig. 7B represent the mean phase shift (with SD) between the

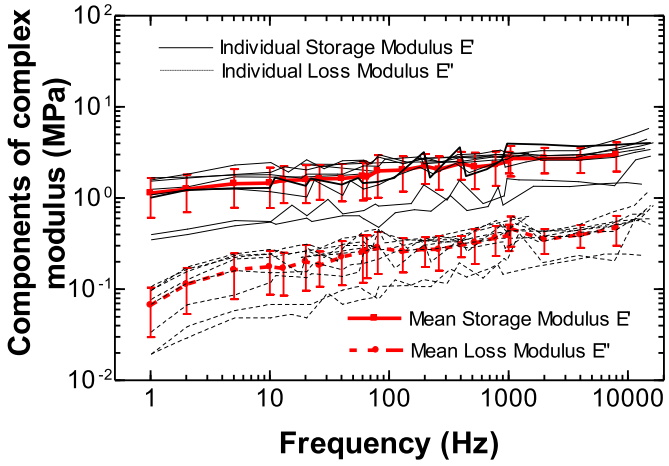


Fig. 6. The master curves of the components of complex modulus at 37 °C from 8 ISJ samples and the mean master curves of the storage and loss modulus with SD.

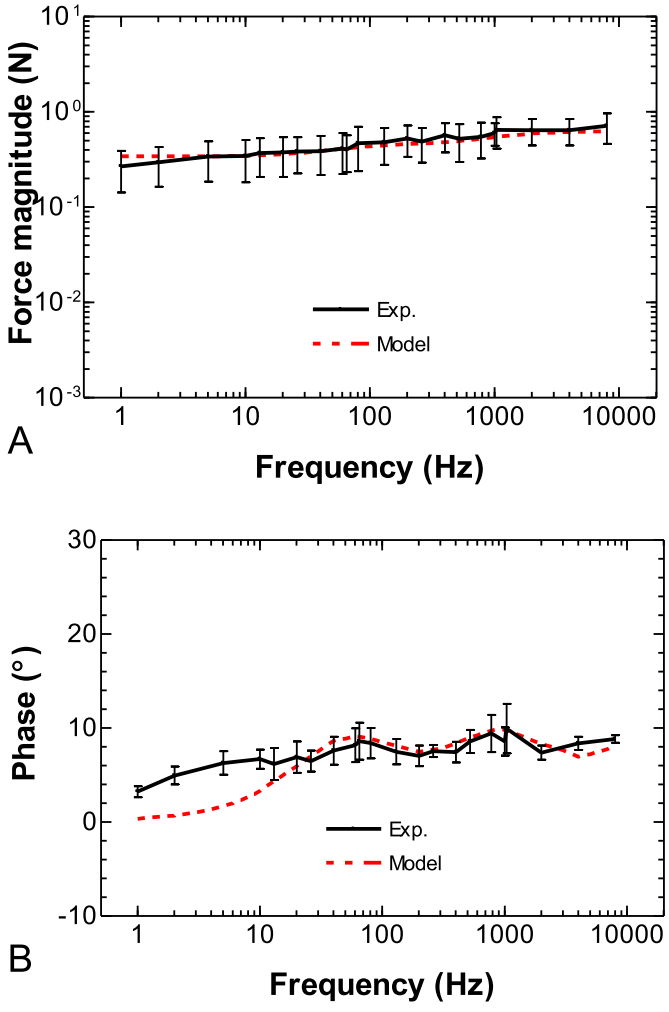


Fig. 7. Comparison between the forces on the lenticular process of the incus obtained from experimental-derived master curves and the FE model simulation. (A) The force magnitude–frequency curves. (B) The phase–frequency curves. (For interpretation of the references to color in the text, the reader is referred to the web version of this article.)

displacement and the force obtained from the experiment and FE model, respectively. Overall, the model predicted results matched the experimental data except for phase values at frequencies below 10 Hz. Since 10 Hz is lower than the normal auditory frequency range, the deviations are acceptable. Note that in the frequency range of 10–80 Hz where the results were directly obtained from the experimental data without any extrapolation by the FTS principle, the experimental data and model prediction still matched well. The good matching between the experimental and model-derived data suggested that the generalized Maxwell model ($n = 3$) was able to characterize the viscoelastic behavior of the joint capsule over the auditory frequency range.

4. Discussion

4.1. Comparison with published data

To the best of our knowledge, though the mechanical properties of human ISJ under quasi-static loading conditions were reported [19], there was no published data on dynamic properties of the ISJ in human or experimental animals by the time this paper was composed. Results from tension, compression, and stress relaxation tests by Zhang and Gan [19] demonstrated that the human ISJ exhibited typical viscoelastic behavior. Considering the displacement amplitude used in the present dynamic test was 0.1 mm, the average elastic modulus obtained from the 0.1 mm quasi-static tension and compression reported by Zhang and Gan was used for comparison. The mean storage modulus at 1 Hz (lowest testing frequency) in current experiment is 1.14 MPa (Fig. 6) and the result from quasi-static tests was approximately 1.17 MPa. Considering the strain rate of the sample in 1 Hz dynamic test was comparable to the condition of the quasi-static test, the mechanical properties of ISJ obtained in this study matched well to that reported in the previous study.

4.2. Contribution of the FE model of ISJ

Even though the quasi-static properties of the ISJ [19] and the analysis of ISJ structural effect on middle ear transfer function [4] have been reported, the dynamic properties of the joint remain unknown. In this study, the complex modulus of ISJ was obtained experimentally, and the mechanical properties of the joint capsule were predicted through the FE model of ISJ. To compare the ISJ mechanical properties obtained in this study with those used in the published FE models of the human ear, the ISJ model in Fig. 3 was replaced by two solid models of ISJ: linear elastic and viscoelastic replaced by two solid models of the ISJ, linear elastic [16] and viscoelastic [18], respectively. The linear elastic model of ISJ was based on the material properties used by Gan and Wang [16] with a Young's modulus of 0.6 MPa. The viscoelastic ISJ model was based on the material properties reported by Zhang and Gan [18] as the standard linear viscoelastic material with $E_0 = 0.4$ MPa, $E_1 = 20$ MPa, and $\tau_1 = 20$ μs. Fig. 8 shows the results of two material models of the ISJ in comparison with the experimental data and FE model results of this study. As shown in Fig. 8A, the linear elastic ISJ is unable to simulate frequency-dependent behavior of the joint, and there is no phase shift for the linear elastic ISJ in Fig. 8B. The force magnitude derived from the viscoelastic ISJ is lower than the experimental results at low frequencies and higher at high frequencies ($f > 800$ Hz). The phase angle of the derived force on the joint shown in Fig. 8B displays a huge increase at $f > 30$ Hz when the ISJ was molded as viscoelastic material. This indicates that the absence of the synovial fluid, cartilage, and viscoelastic joint capsule may not represent the dynamic behavior of the ISJ over a broad frequency range. However, future study on using dynamic properties of the ISJ in the human

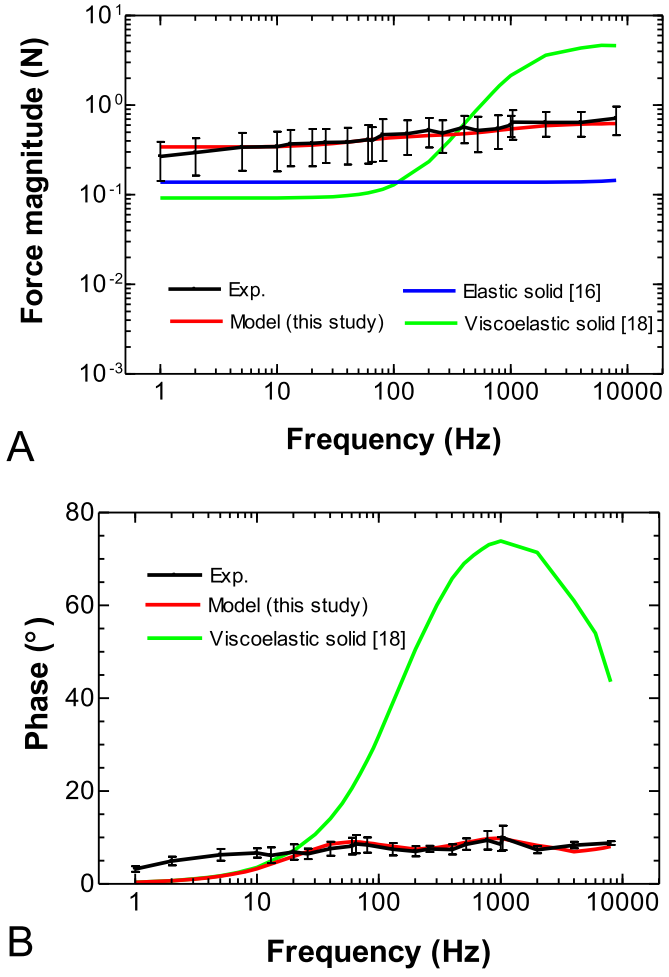


Fig. 8. Comparison between the forces on the lenticular process of the incus obtained from experimental-derived master curves and the FE models based on different material properties. (A) The force magnitude–frequency curves. (B) The phase–frequency curves.

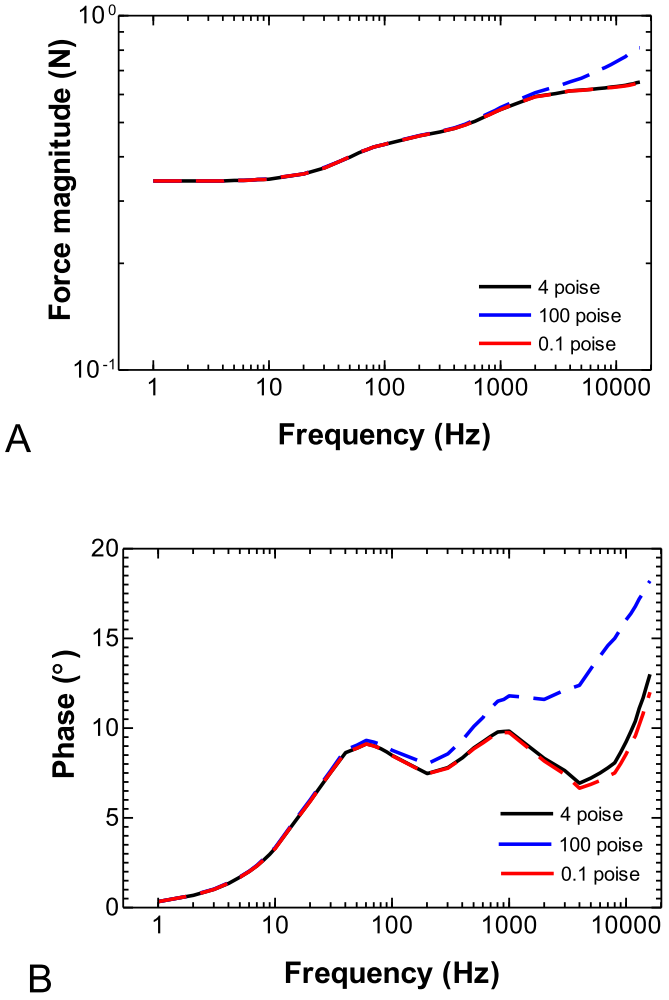


Fig. 9. Curves describing the force on the lenticular process of incus derived from the FE model simulation with different levels of synovial fluid viscosity. (A) The force magnitude–frequency curves. (B) The phase–frequency curves.

ear model may provide more insights for ISJ mechanical function for sound transmission. Fig. 8 demonstrates that the model results can be used to simulate the ISJ in the human middle ear model with higher accuracy comparing to previous models over the auditory frequency range.

In addition to providing the values of mechanical properties of the joint components, the FE model of the ISJ may also be used to evaluate the contribution of each component to the overall stiffness of the joint over the frequency range. The previous ISJ modeling suggested that the behavior of the joint was sensitive to the viscosity of the synovial fluid [4,19]. To confirm this observation, we conducted an analysis in the current ISJ model by varying the viscosity of the synovial fluid from 100 to 0.1 poise and calculating the force induced on the incus over frequencies of 1 Hz to 8 kHz as shown in Fig. 9. The model-derived force magnitude in relation to frequency is shown in Fig. 9A, and the phase shift between the displacement and force is shown in Fig. 9B. Note that the viscosity of the synovial fluid inside the articular joint changed from 100 to 0.1 poise when the shear rate increased from 0 to 5000/s due to the shear-thinning effect of the synovial fluid [31]. During the deformation process of the ISJ, the synovial fluid experienced shearing. Based on a broad frequency range of the results in Fig. 9 (1–8 kHz), the shear rate of the synovial fluid would increase with the testing frequency which might make the shear-thinning effect unneglectable. Considering that the frequency of the results in Fig. 9 was obtained by extrapolation, the values of the shear rate of the synovial fluid was difficult to be determined quantitatively from the frequency values. Therefore, values between 0 and 5000/s were used to make a qualitative estimation on the shear rate of the synovial fluid in the ISJs in this study to illustrate how the thinning effect of the synovial fluid will affect the behavior of the joint. Viscosity of 4 poise was used as the normal value for synovial fluid used in this study. As shown in Fig. 9, there was no significant difference in magnitude or phase of the force at low frequencies. The fluid viscosity started showing effects on the force magnitude at 1 kHz (Fig. 9A) and on the phase at 60 Hz (Fig. 9B). It can be said that the synovial fluid is a typical bioviscoelastic fluid whose storage and loss shear modulus increase with the shear rate [31]. In this study, the shear rate of the fluid is proportional to frequency in dynamic tests. Higher testing frequency results in higher storage and loss modulus of the synovial fluid, which increase the stiffness and energy dissipation of the entire ISJ structure. The change of mechanical properties of the ISJ was demonstrated by the increased force magnitude and phase of the incus in the FE model. Conclusively, the viscosity of the synovial fluid contributes to dynamic behavior of the ISJ mostly at high frequencies.

This study is the first report on dynamic properties of the human ISJ and we attempt to describe the properties of ISJ components based on a FE model of the joint. However, the measurement of the ISJ geometry was relatively coarse, especially the parameters which are unable to be measured directly in this study, such as the *m, L, h* and *D* as shown in the model of Fig. 3. Zhang and Gan [19] reported that the thinner cartilage (*h* decreased) would result in a reduced compressive stiffness of the ISJ. Therefore, if the h value used in the FE model is lower than the value in the experiment, the viscoelastic parameters of the joint capsule (E_0, E_1) obtained from the simulation would be higher than the true values. Moreover, the thickness of the capsule *m* is not directly measured either. Given the displacement-force relationship obtained from the FE model unchanged, the stiffness of the joint capsule would be negatively correlated with the value of *m*. In our future studies, we will explore the optic coherence tomography technique for measuring the ISJ structure. The accurate morphological data of ISJ will improve not only the experimental results, but also the FE model of the joint [32]. In addition to the ISJ's geometry parameters, the material properties of some components such as the cartilage are simplified as linear elastic in FE simulation. The frequent-dependent behavior of the cartilage was not involved in modeling analysis. The results provided by Zhang and Gan [19] indicated that the stiffness of the ISJ increased with the elastic modulus of cartilage, but the effect was less significant than that of cartilage thickness. Gan and Wang [4] suggested that the effect of the elastic modulus of the cartilage on the mobility of the incus was decreased with frequency if the cartilage was linear elastic. Another recent study indicated that the transfer function of the middle ear was closely related to the pretension inside the ossicular chain [33]. In this study, the pretension of the ossicular chain was released during the specimen preparation process and the initial status of the ISJ tested in the experiments was different from the physiological condition. In future studies, we may consider conducting the mechanical measurement with an intact ossicular chain.

5. Conclusion

Dynamic properties of human ISJ samples at 1–80 Hz were measured by DMA and the frequency range of the results was extrapolated by FTS principle to 8 kHz. The experimental data has been analyzed with a FE model of the joint. The mean value of storage modulus increased from 1.14 MPa at 1 Hz to 3.01 MPa at 8 kHz and the loss modulus increased from 0.07 MPa at 1 Hz to 0.47 MPa at 8 kHz. The 3D FE model of the human ISJ was used for identifying mechanical properties of the joint components by matching the model-derived data to the experimental results. The viscoelastic properties of the joint capsule were determined by using a 7-term generalized Maxwell model. The FE analysis indicated that the mechanical properties of the ISJ capsule and the viscosity of the synovial fluid affect the dynamic behavior of the joint. The results reported in this paper provide useful data for improving the accuracy of FE models of the human middle ear and contribute to a better understanding of the structure–function relationship of the ISJ.

Acknowledgments

We thank Don Nakmali for his help in sample preparation. This study was supported by National Institutes of Health (NIH) under grant R01DC011585 and Department of Defense (DOD) under grant W81XWH-14-1-0228.

References

[1] Funnell WRJ, Siah TH, McKee MD, Daniel SJ, Decraemer WF. On the coupling between the incus and the stapes in the cat. J Assoc Res Otolaryngol 2005;6(1):9–18.
[2] Karmody CS, Northrop CC, Levine SR. The incudostapedial articulation: new concepts. Otolo Neurotol 2009;30(7):990–7.
[3] Ortug G, Ortug C, Aydar Y. Configurations of incudostapedial joint surface, an SEM Study. FASEB J 2006;20(4):A442.
[4] Gan RZ, Wang X. Modeling microstructure of incudostapedial joint and the effect on cochlear input. Mechanics of hearing: protein to perception. Karavitaki KD, Corey DP, editors. Melville, NY: AIP; 2015.
[5] Gan RZ, Wood MW, Dormer KJ. Human middle ear transfer function measured by double laser interferometry system. Otol Neurotol 2004;25(4):423–35.
[6] Vishwakarma R, More YI, Joseph ST, Patel KB, Ramani MK, More RI. Incudostapedial joint arthroplasty using temporalis fascia/perichondrium ties. Am J Otolaryngol 2009;30(3):171–5.
[7] Maducdoc MM, Ghavami Y, Shamouelian D, Mahboubi H, Djalilian HR. Congenital anomalies of the incudostapedial joint. Int J Pediatr Otorhinolaryngol 2015;79(12):2277–80.
[8] Suzuki M, Kanebayashi H, Kawano A, Hagiwara A, Furuse H, Yamaguchi T, Shimizu M. Involvement of the incudostapedial joint anomaly in conductive deafness. Acta Otolaryngol 2008;128(5):515–19.
[9] Sim RJ, Chang P. Incudostapedial ankylosis from temporomandibular joint disruption. Otolaryngol Head Neck Surg 2008;139(1):166–7.
[10] Celik H, Aslan Felek S, Islam A, Demirci M, Samim E, Oztuna D. The impact of fixated glass ionomer cement and springy cortical bone incudostapedial joint reconstruction on hearing results. Acta Otolaryngol 2009;129(12):1368–73.
[11] Alian W, Majdalawieh O, Kiefte M, Ejnell H, Bance M. The effect of increased stiffness of the incudostapedial joint on the transmission of air-conducted sound by the human middle ear. Otol Neurotol 2013;34(8):1503–9.
[12] Szymanski M, Rusinek R, Zadrozniak M, Morshed K, Warminski J. The influence of incudostapedial joint separation on the middle ear transfer function. Clin Exp Otorhinolaryngol 2014;7(4):250–3.
[13] Prendergast PJ, Ferris P, Rice HJ, Blayney AW. Vibro-acoustic modelling of the outer and middle ear using the finite-element method. Audiol Neurotol 1999;4(3–4):185–91.
[14] Gan RZ, Feng B, Sun Q. Three-dimensional finite element modeling of human ear for sound transmission. Ann Biomed Eng 2004;32(6):847–59.
[15] Wada H, Koike T, Kobayashi T. Three-dimensional finite-element method (FEM) analysis of the human middle ear. In: Middle ear mechanics in research and otosurgery; 1997. p. 76–80.
[16] Gan RZ, Wang X. Multifield coupled finite element analysis for sound transmission in otitis media with effusion. J Acoust Soc Am 2007;122(6):3527–38.
[17] Gan RZ, Zhang X, Guan X. Modeling analysis of biomechanical changes of middle ear and cochlea in otitis media. In: Shera CA, Olson ES, editors. AIP conference proceedings; 2011. p. 539–44.
[18] Zhang X, Gan RZ. Finite element modeling of energy absorbance in normal and disordered human ears. Hear Res 2013;301:146–55.
[19] Zhang X, Gan RZ. Experimental measurement and modeling analysis on mechanical properties of incudostapedial joint. Biomech Model Mechanobiol 2011;10(5):713–26.
[20] Ferry JD. Mechanical properties of substances of high molecular weight: VI. Dispersion in concentrated polymer solutions and its dependence on temperature and concentration. J Am Chem Soc 1950;72(8):3746–52.
[21] Williams ML, Landel RF, Ferry JD. The temperature dependence of relaxation mechanisms in amorphous polymers and other glass-forming liquids. J Am Chem Soc 1955;77(14):3701–7.
[22] Ferry JD. Viscoelastic properties of polymers. John Wiley & Sons; 1980.
[23] Nielsen LE, Landel RF. Mechanical properties of polymers and composites. second ed. New York: Marcel Dekker; 1994.
[24] Peters GW, Meulman JH, Sauren AA. The applicability of the time/temperature superposition principle to brain tissue. Biorheology 1997;34(2):127–38.
[25] Chan RW. Estimation of viscoelastic shear properties of vocal-fold tissues based on time-temperature superposition. J Acoust Soc Am 2001;110:1548–61.
[26] Miri AK. Mechanical characterization of vocal fold tissue: a review study. J Voice 2014;28(6):657–67.
[27] Zhang X, Gan RZ. Dynamic properties of human tympanic membrane based on frequency-temperature superposition. Ann Biomed Eng 2012;41:205–14.
[28] Zhang X, Gan RZ. Dynamic properties of human stapedial annular ligament measured with frequency–temperature superposition. J Biomech Eng 2014;136:0810041–7.
[29] Hitt BM, Wang X, Gan RZ. Dynamic property changes in stapedial annular ligament associated with acute otitis media in the chinchilla. Med Eng Phys 2017;40:65–74.
[30] Oskui IZ, Hashemi A. Dynamic tensile properties of bovine periodontal ligament: a nonlinear viscoelastic model. J Biomech 2016;49(5):756–64.
[31] Fung YC. Biomechanics: mechanical properties of living tissues. second ed. New York: Springer Science & Business Media; 1993.
[32] Park J, Cheng JT, Ferguson D, Maguluri G, Chang EW, Clancy C, Lee DJ, Iftimia N. Investigation of middle ear anatomy and function with combined video otoscopy-phase sensitive OCT. Opt Express 2016;7(2):238–50.
[33] Koch M, Eßinger TM, Stoppe T, Lasurashvili N, Bornitz M, Zahnert T. Fully implantable hearing aid in the incudostapedial joint gap. Hear Res 2016;340:169–178.

Biomechanical Measurement and Modeling of Human Eardrum Injury in Relation to Blast Wave Direction

Rong Z. Gan, PhD; Kegan Leckness, MS; Don Nakmali, MS; Xiao D. Ji, PhD

ABSTRACT Rupture of the eardrum or tympanic membrane (TM) is one of the most frequent injuries of the ear after blast exposure. To understand how the TM damage is related to blast wave direction, human cadaver ears were exposed to blast waves along three directions: vertical, horizontal, and front with respect to the head. Blast overpressure waveforms were recorded at the ear canal entrance (P0), near the TM (P1), and inside the middle ear (P2). Thirteen to fourteen cadaver ears were tested in each wave direction and the TM rupture thresholds were identified. Results show that blast wave direction affected the peak P1/P0 ratio, TM rupture threshold, and energy flux distribution over frequencies. The front wave resulted in lowest TM rupture threshold and the horizontal wave resulted in highest P1/P0 ratio. To investigate the mechanisms of TM injury in relation to blast wave direction, the recorded P1 waveforms were applied onto the surface of the TM in a three-dimensional finite element model of the human ear and distributions of the stress in TM were calculated. Modeling results indicate that the sensitivity of TM stress change with respect to P1 pressure ($d\sigma/dP_1$) may characterize mechanical damage of the TM in relation to blast waves.

INTRODUCTION

Exposure to high-intensity sound or blast overpressure waves is considered to be an intrinsic situation faced by military personnel involved in combat operations. Over 60% of wounded-in-action service members have tympanic membrane (TM) injuries, tinnitus, and/or hearing loss.[1,2] The primary blast injury to the ear is caused by direct effect of the blast overpressure wave upon the TM and middle ear ossicular chain. Rupture of the TM is one of the most frequent injuries of the ear and has been investigated in animals and humans with wide variability.[3,4]

A recent study on chinchilla blast model by Gan *et al.*[5] reported the relationships between the TM rupture threshold, the TM damage pattern, and the overpressure waveforms. The results demonstrated that the TM rupture threshold was closely related to pressure waveforms at the entrance of the ear canal. The waveforms recorded under the shielded case had almost equal positive–negative pressure phases while the waveforms recorded in the open field had the positive pressure only. The TM rupture threshold measured in the shielded case was much lower than that in the open field. These findings in animal blast model brought further research requests on identifying human TM damage after blast exposure and the TM rupture threshold in relation to blast overpressure wave direction.

This paper reports our current study of measuring blast wave transmission through the human ear under three different incident blast directions with respect to the head or ear. In addition to experimental tests in human cadaver ears, a three-dimensional (3D) finite element (FE) model of the human ear for blast simulation was developed to simulate blast overpressure transduction through the ear.[6] The mechanisms of TM damage in relation to blast wave direction were characterized using this model.

The goal of this study is to determine the relationships between the TM rupture threshold and blast wave directions. Both the experimental measurements and computational modeling of blast wave transduction from the ear canal to middle ear will provide important data for prediction of TM injury and hearing damage induced by blast exposure in the battlefield.

METHODS

Experimental Setup and Protocol

A "head block" attached with human cadaver ear or temporal bone and mounted with two pressure sensors has been developed in our lab to measure the transfer functions of the ear canal and middle ear in response to blast overpressure. In addition to two pressure sensors inside the ear, the third sensor is placed at the entrance of the ear canal. The three pressure sensors are simultaneously monitoring the blast pressure at the entrance of the ear canal (P0), near the TM in the canal (P1), and behind the TM in the middle ear (P2) as shown in Figure 1. The pressure sensor P0 (Model 102B16, PCB Piezotronics, Depew, NY) is placed at 1 cm lateral to the ear canal opening with the sensing surface facing the blast. The other two sensors P1 and P2 (Model 105C02, PCB Piezotronics) are placed at 3 mm from the TM in the canal and inside the middle ear cavity through the Eustachian tube, respectively. The P0 and P1 difference shows the transfer function of the ear canal in response to blast wave, and the difference between P0 and P2 or between P1 and P2 shows the middle ear transfer function or indicate how much sound pressure is transmitted into the middle ear in both time and frequency domains, respectively.

School of Aerospace and Mechanical Engineering, University of Oklahoma, 865 Asp Avenue, Norman, OK 73019

doi: 10.1093/milmed/usx149

© Association of Military Surgeons of the United States 2018. All rights reserved. For permissions, please e-mail: journals.permissions@oup.com.

Downloaded from https://academic.oup.com/milmed/article-abstract/183/suppl_1/245/4959935
by guest
on 07 April 2018

The "head block" was exposed to open-field blast inside an anechoic test chamber along three directions: the vertical, horizontal, and front with respect to the head as shown in Figure 2. A total of 41 fresh human temporal bones (TBs) were used in this study for testing of three wave directions: from the top of the head – the vertical setup (13 TBs, donors' average age 66.2 ± 6.6), from the lateral to the ear – horizontal setup (14 TBs, donors' average age 64.5 ± 9.6), and from the front of the face – the front setup (14 TBs, donors' average age 73.7 ± 7.1). The setups along these three directions with the pictures of head block are displayed in Figure 2. The TBs were obtained from Life Legacy Foundation, a certified human tissue supply source for military research. The study protocol was approved by the US Army Medical Research and Material Command Office of Research Protections.

All experiments on human TBs were performed in the Biomedical Engineering Laboratory at the University of Oklahoma. A well-controlled compressed air (nitrogen) – driven blast apparatus located inside an anechoic chamber was used to create a blast overpressure wave in this study.[5–7] Polycarbonate film (McMaster-Carr, Atlanta, GA, USA) of either 130 µm or 260 µm thick was employed to generate blast overpressure of at least 30 psi (207 kPa or 200 dB SPL). The overpressure level was controlled by varying the distance from the blast reference plane.

The pressure sensor signal was measured by cDAQ 7194 and A/D converter 9215 (National Instruments Inc., Austin, TX, USA) with the sampling rate of 100 k/s (10 µs dwell time). The LabVIEW software package (NI Inc.) was used for data acquisition and analysis. The waveform of each blast test was saved in a PC for further analysis.

It usually took three-to-four iterations of blast tests to reach the TM rupture threshold defined as the peak pressure before the TM rupture. That means if the TM ruptured after the third blast, the threshold was the peak pressure level of the second blast. The initial blast pressure level was selected based on the system calibration using different films and changing the distance between the sensor surface and the blast reference plane. The number of blast tests also varied with individual TBs due to the variation among the human samples and setups. To confirm the TM damage, an otoscopic examination of the ear was performed first and further verification was done using wideband tympanometry to determine whether the TM was ruptured.[5] When the TM was found without rupture, the next blast test was conducted with an increase of overpressure level. The testing stopped when the ear was ruptured. Note that the TM rupture threshold is a parameter to describe TM tissue damage in relation to the pressure force reaching the TM surface during blast exposure, which may not only depend on pressure level but also the exposure times before the rupture. However, in this study, the time interval between exposures was very short and the mechanical change of TM tissue in previous exposure was neglected.

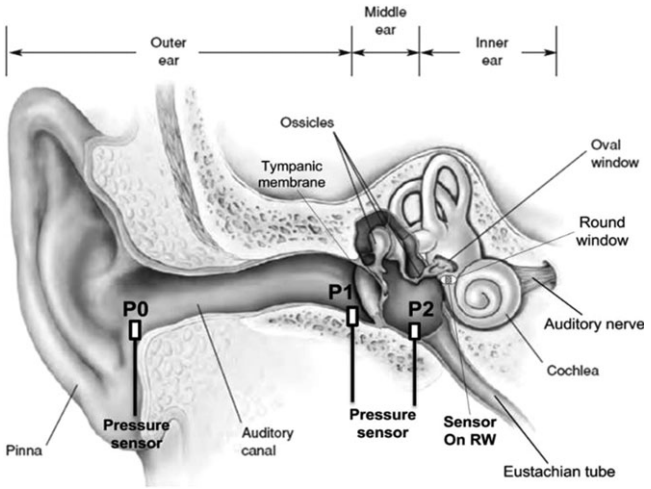


FIGURE 1. Schematic of simultaneously measuring blast overpressure transduction through the ear with three pressure sensors.

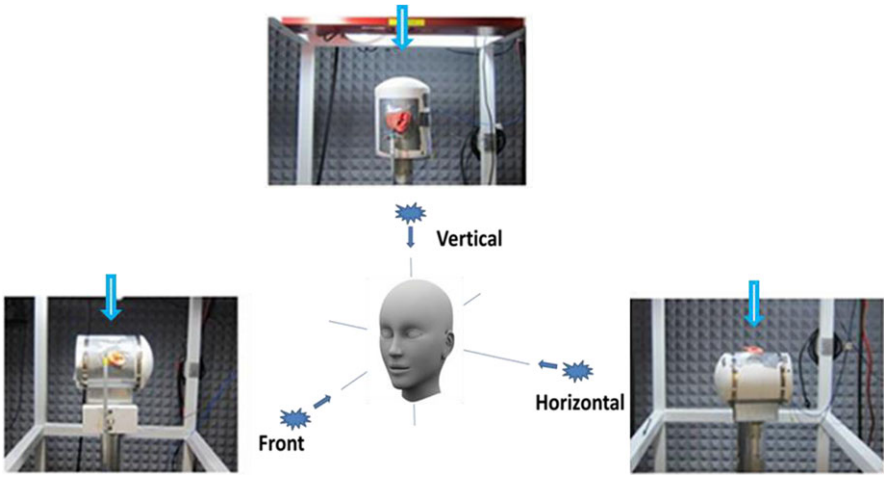


FIGURE 2. Schematic of three blast wave directions with respect to the head and the pictures of experimental setup with the head block along the vertical, horizontal, and front wave directions inside the test chamber. The blue arrow in each picture shows blast wave origination for the vertical, horizontal, and front setup test, respectively.

Downloaded from https://academic.oup.com/milmed/article-abstract/183/suppl_1/245/4959935
by guest
on 07 April 2018

Waveform Analysis

Blast pressure energy spectra analysis on recorded waveforms (P0, P1, and P2) in the time domain was conducted in MATLAB to determine the signal energy distribution over the frequencies under three blast wave directions. First, the recorded pressure waveforms were converted to pressure distributions over the frequencies of 0.2–20 kHz by using FFT spectral analysis. Next, following the methods of impulse signal energy distribution theory reported by Gan et al,[5] the total sound exposure was divided by the standard characteristic impedance of the air ρc as impulse energy flux (energy per unit area) and expressed as:

$$E^* = \frac{1}{\rho c}\int_0^T p^2(t)\,dt, \quad [\mathrm{J/m^2}] \tag{1}$$

where $p(t)$ is the instantaneous value of acoustic pressure in Pa or N/m^2, dt is the time increment for scanning of acoustic pressure in seconds, T is the duration of $P(t)$, and $\rho c = 406$ mks rayls to produce a quantity with units of energy flux (i.e., J/m^2). Both ρ and c are pressure-dependent in the shock front. The duration of $T = 6$ ms was used for calculation in the present study.

Eight octave band-pass filters with center frequencies at 125 Hz, 250 Hz, 500 Hz, 1 kHz, 2 kHz, 4 kHz, 8 kHz, and 16 kHz were designed. A low pass filter L125 and a high pass filter H16k were also designed to catch signals at frequencies lower than 125 Hz and higher than 16 kHz. The filtered signals were then generated and the sound energy in each band was calculated as the distribution of pressure energy flux over 10 bands. Instead of directly comparing the energy flux values in the three wave directions, the energy in each band was normalized with respect to the total sound energy in that band.

Finite Element Modeling

The 3D FE model of the human ear developed by Gan *et al*[8] for sound transmission and being used for TM perforation studies was employed to simulate the blast wave transmission through the ear as shown in Figure 3. The FE model consisted of the ear canal, TM, TM annulus (TMA), three ossicles connected by two joints: incudomelleolar joint (IMJ) and incudostapedial joint (ISJ), middle ear suspensory ligaments/muscle tendons, stapedial annular ligament (SAL), and the middle ear cavity. The cochlea was not included in this initial model, but the cochlear load was applied on the stapes footplate by a mass block-dashpot system with the cochlear input impedance of 20 GΩ.[8] The cochlear impedance was defined as the pressure per unit volume velocity of stapes footplate.

This FE model of the human ear was regenerated in ANSYS Workbench (ANSYS Inc., Canonsburg, PA, USA) where Fluent/ANSYS Mechanical coupled fluid–structure interaction analyses were employed to compute blast overpressure transduction from the environment to the TM and middle ear.[6] Briefly, the viscoelastic material properties were assigned to soft tissues in the middle ear including the TM, TMA, IMJ, ISJ, and SAL. The experimentally recorded P0 waveforms from the head block with cadaver TBs were applied onto the boundary at the entrance of the ear canal and the pressure waveforms P1 and P2 were then calculated and compared with those measured from the experiments. Note that the detailed description and validation of the FE model of the human ear for blast overpressure wave transduction can be found in Leckness' MS thesis (2016).[6]

The FE model was employed to investigate the mechanisms of TM injury under recorded P1 profiles from the vertical, horizontal, and front directions in this study. The P1 overpressure waveforms recorded from multiple iterations of blast tests in 14 temporal bones (four from the vertical direction and five from the horizontal and front directions) were applied to the surface of the TM in the FE model. The equivalent (von Mises) stress was used as a measure of the stress state of the TM and the maximum stress distributions on the TM were calculated. The sensitivity of TM stress with respect to P1 pressure increase, that is the TM stress gradient with respect to P1, $d\sigma/dP_1$, was then calculated from the model based on experimental P1 waveforms of pre-threshold

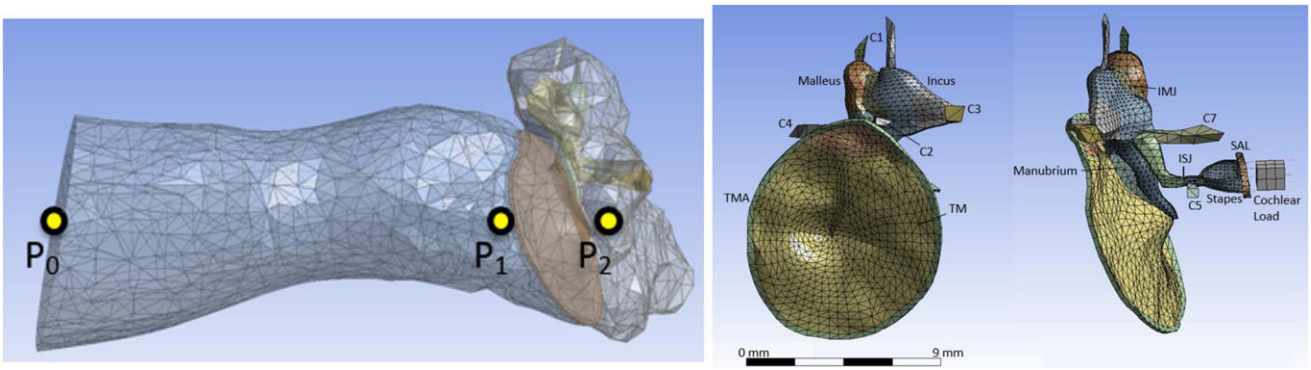


FIGURE 3. (Left) FE model of the human ear comprised of the ear canal, TM, middle ear ossicles, and middle ear cavity. The locations for pressure monitoring points are designated as P0, P1, and P2. (Right) Structural mesh of the model, showing the TM, TMA, middle ear ossicles, IMJ, ISJ, suspensory ligaments/muscle tendons (all Cs and SAL), and cochlear load.

Downloaded from https://academic.oup.com/milmed/article-abstract/183/suppl_1/245/4959935
by guest
on 07 April 2018

up to rupture level. Usually two-to-four pressure waveforms per cadaver ear or temporal bone were involved in modeling calculation for $d\sigma/dP_1$.

RESULTS

Blast Experiment

Figure 4 shows typical overpressure waveforms of P0, P1, and P2 recorded from three cadaver ears in the vertical, horizontal, and front tests (before the TM rupture). The pressure waves are displayed in 2 ms of time duration and the positive overpressure is followed by negative pressure. As shown in Figure 4, the peak P0 level was around 50 kPa or 7.5 psi or 188 dB SPL for all three tests. The P1 peak pressure shows a substantial increase compared to the P0 pressure in all wave direction tests. The results demonstrate the ear canal effect on enhancing the impulse pressure level near the TM in the canal.

The otoscopic photos displayed in Figure 5 illustrate the TM damages observed at the vertical (V), horizontal (H), and front (F) tests with the peak P0 pressure level of 191, 186, and 189 dB SPL (or 11, 6, and 8 psi), respectively. There is no consistent TM rupture pattern observed from the experiments at different wave directions. However, in the most ruptured TM samples, the damage along the TM-radial fiber direction is observed, which is consistent with that the circumferential fibers of the TM have lower fracture strength and would break before the radial fibers. In some TM samples, the rupture area is near the manubrium or inferior side of the TM along the radial direction.

Table I lists the mean and standard deviation (SD) of P0, P1, P2, ratio of P1/P0 and the TM rupture P0 and P1 thresholds obtained from all tests along three blast wave directions: V, H, and F. The P1 rupture threshold was determined by multiplying the P1/P0 ratio and the P0 rupture threshold for each direction. The results in Table I show that the P0 rupture threshold for the V and F directions are comparable and that the P0 threshold in H-direction is significantly lower than the other two directions. Conversely, the P1/P0 ratio in H-direction is well above the others. It is also observed from Table I that the P1 rupture threshold (the pressure that is directly responsible for TM damage) is similar for the V and H directions, at 20.2 and 20.1 psi, respectively. Interestingly, the results indicate that the F direction requires less pressure as measured at P1 to rupture the TM.

Waveform Analysis

Figure 6 displays the comparison of impulse energy flux (energy per unit area in unit J/m^2) distributed in 10 frequency bands from the below 125 Hz to over 16 kHz obtained from waveforms recorded in three wave direction tests. The results demonstrate that (1) P0 pressure-induced energy is mainly distributed at frequencies below 1 kHz and there is a large peak for V direction at 500 Hz as shown in Fig. 6A; (2) P1 pressure-induced energy is distributed mainly at frequencies up to 4 kHz as shown in Fig. 6B; and (3) blast waves at F and H directions

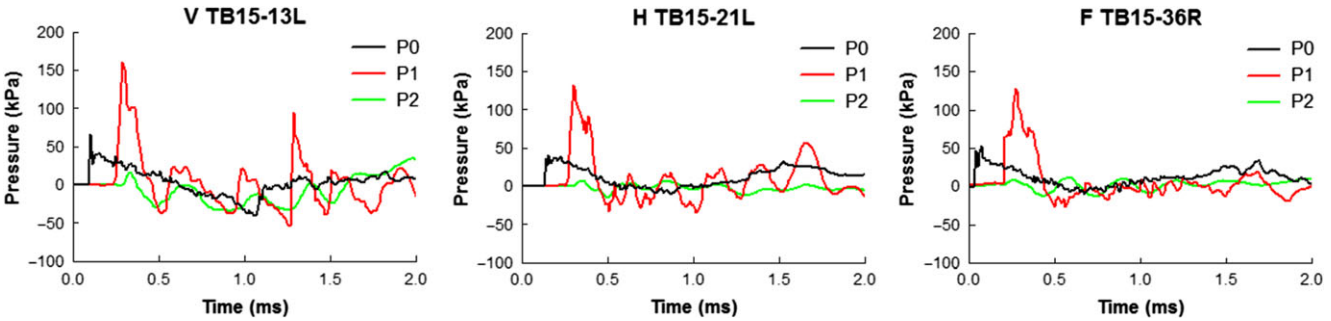


FIGURE 4. Overpressure waveforms of P0 (black), P1 (red), and P2 (green) recorded from three cadaver ears or temporal bones under the vertical (V, left), horizontal (H, medium), and front (F, right) tests. TB15-13L, TB15-21L, and TB15-36R represent the temporal bone (TB) samples.



FIGURE 5. Otoscopic pictures of human TMs ruptured after blast exposure. (A) Vertical test, left ear, TM ruptured in the superior-posterior region; (B) horizontal tests, left ear, TM ruptured in the inferior side; (C) front test, right ear, TM ruptured in the superior-posterior region.

Downloaded from https://academic.oup.com/milmed/article-abstract/183/suppl_1/245/4959935
by guest
on 07 April 2018

TABLE I. Mean and SD of Peak Pressure Values P0, P1, and P2, Ratio of P1/P0 and the TM Rupture P0 and P1 Thresholds

Blast Wave Direction	TB Sample	P0 (psi)	P1 (psi)	P2 (psi)	P1/P0	Threshold P0 (psi)	Threshold P1 (psi)
Vertical	Mean ± SD ($N = 13$)	8.9 ± 1.8	19.3 ± 3.3	2.3 ± 1.6	2.2 ± 0.5	9.2 ± 1.7	20.2 ± 2.2
Horizontal	Mean ± SD ($N = 14$)	6.4 ± 2.1	19.0 ± 6.1	2.2 ± 1.4	3.0 ± 0.7	6.7 ± 1.2	20.1 ± 1.9
Front	Mean ± SD ($N = 14$)	9.8 ± 2.0	16.3 ± 3.3	2.1 ± 0.7	1.7 ± 0.4	9.8 ± 2.1	16.7 ± 2.5

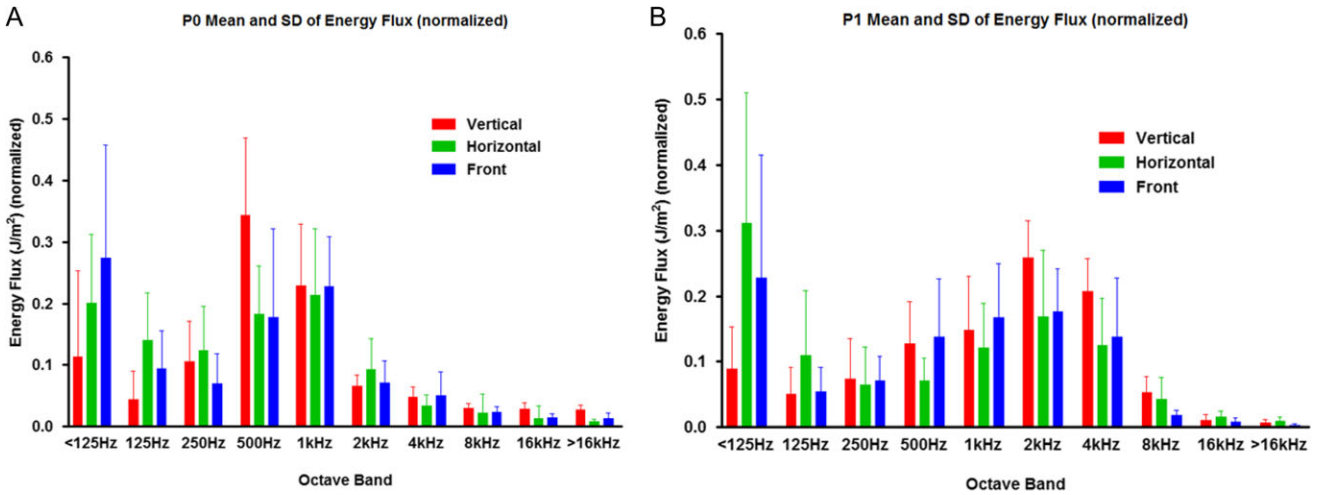


FIGURE 6. Comparison of normalized energy flux over 10 octave bands from below 125 Hz to above 16 kHz between the waveforms recorded in vertical, horizontal, and front tests. (A) Mean and SD of energy flux for P0 waveforms; (B) mean and SD of energy flux for P1 waveforms.

result in relatively large energy flux of both P0 and P1 at frequencies below 125 Hz.

FE Modeling

The average maximum stresses induced by the P1 rupture threshold waveforms were 16.2 ± 3.0, 16.3 ± 2.4, and 14.3 ± 2.5 MPa for the vertical, horizontal, and front directions, respectively. The average maximum stresses induced by the P1 waveforms that caused visible TM damage were 20.3 ± 1.2, 18.8 ± 2.0, and 15.5 ± 3.5 MPa for the vertical, horizontal, and front directions, respectively. An example of TM stress distribution at the time of maximum stress due to an applied P1 waveform of 134 kPa maximum pressure is displayed in Figure 7. As shown in this figure, the maximum stress reached 16 MPa and the regions of highest stress were along the anterior portion of the TMA, the posterior to the center of the manubrium, and the inferior to the bottom of the manubrium. These locations may indicate potential sites for TM rupture.

To understand the mechanism behind the experimental findings, the sensitivity of TM stress with respect to P1 pressure increase as the TM stress gradient with respect to P1, $d\sigma/dP_1$, were calculated from the four cadaver ears at the V direction test and five at the H and F direction tests, respectively. As an example, Figure 8A–C show a series of P1 pressure waveforms over 0.5 ms duration from three temporal bone experiments in V, H, and F direction test, respectively. The P1 waveforms

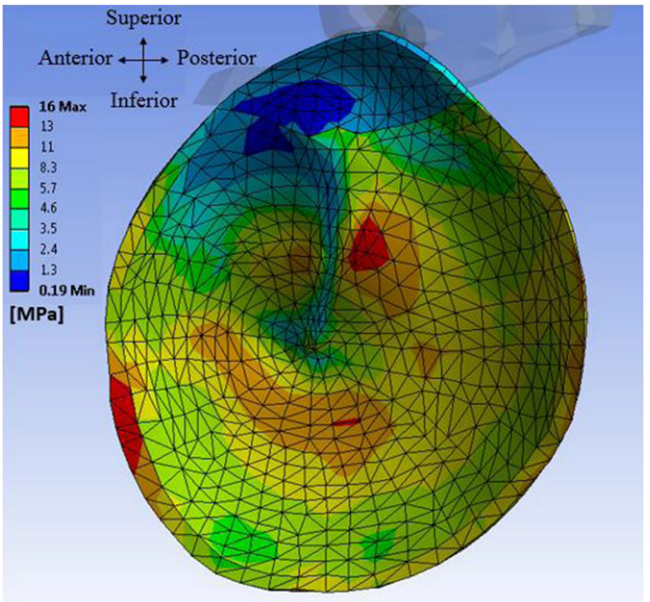


FIGURE 7. FE model-derived distribution of the equivalent (von Mises) stress in the TM when the maximum stress was reached under the vertical wave direction.

recorded from 3 to 4 blasts to reach TM rupture were used to calculate $d\sigma/dP_1$ in V, H, and F directions using the model.

All the data points of the maximum stress in the TM vs. the maximum (peak) P1 pressure obtained along the V, H,

Downloaded from https://academic.oup.com/milmed/article-abstract/183/suppl_1/245/4959935
by guest
on 07 April 2018

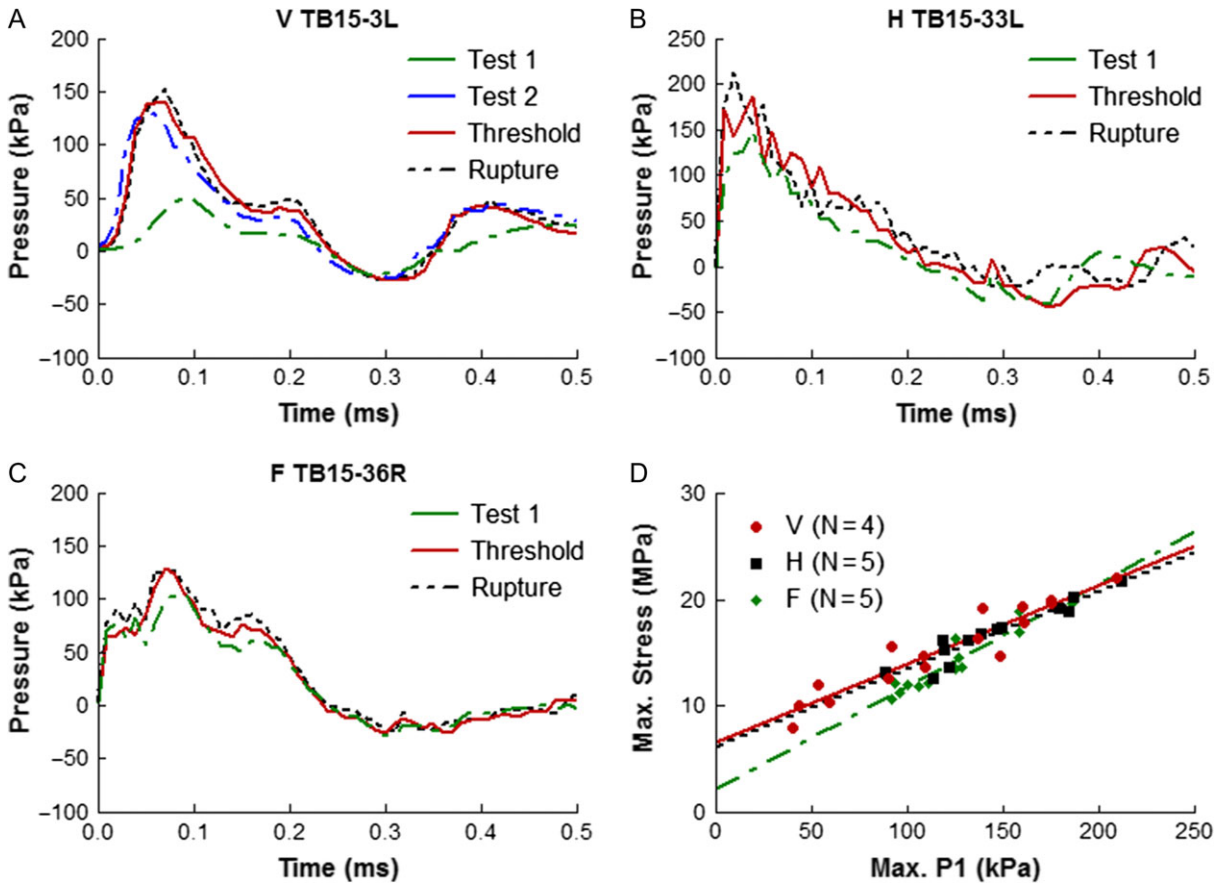


FIGURE 8. (A), (B), and (C) represent the P1 pressure waveforms with incremental peak pressure level from initial test 1 to TM rupture recorded from a temporal bone sample TB15-3L in V direction test, from sample TB15-33L in H-direction test, and from sample TB15-36R in F direction test, respectively. (D) Plots of FE model-derived maximum stress in the TM vs. P1 peak pressure obtained from V direction ($N = 4$), H direction ($N = 5$), and F direction ($N = 5$).

and F blast direction tests were plotted in Figure 8D. Statistical correlation was then applied to determine the best-fit line for the data points at each direction. Figure 8D shows the comparison of the slope (i.e., stress gradient) $d\sigma/dP_1$ at three directions. The mean value of stress gradient with respect to pressure P1 was calculated as 74.1, 73.0, and 96.7 for V, H, and F direction, respectively.

DISCUSSION

Mechanisms of TM Rupture in Relation to Blast Wave Direction

The energy analysis results shown in Figure 6 suggest that P1 pressure waveform should be considered as a primary factor for blast-induced TM damage because P1 energy distributions on octave bands are similar for all three wave directions and concentrated from 500 Hz to 4 kHz. Moreover, the P1 pressure is measured near the TM which represents the pressure force reaching the TM surface during blast exposure. Thus, the P1 threshold for TM damage is more accurately represent the pressure applied to the TM than the P0 threshold. The experimental results shown in Table I indicate that P1 threshold in F direction is lower than V and H directions, or in other words, the blast wave from front of the face (F direction) is easier to cause TM rupture than other blast wave directions. Now the question is: why does the front direction of blast wave result in a lower P1 threshold for TM damage?

To answer this question and understand the mechanism behind the experimental findings, the FE model of the human ear was used to compute the distributions of the stress in the TM and derive the sensitivity of TM stress with respect to P1 pressure increase as the TM stress gradient with respect to P1, $d\sigma/dP_1$. The results shown in Figure 8 indicate that the change of maximum stress in the TM with respect to P1 peak pressure increase in the front direction is higher than other two directions. The high sensitivity of TM stress with respect to the P1 pressure in front setup, or the blast wave coming to the face, may characterize mechanical damage of the TM induced by blast. The average maximum stress was lowest for the front direction, as was the average P1 rupture threshold; this suggests that neither stress level nor P1 level alone determines TM failure, but that TM failure is best predicted by the rate change of stress with respect to maximum P1 pressure reaching the TM.

This finding agrees with the study reported in chinchilla TM damage by Gan *et al.*[5] The variation of TM stress in chinchilla ear with respect to blast overpressure level showed

Downloaded from https://academic.oup.com/milmed/article-abstract/183/suppl_1/245/4959935
by guest
on 07 April 2018

obvious difference between the open and shielded exposures in Gan's paper (Figure 10 of that paper). The rapid change of stress σ to the pressure loading p, or the higher $d\sigma/dp$ value in shielded case than the open case, resulted in a lower threshold of TM rupture in chinchilla blast experiments. The present study in human TM damage during the blast exposure also shows that the rate of stress change with respect to the overpressure loading is a parameter to characterize TM tissue damage caused during the blast exposure.

Additional Insight from This Work

This is the first time the TM damage in relation to blast overpressure wave direction has been investigated using the human cadaver ears and 3D FE model of the human ear. The available studies in the literature on the effect of blast direction on tissue injury are mainly in the areas of brain responses to different blast or impact directions using the computational modeling approach. For example, a recent study by Sarvghad-Moghaddam *et al*[9] reported their FE analysis of the human head model with the helmet and faceshield under three blast wave directions: the front, back, and side of the head. The calculated intracranial pressure and the maximum shear stress were used as the major injury predictors for evaluation of helmet and faceshield protections. Sarvghad-Moghaddam *et al* found that the underwash incidence overpressure greatly changed with the blast direction. However, the main limitation of their study and probably similar blast-head interaction studies is lack of validation of the head model against blast loads as stated in their paper.

Compared with the published works in head injury in relation to blast direction, the present study includes both the experimental tests in human cadaver ears and the FE modeling of the TM maximum stress increasing with blast pressure loads. The results and findings from this study have general contributions for providing the TM rupture threshold data and the mechanisms of TM damage during blast exposure. The results reported in this paper can be used in clinics for understanding or explaining the TM damage in relation to blast exposure for military Service members regarding their specific experiences in the battlefield. However, there are still many questions to be answered, including the TM damage after repetitive blast exposures and the relationship between the mechanical injuries of the TM and the cochlear damage during blast exposure. The investigation along this direction on mechanisms of the TM and other ear tissue damages in relation to blast overpressure waveforms is needed for development of the failure criteria for TM, a multiple layer, viscoelastic membrane tissue, in response to blast overpressure.

CONCLUSIONS

The relationship between the TM damage threshold and blast overpressure wave direction has been investigated in human cadaver ears or temporal bones and the FE model of the human ear. The "head block" attached with the temporal bone was exposed to open-field blast inside the test chamber at three incident wave directions: vertical, horizontal, and front with respect to the head. Results demonstrate that blast overpressure P0 at the ear canal entrance induced the highest peak pressure P1 near the TM in the canal, which determines the TM injury. The P1 pressure differences in vertical, horizontal, and front tests reflect the variations of energy flux distribution over frequencies, peak P1/P0 ratio, and TM rupture threshold. FE modeling results indicate that P1 threshold for TM rupture in front direction is the lowest because of the highest TM stress change rate with respect to P1 pressure increase, $\delta\sigma/\delta p_1$, compared with the vertical and horizontal directions.

PRESENTATIONS

Presented in a breakout session entitled "The Role of Medical Research in Blast Injury" at the 2016 Military Health System Research Symposium. (Abstract number: MHSRS-16-0405).

FUNDING

This work was supported by U.S. Army Medical Research and Material Command (USAMRMC) Military Operational Medicine Research Program, Contract No. W81XWH-14-1-0028.

REFERENCES

1. Helfer TM, Jordan NN, Lee RB: Postdeployment hearing loss in U.S. Army soldiers seen at audiology clinics from April 1, 2003, through March 31, 2004. Am J Audiol 2005; 14: 161–8.
2. Cave KM, Cornish EM, Chandler DW: Blast injury of the ear: clinical update from the global war on terror. J Mil Med 2007; 172(7): 726–30.
3. Cho S-I, Gao SS, Xia A, et al: Mechanisms of hearing loss after blast injury to the ear. PLoS One 2013; 8(7): e67618.
4. Fausti SA, Wilmington DJ, Gallun FJ, Myers PJ, Henry JA: Auditory and vestibular dysfunction associated with blast-related traumatic brain injury. J Rehabil Res Dev 2009; 46(6): 797–810.
5. Gan RZ, Nakmali D, Ji X, Leckness K, Yokell Z: Mechanical damage of tympanic membrane in relation to impulse pressure waveform - a study in chinchillas. Hearing Res 2016; 340: 25–34.
6. Leckness K: Novel finite element method to predict blast wave transmission through human ear. Thesis for Master Degree in Biomedical Engineering at University of Oklahoma, August 2016. Avialable at http://hdl.handle.net/11244/44932; accessed December 30, 2016.
7. Hawa T, Gan RZ: Pressure distribution in a simplified human ear model for the high intensity sound transmission. J Fluids Eng 2014; 136(11): 111108-1–6.
8. Gan RZ, Cheng T, Dai C, Yang F, Wood MW: Finite element modeling of sound transmission with perforations of tympanic membrane. J Acoust Soc Am 2009; 126(1): 243–53.
9. Sarvghad-Moghaddam H, Rezaei A, Ziejewski M, Karami G: Evaluation of brain tissue responses because of the underwash overpressure of helmet and faceshield under blast loading. Int J Numer Mechod Biomed Eng 2017; e02782: 1–13.

Downloaded from https://academic.oup.com/milmed/article-abstract/183/suppl_1/245/4959935
by guest
on 07 April 2018

Computational Modeling of Blast Wave Transmission Through Human Ear

Kegan Leckness, MS; Don Nakmali, MS; Rong Z. Gan, PhD

ABSTRACT Hearing loss has become the most common disability among veterans. Understanding how blast waves propagate through the human ear is a necessary step in the development of effective hearing protection devices (HPDs). This article presents the first 3D finite element (FE) model of the human ear to simulate blast wave transmission through the ear. The 3D FE model of the human ear consisting of the ear canal, tympanic membrane, ossicular chain, and middle ear cavity was imported into ANSYS Workbench for coupled fluid–structure interaction analysis in the time domain. Blast pressure waveforms recorded external to the ear in human cadaver temporal bone tests were applied at the entrance of the ear canal in the model. The pressure waveforms near the tympanic membrane (TM) in the canal (P1) and behind the TM in the middle ear cavity (P2) were calculated. The model-predicted results were then compared with measured P1 and P2 waveforms recorded in human cadaver ears during blast tests. Results show that the model-derived P1 waveforms were in an agreement with the experimentally recorded waveforms with statistic Kurtosis analysis. The FE model will be used for the evaluation of HPDs in future studies.

INTRODUCTION

Hearing loss is the most common disability among veterans, and is often caused by exposure to high-intensity sound or blast overpressure waves that are considered to be an intrinsic eventuality faced by military personnel involved in most operational activities. Blast overpressure is a high-intensity disturbance in the ambient air pressure that is characterized by an intense impulse sound wave of over 170 dB sound pressure level (SPL).[1] When exposed to a blast, the human auditory system is vulnerable to both peripheral and central damage from the overpressure.[2,3]

In a previous study by Gan et al,[4] the experimental measurement and finite element (FE) modeling methods were used to investigate blast-wave-induced tympanic membrane (TM) rupture in two cases in chinchillas: the open-field and shielded cases. Eighteen animals were tested under two cases (nine for each) and the stainless steel cup was used as a shield. A compressed nitrogen-driven blast apparatus located inside an anechoic chamber in the Biomedical Engineering Laboratory at the University of Oklahoma was used to generate blast overpressure. The resulting waveforms were then recorded and TM rupture was observed. Driven by experimentally measured pressure waveforms, the FE model of the chinchilla middle ear[5] was used to develop the stress distributions in the TM for the open-field and shielded cases. The stress gradients with respect to the maximum incident pressure were then derived to explain why the shielded chinchillas' TMs ruptured at much lower pressure levels than those without a shield.

In this article, we report our recently developed three-dimensional (3D) FE model of the human ear to simulate blast wave transmission through the ear. The purpose of this study is to provide a 3D computational model for the improvement of current auditory hazard assessment models and for a better understanding of blast wave transmission through the human ear.

A 3D human ear model published by Gan et al[6] consisting of the ear canal, TM, ossicular chain, and middle ear cavity was used in this study. Fluent/ANSYS Mechanical coupled fluid–structure interaction (FSI) analyses were employed to compute blast overpressure transduction from the environment to the TM and middle ear. Fresh human cadaver temporal bones (TBs) with all soft tissue intacts were subjected to blast exposures from three directions (vertical, horizontal, and front) inside the test chamber. The pressures at the ear canal entrance (P0), near the TM in the canal (P1), and behind the TM in the middle ear cavity (P2) were simultaneously monitored. The P0 waveforms measured in cadaver ears were applied at the entrance of the ear canal of the FE model. The P1 and P2 pressures were calculated from the model. The model-derived results were compared with experimentally measured P1 and P2 waveforms from human cadaver ears. The comparisons show that the FE model of the human ear is able to predict blast overpressure transmission through the ear canal into the middle ear. The model will be used for the evaluation of hearing protection devices (HPDs) in future studies.

METHODS

FE Model

Human ear FE model geometry built on a set of histological cross-sectional images of a human TB reported by Gan et al[6] was remeshed in HyperMesh 12 (Altair Engineering, Inc.,

School of Aerospace and Mechanical Engineering, University of Oklahoma, 865 Asp Avenue, Norman, OK 73019.

doi: 10.1093/milmed/usx226

© Association of Military Surgeons of the United States 2018. All rights reserved. For permissions, please e-mail: journals.permissions@oup.com.

Downloaded from https://academic.oup.com/milmed/article-abstract/183/suppl_1/262/4959995
by guest
on 07 April 2018

Troy, MI, USA) using tetrahedral and wedge elements. The model consists of the ear canal, TM (pars flaccida and pars tensa), TM annulus (TMA), manubrium, ossicles and associated suspensory ligaments, incudo-malleolar joint (IMJ), incudostapedial joint (ISJ), and stapedial annular ligament (SAL). The middle ear structures, ear canal, and middle ear cavity consist of 8,043, 13,805, and 11,884 elements, respectively.

The entire model (Fig. 1) was then imported into the ANSYS Workbench v16.1 (ANSYS Inc., Canonsburg, PA, USA) environment where the strongly coupled FSI analysis method was developed. The structural calculations were carried out in ANSYS Mechanical. Linear viscoelastic material properties reported by Zhang and Gan[7] were assigned to the middle ear soft tissues including the TM, TMA, IMJ, ISJ, and SAL. The manubrium, ossicles, and suspensory ligaments were presented as elastic materials as reported by Gan et al.[6] The TMA, SAL, and ends of the suspensory ligaments where they meet the bony wall were given fixed boundary conditions. As the cochlea was not included in this initial model, its damping effect on stapes footplate motion was modeled by introducing a mass block-dashpot system, with parameters adjusted to reflect the cochlear input impedance of 20 GΩ.[8] The middle ear structures were assumed to react to the oncoming blast wave passively, and so the only loads acting on the structures were transferred via fluid–structure interface applied to both sides of the TM. The FSI between the ossicular chain and middle ear cavity fluid (air) was considered negligible and was not included in this study.

The computational fluid dynamics (CFD) software Fluent was used to determine the air pressure propagation through the ear canal and middle ear cavity. Computational fluid dynamics packages have been shown to be useful in the prediction of blast wave dynamics[9] and Fluent, specifically, has been implemented in impulsive flow studies.[10] Fluent utilizes the finite volume method to numerically solve the equations of mass, momentum, and energy conservation and the equation of state. Standard compressible air properties were employed and the operating pressure was set to ambient air pressure at sea level, or 101,325 Pa and the gravitational effects were neglected. The walls of the canal and middle ear cavity were defined as rigid and a no-slip boundary condition was applied. Fluid–structure interactions were prescribed to the boundaries of the fluid domains coincident with the surfaces of the TM. Experimentally measured P0 pressure profiles from TB tests were applied directly onto the boundary at the entrance of the canal as a pressure inlet. The pressure waveforms at P1 and P2 were calculated. To keep the fluid meshes' cell quality sufficient for convergence under large TM deformation, a dynamic smoothing and remeshing scheme was employed. The FE modeling results included the pressure distribution throughout the fluid domains (ear canal and middle ear cavity) and the associated structural response.

Blast Test with Cadaver Ears

Human cadaveric temporal bones with intact pinna, TM, and ossicular chain were mounted to a specifically designed "head block" inside the blast chamber as shown in Figure 2A (setup for vertical exposure). The temporal bones were divided into three groups to test the blast direction effect: the vertical, horizontal, and front directions (Fig. 2B). A compressed nitrogen-driven blast apparatus was used to mimic blast exposure in this study. Polycarbonate film of varying thicknesses (130 μm or 260 μm) was employed as a diaphragm under compressed nitrogen, the rupture of which generated blast overpressure of at least 207 kPa (30 psi or 200 dB SPL). Overpressure level at the canal entrance was controlled by varying the distance of the head block from the blast reference plane.

A pressure sensor (Model 102B16; PCB Piezotronics, Depew, NY, USA) was placed at the entrance of the ear canal (approximately 1 cm off the center of the ear canal opening) to monitor the overpressure waveform entering the ear canal (P0). Two holes were drilled into the temporal bone for the insertion of additional pressure sensors. These additional sensors were inserted to measure P1 and P2. The P1 and P2 sensors (Model 105C02; PCB Piezotronics) were placed at 3 mm from the TM in the ear canal and inside the middle ear cavity through the Eustachian tube, respectively. The pressure sensor signal was measured by cDAQ 7194 and A/D converter 9215 (National Instruments Inc., Austin, TX, USA) with the sampling rate of 100 k/s (10 μs dwell time). The LabVIEW software package (NI Inc.) was used for data acquisition and analysis. The

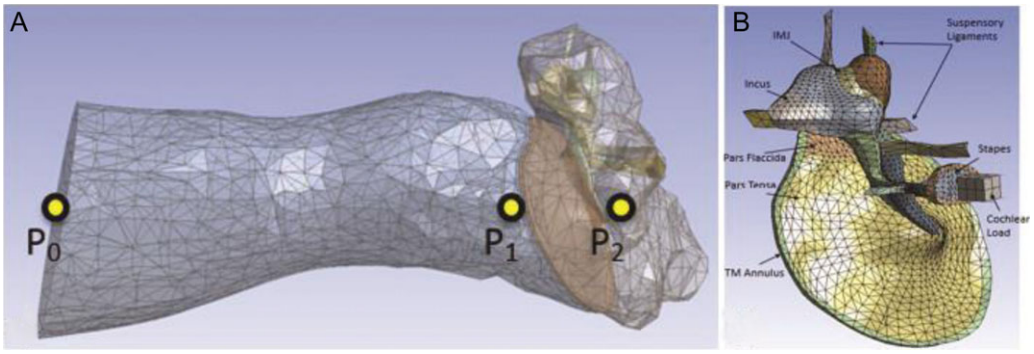


FIGURE 1. (A) Finite element model of the human ear including ear canal, middle ear cavity, and middle ear structures. Shows the pressure monitor locations P0, P1, and P2 as they exist in the model. (B) The middle ear structures isolated.

Downloaded from https://academic.oup.com/milmed/article-abstract/183/suppl_1/262/4959995
by guest
on 07 April 2018

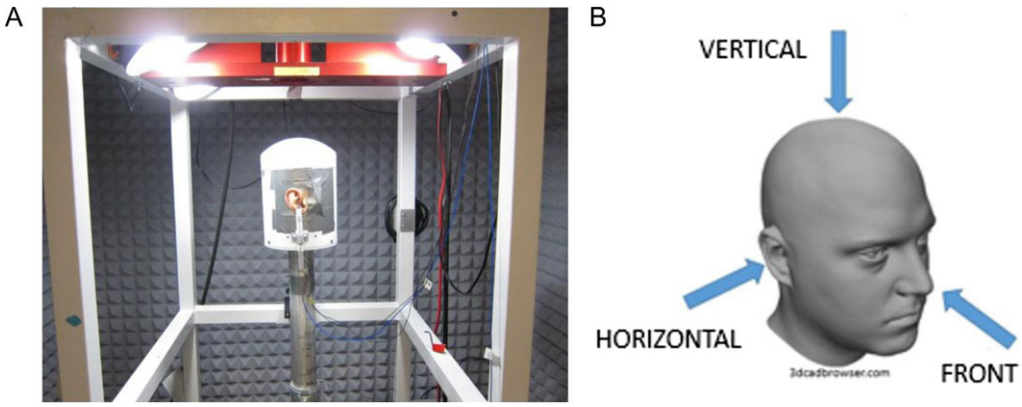


FIGURE 2. (A) Cadaver temporal bone mounted on head block under blast apparatus in blast chamber. Shows vertical exposure setup. (B) Display of blast exposure directions.

waveform of each blast test was then saved for further analysis. Note that the sampling rate is sufficient for the waveform recorded in this study.

Comparison of Model Data with Experimental Results

The 3D FE model-predicted pressure waveforms were compared with those measured in cadaver ears during experiments. The P1 pressure waveforms were the most important because this is the pressure directly responsible for TM damage and ossicular chain motion. Three metrics of the P1 waveforms in the time domain were considered for comparison: peak pressure level, A-duration, and Kurtosis. These three parameters describe the P1 waveforms from different aspects. The peak pressure P1 represents the intensity of blast overpressure reaching the TM; the A-duration is defined as the measure of time (in ms) that the positive portion of the peak pressure is sustained and describes the shape of the P1 peak wave; Kurtosis is the statistics measure of impulse pressure wave shape to compare two P1 waveforms: recorded from the experiment and derived from the FE model. Note that Kurtosis analysis has been used for prediction of human hearing loss in impulsive noise environment.[11–13] In this study, however, the statistic Kurtosis was only employed to compare two P1 waveforms for validation of the FE model. During the calculation, 1 ms of the P1 pressure profile was enough to assess the characteristics of the waveform.

Via FFT analysis, the impulse pressure spectra were then obtained from the experimental and predicted P1 waveforms to derive the energy spectra in the frequency domain. Next, following the methods of impulse signal energy distribution theory reported by Gan et al,[4] the total sound exposure was divided by the standard characteristic impedance of the air ρc as impulse energy flux (energy per unit area) and expressed as:

$$E^* = \frac{1}{\rho c}\int_0^T p^2(t)\,dt, \ [\mathrm{J/m^2}]$$

where $p(t)$ is the instantaneous value of acoustic pressure in Pa, dt is the time increment for scanning of acoustic pressure in seconds, and $\rho c = 406$ mks rayls to produce the quantity with units of energy flux (i.e., $\mathrm{J/m^2}$). Both ρ and c are pressure-dependent in the shock front. The duration $T = 6$ ms was used for calculation in the current study.

Eight octave band-pass filters with center frequencies at 125 Hz (88–177), 250 Hz (177–354), 500 Hz (354–707), 1 kHz (0.707–1.414), 2 kHz (1.414–2.828), 4 kHz (2.828–5.657), 8 kHz (5.657–11.314), and 16 kHz (11.314–22.627) were designed. To catch signals at frequencies lower than 125 Hz and higher than 16 kHz, additional low-pass (L125, cutoff at 88 Hz) and high-pass (H16k, cutoff at 22.627 kHz) filters were designed. The MATLAB SPTOOL was used to create all the filters with IIR (infinite impulse response) Butterworth filter with 6 order, signal sample rate Fs = 100,000. The impulse pressure spectra were filtered and the sound energy in each band was calculated as the distribution of pressure energy flux over 10 bands. The energy in each band was normalized with respect to the total sound energy in that band, and the resulting energy fluxes of the experimental and predicted waveforms were compared.

RESULTS

The experimentally measured and FE model-predicted pressure waveforms for the vertical, horizontal, and front blast directions are shown in Figure 3A and B, respectively. The peak pressure level of waveforms (P0) ranged from approximately 50 kPa to 80 kPa across the incident wave directions of vertical, horizontal, and front, and the A-duration for P0 waveforms ranged from approximately 0.5 ms to 1.0 ms. Note that in the experiment, the P0 sensor was placed 1 cm lateral to the canal entrance, but in the model, the P0 waveform was applied directly at the canal entrance; this resulted in experimental P1 response times (the time it takes for P1 to respond after initial P0 response) that were longer than those predicted by the model. As can be seen when comparing the P0 and P1 waveforms

Downloaded from https://academic.oup.com/milmed/article-abstract/183/suppl_1/262/4959995
by guest
on 07 April 2018

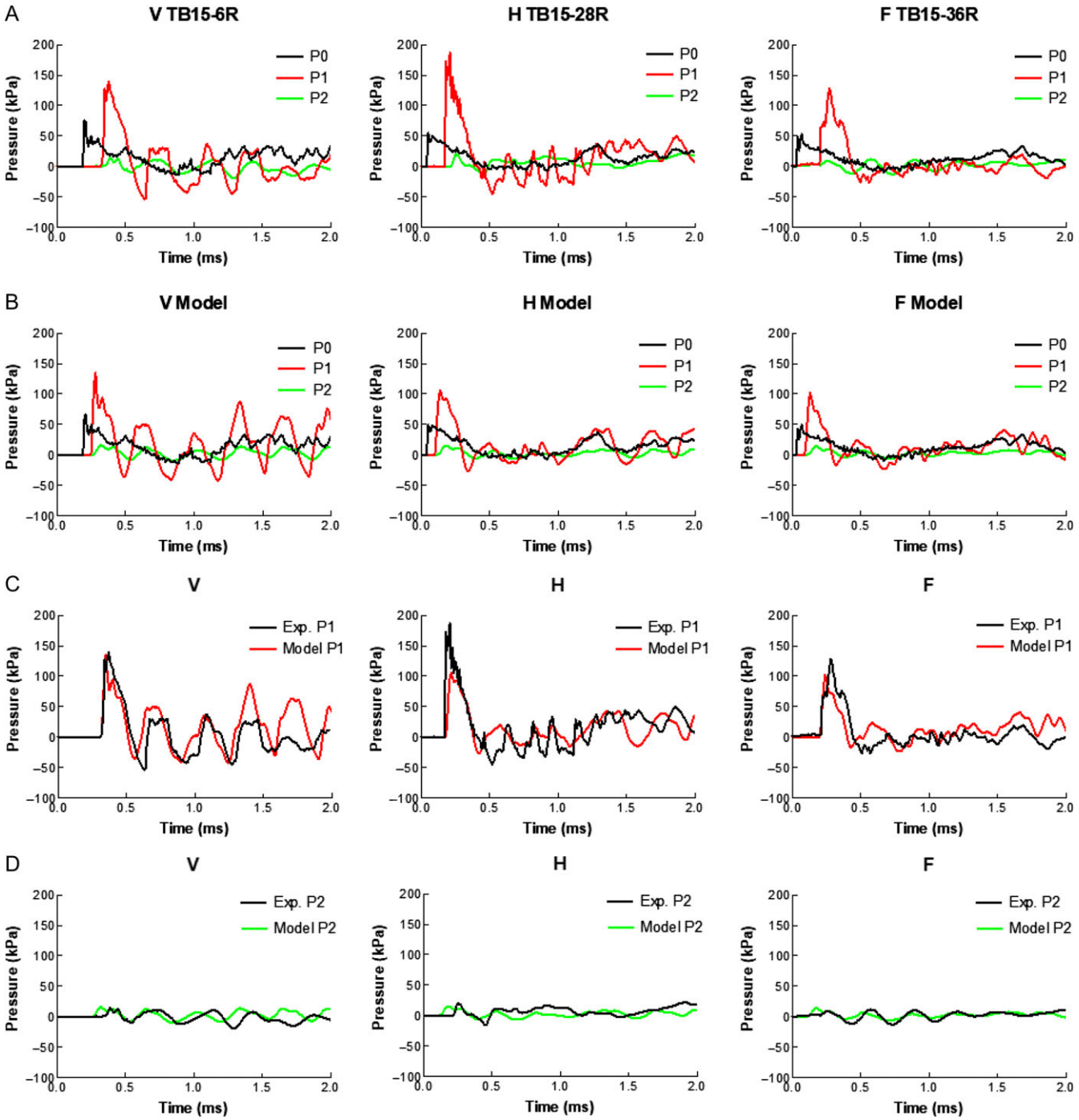


FIGURE 3. (A) Experimental recordings of the P0, P1, and P2 waveforms from vertical, horizontal, and front blast exposures. (B) Predicted P1 and P2 waveforms induced by experimental P0 waveforms from each blast direction. (C) Comparison of experimental and model-predicted P1 waveforms from each blast direction. (D) Comparison of experimental and model-predicted P2 waveforms from each blast direction.

in Figure 3A, the pressure magnitude increases significantly by the time the wave has reached the TM; the model captures this behavior. The peak pressure ratios, P1:P0, of the experimental vs. predicted waveforms were 1.83 vs. 1.78, 3.37 vs. 2.72, and 2.42 vs. 1.92 for the vertical, horizontal, and front directions, respectively. The experimental and model-derived P1 waveforms from each direction are compared in Figure 3C, accounting for the difference in P1 response time. Qualitatively, the three predicted P1 pressure profiles agree quite well with the experimental waveforms. Figure 3D shows the comparison of P2 pressure waveforms recorded from experiments and derived from the model in V, H, and F direction, respectively. As shown in this figure, the P2 waves are no longer as the impulse pressure profiles and the peak-to-peak pressure values are lower than

Downloaded from https://academic.oup.com/milmed/article-abstract/183/suppl_1/262/4959995
by guest
on 07 April 2018

20 kPa or lower than 20% of P1 peak pressure value. The experimental and modeling results overlap each other, which indicates the model is also able to predict P2 pressure. However, as pointed at the beginning of the 3rd Section under 'Methods' that it is important to understand P1 waveform behavior since it is the pressure that acts directly on the TM.

Table I lists the three quantitative metrics by which the experimental and model-derived P1 waveforms were evaluated and compared in peak pressure level, A-duration, and 1 ms kurtosis. Percent error calculations were performed to assess the FE model's predictability. The model-predicted percent errors in the peak pressure level, A-duration, and 1 ms kurtosis were found to be 3.0%, 9.1%, and 15%; 25%, 17%, and 1.0%; and 20%, 13%, and 9.8% for the vertical, horizontal, and front blast directions, respectively.

Obtained from FFT analysis, the spectral behavior of the vertical P1 waveforms (sample TB15-6R) in Figure 3C is displayed for comparison in Figure 4A. These data were utilized to perform the energy flux analysis over 10 octave bands in Figure 4B. Note that the data were normalized with respect to the total signal energy and the total value was 1.0. Also note that the P0 waveform applied as input to the FE model was taken from the experiment, and so the energy flux for the experimental and predicted P0 is the same for all octave bands. The majority of the experimental P1 energy flux is in the 2 kHz and 4 kHz octave bands, peaking around 0.3 J/m^2 in the 2 kHz band. The majority of the energy flux determined from the model-derived P1 pressure spectra was also concentrated in the 2 kHz and 4 kHz octave bands, with a maximum at 4 kHz. The results demonstrate that the model is capable of predicting which frequencies the majority of P1 energy flux occupies.

Figure 5 displays the displacement (Fig. 5A) and stress distributions (Fig. 5B) plotted onto the TM at the time maximum displacement or maximum stress occurred, for the vertical exposure. The maximum TM deformation of 1.4 mm occurs approximately 2 mm inferior and anterior to the umbo. The stress contours indicate maximum stresses at three locations on the TM (the anterior TMA, inferior to the umbo, and posterior to the manubrium) and may indicate possible locations prone to TM rupture. Structural stress, strain rates, and displacement distributions may be implemented in analyses of all modeled middle ear structures.

DISCUSSION

The peak pressure metric showed the most variability when quantitatively comparing experimental and model-predicted P1 waveforms, with percent error ranging from 3.0% in the

TABLE I. List of P1 Waveform Metric Data from Experiment and FE Model at Vertical (V), Horizontal (H), and Front (F) Wave Directions.

	ID	P1	Peak (kPa)	Peak (dB SPL)	A-Duration (ms)	Kurtosis (1 ms)
V	TB15-6R	Experiment	139.3	196.9	0.22	3.85
		Model	135.1	196.6	0.20	3.28
H	TB15-28R	Experiment	187.1	199.4	0.24	5.54
		Model	139.8	196.9	0.20	5.50
F	TB15-36R	Experiment	128.4	196.2	0.23	4.48
		Model	102.3	194.2	0.20	4.92

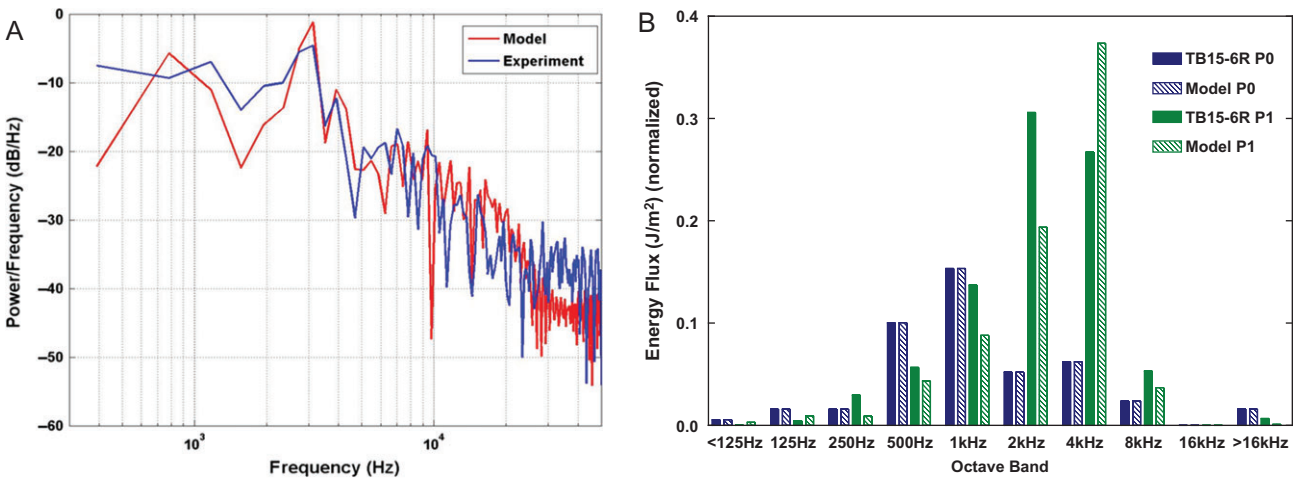


FIGURE 4. (A) Spectral behavior of the model-predicted and experimentally measured P1 waveforms from vertical blast exposure. (B) Comparison of the normalized energy flux distributions of model-predicted and experimental P0 (blue) and P1 (green) waveforms.

Downloaded from https://academic.oup.com/milmed/article-abstract/183/suppl_1/262/4959995
by guest
on 07 April 2018

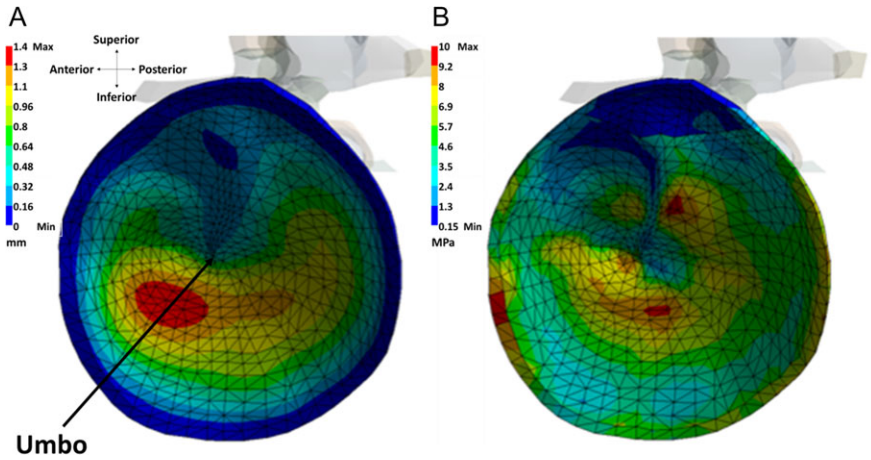


FIGURE 5. (A) TM displacement distribution at the time of maximum displacement for vertical exposure. TM is fixed to the bony wall along its annulus and experiences a maximum displacement of 1.4 mm approximately 2 mm inferior and anterior to the umbo. (B) TM stress distribution at the time of maximum stress. Displays three stress concentrations indicating possible locations for TM rupture.

vertical direction to 25% in the horizontal direction. This variability may be due to the entrance velocity effect. In experiments with three incident wave directions, the blast wave front enters the ear canal at different rates because of the orientation of the ear canal with respect to wave front. It is possible that the effects of ear canal geometry on overpressure amplification (P1/P0) are magnified due to a higher entrance velocity in the horizontal orientation (in which the ear canal is parallel to the wave front). Future blast experiments designed to measure the velocity at the ear canal entrance may provide additional data that will allow for more accurate modeling of the initial conditions of the blast wave propagation.

The percent error in the model-predicted P1 A-duration metric ranged from 9.1% to 17% for the vertical and horizontal directions, respectively. Interestingly, the predicted P1 A-durations were determined to be 0.2 ms for all directions, suggesting that A-duration near the TM is a function of ear canal geometry. The best-predicted metric was 1 ms kurtosis, ranging from 1.0% to 15% error for the horizontal and vertical directions, respectively. These results demonstrate that the statistic Kurtosis method used in this study has fulfilled the quantitative comparison of two signal shape measurements or waveforms, one from the experiments and one from the model.

The model-predicted P1 energy flux was in general agreement with the experimental energy flux, both showing the pressure spectra being concentrated in the 2 kHz and 4 kHz octave bands. The shift of the predicted P1 pressure spectra to higher frequencies may be attributed to ear canal geometry or the absence of skin in the model. The ear canal skin was not included in the model because the original FE model published by Gan et al[6] does not have the canal skin. However, to simulate blast overpressure transduction through the ear canal with the earplug inserted, the ear canal skin was added to the model.[8] The preliminary data showed that the effect of skin on overpressure transmission through the ear canal was limited. Although the addition of skin to the model did not significantly alter the pressure magnitude or P1 waveform, it is not clear how skin may affect the pressure spectra and the future study is needed. Moreover, the model-derived P1 pressure spectra were in greater agreement with the experimental data than were the predicted P2 pressure spectra; however, due to the relatively low pressure levels of the P2 waveforms, this disagreement was not considered crucial.

No experimental data currently exist that detail the response of the TM to blast exposure. The FE method is thus the best available method to investigate impulse overpressure and its effects on the TM. Future blast experiments will be designed to measure TM motion under high-intensity pressure propagation; those data will then be used to further verify the current FE model.

CONCLUSION

A FE model of the human ear including the ear canal, TM, ossicular chain, and middle ear cavity for blast wave transmission analysis has been developed. The FE model was used to predict P1 and P2 pressures induced by P0 pressure applied at the canal entrance. Further, the stress and displacement distributions on the TM were also calculated. The model was validated against experimental data with the satisfied prediction of P1 waveforms induced by P0 pressures from the vertical, horizontal, and front directions.

This model can be used for the investigation of biomechanical response of the human ear when exposed to blast overpressure. The application of experimentally measured overpressure waveforms as input to the entrance of the ear canal in the model permits the user to investigate particular disturbance sources and their impact on the ear, instead of simply the effect of altered Friedlander waveforms. The level of detail afforded by the FE method may allow for the model's application in the investigation of auditory blast injury, such as TM rupture. Hearing protection devices may be introduced to the model to

Downloaded from https://academic.oup.com/milmed/article-abstract/183/suppl_1/262/4959995
by guest
on 07 April 2018

study the effect of earplugs' material properties, structural designs, and insertion depths. Additionally, this model may aid in the evaluation and optimization of orifice geometries in nonlinear earplugs. This model promises to be of great value in the investigation of ear injury and in providing means to test and design protective measures for those subjected to high-intensity blast overpressures in the armed forces.

ACKNOWLEDGMENTS

The authors thank Dr. Xiao Ji, Research Associate in the Biomedical Engineering Laboratory at the University of Oklahoma, for his energy analysis expertise.

FUNDING

This work was supported by U.S. Army Medical Research and Material Command (USAMRMC) Military Operational Medicine Research Program, Contract No. W81XWH-14-1-0028.

PRESENTATIONS

Presented in a breakout session entitled "The Role of Medical Research in Blast Injury" at the 2016 Military Health System Research Symposium (abstract number: MHSRS-16–0405).

REFERENCES

1. Stuhmiller JH, Phillips YY, Richmond DR: The physics and mechanisms of primary blast injury. In: Conventional Warfare: Ballistic, Blast, and Burn Injuries, pp 241–70. Edited by Bellamy RF, Zajtchuk R, Buescher TM. Washington, DC, Department of the Army, Office of the Surgeon General, 1991.
2. Fausti S, Wilmington D, Gallun F, Myers P, Henry J: Auditory and vestibular dysfunction associated with blast-related traumatic brain injury. J Rehabil Res Dev 2009; 46(6): 797–810.
3. Saunders G, Echt K: Blast exposure and dual sensory impairment: an evidence review and integrated rehabilitation approach. J Rehabil Res Dev 2012; 49(7): 1043–58.
4. Gan RZ, Nakmali D, Xiao J, Leckness K, Yokell Z: Mechanical damage of tympanic membrane in relation to impulse pressure waveform – a study in chinchillas. Hear Res 2016; 340: 25–34.
5. Wang X, Gan R: 3D finite element model of the chinchilla ear for characterizing middle ear functions. Biomech Model Mechanobiol 2016; 15 (5): 1263–77.
6. Gan R, Reeves B, Wang X: Modeling of sound transmission from ear canal to cochlea. Ann Biomed Eng 2007; 35(12): 2180–94.
7. Zhang X, Gan R: Finite element modeling of energy absorbance in normal and disordered human ears. Hear Res 2013; 301: 146–55.
8. Leckness K: Novel finite element method to predict blast wave transmission through human ear. Thesis for Master Degree in Biomedical Engineering at University of Oklahoma, August 2016. Available at http://hdl.handle.net/11244/44932; accessed December 30, 2016.
9. Hansen OR, Hinze P, Engel D, Davis S: Using computational fluid dynamics (CFD) for blast wave predictions. J Loss Prev Process Ind 2013; 23: 885–906.
10. Cyklis P, Mlynarczyk P: The influence of the spatial discretization methods on the nozzle impulse flow simulation results. Procedia Eng 2016; 157: 396–403.
11. Davis R, Qui W, Heyer N, et al: The use of the kurtosis metric in the evaluation of occupational hearing loss in workers in China: implications for hearing risk assessment. Noise Health 2012; 14(61): 330–42.
12. Qui W, Hamernik R, Davis R: The value of a kurtosis metric in estimating the hazard to hearing of complex industrial noise exposures. J Acoust Soc Am 2013; 133(5): 2856–66.
13. Ganesh JS, Rao VS, Srinivas K: Enhanced noise type recognition using statistical measures. IOSR J Comput Eng 2012; 2(1): 19–23.

Downloaded from https://academic.oup.com/milmed/article-abstract/183/suppl_1/262/4959995
by guest
on 07 April 2018

Biomechanical Changes of Tympanic Membrane to Blast Waves

Rong Z. Gan

Abstract

Eardrum or tympanic membrane (TM) is a multilayer soft tissue membrane located at the end of the ear canal to receive sound pressure and transport the sound into the middle ear and cochlea. Rupture of the TM is one of the most frequent injuries of the ear after blast exposure in military service members. The TM mechanical property changes induced by blast waves also affect progressive hearing loss in veterans. This chapter describes the biomechanical measurements and modeling of blast wave transduction through the ear and the TM mechanical property changes after blast exposure. The human TM rupture thresholds were determined with a relationship to blast wave direction. It is found that the sensitivity of TM stress change with respect to the pressure reaching on TM surface characterizes the mechanical damage of the TM in relation to blast waves. Mechanical properties of the human TM after exposure to blasts were measured using acoustic loading and laser Doppler vibrometry with the inverse problem-solving method. The complex modulus of the TM exposed to blast waves had significant reduction compared to normal tissue. The SEM images of post-blast TM showed obvious microstructural changes from the normal TM which indicate the tissue damage caused by blast exposures. This chapter provides important data on human TM damage and mechanical changes induced by blast overpressure waves.

1 Introduction

The eardrum or tympanic membrane is a soft tissue membrane separating the ear canal from the middle ear. The tympanic membrane (TM) plays an important role in transmission of sound pressure from the environment into mechanical vibration of the ossicular chain in the middle ear, which is transported into the inner ear or cochlea and then to the brain for hearing. Exposure to high-intensity sound or blast overpressure waves causes injuries to auditory system and results in acute hearing loss in military service members and the long-term hearing disabilities in veterans (Cave et al. 2007; Dougherty et al. 2013). The primary blast injury to the ear is induced by direct effect of blast overpressure waves upon the TM and middle ear ossicular chain. Rupture of the

R. Z. Gan (✉)
Biomedical Engineering Laboratory, School of Aerospace and Mechanical Engineering, University of Oklahoma, Norman, OK, USA
e-mail: rgan@ou.edu

© Springer International Publishing AG, part of Springer Nature 2018

B. M. Fu, N. T. Wright (eds.), *Molecular, Cellular, and Tissue Engineering of the Vascular System*, Advances in Experimental Medicine and Biology 1097,
https://doi.org/10.1007/978-3-319-96445-4_17

rgan@ou.edu

TM is one of the most frequent injuries of the ear and has been investigated in animals and humans with wide variability (Cho et al. 2013; Fausti et al. 2009).

The TM perforation induces the reduction of energy transfer efficiency and has been measured in human temporal bones (Voss et al. 2007; Gan et al. 2009), animals (Bigelow et al. 1996; Santa Maria et al. 2007), and clinical studies (Ahmad and Ramani 1979; Mehta et al. 2006). Gan et al. (2007, 2009) used a three-dimensional finite element (FE) model of the human ear including the external ear canal, middle ear, and uncoiled cochlea with two straight fluid channels separated by the basilar membrane to predict the perforation-induced change of middle ear function for sound transmission. The acoustic-structure-fluid coupled FE analysis was employed in the model to evaluate a complex combination of two sound conduction routes: the mechanical route through the ossicular chain and the acoustic route through the air in the middle ear cavity. Perforations created in the FE model were also produced in human cadaver ears or temporal bones to verify the FE model results by Gan et al. (2009). A good agreement between the model and experimental data indicated that the TM perforation mainly affects the middle ear transfer function at low frequencies for normal sound.

Blast overpressure is a high-intensity disturbance in the ambient air pressure that creates high-intensity sound (impulse) over 170 dB SPL. In addition to TM perforation or rupture, any damage induced by blast waves to the TM tissue would affect its mechanical properties and alter the normal performance of the TM for sound transmission. There are two basic types of experimental data which are used to assess the extent and nature of blast-induced damage to the TM: mechanical property changes and microstructural variations of the TM (Engles et al. 2017; Liang et al. 2017).

A recent study on chinchilla blast model by Gan et al. (2016) reported the relationships between the TM rupture threshold, the TM damage pattern, and the overpressure waveforms. The results demonstrated that the TM rupture threshold was closely related to overpressure waveforms at the entrance of the ear canal. The waveforms recorded under the shielded case had almost equal positive-negative pressure phases, while the waveforms recorded in the open field had the positive pressure only. The TM rupture threshold measured in the shielded case was much lower than that in the open field. These findings in animal blast model brought further research requests on identifying human TM damage after blast exposure and the TM rupture threshold in relation to blast overpressure level and wave direction.

The first part of this chapter reports our current study on measuring blast wave transmission through the human ear and the relationship between the TM damage and the incident blast wave direction. In addition to experimental tests in human cadaver ears, a 3D FE model of the human ear for blast simulation based on the model published by Gan et al. (2004, 2007) was developed to modeling blast overpressure transduction through the ear (Leckness 2016). The mechanisms of TM injury in relation to blast wave direction were investigated using this model. The study was completed in the Biomedical Engineering Laboratory at the University of Oklahoma, and the results were presented at the 2016 Military Health System Research Symposium (MHSRS).

The second part of this chapter reports the changes of TM tissue mechanical properties after multiple blast exposures of human cadaver ears based on our recent study by Engles et al. (2017). Microstructural variations of the TM were detected by scanning electron microscopy (SEM) images, which provide an insight into the structural aspects of the injury on the surface of the TM. Changes of the structure and mechanical properties of the TM directly affect sound transmission and result in conductive hearing loss. We have also measured the changes of TM mechanical properties in chinchilla blast model using a micro-fringe protection method, but the results are not included in this chapter. The readers can find the information from the current publication by Liang et al. (2017).

rgan@ou.edu

2 Part I. Human TM Rupture in Relation to Blast Overpressure Direction

2.1 Experimental Setup, Procedure, and Results from Blast Tests

A "head block" attached with human cadaver ear or temporal bone and mounted with two pressure sensors was developed in our lab to measure the transfer functions of the ear canal and middle ear in response to blast overpressure. Three pressure sensors are simultaneously monitoring the blast pressure at the entrance of the ear canal (P0), near the TM in the canal (P1), and behind the TM in the middle ear (P2). The P0 sensor (Model 102B16, PCB Piezotronics, Depew, NY) was placed at 1 cm lateral to the ear canal opening with the sensing surface facing the blast. The P1 and P2 sensors (Model 105C02, PCB Piezotronics) were placed at 3 mm from the TM and inside the middle ear cavity through the Eustachian tube, respectively.

The "head block" was exposed to open-field blast inside an anechoic test chamber in our lab along three directions, the vertical, horizontal, and front, with respect to the head as shown in Fig. 1. A well-controlled compressed air (nitrogen)—driven blast apparatus located inside the test chamber—was used to create a blast overpressure wave (Gan et al. 2016; Hawa and Gan 2014). Polycarbonate film (McMaster-Carr, Atlanta, GA) of varying thickness (0.13–1.0 mm) was employed to generate blast overpressure of at least 30 psi (207 kPa or 200 dB SPL). The overpressure level was controlled by changing the thickness of the film or the distance from the blast reference plane. By increasing the blast peak pressure P0, the TM was finally ruptured, and all three pressure waveforms (P0, P1, and P2) were recorded simultaneously at each pressure level.

The pressure sensor signal was measured by cDAQ 7194 and A/D converter 9215 (National Instruments Inc., Austin, TX) with the sampling rate of 100 k/s (10 μs dwell time). The LabVIEW software package (NI Inc.) was used for data acquisition and analysis. The waveform of each blast test was saved in a PC for further analysis.

A total of 41 fresh human temporal bones (TBs) were used in this study for testing of three wave directions: from the top of the head (the vertical setup), from the lateral to the ear (the horizontal setup), and from the front of the face (the front setup). The schematic of the setup along these three directions is shown in Fig. 1a. Figure 1b displays the head block with a right cadaver ear exposed to the vertical wave direction. The P0 pressure sensor was fixed near the ear canal entrance. All the TBs were obtained from the Life Legacy Foundation, a certified human tissue supply source for military research. The study protocol was approved by the US Army Medical

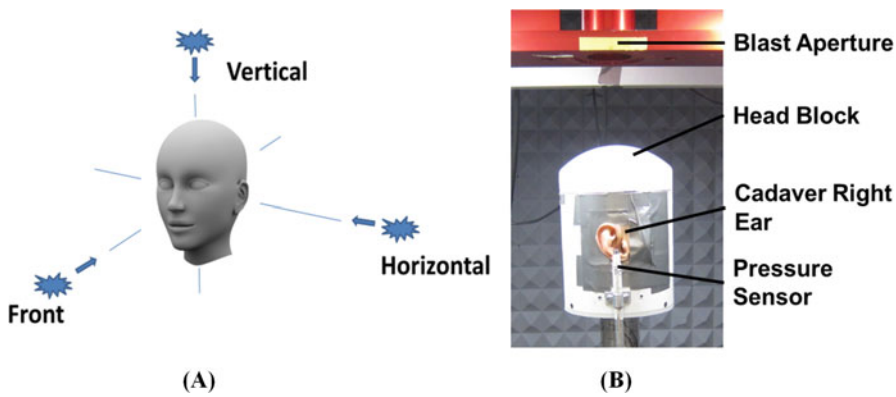


Fig. 1 (**a**) Schematic of three blast wave directions with respect to the head. (**b**) The picture of experimental setup with the head block along the vertical wave direction inside the test chamber

rgan@ou.edu

Research and Materiel Command (USAMRMC) Office of Research Protections (ORP).

It usually took 3–4 iterations of blast tests to reach the TM rupture threshold defined as the peak pressure before the TM rupture. That means if the TM ruptured after the third blast, the threshold was the peak pressure level of the second blast. The initial blast pressure level was selected based on the system calibration using different films and changing the distance between the sensor surface and the blast reference plane. The number of blast tests also varied with individual TBs due to the variation among the human samples and setups. To confirm the TM damage, an otoscopic examination of the ear was performed first, and further verification was done using wideband tympanometry to determine whether the TM was ruptured (Gan et al. 2016). When the TM was found without rupture, the next blast test was conducted with an increase of the overpressure level. The testing stopped when the TM was ruptured.

Figure 2a shows typical overpressure waveforms of P0 (black), P1 (red), and P2 (green) recorded from three cadaver ears in the vertical, horizontal, and front tests (before the TM rupture). The pressure waves are displayed in 2 ms of time duration, and the positive overpressure is followed by negative pressure. As shown in Fig. 2a, the peak P0 level was around 50 kPa or 7.5 psi or 188 dB SPL for all three tests. The P1 peak pressure shows a substantial increase compared to the P0 pressure in all wave direction tests. The results demonstrate the effect of the ear canal on enhancing the impulse pressure level near the TM in the canal.

The otoscopic photographs displayed in Fig. 2b illustrate the TM damages observed at the vertical (V), horizontal (H), and front (F) tests with the peak P0 pressure levels of 191, 186, and 189 dB SPL (or 11, 6, and 8 psi), respectively. There is no consistent TM rupture pattern observed from the experiments at different wave directions. However, the damage along the

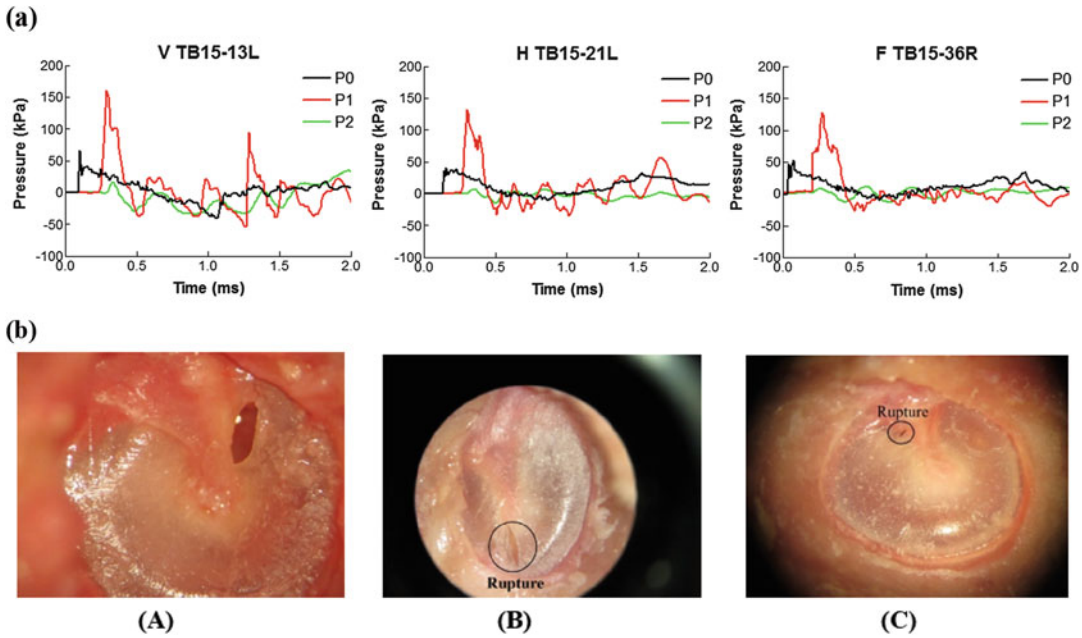


Fig. 2 (**a**) Overpressure waveforms of P0 (black), P1 (red), and P2 (green) recorded from three cadaver ears or temporal bones under the vertical (left), horizontal (medium), and front (right) tests. (**b**) Otoscopic pictures of human TMs ruptured after blast exposure. (**A**) Vertical test, left ear, TM ruptured in the superior-posterior region; (**B**) horizontal test, left ear, TM ruptured in the inferior side; (**C**) front test, right ear, TM ruptured in the superior-posterior region

rgan@ou.edu

TM-radial fiber direction is commonly observed from the experiments. Another area is near the manubrium or inferior side of the TM along the radial direction.

Table 1 lists the mean and standard deviation (SD) of P0, P1, and P2 ratio of P1/P0 and the TM rupture P0 and P1 thresholds obtained from all tests along three blast wave directions: V, H, and F. The P1 rupture threshold was determined by multiplying the P1/P0 ratio and the P0 rupture threshold for each direction. The results in Table 1 show that the P0 rupture threshold for the V and F directions are comparable and that the P0 threshold in H-direction is significantly lower than the other two directions. Conversely, the P1/P0 ratio in H direction is well above the others. It is also observed from Table 1 that the P1 rupture threshold (the pressure that is directly responsible for TM damage) is similar for the V and H directions, at 20.2 and 20.1 psi, respectively. Interestingly, the results indicate that the F direction requires less pressure as measured at P1 to rupture the TM.

The recorded waveforms (P0 and P1) from blast tests in TBs are impulse pressure profiles (short duration and nonperiodic). The impulse pressure energy spectra analysis on recorded waveforms in the time domain was conducted in MATLAB to determine the signal energy distribution over the frequencies (ten octave frequency bands) under three blast wave directions. First, the recorded pressure waveforms were converted to pressure distributions over the frequencies of 20–20 kHz by using FFT spectral analysis. Next, following the methods of impulse signal energy distribution theory reported by Hamernik et al. (1991), Hamernik and Keng (1991), Hamernik and Qiu (2001), and Gan et al. (2016), the total sound exposure was divided by the standard characteristic impedance of the air ρc as impulse energy flux (energy per unit area) and expressed as

$$E^* = \frac{1}{\rho c}\int_0^T p^2(t)dt, \quad \left[\mathrm{J/m^2}\right] \qquad (1)$$

where $p(t)$ is the instantaneous value of acoustic pressure in Pa or N/m^2, dt is the time increment for scanning of acoustic pressure in seconds, and $\rho c = 406$ mks rayls to produce a quantity with units of energy flux (i.e., J/m^2). Both ρ and c are pressure-dependent in the shock front. The duration of $T = 6$ ms was used for calculation in the present study.

Eight octave band-pass filters with center frequencies at 125 Hz, 250 Hz, 500 Hz, 1 kHz, 2 kHz, 4 kHz, 8 kHz, and 16 kHz were designed. A low-pass filter L125 and a high-pass filter H16k were also designed to catch signals at frequencies lower than 125 Hz and higher than 16 kHz. The filtered signals were then generated, and the sound energy in each band was calculated as the distribution of pressure energy flux over ten bands. Instead of directly comparing the energy flux values in the three wave directions, the energy in each band was normalized with respect to the total sound energy in that band.

The comparison of impulse energy flux (energy per unit area in unit J/m^2) distributed in ten frequency bands from below 125 Hz to over 16 kHz obtained from waveforms recorded in three wave direction tests demonstrates that (1) P0 pressure-induced energy is mainly distributed at frequencies below 1 kHz and there is a large peak for V direction at 500 Hz; (2) P1 pressure-induced energy is distributed at frequencies up to 4 kHz; and (3) blast waves at F and H directions result in relatively large energy flux of both P0 and P1 at frequencies below 125 Hz. This energy analysis suggests that P1 pressure waveform should be considered as a primary factor for blast-induced TM damage because P1 energy distributions on octave bands are similar for all three wave directions and concentrated from 500 Hz to 4 kHz.

2.2 Finite Element Modeling Prediction

The 3D FE model of the human ear developed by Gan et al. (2004, 2007) for sound transmission and being used for TM perforation studies (Gan et al. 2009) was modified to simulate the blast wave transmission through the ear as shown in Fig. 3a. The FE model consisted of the ear

rgan@ou.edu

Table 1 Mean and SD of peak pressure values of P0, P1, and P2, ratio of P1/P0, and the TM rupture P0 and P1 thresholds

Blast wave direction	TB sample	P0 (psi)	P1 (psi)	P2 (psi)	P1/P0	Threshold P0 (psi)	Threshold P1 (psi)
Vertical	Mean ± SD($N = 13$)	8.9 ± 1.8	19.3 ± 3.3	2.3 ± 1.6	2.2 ± 0.5	9.2 ± 1.7	20.2 ± 2.2
Horizontal	Mean ± SD($N = 14$)	6.4 ± 2.1	19.0 ± 6.1	2.2 ± 1.4	3.0 ± 0.7	6.7 ± 1.2	20.1 ± 1.9
Front	Mean ± SD($N = 14$)	9.8 ± 2.0	16.3 ± 3.3	2.1 ± 0.7	1.7 ± 0.4	9.8 ± 2.1	16.7 ± 2.5

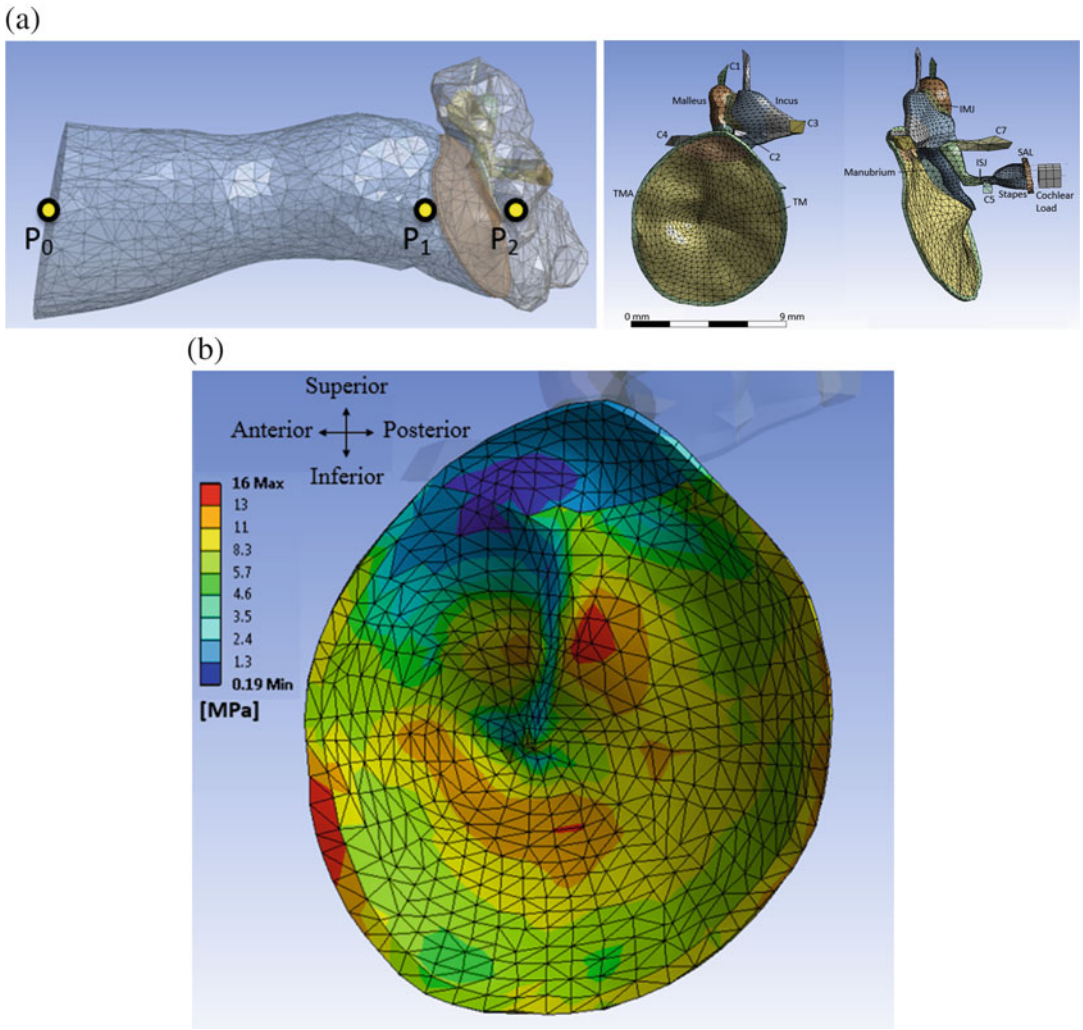


Fig. 3 (**a**) (Left) FE model of the human ear comprised of the ear canal, TM, middle ear ossicles, and middle ear cavity. The locations for pressure monitoring points are designated as P0, P1, and P2. (Right) Structural mesh of the model, showing the TM, TMA, middle ear ossicles, IMJ, ISJ, suspensory ligaments/muscle tendons (all Cs and SAL), and cochlear load. (**b**) FE model-derived distribution of the equivalent (von Mises) stress in the TM when the maximum stress was reached under the vertical wave direction

rgan@ou.edu

canal, TM, TM annulus (TMA), three ossicles connected by two joints (incudomalleolar joint (IMJ) and incudostapedial joint (ISJ)), middle ear suspensory ligaments/muscle tendons (Cs), stapedial annual ligament (SAL), and middle ear cavity. The cochlea was not included in this initial model for blast simulation, but the cochlear load was applied on the stapes footplate by a mass block-dashpot system with the cochlear input impedance of 20 GΩ (Gan et al. 2004).

This FE model of the human ear was regenerated in ANSYS Workbench (ANSYS Inc., Canonsburg, PA) where Fluent and ANSYS Mechanical coupled with fluid-structure interaction analyses were employed to compute blast overpressure transduction from the environment to the TM and middle ear (Leckness 2016). Briefly, the viscoelastic material properties were assigned to soft tissues in the middle ear including the TM, TMA, IMJ, ISJ, and SAL. The experimentally recorded P0 waveforms from the head block with cadaver TBs were applied onto the boundary at the entrance of the ear canal, and the pressure waveforms P1 and P2 were then calculated and compared with those measured from the experiments. The FE model was then employed to investigate the mechanisms of TM injury under recorded P1 profiles from the vertical, horizontal, and front directions. P1 overpressure waveforms recorded from multiple iterations of blast tests in 14 temporal bones (4 from the vertical direction and 5 from the horizontal and front directions) were applied to the surface of the TM in the FE model, and the maximum stress distributions were calculated. Note that the detailed description and validation of the FE model of the human ear are not included in this paper, which can be found from Leckness (2016).

The equivalent (von Mises) stress was used as a measure of the stress state of the TM. The average maximum stresses induced by the P1 rupture threshold waveforms were 16.2 ± 3.00 MPa, 16.3 ± 2.44 MPa, and 14.3 ± 2.53 MPa for the vertical, horizontal, and front directions, respectively. The average maximum stresses induced by the P1 waveforms that caused visible TM damage were 20.3 ± 1.18 MPa, 18.8 ± 1.99 MPa, and 15.5 ± 3.46 MPa for the vertical, horizontal, and front directions, respectively. An example of TM stress distribution at the time of maximum stress due to an applied P1 waveform of 134 kPa peak pressure in the vertical wave direction is displayed in Fig. 3b. As shown in this figure, the maximum stress reached 16 MPa, and the regions of the highest stress were along the anterior portion of the TMA, the posterior to the center of the manubrium, and the inferior to the bottom of the manubrium. These locations may indicate potential sites for TM rupture.

2.3 Mechanisms of TM Rupture in Relation to Blast Wave Direction

The P1 threshold for TM damage should more accurately represent the pressure applied to the TM than the P0 threshold. The experimental results shown in Table 1 indicate that P1 threshold in F direction is lower than V and H directions, or in other words, the blast wave from the front of the face (F direction) is easier to cause TM rupture than other blast wave directions. *Why does the F direction result in a lower P1 threshold for TM damage?* To answer this question and understand the mechanism behind the experimental findings, the FE model of the human ear was used to compute the distributions of the stress in the TM and derive the sensitivity of TM stress with respect to P1 pressure increase as the TM stress gradient with respect to P1, $d\sigma/dP_1$. The stress gradient was calculated based on experimental P1 waveforms of pre-threshold up to the rupture level, usually 2–4 pressure waveforms per cadaver ear or temporal bone. Fourteen cadaver ears (four from the V direction and five from the H and F directions) were selected for calculation. As an example, Fig. 4a–c shows a series of P1 pressure waveforms over 0.5 ms duration from three temporal bone experiments in V, H, and F direction tests, respectively. The P1 waveforms were used to calculate $d\sigma/dP_1$ in V, H, and F directions using the model.

rgan@ou.edu

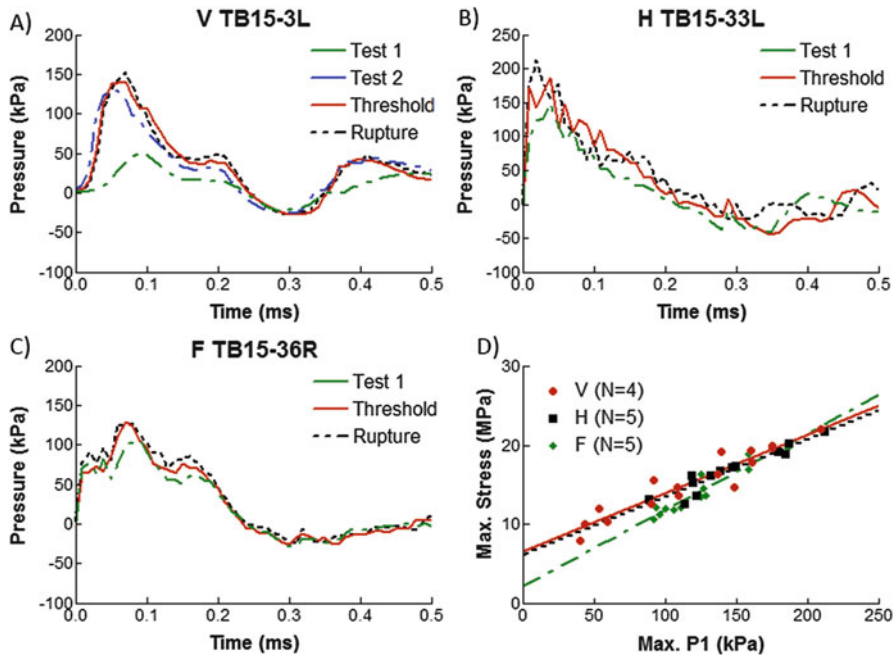


Fig. 4 (**a**–**c**) represent the P1 pressure waveforms with incremental peak pressure level from initial test 1 to TM rupture recorded from a temporal bone sample TB15-3L in V direction test, from sample TB15-33L in H direction test, and from sample TB15-36R in F direction test, respectively. (**d**) Plots of FE model-derived maximum stress in the TM vs. P1 peak pressure obtained from V direction ($N = 4$), H direction ($N = 5$), and F direction ($N = 5$)

All the data points of the maximum stress in the TM vs. the maximum (peak) P1 pressure obtained along the V, H, and F blast direction tests were plotted in Fig. 4d. Statistical correlation was then applied to determine the best-fit line for the data points at each direction. Figure 4d shows the comparison of the slope (i.e., stress gradient) $d\sigma/dP_1$ at three directions. The mean value of stress gradient was calculated as 74.1, 73.0, and 96.7 for V, H, and F direction, respectively. This indicates that the change of maximum stress in the TM with respect to P1 peak pressure in F direction is higher than the other two directions. The high sensitivity of TM stress with respect to the P1 pressure in F direction may characterize mechanical damage of the TM induced by blast. The average maximum stress was lowest for the front direction, as was the average P1 rupture threshold; this suggests that neither the stress level nor P1 level alone determines TM failure but that TM failure is best predicted by the rate change of stress with respect to maximum P1 pressure reaching the TM.

3 Part II. TM Tissue Mechanical Property Changes After Exposure to Blast Waves

3.1 Summary of TM Mechanical Property Measurements

The TM or eardrum is a multilayer membrane including the epidermal, collagen fibrous, and mucosal layers from the lateral to the medial side. The collagen fibers provide primarily the mechanical stiffness of the TM. It consists of a matrix of ground substance embedding approximately 22-μm-thick collagen fiber layer aligned primarily along the radial direction emanating from the umbo and approximately 15-μm-thick collagen fiber layer along the circumferential direction (Lim 1995). A major part of the TM is the

rgan@ou.edu

pars tensa, which is within tympanic annulus ring located at the boundary; the malleus manubrium bone is attached in the central portion at the medial side. The small dimensions of the TM (about 70 μm thick and 9 mm in diameter) make it difficult to measure the mechanical properties. Numerous investigations of the mechanical behavior of human TMs have been performed at static or low strain rates (von Békésy 1960; Dirckx and Decraemer 2001; Fay et al. 2005; Cheng et al. 2007; Huang et al. 2007; Daphalapurkara et al. 2009).

The static properties of the human TM were first reported by von Békésy (1960) as 20 MPa from a bending test on a rectangular cadaver TM strip. Further investigations into mechanical properties of human TM have been performed at quasi-static or low-frequency range (Cheng et al. 2007; De Greef et al. 2014; Fay et al. 2005; Huang et al. 2007). However, the TM works under the auditory frequency range of 20–20,000 Hz, and the dynamic properties of the TM need to be measured over the auditory frequency range. Kirikae (1960) determined Young's modulus in the circumferential direction to be 40 MPa at 890 Hz. Zhang and Gan (2010) reported an investigation on dynamic properties of human TM using acoustic stimulation and laser Doppler vibrometry (LDV) measurement. Utilizing various techniques, the dynamic properties of the human TM in the auditory frequency range have been further characterized (Luo et al. 2009; Zhang and Gan 2012). Nevertheless, there are only a few investigations providing accurate mechanical data for the damaged TM after exposure to blast overpressure (Luo et al. 2015; Gan et al. 2016; Engles et al. 2017).

A better understanding of dynamic properties of the human TM exposed to blast waves is of considerable interest for assessment of blast-induced damage of the auditory system as well as for hearing protection devices. Luo et al. (2015) used a highly sensitive miniature split Hopkinson tension bar (SHTB) to measure the mechanical properties of the TM at high strain rates and derive Young's modulus changes of the TM after multiple blast exposures. The SHTB provided a uniaxial tensile test for TM strip specimens in the time domain. The tensile strain of the TM specimens in SHTB tests was typically 10–30%. Due to the sensitivity of the TM's stiffness characteristics to strain rates, the results from SHTB test can be utilized to characterize the failure behavior and nonlinear stress-strain curve of the TM in relation to impact loading. However, from the view of TM transmitting sound vibration, mechanical property changes of the TM induced by blast waves should be quantified in response to sound stimulation.

Despite the progress made in understanding the change of mechanical properties induced by blast exposure, accurate measurement of the mechanical properties of damaged TM is still needed as addressed (Engles et al. 2017). First, due to the nonlinear stiffness characteristics of the TM, the mechanical properties vary with strain. It is necessary to determine how mechanical stiffness of the TM decreases when the TM is exposed to repeated blast exposures. Second, the residual stiffness of damaged TM reflects the severity of injury to the TM, and the property data gives us an insight into the mechanical state of the TM immediately after exposure. Third, the material properties can be used to validate the biomechanical modeling of TM perforation induced by blast exposure. Thus, the knowledge about residual TM stiffness after blast exposure may assist emergency medical personnel in the evaluation and treatment of blast-injured TM, avoiding further auditory injury.

3.2 Dynamic Properties of Human TM After Blast Exposure

A study on dynamic properties of human TM after exposure to blast waves by using acoustic loading and laser Doppler vibrometry measurement with an inverse problem-solving method to determine the complex modulus of the TM specimen was recently completed in our lab (Engles et al. 2017). The TM specimens were prepared from human temporal bones following exposures to blast overpressure using the established methodologies described in Sections I–

rgan@ou.edu

A and shown in Fig. 1b. It usually took three iterations of blasts to reach the TM rupture. The peak pressure before the TM rupture defined as the TM rupture threshold ranged from 7.6 to 9.0 psi (52.4–62.1 kPa) from ten human cadaver ears or temporal bones. The TM specimen for mechanical test was the rectangular strip with approximate dimensions of 6 × 2 mm cut from either the posterior or anterior site of the pars tensa with the tympanic annulus attached. The specimen was then mounted to the material testing system (MTS).

The experimental setup with LDV to measure dynamic properties of the TM specimen can be found in Fig. 3 of Engles et al. (2017). Briefly, the sound was delivered from a speaker through a 1-mm-diameter sound delivery tube at 2 mm away from the center of the lateral side of the specimen. A dynamic signal analyzer (DSA) (PSA, HP 35670A, CA) coupled to a power amplifier (B&K 2718, Norcross, GA) was used to generate a pure tone sound of 90 dB SPL over the frequency range of 200–8000 Hz. To monitor the input sound pressure level, a probe microphone (ER-7C, Etymotic Research, IL) was attached to the sound delivery tube at 1 mm from the TM surface. Specimen vibrations were measured with the LDV (HLV-1000, Polytech PI, Austin, CA) while focusing the beam at the reflective tape. The vibration velocity of the specimen was acquired by the DSA and recorded on a PC for further analysis.

Dynamic testing of each specimen was simulated in a FE model in ANSYS using acoustic-structure coupled analysis. To mimic the vibration of the TM specimen in response to sound stimuli in an open field, a FE model including the solid structure of the specimen and a spherical area of air surrounding the TM was built. To facilitate acoustic pressure coupled to the TM surface, the surface of acoustic elements (air) in contact with the TM solid structure was defined as a fluid-structure interface. The standard linear solid model or Weichert model was used to describe the viscoelastic behavior of the TM (O'Connor et al. 2008; Zhang and Gan 2010). The relaxation modulus of the TM can be expressed as

$$E(t) = E_0 + E_1 \exp\left(-\frac{t}{\tau_1}\right) \tag{2}$$

where E_0 is the relaxed elastic modulus at $t = \infty$, $E_0 + E_1$ is the initial elastic modulus at $t = 0$, and τ_1 is the relaxation time. The relaxation modulus in the time domain can be converted to the complex modulus in the frequency domain. The complex modulus E^* is expressed as

$$E^*(\omega) = E'(\omega) + iE''(\omega) \tag{3}$$

where $E'(\omega)$ is the storage modulus, $E''(\omega)$ is the loss modulus, and ω is the angular frequency. Further, $E'(\omega)$ and $E''(\omega)$ can be expressed as

$$E'(\omega) = E_0 + \frac{E_1\tau_1^2\omega^2}{1+\tau_1^2\omega^2} \tag{4}$$

$$E''(\omega) = \frac{E_1\tau_1\omega}{1+\tau_1^2\omega^2} \tag{5}$$

The loss factor $\eta(\omega)$ can be expressed as

$$\eta(\omega) = \tan(\delta) = \frac{E''(\omega)}{E'(\omega)} \tag{6}$$

where δ is the phase angle.

An iterative FE simulation of the dynamic test was performed to find material constants that achieve the best match between the modeling results and actual measurements. A short description of the process was given by Engles et al. (2017). An example of the experimental results of the amplitude-frequency curve from two TM samples (47 L and 41 L) compared with the FE model-derived curves was shown in Fig. 6 of their paper. The three parameters E_0, E_1, and τ_1 for each specimen were determined through the FE model, and the experimental curves were represented by the resonance frequency f_n and the amplification ratio R (ratio between the amplitude at the resonance frequency and the amplitude at the lowest frequency measured).

To determine the effect of blast waves on mechanical properties of the TM, the complex modulus for post-blast TMs was plotted against normal TMs published by Zhang and Gan (2010)

rgan@ou.edu

using acoustic stimulation and LDV in Fig. 5. The blast exposure caused the storage modulus to become significantly reduced across the frequency range. Similarly, the loss modulus for post-blast TMs was also much lower than the normal TMs. The decrease of loss modulus was significant (Student's t test, $p < 0.0065$). These data reveal that the blast overpressure causes a frequency-dependent stiffness reduction of the TM. Loss factor is the ratio between the loss modulus and storage modulus. The post-blast TMs had a lower loss factor at frequencies below 2 kHz and a larger loss factor at frequencies over 2 kHz compared to the normal TMs. As shown in Fig. 5, the blast resulted in a flat storage modulus curve in the high-frequency range. This is one of the reasons that caused the larger loss factor in the post-blast TMs at high frequencies.

An additional insight from this study is the data clearly show that retained complex modulus of the TM after blast exposure was reduced more than 50%. The TM rupture caused by blast exposure includes perforation of the TM and reduction of complex modulus in the remaining part of the TM. The TM perforation and alteration in mechanical properties can contribute to a conductive hearing loss. The effect of TM perforations on sound transmission through the middle ear was investigated in temporal bone models by Gan et al. (2009). Their results indicated that TM perforations caused more than 20 dB reduction in the TM and stapes footplate displacements at frequencies below 1 kHz.

3.3 Microstructural Changes in Post-Blast TM

TM is a complex trilaminar membrane. Its middle layer, the lamina propria, has a composite structure consisting of radially and circumferentially oriented collagen fibers embedded in the ground substance (Lim 1995). To evaluate the microstructural changes of the TM after expo-

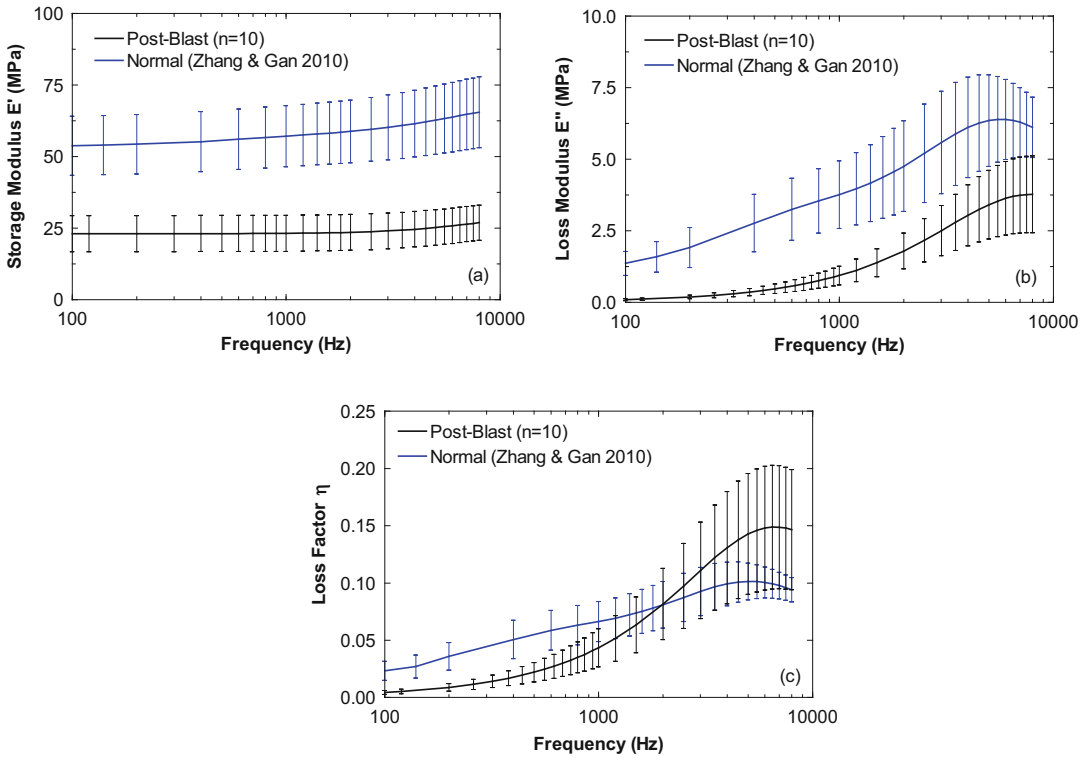


Fig. 5 Comparison of complex modulus between blast-exposed and normal TMs over the frequency range of 100–8000 Hz. (**a**) Storage modulus, (**b**) loss modulus, and (**c**) loss factor

rgan@ou.edu

sure to blast, the SEM images were obtained for both pre- and post-blast human TMs and examined with electron microscopes (NEON 40 EsB, Zeiss, Oberkochen, Germany; JSM-840, JEOL Ltd., Tokyo, Japan) in the Samuel Roberts Noble Microscopy Laboratory at the University of Oklahoma.

Figure 6 shows the SEM image obtained from a post-blast TM (left panel) and a normal TM (right panel). The images were viewed from the lateral side and focused on areas where the epithelial layer separated from the TM during SEM preparation. The effect of blast waves on the fiber bundles can be observed from Fig. 6 as shown by the radial orientation of the post-blast TM tears, which was a result of the circumferential fiber fractures. The normal TM shows a generally smoother appearance, reflecting the normal state of the TM. The SEM images suggested that the TM damage along the radial direction may be more severe than that along the circumferential direction after blast exposure.

In a study performed by Luo et al. (2015), the results indicated that Young's modulus is higher in the radial direction than in the circumferential direction and the fracture strength in the radial direction is also higher than that in the circumferential direction under the condition of the same strain rate. When the TM is exposed to blast waves, it is more probable that the circumferential fibers, which have a lower fracture strength, would break before the radial fibers. Figure 6 demonstrates that the post-blast TM tears were oriented in the radial direction, indicating the microstructure changes caused by blast exposures. However, it is difficult to quantify the extent of microstructure damage of TM by using SEM images. The weakened mechanical properties are the reflection of microstructure damage, but it is not applicable to build a direct relation between microstructure damage of TM and changes of macro-mechanical properties at the present stage.

4 Conclusions

1. The relationship between the TM damage threshold and blast overpressure wave direction has been investigated in human cadaver ears and the FE model of the human ear. The "head block" attached with the temporal bone was exposed to open-field blast inside the test chamber at three incident wave directions, vertical, horizontal, and front, with respect to the head. Results demonstrate that blast overpressure P0 at the ear canal entrance induced the highest peak pressure P1 near the TM in the canal, which determines the TM injury. The P1 pressure differences in vertical, horizontal, and front tests reflect the variations of energy flux distribution over frequencies, peak P1/P0 ratio, and TM rupture threshold. FE modeling results indicate that P1 threshold for TM rupture in front direction is the lowest because of the highest TM stress change rate with respect to P1 pressure increase, $\delta\sigma/\delta p_1$, compared with the vertical and horizontal directions.
2. The dynamic properties of post-blast TMs were measured on ten human cadaver TM

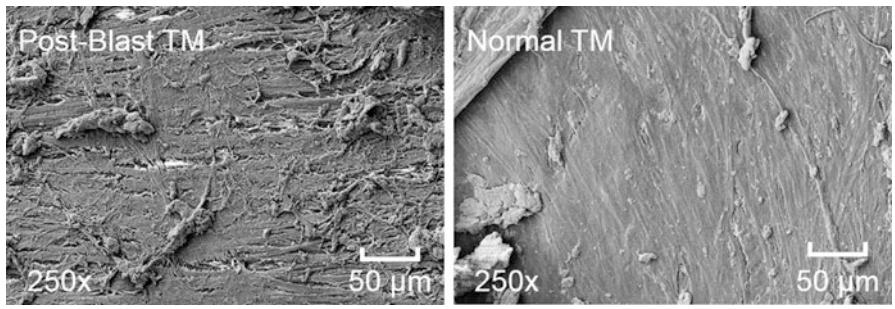


Fig. 6 SEM images of the TM surface. The left image shows the damage of the post-blast TM. The right panel shows the SEM image of the normal TM surface

rgan@ou.edu

samples following the blast. Acoustic stimulation was used as a driving force to induce vibrations of the TM over a frequency range of 200–8000 Hz, and LDV was used to measure the sample vibrations. The inverse problem-solving method with the FE modeling of each TM specimen test was used to determine the complex modulus. Results include the storage modulus and the loss modulus over the frequency range of 100–8000 Hz obtained from all TM specimens. The mean storage modulus was ranging from 23.1 to 26.9 MPa at frequencies from 100 to 8000 Hz. The mean loss modulus was from 0.10 to 3.78 MPa at frequencies of 100–8000 Hz. Compared to the mechanical properties of normal TMs determined previously using the same method, the storage and loss modulus of the TMs exposed to blast waves had significant reduction. The SEM images of post-blast TMs compared with normal TMs showed obvious microstructural changes which indicate the tissue damage caused by the multiple blast exposures. This study provides important data on the human TM mechanical changes after exposure to blast overpressure waves.

Acknowledgments This work was supported by the US Army Medical Research and Materiel Command (USAMRMC) Grant W81XWH-14-1-0228. The author would like to thank Kegan Leckness, MS; Don Nakmali, MS; Warren Engles, MS; Xiao D. Ji, PhD; and Xuelin Wang, PhD, for their work involved in the projects reported in this chapter.

References

Ahmad SW, Ramani GV (1979) Hearing loss in perforations of the tympanic membrane. J Laryngol Otol 93:1091–1098

von Békésy G (1960) Experiments in hearing. McGraw Hill, New York

Bigelow DC, Swanson PB, Saunders JM (1996) The effect of tympanic membrane perforation size on umbo velocity in the rat. Laryngoscope 106:71–76

Cave KM, Cornish EM, Chandler DW (2007) Blast injury of the ear: clinical update from the global war on rerror. Mil Med 172:726–730

Cheng T, Dai C, Gan RZ (2007) Viscoelastic properties of human tympanic membrane. Ann Biomed Eng 35:305–314

Cho S-I, Gao SS, Xia A, Wang R, Salles FT, Raphael PD, Abaya H, Wachtel J, Baek J, Jacobs D, Rasband MN, Oghalai JS (2013) Mechanisms of hearing loss after blast injury to the ear. PLoS One 8(7):e67618

Daphalapurkara NP, Dai C, Gan RZ, Lu H (2009) Characterization of the linearly viscoelastic behavior of human tympanic membrane by nanoindentation. J Mech Behav Biomed Mater 2(1):82–92

De Greef D, Aernouts J, Aerts J, Cheng JT, Horwitz R, Rosowski JJ, Dirckx JJJ (2014) Viscoelastic properties of the human tympanic membrane studied with stroboscopic holography and finite element modeling. Hear Res 312:69–80

Dirckx JJ, Decraemer WF (2001) Effect of middle ear components on eardrum quasi-static deformation. Hear Res 157:124–137

Dougherty AL, MacGregor AJ, Han PP, Viirre E, Heltemes KJ, Galarneau MR (2013) Blast-related ear injuries among U.S. military personnel. JRehabil Res Dev 50:893–904

Engles WG, Wang X, Gan RZ (2017) Dynamic properties of human tympanic membrane after exposure to blast waves. Ann Biomed Eng 45(10):2383–2394. https://doi.org/10.1007/s10439-017-1870-0

Fausti SA, Wilmington DJ, Gallun FJ, Myers PJ, Henry JA (2009) Auditory and vestibular dysfunction associated with blast-related traumatic brain injury. J Rehabil Res Dev 46(6):797–810

Fay J, Puria S, Decraemer WF, Steele C (2005) Three approaches for estimating the elastic modulus of the tympanic membrane. J Biomech 38:1807–1815

Gan RZ, Feng B, Sun Q (2004) Three-dimensional finite element modeling of human ear for sound transmission. Ann Biomed Eng 32(6):847–859

Gan RZ, Reeves BP, Wang X (2007) Modeling of sound transmission from ear canal to cochlea. Ann Biomed Eng 35(12):2180–2195

Gan RZ, Cheng T, Dai C, Yang F, Wood MW (2009) Finite element modeling of sound transmission with perforations of tympanic membrane. J Acoust Soc Am 126:243–253

Gan RZ, Nakmali D, Ji X, Leckness K, Yokell Z (2016) Mechanical damage of tympanic membrane in relation to impulse pressure waveform - A study in chinchillas. Hear Res 340:25–34

Hamernik RP, Keng D (1991) Impulse noise: some definitions, physical acoustics and other considerations. J Acoust Soc Am 90:189–196

Hamernik RP, Qiu W (2001) Energy-independent factors influencing noise-induced hearing loss in the chinchilla model. J Acoust Soc Am 110:3163–3168

Hamernik RP, Ahroon WA, Hsueh KD (1991) The energy spectrum of an impulse: Its relation to hearing loss. J Acoust Soc Am 90:197–204

Hawa T, Gan RZ (2014) Pressure distribution in a simplified human ear model for the high intensity sound transmission. J Fluids Eng 136:111108-1–111108-6

Huang G, Daphalapurkar NP, Gan RZ, Lu H (2007) A method for measuring linearly viscoelastic properties

rgan@ou.edu

of human tympanic membrane using nanoindentation. J Biomech Eng 130:014501

Kirikae I (1960) The structure and function of the middle ear. University Press, Tokyo

Leckness K (2016) Novel finite element method to predict blast wave transmission through human ear. MS Thesis. University of Oklahoma, Oklahoma

Liang J, Yokell Z, Nakmali D, Gan RZ, Lu H (2017) The effect of blast overpressure on the mechanical properties of a chinchilla tympanic membrane. Hear Res 354:48–55

Lim DJ (1995) Structure and function of tympanic membrane: A review. Acta Otorhinolaryngolog Belg 49:101–115

Luo H, Dai C, Gan RZ, Lu H (2009) Measurement of young's modulus of human tympanic membrane at high strain rates. J Biomech Eng 131: 064501–064501

Luo H, Jiang S, Nakmali D, Gan RZ, Lu H (2015) Mechanical properties of a human eardrum at high strain rates after exposure to blast waves. J Dyn Behav Mater 2:59–73

Mehta RP, Rosowski JJ, Voss SE, O'Neil E, Merchant SN (2006) Determinants of hearing loss in perforations of the tympanic membrane. Otol Neurotol 27:136–143

O'Connor KN, Tam M, Blevins NH, Puria S (2008) Tympanic membrane collagen fibers: a key to high-frequency sound conduction. Laryngoscope 118:483–490

Santa Maria PL, Atlas MD, Ghassemifar R (2007) Chronic tympanic membrane perforation: a better animal model is needed. Wound Repair Regen 15:450–458

Voss SE, Rosowski JJ, Merchant SN, Peake WT (2007) Non-ossicular signal transmission in human middle ears: experimental assessment of the 'acoustic route' with perforated tympanic membranes. J Acoust Soc Am 122(4):2135–2153

Zhang X, Gan RZ (2010) Dynamic properties of human tympanic membrane – experimental measurement and modelling analysis. IJECB 1:252–270

Zhang X, Gan RZ (2012) Dynamic properties of human tympanic membrane based on frequency-temperature superposition. Ann Biomed Eng 41:205–214

rgan@ou.edu

Hearing Research 354 (2017) 48–55

Contents lists available at ScienceDirect

Hearing Research

journal homepage: www.elsevier.com/locate/heares

Research Paper

The effect of blast overpressure on the mechanical properties of a chinchilla tympanic membrane

Junfeng Liang [a], Zachery A. Yokell [b], Don U. Nakmaili [b], Rong Z. Gan [b], Hongbing Lu [a, *]

[a] Department of Mechanical Engineering, The University of Texas at Dallas, Richardson, TX, 75080, USA
[b] School of Aerospace and Mechanical Engineering, University of Oklahoma, Norman, OK, 73019, USA

ARTICLE INFO

Article history:
Received 25 December 2016
Received in revised form
30 July 2017
Accepted 15 August 2017
Available online 18 August 2017

Keywords:
Hearing damage
Blast overpressure
Tympanic membrane
Micro-fringe projection
Mechanical properties
Chinchilla

ABSTRACT

The rupture of tympanic membrane (TM) has long been viewed as an indicator of blast injury, especially for hearing loss. However, little is known about damage to the TM caused by blast with pressure lower than the rupture threshold. In this paper, we present our study on the effect of blast overpressure on the static mechanical properties of TM. Chinchilla was used as the animal model and exposed to multiple blasts with pressures lower than the rupture threshold of the TM. Using a micro-fringe projection method, we observed the alteration of the static mechanical properties of post-blast chinchilla's TMs as compared to those of control TMs. Specifically, after exposing to multiple blasts, the Young's modulus of chinchilla TM decreased by ~53% while the ultimate failure pressure decreased by ~33%. Scanning Electron Microscope (SEM) images show the damage formation in the post-blast TM as compared with its control counterpart.

© 2017 Elsevier B.V. All rights reserved.

1. Introduction

Blast injury is one of the common types of injury in the modern military conflicts (Dougherty et al., 2013; Eskridge et al., 2012; Vanderploeg et al., 2012). The high pressure shock wave and overpressure blast wind generated in the battle field from the explosion can directly traumatize exposed victims' organs that encompass an air-fluid interface (Chaloner, 2005; Yeh and Schecter, 2012). Among these organs, the ear is the most vulnerable and typically the first organ to incur primary blast injury. Exposure to the high pressure of the blast wave can potentially cause a series of otologic injuries including: perforation of tympanic membrane, dislocation or fracture of ossicular chain, and gross trauma in cochlea such as rupture of basilar membrane and permanent loss of hair cells (Cho et al., 2013; Darley and Kellman, 2010; Patterson and Hamernik, 1997; Wani et al., 2016). Sequelae of the primary blast traumas on the ear can affect immediate situational awareness and cause permanent hearing disabilities (Darley and Kellman, 2010; Ewert et al., 2012; Luo et al., 2017).

Rupture of tympanic membrane (TM) or eardrum is usually considered as an indicator for blast induced otologic injury. Locating between outer ear and middle ear, TM is the first vulnerable tissue exposed to the overpressure wave. TM rupture may occur at a blast pressure as low as 35 kPa while a pressure of 105 kPa leads to rupture in 50% of eardrums in adults (Sprem et al., 2001). It is observed that the transmission function of the TM can be remarkably altered if the TM is ruptured (Gan et al., 2016). However, a TM is a complex tri-laminar membrane. Its acoustic functional layer, the lamina propia has a composite structure consisting of radially and circumferentially oriented collagen fibers embedded in the ground substance (Lim, 1995). Due to the arrangement and the viscoelastic characteristic of the collagen fibers, the mechanical properties of TM, in whole, vary significantly depending on the orientation and the strain rate (Daphalapurkar et al., 2008; Luo et al., 2009). In a blast exposure, even before the overpressure reaches its rupture threshold, a TM has already experienced deformation at an extremely high strain rate, which could induce damage at the collagen fiber level. The damage is usually too small to observe directly but still severe enough to alter the overall mechanical properties and thus the transmission function of TM (Luo et al., 2016). Unlike other injuries with explicit symptoms, such a subtle effect of alteration of material properties of TM tends to be overlooked or hidden by some more observable sequelae from other damages of the auditory system. Nevertheless,

* Corresponding author. Department of Mechanical Engineering, University of Texas at Dallas, 800 W Campbell Rd, ECSN 2.528, Richardson, 75080-3021, TX, USA.
E-mail address: hongbing.lu@utdallas.edu (H. Lu).

http://dx.doi.org/10.1016/j.heares.2017.08.003
0378-5955/© 2017 Elsevier B.V. All rights reserved.

it is important to investigate the change of mechanical properties of TM because it provides the foundation to understand the effect of structural change of the TM from the blast wave on the sound transmission. This subsequently will help to evaluate and diagnose conductive hearing loss induced by blast exposure.

In this paper, we describe our animal study on the change of mechanical properties of TM caused by the exposure to over-pressure blast wave. Chinchillas were used in this study because the size of their TM and the frequency range of their hearing are similar to those of humans (Heffner and Heffner, 1991; Jensen and Bonding, 1993; Richmond et al., 1989). The adult chinchillas were exposed to blast waves multiple times *in vivo* with pressure lower than the rupture threshold (9.1 psi) of TM (Gan et al., 2016). The mechanical properties of post-blast TMs were measured and compared with control (normal) TMs using a micro-fringe projection method. In this method, deformation of an intact TM *in situ* was measured by projecting fringes with submillimeter pitch onto the TM as quasi-static air pressure was applied. Mechanical properties were determined by an inverse method with the assistance of finite element simulations.

2. Methods

2.1. Blast chamber

A compressed air (nitrogen)-driven blast apparatus located inside an anechoic chamber in the Biomedical Engineering Laboratory at the University of Oklahoma was used to generate a blast overpressure wave in this study (Gan et al., 2016). Fig. 1 shows the schematic of the blast apparatus with an animal holder placed at the center. A polycarbonate film (McMaster-Carr, Atlanta, GA) was used to induce initial blast overpressure of ~200 kPa (200 dB SPL) or higher at the exit of the pressure reservoir. The overpressure level on the animal was controlled by varying the thickness (0.13 mm and 0.26 mm) of the film as well as the distance from the sample to the blast reference plate.

Blast overpressure was monitored using a high-frequency piezoelectronic pressure transducer (PCB Group Inc., Model102B16) with the face of the sensor toward the incident blast wave. The recorded pressure signal was amplified by a Piezotronic Signal Conditioner (PCB Group Inc., Model 482C) and acquired by a data acquisition system with LabView interface (National Instrument, N1 cDAQ-9174). Two typical pressure waveforms of blasts are demonstrated in Fig. 2. In this study, 0.26 mm thickness of polycarbonate film was used to produce a blast with a peak pressure between 21 kPa and 48 kPa lasting approximately 1.0 μs at 30 cm from the blast reference plate. It was found that chinchilla TMs exposed to this level of blast wave multiple times did not rupture but experienced enough damage for observing the changes of mechanical properties.

2.2. Animal exposure to the blast

Six healthy adult chinchillas weighed from 500 to 800 g were used in this study. The study protocol was approved by the Institutional Animal Care and Use Committee of the University of Oklahoma and met the guidelines of the National Institutes of Health and the United States Department of Agriculture (USDA). All animals were raised to be free from middle ear disease, as evaluated by wideband tympanometry. An animal holder made of 4 inch inner diameter polyvinyl chloride (PVC) pipe was used to protect the body of a chinchilla below the neck from the force of the blast and to maintain the position of the head of chinchilla. The chinchilla was deeply anesthetized with 35 mg/kg of ketamine and 7 mg/kg of xylazine and placed into the holder with only its head exposed to the base of the pinna, securing with a c-shaped clamp around its neck. As shown in Fig. 1, the animal holder with the chinchilla was placed inside the test chamber. The pressure transducer was then positioned at the entrance of the ear canal of chinchilla as described in Gan et al. (2016). Multiple blasts were subsequently applied to simulate the battlefield environment where deployed military members in the front line are frequently exposed to multiple blast waves. Repeated blast exposures were given 3 times at 2 min intervals. Following the final exposure, the animal ear was examined using an otoscope to confirm the TM was intact. TMs with observable rupture were excluded from the study.

2.3. Sample preparation

After blast, the chinchillas were euthanized by the intraperitoneal (IP) administration of 1.0 mL Euthasol (390 mg/mL pentobarbital sodium, 50 mg/mL phenytoin sodium). Intact bullas were harvested 10 min *post mortem*. The medial side of the TM was fully exposed by opening the bulla wall from the middle ear side and removing the cochlea, stapes, and tensor tympani muscle. The

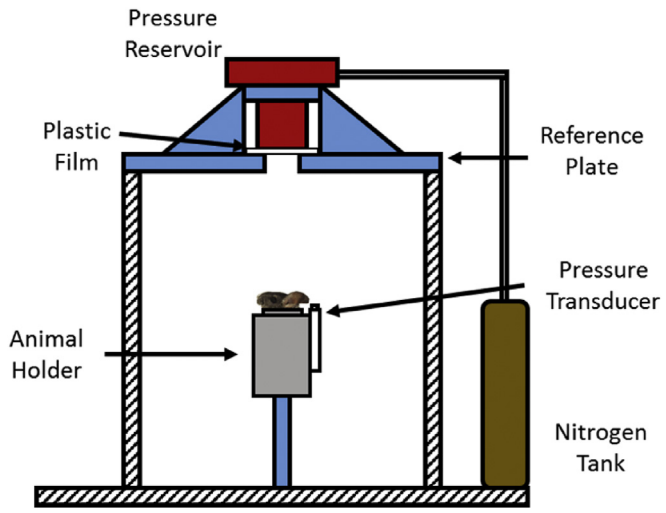


Fig. 1. Schematic of the blast testing chamber and the animal experimental setup. For demonstration purpose, the components are not drawn in scale.

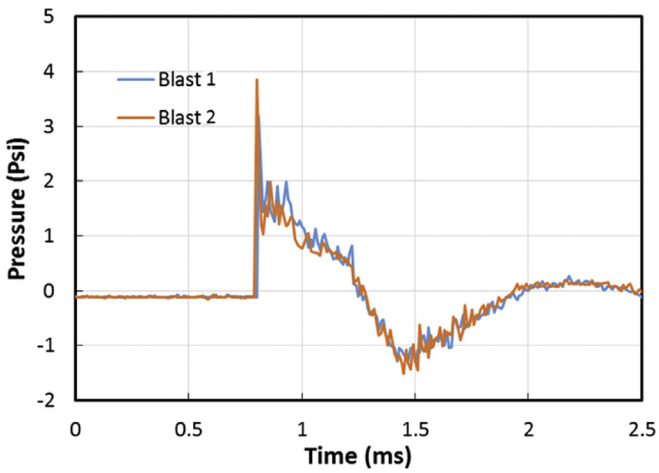


Fig. 2. Typical waveforms of the blast overpressure as measured by a piezo pressure transducer at the entrance of ear canal close to the TM of a chinchilla. The two blast waveforms demonstrate the repeatability.

malleus-incus complex was then immobilized by applying a droplet of gel type superglue (Superglue, Co. Find the Right Glue, Fast™) between the incus section and the petrous wall behind to maintain the conical geometry of the TM. A PVC tubing with 1/16 inch inner diameter, 1/8 inch outer diameter, and about 3 inch long, was inserted into the ear canal and hermetically fixed on the bulla by applying two-part epoxy (Illinois Tool Works, Devcon 5 Minute) at the entrance of the ear canal. The ear canal and the TM formed a concealed chamber and the PVC tube was then connected to a pressure monitor system to either inflating or deflating the TM from the lateral side. During the sample preparation, a droplet of saline solution was applied on the TM every 5 min to prevent the TM from desiccation. Meanwhile, a small piece of Kimwipes paper saturated with saline solution was used to cover the TM during the curing period of the two-part epoxy.

Micro-fringe projection was used to measure deformation of the TM in terms of volume displacement. This technique requires the object to have a diffusive reflecting surface to form fringes with sharp contrast for imaging. Therefore the medial side of TM was coated with a thin layer of titanium oxide in saline solution (100 mg/ml) to improve the reflectiveness of the surface. Titanium oxide was chosen because it has good reflection and is a non-toxic material commonly used for cosmetic (Dirckx and Decraemer, 1997).

As TM, like other soft tissues, is a viscoelastic material (Fung, 1993; Cheng et al., 2007; Ladak et al., 2004), preconditioning needs to be carried out to allow the TM to reach a steady state. For our case, each TM sample was preconditioned by applying five cycles of a small alternating (negative and positive) pressures with magnitudes less than 100 Pa. For each preconditioning cycle, a negative pressure was applied first to the bulla, then the pressure was increased to a positive value, and finally the pressure was released back to zero. Here, the negative pressure was introduced by applying a vacuum pressure from the lateral side of TM, causing the pressure on the medial side of the TM to be higher than the pressure applied on the lateral side. The positive compressed air pressure was introduced into the bulla from the lateral side of TM, causing the pressure on the medial side of the TM to be lower than the pressure applied on the lateral side of the TM. The total duration of preconditioning lasted approximately 1 min.

2.4. Measurement procedure with micro-fringe projection

Each bulla specimen was positioned on a gimbal sample holder mounted on a xyz translation stage which allowed the adjustment of the orientation and position of the bulla with six degrees of freedom. A self-developed projection system was used to project the parallel line pattern of a grating with a pitch of 20 cycles/mm to form micro-fringes onto the TM surface (Liang et al., 2016). The image of distorted fringes on the TM surface containing the topography information of the TM was captured by a digital camera (Nikon D7000, 4928 × 3264 pixels) connected to a surgical microscope (Carl Zeiss, OPMI-1). The acquired images were analyzed for 3-dimensional reconstruction of the TM surface using a five phase-shifting algorithm (Ortiz and Patterson, 2005). During the measurement, the bulla was first secured with molding clay in the sample holder and coarsely positioned with the xyz translation stage so that the entire TM faced the microscope and stayed within the field of view of the camera. Next, the bulla was fixed with the swivel screws in the gimbal sample holder and the angle was finely adjusted until a full view of the TM free of shadow can be seen in the camera through the microscope.

Air pressure was applied to the bulla using a syringe in a pressure monitoring system. Both positive and negative pressures were applied to the bulla for measuring the response of the TM to the pressures to determine mechanical properties of the TM. Pressure was applied with a magnitude between −1.0 kPa and 1.0 kPa with an increment of 0.125 kPa inside the bulla. The stopcock in the pressure monitoring system was set to lock-up mode and a constant pressure was maintained at each step for a few seconds. Due to the reduction of the strength of the TM after experiencing multiple blasts, some TM samples failed before the pressure reached 1.0 kPa. As air pressure was used as loading, the middle ear cavity needed to be air-tightly sealed. The TM must remain intact and free from any perforation. To ensure this condition, for measuring the post-blast chinchilla TMs, the applied pressure cycle was different from that in the previous work on control chinchilla TMs. The pressure started with zero and was ramped up in the positive direction until the TM sample failed or pressure reached 1.0 kPa. The pressure was subsequently released back to zero and ramped up in the negative direction. If the TM sample did not rupture in a full measurement cycle, a failure test immediately followed: positive pressure was applied on the TM continuously until the TM was ruptured, and the final value of pressure was recorded and reported as the ultimate failure pressure. For those TM samples ruptured in the measurement cycle, data were only collected in the pressure range where the TM was not ruptured, and the maximum positive pressures applied were recorded as the failure pressure. If the TM sample was ruptured when a negative pressure was applied, it was excluded from the failure data.

2.5. Finite element model and inverse method

To determine the mechanical properties of the post-blast TMs with an inverse method, a finite element method (FEM) model was developed using the surface typography of a TM at zero-pressure state on ANSYS15.0 (ANSYS, Inc.). The boundary and the location of manubrium were determined by the optical image of the TM sample. The malleus was constructed as a part of the TM but with properties of a bone tissue (with 10 GPa Young's modulus, and 0.2 Poisson's ratio). The rest of the TM was modelled as a homogeneous and isotropic hyperelastic membrane with the boundary, the annulus, completely fixed for all degrees of freedom. The entire model (including the membrane and the manubrium) was discretized with 10,000 4-node tetrahedral shell elements (shell-181) with a thickness of 10 μm.

For each specimen, the dimensions of the FEM model were adjusted according to the experimental measurement (Table 1). Uniaxial form of 2nd-order Ogden model was used as the constitutive model to describe the mechanical behavior of the TM. The uniaxial form of 2nd-order Ogden model is given as (Aernouts et al., 2010; Wang et al., 2002)

$$T_U = \sum_{i=1}^{2} \frac{2\mu_i}{\alpha_i}\left(\lambda_U^{\alpha_i - 1} - \lambda_U^{-0.5\alpha_i - 1}\right) \tag{1}$$

where T_U is the uniaxial stress; λ_U is the uniaxial stretch ratio, and $\lambda_U = 1 + \varepsilon_U$, with ε_U being the uniaxial strain. Parameters μ_i and α_i are constants representing the material hyperelastic properties. Under uniaxial stretch, assuming incompressibility of the TM, the principal stretch ratios λ_i (i = 1, 2, 3) are given as $\lambda_1 = \lambda_U$, $\lambda_2 = \lambda_3 = \lambda_U^{-\frac{1}{2}}$.

During the inverse method process, values of μ_i and α_i were first set to be identical to those of normal chinchilla TM reported by Liang et al. (2016). Uniform pressure in the range of 0 kPa–1.0 kPa was applied on the medial side and the lateral side, corresponding to the pressures used in the experiments. The volume displacement under each static pressure was calculated. An iteration procedure was used to modify μ_i and α_i until the volume displacement

Table 1
Dimensions, average pressures for the blasts and parameters of Ogden model for each Chinchilla TM.

Sample Number	Superior-inferior Diameter (mm)	Anterior-posterior Diameter (mm)	Average Blast Pressure (Psi)	μ_1	α_1	μ_2	α_2
16-3-2L	8.24	8.13	4.95	1.5	4.4	3.2	−7.0
16-3-2R	8.86	9.26	4.95	1.1	3.7	2.9	−6.1
16-3-11L	8.58	9.30	4.90	1.0	2.7	2.8	−5.6
16-3-11R	8.16	9.23	4.90	1.4	3.7	3.1	−6.8
16-3-5L	8.81	7.91	5.56	1.6	4.0	3.2	−6.9
16-3-6R	8.38	8.56	4.05	1.5	3.3	3.2	−6.3
16-3-7R	7.41	8.93	4.75	1.5	3.1	3.2	−6.2
16-3-10L	8.40	9.12	4.23	1.1	2.6	2.9	−5.0
Average	8.36 ± 0.43	8.81 ± 0.51	4.79 ± 0.65	1.3 ± 0.2	3.4 ± 0.6	3.1 ± 0.2	−6.2 ± 0.6

computed from the FEM model agreed well with the corresponding experimental volume displacement.

To compare with the mechanical properties of control chinchilla TMs from our previous work, the data was also analyzed to determine the Young's modulus and the tangent modulus. The former is defined as the slope in the linear region of stress-strain curve under small deformations. The latter is the slope of the stress-strain curve at any point. The Young's modulus and the tangent modulus are identical at the initial linear portion of a stress-strain curve. For hyperelastic material, the tangent modulus can be obtained by taking derivative of stress with respect to strain from Equation (1), given as

$$\frac{dT_U}{d\varepsilon_U} = \sum_{i=1}^{2} \frac{2\mu_i}{\alpha_i} \left[(\alpha_i - 1)(1+\varepsilon_U)^{\alpha_i - 2} + (0.5\alpha_i + 1)(1+\varepsilon_U)^{-0.5\alpha_i - 2} \right] \quad (2)$$

Additional details of the FEM model and the procedure of the inverse method can be found in our previous work (Liang et al., 2015; 2016).

3. Results

The pressure-volume displacement relationships of eight post-blast chinchilla TMs were calculated from the topographies reconstructed with micro-fringe projection. The applied pressures were plotted against the volume displacements as shown in Fig. 3. The volume displacements were calculated from the TM surface profiles during the pressure ramping-up phase.

Closely observing this plot reveals a short initial linear stage where the TM deforms significantly with the increase of pressure followed by a nonlinear stage where the deformation of TM becomes stable. At the initial stage of the loading, linear behavior is observed and it is due to the relaxed collagen fibers and the elastic behavior of the TM's soft tissue. As the loading increases, however, the collagen fibers start to align in the loading direction to bear the loads, causing an alternation in stiffness. The strong nonlinearity exhibited in the pressure-volume displacement curves is similar to our previous reported results on control chinchilla TMs (Liang et al., 2016).

The curves shown in Fig. 3 are overall fairly asymmetrical with respect to the origin. The average lower volume displacement in the positive direction is about 29% lower than that in the negative direction. The asymmetry is attributed to the nearly conical geometry of the TM and the boundary structure: the malleus on the medial side of the TM holding the convex geometry of TM in a pre-stretched condition hinders the TM to further deform as pressure increases in the positive direction (Dirckx and Decraemer, 1992; Qi et al., 2008). Even though the tensor tympani muscle has been removed, the immobility of the malleus-incus complex from sample preparation still serves as a strong constraining boundary for the TM deformation under positive pressure. This can also be the reason why most of the TM samples fail under the positive pressure loading. The asymmetrical deformation under volume-displacement overpressure agrees with our previous work (Liang et al., 2016) and findings from TMs of other mammals such as gerbil (Gea et al., 2010), cat (Funnell and Decraemer, 1996).

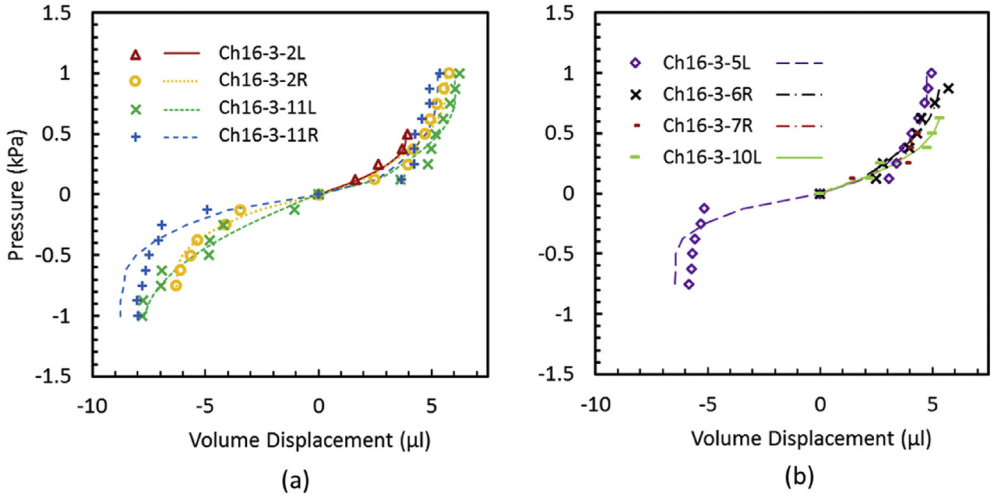


Fig. 3. Pressure-volume displacement relationships for eight post-blast chinchilla TMs. The makers show the experimental results during of ramping up of the pressure and the smooth curves show the FEM simulation results. Data were plotted in two figures for the convenience of reading.

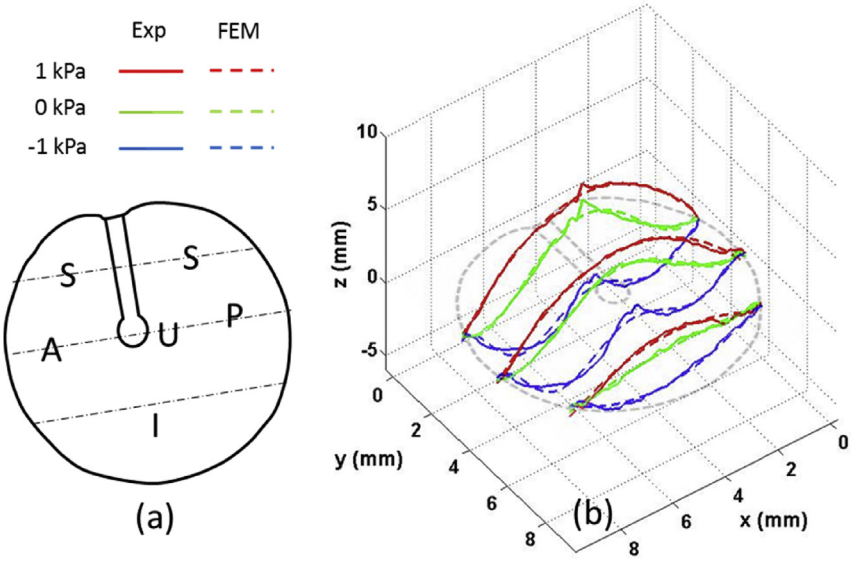


Fig. 4. Comparison of surface profile of a typical TM sample between experimental (Exp) results and FEM simulation under −1.0 kPa, 0 kPa and +1.0 kPa pressures. The three dash-dot lines along anterior-posterior direction in the schematic in (a) shows the cross-sections for comparison in the right figure. The labels in the schematics are: A (anterior quadrant), P (posterior quadrant), S (superior quadrant), I (inferior quadrant) and U (umbo).

The dimensions and the material properties parameters for Ogden model of each TM are listed in Table 1. These parameters were obtained with the entire pressure history of the measurement for each sample. Simulated pressure-volume displacement curves are plotted with the solid lines in Fig. 3 to compare with their experimental counterparts. The simulation results generally agree well with the experimental data with less than 10% error. For validation purpose, height profiles of a typical sample are also compared between experiment and simulation in three cross-sections at three different pressure levels (−1.0 kPa, 0 kPa and +1.0 kPa) shown in Fig. 4. With positive pressure applied, simulation height profiles are almost identical to the experimental results with error less than 5%, while with negative pressure the error is relatively large-at around 15%. The reasonable good agreement between the simulation results and experimental data shows that the non-uniformity of TM were reduced through the summation process in the calculation of volume displacement.

The stress-strain relationships of the eight post-blast chinchilla TMs determined using Equation (1) and the parameters from Table 1 are shown in Fig. 5. The curves shown in Fig. 5 indicate that the material properties of chinchilla TM are highly nonlinear above 10% strain. The TM first becomes softer between 10% and 20% strain and then gradually stiffens after 20% strain.

The tangent modulus is plotted against the uniaxial strain as shown in Fig. 6. The curves in this figure indicate that, as the strain increases, the tangent modulus exhibits a decrease followed by a gradual increase in value. At 46% strain, which is the maximum strain on the TM determined by FEM model, the maximum stress reaches an average of 1.0 MPa as shown in Fig. 5.

The average Young's modulus is also calculated based on the

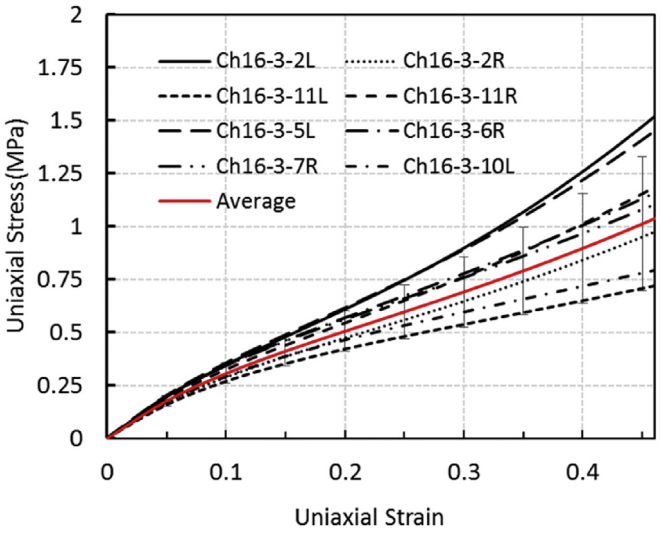


Fig. 5. Uniaxial tensile stress-strain curves of eight chinchilla TMs post blast (determined from an inverse method using the 2nd order uniaxial Ogden hyperplastic model).

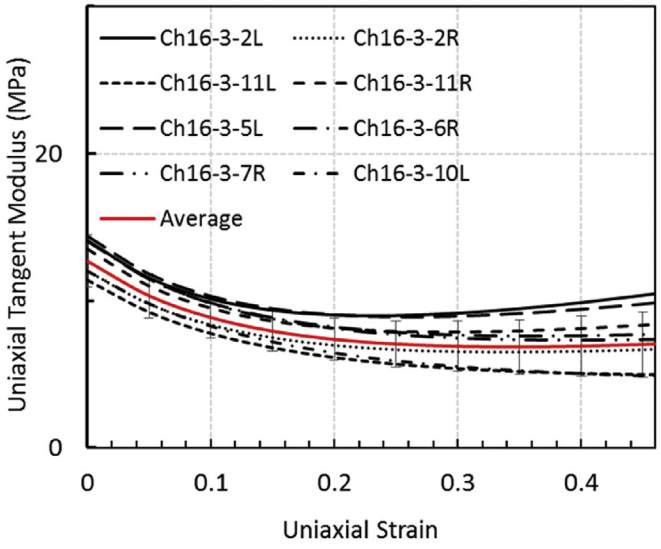


Fig. 6. Tangent modulus as a function of strain for eight post blast chinchilla TMs (determined from an inverse method using the 2nd order uniaxial Ogden hyperplastic model).

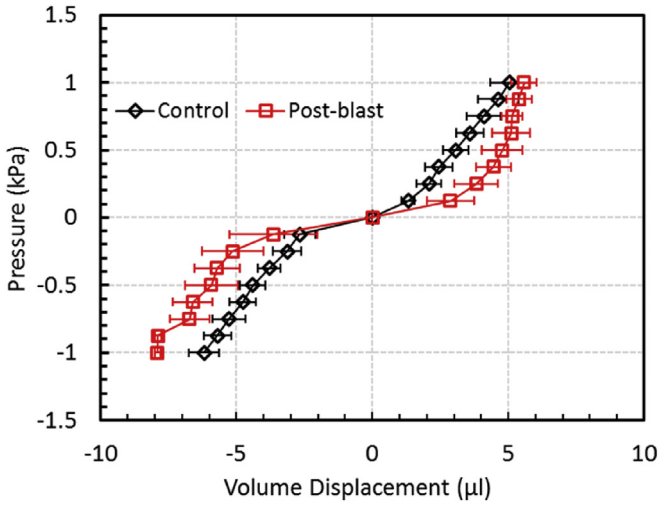


Fig. 7. Pressure-volume displacement relationships for post-blast and control chinchilla TMs (n = 10 for the control group and n = 8 for the post-blast group). The error bar in the figure shows the standard deviation. Note that the average and the standard deviation for the post-blast samples are calculated from the available data at each pressure level (See Fig. 3). Thus n may be smaller than 8 at some pressures due to premature rupture of some samples.

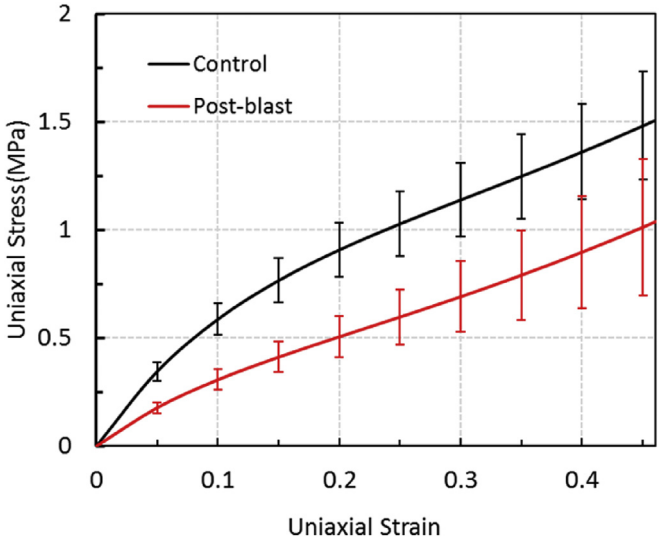


Fig. 8. Uniaxial tensile stress-strain relationships for post-blast and control chinchilla TMs (n = 10 for the control group and n = 8 for the post-blast group. The error bar in the figure shows the standard deviation.).

results obtained from eight TMs using Equation (2). At strain close to zero, the tangent modulus is 12 MPa. Then it decreases to 7.0 MPa at 46% strain. The average tangent modulus, at strains less than 25%, is chosen as the representative Young's modulus. Therefore, the average value of ~9 MPa is quoted as the Young's modulus for the post-blast TMs.

4. Discussion

4.1. Comparison between post-blast and control TMs

The mechanical properties of chinchilla TMs without exposure to a blast (control samples) have been measured and reported previously (Liang et al., 2016). In this study, we make a comparison between the mechanical properties of control and post-blast

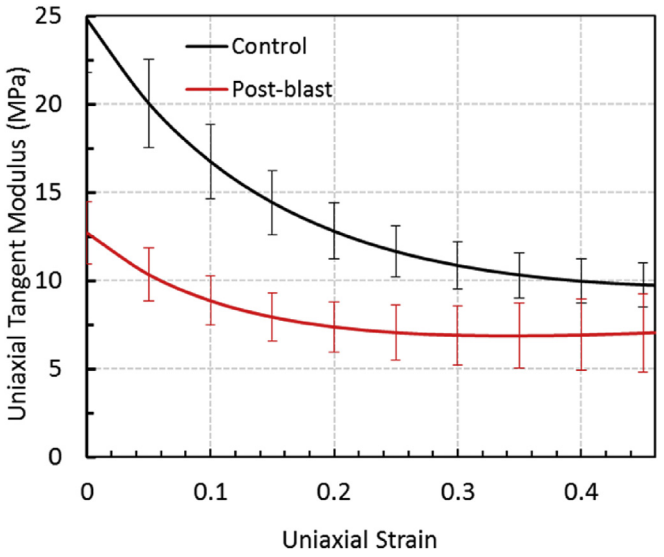


Fig. 9. Tangential modulus for post-blast and control chinchilla TMs (n = 10 for the control group and n = 8 for the post-blast group. The error bar in the figure shows the standard deviation.).

Table 2
Comparison of failure pressures between control chinchilla TMs and post-blast chinchilla TMs (p = 0.036).

Group	Number of Samples	Failure Pressure (kPa)	Standard Deviation (kPa)
Control	10	1.14	0.3
Post-blast	8	0.77	0.37

chinchilla TMs. Specifically, in order to investigate the effect of the blast on the chinchilla TM, the average value of pressure-volume displacement relationships, stress-strain relationships and tangential modulus of TMs of two groups of animals (control and post-blast chinchilla) are plotted in Figs. 7–9 respectively. The results are based on the average values for eight post-blast TMs and ten control samples respectively. The comparison indicates notable differences as described below.

When comparing the pressure-volume displacement relationship between the post-blast and the control TM (Fig. 7), independent two sample *t*-test at each pressure level shows that there is a significant difference between these two groups of data ($p < 0.05$) except at the pressure of 1.0 kPa ($p = 0.123$). In the positive direction, the volume displacement significantly increases below 0.5 kPa and this increase gradually drops down. At 1.0 kPa, the volume displacements of control and post-blast TMs are similar. Pressure-volume displacement relationship reflects the mechanical response of the entire structure including TM and the malleus-incus complex. The notable rise of volume displacement of the post-blast TMs at the low pressure level indicates the decrease of the stiffness of the structure. As the pressure increases, malleus starts to carry more load and becomes the major constraint for the TM deformation, thus the difference of volume displacements between control and post-blast TMs becomes small. The volume displacement in the negative pressure range generally shows a similar pattern except for the pressures at −0.875 kPa and −1.0 kPa. This is probably due to uncertainty associated with small sample size (n = 2). As pointed out in measurement procedure section, some TM samples ruptured before the maximum positive pressures were applied, or ruptured at magnitude of low pressure levels when negative pressure was applied. Only two of the post-blast

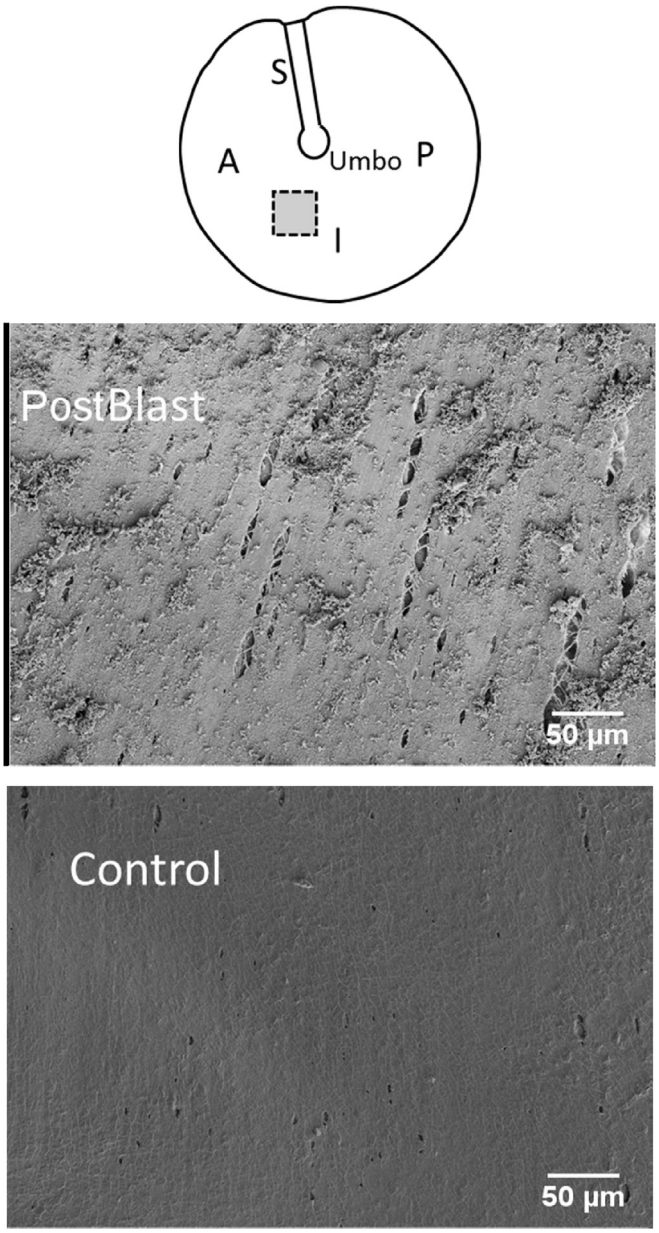


Fig. 10. Typical SEM images for post-blast and control chinchilla TMs. The grey box in the schematic on the top shows the location where the SEM images were acquired. The labels in the schematics are: A (anterior quadrant), P (posterior quadrant), S (superior quadrant), and I (inferior quadrant).

TMs were able to provide the volume displacement at these two pressure levels. The increase in volume displacement generally occurs as the TM-malleus structure becomes less stiff after experiencing multiple blasts.

To further investigate the change of material properties of the TM instead of alternation of the structural properties of the system, a comparison is made on the stress-strain curves of TM determined from the inverse method. Fig. 8 confirms the hypothesis that the TM becomes softer after experiencing multiple blasts, in that the stress is lower in post-blast samples when compared to the control samples at the same strain. The difference of stresses between normal and post-blast TMs at strain levels above 20% is generally identical ($p < 0.01$ at all the strain levels), although at high strain both control and post-blast TMs show large scattering and the scattering areas partly overlap with each other.

Fig. 9 shows that the tangent modulus has a pronounced decrease ($p < 0.006$ at all the strain levels) after the TM has experienced multiple blasts especially below 20% strain. Above 20% strain, the difference in modulus gradually decreases, which also agrees with the pattern of the difference in volume displacement between control and post-blast TMs. Within the linear range (below 25% strain), tangential modulus decreases about 10 MPa, which is about a 53% decrease when compared to the control samples.

Table 2 shows the comparison of ultimate failure pressures between control and post-blast chinchilla TMs. The ultimate failure pressure decreases significantly: the ultimate failure pressure drops down from 1.14 kPa to 0.77 kPa ($p = 0.036$), representing a 33% reduction. This implies that TMs were generally significantly weakened through the exposure to multiple blasts, even though the blast pressure level does not reach the rupture threshold.

The decrease of the stiffness of the structure and the weakening of the TM are related to the microscopic damages that were caused by the multiple blasts. Fig. 10 shows the Scanning Electron Microscope (SEM) image of the TM in the control case and post-blast case. The surface layers of post-blast TM are much rougher than the control counterpart. While the blast was not severe enough to perforate the entire TM structure, it clearly damaged the surface of the TM as well as induced micro-cracks in the fiber layers. Damaged epidermis is also clearly observed all over the post-blast TM surface. Due to the *in vitro* nature of the measurement in the present study, it is unclear whether these microstructural damages of the TM by blast are recoverable or long-term in a live chinchilla. Investigation of the effect of damage on the threshold and transfer function of the hearing in live chinchillas can potentially address this issue.

4.2. Comparison with other studies

The results reported herein are in line with other results available in the literature. Although there are various researches on blast induced traumas in brain (Alshareef et al., 2015; Elliott et al., 2008; Ling et al., 2009), eyes (DeMar et al., 2016; Jones et al., 2016), and auditory system (Gan et al., 2016; Wani et al., 2016), to the best of our knowledge, studies on change of mechanical properties of auditory tissues are very rare. Most recently, Luo, et al. reported the mechanical properties of human eardrum at high strain rates after exposure to blast waves (Luo et al., 2016), which is the only work on change of TM mechanical properties after blast. In their study, it was found that the average Young's moduli of the human TMs exhibit 27% reduction after exposure to blast in radial direction but remain nearly identical in circumferential directions at strain rates below $300s^{-1}$. Our finding on decrease of Young's modulus of chinchilla TM after blast agrees with Luo's observation on human TM. The decrease of mechanical properties of the chinchilla TM reported in this work is larger than that was found in human as reported by Luo et al. This is probably due to the thickness difference of TMs between chinchilla and human (15 μm of chinchilla vs. 70 μm of human). Exposing to similar level of blast pressure may generate more damage to chinchilla TM than to human TM.

Compared to Luo's work, the method in this study has two advantages: Firstly, animal study allows investigation of TM exposed to blast *in vivo*. It is well known that the stapedius and tensor tympani muscles of the middle ear contract when the ear is exposed to high-intensity sound (Fox, 2006), potentially reducing the damage to the TM. Therefore, the decrease of TM properties could be smaller in the *in vivo* case than that in the *post mortem* case. Secondly, the micro-fringe projection used in this study is a non-contact technique. The procedure of the method does not require cutting the TM into strips or harvesting the TM as in some

other mechanical testing techniques (Cheng et al., 2007; Huang et al., 2008; Luo et al., 2009; Zhang and Gan, 2013). Therefore the potential damage to the TM structure caused by sample preparation is excluded from damage caused by blast overpressure. It is worth noting that fringe projection measurement requires the scarification of the chinchilla to harvest the bullas, thus individual TM was used either in control or blast exposure experiment. The observation of effect of the blast is based on group comparison. In this study, micro-fringe projection is used to determine the surface topography of the TM, this technique is not sensitive enough to detect the damage that is highly localized. As a result, the homogenized (or effective) mechanical properties are determined under the assumption that the TM behaves as an isotropic material. The values of mechanical properties reported herein globally represent the average alternation of mechanical performance of the TM after blast exposure. This work should be considered as a supplement to the existing study on the effect of blast overpressure on human TM properties. Future study is needed to identify local damage, and its effect on the local mechanical properties, including the alteration of material anisotropic properties.

5. Conclusion

The effect of blast overpressure on mechanical properties of the TM in chinchillas were reported in this paper using a micro-fringe projection system with pressure as loading. FEM models of the chinchilla TMs were developed to characterize the mechanical properties of the TMs through an inverse method. Compared to the results from previous work on the control chinchilla TMs, it is found that Young's modulus of the post-blast chinchilla TMs decreased by about 53% while the failure pressure reduced by about 33%. Based on the measured post-blast mechanical properties of TM, more accurate simulation model of the middle ear for blast wave transmission can be established for further investigating hearing damage.

Acknowledgements

We acknowledge the support of DOD W81XWH-13-MOMJPC5-IPPEHA. Dr. Lu also acknowledges the Louis A. Beecherl Jr. Chair for additional support. We thank Kegan Leckness for the assistance in SEM imaging and Dr. Dani Z. Fadda for editing the manuscript.

References

Aernouts, J., Soons, J.A.M., Dirckx, J.J.J., 2010. Quantification of tympanic membrane elasticity parameters from in situ point indentation measurements: validation and preliminary study. Hear. Res. 263, 177–182.
Alshareef, A.A., Gabler, L.F., Stone, J.R., Panzer, M.B., 2015. Changes in the mechanical response of brain tissue following proimary blast injury. In: 2015 Ohio State University Injury Biomechanics Symposium.
Chaloner, E., 2005. Blast injury in enclosed spaces - all doctors should know the basic management of patients injured by explosive blast. Br. Med. J. 331 (7509), 119–120.
Cho, S., Gao, S.S., Xia, A., Wang, R., Salles, F.T., Raphael, P.D., Abaya, H., Wachtel, J., Baek, J., Jacobs, D., Rasband, M.N., Oghalai, J.S., 2013. Mechanisms of hearing loss after blast injury to the ear. PLoS One 8 (7), e67618.
Cheng, T., Dai, C.K., Gan, R.Z., 2007. Viscoelastic properties of human tympanic membrane. Ann. Biomed. Eng. 35 (2), 305–314.
Daphalapurkar, N.P., Dai, C., Gan, R.Z., Lu, H., 2008. Characterization of the linearly viscoelasic behavior of human tympanic membrane by nanoindentation. J. Mech. Behav. Biomed. Mater. 2 (1), 82–92.
Darley, D.S., Kellman, R.M., 2010. Otologic considerations of blast injury. Disaster Med. Public 4 (2), 145–152.
DeMar, J., Sharrow, K., Hill, M., Berman, J., Oliver, T., Long, J., 2016. Effects of primary blast overpressure on retina and optic tract in rats. Front. Neurol. 7, 59.
Dirckx, J.J.J., Decraemer, W.F.S., 1992. Area change and volume displacement of the human tympanic membrane under static pressure. Hear. Res. 62 (1992), 99–104.
Dirckx, J.J.J., Decraemer, W.F., 1997. Coating techniques in optical interferometric metrology. Appl. Opt. 36 (13), 2776–2782.
Dougherty, A.L., MacGregor, A.J., Han, P.P., Viirre, E., Heltemes, K.J., Galarneau, M.R., 2013. Blast-related ear injuries among U.S. miliary personnel. J. Rehabil. Res. Dev. 50 (6), 893–904.
Elliott, M.B., Jallo, J.J., Tuma, R.F., 2008. An investigation of cerebral edema and injury volume assessments for controlled cortical impact injury. J. Neurosci. Methods 168 (2), 320–324.
Eskridge, S.L., Macera, C.A., Galarneau, M.R., Holbrook, T.L., Woodruff, S.I., MacGregor, A.J., Morton, D.J., Shaffer, R.A., 2012. Injuries from combat explosions in Iraq: injury type, location, and severity. Injury 43 (10), 1678–1682.
Ewert, D.L., Lu, J.Z., Li, W., Du, X.P., Floyd, R., Kopke, R., 2012. Antioxidant treatment reduces blast-induced cochlear damage and hearing loss. Hear. Res. 285 (1–2), 29–39.
Fox, S., 2006. Human Physiology, ninth ed., pp. 267–269 New York.
Fung, Y.C., 1993. Biomechanics: Mechanical Properties of Living Tissues, second ed. Springer, New York.
Funnell, W.R.J., Decraemer, W.F., 1996. On the incorperation of moire shape measurements in finite-element models of the cat eardrum. J. Acoust. Soc. Am. 100 (2 Pt 1), 925–932.
Gan, R.Z., Nakmali, D., Ji, X.D., Leckness, K., Yokell, Z., 2016. Mechanical damage of tympanic membrane in relation to impulse pressure waveform-A study in chinchillas. Hear Res. 340, 25–34.
Gea, S.L.R., Decraemer, W.F., Funnell, W.R.J., Dirckx, J.J., Maier, H., 2010. Tympanic membrane boundary deformations derived from static displacements observed with computerize tomography in human and gerbil. J. Assoc. Otolaryngol. 11 (1), 1–17.
Heffner, R.S., Heffner, H.E., 1991. Behavioral hearing range of the chinchilla. Hear Res. 52 (1), 13–16.
Huang, G., Daphalapurkar, N.P., Gan, R.Z., Lu, H.B., 2008. A method for measuring linearly viscoelastic properties of human tympanic membrane using nano-indentation. J. Biomech. Eng. 130 (1), 014501.
Jensen, J.H., Bonding, P., 1993. Experimental pressure induced rupture of the tympanic membrane in man. Acta Otolaryngol. 113 (1), 62–67.
Jones, K., Choi, J.H., Sponsel, W.E., Gray, W., Groth, S.L., Glickman, R.D., Lund, B.J., Reilly, M.A., 2016. Low-level primary blast causes acute ocular trauma in rabbits. J. Neurorauma 33 (13), 1194–1201.
Ladak, H.M., Decraemer, W.F., Dirckx, J.J.J., Funnell, W.R.J., 2004. Response of the cat eardrum to static pressures: mobile versus immobile malleus. J. Acoust. Soc. Am. 116 (5), 3008–3021.
Liang, J., Fu, Bo., Luo, H., Nakmali, D., Gan, R.Z., Lu, H., 2015. Characterization the nonlinear elastic behavior of Guinea pig tympanic membrane using micro-fringe projection. Int. J. Exp. Comput. Biomech. 3 (4), 319–344.
Liang, J., Luo, H., Yokell, A.Z., Nakmali, U.D., Gan, R.Z., Lu, H., 2016. Characterization of the nonlinear elastic behavior of chinchilla tympanic membrane using micro-fringe projection. Hear. Res. 339, 1–11.
Lim, D.J., 1995. Structure and function of the tympanic membrane:a review. Acta oto-rhino-laryngologica belg 49 (2), 101–115.
Ling, G., Bandak, F., Armonda, R., Grant, G., Ecklund, J., 2009. Explosive blast neurotrauma. J. Neurotrauma 26 (6), 815–825.
Luo, H.Y., Dai, C.K., Gan, R.Z., Lu, H.B., 2009. Measurement of Young's modulus of human tympanic membrane at high strain rates. J. Biomech. Eng. 131 (6), 064501.
Luo, H., Jiang, S., Nakmali, D.U., Gan, R.Z., Lu, H., 2016. Mechanical properties of a human eardrum at high strain rates after exposure to blast waves. J. Dyn. Behav. Mater. 2 (1), 59–73.
Luo, H., Pace, E., Zhang, J., 2017. Blast-induced tinnitus and hyperactiveity in the auditory cortex of rats. Neuroscience 340, 515–520.
Ortiz, M.H., Patterson, E.A., 2005. Location and shape measurement using a portable fringe projection system. Exp. Mech. 45, 197–204.
Patterson, J.H., Hamernik, R.P., 1997. Blast overpressure induced structural and functional changes in the auditory system. Toxicology 121 (1), 29–40.
Qi, L., Funnell, W.R., Daniel, S.J., 2008. A nonlinear finite-element model of the newborn ear. J. Acoust. Soc. Am. 124 (1), 337–347.
Richmond, D.R., Yelverton, J.T., Fletcher, E.R., Phillips, Y.Y., 1989. Physical correlates of eardrum rupture. Ann. Otol. Rhinol. Laryngol. Suppl. 140, 35–41.
Sprem, N., Branica, S., Dawidowsky, K., 2001. Tympanoplasty after war blast lesions of the eardrum: retrospective study. Croat. Med. J. 42 (6), 642–645.
Vanderploeg, R.D., Belanger, H.G., Horner, R.D., Spehar, A.M., Powell-Cope, G., Luther, S.L., Scott, S.G., 2012. Health outcomes associated with military deployment: mild traumatic brain injury, blast, trauma, and combat associations in the Florida National Guard. Arch. Phys. Med. Rehab. 93 (11), 1887–1895.
Wang, B., Lu, H., Kim, G., 2002. A damage model for the fatigue life of elastomeric materials. Mech. Mater. 34 (8), 475–483.
Wani, A., Rehman, A., Lateef, S., Malik, R., Ahmed, A., Ahmad, W., Kirmani, M., 2016. Traumatic tympanic membrane perforation: an overview. Indian J. Otol. 22 (2), 100–104.
Yeh, D.D., Schecter, W.P., 2012. Primary blast injuries-an updated concise review. World J. Surg. 36 (5), 966–972.
Zhang, X.M., Gan, R.Z., 2013. Dynamic properties of human tympanic membrane based on frequency-temperature superposition. Ann. Biomed. Eng. 41 (1), 205–214.

Annals of Biomedical Engineering, Vol. 45, No. 10, October 2017 (© 2017) pp. 2383–2394
DOI: 10.1007/s10439-017-1870-0

Dynamic Properties of Human Tympanic Membrane After Exposure to Blast Waves

WARREN G. ENGLES, XUELIN WANG, and RONG Z. GAN

School of Aerospace and Mechanical Engineering, University of Oklahoma, Norman, OK 73019, USA

(*Received 29 January 2017; accepted 7 June 2017; published online 20 June 2017*)

Associate Editor Eiji Tanaka oversaw the review of this article.

Abstract—Blast overpressure causes dynamic damage to middle ear components, and tympanic membrane (TM) rupture is the most frequent middle ear injury. However, it is unclear how the blast waves change mechanical properties of the TM and affect sound transmission through the ear. This paper reports the current study on dynamic properties of the TM after exposure to blast waves by using acoustic loading and laser Doppler vibrometry (LDV). The TM specimens were prepared from human temporal bones following exposures to blast overpressure. Vibration of the TM specimen induced by acoustic loading was measured by LDV over a frequency range of 200–8000 Hz. An inverse-problem solving method with finite element modeling was used to determine the complex modulus of the TM specimen. The post-blast storage modulus ranged from 23.1 to 26.9 MPa, and loss modulus ranged from 0.09 to 3.78 MPa as frequency increased from 200 to 8000 Hz. Compared to the complex modulus of normal TM reported in the literature, the post-blast storage and loss modulus decreased significantly across the frequency range. The scanning electron microscopy (SEM) images of the post-blast TM samples showed microstructural changes of the tissue, which explained the alteration of mechanical properties of the TM samples.

Keywords—Tympanic membrane, Complex modulus, Blast overpressure, Ear injury.

INTRODUCTION

Auditory damage is one of the primary blast injuries in service members on the battlefield and civilians that suffered from blast exposure. Dougherty *et al.*[7] reported a study on 3981 military personnel that suffered a blast-related injury and found that tympanic membrane (TM) perforation occurred in 8% of the individuals. Other studies of blast-exposed patients showed the incidence of TM rupture ranged from 10 to 20%.[12,13,25] In addition to TM rupture, the blast overpressure can also interrupt the ossicular chain, and damage the cochlear hair cells.[4] While the mechanisms of blast-induced hearing loss are not well understood, mechanical damage to TM has been associated with a higher chance of hearing loss at medium and high frequencies.[7,21]

The TM is located at the end of the external ear canal and forms the boundary between the outer ear and middle ear. The TM plays an important role in transmitting sound from the environment to the middle ear and inner ear. As a multi-layer membrane tissue, mechanical properties of the TM directly affect its vibration response to sound pressure. Any damage to the TM would affect its mechanical properties and alter the normal performance of the TM for sound transmission.

There are two basic types of experimental data which are used to assess the extent and nature of blast-induced damage to the TM: mechanical property changes and microstructural variations of the TM. Mechanical properties provide an indication of the residual stiffness of the damaged TM as a function of the frequency. By comparing mechanical properties at various frequencies before and after an exposure, it is possible to derive a stiffness shift measure of the TM. Microstructural variations can be detected by scanning electron microscopy (SEM) images, which provide an insight into the structural aspects of the injury on the surface of the TM, but SEM images are difficult to quantify the damage throughout TM.

Mechanical properties of the TM under normal conditions have been characterized by numerous researchers. The static properties of the human TM

Address correspondence to Rong Z. Gan, School of Aerospace and Mechanical Engineering, University of Oklahoma, Norman, OK 73019, USA. Electronic mail: rgan@ou.edu

0090-6964/17/1000-2383/0 © 2017 Biomedical Engineering Society

were first reported by von Békésy[24] as 20 MPa from a bending test on a rectangular cadaver TM strip. Further investigations into mechanical properties of human TM have been performed at quasi-static or low frequency range.[3,5,8,14,24] However, the TM works under the auditory frequency range of 20–20,000 Hz, and the dynamic properties of the TM need to be measured over the auditory frequency range. Kirikae determined Young's Modulus in the circumferential direction to be 40 MPa at 890 Hz.[16] Zhang and Gan reported an investigation on dynamic properties of human TM using acoustic stimulation and laser Doppler vibrometry (LDV) measurement.[27] Utilizing various techniques, the dynamic properties of the human TM in the auditory frequency range have been further characterized.[18,27,28] Nevertheless, there are only a few investigations providing accurate mechanical data for the damaged TM after exposure to blast overpressure.[11,19]

A better understanding of dynamic properties of the human TM exposed to blast waves is of considerable interest for assessment of blast-induced damage of the auditory system as well as for hearing protection devices. Luo *et al.*[19] used a highly sensitive miniature split Hopkinson tension bar (SHTB) to measure the mechanical properties of the TM at high strain rates, and derive the Young's modulus changes of the TM after multiple blast exposures. The SHTB provided an uniaxial tensile test for TM strip specimens in the time-domain. The tensile strain of the TM specimens in SHTB tests was typically 10–30%.[19] Due to the sensitivity of the TM's stiffness characteristics to strain rates, the results from SHTB test can be utilized to characterize the failure behavior and nonlinear stress–strain curve of the TM in relation to impact loading. However, from the view of TM transmitting sound vibration, mechanical property changes of the TM induced by blast waves should be quantified in response to sound stimulation.

Despite the progress made in understanding the change of mechanical properties induced by blast exposure, accurate measurement of the mechanical properties of damaged TM is still needed. First, due to the nonlinear stiffness characteristics of the TM, the mechanical properties vary with strain. It is necessary to determine how mechanical stiffness of the TM decreases when the TM is exposed to repeated blast exposures. Second, the residual stiffness of damaged TM reflects the severity of injury to the TM, and the mechanical property data give us an insight into the mechanical state of the TM immediately after exposure. Third, the material properties can be used to validate the biomechanical modeling to predict TM perforation induced by blast exposure. Finally, the knowledge about residual TM stiffness may assist emergency medical personnel in the evaluation and treatment of blast-injured TM, avoiding further auditory injury.

The goal of this study is to determine the mechanical properties of damaged human TMs in response to sound stimulation. After the TM was exposed to multiple blast waves, a technique coupling LDV measurement with acoustic stimulation was utilized to measure the dynamic response of the TM specimen over the auditory frequency range following the previously established methodologies.[27] Then an inverse-problem solving method with finite element (FE) modeling was employed to determine the complex modulus of the TM samples. The results quantified the stiffness characteristic of the TM after it suffered multiple blast exposures.

METHODS

TM Specimen Preparation

Exposure of Human Temporal Bones to Blast Waves

Fresh human cadaveric temporal bones were supplied by LifeLegacy Foundation, a certified human tissue supply source for military research. The study protocol was approved by the US Army Medical Research and Material Command (USAMRMC), Office of Research Protections (ORP). 10 fresh temporal bones (6 female and 4 male) from 7 donors with an average age of 73.7 ± 5.8 years, ranging from 66 to 84 years, were involved in this study. Comparing the TM samples reported by Zhang and Gan,[27] they used 8 specimens from 5 donors with a mean age of 67.5 years yielding a 8.8% difference. All temporal bones provided by LifeLegacy Foundation were shipped with dry ice to our laboratory within 12 h. The experiments were conducted within one week after the temporal bones arrived. The samples were processed with a solution of 0.9% saline and 15% povidone at 5 °C to maintain the physiological condition before the experiment. Each sample was examined under an operating microscope (OPMI-1, Zeiss, Thornwood, NY) to confirm a normal ear canal and an intact TM.

As shown in Fig. 1 a temporal bone including a complete normal organ of the ear was mounted to a "head block" inside an anechoic test chamber in our lab at the University of Oklahoma. Following previously established methodologies, a compressed nitrogen-driven blast apparatus was utilized to produce blast overpressure by rupturing a polycarbonate film (McMaster-Carr, Atlanta, GA).[11] Blast overpressure level was controlled by changing the thickness of the film, or the distance from the blast reference plane. A pressure sensor (Model 102B16, PCB Piezotronics,

Depew, NY) was mounted on a column to monitor the blast pressure. The pressure sensor was positioned approximately 1 cm lateral to the ear canal opening. The pressure signal was acquired using a sampling rate of 100 kilo-samples per second (10 μs dwell time) by the cDAQ 7194 and A/D converter 9215 (National Instruments Inc., Austin, TX), and acquired by the software package LabVIEW (NI Inc.). The pressure waveform of each blast had a single positive over-pressure peak, and the peak pressure was used to assess the pressure level of blast. Following the previously established method,[19] it usually took three iterations of blasts to reach the TM rupture. The peak pressure before the TM rupture was defined as the TM rupture threshold. For this study, the TM rupture threshold ranged from 7.6 to 9.0 psi (52.4–62.1 kPa), which is representative of an explosion of 0.45 kg of TNT at distance 3.35 m from the person.[15] The perforations were mainly observed in the anterior or inferior portion of the TM along the radial direction.

TM Specimen Preparation

A rectangular strip cut from the pars tensa of the TM was used to identify material properties. The human middle ear includes the TM or eardrum, three ossicular bones connected by two joints, and suspensory ligaments. If an intact middle ear is used to measure the material properties of TM, a large number of unknown variables including the shape of the TM, the material properties of the malleus–incus joint, incus–stapes joint, and suspensory ligaments will be involved. To reduce the number of variables and the difficulty of parameter identification, a rectangular strip TM specimen was utilized.

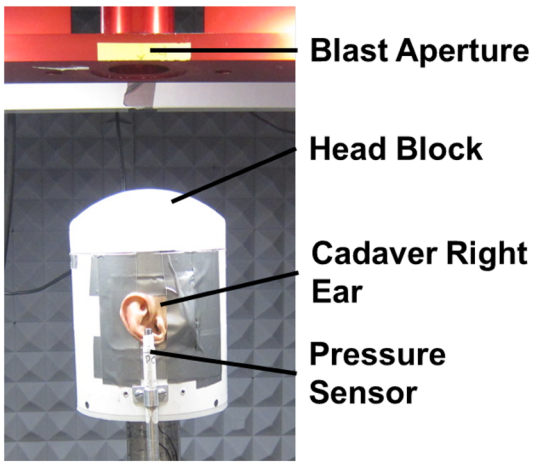


FIGURE 1. Setup to induce blast waves on human temporal bones.

After the temporal bone was exposed to blast waves, the tympanic annulus was detached from the tympanic sulcus. The TM was then removed with an intact malleus, and placed in 0.9% saline solution. A rectangular strip with approximate dimensions of 6 × 2 mm was cut from either the posterior or anterior site of the pars tensa as shown in Fig. 2a. A total of ten TM samples were collected for this study.

Experimental Setup for LDV Measurement

The TM specimen was fixed to two aluminum fixture adapters with cyanoacrylate liquid glue (Super Glue), and two plastic panels were used to support the fixture adapters during the mounting process. A laser reflective tape (3 M Co., St. Paul, MN) with an area of 0.5 mm^2 and a mass of 0.04 mg was placed at the center of the specimen to serve as the laser target for LDV measurement. Once the specimen was aligned in the grips of the material testing system (MTS) (TestResource, MN), the support panels were cut. The initial state of a mounted specimen was setup as shown in Fig. 2b.

Figure 3 is a schematic diagram of the experimental setup with LDV to measure dynamic properties of the TM specimen. The sound was delivered from a speaker through a 1 mm diameter sound delivery tube at 2 mm away from the center of the lateral side of the specimen. A dynamic signal analyzer (DSA) (PSA, HP 35670A, CA) coupled to a power amplifier (B&K 2718, Norcross, GA) was used to generate a pure tone sound of 90 dB SPL over the frequency range of 200–8000 Hz. To monitor the input sound pressure level a probe microphone (ER-7C, Etymotic Research, IL) was attached to the sound delivery tube 1 mm from the TM surface. Specimen vibrations were measured with a LDV (HLV-1000, Polytech PI, Austin, CA) while focusing the beam at the reflective tape. The vibration velocity of the specimen was acquired by the DSA and recorded on a personal computer for further analysis.

It is well known that the stabilized mechanical state of biological soft tissue can be reached through preconditioning. In this study, preconditioning was achieved by conducting five loading and unloading cycles in the MTS. The specimens were elongated at 0.5 mm/s with a longitudinal stretch ratio of 10%. The TM specimens were moistened with a saline solution during the testing process to maintain physiological conditions.

Determination of Complex Modulus

Dynamic testing of each specimen was simulated in a FE model in ANSYS (ANSYS, Inc., Canonsburg, PA) using acoustic-structure coupled analysis. The

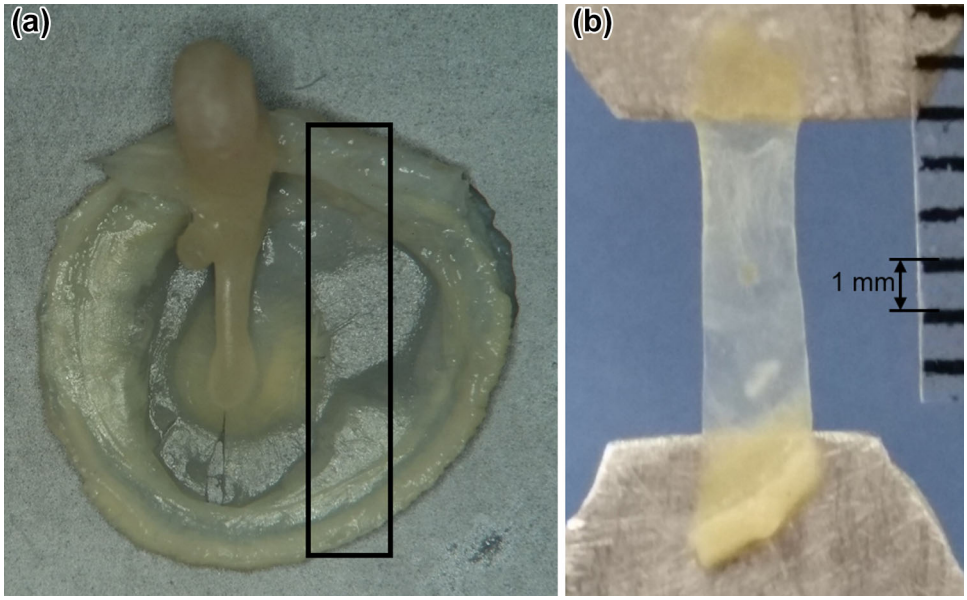


FIGURE 2. (a) TM sample harvested from blast exposed temporal bone. The black rectangle shows the area where the specimen was cut from. (b) TM strip specimen fixed to a metal adapter and mounted into the MTS.

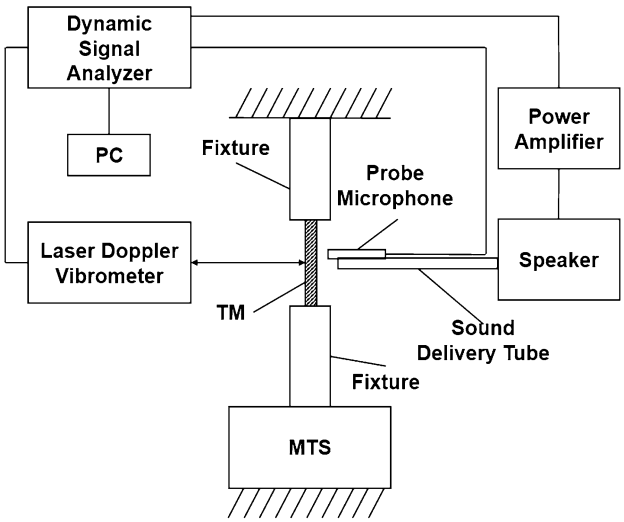


FIGURE 3. The schematic of the experimental setup for dynamic testing of TM specimens.

inverse-problem solving method was applied to determine the dynamic properties of the TM sample using the experimental data.

FE Model

To mimic the vibration of the TM specimen in response to sound stimuli in an open field, a FE model including the solid structure of the specimen and a spherical area of air surrounding the TM was built. To facilitate acoustic pressure coupled to the TM surface, the surface of acoustic elements (air) in contact with the TM solid structure was defined as a fluid–structure interface (FSI). The air had a density of 1.21 kg/m^3, and the specimen was simplified to a rectangular strip and assumed as a homogeneous isotropic material with a density of 1200 kg/m^3 and Poison's ratio 0.3.[9] A review of computational studies of human TM biomechanics was conducted by Volandri *et al.*[23] (see Table 2 of their paper) with the TM Poisson's ratio values reported in the literature. There was a general agreement on setting a value of 0.3 for the TM Poisson's ratio in the absence of experimental data. Although some researchers used TM Poisson's ratio close to 0.5 to approximately simulate incompressibility,[1] the Poisson's ratio of the TM has never been experimentally measured.

Four-node tetrahedral solid elements (Type 185 in ANSYS) were used for the meshing of the TM in ANSYS. The air surrounding the TM within 0.1 m radius was meshed using four-node tetrahedral fluid elements (Type 30 in ANSYS). The exterior surface of the air sphere was covered in three-node triangular fluid elements, which simulated the sound absorbance effect in an infinite open field.[25]

The TM specimen was considered to be fully clamped at either end. The input sound pressure delivered through the tube was considered to be acoustic loading applied at 1 mm away from the specimen surface. The real pressure distribution to drive the specimen vibration was solved by the FE modeling.

Before the FE model was used for determination of complex modulus, convergence tests were performed to assess the adequacy of the mesh density. The

elements of the TM sample were refined three times. The number of elements along width for the specimen was 13, 20 or 40, and the number of elements along length were 34, 60 or 80. The increase of the resulting displacement varied across the range of input sound frequencies. The difference of the first resonance frequency between the initial mesh and the first refinement was less than 15%, and the difference between the first and second refinement was less than 7%. The peak displacement magnitudes for the first refinement deviated by 44%, but for the second refinement the displacement deviated by less than 5%. Thus, we used the mesh resulting from the second refinement for simulations.

In FE model, the TM specimen was surrounded by the air without net flow. The continuity conditions between the structure (TM) and the air were well defined by Bouillard and Ihlenbury[2] and the acoustic fluid–structure interaction was used in published works on TM dynamic properties by Yokell *et al.*[26] and Zhang and Gan.[27] In this study, the air surrounding the TM was meshed with four-node tetrahedral acoustic elements. The well-known rule for the linear elements is to resolve a wavelength λ by six elements. Following this 'rule of the thumb' that at least six elements per shortest acoustic wavelength should be adopted for acoustic scattering.[2] The maximum acoustic element edge size of 0.0071 m was estimated at 8000 Hz, i.e., $1/6\ \lambda = 1/6\ (c/f) = 1/6$ (343 m/s/8000/s) = 0.0071 m, where c is the sound speed in air and f is the frequency. Thus, the maximum element edge size in this study was much smaller than 0.007 m and the mesh was fine enough.

Figure 4 displays a typical model of TM specimen with plane and lateral views. The figure shown was the initial meshes, and the mesh density was coarser than that of the final refinement.

Sound pressure of 90 dB SPL over the frequency range of 200–8000 Hz was applied at 1 mm away from the surface of the TM. The harmonic analysis was conducted in the model using ANSYS, and the predicted displacement at the center of the TM specimen was derived to compare with the measured result.

Constitutive Equation of TM Specimen

The standard linear solid model or Weichert model was used to describe the viscoelastic behavior of the TM.[20,27] The relaxation modulus of the TM can be expressed as

$$E(t) = E_0 + E_1 \exp\left(-\frac{t}{\tau_1}\right), \tag{1}$$

where E_0 is the relaxed elastic modulus at $t = \infty$, $E_0 + E_1$ is the initial elastic modulus at t = 0, and τ_1 is the relaxation time. The relaxation modulus in the time domain can be converted to the complex modulus in the frequency domain. The complex modulus E^* is expressed as

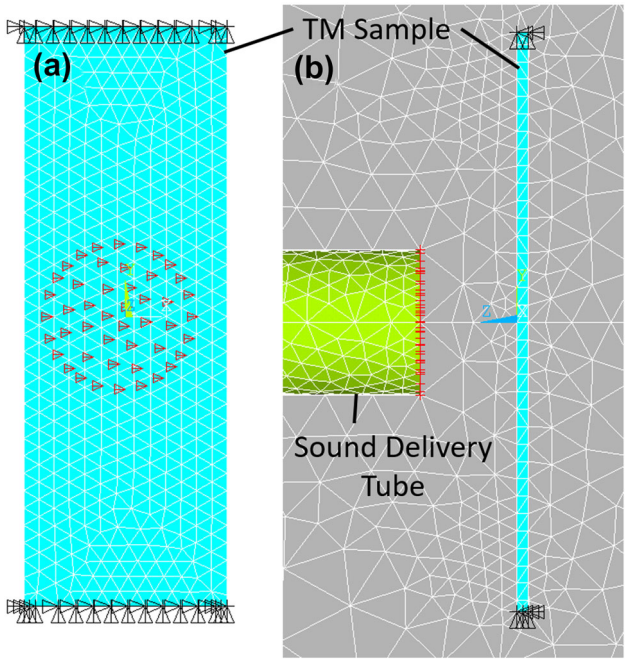


FIGURE 4. The FE model of dynamic experiment on the TM specimen. (a) Plane view of the FE model with fixed boundary condition (triangles) at both ends of the TM specimen and the acoustic pressure applied at the central area of the specimen. (b) Lateral view of the FE model including the TM specimen, sound delivery tube, and surrounding acoustic elements.

$$E^*(\omega) = E'(\omega) + iE''(\omega) \tag{2}$$

where $E'(\omega)$ is the storage modulus, $E''(\omega)$ is the loss modulus, and ω is the angular frequency. Further, $E'(\omega)$ and $E''(\omega)$ can be expressed as

$$E'(\omega) = E_0 + \frac{E_1\tau_1^2\omega^2}{1+\tau_1^2\omega^2} \tag{3}$$

$$E''(\omega) = \frac{E_1\tau_1\omega}{1+\tau_1^2\omega^2}. \tag{4}$$

The loss factor $\eta(\omega)$ can be expressed as

$$\eta(\omega) = \tan(\delta) = \frac{E''(\omega)}{E'(\omega)}, \tag{5}$$

where δ is the phase angle.

Inverse-Problem Solving

The inverse-problem solving method was used to obtain the complex modulus, following the methods

TABLE 1. Dimensions, resonance frequency, amplitude ratio, and viscoelastic parameters of post-blast TM specimens (n = 10).

TM specimen	35L	36R	38R	39L	41L	43L	44R	47L	48R	49L	Mean ± SD
Length (mm)	5.9	5.7	6.0	6.1	6.3	5.9	6.0	5.9	6.2	5.2	5.9 ± 0.3
Width (mm)	2.1	2.2	2.2	2.1	2.2	2.2	2.1	1.9	2.2	2.0	2.1 ± 0.1
Thickness (mm)	0.09	0.10	0.10	0.10	0.09	0.12	0.12	0.09	0.08	0.09	0.10 ± 0.01
f_n (Hz)	707	707	1019	707	778	1214	1311	811	712	1019	899 ± 277
R	17.3	11.1	20.8	21.2	15.3	17.6	28.9	13.5	17.4	14.6	17.8 ± 5.0
E_0 (MPa)	17.1	12.9	29.4	20.7	26.5	29.7	33.0	19.9	21.2	20.8	23.1 ± 6.3
E_1 (MPa)	7.0	5.0	5.9	9.9	11.6	5.3	3.5	7.6	9.0	10.7	7.6 ± 2.7
τ_1 (μs)	20.0	20.0	21.8	20.0	20.0	20.0	20.0	20.0	20.0	20.0	20.2 ± 0.6

reported by Zhang and Gan[27] of measuring dynamic properties of human TMs. An iterative process was used to determine the three viscoelastic parameters E_0, E_1, and τ_1 in Eqs. (3), (4), and (5) through comparing each experimental displacement-frequency curve with the curve derived from the FE model of each specimen. The comparison was focused on four primary features: the resonance frequency ω_n, the amplitude displacement at low-frequency (f = 200 Hz), the displacement amplification ratio R of peak amplitude to low-frequency amplitude, and the bandwidth at the peak amplitude. Finally, E_0, E_1, and τ_1 were substituted into Eqs. (3), (4), and (5) to calculate the storage modulus, loss modulus, and loss factor.

An iterative FE simulation of the dynamic test was performed to find material constants that achieved the best match between the modeling results and actual measurements. A short description of the process is given below. (1) The loss factor at the resonance frequency was assumed with various values, the storage modulus at the resonance frequency was determined by comparing the computed resonance frequency and the amplitude ratio R with those of the actual measurement. This was implemented by a golden-section in the MATLAB program. The values best matching between computed and actual measurements were used as the storage modulus and loss factor at resonance frequency. (2) An iterative process was used to find the estimation of E_0, E_1, and τ_1 by matching the storage modulus and loss factor that obtained from step (1). The storage modulus $E'(\omega)$ and loss factor $\eta(\omega)$ were calculated over the frequency range of 200–8000 Hz using Eqs. (3) and (5). (3) The calculated displacement-frequency curve from the model was compared to the experimental data based on the primary features described above. If the lower frequency displacement and bandwidth did not match well with the experimental data, the iteration continued until the two curves fit well. The process was terminated when the mean percentage error between two iterations or between computed and actual measurements were lower than a prespecified tolerance of 10%.

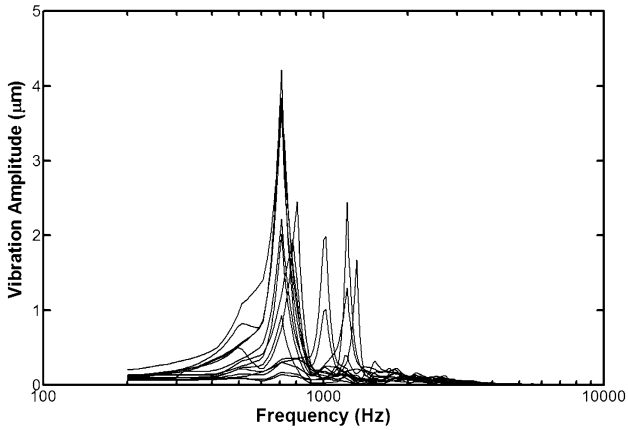


FIGURE 5. Vibration amplitude measured from dynamic tests on ten TM specimens over the frequency range 200–8000 Hz.

SEM Images

To evaluate the microstructural changes of the TM after exposure to blast, SEM imaging was performed for both pre- and post-blast TMs. TMs were fixated using paraformaldehyde, dehydrated in ethanol, dried using Hexamethyldisilizane solution, and sputter coated with gold palladium. Finally, the prepared samples were examined with electron microscopes (NEON 40 EsB, Zeiss, Oberkochen, Germany) (JSM-840, JEOL Ltd., Tokyo, Japan) in the Samuel Roberts Noble Microscopy Laboratory at the University of Oklahoma.

RESULTS

The length, width, and thickness of ten TM specimens are listed in the first three rows of Table 1. The length ranged from 5.2 to 6.3 mm with a mean of 5.9 ± 0.3 mm, the width ranged from 2.0 to 2.2 mm with a mean of 2.1 ± 0.1 mm, and the thickness ranged from 0.08 to 0.12 mm with a mean of 0.10 ± 0.1 mm. Figure 5 displays the measured frequency-displacement response curves from ten speci-

mens. The resonance frequency f_n and the amplification ratio R (ratio between the amplitude at the resonance frequency and the amplitude at the lowest frequency measured) are both listed in Table 1. The average resonance f_n was 899 ± 277 Hz, and the median for the group occurred at 795 Hz. The amplitude ratio R averaged 17.8 ± 5.0 with the maximum value of 28.9 corresponding to the specimen with the highest resonance frequency of 1311 Hz.

FE models were generated to simulate the dynamic experiments of all TM samples. As an example Fig. 6 shows the experimental results of the amplitude-frequency curve from two TM samples 47L and 41L (solid lines), compared with the FE model-derived curves (dashed lines). The three parameters E_0, E_1, and τ_1 for each specimen determined through the FE model are listed in Table 1. E_0 ranged from 12.9 to 33.0 MPa with a mean of 23.1 ± 6.3 MPa, E_1 ranged from 3.5 to 11.6 MPa with a mean of 7.6 ± 2.7 MPa, and τ_1 ranged from 20.0 to 21.8 μs with a mean of 20.2 ± 0.6 μs. Discrepancies across the specimens can be a result of either differences in the blast history of the temporal bone, geometry of the specimens, or experimental setup.

Figure 7 shows the storage modulus E', loss modulus E'', and loss factor η as functions of frequency of all ten specimens based on their viscoelastic parameters of E_0, E_1, and τ_1 listed in Table 1. In Fig. 7a, the storage modulus remained generally constant from 100 to 2000 Hz, but in frequencies over 2000 Hz there was a slight increase. The storage modulus for post-blast TMs ranged from 12.9 to 33.0 MPa at 100 Hz, and at 8000 Hz the storage modulus ranged from 15.4 to 34.8 MPa. On average the storage modulus was 23.1 ± 6.3 MPa at 100 Hz and was 26.9 ± 6.1 MPa at 8000 Hz.

The loss modulus (Fig. 7b) showed a gradual increase from 100 to 1000 Hz, followed by a rapid increase to 7000 Hz without further variation to 8000 Hz. The value increased with increasing frequency until 6000–7000 Hz, where the loss modulus reached its maximum value. The loss modulus at 100 Hz for post-blast TMs ranged from 0.04 to 0.15 MPa. At 8000 Hz the loss modulus ranged from 1.77 to 5.79 MPa. On average the loss modulus was 0.10 ± 0.03 MPa at 100 Hz and was 3.78 ± 1.34 MPa at 8000 Hz.

The loss factor (Fig. 7c) featured a similar trend as the loss modulus except a peak occurred from 6000 to 7000 Hz afterwards it had a gradual decrease with increasing frequency up to 8000 Hz. The loss factor increased steadily until 6000–7000 Hz, after which the loss factor decreased with increasing frequency. The loss factor at 100 Hz ranged from 0.001 to 0.0065, and at the peak the loss factor ranged from 0.050 to 0.210. On average, the loss factor was 0.004 ± 0.002 at 100 Hz and was 0.150 ± 0.054 at the peak frequency of 6500 Hz.

Figure 8 shows the SEM image obtained from a post-blast TM. As a comparison, a SEM image of the normal TM was displayed in the same figure. The images were viewed from the lateral side and focused on areas where the epithelial layer separated from the TM during SEM preparation. The effect of blast waves on the fiber bundles can be observed from Fig. 8 as shown by the radial orientation of the post-blast TM tears, which was a result of the circumferential fibers fractures. The normal TM shows a generally smoother appearance, reflecting the normal state of the TM. Figure 8 suggested that the TM damage along the radial direction may be more serious than that along the circumferential direction after blast exposure.

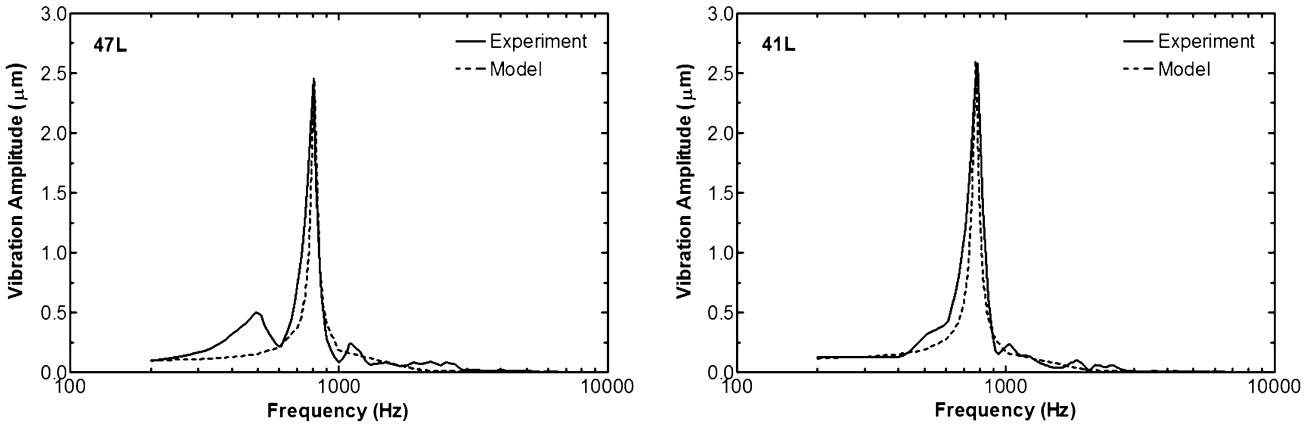


FIGURE 6. The FE fitting results obtained from two typical specimens in comparison with the corresponding experimental curves.

BMES BIOMEDICAL ENGINEERING SOCIETY™ www.bmes.org

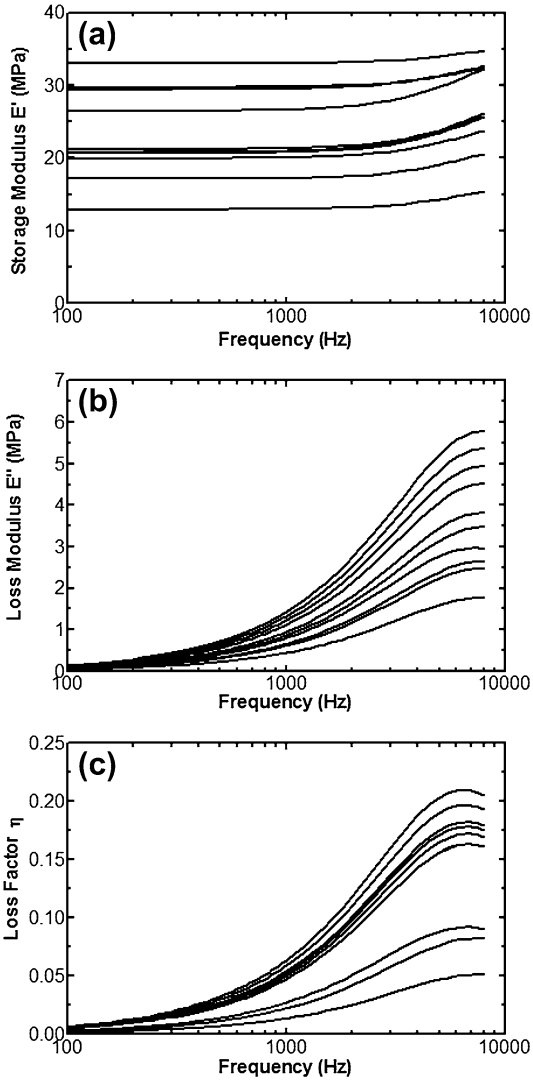


FIGURE 7. Dynamic properties of specimens ($n = 10$) determined from the FE modeling over the frequency range of 100–8000 Hz. (a) Storage modulus, (b) loss modulus, and (c) loss factor.

DISCUSSION

Microstructural Changes in Post-Blast TM

The TM is composed of three distinct layers. The lateral side is an epidermal layer, and the medial side is a mucosal layer. The middle layer is comprised of collagen fibers, aligning primarily along the radial and circumferential directions.[17] In a study performed by Luo *et al.*,[18] the results indicated that the Young's modulus is higher in the radial direction than in the circumferential direction, and the fracture strength in the radial direction is also higher than that in the circumferential direction under the condition of the same strain rate.[19] When the TM is exposed to blast waves it is more probable that the circumferential fibers, which have a lower fracture strength, would break before the radial fibers. Figure 8 demonstrates that the post-blast TM tears were oriented in the radial direction, indicating the microstructure changes caused by blast exposures. However, it is difficult to quantify the extent of microstructure damage of TM by using SEM images. The weakened mechanical properties are the reflection of microstructure damage, but it is not applicable to build a direct relation between microstructure damage of TM and changes of macromechanical properties at the present stage.

Effect of Exposure to Blast Waves on the Complex Modulus of the TM

The earlier work of Zhang and Gan reported dynamic properties of the normal TM using acoustic stimulation and LDV.[27] The same technique was used in this study. A comparison between Zhang and Gan's data and the present results allows us to observe the difference of TM properties and stiffness shift before and after blast exposure. To determine the effect of blast waves on mechanical properties of the TM, the complex modulus for post-blast TMs was plotted against normal TMs in Fig. 9. The mean storage modulus at 100 Hz was 23.1 MPa for the post-blast TMs and 53.8 MPa for normal TMs. At 8000 Hz the mean storage modulus of post-blast TMs was 26.9 MPa, and the normal was 65.5 MPa. The blast exposure caused the storage modulus to become significantly reduced across the frequency range. Similarly, the loss modulus for post-blast TMs was also much lower than the normal TMs. At 100 Hz the mean loss modulus was 0.09 MPa for post-blast TMs, and 1.37 MPa for normal TMs. At 8000 Hz the loss modulus of post-blast TMs was 3.78 MPa while that of the normal TMs was 6.11 MPa. The decrease of loss modulus was significant (Student's t test, $p < 0.0065$). These data reveal that the blast overpressure causes a frequency-dependent stiffness reduction of the TM.

Loss factor is the ratio between the loss modulus and storage modulus. The post-blast TMs had a lower loss factor at frequencies below 2 kHz and a larger loss factor at frequencies over 2 kHz compared to the normal TMs. As shown in Fig. 9, the blast resulted in a flat storage modulus curve in the high frequency range. This is one of reasons that caused the larger loss factor in the post-blast TMs at high frequencies.

Comparing the resonance frequencies of the specimens collected in this study to those in Zhang and Gan,[27] there is also a large alteration between the post-blast specimen and the normal. The mean resonance frequency of the post-blast TMs was 899 ± 277 Hz, ranging from 707 to 1311 Hz. For the normal TMs, the mean resonance frequency was 2681 ± 277 Hz for

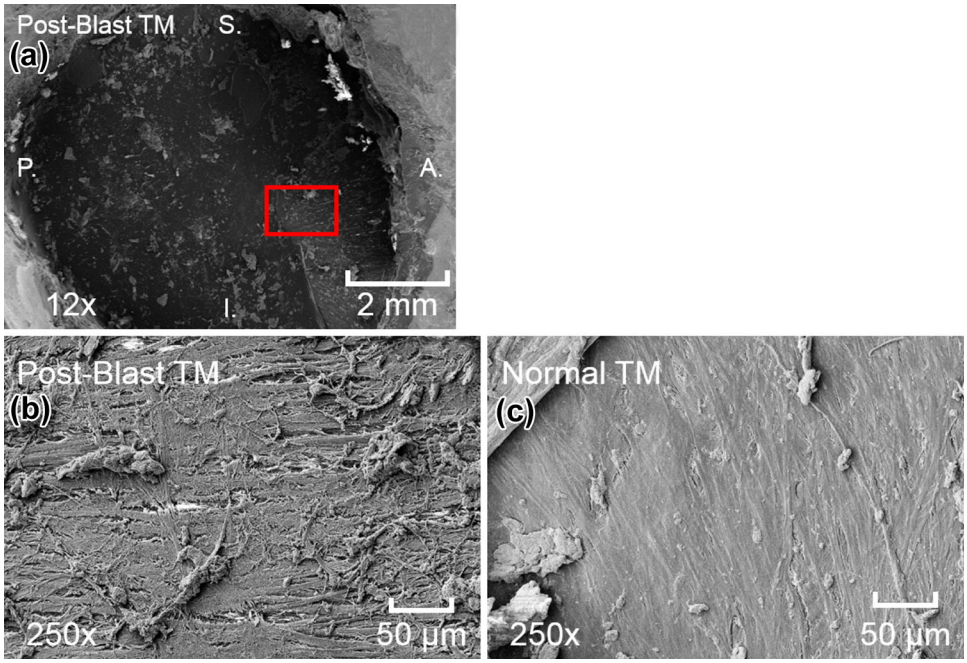


FIGURE 8. SEM images of the TM surface. (a) An image of the whole TM with the indicated location where the SEM image was taken, (b) image showing the damage of the post-blast TM, and (c) image showing the normal TM surface. S., P., I., and A. represent the superior, posterior, inferior, and anterior, respectively.

eight specimens. A reduction of mean resonance frequency in the TMs exposed to blast was up to 66%. Although the specimen geometry is nearly identical between Zhang and Gan's study and the current one, the resonance frequencies of the TM specimens obtained in this study were much lower than those measured by Zhang and Gan, supporting the conclusion that the Young's Modulus is reduced in the post-blast TM.

In a recent SHTB test performed by Luo *et al.*,[19] the mechanical properties of post-blast human TM were measured in the radial direction and circumferential direction. Luo *et al.*[19] reported that Young's modulus of the post-blast TMs was reduced in the circumferential direction across the whole strain rate range, while the modulus in the radial direction was reduced only at low strain rate. In this study, the cutting orientation of the rectangular strips was mainly along the circumferential direction as shown in Fig. 2a, which resulted in a greater number of circumferential fibers retained in the specimen than radial fibers. Therefore, the present results should be more closely related to the TM mechanical properties in the circumferential direction. The blast-induced change of storage modulus in the circumferential direction followed the same trend as that of the measurements by Luo *et al.*, but the reduced magnitude was larger in the present study. The reason for the different change of dynamic modulus between the two experiments in the blast-exposed TM needs further study. However, it should be noted that the deformation direction and strain rate for samples in two experiments were different. In the SHTB study, the TM specimen was tested for axial tensile at a high strain rate, while the post-blast specimen in this study experienced transverse vibration in a small deformation.

Additional Insight from This Study

In this study, the data clearly show that retained complex modulus of the TM after blast exposure was reduced more than 50%. The TM rupture caused by blast exposure includes perforation of the TM and reduction of complex modulus in the remaining part of the TM. The TM perforation and alteration in mechanical properties can contribute to a conductive hearing loss. The effect of TM perforations on sound transmission through the middle ear was investigated in temporal bone models by Gan *et al.*[9] Their results indicated that TM perforations caused more than 20 dB reduction in the TM and stapes footplate displacements at frequencies below 1 kHz.

The reduction of TM complex modulus affects the middle ear dynamic behavior in two ways due to the weakened TM stiffness: change of the magnitude and phase of the TM vibration and alteration of the motion correlation between the umbo and other locations of the TM. The middle ear transfer function or frequency-displacement response of stapes footplate is directly related to the TM motion. The reduction of TM stiff-

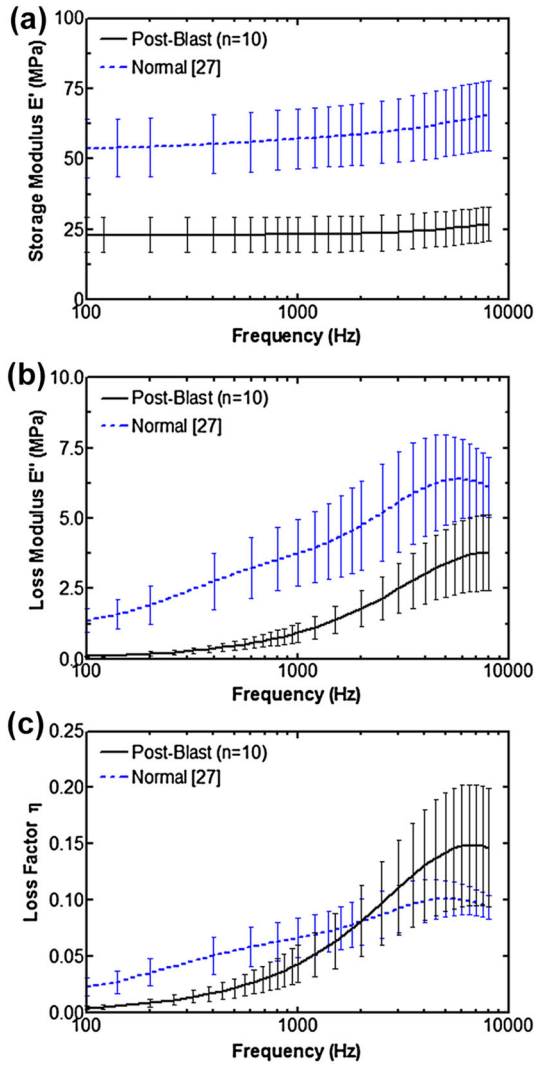


FIGURE 9. Comparison of complex modulus between blast-exposed and normal TMs over the frequency range of 100–8000 Hz. (a) Storage modulus, (b) loss modulus, and (c) loss factor.

ness resulted in an increased displacement of the stapes footplate at low frequencies and a decreased displacement at high frequencies.[10] The changes of the TM stiffness and damping properties affect the TM vibration waveforms or modes.[6] Such a change in vibration waveforms may result in an alteration of the motion correlation between the umbo and other locations of the TM from the normal condition. The spatially or temporally altered TM motion correlation may interrupt the efficient transduction of sound energy from a given portion of the TM to the umbo and malleus, and affect the acoustic input to the cochlea. O'Connor *et al.*[20] investigated the significance of TM fiber layers in high frequency sound transmission, and their results showed that radial collagen fibers of the TM play an important role in the conduction of sound above 4 kHz. Accordingly, the weakened stiffness in the radial direction also affects high-frequency sound conduction.

Tympanoplasty can restore the anatomic integrity of the TM. Various materials have been used in clinical practice for reconstructing the ruptured TM including different types of fascial grafts, cartilage, fat, *etc*. The stiffness of the resulting TM reconstructions varies with a wide range. It should be mentioned that the weakened stiffness of the residual TM may affect hearing outcomes when tympanoplasty is performed for closure of the TM perforation due to blast exposure. Further study of tympanoplasty for restoration of hearing in the blast damaged TM is needed.

A series of studies have demonstrated the similarities of sound transmission through the ear between live human and the cadaveric temporal bones.[22] Human temporal bones are the major source for measuring mechanical properties of the ear tissues and evaluating functions of various middle ear implants or implantable devices. The limitations of this study can also be related to the viscoelastic material model. The TM material in this study was assumed to be isotropic and homogenous, and the directional TM damage was also ignored. In reality, these collagen fibers of TM are aligned primarily along the radial and circumferential directions, and the tears in the TM due to blast exposures were along radial direction. It should be mentioned that the proposed approach is good enough to describe at least the first resonance frequency of the TM specimen. However, the measurement of multiple points will probably obtain multiple resonance frequencies and provide more complete data for calculating the frequency dependent properties of the TM. In this condition, the multiple constant model will improve the estimation of the complex modulus.

In addition, the Poisson's ratio of the TM may still be an open question due to the difficulties in measuring this value. Currently, the value of Poisson's ratio of 0.3 can be seen as a compromise between an incompressible material and a material composed of parallel fibers without lateral interaction among the fibers. It has been shown that Poisson's ratio was necessary as input data for determination of the complex modulus in this process. Therefore, the identified complex modulus was closely related to the value of Poisson's ratio selected in the inverse-problem solving.

CONCLUSIONS

The dynamic properties of post-blast TMs were measured on ten TM samples after exposure to blast waves in this study. Acoustic loading was used as a driving force to induce vibrations on the TM over a

frequency range of 200–8000 Hz, and LDV was used to measure the resulting vibrations. FE models were created for each TM specimen and the inverse problem solving method was used to determine the complex modulus. The storage modulus and the loss modulus over the frequency range of 100–8000 Hz were obtained from all ten specimens. The mean storage modulus was 23.1 ± 6.3 MPa at 100 Hz and 26.9 ± 6.1 MPa at 8000 Hz. The mean loss modulus was 0.10 ± 0.03 MPa at 100 Hz and 3.78 ± 1.34 MPa at 8000 Hz. Compared to the mechanical properties of normal TMs determined previously using the same method, the storage and loss modulus of the TMs exposed to blast waves had significant reduction. The SEM images of post-blast TMs compared with normal TMs showed obvious microstructural changes which indicate the tissue damage caused by the multiple blast exposures. This study provided important data on the human TM mechanical changes after exposure to blast overpressure waves.

ACKNOWLEDGMENTS

The authors thank Don Nakmali, M.S. research associate, and Kyle Smith, research undergraduate student in BME Lab for technical assistance. This work was supported by DOD W81XWH-14-1-0228.

REFERENCES

[1]Aernouts, J., J. A. Soons, and J. J. Dirckx. Quantification of tympanic membrane elasticity parameters from in situ point indentation measurements: validation and preliminary study. *Hear. Res.* 263:177–182, 2010.

[2]Bouillard, Ph., and F. Ihlenbury. Error estimation and adaptivity for the finite element method in acoustics: 2D and 3D applications. *Comput. Methods Appl. Mech. Eng.* 176:147–163, 1999.

[3]Cheng, T., C. Dai, and R. Z. Gan. Viscoelastic properties of human tympanic membrane. *Ann. Biomed. Eng.* 35:305–314, 2006.

[4]Choi, C. H. Mechanisms and treatment of blast induced hearing loss. *Korean J. Audiol.* 16:103–107, 2012.

[5]Daphalapurkar, N. P., C. Dai, R. Z. Gan, and H. Lu. Characterization of the linearly viscoelastic behavior of human tympanic membrane by nanoindentation. *J. Mech. Behav. Biomed.* 2:82–92, 2009.

[6]De Greef, D., J. Aernouts, J. Aerts, J. T. Cheng, R. Horwitz, J. J. Rosowski, and J. J. J. Dirckx. Viscoelastic properties of the human tympanic membrane studied with stroboscopic holography and finite element modeling. *Hear. Res.* 312:69–80, 2014.

[7]Dougherty, A. L., A. J. MacGregor, P. P. Han, E. Viirre, K. J. Heltemes, and M. R. Galarneau. Blast-related ear injuries among U.S. military personnel. *J. Rehabil. Res. Dev.* 50:893–904, 2013.

[8]Fay, J., S. Puria, W. F. Decraemer, and C. Steele. Three approaches for estimating the elastic modulus of the tympanic membrane. *J. Biomech.* 38:1807–1815, 2005.

[9]Gan, R. Z., T. Cheng, C. Dai, and F. Yang. Finite element modeling of sound transmission with perforations of tympanic membrane. *J. Acoust. Soc. Am.* 126:243–253, 2009.

[10]Gan, R. Z., B. Feng, and Q. Sun. Three-dimensional finite element modeling of human ear for sound transmission. *Ann. Biomed. Eng.* 32:847–859, 2004.

[11]Gan, R. Z., D. Nakmali, X. D. Ji, K. Leckness, and Z. Yokell. Mechanical damage of tympanic membrane in relation to impulse pressure waveform—a study in chinchillas. *Hear. Res.* 340:25–34, 2016.

[12]Garth, R. J. N. Blast injury of the auditory system: a review of the mechanisms and pathology. *J. Laryngol. Otol.* 108:925–929, 1994.

[13]Gondusky, J. S., and M. P. Reiter. Protecting military convoys in Iraq: an examination of battle injuries sustained by a mechanized battalion during operation Iraqi Freedom II. *Mil. Med.* 170:546–549, 2005.

[14]Huang, G., N. P. Daphalapurkar, R. Z. Gan, and H. Lu. A method for measuring linearly viscoelastic properties of human tympanic membrane using nanoindentation. *J. Biomech. Eng.* 130:014501, 2008.

[15]Kingery, C. N., and B. F. Pannill. Peak overpressure vs scaled distance for TNT surface bursts (hemispherical charges). Ballistics Research Laboratory. Report No. 1518, 1964.

[16]Kirikae, I. The Structure and Function of The Middle Ear. Tokyo: University Press, 1960.

[17]Lim, D. J. Structure and function of the tympanic membrane: a review. *Acta Otorhinolaryngol. Belg.* 49:101–115, 1995.

[18]Luo, H., C. Dai, R. Z. Gan, and H. Lu. Measurement of Young's modulus of human tympanic membrane at high strain rates. *J. Biomech. Eng.* 131:064501, 2009.

[19]Luo, H., S. Jiang, D. U. Nakmali, R. Z. Gan, and H. Lu. Mechanical properties of a human eardrum at high strain rates after exposure to blast waves. *J. Dyn. Behav. Mater.* 2:59–73, 2015.

[20]O'Connor, K. N., M. Tam, N. H. Blevins, and S. Puria. Tympanic membrane collagen fibers: a key to high-frequency sound conduction. *Laryngoscope* 118:483–490, 2008.

[21]Ritenour, A. E., and T. W. Baskin. Primary blast injury: update on diagnosis and treatment. *Crit. Care Med.* 36:S311–S317, 2008.

[22]Rosowski, J. J., P. J. Davis, S. N. Merchant, K. M. Donahue, and M. D. Coltrera. Cadaver middle ears as models for living ears: comparisons of middle-ear input immittance. *Ann. Otol. Rhinol. Laryngol.* 99:403–412, 1990.

[23]Volandri, G., F. Di Puccio, P. Forte, and C. Carmignani. Biomechanics of the tympanic membrane. *J. Biomech.* 44:1219–1236, 2011.

[24]Von Békésy, G. Experiments in Hearing. Oxford: McGraw Hill, 1960.

[25]Xydakis, M. S., V. S. Bebarta, C. D. Harrison, J. C. Conner, G. A. Grant, and A. S. Robbins. Tympanic-

membrane perforation as a marker of concussive brain injury in Iraq. *N. Engl. J. Med.* 357:830–831, 2007.
[26]Yokell, Z., X. Wang, and R. Z. Gan. Dynamic properties of tympanic membrane in a chinchilla otitis media model measured with acoustic loading. *J. Biomech. Eng.* 137:081006-1–081006-9, 2015.
[27]Zhang, X., and R. Z. Gan. Dynamic properties of human tympanic membrane—experimental measurement and modelling analysis. *Int. J. Exp. Comput. Biomech.* 1:252–270, 2010.
[28]Zhang, X., and R. Z. Gan. Dynamic properties of human tympanic membrane based on frequency-temperature superposition. *Ann. Biomed. Eng.* 41:205–214, 2012.

Research Article | Vol. 24, No. 26 | 26 Dec 2016 | OPTICS EXPRESS 29822

Optics EXPRESS

Measurement of thickness and profile of a transparent material using fluorescent stereo microscopy

ZHENXING HU,[1] TINGGE XU,[1] HUIYANG LUO,[1] RONG Z. GAN,[2] AND HONGBING LU[1,*]

[1]*Department of Mechanical Engineering, the University of Texas at Dallas, Richardson, TX 75080, USA*
[2]*School of Aerospace and Mechanical Engineering, the University of Oklahoma, Norman, OK 73019, USA*
**hongbing.lu@utdallas.edu*

Abstract: Full-field thickness measurement for a thin transparent film is of interest for biological, medical, electronic, and packaging materials. It is a challenging task when the film is curvy, delicate and its thickness varies with location. We report herein a method to measure the thickness of a transparent (flat or curved) material and its topography using a stereo fluorescent profilometry technique. In this technique, two different types of fluorescent particles are deposited to both sides of the transparent film. Selected fluorescent excitation and emission are used to allow the observation of each one surface of the film at a time to determine the surface profile using stereo-based digital image correlation techniques. After the surface profiles for both surfaces are determined, subtraction of one surface profile from the other provides accurate thickness distribution of the film. Validation experiments were conducted using transparent films with known thickness. As an application, a measurement on a contact lens was conducted. The technique is appropriate for measurement of the full-field thickness of objects at other scales, such as soft transparent or translucent biofilms, with which thickness can hardly be measured accurately with other techniques.

© 2016 Optical Society of America

OCIS codes: (120.0120) Instrumentation, measurement, and metrology; (150.6910) Three-dimensional sensing; (180.2520) Fluorescence microscopy; (180.6900) Three-dimensional microscopy; (160.1435) Biomaterials.

References and links

1. L. C. Kuypers, W. F. Decraemer, and J. J. Dirckx, "Thickness distribution of fresh and preserved human eardrums measured with confocal microscopy," Otol. Neurotol. **27**(2), 256–264 (2006).
2. A. Piegari and E. Masetti, "Thin film thickness measurement: A comparison of various techniques," Thin Solid Films **124**(3-4), 249–257 (1985).
3. I. Grulkowski, J. J. Liu, B. Potsaid, V. Jayaraman, J. Jiang, J. G. Fujimoto, and A. E. Cable, "High-precision, high-accuracy ultralong-range swept-source optical coherence tomography using vertical cavity surface emitting laser light source," Opt. Lett. **38**(5), 673–675 (2013).
4. H. Ishikawa, M. L. Gabriele, G. Wollstein, R. D. Ferguson, D. X. Hammer, L. A. Paunescu, S. A. Beaton, and J. S. Schuman, "Retinal nerve fiber layer assessment using optical coherence tomography with active optic nerve head tracking," Invest. Ophthalmol. Vis. Sci. **47**(3), 964–967 (2006).
5. S. Konno, J. Akiba, and A. Yoshida, "Retinal thickness measurements with optical coherence tomography and the scanning retinal thickness analyzer," Retina **21**(1), 57–61 (2001).
6. J. S. Fernandes, C. R. Appoloni, and C. P. Fernandes, "Accuracy evaluation of an X-ray microtomography system," Micron **85**, 34–38 (2016).
7. Z. Hu, Y. Du, H. Luo, B. Zhong, and H. Lu, "Internal deformation measurement and force chain characterization of mason sand under confined compression using incremental digital volume correlation," Exp. Mech. **54**(9), 1575–1586 (2014).
8. Z. Hu, H. Luo, S. Bardenhagen, C. Siviour, R. Armstrong, and H. Lu, "Internal deformation measurement of polymer bonded sugar in compression by digital volume correlation of *in-situ* tomography," Exp. Mech. **1**(1), 289–300 (2015).
9. L. C. Kuypers, J. J. Dirckx, W. F. Decraemer, and J.-P. Timmermans, "Thickness of the gerbil tympanic membrane measured with confocal microscopy," Hear. Res. **209**(1-2), 42–52 (2005).
10. Z. Hu, H. Luo, Y. Du, and H. Lu, "Fluorescent stereo microscopy for 3D surface profilometry and deformation mapping," Opt. Express **21**(10), 11808–11818 (2013).

#278553 http://dx.doi.org/10.1364/OE.24.029822
Journal © 2016 Received 18 Oct 2016; revised 9 Dec 2016; accepted 13 Dec 2016; published 15 Dec 2016

Optics EXPRESS

11. P. Luo, Y. Chao, M. Sutton, and W. Peters III, "Accurate measurement of three-dimensional deformations in deformable and rigid bodies using computer vision," Exp. Mech. **33**(2), 123–132 (1993).
12. J.-J. Orteu, "3-D computer vision in experimental mechanics," Opt. Lasers Eng. **47**(3-4), 282–291 (2009).
13. Z. Hu, H. Xie, J. Lu, T. Hua, and J. Zhu, "Study of the performance of different subpixel image correlation methods in 3D digital image correlation," Appl. Opt. **49**(21), 4044–4051 (2010).
14. T. A. Berfield, J. K. Patel, R. G. Shimmin, P. V. Braun, J. Lambros, and N. R. Sottos, "Fluorescent image correlation for nanoscale deformation measurements," Small **2**(5), 631–635 (2006).
15. M. Asally, M. Kittisopikul, P. Rué, Y. Du, Z. Hu, T. Çağatay, A. B. Robinson, H. Lu, J. Garcia-Ojalvo, and G. M. Süel, "Localized cell death focuses mechanical forces during 3D patterning in a biofilm," Proc. Natl. Acad. Sci. U.S.A. **109**(46), 18891–18896 (2012).
16. H. A. Bruck, S. R. McNeill, M. A. Sutton, and W. H. Peters III, "Digital image correlation using Newton-Raphson method of partial-differential correlation," Exp. Mech. **29**(3), 261–267 (1989).
17. B. Pan, "Reliability-guided digital image correlation for image deformation measurement," Appl. Opt. **48**(8), 1535–1542 (2009).
18. Z. Hu, H. Xie, J. Lu, H. Wang, and J. Zhu, "Error evaluation technique for three-dimensional digital image correlation," Appl. Opt. **50**(33), 6239–6247 (2011).
19. Y. Q. Wang, M. Sutton, X. D. Ke, H. Schreier, P. Reu, and T. Miller, "On error assessment in stereo-based deformation measurements," Exp. Mech. **51**(4), 405–422 (2011).
20. Correlated Solutions Inc, "Correlated Solutions - Microscopy" *http://correlatedsolutions.com/vic-3d/microscopy/*.

1. Introduction

Thickness of a thin film is an important geometric parameter that needs to be measured accurately in various situations, such as in the mechanical characterization of a tympanic membrane (TM) [1]. The available options for appropriate thickness measurement techniques are often times limited, especially when the thickness is small and the material is soft and delicate, or under moisturized conditions. In the case of a biofilm, or bio-membranes, the surface is curved, and the thickness varies with locations. Examples of such materials include TMs for human and animals (e.g., chinchilla, guinea pig), and cornea and lenses in eyes. The role of the thickness is important; an example is the assessment of retinal thickness, which is vital to understand the macular pathologies. It is very difficult to measure the location-dependent thickness of those curvy and delicate films. Existing techniques [2] for thickness measurement include micrometer, caliper, stylus profilometry, interferometry, reflectometry, ellipsometry, spectrophotometry, ultrasound, advanced light focused microscopy, laser scanning microscopy, optical coherence tomography (OCT) [3], ion beam analysis, X-ray refelctometry and tomography, electron microscopy and others. Some of these contacting methods are point-to-point measurement technique. Most of the existing thickness measurement techniques are used at the nanoscale for solid-state samples or relatively stiff samples. It remains a challenge for thickness measurement for a soft material at the microscale. Taking the full-field thickness measurement of the chinchilla eardrum as an example, the thickness is in the neighborhood of 20 μm, and varies with location. The thickness is out of capability of the ultrasonic method, which is in the range above 0.1 mm. Because eardrums are soft and delicate, a contact method is not appropriate. Instead, a non-contact method should be used. Non-contact methods, such as interferometry and reflectrometry, have a capability for thickness measurement in the range of visible light wavelength. They are not suitable for samples with a thickness of tens of μm. A commercial OCT has resolution approximately 6 μm [4], it is not accurate enough for thickness measurement in many situations, such as measurement of TMs. Although OCT has been applied for measurement of the thickness of retinal, the standard deviation is on the order of 10 μm [5]. A sensitive method is needed to measure the thickness of a variety of films as described above. For a typical commercially available X-ray micro-computed topography, the highest resolution is approximately 2 μm/voxel [6–8]. In addition, a TM, like many other bio-tissues, is not X-ray sensitive, so that it is difficult to detect the surface edges of an eardrum for accurate thickness measurement. Laser scanning microscope will work for a sample cut from a TM, in which case the sample thickness can be different from the thickness of an intact TM [9]. In addition, it is very tedious, and as a result it is not possible to use it to

Optics EXPRESS

determine the thickness map of a TM. Other alternative methods such as scanning electron microscope (SEM), and transmission electron microscope, measure only thickness at edges in particular locations for a sample that is not in physiological condition. The thickness can be different from an intact full-size TM. Transmission electron microscope is suitable for very thin small samples, which are subject to very high-energy electronic beam bombarding, making it vulnerable to the beam damage. Currently, none method is available for non-contact, accurate, and full-field measurement of location-dependent thickness for a relatively soft, delicate and transparent material.

In this study, we report a new technique for full-field thickness measurement, and also the surface profile for a transparent, soft material at the microscale. The technique is based on a three-dimensional (3D) fluorescent stereo technique we developed for surface shape measurement at the microscale [10]. In the sequel, we describe the principal and the experimental setup for the technique, followed by validation and an example for application.

2. Principles and setup

The technique reported herein for thickness measurement for a transparent material with thickness on the order of microns or thicker is based on stereo digital image correlation of dual-path fluorescent images acquired for both surfaces of the film. This technique, referred to as stereo digital image correlation (also referred as 3D digital image correlation), is based on the principle of binocular stereo vision. It has been widely used in the research in experimental mechanics and materials science [11–13].

Figure 1 shows a schematic diagram for a binocular stereo-vision system. In a local Cartesian frame, a point (e.g., P_1) at the top surface of the film is projected into two points (P_1^L, P_1^R) in the imaging planes of the left and right cameras, respectively. Digital image correlation is used to find the corresponding points in the two images acquired by the two cameras. The binocular system is calibrated to determine parameters of cameras, so that the coordinates of the projected points in both images are obtained. Subsequently, the world coordinates for P_1 are reconstructed using triangulation method.

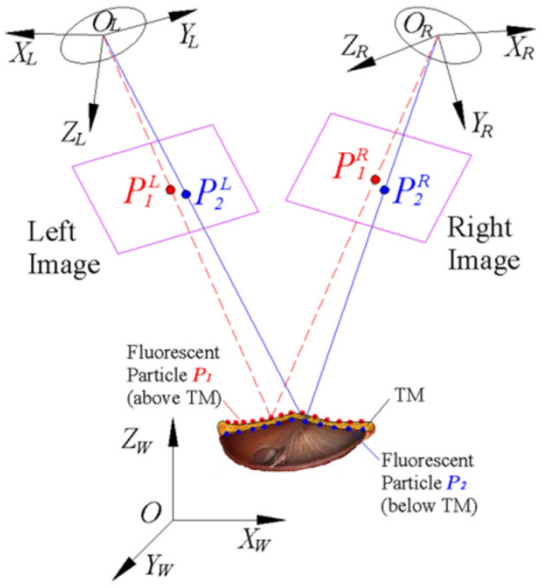


Fig. 1. A schematic diagram of the multi-fluorescent imaging system for thickness measurement on transparent materials.

In a previous study [10], we extended fluorescent digital image correlation for in-plane deformation measurement [14] to 3D profilometry and deformation measurements using the

Optics EXPRESS

fluorescent stereo microscopy based on stereo digital image correlation. The fluorescent particles are randomly sprayed onto the surface of a biofilm to form unique speckle pattern surrounding each point, and appropriate filters for excitation and emission are installed in the stereomicroscope.

In the biomedical imaging fields, tissues dyed with different fluorescent particles are observed using multi-path fluorescent imaging [15]. Two kinds of fluorescent particles are used to separate the top and the bottom surface. Dual-path fluorescent imaging provides an active technique to control the exciting of the particles. Thus, the dual-path fluorescent imaging technique is adopted for purpose of thickness measurement.

We refined a fluorescent stereo microscope (FSM) to allow the use of two fluorescent imaging paths for a transparent specimen. Two types of fluorescent particles are sprayed onto the top and bottom surfaces of a transparent curvy film as shown in Fig. 1. When turning on one excitation light, and the emission filter is rotated to match the excitation light, one particular layer of sprayed fluorescence is excited and the images are acquired by both left and right cameras. Using stereo digital image correlation, the 3D coordinates of the excited layer, representing geometry of one surface are reconstructed. Then the excitation layer for this particular surface is turned off. Subsequently the excitation light on the other surface is turned on, and the images are acquired by both cameras, and analyzed to determine surface topography of the other surface. With the coordinates for both top and bottom surfaces determined, by subtracting the 3D coordinates of the bottom surface from those for the bottom surface in Z-direction, the thickness distribution of the specimen can be obtained. For more complicated curvy transparent objects, the thickness can be determined using the coordinates in three directions accordingly.

Two appropriate fluorescent particles were selected in order to distinguish themselves under different excitation and emission wavelengths. Two types of fluorescent particles with diameter of 1 μm are chosen; they are blue-green fluorescent particles (430/465, Life Technology Corp., #F13080) and red fluorescent particles (580/605, Life Technology Corp., #F13083). Excitation and emission filters are used for fluorescent imaging. It is noted that the primary function of the emission/barrier filter in any fluorescent imaging system is to block the excitation wavelengths used and allow only the excited light from the fluorescent particles to pass. For the blue-green fluorescent, the matching filters are selected as the excitation filters EX420/40x and ET480/40m (Chroma Technology Corp.). For the other fluorescent particles, the matching filters are ET560/40x and ET615/40m.

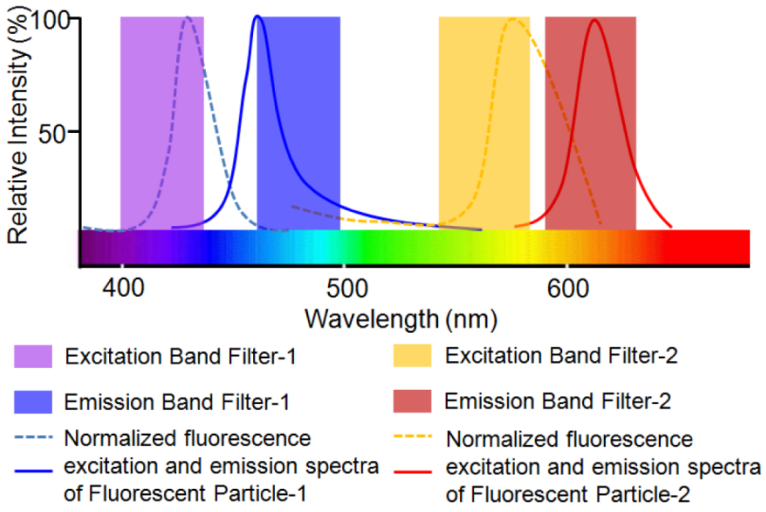


Fig. 2. Band filters and properties of two types of fluorescent particles.

Optics EXPRESS

The properties of the band filters and fluorescent particles used in the setup are shown in Fig. 2. Blue and red are selected because the two colors are relatively far away from each other in the visible light spectrum. As shown in Fig. 2, the intensities associated with the two fluorescent imaging paths are clearly visible. The excitation band filter-1, and filter-2, and emission band filter-1, and filter-2 are used for the fluorescent imaging for fluorescent particle-1, and fluorescent particle-2, respectively.

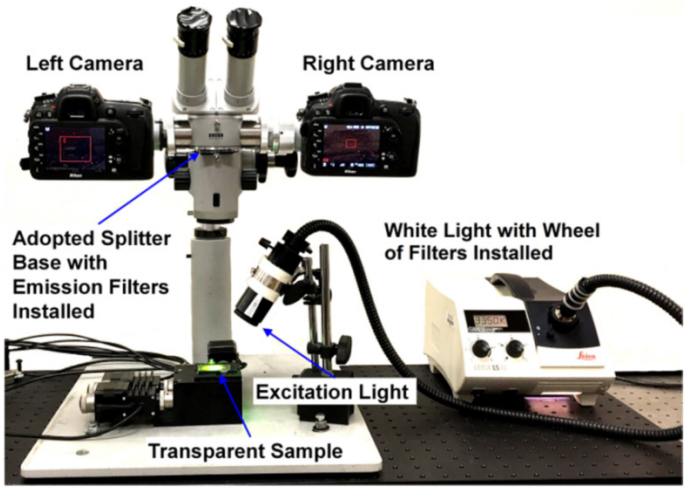


Fig. 3. Experimental setup of dual-path fluorescent stereo microscope for thickness measurement (Green excitation light is turned on).

Figure 3 shows the experimental setup, which is modified from a Zeiss OPMI stereo microscope to include dual fluorescent imaging paths. This microscope has a large working distance, up to 150 mm (the objective lens is 150 mm), and up to 5 mm depth of field. The viewing field is 5~18 mm in diameter, to allow measurements of relatively large surface profile and deformations. Two Nikon D7100 cameras are installed on the observation tubes of the stereomicroscope to acquire images of speckle patterns on either top or bottom surface of the sample. A beam splitter base is used to place the emission filters. A pair of aforementioned emission filters is placed under the base of the splitter base. Two different excitation filters (excitation band filter-1 and excitation band filter-2) are installed on the filter wheel on the white light illuminator Leica L5. When the fluorescent excitation filter is switched by rotating the filter wheel on the illumination, the pair of the emission filters can be removed and replaced with the other pair.

3. Experiments and application

A transparent glass slide is placed at the stage as shown in Fig. 3. The top surface of the sample is randomly sprayed with blue-green fluorescent particles and the bottom surface is sprayed with red fluorescent particles. The fluorescent random texture patterns on both surfaces are generated by an airbrush (Iwata Inc.). Before conducting the measuring experiment, it should take care to set the parameters for both cameras, such as exposure time, setting of ISO, and the intensity of illumination light should be adjusted for different fluorescent imaging paths, in order to eliminate the residual fluorescence effects under the unmatched fluorescent imaging paths. In this system, the residual fluorescent effect occurs as blue-green fluorescent particles (fluorescent particle-1) is excited when the red fluorescent imaging path (excitation band filter-2 and emission band filter-2) is used and vice versa. It is noted that it is important to detect the residual fluorescent effects in the system. For example, if the excitation band filter-2 and emission band filter-2 are used, the cameras should see

Optics EXPRESS

nothing of a sample covered with only the blue-green fluorescent particles, and vice versa. If there is an effect on certain extent of residual fluorescent, the imaging parameters must be altered to eliminate the residual fluorescence effects. Figure 4 shows the fluorescent images of a sample acquired by the left and right cameras using the dual fluorescent imaging paths. The images have a resolution of 6000 × 4000 pixels. Figures 4(a) and 4(b) show the speckle patterns of the excited blue-green fluorescent particles using excitation band filter-1 and emission band filter-1. Then the excitation filter was changed to excitation filter-2 and the pair of emission filter-2 was replaced at the splitter modified base. Figures 4(c) and 4(d) show the speckle pattern of the excited red fluorescent particles using excitation band filter-2 and emission band filter-2. While the fluorescent paths are switched, the sample stays at the same position. The stereo microscope (with modified splitter base as shown in Fig. 3), provides an overall field of view of 8.22 × 5.48 mm with a resolution of 1.37 μm/pixel.

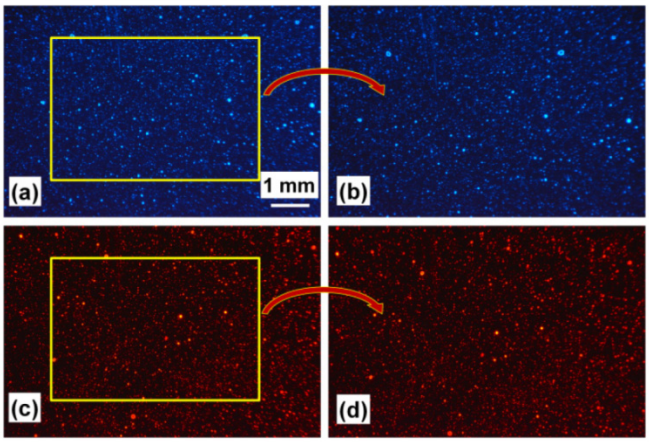


Fig. 4. Fluorescent images acquired by left and right cameras. (a)(b) blue-green fluorescent particles covering the top surface; (c)(d) red fluorescent covering the bottom surface.

It is seen clearly that the speckle patterns formed at the top and bottom surfaces are different. It shows that the two surfaces are distinguishable using the setup with dual-path fluorescent imaging. To obtain the thickness of the transparent sample, the same area of interest, as indicated by the yellow rectangle area, is viewed in Figs. 4(a) and 4(c).

If the X-Y plane is built on the glass slides, the Z-direction is in the thickness direction. After calibration of the system and stereo matching, the 3D coordinates of the top and bottom surfaces in the rectangle area can be reconstructed. Thus, the thickness is determined by subtracting the coordinates in Z-direction.

Additional experiments were conducted to examine the technique. A series of thin polyester films (McMaster, #8567k14, #8567k24 and 8567K44) with known thickness of one, two and four thousandth of inch (milliinch), were used. The top surface was sprayed with random blue-green fluorescent particles and the bottom surface was spared with red fluorescent particles. Two glass slides with thickness of 0.15 mm and 0.96 mm were also used for validation. Table 1 shows the data from experiments.

Table 1. Thickness results on five transparent films.

Sample thickness	Measured thickness
1 milliinch (25.4 ± 2.54 μm)	23.8 ± 2.8 μm
2 milliinch (50.8 ± 5.08 μm)	48.2 ± 4.6 μm
4 milliinch (101.6 ± 10.2μm)	97.6 ± 7.3 μm
150 ± 20 μm	157.7 ± 13.2 μm
960 ± 20 μm	893.3 ± 34.7 μm

Optics EXPRESS

Table 1 shows that the measured results are very close to the thicknesses of the samples except for the glass slide with a thickness of 0.96 mm. The large error on the glass slide of 0.96 mm thickness is due to the fact that while one surface is in focus, the other surface is not in focus. Once the speckle pattern on the surface is out-of-focus, it causes the decorrelation for the stereo-matching using digital image correlation. In our algorithm, the Newton-Raphson iterative method [13, 16] and reliability-guided digital image correlation [17] are employed to identify the corresponding points in matching images. It is noted that the accuracy of this thickness measurement technique should be at the same order as the displacement measurement of an object translated in Z-direction because the principles are the same [10]. The determination of the accuracy of the stereo digital image correlation could be very complex. Many factors play a role, these include quality of cameras, fluorescent particle size, speckle patterns, optical accessories, calibration, system configuration, stereo matching and algorithms [18, 19]. In this system, a modified base for the emission filters may affect the results. In addition, the fluorescent particle size is approximately 1 μm. The aggregate of the particle size can be even larger, so that the accuracy cannot be lower than the size of the aggregated fluorescent particle size. Furthermore, the residual fluorescent effects could affect the accuracy, despite that we have already set the exposure time and ISO setting carefully. However, there is room for further improvement in accuracy. For example, commercially available stereo digital image correlation system at the microscale, such as VIC-3D stereo microscope measurement system manufacture by Correlated Solutions, Inc [20]. can achieve out-of-plane displacement resolution of ± 120 nm. Thus, the potential for improvement in accuracy is promising.

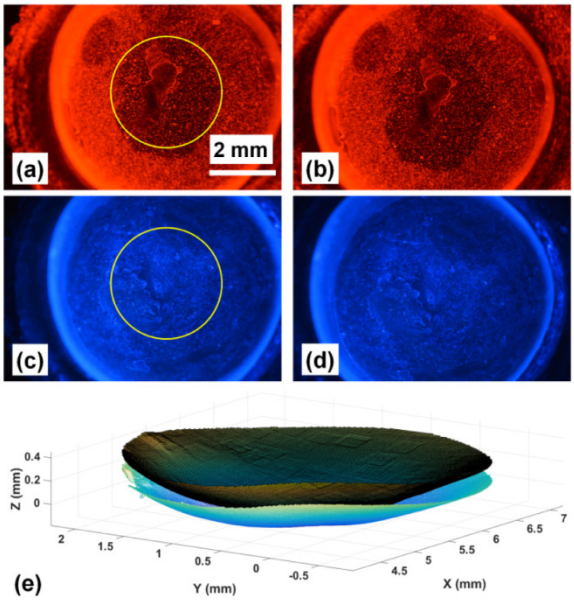


Fig. 5. Measurement of thickness of a contact lens. (a)(b) images for the inner surface covered with red fluorescent particles acquired by left and right cameras, respectively; (c)(d) images for the outer surface with blue-green fluorescent particles by left and right cameras, respectively; (e) 3D reconstructed shape of the inner and outer surfaces.

For application, we conducted thickness measurement on a contact lens. Contact lenses are transparent. The thickness distribution and surface shape are vitally important to achieve the desired optical properties. As an example for application of this technique, a measurement of the thickness of a contact lens (Bausch + Lomb, Daily disposable contact lens –4.00, diameter 14.2 mm) was conducted. The inner surface making contact with an eye was

Optics EXPRESS

covered with red fluorescent particles. The outer surface making contact with air is covered with blue-green yellow fluorescent particles. Figure 5 shows the red and blue fluorescent images, and the 3D reconstructed surfaces. The same area of interest was chosen as shown in Figs. 5(a) and 5(c). Using this technique, both surfaces of the contact lens are reconstructed. The full-field thickness is obtained as shown in Fig. 5(e). The average thickness in the central region is 76.0 ± 6.6 μm.

4. Conclusions

In conclusion, a new optical technique for measurement of full-field thickness and also surface topography of a transparent material was developed. In this technique, a combination of dual-path fluorescent imaging and stereo digital image correlation were used. Compared with other thickness measurement techniques, this technique is a non-contact full-field, and robust method for measurement of a soft transparent sample with complex and curvy surfaces. It is noted that in addition to measurement at the microscale, this technique is suitable for thickness and surface profile measurement at larger scales. With the use of stereo imaging at larger scales the method can be used for thickness measurement in the range of millimetres to meters.

Funding

Department of Defense (DOD) (W81XWH-13-MOMJPC5-IPPEHA, W81XWH-14-1-0228); National Institutes of Health (NIH) (1R01DC011585); National Science Foundation (NSF) (ECCS-1307997).

Acknowledgment

Lu acknowledges Louis A. Beecherl Jr. Chair and SpeckleTrack LLC for support.

107.223.136.45 {ts '2016-12-15 11:17:52'}

Hearing Research 340 (2016) 25–34

Contents lists available at ScienceDirect

Hearing Research

journal homepage: www.elsevier.com/locate/heares

Research paper

Mechanical damage of tympanic membrane in relation to impulse pressure waveform – A study in chinchillas

Rong Z. Gan*, Don Nakmali, Xiao D. Ji, Kegan Leckness, Zachary Yokell

School of Aerospace and Mechanical Engineering and Biomedical Engineering Center, University of Oklahoma, Norman, OK, USA

ARTICLE INFO

Article history:
Received 1 August 2015
Received in revised form
27 December 2015
Accepted 11 January 2016
Available online 22 January 2016

Keywords:
Tympanic membrane
Blast overpressure
Ear injury biomechanics
Helmet
Finite element modeling

ABSTRACT

Mechanical damage to middle ear components in blast exposure directly causes hearing loss, and the rupture of the tympanic membrane (TM) is the most frequent injury of the ear. However, it is unclear how the severity of injury graded by different patterns of TM rupture is related to the overpressure waveforms induced by blast waves. In the present study, the relationship between the TM rupture threshold and the impulse or overpressure waveform has been investigated in chinchillas. Two groups of animals were exposed to blast overpressure simulated in our lab under two conditions: open field and shielded with a stainless steel cup covering the animal head. Auditory brainstem response (ABR) and wideband tympanometry were measured before and after exposure to check the hearing threshold and middle ear function. Results show that waveforms recorded in the shielded case were different from those in the open field and the TM rupture threshold in the shielded case was lower than that in the open field (3.4 ± 0.7 vs. 9.1 ± 1.7 psi or 181 ± 1.6 vs. 190 ± 1.9 dB SPL). The impulse pressure energy spectra analysis of waveforms demonstrates that the shielded waveforms include greater energy at high frequencies than that of the open field waves. Finally, a 3D finite element (FE) model of the chinchilla ear was used to compute the distributions of stress in the TM and the TM displacement with impulse pressure waves. The FE model-derived change of stress in response to pressure loading in the shielded case was substantially faster than that in the open case. This finding provides the biomechanical mechanisms for blast induced TM damage in relation to overpressure waveforms. The TM rupture threshold difference between the open and shielded cases suggests that an acoustic role of helmets may exist, intensifying ear injury during blast exposure.

© 2016 Elsevier B.V. All rights reserved.

1. Introduction

Exposure to high intensity sound or blast overpressure waves is considered to be an intrinsic situation faced by military personnel involved in most operational activities. The direct consequences of high-intensity noise and blast injuries to the auditory system are acute hearing loss, which immediately affects the normal functioning of soldiers in combat operations, and the resultant long-term hearing disabilities that occur in a significant fraction of veterans (Patterson and Hamernik, 1997; Garth, 1994; Karmy-Jones et al., 1994; Gondusky and Reiter, 2005; Fausti et al., 2009).

Blast overpressure is a high intensity disturbance in the ambient air pressure that creates high intensity sound (impulse) over 170 dB SPL. When exposed to a blast, the human auditory system is vulnerable to both peripheral and central damage from the overpressure (Patterson and Hamernik, 1997; Mayorga, 1997). Rupture of the eardrum or tympanic membrane (TM) is the most frequent injury of the ear and has been investigated in animals and humans with wide variability (Hirsch, 1966; Patterson and Hamernik, 1997; Richmond et al., 1989). The literature indicates that mechanical damage to components of the auditory system is the major cause for hearing loss after blast exposure. However, it is not clear how the severity of injury graded by different patterns of TM rupture is related to the overpressure waveforms induced by blast exposure. Particularly, no quantitative study on biomechanical changes of the TM in response to different pressure waveforms has been reported

Abbreviation: ABR, Auditory Brainstem Response; AML, Anterior Malleal Ligament; EA, Energy Absorbance; FE, Finite Element; FSI, Fluid–Structure Interaction; PIL, Posterior Incudal Ligament; PST, Posterior Stapedial Tendon; SAL, Stapedial Annual Ligament; S.D., Standard Deviation; TM, Tympanic Membrane; TMA, Tympanic Membrane Annulus; TTT, Tensor Tympani Tendon

* Corresponding author. School of Aerospace and Mechanical Engineering and Bioengineering Center, University of Oklahoma, 865 Asp Avenue, Room 200, Norman, OK 73019, USA.
E-mail address: rgan@ou.edu (R.Z. Gan).

http://dx.doi.org/10.1016/j.heares.2016.01.004
0378-5955/© 2016 Elsevier B.V. All rights reserved.

in the literature.

In this paper, we report our currently completed study on relationships between the TM rupture threshold, the TM damage pattern, and the overpressure waveforms using a chinchilla animal model. The chinchilla is a commonly used animal model for auditory research with large TMs, ossicular dimensions, and middle ear spaces for an animal of its size. The chinchilla's range of hearing is similar to that of humans (Heffner and Heffner, 1991; Richmond et al., 1989; Jensen and Bonding, 1993). In the present study, two groups of animals were exposed to high intensity sound pressure under two conditions: the open field without a shield and the shielded case with a stainless steel cup covering the animal head. By increasing the blast peak pressure level, the TM was finally ruptured and the pressure waveforms at the entrance of the ear canal were recorded simultaneously. The goal of this study was to determine whether there is a change of overpressure waveform under the shield and how the waveform change affects the TM rupture threshold.

In addition to experimental testing in animals, impulse pressure energy spectra analysis of the waveforms recorded under open and shielded conditions was performed to determine signal energy flux over 10 frequency bands. The 3D finite element (FE) model of the chinchilla middle ear recently developed in our lab was employed to calculate the distributions of the stress and strain in the TM with impulse pressure profiles recorded in open and shielded conditions. The FE modeling results reveal that a waveform pattern consisting of both positive and negative pressures in the shield case (under a stainless steel cup) contributes more greatly to TM damage than the positive overpressure in the open case. This finding provides the biomechanical mechanisms for blast induced TM damage in relation to overpressure waveforms. The TM rupture threshold difference between the open and shielded cases suggests that an acoustic role of helmets may exist, intensifying ear injury during blast exposure.

2. Methods

2.1. Animal study protocol

Eighteen chinchillas (*Chinchilla laniger*) weighing between 600 and 800 g were included in this study. The study protocol was approved by the Institutional Animal Care and Use Committee of the University of Oklahoma and met the guidelines of the National Institutes of Health and the United States Department of Agriculture (USDA). All animals were established to be free from middle ear disease, as evaluated by wideband tympanometry.

A well-controlled compressed air (nitrogen)-driven blast apparatus located inside an anechoic chamber in the Biomedical Engineering Laboratory at the University of Oklahoma was used to create a blast overpressure wave or blast exposure in this study (Hawa and Gan, 2014). Polycarbonate film (McMaster-Carr, Atlanta, GA) of varying thickness (130 μm and 260 μm) was employed to generate blast overpressure of at least 30 psi (200 dB SPL). The overpressure level was controlled by varying the distance from the blast reference plate. Fig. 1A shows a schematic of the blast apparatus with the animal holder placed at the center.

The animals were divided into two groups: one group of 9 animals was exposed to blast in an “open field” (Fig. 1A) and another group of 9 animals was exposed to blast with a shield covering the animal head as shown in the schematic of Fig. 1B and the picture of Fig. 1C. The animals in both groups were first tested with the pre-exposure measurements, including middle ear energy absorbance (EA) using wideband tympanometry (Model AT235h, Interacoustics, MN) and auditory brainstem response (ABR) using TDT system III (Tucker–Davis Technologies, Alachua, FL). The EA measurement applied tone-burst stimuli at frequencies of 0.5, 1, 2, 4, and 8 kHz in the ear canal (Guan and Gan, 2011; Jeselsohn et al., 2005; Petrova et al., 2006; Qin et al., 2010). The EA measurement was used as a check of the TM integrity and normal function of the middle ear. The ABR measurements provided the change of hearing threshold of the ear after blast exposure. The animal was anesthetized with mixed ketamine (10 mg/kg) and xylazine (2 mg/kg). To maintain consistent measurement of ABR, tympanometry, and blast pressure level, the pinna was removed.

After pre-exposure testing, the animal was placed into a specially designed animal holder. A pressure sensor (Model 102B16, PCB Piezotronics, Depew, NY) was placed at the entrance of the ear canal (1 cm lateral to the ear canal opening) with the sensing surface facing the blast in both open and shielded conditions. During the shielded test, the entire animal head was covered by a stainless steel cup with a thickness of 2 mm. The edge of the cup was flushed with the sensor which was also covered by the shield (Fig. 1C). Note that the chinchilla head shield was adjustable with relative position from the animal head and there was a distance of about 3 cm from the animal head to the internal top surface of the shield. The stainless steel shield was finally fixed on the animal holder. The animal within the holder was then moved to the testing chamber for blast exposure.

The pressure sensor signal was measured by cDAQ 7194 and A/D converter 9215 (National Instruments Inc., Austin, TX) with the sampling rate of 100k/s (10 μs dwell time). The LabVIEW software package (NI Inc.) was used for data acquisition and analysis. The waveform of each blast test was saved in a PC for further analysis.

It usually took 2–3 iterations of blast tests to reach the TM rupture threshold defined as the peak pressure before the TM rupture. That means if the TM ruptured after the third blast, the threshold was the peak pressure level of the second blast. The initial blast pressure level was selected based on the system calibration using different films and changing the distance between the sensor surface and the blast reference plane. The number of blast tests also varied with individual chinchillas due to the variation among the animals and setups. To confirm the TM damage, an otoscopic examination of both ears was performed first and further verification was done using wideband tympanometry to determine whether the TM was ruptured. When the TM was found without rupture, the next blast test was conducted with an increase of overpressure level. The testing stopped when one ear was ruptured.

Post-exposure measurements included wideband tympanometry to verify whether the TM was ruptured or damaged in both ears and ABR measurement in the ears with intact TMs to determine the hearing threshold shift after exposure. The TM damage pattern was recorded by taking pictures after the animal was euthanized and the bulla was dissected.

2.2. Waveform analysis

Impulse pressure energy spectra analysis on recorded waveforms in the time domain was conducted in MATLAB to determine the signal energy distribution over the frequencies under open and shielded conditions. First, the recorded pressure waveforms were converted to pressure distributions over the frequencies of 20–5000 Hz by using FFT spectral analysis. Next, following the methods of impulse signal energy distribution theory reported by Hamernik et al. (1991), Hamernik and Keng (1991), Hamernik and Qiu (2001) and Young (1970), the total sound exposure was divided by the standard characteristic impedance of the air ρc as impulse energy flux (energy per unit area) and expressed as:

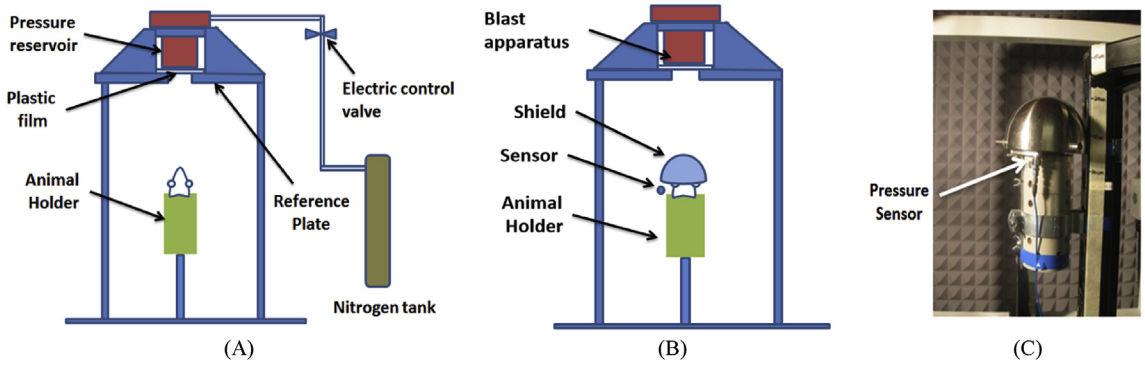


Fig. 1. (A) Schematic of animal experimental setup with blast apparatus in the open field testing. (B) Schematic of animal experimental setup in the shielded test with a stainless steel cup. (C) Picture of the animal inside the holder with its head covered by a stainless steel cup in the testing chamber.

$$E^* = \frac{1}{\rho c}\int_0^T p^2(t)dt, \quad \left[\mathrm{J}/\mathrm{m}^2\right] \tag{1}$$

where $p(t)$ is the instantaneous value of acoustic pressure in Pa or N/m^2, dt is the time increment for scanning of acoustic pressure in seconds, and $\rho c = 406$ mks rayls to produce a quantity with units of energy flux (i.e., J/m^2). Both ρ and c are pressure-dependent in the shock front. The duration of T = 50 ms was used for calculation in the present study.

Eight octave band-pass filters with center frequencies at 125 Hz, 250 Hz, 500 Hz, 1 kHz, 2 kHz, 4 kHz, 8 kHz, and 16 kHz were designed. A low pass filter L125 and a high pass filter H16k were also designed to catch signals at frequencies lower than 125 Hz and higher than 16 kHz. The filtered signals were then generated and the sound energy in each band was calculated as the distribution of pressure energy flux over 10 bands. Instead of directly comparing the energy flux values in the open field and shielded case, the energy in each band was normalized with respect to the total sound energy in that band.

2.3. Finite element modeling prediction

A 3D finite element model of the chinchilla ear has been developed in our lab and is currently under review for publication. The model was built based on X-ray micro-CT images of an entire chinchilla bulla, consisting of the ear canal, TM, middle ear ossicles and suspensory ligaments, and middle ear cavity. In this study, the FE model was used to calculate the distribution of the stress and strain in the TM with impulse pressure waveforms measured under open and shielded conditions. To simplify the modeling process, the ear canal and middle ear cavity were not included in the model as shown in Fig. 2. Fig. 2A shows the lateral view of the model with a TM diameter of 8.83 mm along the manubrium or malleus long process and 9.72 mm perpendicular to the manubrium. Surface area of the TM was 74.71 mm^2 and the thickness was 15 μm. Fig. 2B shows the posterior view of the model with a height of cone at 1.65 mm. The TM and ossicles were suspended by the TM annulus (TMA), anterior malleal ligament (AML), posterior incudal ligament (PIL), posterior stapedial tendon (PST), tensor tympani tendon (TTT), and stapedial annual ligament (SAL). In the chinchilla ear, the malleus and incus are fused as the malleus-incus complex and the incus-stapes joint still exists. The mechanical properties of the TM and middle ear tissues are listed in Table A1 in the Appendix.

The effect of cochlear fluid on acoustic-mechanical transmission through the ossicular chain or cochlear load was modeled as a mass block and 10 dashpots attached between the stapes footplate and fixed boundary. The average cochlear impedance was about 100 GΩ as reported by Slama et al. (2010). The impedance value of 100 GΩ was applied on 2.45 mm^2 of the stapes footplate to determine the dashpot damping, which resulted in a damping coefficient of 0.06 Nm/s for each dashpot.

Representative pressure waveforms (i.e., same magnitude and impulse duration, but more smooth) analogous to the recorded open and shielded waveforms (pressure vs. time plots) were directly applied on the TM surface and the calculation was performed in ANSYS APDL (ANSYS Inc., Canonsburg, PA). FE modeling of the TM and other soft tissue responses to impulse pressure waves used structural analysis with geometry nonlinearity of the tissues. The analysis was conducted in the time domain, utilizing the automatic time step function offered by ANSYS. Sensitivity analyses resulted in a calculated error of less than 1%. The output from modeling included the stress and strain distributions in the TM and the TM displacement distribution. The FE modeling results characterized mechanical damage of the TM in relation to impulse pressure waveforms.

3. Results

3.1. Experimental results

The damage of the TM observed from chinchilla ears after exposure in both open and shielded conditions showed certain TM rupture patterns. Fig. 3 displays otoscopic photographs of chinchilla TMs in a normal or intact ear (Fig. 3A) and injured ears (Fig. 3B–D). The severity of TM rupture increased from Fig. 3B to D. A small split along the radial direction of the TM was shown in Fig. 3B (chin-7s, shielded) and a large split along the radial direction was shown in Fig. 3C (chin-6s, shielded). These damage patterns show that the TM tissue strength varies in radial and circumferential directions and the collagen fibrous structure of the TM results in relatively weak mechanical properties along the circumferential direction. Under high intensity sound or blast overpressure, the TM damage pattern is closely related to variation of mechanical properties across the TM membrane. Fig. 3D shows a large perforation about the half of the TM surface in the inferior side (chin-7, unshielded). The TM rupture patterns shown in Fig. 3 were observed in both open and shielded conditions, and in most animals, the both ears were damaged with different patterns. Our observations are similar to those of TM perforations in mice after blast exposure reported by Cho et al. (2013): larger blast pressure did not make larger perforations. Thus, the present study could not provide any relationship between the TM rupture pattern and exposure condition: shielded

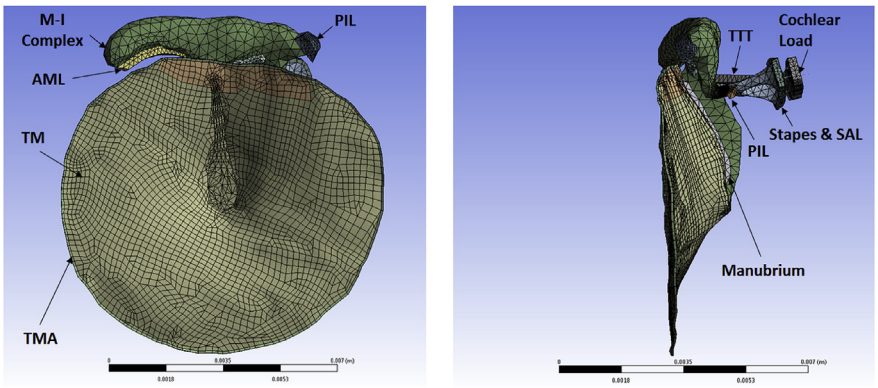


Fig. 2. Finite element (FE) model of chinchilla middle ear. (A) Lateral view of the FE model with the tympanic membrane (TM), malleus-incus (M–I) complex, anterior malleal ligament (AML), posterior incudal ligament (PIL), and TM annulus (TMA). (B) Posterior view of the FE model with manubrium, PIL, tensor tympani tendon (TTT), stapes, stapedial annual ligament (SAL), and cochlear load.

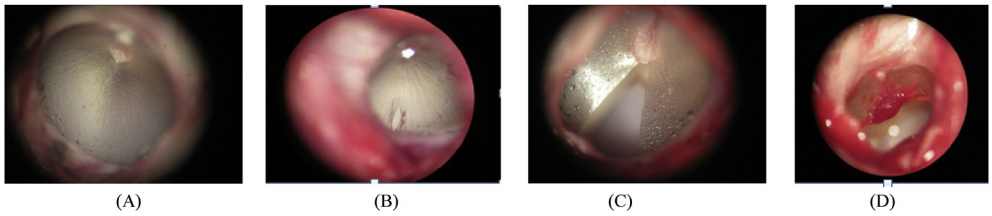


Fig. 3. Otoscopic pictures of chinchilla TMs. (A) Normal chinchilla TM. (B–D) TM ruptured after blast exposure with different severity: (B) a small split along the radial direction; (C) a large split along the radial direction; and (D) severe rupture of the TM.

and unshielded.

Fig. 4A and B shows the typical waveforms of pressure amplitude (rupture threshold level) in units of psi over a time of 10 ms recorded from two chinchillas in open field testing. A single positive overpressure peak was observed and peak pressures of 9.8 psi (Fig. 4A) and 11.3 psi (Fig. 4B) were reached within 3 ms as shown in these two figures. The spectral behavior of the waveforms in Fig. 4A and B at frequencies of 20–50,000 Hz by FFT analysis is displayed in Fig. 4C and D, respectively. There was a plateau of 50–55 dB at low frequencies (<200 Hz), and then the pressure level monotonically decreased to around zero as frequency increased to 50,000 Hz.

Table 1 lists the measured TM rupture thresholds (positive-peak in both psi and dB SPL) for animals tested in open field. The mean value of the TM rupture threshold measured from 9 animals in open field was 9.1 psi or 190 dB SPL or 62.7 kPa with a standard deviation (S.D.) of ±1.7 psi (N = 9).

Fig. 5A and B shows the waveforms of pressure (rupture threshold level) recorded from two animals in shielded testing. The waveform under the shield is obviously different from that in open field. Both positive and negative peaks were reached at less than 3 ms. The peak-to-peak pressure levels were 3.5 psi and 3.4 psi for Fig. 5A and B, respectively. This suggests that under the shield, the TM was ruptured at a lower pressure level than that without the shield. The spectral behavior of the waveforms in Fig. 5A and B is displayed in Fig. 5C and D, respectively. It can be seen that under the shielded test there was no perfect plateau like that observed in open field at lower frequencies (Fig. 4C and D) and the peak pressure around 50 dB was reached at about 1000 Hz and decreased to zero as frequency increased to 50,000 Hz.

Table 2 lists the measured TM rupture thresholds for animals tested with the shielded. The positive-peak and negative–peak in psi as well as the peak-to-peak pressures in both psi and dB SPL are included in Table 2. The mean value of the TM rupture thresholds measured from 9 animals with the shield was 3.4 ± 0.7 psi (N = 9) or 181 dB SPL. Comparing the results listed in Tables 1 and 2, a significant difference in the TM rupture thresholds between the open and shielded cases was revealed. With the shield, the TM rupture occurred at a much lower impulse pressure than that in the open field. This difference shows the biphasic nature of the shielded impulse.

Wideband tympanometry was used as an effective tool to detect TM damage in this study. The pre- and post-exposure tympanometry measurements were focused on the change of energy absorbance of the middle ear. The peak EA happens when the pressure of the middle ear equals that of the external ear in a normal ear with intact TM. When there is a perforation, the EA is low and flat. However, if the TM was not ruptured after blast, the EA measured at the pre- and post-blast exposure from 8 ears did not show significant difference between the pre- and post-exposure by paired t-test (detailed results not included here). This indicates that a TM rupture, even a small split, affects the EA measurement substantially.

Hearing threshold shift data were obtained by taking the difference of ABR measurements obtained pre- and post-blast exposure for ears without rupture. The tests were only conducted for animals in the open condition. The threshold shift indicates the hearing loss induced by blast exposure, which may involve outer ear and middle ear disorder. Fig. 6 shows the ABR hearing threshold shift obtained from 13 ears (4 animals had both ears tested). The hearing threshold was measured at 5 frequencies: 0.5, 1, 2, 4 and 8 kHz. It can be seen that the blast exposure caused ABR hearing threshold shift, particularly at high frequencies. A 10–20 dB threshold increase was measured at frequencies of 2–8 kHz, which means the high frequency hearing loss is greater than the low

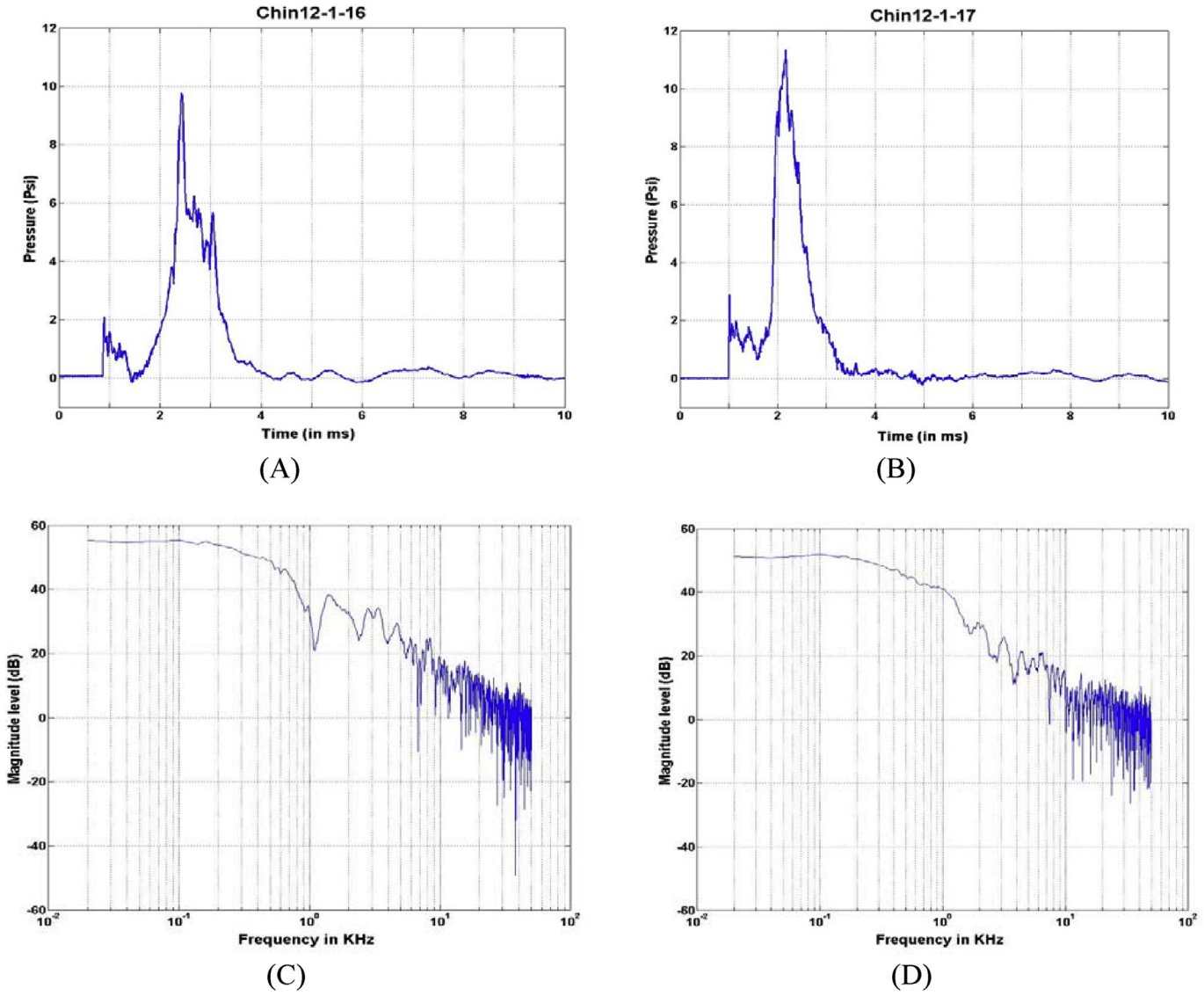


Fig. 4. (A) The overpressure waveform recorded in one chinchilla in open field testing and (C) the impulse pressure spectra obtained from this animal's waveform. (B) The overpressure waveform recorded in another chinchilla in open field testing and (D) the impulse pressure spectra obtained from this animal's waveform.

Table 1
List of TM rupture thresholds measured from a group of chinchillas tested in open field.

Animal	Chin-1	Chin-2	Chin-3	Chin-4	Chin-5	Chin-6	Chin-7	Chin-8	Chin-9	Mean ± S.D.
Positive peak (psi)	10.7	6.9	9.8	11.3	10.2	9.8	9.1	9.0	5.5	9.1 ± 1.7
Positive peak (dB SPL)	191.3	187.5	190.6	191.8	190.9	190.6	189.9	189.8	185.6	189.8 ± 1.9

frequency hearing loss induced by blast exposure. While there was no mechanical damage observed visibly in the middle ear, damage of the cochlea after blast may contribute to the hearing threshold shift as suggested by Cho et al. (2013).

3.2. Impulse energy spectra analysis

The sound pressure signal in the open field (Fig. 4A and B) is a shock wave-like impulse and the pressure signal in the shielded case (Fig. 5A and B) is a complex wave-like waveform as observed in our experiments. The impulse wave is completely changed under the shield. However, both waveforms are impulse pressure profiles (short duration and non-periodic) and the signal energy flux calculation was performed for all recorded waveforms in open and shielded groups over 10 octave frequency bands. Table 3 lists the calculated normalized energy flux for the open and shielded groups (N = 9 for each group) over 10 bands with mean and S.D. Note that the data were normalized with respect to the total signal energy in each group and the total value was 1.0 as shown in the table.

Fig. 7 displays the distribution of energy flux (normalized) based on the data in Table 3. It clearly shows the different energy flux over frequencies in the open and shielded cases. Under the open field condition, the majority of energy flux is presented at lower frequencies below 500 Hz. However, under shielded condition, the

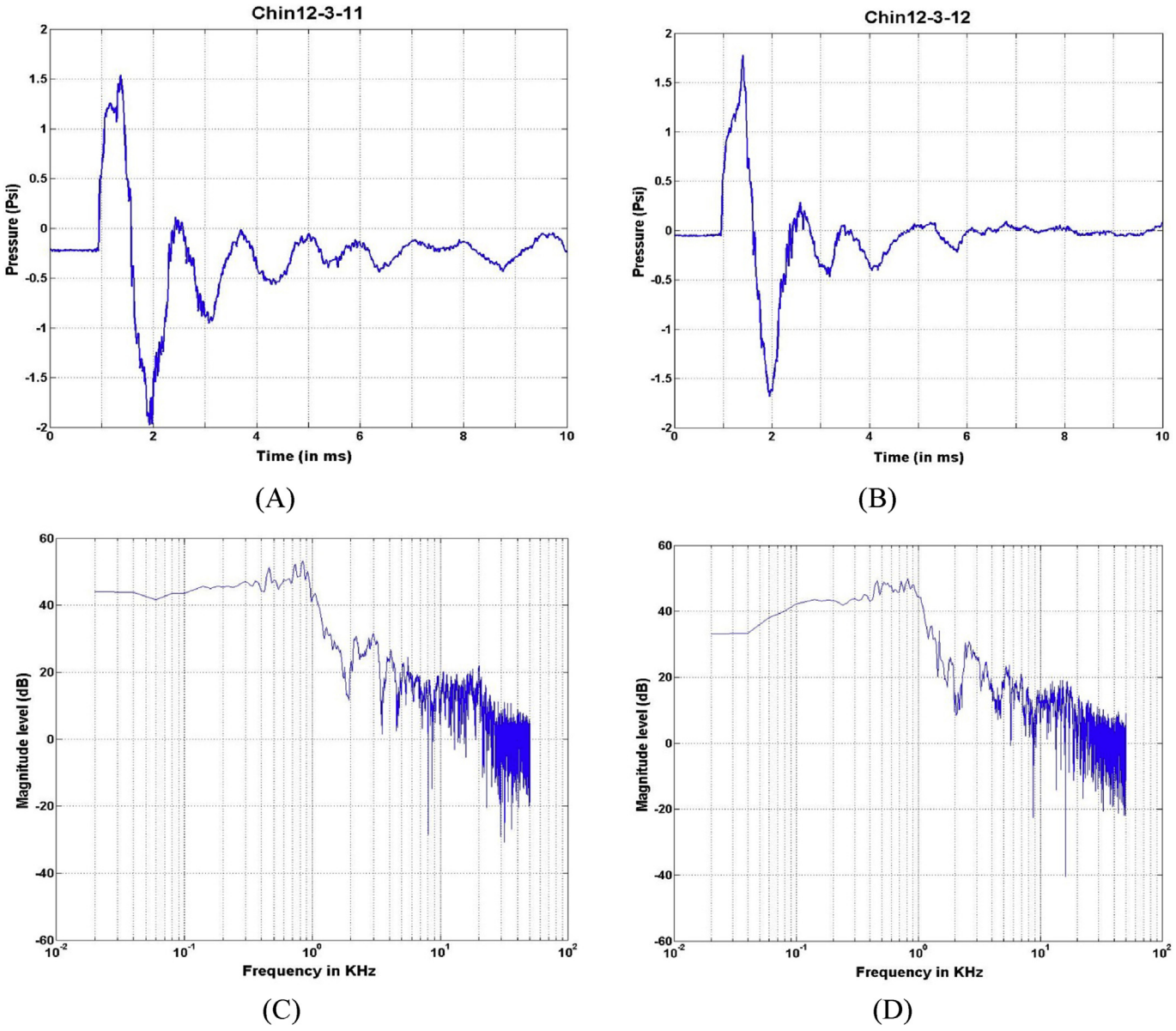


Fig. 5. (A) The overpressure waveform recorded in one chinchilla in shielded testing and (C) the impulse pressure spectra obtained from this animal's waveform. (B) The overpressure waveform recorded in another chinchilla in shielded testing and (D) the impulse pressure spectra obtained from this animal's waveform.

Table 2
List of TM rupture thresholds measured from a group of chinchillas tested with a shield.

Animal	Chin-1s	Chin-2s	Chin-3s	Chin-4s	Chin-5s	Chin-6s	Chin-7s	Chin-8s	Chin-9s	Mean ± S.D.
Positive-peak (psi)	1.5	2.2	1.5	1.5	2.3	2.3	1.8	1.4	1.1	1.7 ± 0.4
Negative-peak (psi)	2.6	2.7	1.5	1.3	1.3	1.2	1.6	1.4	1.6	1.7 ± 0.5
Peak-to-peak (psi)	4.1	4.9	3.0	2.8	3.6	3.5	3.4	2.8	2.7	3.4 ± 0.7
Peak-to-peak (dB SPL)	183.0	184.6	180.3	179.7	181.9	181.6	181.4	179.7	179.4	181.3 ± 1.6

energy flux is mainly involved at 500 and 1000 Hz. The results demonstrate that the different pressure waveforms in the open and shielded cases implicate the different energy distribution characteristics involved in these two exposures.

3.3. FE modeling results

The pressure waveforms recorded from the open field test (Fig. 4B) and the shielded test (Fig. 5B) were selected as blast pressure loading on the TM in the FE model of the chinchilla ear shown in Fig. 2. Two simulations were created: the open case with a positive peak pressure of 11.3 psi and the shielded case with peak pressures of positive 1.7 psi and negative 1.7 psi, or 3.4 psi peak-to-peak. The duration of open case simulation was set to 1 ms, to reflect the majority of the impulse of the measured open waveform. The small initial peak in the measured open waveform was not

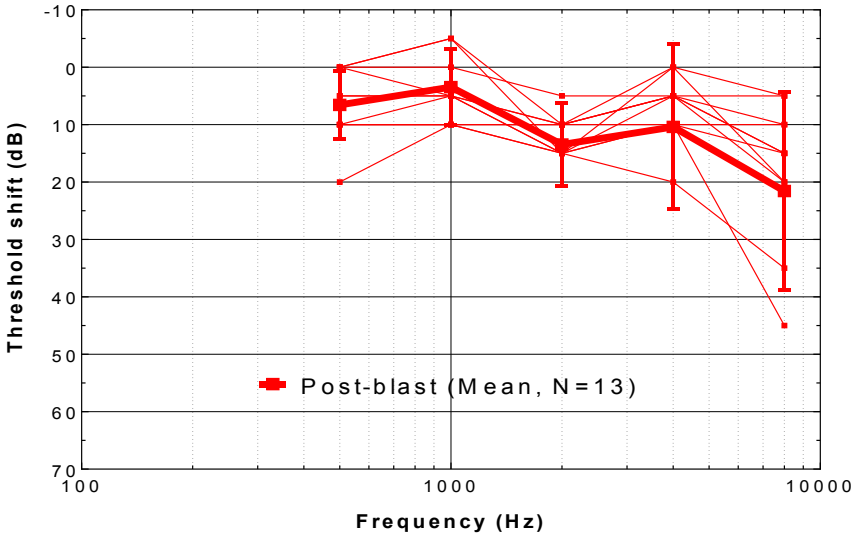


Fig. 6. ABR hearing threshold shift at frequencies of 0.5, 1, 2, 4, and 8 kHz obtained from 13 animal ears after exposures to blast waves (open field).

Table 3
Octave-band energy flux (J/m^2) (normalized) for the open and shielded groups.

Octave band CF(kHz)	Open		Shielded	
	Mean	±S.D.	Mean	±S.D.
<0.125	0.2557	0.0512	0.0343	0.0225
0.125	0.1797	0.0356	0.0444	0.0157
0.25	0.2159	0.0653	0.1310	0.0285
0.5	0.1628	0.0631	0.3922	0.0417
1.0	0.0935	0.0643	0.3118	0.0914
2.0	0.0421	0.0531	0.0737	0.0615
4.0	0.0211	0.0162	0.0270	0.0177
8.0	0.0113	0.0084	0.0114	0.0109
16.0	0.0121	0.0215	0.0051	0.0019
>16.0	0.0125	0.0278	0.0035	0.0024
Total	***1.0066***		***1.0344***	

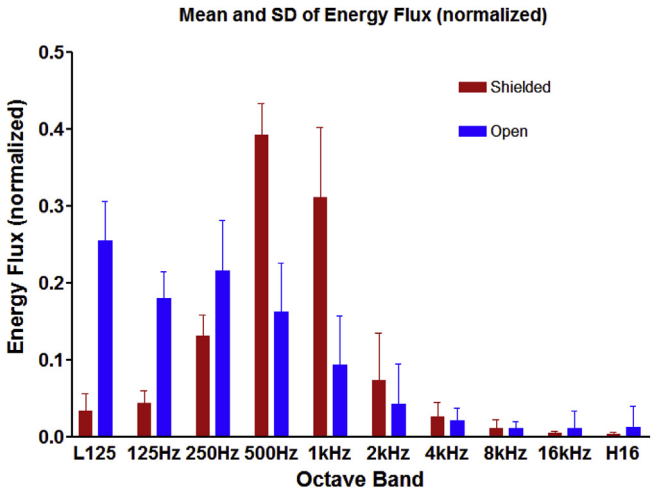


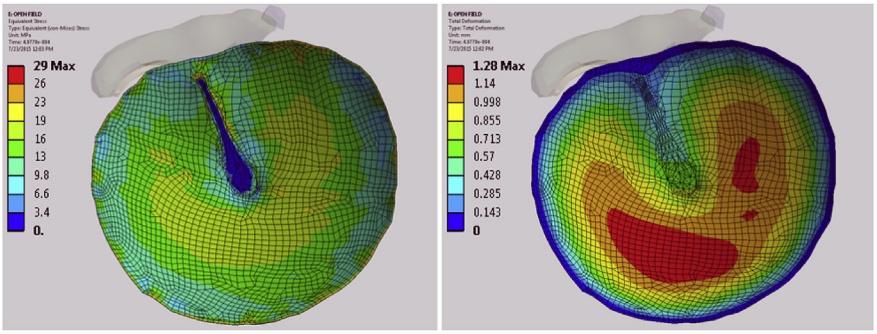
Fig. 7. Comparison of normalized energy flux over 10 frequency bands from below 125 Hz to above 16 kHz between the waveforms recorded in the open and shielded groups of chinchillas.

included in the simulation and the modeling analysis showed that the addition of the initial peak did not alter the results significantly. The shielded case was simulated using 1.5 ms of the experimental waveform so as to capture the initial pressure oscillations.

Fig. 8 shows the model-derived distributions or contours of stress in the TM (Fig. 8A) and the displacement of the TM (Fig. 8B) in the open case (or under positive pressure waveform) at the time of maximum stress was reached. In this study, the equivalent (von Mises) stress was used as a measure of the stress state of the TM. As shown in Fig. 8A, the stress varied from 29 to 0.13 MPa in the TM. The maximum stress of 29 MPa was at the top of the manubrium or near the flaccida above the handle of malleus. The second high-stress region of the TM was located in the inferior side along the middle region between the annulus and umbo with the stress ranging from 16 to 19 MPa. Fig. 8B displays the FE model-predicted TM displacement distribution. The maximum displacement of 1.28 mm was located in the inferior-posterior quadrant, approximately midway between the annulus and umbo. The displacement in the region of the manubrium was the smallest.

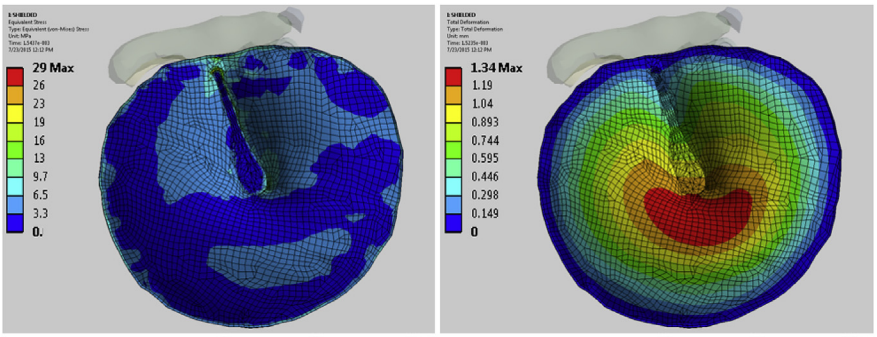
Fig. 9 displays the FE model-derived equivalent stress distribution in the TM (Fig. 9A) and the TM displacement (Fig. 9B) in the shielded case (or under positive-negative pressure waveform) at the time when the maximum stress was reached. The maximum stress occurred as the peak negative pressure was reached. As shown in Fig. 9A, in the superior region of the TM, the location of the maximum stress was the same as that of the open condition, i.e., at the top of the manubrium, and the value of maximum stress was also about 29 MPa. In the inferior side, the maximum stress of the TM was next to the umbo with a value about 15 MPa. The maximum displacement was located in the inferior portion of the TM, directly below the umbo with a value of 1.33 mm.

A comparison of the results obtained in the shielded case (Fig. 9) with those obtained in open field (Fig. 8) indicates a similar stress distribution on the TM surface in both open and shielded cases, with the maximum stress of about 29 MPa at the top of the manubrium. It is also found that for both open and shielded conditions, the maximum TM displacements were similar, but the location of maximum displacement in the shielded condition was closer to the umbo than that of the open condition. The model-predicted high stress level regions on the TM surface induced by impulse pressure waves recorded in blast tests were generally consistent with the observed TM rupture locations in experiments, suggesting the high stress levels may result in the TM rupture. The calculated location of maximum stress on the TM may not match the common mode of failure as seen in Fig. 3 – a radial tear caused



(A) (B)

Fig. 8. FE model-derived distributions of the equivalent (von Mises) stress in the TM (A) and the displacement of the TM (B) in the open case at the time when the maximum stress was reached. The recorded pressure waveform is listed in Fig. 4B. The stress and displacement levels are shown by color code.



(A) (B)

Fig. 9. FE model-derived distributions of the equivalent stress in the TM (A) and the displacement of the TM (B) in the shielded case at the time when the maximum stress was reached. The recorded pressure waveform is listed in Fig. 5B. The stress and displacement levels are shown by color code.

by failure of the TM circumferential fibers. The TM in current model was assumed as an isotropic membrane material, and thus does not capture the intricacies of the physiological, 3-layer membrane. Creation and implementation of a multi-layer TM is a future direction of this study.

Luo et al. (2009) measured the TM failure stress using a miniature split Hopkinson tension bar, and their results showed that the ultimate tensile stress of the TM increased with increasing strain rate, and the orientation of TM sample had a strong influence on the ultimate tensile stress. The mean ultimate stress of TM in the circumferential direction was 7.7 MPa with a strain rate of 772/s, and 13.7 MPa with a strain rate 1353/s. Since the strain rate was not derived from the two waveforms in the present study, the TM strain rate associated with the two waveforms and its effect on the rupture threshold need further investigation.

4. Discussion

4.1. What we found from the chinchilla study?

In this study, mechanical damage of the TM in chinchilla ears after exposure to high intensity sound or blast has been investigated in two groups of animals under two exposure conditions: open field and shielded. The results show that the TM rupture threshold in the shielded case was lower than that in the open field with the mean values obtained from 9 animals in each condition. The waveforms recorded during the tests from these two groups are different: a single positive impulse pressure wave obtained from the open test and the almost equal positive-negative waves obtained from the shielded test. These experimental results provide the evidence that the TM damage induced by blast overpressure is closely related to impulse pressure waveforms at the entrance of the ear canal which determine the energy level and frequency components of the sound signal to be transmitted into to the ear.

4.2. How to explain the results?

Two methods have been used for analysis of the TM damage results in this study with a focus on the relationship between the TM rupture threshold and impulse pressure waveform.

(1) The impulse pressure energy spectra for waveforms recorded from each animal was analyzed over 10 octave frequency bands. The normalized energy flux at each band was then calculated from each animal and the mean values with S.D. were derived and displayed in Fig. 7 for both open and shielded groups. The spectra difference between these two groups suggests that the positive-negative pressure waveform in the shielded case carried more energy at higher frequencies than that of the open case. This finding verifies that the spectra behavior of impulse signal energy distribution over frequency bands is different in these two waveforms for the open and shielded conditions. However, the direct analysis of TM mechanical damage in relation to impulse pressure waveform needs further clarification.
(2) The 3D finite element model of the chinchilla middle ear (Fig. 2) was used to derive the stress/strain distribution in the TM and the TM displacement when the pressure waves were applied on the TM over a very short time duration (<3 ms, Figs. 4B and 5B). The FE modeling results shown in Figs. 8 and

9 provide the contour distributions of the stress and displacement at the time when the maximum stress was reached, which reflected the stress and movement of the TM at the rupture threshold level. To examine the change of stress in the TM in response to rapid pressure loading, we applied the pressure waves on the TM at four levels: 25%, 50%, 75%, and 100% of the rupture pressure level. The results are shown in Fig. 10 as the variation of TM stress with respect to the impulse pressure level.

As can be seen in Fig. 10, the change of stress in response to change in pressure loading in the shielded case was much higher than that in the unshielded case. This finding reveals that the biomechanical mechanisms for blast-induced TM damage in relation to overpressure waveforms may consist of the following two standard points: 1) the negative pressure component of the shielded waveform may play a crucial role for TM rupture, even though the negative peak is smaller than the positive peak; 2) the sensitivity of TM stress with respect to peak-to-peak pressure amplitude, $\delta\sigma/\delta p$, may characterize mechanical damage of the TM in relation to the impulse pressure waveform.

4.3. Future studies

This is the first time the TM damage in relation to blast pressure waveforms has been investigated by using the 3D FE model of the chinchilla ear. This approach is based on experimental measurements in animals and the FE mechanical analysis of the TM or middle ear structure response to blast overpressure waves. The results and findings from this study, though limited to two cases, may have general contributions for understanding the mechanisms of TM damage during the blast exposure. In our future studies, we will continue the investigation along this direction on mechanisms of the TM and other ear tissue damages in relation to blast overpressure waveforms. We will also face challenges for development of the failure criteria for TM, a multiple layer, viscoelastic membrane tissue, in response to high intensity sound and blast overpressure.

It is also worth noting that the present study has demonstrated that the TM rupture threshold in the shielded case with the shield covering the animal head was lower than that in the open field, when the animal was exposed to blast overpressure. This suggests that an acoustic role of helmets may exist which intensifies ear injury during blast exposure. However, more studies on a helmet's effect on possible TM damage are needed in addition to its protection function to traumatic brain injury.

5. Conclusions

The relationship between the TM rupture threshold and the impulse or overpressure waveform has been investigated in chinchillas. Two groups of animals were exposed to blast overpressure under two conditions: open field and shielded with a stainless steel cup covering the animal head. The waveforms recorded in the shielded case had almost equal positive-negative pressure phases while the waveforms recorded in the open field had the positive pressure only. The average TM rupture threshold measured in the shielded case was lower than that in the open field (3.4 peak-to-peak vs. 9.1 psi or 181 vs. 190 dB SPL, and the positive peak for the shielded case was even smaller). The positive-negative pressure waveform in the shielded case delivered more energy at high frequencies to the ear canal while the positive pressure only waveform in the open case carried energy limited at lower frequencies. The FE modeling results further revealed that the biomechanical mechanisms for blast induced TM damage in relation to the overpressure waveform may consist of two standard points: the role of the negative pressure component and the rate of stress change with respect to impulse pressure loading increasing. The TM rupture threshold difference between the open and shielded cases may suggest that an acoustic role of the helmet may exist which intensifies ear injury during blast exposure.

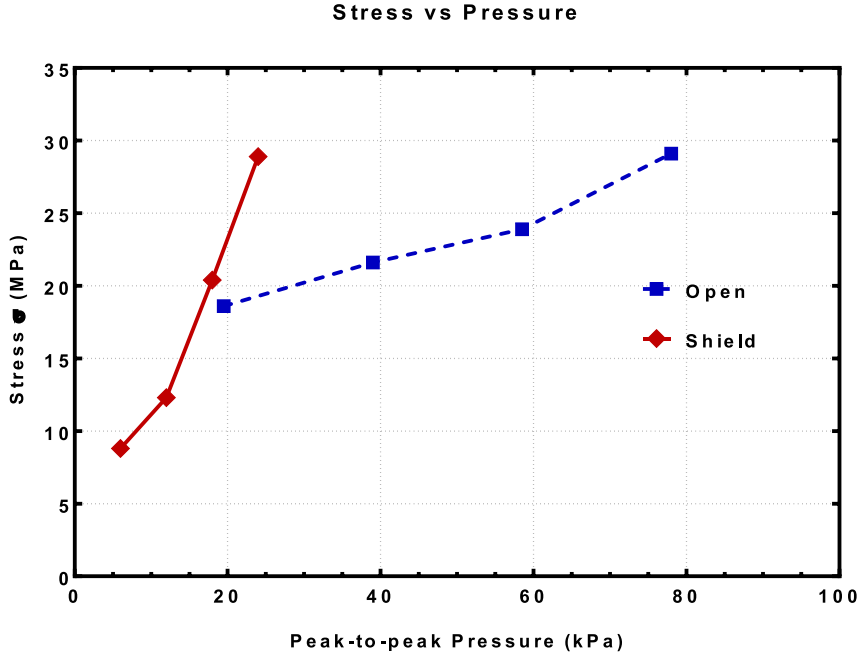


Fig. 10. Plots of FE model-derived stress increase with the peak-to-peak pressure loading in open and shielded cases. The blue broken line with symbols was obtained from Fig. 8 in open case and the red solid line with symbols was obtained from Fig. 9. (For interpretation of the references to colour in this figure legend, the reader is referred to the web version of this article.)

Acknowledgments

We thank Prof. Ning Xiang, Ph.D., Architectural Acoustics at Rensselaer Polytechnic Institute for his valuable discussions on acoustics analysis. This work was supported by DOD W81XWH-14-1-0228 and NIH R01DC011585 grants.

Appendix

Table A1
Mechanical properties of middle ear soft tissues of chinchilla ear

Structure	Parameters
Tympanic membrane	
Elastic modulus (MPa):	
Pars tensa	200
Pars flaccida	15
Density (kg/m^3)	1100
Damping coefficient	1.00×10^{-4}
Manubrium	
Elastic modulus (MPa)	800
Density (kg/m^3)	1200
Damping coefficient	7.5×10^{-5}
Incudomalleolar (IS) joint	
Elastic modulus (MPa)	6
Density (kg/m^3)	1000
Damping coefficient	7.5×10^{-5}
Stapedial annular ligament (SAL)	
Elastic modulus (MPa)	0.1
Density (kg/m^3)	1000
Damping coefficient	7.5×10^{-5}
Anterior malleal ligament (AML)	
Elastic modulus (MPa)	3.2
Density (kg/m^3)	1000
Damping coefficient	1.0×10^{-4}
Posterior incudal ligament (PIL)	
Elastic modulus (MPa)	2.5
Density (kg/m^3)	1000
Damping coefficient	7.5×10^{-4}
Posterior stapedial tendon (PST)	
Elastic modulus (MPa)	2.0
Density (kg/m^3)	1000
Damping coefficient	7.5×10^{-5}
Tensor tympani tendon (TTT)	
Elastic modulus (MPa)	2.0
Density (kg/m^3)	1000
Damping coefficient	7.5×10^{-5}
Malleus-incus complex	
Elastic modulus (GPa)	14.1
Density (kg/m^3)	2000
Mass (mg)	12.05
Damping coefficient	1.5×10^{-4}
Stapes	
Elastic modulus (GPa)	14.1
Density (kg/m^3)	1300
Mass (mg)	0.55
Damping coefficient	1.0×10^{-4}

References

Cho, S.-I., Gao, S.S., Xia, A., Wang, R., Salles, F.T., Raphael, P.D., Abaya, H., Wachtel, J., Baek, J., Jacobs, D., Rasband, M.N., Oghalai, J.S., 2013. Mechanisms of hearing loss after blast injury to the ear. PLoS One 8 (7), e67618.

Fausti, S.A., Wilmington, D.J., Gallun, F.J., Myers, P.J., Henry, J.A., 2009. Auditory and vestibular dysfunction associated with blast-related traumatic brain injury. J. Rehabil. Res. Dev. 46 (6), 797–810.

Garth, R.J., 1994. Blast injury of the auditory system: a review of the mechanisms and pathology. J. Laryngol. Otol. 108 (11), 925–929.

Gondusky, J.S., Reiter, M.P., 2005. Protecting military convoys in Iraq: an examination of battle injuries sustained by a mechanized battalion during operation Iraqi freedom II. Mil. Med. 170 (6), 546–549.

Guan, X., Gan, R.Z., 2011. Effect of middle ear fluid on sound transmission and auditory brainstem response in guinea pigs. Hear Res. 277, 96–106.

Hamernik, R.P., Ahroon, W.A., Hsueh, K.D., 1991. The energy spectrum of an impulse: its relation to hearing loss. J. Acoust. Soc. Am. 90, 197–204.

Hamernik, R.P., Keng, D., 1991. Impulse noise: some definitions, physical acoustics and other considerations. J. Acoust. Soc. Am. 90, 189–196.

Hamernik, R.P., Qiu, W., 2001. Energy-independent factors influencing noise-induced hearing loss in the chinchilla model. J. Acoust. Soc. Am. 110, 3163–3168.

Hawa, T., Gan, R.Z., 2014. Pressure distribution in a simplified human ear model for the high intensity sound transmission. J. Fluids Eng. 136, 111108-1 to -6.

Heffner, R.S., Heffner, H.E., 1991. Behavioral hearing range of the chinchilla. Hear. Res. 52, 13–16.

Hirsch, F.G., 1966. Effects of Overpressure on the Air – a Review. Technical progress report on contract DA-49-146-XZ-372 (Department of Defense).

Jensen, J.H., Bonding, P., 1993. Experimental pressure induced rupture of the tympanic membrane in man. Acta Otolaryngol. Stockh. 113, 62–67.

Jeselsohn, Y., Freeman, S., Segal, N., Sohmer, H., 2005. Quantitative experimental assessment of the factors contributing to hearing loss in serous otitis media. Otol. Neurotol. 26, 1011–1015.

Karmy-Jones, R., Kissinger, D., Golocovsky, M., Jordan, M., Champion, H.R., 1994. Bomb-related injuries. Mil. Med. 159 (7), 536–539.

Luo, H., Dai, C., Gan, R.Z., Lu, H., 2009. Measurement of Young's modulus of human tympanic membrane at high strain rates. J. Biomech. Eng. 131, 064501-1 to -8.

Mayorga, M.A., 1997. The pathology of primary blast overpressure injury. Toxicology 121 (1), 17–28.

Patterson Jr., J.H., Hamernik, R.P., 1997. Blast overpressure induced structural and functional changes in the auditory system. Toxicology 121 (1), 29–40.

Petrova, P., Freeman, S., Sohmer, H., 2006. The effects of positive and negative middle ear pressures on auditory threshold. Otol. Neurotol. 27, 734–738.

Qin, Z., Wood, M., Rosowski, J.J., 2010. Measurement of conductive hearing loss in mice. Hear Res. 263, 93–103.

Richmond, D.R., Yelverton, J.T., Fletcher, E.R., Phillips, Y.Y., 1989. Physical correlates of eardrum rupture. Ann. Otol. Rhinol. Laryngol. 98, 35–41.

Young, R.W., 1970. On the energy transported with a sound pulse. J. Acoust. Soc. Am. 47, 441–442.

Hearing Research 339 (2016) 1–11

Contents lists available at ScienceDirect

Hearing Research

journal homepage: www.elsevier.com/locate/heares

Research Paper

Characterization of the nonlinear elastic behavior of chinchilla tympanic membrane using micro-fringe projection

Junfeng Liang [a], Huiyang Luo [a], Zachary Yokell [b], Don U. Nakmali [b], Rong Zhu Gan [b], Hongbing Lu [a, *]

[a] Department of Mechanical Engineering, The University of Texas at Dallas, Richardson, TX 75080, USA
[b] School of Aerospace and Mechanical Engineering, The University of Oklahoma, Norman, OK 73019, USA

ARTICLE INFO

Article history:
Received 25 May 2015
Received in revised form
1 April 2016
Accepted 8 May 2016
Available online 27 May 2016

Keywords:
Chinchilla
Tympanic membrane
Micro-fringe projection
Static pressure
Hyperelastic model

ABSTRACT

The mechanical properties of an intact, full tympanic membrane (TM) inside the bulla of a fresh chinchilla were measured under quasi-static pressure from −1.0 kPa to 1.0 kPa applied on the TM lateral side. Images of the fringes projected onto the TM were acquired by a digital camera connected to a surgical microscope and analyzed using a phase-shift method to reconstruct the surface topography. The relationship between the applied pressure and the resulting volume displacement was determined and analyzed using a finite element model implementing a hyperelastic 2nd-order Ogden model. Through an inverse method, the best-fit model parameters for the TM were determined to allow the simulation results to agree with the experimental data. The nonlinear stress-strain relationship for the TM of a chinchilla was determined up to an equibiaxial tensile strain of 31% experienced by the TM in the experiments. The average Young's modulus of the chinchilla TM from ten bullas was determined as approximately 19 MPa.

© 2016 Elsevier B.V. All rights reserved.

1. Introduction

An eardrum or tympanic membrane (TM) couples acoustic waves from ambient air in the ear canal to the middle ear; it is a key component for transmitting sound pressure to ossicular chains. The function of the TM can be affected by ambient pressure, which changes widely from a few pascal (Pa) to a few kPa. In some extreme cases, for instance, under blast in conflict zones, the overpressure can be as high as 100 kPa, which could cause damage to the TM (Ritenour et al., 2008). As TM deforms under different ambient pressures, the transmission of sound energy across the middle ear can be significantly altered (Dirckx and Decraemer, 1991; Volandri et al., 2011; Ghadarghadar et al., 2013; Thornton et al., 2013; Rosowski et al., 2014). In efforts made to understand the effect of ambient pressure on TM function for the sound transmission, the mechanical response of TMs has been investigated under various static pressures. The deformation of a TM, induced by either negative or positive pressure in the middle ear, was measured using shadow moiré technique on human temporal bones (Dirckx and Decraemer, 1991). The TM vibration under different middle-ear pressures was measured on gerbil ears (Lee and Rosowski, 2001; Rosowski and Lee, 2002), where the alterations of acoustic stiffness and impedance by static pressures were observed. The stiffening of a TM under the repetitive pressure loading from habitual sniffing was investigated on gerbil using shadow moiré (von Unge and Dricks, 2009).

In addition to experimental investigations, finite element methods (FEM) have been used to study the sound transmission in the middle ear under various static pressures. The effect of geometrical nonlinearity was reported on the movement of a cat eardrum under static pressures on TM (Ladak et al., 2006). The middle ear transfer function was also analyzed under various static pressures on a human middle ear (Wang et al., 2007). It is noted that, the fidelity of the simulation results depends, to a large extent, on the accuracy of the mechanical properties of a TM, as a function of pressure.

The mechanical properties of TMs have been measured using numerous experimental techniques. The viscoelastic properties of a human TM were measured under tension using dynamic

List of the abbreviations: A, anterior; CAD, computer-aided design; FEM, finite element method; I, inferior; IACUC, institutional animal care and use committee; IM, intramuscular; LDV, laser Doppler vibrometery; P, posterior; PVC, polyvinyl chloride; S, superior; TM, tympanic membrane; U, umbo; XYZ, x-, y- and z-axes

* Corresponding author.
E-mail address: hongbing.lu@utdallas.edu (H. Lu).

http://dx.doi.org/10.1016/j.heares.2016.05.012
0378-5955/© 2016 Elsevier B.V. All rights reserved.

mechanical analysis (Cheng et al., 2007) and acoustic pressure using laser Doppler vibrometery (LDV) (Gan et al., 2010; Zhang and Gan, 2010). A miniature split Hopkinson tension bar was used to measure the dynamic properties of human TMs under high strain rates (Luo et al., 2009a,b, 2016). Another method used was nanoindentation, it has been used to measure the mechanical properties of different quadrants of a TM. The linear viscoelastic properties of TMs were reported using nanoindentation (Huang et al., 2008). The method was also used to measure both in-plane and out-of-plane mechanical properties at different locations of a TM (Daphalapurkar et al., 2009). In all these methods, strip or cut TM specimens were used. This approach causes the collagen fibers in the radial or circumferential directions in pars tensa to shrink (O'Connor et al., 2008), and alters the physiological condition of TM, leading potentially to erroneous results. To circumvent this problem, it is necessary to employ a new method to measure the mechanical properties for the full, intact TM, which is the focus of this paper.

Full-field measurement methods have been used in the last several years to measure the mechanical responses of a TM. Using LDV and stroboscopic holography, deformations of a human TM were measured with acoustic loading, and viscoelastic properties were determined through a hybrid method allowing FEM simulated umbo displacement to agree with the experimental measurement (De Greef et al., 2014a,b). Another full-field method to probe mechanical properties was developed to measure the TM elastic properties (Aernouts et al., 2010; Buytaert and Drickx, 2009) using geometric moiré and indentation loading. The geometric moiré was used to determine the surface topography while the indentation was applied; the mechanical response of the TM was simulated by FEM to determine the elastic properties and the viscoelastic properties under low frequencies (Aernouts and Drickx, 2012a,b; Aernouts et al, 2012) using an inverse problem solving scheme. The Young's modulus was measured as approximately 20 MPa by nano/micro-indentation (Aernouts et al., 2010, Aernouts and Drickx, 2012a,b; Hesabgar et al., 2010; Soons et al., 2010; Salamati et al., 2012). Both methods measure TM properties under indentation loading, which is applied on a small local region; that is a loading situation that is different from the condition under normal hearing or under blast, in which air pressure is applied on the entire TM. In addition, for the latter method, the contact nature and the localization of force applied on a small region could impose challenges to maintain the indenter positioning under increasing load. There is also a potential issue on convergence in the analysis considering a contact mechanics problem. An alternative computer-based method was developed; in which case, the pressure was used instead of indentation (Ghadarghadar et al., 2013). In that method, the Young's modulus of TM was estimated by minimizing the difference in displacements over the entire TM calculated from model with that measured from experiment. The replacement of indentation loading with pressure loading simplified the experimental setup. Ghadarghadar et al. (2013) showed a rather good agreement between the computational displacement and experimental results on the pars tensa of the TM, but not on the pars flaccida (a small portion of the dataset). They also pointed out that the material property of pars flaccida can be significantly different from pars tensa. It is noted that, the nonlinearity of the mechanical behavior of TM under different pressures has not been considered.

In this paper, we provide a non-contact, full-field optical method on the measurement of mechanical properties of an intact TM under quasi-static pressure. An inverse method combining experimental and numerical investigation is used to determine the mechanical properties of a chinchilla TM. The TM inside a bulla is pressurized while its topography is determined by a full-field micro-fringe projection technique. Volumetric displacement is then calculated from the topography. FEM with a nonlinear material model is applied to model the topography of TM under pressure, to provide the simulated relationship between pressure and volume displacement that is consistent with experiment. The nonlinear mechanical properties of TM under different quasi-static pressures are thus determined.

2. Method

2.1. Micro-fringe projection technique

A micro-fringe projection technique was used to determine the deformed surface topography of the TM under a prescribed static pressure. In micro-fringe projection, a grating is projected onto an object and the image of the projected fringe on the surface of the object is acquired by a digital camera. Another image of fringe projected onto a reference plane under the same setup is also acquired. The object image is subsequently digitally superimposed with the reference image to generate interferometry (Ortiz and Patterson, 2003, 2005). Virtual shifting is conducted by utilizing five phase-shifted images of the original image to calculate the phase difference between reference plane and the object from the interferometry map (Ortiz and Patterson, 2005).

The inverse tangent function outputs phase angle within the interval $[-\pi, \pi]$ with 2π discontinuity at the end of the period. In order to determine the surface profile from the direct output, phase angle has to be unwrapped. A quality bins algorithm is used to unwrap the phase map for surface profile reconstruction (Ghiglia and Pritt, 1998; Ortiz, 2004). In the case where the projection is telecentric, the out-of-plane position Z is determined from the phase angle difference $\Delta\Phi$ for any point on the object surface:

$$Z = \frac{ph}{d}\frac{\Delta\Phi}{2\pi} \tag{1}$$

where h is the distance between the camera and the object, and d is the distance between the camera and the light source, as shown schematically in Fig. 1(a). In the actual situation, it is difficult to measure accurately these parameters directly from the apparatus. A calibration procedure is thus used to determine the ratio between h and d in Eqn (1) (Ortiz and Patterson, 2003). A cone with known dimensions that approximately match the features (radius and depth) of the TM was used for calibration. By comparing the phase map with the known geometry, the ratio of h to d was determined.

2.2. Experimental setup

Fig. 1(b) shows the actual experimental setup. The chinchilla bulla was placed on a gimbal holder attached to a temporal bone bowl, which allowed the orientation of the TM surface to be adjusted for micro-fringe projection as well as for observation by a camera. A set of X-, Y- and Z- (*XYZ*) linear translation stages was used to hold the temporal bone bowl, to position the TM within the field of the projected fringes and field of view of the camera. A micro-fringe projector, including a set of lenses, grating, and fiber optic light source was used to project fringes onto the TM in the bulla. The projector consisted of a 100 W fiber optic lamp, two condenser lenses (Edmund Optical Sci., #89-038), a grating and an objective lens (Fujinon Photo Optical Co., 611374). The focal length of the objective lens was adjustable so that an in-focus pattern of equidistant pitch fringes was projected onto the reference plane and the object. The grating used had a square wave transmission profile, namely the Ronchi rulings (Edmund Optical Sci., #58-777) with pitch density of 20 cycle/mm. A digital camera (Nikon D7000,

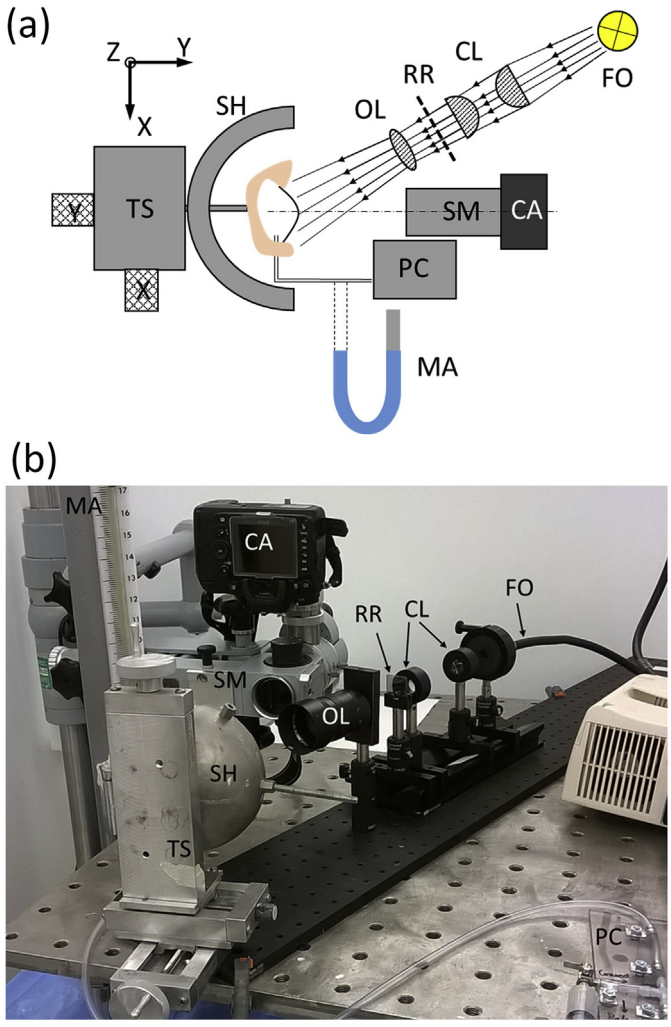


Fig. 1. The experimental setup of the micro-fringe projection system and the pressure loading and monitoring system. (a) Schematic diagram; (b) Actual setup. The components include: manometer (MA), camera (CA), surgical microscope (SM), sample holder (SH), XYZ-translation stage (TS), objective lens (OL), Ronchi rulings (RR), condenser lenses (CL), fiber optics illuminator (FO) and pressure control (PC).

4928 × 3264 pixels) was attached to a beam splitter on a surgical microscope (Carl Zeiss, OPMI-1) with an objective lens of 250 mm. The microscope head was connected to a finely adjustable arm mounted on a movable stand, which allowed optical axis of the microscope to remain perpendicular to the sample holder plane. The projection lens of micro-fringe projector was located about 88 mm away from the microscope objective lens; an angle of approximately 19° was formed between the axis of the microscope-camera assembly and axis of the projector. The combination of a finer grating and a smaller angle generally produces higher sensitivity than a coarser grating and a larger angle. In addition, the distance between the objective lens in Fig. 1 and the object should be at least one order of magnitude larger than the height of the object (von Unge et al., 1993). The height of chinchilla TM was about 2 mm, which was much smaller than the working distance (250 mm) of the microscope. Therefore, the telecentric condition was satisfied.

A pressure monitoring system was used to load the specimen with either positive or negative static pressure. The system consists of two three-way stopcocks, a 20 mL syringe and a water manometer with a resolution of 2.5 mm water bar (Dwyer Instruments, #1235). A three-way stopcock serves as a valve to control the pressure applied on the specimen; it allows for releasing and applying pressure to the specimen, and locking up the pressure in the specimen. Another three-way stopcock, serving as pressure direction control, was utilized to switch between positive pressure and negative pressure applied on the specimen.

2.3. Sample preparation

Ten TMs of adult chinchillas weighing between 535 g and 855 g, without middle ear diseases were used. Chinchilla was used because the diameter and the shape of its TM are close to human. The study protocol was approved by the Institutional Animal Care and Use Committee (IACUC) of the University of Oklahoma and met the guidelines of the National Institutes of Health. After examination with an otoscope, the chinchilla was sacrificed with ketamine (100 mg/kg IM) and xylazine (10 mg/kg IM) injected directly to the heart. An intact temporal bone or bulla was harvested from the skull 10 min *post mortem*. The bulla wall was opened widely from the middle ear side and both the cochlea and the stapes along with the tensor tympani muscle were removed until the medial side of TM was fully exposed (Fig. 2(a)). In order to maintain the geometry of the TM and simplify the boundary conditions for modeling, the malleus-incus complex was immobilized by applying a droplet of gel type superglue (Superglue, Co., Fast™) between the incus section and the petrous wall behind. A polyvinyl chloride (PVC) tubing with 3/16 inches inner diameter, 1/4 inches outer diameter, and about 3 inches long, was inserted into the ear canal and hermetically fixed on the bulla by applying two-part epoxy (Illinois Tool Works Inc, Devcon and 5 Minute) at the entrance of the ear canal. The two-part epoxy was mixed and cured for 2 min before it was applied on the bulla to ensure that it was viscous and would not flow into the middle ear. The outer end of the tubing was then connected to the pressure monitoring system for applying static pressure on the TM from the lateral side (Fig. 2(b)). The overall time for sample preparation for each bulla in an experiment in this section was about 45 min. In order to protect the TM from desiccation, during the process of opening the bulla, a droplet of saline solution was applied on the TM every 5 min. Also, during the curing period of the two-part epoxy, a small piece of Kim wipe paper saturated with saline solution was used to cover the TM.

Similar to shadow moiré, fringe projection requires the object to have a diffusive reflecting surface. Therefore the medial side of TM was coated with a thin layer of titanium oxide in saline solution (100 mg/ml) to provide good reflection. Titanium oxide was chosen because it is a typical material used in cosmetics and a thin layer of the coating is not anticipated to affect the mechanical response of the TM (Dirckx and Decraemer, 1997).

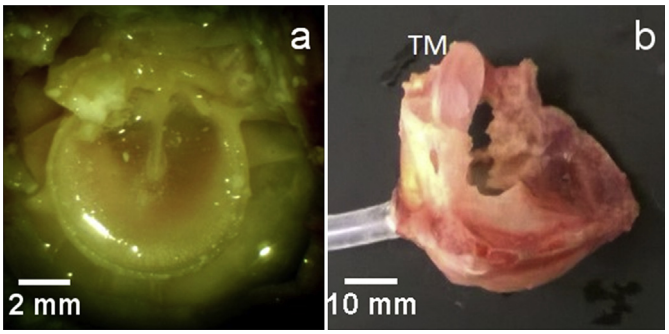


Fig. 2. A chinchilla bulla sample for measurements: (a) The medial side of TM with intact malleus-incus complex immobilized; (b) A typical bulla sample with TM exposed, and a sealed PVC tube inserted into ear canal for applying pressure.

2.4. Measurement procedures

After the bulla specimen was prepared, it was mounted on the gimbal sample holder. The bulla was first secured with molding clay to adjust coarsely the position of the bulla so that TM faced the microscope and then fixed with the use of screwed arms of the holder; and the orientation of the bulla was finely adjusted to allow a full view of the TM without any shadow. The aforementioned PVC tubing was connected to the first three-way stopcock in the pressure monitoring system, and the stopcock was switched to change-pressure mode. Pressure was then applied to the bulla manually through the syringe in the pressure monitoring system. As a TM, like other soft tissue, is a viscoelastic material (Fung, 1993; Ladak et al., 2004), preconditioning must be carried out to allow the specimen to give consistent results. Each bulla was preconditioned by applying a small pressure with magnitudes less than 100 Pa by five cycles prior to test. A positive pressure was induced by pumping compressed air into bulla from ear canal; as such, the pressure on the medial side of the TM was lower than that applied on the lateral side of the TM. A negative pressure was induced by a vacuum in the ear canal; in such a case the pressure on the medial side of the TM was higher than that applied on the lateral side. In each cycle in preconditioning, a negative pressure was applied first to the bulla, and then the pressure was increased to a positive value, and finally the pressure was released back to zero. Both positive and negative pressures were applied to the bulla for measurement of the response of the TM to pressure to determine the mechanical response of the TM. The magnitude of pressure applied was between 0 and 1.0 kPa with an increment of 0.125 kPa inside the bulla with stopcock set to lock-up mode. A constant pressure was maintained at each step. The entire measurement took about 2 min for each sample; therefore no special care was needed to maintain moisture in the TM.

At each state of pressure, including the zero-pressure state, an image was acquired by a digital camera attached to the microscope. For each image, reconstruction of TM surface was conducted using the method described in Section 2.1. The reconstructed TM surface profiles were then used to calculate the volume displacement based on the surface topography under pressure and the surface profile under the zero-pressure state.

2.5. Finite element simulations

The FEM software, ANSYS-15 was used for simulations of chinchilla TM under quasi-static pressure. A FEM model was established using the surface typography of the TM determined at the zero-pressure state. For each specimen, an individualized FEM model was established and the volume displacement under static pressure was calculated. Simulations were conducted by selecting the material parameters in the Ogden hyperelastic constitutive law until the volume displacement obtained from the FEM model matched well with the corresponding experimental data. The surface topography under the zero-pressure state, reconstructed from the micro-fringe projection, was converted to a three-dimensional model using the computer-aided design (CAD) software, SolidWorks 2013. Since the TM thickness is small compared with its major or minor axis, TM was modeled as a shell with a thickness of 10 μm (Ghadarghadar et al., 2013; Wang et al., 2002). The CAD model was then converted to a shell model for simulations in ANSYS. The boundary and the location of malleus were determined by the optical image of the TM sample. Malleus was constructed using SolidWorks as a part of the TM assigned with properties of a bone (with 10 GPa Young's modulus, and 0.2 Poisson's ratio). The outer boundary (annulus tympanicus) of the TM was fixed for all degrees of freedom (no translations or rotations), and a uniform pressure in the range of 0 kPa−1.0 kPa was applied from the medial side (negative pressure) or lateral side (positive pressure), corresponding to the pressure used in experiments.

Each meshed FEM model has nearly 10,000 4-node tetrahedral shell elements (shell-281) as shown in Fig. 3(a) and (b); the boundary determined from optical image as shown in Fig. 3(c) was used in FEM simulation. In practice, due to the continuation between epithelial layer of the TM and annulus, there is about 1–2 pixels of uncertainty for determining the boundary in the annulus area; this uncertainty induced less than 2% variation for the total area of TM. The uncertainty can be higher at the pars flaccida area. However, since the area of pars flaccida is less than 1/15 of pars tensa (Vrettakos et al., 1988) and the displacement in pars flaccida area is usually much smaller than that of pars tensa (Ghadarghadar et al., 2013), the uncertainty on the identification of the entire boundary is expected to induce less than 3% of error in the determination of volume displacement. Experimental data do not show any abrupt change of deformation in the neighborhood of pars flaccida area, therefore, only pars tensa was considered in both reconstruction and the FEM modeling. The medial and posterior views of a meshed TM model are shown in Fig. 3(a) and (b), respectively, without showing the boundary conditions and the applied pressure. Fig. 3(c) shows the medial-lateral views of the TM surface topography with boundary conditions. The outer boundary (annulus tympanicus) of the TM was fixed for all degrees of freedom (no translations or rotations) and a uniform pressure in the range of −1.0–1.0 kPa, was applied from the medial side (negative pressure) or lateral side (positive pressure), same as the

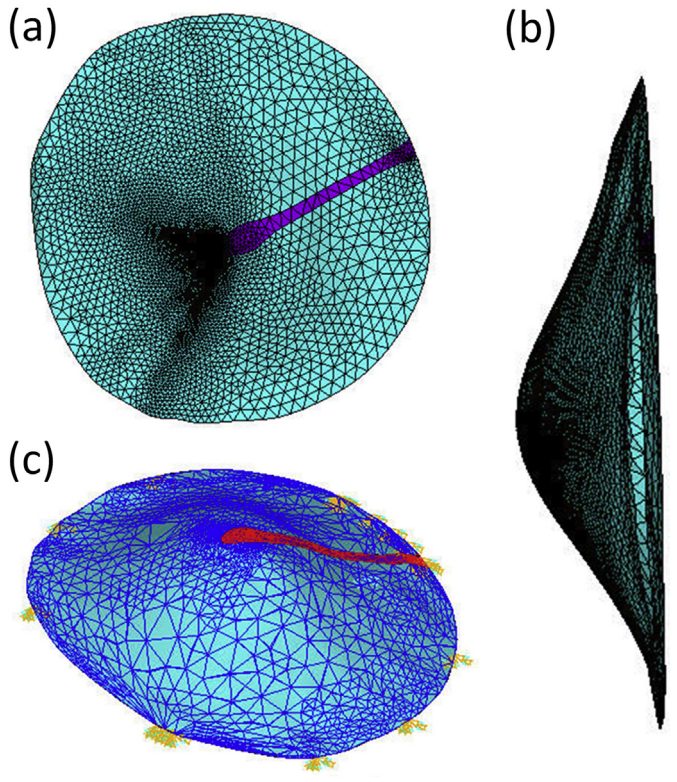


Fig. 3. Finite element model of chinchilla TM in different views. The model consists of 10,000 shell elements (shell-181). The annular ring of the TM is fixed for all degrees of freedom. The area marked in red color is the manubrium whose material properties are set as those (Young's modulus, etc.) for bones. (a). Medial-view of meshed TM; (b). Posterior view of meshed TM; (c). Boundary conditions for TM, as shown with yellow arrows. (For interpretation of the references to color in this figure legend, the reader is referred to the web version of this article.)

pressure values used in experiments.

To simulate the pressure – volume deformation response observed in experiments, FEM analysis with the use of an appropriate constitutive model was conducted. Since a TM is essentially a biomaterial in rubbery state, a hyperelastic model traditionally developed for materials in the rubbery state such as elastomers was used in this study, to describe the constitutive behavior of a chinchilla TM under tension. The pressure-volume displacement response of TM shows behavior similar to an elastomer (Aerts and Drickx, 2010), including stiffening after reaching a certain pressure, the Ogden model was used to describe the mechanical behavior of TM under large deformations. The Ogden strain energy potential is given as:

$$U = \sum_{i=1}^{N} \frac{2\mu_i}{\alpha_i}\left(\lambda_1^{\alpha_i} + \lambda_2^{\alpha_i} + \lambda_3^{\alpha_i}\right), \quad i = 1, 2, \ldots N \tag{2}$$

where N is the number of terms; λ_j (j = 1, 2, 3) are the principle stretch ratios; μ_i and α_i are constants. In this study, N was taken as 2. In order to determine the model parameters μ_i and α_i, an inverse problem-solving scheme was used by allowing the FEM simulated TM volume displacement data to match the measured values under a given pressure. The procedures are described as follows.

(1) Give vector of initial values, p containing μ_i and α_i, as $p^{\mathrm{T}} = [\mu_1, \alpha_1, \mu_2, \alpha_2]$.
(2) Generate a FEM model for the TM, consistent with the geometry of the TM under the zero-pressure state. The TM is assigned with hyperelastic parameters (Ogden model). The out-of-plane displacement (i.e., displacement perpendicular to the image plane of the camera), and height Z of each node was obtained.
(3) Interpolate nodal displacement obtained in Step 2 to the background grid with point density identical to the pixel density of images obtained in experiments using the bilinear interpolation scheme.
(4) Calculate the volume displacement from the out-of-plane displacement of the background grid, and compare it with the experimental volume displacement data, which is calculated as:

$$\Delta V = \iint_{\Omega} [z(x,y) - z_0(x,y)]\mathrm{d}x\mathrm{d}y \tag{3}$$

where, z (x,y) and z_0 (x,y) are the height profiles under a finite pressure and the zero pressure, respectively, Ω is the area enclosed by the annulus. Optimization of a cost function is used to determine the Ogden parameters using ΔV at different pressures. The cost function is defined as:

$$f = \sum_{i=1}^{M} \left(\Delta V_i^{exp} - \Delta V_i^{FEM}\right)^2 \tag{4}$$

where ΔV_i^{exp} is the volume displacement obtained in experiment under a pressurized state, ΔV_i^{FEM} is the corresponding FEM simulated volume displacement, M is the number of pressurized states.

(5) Update p using a gradient descent algorithm, and repeat Steps (1) through (4) until $f < 0.05$ mm^6. The equation for gradient descent is given as:

$$p' = p - \gamma \nabla f(p) \tag{5}$$

where γ is the learning rate, set to be 0.1, $\nabla f(p)$ is a vector of discrete form of gradient of f with 4 elements, where each element is the difference of the cost function f when one parameter in p changes by 0.1.

In this study, the initial parameters are set to the parameters for human (Cheng et al., 2007). A range of initial values in the neighborhood of this set of initial parameters has been tried and it was found that within this range, the results converge to the same solution.

3. Results

3.1. Reconstruction of the TM surface under pressure

The TM surface topography under different pressures was obtained from the micro-fringe projection system. Fig. 4 shows the pressure-volume displacement relationships for five cycles of preconditioning at small pressure levels with amplitudes less than 0.1 kPa. Since chinchilla TMs are thin and fragile, some of the TMs ruptured during the process of loading. Therefore the pressure range for those samples was smaller than other samples. The preconditioning has significantly reduced the hysteresis: the difference in volume displacement between loading and unloading is in general less than 10% after preconditioning (Fig. 4(b)). After five cycles of preconditioning, the pressure-volume displacement curves were gradually converged and the hysteresis loops became stable. It indicates that the mechanical behavior became steady, thus the TM was ready for characterization of the nonlinear elastic behavior. Fig. 5(a) shows the TM image under projected micro-fringes before reconstruction of the surface. The four sections of TM, namely superior, posterior, inferior, anterior, and umbo are shown and marked as S, P, I, A and U, respectively. Fig. 5(b) shows a typical surface height color contours of TM under the zero-pressure state from the reconstruction. Fig. 5(c) and (d) show the corresponding z-displacement, U_3 contours under pressures. For the purpose of illustration, in the interest of space, only two cases are shown here: TM under −1.0 kPa and 1.0 kPa pressures.

Under −1.0 kPa, the edge of a TM close to inferior-posterior region has nearly zero displacement. Like other rodent, the manubrium of chinchilla is a thin bony edge, with thickness decreasing from about 1.0 mm at superior of annulus to roughly 0.1 mm at umbo. However, the region of low displacement is relatively large, which covers more than 1/3 of the TM area around the manubrium. Likewise, around the annulus ring, a ring of low displacement region with width about 1.0 mm can be also observed. The maximum displacement is found to locate at the ring-shaped belt concentric with the annulus and about 1.5 mm from annulus ring covering the posterior, inferior and anterior. This probably stems from the thickness distribution of the TM, which is thicker at location around the bony boundary and thinner at location away from the bony boundary (Gea et al., 2010). Similar displacement distribution is also seen in Fig. 5(d) under positive pressure 1.0 kPa. However, the region with low displacement under a positive pressure is small around the manubrium. The displacement at location close to the annulus increases smoothly to maxima at the location about 2.5 mm away from the annulus and then gradually decreases to zero. Due to the complex cone-shape geometry, a TM under positive and negative pressures exhibits different responses.

3.2. Mechanical response of TM to various static pressures

Using Eqn (3), the pressure-volume displacement relationship can be calculated from the Z-displacement, U_3 profile. Fig. 6(a) shows the pressure as a function of the volume displacement, plotted in terms of the curves from the experimental results of ten chinchilla TMs with intact immobilized malleus-incus complex attached. It is noted that, results from some TMs have smaller range

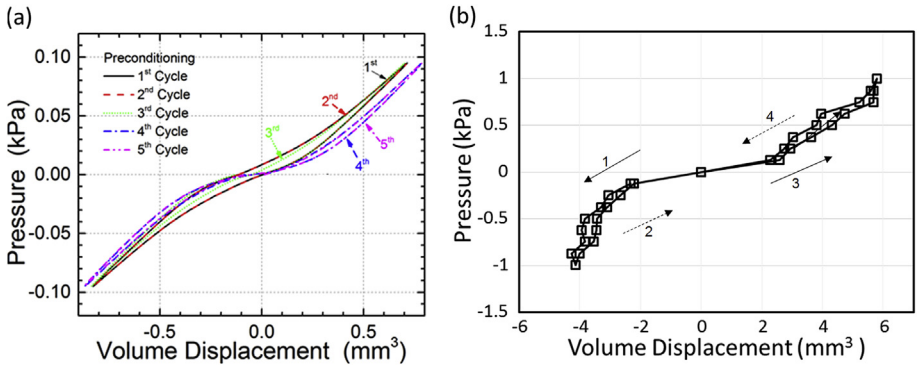


Fig. 4. Pressure-volume displacement curves. (a) Typical 5 cycles of preconditioning for a chinchilla TM. (b) Typical one cycle of loading and unloading. The sequence of loading is as follows: negative pressure was first applied on the TM (creating a vacuum from ear canal side) up to −1.0 kPa and then released to zero; subsequently, positive pressure was applied onto TM (pumping air on the ear canal side) up to 1.0 kPa and then released to zero. The loading sequence is 1-2-3-4 as shown by the arrows.

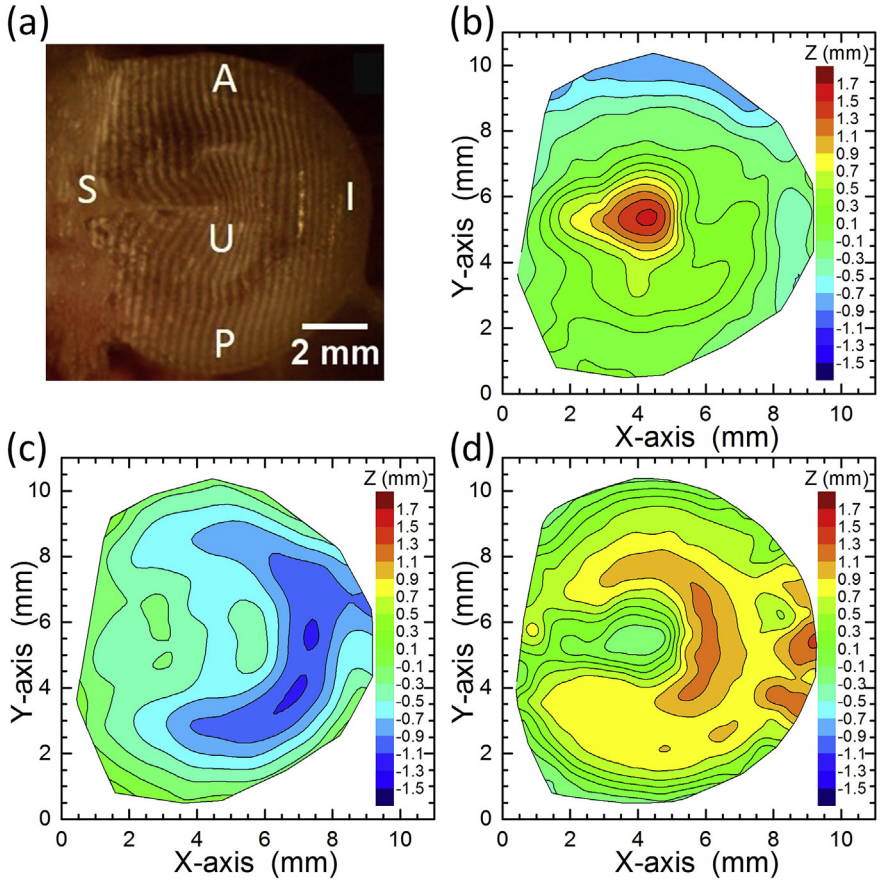


Fig. 5. Measurements of projected micro-fringes for chinchilla TM surface topography. (a). Micro-projected fringes on a chinchilla TM; (b). Height profile z (x,y) under zero pressure; (c). Z-displacement U_3 under −1.0 kPa pressure (medial side pressure is higher than lateral side pressure); (d). Z-displacement U_3 under 1.0 kPa pressure (lateral side pressure is higher than medial side pressure). Note, the reference plane is not necessarily coincident with the annular ring because the annular ring is not on the same plane. Thus there is a slight inclination in the reconstructed surface profile.

of volume displacement values due to the rupture of these TMs in experiment. To distinguish the TM samples, markers were used at certain data points. The pressure-volume displacement curves exhibit strong nonlinearity. The increasing stress with the increase of strain indicates the stiffening behavior of the chinchilla TM, and therefore the alternation of stiffness as pressure increases. This is likely due to the stiffening of the collagen fibers in the soft tissue. At the initial stage of the loading, collagen fibers are relaxed, showing a linear behavior. As the loading increases, the collagen fibers tend to align in the loading direction in response to the increasing load, to provide change in stiffness.

Due to the nearly conical geometry of TM, volume displacements show significant difference between negative and positive pressures as shown in Fig. 6. The deformation under positive pressure is larger than the deformation under negative pressure. The asymmetry of volume-displacement over positive/negative pressures is consistent with that was observed from TMs of other mammals, such as gerbil (Gea et al., 2010), cat (Funnell and

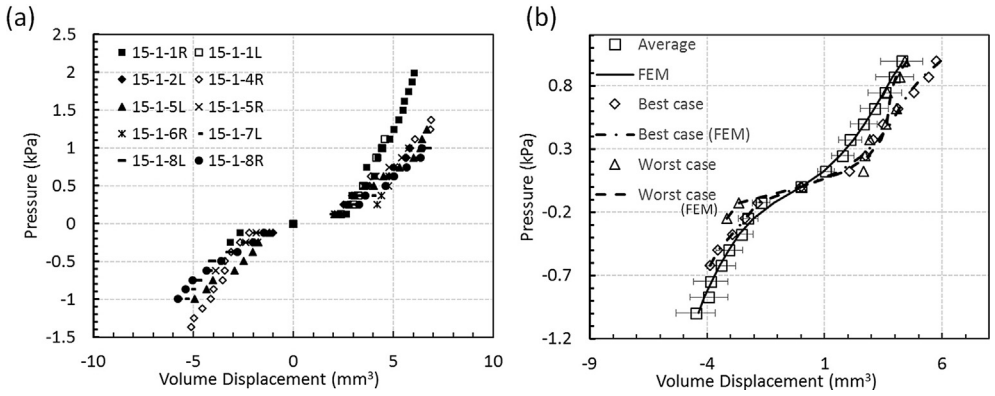


Fig. 6. Pressure-volume displacement relationships for ten chinchilla TMs under different pressures measured with the micro-fringe projection system. (a). Experimental results for10 TMs; (b). A comparison between the finite element simulation results and experimental data. The error bar represents the standard deviation from the experiments. Both best and worst fitting results are given in (b).

Decraemer, 1995), and human (Gaihede et al., 2007). Fig. 6(b) shows a curve-fitting of the average pressure-volume displacement curve between FEM results and experimental data for ten TMs. Two extreme cases are also plotted in Fig. 6(b), which are the best cases of fitting (smallest average error at each pressure point) for one of the animals and the worst case of fitting (largest average error at each pressure point) for another animal. The error is less than 10% between FEM and experimental data, indicating that the Ogden model is appropriate to describe the TM mechanical behavior. The model parameters are obtained under both positive and negative pressures. The dimensions of the TM and the material property parameters for Ogden model of each TM are listed in Table 1.

3.3. Young's modulus of TM

Since the TM is under biaxial stress state when a pressure is applied on it. An equibiaxial stress-strain relationship is used to describe the behavior of TM. The equibiaxial form of N^{th}-order Ogden model is given as (Ogden, 1972)

$$T_B = \sum_{i=1}^{N} \frac{2\mu_i}{\alpha_i}\left(\lambda_B^{\alpha_i - 1} - \lambda_B^{-2\alpha_i - 1}\right), \quad i = 1, 2, \ldots N \tag{6}$$

where T_B is the equibiaxial stress; λ_B is the equibiaxial stretch ratio, and $\lambda_B = 1 + \varepsilon_B$, with ε_B being the equibiaxial strain. Under an equibiaxial stretch, assuming incompressibility of the TM, the principal stretch ratios λ_i (i = 1, 2, 3) are given as $\lambda_1 = \lambda_2 = \lambda_B$, $\lambda_3 = \lambda_B^{-2}$. Fig. 7(a) shows the plot of the equibiaxial stress-strain relationship describing the equibiaxial state of the chinchilla TM. The tissue has a linear mechanical behavior within a small range of strain and the mechanical behavior becomes nonlinear after strain becomes larger. The TM tissue becomes stiffer when it is under higher strain. The stiffening effect is evident when the mechanical behavior of the TM is plotted in equibiaxial tangent modulus, which is defined as the derivative of equibiaxial stress with respect to equibiaxial strain from Eqn (6), given as (Thurn and Hughey, 2004)

$$\frac{dT_B}{d\varepsilon_B} = \sum_{i=1}^{N} \frac{2\mu_i}{\alpha_i}\Big[(\alpha_i - 1)(1 + \varepsilon_B)^{\alpha_i - 2} + (2\alpha_i + 1)(1 + \varepsilon_B)^{-2\alpha_i - 2}\Big], \quad i = 1, 2, \ldots N \tag{7}$$

The equibiaxial tangent modulus under biaxial stress state for the TM is shown in Fig. 7(b). The stiffening effect is observed and the mechanical behavior is linear when the strain is within 0%–5%. At strains smaller than 5%, the equibiaxial tangent modulus, which is equal to the equibiaxial modulus, is 52.8 ± 6.2 MPa.

Since uniaxial tensile test is the most commonly used test for TM measurement, for the purpose to compare our results to others' work, it is convenient to estimate the uniaxial behavior of TM with the parameters in Ogden model. The uniaxial form of N-order Ogden model is given as (Aernouts et al., 2010; Wang et al., 2002)

$$T_U = \sum_{i=1}^{N} \frac{2\mu_i}{\alpha_i}\left(\lambda_U^{\alpha_i - 1} - \lambda_U^{-0.5\alpha_i - 1}\right), \quad i = 1, 2, \ldots N \tag{8}$$

where T_U is the uniaxial stress; λ_U is the uniaxial stretch ratio, and $\lambda_U = 1 + \varepsilon_U$, with ε_U being the axial strain. Under uniaxial stretch, assuming incompressibility of the TM, the principal stretch ratios λ_i

Table 1
Dimensions of chinchilla TMs and parameters for the 2nd-order Ogden hyperelastic model.

Sample number	Superior-inferior diameter (mm)	Anterior-posterior diameter (mm)	μ_1 (MPa)	α_1	μ_2 (MPa)	α_2
15-1-1L	7.66	8.89	1.4	4.3	7.8	−3.6
15-1-1R	7.71	8.08	1.6	3.7	8.7	−4.1
15-1-2L	8.68	8.59	1.0	4.3	5.7	−4.0
15-1-4R	7.37	7.93	1.2	4.5	7.8	−4.4
15-1-5L	7.57	8.53	1.3	4.1	7.2	−4.9
15-1-5R	6.84	7.97	1.2	3.4	7.9	−4.0
15-1-6R	7.99	9.15	1.0	3.1	6.9	−5.0
15-1-7L	7.65	8.42	1.1	3.3	6.6	−5.0
15-1-8L	7.56	8.76	1.1	4.2	6.7	−4.7
15-1-8R	7.49	9.08	1.0	3.9	6.2	−3.8
Average	7.65	8.54	1.2 ± 0.2	3.9 ± 0.4	7.1 ± 0.8	−4.3 ± 0.5

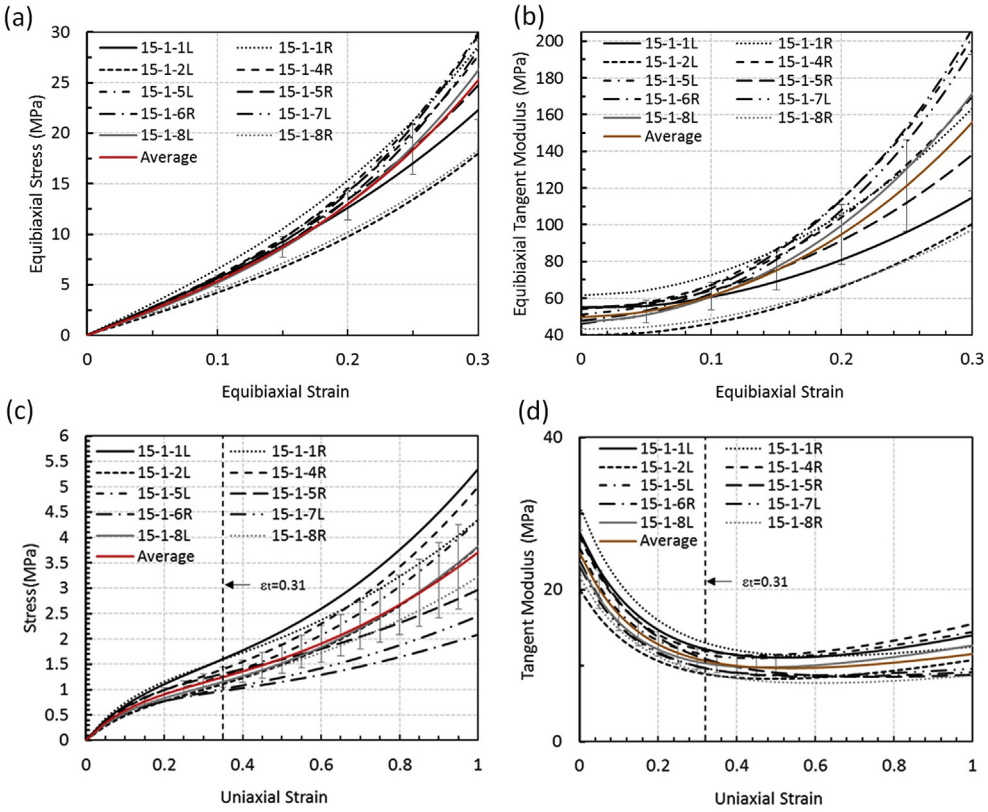


Fig. 7. Mechanical response and mechanical properties of all ten chinchilla TMs derided from the FEM analysis using a second order Ogden model under: (a) Equibiaxial stress-strain curves; (b) Biaxial modulus; (c) Uniaxial tensile stress-strain curves; (d) Tangent modulus of chinchilla TMs. The error bar represents standard deviation. The dash line in (c) and (d) shows the actual maximum strain in the experiment.

($i = 1, 2, 3$) are given as $\lambda_1 = \lambda_U$, $\lambda_2 = \lambda_3 = \lambda_U^{-0.5}$.

The Young's modulus is defined as the slope in the linear region of the uniaxial stress-strain curve under small deformations. The slope of the stress-strain curve at any point is the tangent modulus. The Young's modulus and the tangent modulus are identical at the initial, linear portion of a stress-strain curve. In the case of a hyperelastic material, the tangent modulus, E_t, can be obtained by taking derivative of stress with respect to strain from Eqn (8)

$$E_t = \frac{dT_U}{d\varepsilon_U} = \sum_{i=1}^{N} \frac{2\mu_i}{\alpha_i}\left[(\alpha_i - 1)(1+\varepsilon_U)^{\alpha_i - 2} + (0.5\alpha_i + 1)(1+\varepsilon_U)^{-0.5\alpha_i - 2}\right], \quad i = 1, 2, \ldots, N \tag{9}$$

With known material parameters, Eqn (8) is plotted in Fig. 7(c). The uniaxial stress-strain curve of the chinchilla TM, which represents the mechanical behavior under a tensile test, also exhibits a strong nonlinearity. But the trend is different from that under equibiaxial state: the stiffening effect starts at a much higher strain level (~100%), which will be higher than the strain (~31%) used in the current experiment. In Fig. 7 (d), the tangent modulus in general decreases with the increase of strain up to 31% of axial strain. At 31% strain, which is the maximum strain of the TM determined by FEM model when 1.0 kPa air pressure was applied on the TM, the maximum stress reaches 1.1 MPa. Eqn (9) is plotted in Fig. 7(d), showing the tangent modulus as a function of strain for 10 chinchilla TMs, and the average. At a strain close to zero, the average tangent modulus is 25 MPa, and it decreases to 11 MPa at 31%. The average tangent modulus, at strains less than 25%, is chosen as the representative Young's modulus. Therefore, the average value of approximately 19 MPa is quoted as the Young's modulus. For comparison equibiaxial tangent modulus and Young's modulus values at different strains are given in Table 2. Under equibiaxial stress state the modulus is consistently higher than the corresponding modulus under uniaxial stress state.

4. Discussions

The mechanical properties of TM are difficult to measure due to its small size. The traditional measurement using strips cut from the intact TM induces not only damage to the TM structures, but also leads to difficulty in controlling the exact dimensions and extension of a sample. For example, in tensile test, the gauge length to width ratio was usually chosen as about 3 (Cheng et al., 2007), which is less than the standard value used in the material tensile testing (typically 5) (ASTM E8/E8M-13a standard, 2015). Also, it is a challenge to clamp the soft tissue without inducing boundary effects. An *in-situ* indentation technique was proposed on the TM, to avoid cutting of the TM (Aernouts et al., 2010, 2012; Aernouts and Drickx, 2012a,b). However, that approach is a contact method and does not yield the TM mechanical responses under pressure directly. The present approach is a non-contact method, which does not induce any local damage to the TM structures under test; and air pressure is directly applied as loading. Instead of matching directly calculated deformation field with its experimental counterpart at a given pressure. In this work, volume displacement was used to determine the nonlinear mechanical properties of a TM

Table 2
Equibiaxial and uniaxial modulus values for 10 chinchilla TMs at different strains.

Stain (%)	0	5	10	15	20	25	30	Average
Equibiaxial Modulus (MPa)	49.6 ± 6.0	52.8 ± 6.2	61.3 ± 7.5	75.1 ± 10.8	94.8 ± 16.4	121.3 ± 26.1	155.7 ± 37.2	87.2 ± 14.4
Uniaxial Modulus (MPa)	24.8 ± 3.0	20.0 ± 2.5	16.7 ± 2.1	14.4 ± 1.8	12.8 ± 1.6	11.7 ± 1.4	10.9 ± 1.3	15.9 ± 2.0

under a series of pressure states from negative pressures to positive pressures. Because the simulations were based on the assumption that chinchilla TM consists of a homogeneous, isotropic material, and its thickness is uniform over the entire pars tensa, the Young's modulus obtained in this study represents an overall effective Young's modulus. In the actual situation, due to the nonuniform distribution of the collagen fibers over TM, the variation of thickness of TM at different locations (Kuypers et al., 2006; Kuypers et al., 2005; van der Jeught et al., 2013) was not considered.

In addition, the mechanical properties can also change with locations. Therefore, even though the model was developed from a 3D surface reconstruction of the specimen, there are still pronounced discrepancies between simulations and experiments at different locations. Shape difference of chinchilla TM between FEM simulations and experiments is given in Fig. 8(a) and (b), respectively, at two extreme loading cases under 1.0 kPa and −1.0 kPa. Fig. 8(c) and (d) show the error map, which is determined by subtracting the experimental z-height data from the corresponding FEM simulated height data at 1.0 kPa and −1.0 kPa, respectively.

Although at some small local region, a relatively large error as high as 0.15 mm occurs, most area has error less than 0.017 mm. Overall a reasonably good agreement has been reached. It is seen that discrepancy is generally small in areas with small deformations and high in areas with large deformations. That observation is similar to what was reported in a rat model (Ghadarghadar et al., 2013). Despite of the discrepancy in local displacements, a good agreement is achieved between computational volume displacements and the corresponding experimental values. Fig. 8(a) and (b) show comparison of shape profile in Z-height between FEM simulation and experimental data under pressures 1.0 kPa and −1.0 kPa, respectively, along with the profile along the posterior-anterior section shown in black dash line, through umbo, and along superior-inferior shown as red dash line, which is 2.0 mm from umbo. The small positive and negative errors induced by thickness and properties nonuniformity are reduced through the summation process for the calculation of volume displacement. Therefore in order to reduce the complexity to determine mechanical properties using a hybrid approach, the use of volume displacement for optimization has certain benefit.

In the simulations, the thickness of TM was set as 10 μm. The value is the average from the thickness measured at different locations of chinchilla TM based on histology results (Vrettakos et al., 1988). It is noted that Young's modulus value of TM from FEM analysis is very sensitive to the TM thickness, especially when the thickness is small. The Young's modulus value increases as the assumed thickness of TM decreases. If the thickness of TM was set as

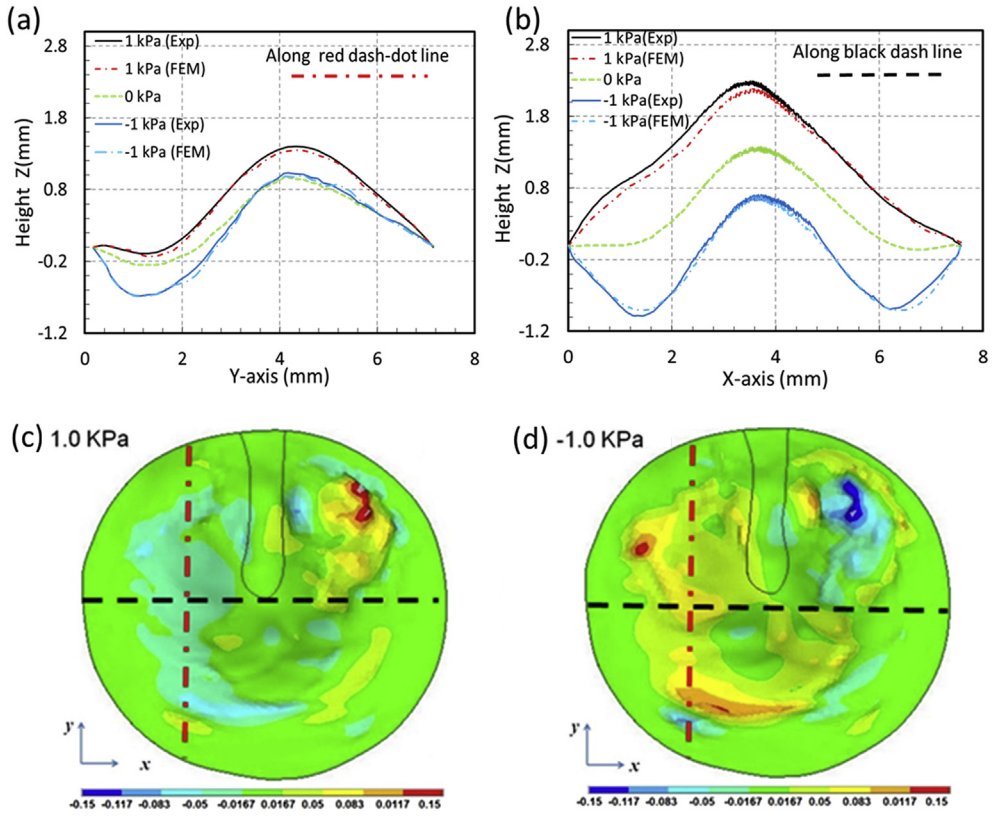


Fig. 8. A comparison of shape profile calculated as z-coordination height between FEM simulation and experimental data at ±1.0 kPa (a). The experimental and FEM simulated Z height profiles along posterior-anterior section (as shown black dash line, through umbo); (b). Experimental and FEM simulated Z height profiles along superior-inferior (as shown red dash line, 2.0 mm off umbo). (c) Error map (FEM simulated map of height subtracted by experimental map of height) at 1.0 kPa; (d) Error map at −1.0 kPa; A reasonably good agreement has been reached. (For interpretation of the references to color in this figure legend, the reader is referred to the web version of this article.)

5 μm, the Young's modulus would be on the 54 MPa, which is three times of the current value. This could be responsible for the large scatter in literature data for TM mechanical properties. In literature, TM thickness was usually assumed to be uniform. Nevertheless, the range of chinchilla TM thickness is often measured from 8 μm to 12 μm. Within this range, the variation of Young's modulus is only about 15%, which is an acceptable range of fluctuation.

Fringe projection was utilized in this study due to its ability for full-field surface topography measurement, high accuracy (about 0.2% out-of-plane error) (Liang, 2010) and acceptable resolution (about 15 μm) for the relatively large deformation induced by pressure. As compared with other Moiré techniques, such as shadow moiré, projection moiré and reflection moiré, it does not require precise alignment of optical setup. It also does not require an accurate control system for phase-shifting, which is a benefit from a virtual phase-shifting applied on a single experimental image through the computerized processing. The aforementioned benefits show that micro-fringe projection technique also has potential for measurement of dynamic properties with the use of a high speed camera.

Young's modulus data in literature on chinchilla TM is sparse, we therefore compare Young's modulus, obtained in this study with measurement obtained for other animals. For rodent TM, using an indentation technique, Young's modulus of rat was measured as around 21 MPa, which is close to the average Young's modulus obtained in this study. Young's moduli of TM of other animals around the size of chinchilla were also reported in a few of papers. Young's modulus of rabbit TM was reported as 30 MPa (Aernouts et al., 2010); and for cat the Young's modulus was estimated as 100–400 MPa (Fay et al., 2005). The diameter of chinchilla TM is similar to human TM. For human, Young's moduli were reported under different situations. The 20 MPa was reported under an *in-vivo* condition (von Békésy, 1960), similar values were obtained on TM samples along radial and circumferential directions (Luo et al., 2009a,b) under high strain rates. The Young's modulus of human TM measured by uniaxial tension of strips cut from TM was measured to be at 10 MPa and 23 MPa, respectively (Decraemer et al., 1980; Kirikae, 1960). It is noted that, cutting TM breaks the collagen fibers, which subsequently shrink. This could induce variations from one specimen to another, causing a large variation of measurement results. Direct measurement of the mechanical properties from the entire pars tensa TM sample can maintain the integrity of TM and yields more reliable data. To the best of our knowledge there was only one study on full-field intact rat TM reported (Ghadarghadar et al., 2013). Young's storage and loss modulus values of intact TM have been measured at frequency 0.1 Hz, they are 40 MPa and 19 MPa, respectively at frequency 0.1 Hz (Ghadarghadar et al., 2013). The results from this study show that the Young's modulus of chinchilla TM is in the range of 11–30 MPa at strains below 25%, slightly higher than the reported values for human TM. While data has been reported for elastic coefficients determined from numerous TMs, including human TM and guinea pig TM (Békéy, 1949; Gan et al., 2010; Guan and Gan, 2013; Zhang and Gan, 2013a,b), the stress-strain curve of chinchilla TM was not reported in literature, especially when it is measured from the intact TM. This study fills the gap by providing the nonlinear stress-strain relationship, including Young's modulus of chinchilla TM, measured at 19.0 ± 4.5 MPa, and tangent modulus at strains up to 31%.

5. Conclusion

The nonlinear mechanical response of chinchilla TM was determined using micro-fringe projection technique. Quasi-static air pressure was applied to a chinchilla TM at the lateral side through the ear canal inside the bulla. A micro-fringe projection method was used to measure the surface topography of the TM. The volume displacement of the TM was used as input to a finite element model for simulation. The Ogden hyperelastic model was used to describe the constitutive behavior of the TM in FEM for simulations. An inverse method was used to allow the pressure-volume displacement relationship simulated by FEM to match with the experimental results. The model parameters were then used to describe the mechanical behavior of chinchilla TM, and stress-strain curve under both equibiaxial and uniaxial stress states. Under equibiaxial stress state, the equibiaxial tangent modulus increases with the increase of strain, while under uniaxial stress state, the tangent modulus decreases with the increase of strain. The Young's modulus of the chinchilla TMs was determined to be approximately 19 MPa, up to a strain level of 25%. As strain increases from 0 to 31%, the tangent modulus decreases from 25 MPa to 11 MPa. The maximum stress experienced by the TM used in these experiments reaches 1.1 MPa.

Acknowledgments

We acknowledge the support of NIH R01DC011585, DOD W81XWH-14-1-0228, DOD W81XWH-13-MOMJPC5-IPPEHA, and NSF CMMI-1031829, CMMI-1132174, ECCS-1307997 and NSF IIP-1522559. Lu acknowledges the Louis A. Beecherl Jr., Chair for additional support.

References

Aernouts, J., Dirckx, J.J.J., 2012a. Static versus dynamic gerbil tympanic membrane elasticity: derivation of the complex modulus. Biomech. Model Mechan. 11, 829–840.
Aernouts, J., Dirckx, J.J.J., 2012b. Viscoelastic properties of gerbil tympanic membrane at very low frequencies. J. Biomech. 45, 919–924.
Aernouts, J., Soons, J.A.M., Dirckx, J.J.J., 2010. Quantification of tympanic membrane elasticity parameters from in situ point indentation measurements: validation and preliminary study. Hear. Res. 263, 177–182.
Aernouts, J., Aerts, J.R.M., Dirckx, J.J.J., 2012. Mechanical properties of human tympanic membrane in the quasi-static regime from in situ point indentation measurements. Hear. Res. 290, 45–54.
Aerts, J.R.M., Dirckx, J.J.J., 2010. Nonlinearity in eardrum vibration as a function of frequency and sound pressure. Hear. Res. 263, 26–32.
ASTM E8/E8M-13a, 2015. Standard Test Methods for Tension Testing of Metallic Materials. ASTM International, West Conshohocken, PA.
Békéy, G.V., 1949. The structure of the middle ear and the hearing of one's own voice by bone conduction. J. Acoust. Soc. Am. 21, 217–232.
Buytaert, J.A.N., Dirckx, J.J.J., 2009. Tomographic imaging of macroscopic biomedical objects in high resolution and three dimensions using orthogonal-plane fluorescence optical sectioning. Appl. Opt. 48, 941–948.
Cheng, T., Dai, C.K., Gan, R.Z., 2007. Viscoelastic properties of human tympanic membrane. Ann. Biomed. Eng. 35, 305–314.
Daphalapurkar, N.R., Dai, C.K., Gan, R.Z., Lu, H.B., 2009. Characterization of the linearly viscoelastlic behavior of human tympanic membrane by nano-indentation. J. Mech. Behav. Biomed. 2, 82–92.
De Greef, D., Soons, J., Dirckx, J.J.J., 2014a. Digital stroboscopic holography setup for deformation measurement at both quasi-static and acoustic frequencies. Int. J. Optomech. 8, 275–291.
De Greef, D., Aernouts, J., Aerts, J., Cheng, J.T., Horwitz, R., Rosowski, J.J., Joris, J.J., Dirckx, J.J.J., 2014b. Viscoelastic properties of the human tympanic membrane studied with stroboscopic holography and finite element modeling. Hear. Res. 312, 69–80.
Decraemer, W.F., Maes, M.A., Vanhuyse, V.J., 1980. An elastic stress-strain relation for soft biological tissues based on a structural model. J. Biomech. 13, 463–468.
Dirckx, J.J.J., Decraemer, W.F., 1991. Human tympanic membrane deformation under static pressure. Hear. Res. 51, 93–106.
Dirckx, J.J.J., Decraemer, W.F., 1997. Coating techniques in optical interferometric metrology. Appl. Opt. 36, 2776–2782.
Fay, J., Puria, S., Decraemer, W.F., Steele, C., 2005. Three approaches for estimating the elastic modulus of the tympanic membrane. J. Biomech. 38, 1807–1815.
Fung, Y.C., 1993. Biomechanics: Mechanical Properties of Living Tissues, second ed. Springer, New York.
Funnell, W.R.J., Decraemer, W.F., 1995. On the incorperation of Moire shape measurements in finite-element models of the cat eardrum. J. Acoust. Soc. Am. 100, 925–932.
Gaihede, M., Liao, D., Gregersen, H., 2007. In vivo arealmodulus of elasticity estimation of the human tympanic membrane system: modelling of middle ear mechanical function in normal young and aged ears. Phys. Med. Biol. 52, 803–814.

Gan, R., Dai, C., Wang, X., Nakmali, D., Wood, M.W., 2010. A totally implantable hearing system - design and function characterization in 3D computational model and temporal bones. Hear. Res. 263, 138–144.
Gea, S.L.R., Decraemer, W.F., Funnell, W.R.J., Dirckx, J.J., Maier, H., 2010. Tympanic membrane boundary deformations derived from static displacements observed with computerize tomography in human and gerbil. J. Assoc. Res. Otolaryngol. 11, 1–17.
Ghadarghadar, N., Agrawal, S.K., Samani, A., Ladak, H.M., 2013. Estimation of the quasi-static Young's modulus of the eardrum using a pressurization technique. Comput. Meth Prog. Biomed. 110, 231–239.
Ghiglia, D.C., Pritt, M.D., 1998. Two-dimensional Phase Unwrapping, Theory, Algorithms, and Software. John Wiley and Sons, New York.
Guan, X., Gan, R., 2013. Mechanisms of tympanic membrane and incus mobility loss in acute otitis media model of guinea pig. J. Assoc. Res. Otolaryngol. 14, 295–307.
Hesabgar, S.M., Marshall, H., Agrawal, S.K., Samani, A., Ladak, H.M., 2010. Measuring the quasi-static Young's modulus of the eardrum using an indentation technique. Hear. Res. 263, 168–176.
Huang, G., Daphalapurkar, N.P., Gan, R.Z., Lu, H.B., 2008. A method for measuring linearly viscoelastic properties of human tympanic membrane using nano-indentation. J. Biomech. Eng-Trans ASME 130, 014501.
Kirikae, I., 1960. The Structure and Function of Middle Ear. University of Tokyo Press, Tokyo.
Kuypers, L.C., Decraemer, W.F., Dirckx, J.J.J., Timmermans, J.P., 2005. Thickness distribution of fresh eardrums of cat obtained with confocal microscopy. J. Assoc. Res. Otolaryngol. 6, 223–233.
Kuypers, L.C., Decraemer, W.F., Dirckx, J.J.J., 2006. Thickness distribution of fresh and preserved human eardrums measured with confocal microscopy. Otol. Neurotol. 27, 256–264.
Ladak, H.M., Decraemer, W.F., Dirckx, J.J.J., Funnell, W.R.J., 2004. Response of the cat eardrum to static pressures: mobile versus immobile malleus. J. Acoust. Soc. Am. 116, 3008–3021.
Ladak, H.M., Funnell, W.R.J., Decraemer, W.F., Dirckx, J.J.J., 2006. A geometrically nonlinear finite-element model of the cat eardrum. J. Acoust. Soc. Am. 119, 2859–2868.
Lee, C.Y., Rosowski, J.J., 2001. Effects of middle-ear static pressure on pars tensa and pars flaccida of gerbil ears. Hear. Res. 153, 146–163.
Liang, J., 2010. Determination of the Mechanical Properties of Guinea Pig Tympanic Membrane Using Combined Fringe Projection and Simulations (Master thesis). Oklahoma State University, Stillwater, OK, USA.
Luo, H., Dai, C., Gan, R., Lu, H., 2009a. Measurement of Young's modulus of human tympanic membrane at high strain rates. J. Biomech. Eng. Trans. ASME 131, 064501.
Luo, H., Lu, H., Dai, C., Gan, R., 2009b. A comparison of Young's modulus for normal and diseased human eardrums at high strain rates. Int. J. Exp. Comput. Biomech. 1, 1–22.
Luo, H., Jiang, S., Nakmali, D.U., Gan, R.Z., Lu, H., 2016. Mechanical properties of a human eardrum at high strain rates after exposure to blast waves. J. Dyn. Behav. Mater. 2, 59–73.
O'Connor, K.N., Tam, M., Blevins, N.H., Puria, S., 2008. Tympanic membrane collagen fibers: a key to high-frequency sound conduction. Laryngoscope 118, 483–490.
Ogden, R.W., 1972. Large deformation isotropic elasticity – on the correlation of theory and experiment for incompressible rubberlike solids. Proc. Roy. Soc. Lon. A Math. Phys. Sci. 326, 565–584.
Ortiz, M.H., 2004. Novel Development of Moire Techniques for Industrial Application. University of Sheffield.
Ortiz, M.H., Patterson, E.A., 2003. On the industrial applications of Moire and fringe projection techniques. Strain 39, 95–100.
Ortiz, M.H., Patterson, E.A., 2005. Location and shape measurement using a portable fringe projection system. Exp. Mech. 45, 197–204.
Ritenour, A.E., Wickley, A., Ritenour, J.S., Kriete, B.R., Blackbourne, L.H., Holcomb, J.B., Wade, C.E., 2008. Tympanic membrane perforation and hearing loss from blast overpressure in operation enduring freedom and operation Iraqi freedom wounded. J. Trauma 64, 174–178.
Rosowski, J.J., Lee, C.Y., 2002. The effect of immobilizing the gerbil's pars flaccida on the middle-ear's response to static pressure. Hear. Res. 174, 183–195.
Rosowski, J.J., Nakajima, H.H., Cheng, J.T., 2014. Current topics in the study of sound conduction to the inner ear, Chapter 26. In: Popper, A.N., Fay, R.R. (Eds.), Perspectives on Auditory Research, Handbook of Auditory Research, vol. 50. Springer, pp. 493–511.
Salamati, E., Agrawal, S.K., Samani, A., Ladak, H.M., 2012. Estimation of the orthotropic elastic properties of the rat eardrum. J. Med. Biol. Eng. 32, 225–234.
Soons, J.A.M., Aernouts, J., Dirckx, J.J.J., 2010. Elasticity modulus of rabbit middle ear ossicles determined by a novel micro-indentation technique. Hear. Res. 263, 33–37.
Thornton, J.L., Chevallier, K.M., Koka, K., Gabbard, S.A., Tollin, D., 2013. Conductive hearing loss induced by experimental middle-ear effusion in a chinchilla model reveals impaired tympanic membrane-couple ossicular chain movement. J. Assoc. Res. Otolaryngol. 14, 451–465.
Thurn, J., Hughey, M.P., 2004. Evaluation of film biaxial modulus and coefficient of thermal expansion from thermoelastic film stress measurements. J. Appl. Phys. 95, 7892.
Van der Jeught, S., Dirckx, J.J.J., Aerts, J.R.M., Bradu, A., Podoleanu, A.G., Buytaert, J.A.N., 2013. Full-field thickness distribution of human tympanic membrane obtained with optical coherence tomography. J. Assoc. Res. Otolaryngol. 14, 483–494.
Volandri, G., Di Puccio, F., Forte, P., Carmignani, C., 2011. Biomechanics of the tympanic membrane. J. Biomech. 44, 1219–1236.
von Békésy, G., 1960. Experiments in Hearing. McGraw-Hill Book Company, New York.
von Unge, M., Dircks, J.J., 2009. Functional effects of repeated pressure loads upon the tympanic membrane: mechanical stiffness measurements after simulated habitual sniffing. Eur. Arch. Oto-Rhino-L 266, 1219–1224.
von Unge, M., Decraemer, W.F., Baggersjoback, D., Dirckx, J.J., 1993. Displacement of the gerbil tympanic membrane under static pressure variations measured with a real-time differential Moire interferometer. Hear. Res. 70, 229–242.
Vrettakos, P.A., Dear, S.P., Saunders, J.C., 1988. Middle ear structure in the chinchilla: a quantitative study. Am. J. Otolaryngol. 9, 58–67.
Wang, B., Lu, H., Kim, G., 2002. A damage model for the fatigue life of elastomeric materials. Mech. Mater 34, 475–483.
Wang, X., Cheng, T., Gan, R., 2007. Finite-element analysis of middle-ear pressure effects on static and dynamic behavior of human ear. J. Acoust. Soc. Am. 122, 906–917.
Zhang, X., Gan, R., 2010. Dynamic properties of human tympanic membrane - experimental measurement and modelling analysis. Int. J. Exp. Comput. Biomech. 1, 252–270.
Zhang, X., Gan, R., 2013a. Finite element modeling of energy absorbance in normal and disordered human ears. Hear. Res. 301, 146–155.
Zhang, X., Gan, R., 2013b. Dynamic properties of human tympanic membrane based on frequency-temperature superposition. Ann. Biomed. Eng. 41, 205–214.

Biomech Model Mechanobiol (2016) 15:1263–1277
DOI 10.1007/s10237-016-0758-5

ORIGINAL PAPER

3D finite element model of the chinchilla ear for characterizing middle ear functions

Xuelin Wang[1,2] · **Rong Z. Gan**[1]

Received: 28 May 2015 / Accepted: 5 January 2016 / Published online: 19 January 2016
© Springer-Verlag Berlin Heidelberg 2016

Abstract Chinchilla is a commonly used animal model for research of sound transmission through the ear. Experimental measurements of the middle ear transfer function in chinchillas have shown that the middle ear cavity greatly affects the tympanic membrane (TM) and stapes footplate (FP) displacements. However, there is no finite element (FE) model of the chinchilla ear available in the literature to characterize the middle ear functions with the anatomical features of the chinchilla ear. This paper reports a recently completed 3D FE model of the chinchilla ear based on X-ray micro-computed tomography images of a chinchilla bulla. The model consisted of the ear canal, TM, middle ear ossicles and suspensory ligaments, and the middle ear cavity. Two boundary conditions of the middle ear cavity wall were simulated in the model as the rigid structure and the partially flexible surface, and the acoustic-mechanical coupled analysis was conducted with these two conditions to characterize the middle ear function. The model results were compared with experimental measurements reported in the literature including the TM and FP displacements and the middle ear input admittance in chinchilla ear. An application of this model was presented to identify the acoustic role of the middle ear septa—a unique feature of chinchilla middle ear cavity. This study provides the first 3D FE model of the chinchilla ear for characterizing the middle ear functions through the acoustic-mechanical coupled FE analysis.

Keywords Middle ear · Fluid–structure interaction · Finite element model · Biomechanics of hearing

1 Introduction

Chinchilla is a commonly used animal model in hearing research. The chinchilla ear has a large tympanic membrane (TM), ossicular dimensions and middle ear space for an animal of its size. The chinchilla's range of hearing is similar to that of humans (Vrettakos et al. 1988; Rosowski et al. 2006). Experiments have been conducted to identify the acoustic and mechanical properties of chinchilla ears for sound transmission (Browning and Granich 1978; Hanamure and Lim 1987; Vrettakos et al. 1988; Ruggero et al. 1990; Rosowski et al. 2006; Ravicz and Rosowski 2013; Wang et al. 2015).

Ruggero et al. (1990) reported the vibration measurements of the malleus and stapes using the Mössbauer technique in chinchillas and assessed the effects of opened middle ear cavity on ossicular motion. Rosowski et al. (2006) investigated the contributions of different middle ear components to middle ear admittance in chinchillas. Their results showed that the middle ear admittance curve had a narrow notch near 2600 Hz under the experimentally vented cavity condition. Ravicz and Rosowski (2012, 2013) further presented the middle ear velocity transfer function and cochlear input admittance in chinchillas with openings in the bulla. Recently, Guan et al. (2014) reported the effects of acute otitis media on mobility of chinchilla TM. In their control experiment, the middle ear cavity was vented before the measurements, and a notch of TM displacement at about 2400 Hz was observed. These

✉ Rong Z. Gan
rgan@ou.edu

[1] School of Aerospace and Mechanical Engineering and Biomedical Engineering Center, University of Oklahoma, 865 Asp Avenue, Room 200, Norman, OK 73019, USA

[2] School of Mechanical Engineering and Science, Huazhong University of Science and Technology, Wuhan, China

published experimental studies suggested that the middle ear cavity boundary condition extensively affects middle ear transfer function in chinchilla ears. In addition to the middle ear cavity boundary condition, the configuration of the middle ear air space was shown to have a significant effect on the middle ear resonance. Guinan and Peake (1967), Rosowski et al. (2000) and Tuck-Lee et al. (2008) investigated the role of septum in functions of the middle ear in cat, but no such studies have yet been reported for the chinchilla.

To fully understand the measurements of TM and stapes footplate (FP) vibrations in chinchilla, the anatomy and function relationship must be established through theoretical analysis. Songer and Rosowski (2007) proposed a transmission matrix method to study the chinchilla middle ear mechanics based on the experimental data obtained in the open middle ear cavity. The model was able to replicate some experimental data of opened cavity, but it simplified the complex middle ear with very limited degrees of freedom, lacking the detailed middle ear anatomical information and material properties. The finite element (FE) model simulates the ear anatomy precisely, and the sound transmission through middle ear ossicles can be analyzed by incorporating middle ear components with mechanical properties and boundary conditions of the middle ear cavity (Gan et al. 2004; Wang et al. 2014).

There are several animal FE models of the ear published in the literature, such as cat (Ladak and Funnel 1996; Tuck-Lee et al. 2008), gerbil (Elkhouri et al. 2006) and guinea pig (Koike et al. 2002). However, there is no FE model of the chinchilla ear reported in the literature. The chinchilla ear has a few distinctive features from other rodents, such as large TM size, exceptionally heavy ossicles relative to skull mass (Nummela 1995), and large middle ear air space divided into multiple sub-cavities (Browning and Granich 1978; Rosowski et al. 2006). The difference in the anatomical structure in the middle ear cavity of chinchilla from other species would logically lead to a specialization in the middle ear function in relation to cavity conditions.

This paper reports a recently completed 3D FE model of the chinchilla ear based on X-ray micro-computed tomography (μCT) images. The model consisted of the bony external ear canal, TM, middle ear ossicles and suspensory ligaments, and the middle ear cavity. Two boundary conditions of the middle ear cavity wall were simulated in the model as the rigid structure and the partially flexible structure to investigate the acoustic-mechanical coupled characteristics of the chinchilla middle ear. The FE model was validated with experimental measurements reported in the literature. As an application of the model, acoustic function of septa was identified by complete and partial removal of the septa. This study provides the first 3D FE model of the chinchilla ear for characterizing middle ear function through the acoustic-mechanical coupled FE analysis.

2 Methods

2.1 3D reconstruction of chinchilla bulla

An adult chinchilla (Chinchilla lanigera) was decapitated after anesthesia overdose euthanasia. The ear canals were excised, and the bullae were bilaterally removed. The left bulla was processed for X-ray micro-computed tomography (μCT) scanning, and the right bulla was dissected for visual observation of middle ear structure under a light microscope. The study protocol was approved by the Institutional Animal Care and Use Committee of the University of Oklahoma and met the guidelines of the National Institutes of Health.

The left bulla was trimmed to fit in a cylindrical scan container 20 mm in diameter. The bulla inside the container was scanned at the Skyscan 1127 μCT (Skyscan, Belgium) at the resolution of 13.4 μm. A total of 2040 μCT images covering the entire bulla were collected as section images. Figure 1a shows a typical μCT image of the chinchilla bulla including the outer ear canal, eardrum, manubrium, middle ear cavity and cochlear bony wall.

A total of 519 μCT images that contained the entire middle ear cavity and cochlea were segmented in Amira software (Visage imaging, Inc.) and served as the information source for 2D geometry contours. At first, the ear canal, eardrum, ossicular chain, and interior wall of the middle ear cavity were identified and generated from the contours or object boundaries using the SurfaceGen function in Amira. The segmentation was done manually for the selected sections. The marching cubes algorithm in Amira was used for extracting polygonal meshes and creating closed surfaces. The ear canal was truncated about 4.2 mm from the tympanic ring. Figure 1b displays the medial view of the chinchilla left bulla in Amira with the surface triangulation meshes.

Considering the complex internal bonny structures of the bulla, we performed visual observation of the space and shape of the internal structures within the bulla to identify the anatomical details in the object images. As an example of the visual observation, Fig. 2 displays the lateral view of the chinchilla right temporal bone after the lateral bony wall of the bulla was removed to exhibit the region surrounding the TM.

Table 1 lists characteristic dimensions of the chinchilla middle ear including those of the ear canal, TM, malleus-incus complex, stapes, and middle ear cavity. Note that the model of the cochlea was not included in this paper for the sake of conciseness and to avoid distracting from the focus on the middle ear.

2.2 FE model of middle ear components

All surfaces of the geometry model built in Amira were translated into HyperMesh (Altair Computing, Inc., Troy, MI) to

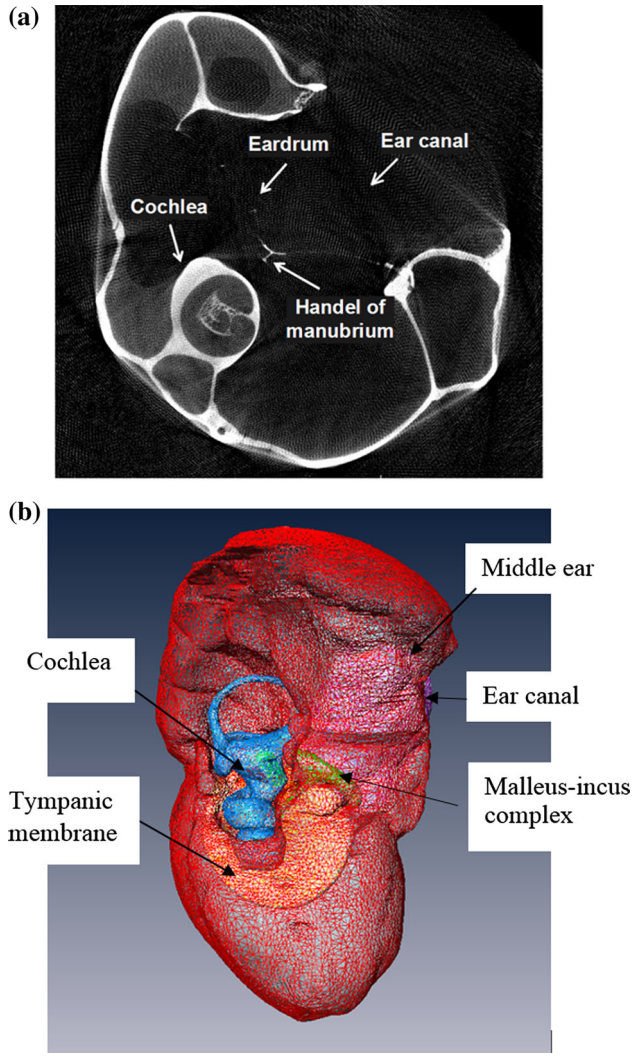


Fig. 1 A typical μCT image and the 3D geometrical model of a chinchilla left ear. **a** A μCT image of the chinchilla bulla, showing a portion of the outer ear canal, eardrum, manubrium, middle ear cavity and cochlea. **b** Lateral view of the 3D model of chinchilla middle ear and cochlea reconstructed from μCT images

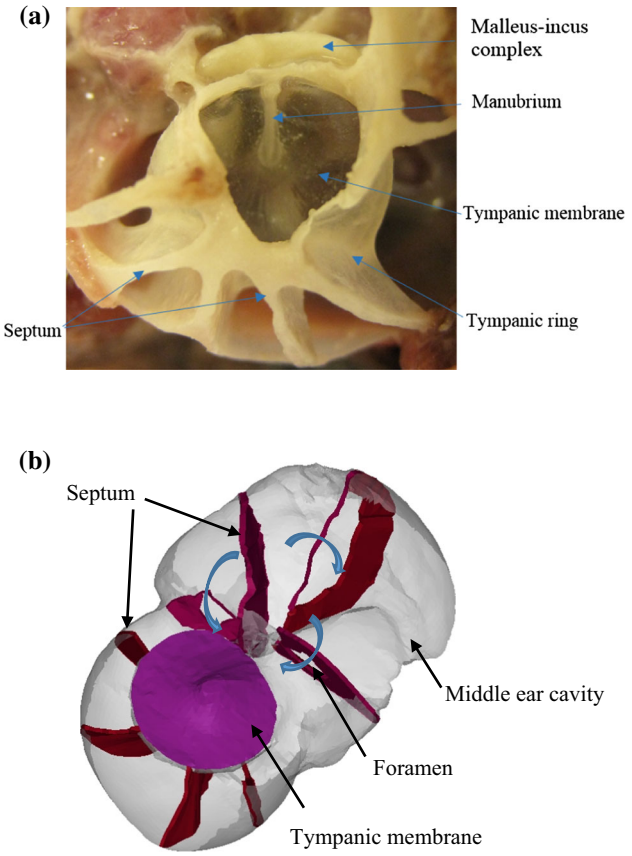


Fig. 2 The septum configuration in the chinchilla middle ear cavity. **a** Lateral view of a chinchilla right temporal bone displaying the structures surrounding the TM. The lateral bony wall of the bulla was removed to exhibit the multiple bone struts supporting the bony meatus and tympanic ring. **b** Medial view of the septum configuration in the model showing superior and inferior bullae and their interconnecting foramina

generate FE meshes for the middle ear components. The ossicles, the bony walls of the middle ear cavity, and the ear canal had clear geometry after reconstruction in Amira. The middle ear ligaments and muscle tendons were generated based on μCT images, visual observation, and the descriptions of those tissues by Vrettakos et al. (1988). The middle ear components of the FE model included the TM, malleus-incus complex, incudostapedial (IS) joint, stapes, posterior incudal ligament (PIL), anterior malleolar ligament (AML), stapedial annular ligament (SAL), posterior stapedial tendon (PST), tensor tympani tendon (TTT), bony septa, and the outer skull of middle ear cavity.

The chinchilla middle ear cavity is naturally divided into two main chambers, the superior and inferior bullae, by thin bony plates called septa (Hanamure and Lim 1987). Figure 2a shows that the multiple septa support the bony meatus and tympanic ring belonging to the inferior bulla. The superior bulla is also divided by septa. Based on observation of the chinchilla bony structure, three septa were built inside the superior bulla cavity, and five septa in the inferior bulla cavity in the FE model. The real geometry of the septum was extremely irregular, and a simplified treatment of the shape and thickness of the septa was adopted in the model. Each septum was assumed to be a constant thickness and connected the tympanic ring to the cavity wall in the inferior bulla and buttressed the cavity wall in the superior bulla. Figure 2b shows the simplified septum structure and configuration of the model in medial view. The curved arrows represent the connection of the air chambers through the foramina.

Figure 3 shows the FE model of chinchilla ear consisting of the bony ear canal, TM, ossicular chain, middle ear ligaments and tendons, septa, and middle ear cavity from medial view (Fig. 3a) and lateral view (Fig. 3b). All of the

Table 1 Dimensions in the FE model of chinchilla middle ear

Structure	Model	Published data
Ear canal		
Volume (mm^3)	43.73	
Tympanic membrane		
Diameter along manubrium (mm)	8.83	8.32[a]
Diameter perpendicular to manubrium (mm)	9.72	8.53[a]
Height of the cone (mm)	1.65	1.78[a]
Surface area (mm^2)	74.71	60.44[a], 61.48[b]
Thickness (μm)	15	7−10[c], ∼ 25[d]
Malleus-incus complex		
Malleus lever arm (manubrium) (mm)	4.59	4.50[a], 5.13[b]
Total length of malleus (mm)	5.92	
Incus level arm (mm)	1.22	1.58[a], 1.40[b]
Length of rotational axis (mm)	6.31	6.08[a]
Distance between Levels (mm)	1.93	1.90[a]
Lever ratio	3.76	2.84[a], 3.66[b]
Stapes		
Height (mm)	1.58	
Length of footplate (mm)	2.32	
Width of footplate (mm)	1.04	
Area of footplate	2.43	1.98[a], 1.90[b]
Middle ear Cavity		
Volume (mm^3)	2668	1530[a], 2313[b], 2800[e]

[a] Vrettakos et al. (1988), [b] Mason (2001), [c] Masaki et al. (1989), [d] Hsu et al. (2000), [e] Teas and Nielsen (1975)

elements were meshed by four-node elements. The air spaces in the ear canal and middle ear cavity were meshed by 17,798 and 179,249 acoustic elements, respectively. The TM was meshed by 951 solid elements, and the manubrium had 535 solid elements. The chinchilla possesses a fused malleus and incus (Vrettakos et al. 1988). In this study, the whole malleus-incus complex was treated as a homogeneous material. The malleus-incus complex and stapes had 5515 and 3854 solid elements, respectively. The IS joint was meshed by 8,638 solid elements. The suspensory ligaments and SAL were divided into 1474 and 1415 solid elements, respectively. The whole FE model consisted of 219,689 elements and 47,240 nodes.

2.3 Boundary conditions

The displacement boundaries of the middle ear vibration system (TM and ossicular chain) consisted of the tympanic annulus, middle ear suspensory ligaments/muscle tendons, and SAL. The tympanic annulus, SAL, and suspensory ligaments were all fixed at the middle ear cavity wall.

Two types of fluid–structure interactions were defined in the acoustic elements of the ear canal and middle ear. Each surface next to a movable structure, such as the TM, ossicles and round window membrane (RWM), was defined in the model as a fluid-structure interface (FSI) where the acoustic pressure was coupled into structural analysis. Each surface next to a fixed bony structure, such as the ear canal wall and middle ear cavity wall, was assumed to be fixed and assigned with an acoustic impedance.

In published experimental studies on chinchilla middle ear function, different conditions on the middle ear cavity wall were reported: the natural structure of sealed cavity, the experimentally vented cavity, and the opened cavity. It was a common process to place a long, narrow ventilation tube in the cavity for obtaining "closed-cavity" conditions without the build-up of static pressure (Ruggero et al. 1990; Rosowski et al. 2006). The cavity with the small ventilation tube is considered equivalent to a completely closed cavity except at very low frequencies.

In FE models of the middle ear, the sealed middle ear cavity was commonly simulated as an acoustically rigid boundary for human (Gan et al. 2004) and guinea pig (Koike et al. 2002). In acoustics, the rigid boundary implied the Neumann boundary with $\nabla P \cdot \mathbf{n} = 0$ ($\mathbf{n}$ is the normal vector of the boundary) along the bony wall. In addition to the rigid wall model of cavity boundary, Tuck-Lee et al. (2008) applied an elastic boundary to model the closed middle ear cavity of

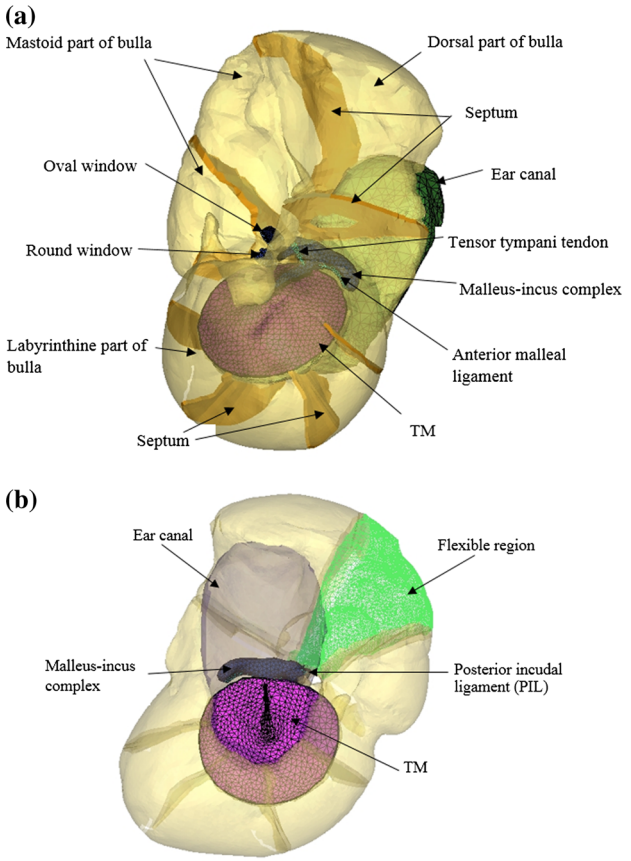


Fig. 3 FE model of the chinchilla ear with the external ear canal and middle ear inside the bulla. **a** Medial view of the model. The middle ear cavity was rendered transparently and the septa were displayed as 3D solid. **b** Lateral view of the model. The ear canal, middle ear cavity and septa were rendered transparently. The flexible region was used for modeling the acoustic coupling boundary of BC2 and displayed as mesh lines

cat in which the epithelial and mucosal linings of the whole cavity wall were simulated as elastic structures.

The air chambers and boundary conditions of the middle ear cavity may contribute fundamental features to the acoustic coupling of the ear (Rabbitt 1990). It is a challenge to accurately identify and simulate the acoustic boundary conditions of the middle ear cavity. In this study, we created two boundary conditions for the middle ear cavity wall to model the different cavity boundaries as described below:

Acoustic Boundary Condition 1 (BC1): BC1 represents the natural or sealed middle ear cavity wall as a rigid structure. Considering the acoustic absorption condition of the middle ear cavity wall, the surfaces of acoustic elements next to the cavity bony wall were assigned the impedance value of 150,000 Pa · s/m^3. This value was based on the estimate of acoustic absorption coefficient between the epithelial and mucosal linings of the bony structure and air media (Gan et al. 2006).

Acoustic Boundary Condition 2 (BC2): BC2 represents the middle ear cavity wall as a partially flexible structure, in which the cavity wall was divided into two regions: rigid region and flexible region. The flexible region is capable of either representing a deformable structure on the cavity surface or approximately simulating a vented wall as an equivalent flexible component, where the boundary impedance is unknown. For the model of the partially flexible cavity wall, inspired by the dynamic model of a micro-perforated or porous plate coupled with acoustic wave (Horoshenkov and Sakagami 2001; Takahashi and Tanaka 2002; Yu et al. 2014), the fluid–structure interaction was used to represent the boundary impedance. An approximate approach to treat the acoustic coupling due to the small ventilation holes or a deformable structure was employed in the BC2 boundary. Assuming the fluid-structure interaction takes place within a limited region, the affected region was simplified as an equivalent flexible shell structure. Applying the definition of boundary admittance, the boundary conditions for acoustic media at the surface of the shell is written as (Horoshenkov and Sakagami 2001)

$$\nabla P \cdot \mathbf{n} = i\rho_0 \omega V_p + i\omega\rho_0 P / Z_{in} \tag{1}$$

where ρ_0 is the density of air, and the shell's velocity, frequency, and surface acoustic impedance are V_p, ω, and Z_{in}, respectively.

To achieve the boundary condition of the affected region in Eq. (1), the flexible shell was parameterized by the thickness, density, and Young's modulus. When a FSI is applied to couple the shell and acoustic domain within the bulla, the partially flexible boundary can simulate the pressure gradient across the cavity wall in the assumed region. Moreover, utilizing the partially flexible boundary condition, the elastic structure existing on the cavity wall can be directly modeled as an elastic shell applied FSI coupling condition. In this study, a thickness of 0.1 μm, Young's modulus of 2 MPa and Raleigh damping coefficient (β) of 1.5 × 10^{-5}s were used for the material properties of the shell elements. The effect of the location of flexible region was analyzed, and it was found that there was a very small effect on the middle ear admittance when the flexible region was located within the area of the superior bulla wall. The flexible region used in this paper is shown in Fig. 3b with mesh lines. The rest of the cavity wall except for the flexible region (Fig. 3b) was defined as the rigid structure; the acoustic elements next to the rigid region were assigned the impedance value of 150,000 Pa · s/m^3.

The effect of cochlear fluid on acoustic-mechanical transmission through the ossicular chain was modeled as dashpots attached between the stapes footplate (FP) and fixed bony wall. The average cochlear impedance was about 100 GΩ as reported by Slama et al. (2010). The cochlear load was modeled as a mass block and 10 dashpots. The mass block

was assumed to be 0.55 mg. The value of 100 GΩ cochlear impedance applied on 2.45 mm^2 of oval window was used to determine the dashpot damping, which resulted in a damping coefficient of 0.06 Nm/s for each dashpot.

2.4 Material properties

Table 2 lists the mechanical properties of the middle ear soft tissues used in the model. Due to small displacements of the TM and middle ear ossicles in response to sound pressure, all solid materials in the model were assumed to be linear and elastic.

Material properties of the TM have major effects on the middle ear response to sound stimulation in the ear canal. As reported by Zhang and Gan (2013), the mean storage modulus of the human TM was from 15.1 to 27.6 MPa across the frequency range from 1 to 3800 Hz. For the Young's moduli of small animals, Aernouts and Dirckx (2012) estimated the Young's modulus ranging from 79 to 118 MPa at 8.2 Hz for the pars tensa of gerbils. Fay estimated the Young's modulus of fiber layer ranged 100–220 MPa posterior and 200–400 MPa anterior for the cat TM. Recently, our experimental results showed that the Young's modulus of the chinchilla pars tensa was about 6-10 times higher than that of the human pars tensa (Yokell et al. 2015). The Young's modulus of the TM was determined by the cross-calibration of the TM and FP displacements (Sun et al. 2002), and a modulus value of 200 MPa was achieved for the pars tensa of TM in this study. Young's modulus of the pars flaccida was assumed to be 12 MPa.

There is no published data for material properties of chinchilla middle ear ligaments. The material property data of chinchilla middle ear ligaments in the model were based on the data of the human ear. Cheng and Gan (2008a) reported that the Young's modulus of the anterior malleolar ligament of human ear varied from 0.22 to 4.7 MPa as the stress increased from 0 to 0.5 MPa. They also reported that the stapedial and tensor tympani tendons had almost the same Young's modulus (Cheng and Gan 2007, 2008b). In the guinea pig model reported by Koike et al. (2002), Young's modulus of the PIL, PST, TTT and AML was assumed to be 2, 4, 1 and 5 MPa, respectively. In this study (see Table 2), the Young's modulus of the PIL was set to 2.5 MPa, and Young's moduli of the PST, TTT and AML were assumed to be 2.0, 2.0 and 3.2 MPa, respectively. In a recent measurement by Zhang and Gan (2014) in human temporal bones, the mean storage shear modulus of the SAL ranged from 31.7 to 61.9 kPa at frequency ranging from 1 to 3760 Hz. Using this result and considering the relationship between shear modulus and

Table 2 Mechanical properties of middle ear soft tissues

Structure	Parameters
Tympanic membrane	
Elastic modulus (MPa):Pars tensa	200
Pars flaccida	15
Density (kg/m^3)	1100
Damping coefficient	1.00×10^{-4}
Manubrium	
Elastic modulus (MPa)	800
Density (kg/m^3)	1200
Damping coefficient	7.5×10^{-5}
Incudostapedial (IS) joint	
Elastic modulus (MPa)	6
Density (kg/m^3)	1000
Damping coefficient	7.5×10^{-5}
Stapedial annular ligament (SAL)	
Elastic modulus (MPa)	0.1
Density (kg/m^3)	1000
Damping coefficient	7.5×10^{-5}
Anterior malleolar ligament (AML)	
Elastic modulus (MPa)	3.2
Density (kg/m^3)	1000
Damping coefficient	1.0×10^{-4}
Posterior incudal ligament (PIL)	
Elastic modulus (MPa)	2.5
Density (kg/m^3)	1000
Damping coefficient	7.5×10^{-4}
Posterior stapedial tendon (PST)	
Elastic modulus (MPa)	2.0
Density (kg/m^3)	1000
Damping coefficient	7.5×10^{-5}
Tensor tympani tendon (TTT)	
Elastic modulus (MPa)	2.0
Density (kg/m^3)	1000
Damping coefficient	7.5×10^{-5}
Malleus-incus complex	
Elastic modulus (GPa)	14.1
Density (kg/m^3)	2000
Mass (mg)	12.05
Damping coefficient	1.5×10^{-4}
Stapes	
Elastic modulus (GPa)	14.1
Density (kg/m^3)	1300
Mass (mg)	0.55
Damping coefficient	1.0×10^{-4}

Young's modulus, an elastic modulus of 0.1 MPa was set for the chinchilla SAL. The Young's modulus of the IS joint was determined by the cross-calibration of the stapes FP displacement. A modulus value of 6 MPa was finally used in the model.

The ossicles were modeled with a Young's modulus of 14.1 GPa and a Poisson's ratio of 0.3, which were the same as those used in the FE model of the human ear (Gan et al. 2004).

Considering the complexity of dynamic properties of middle ear tissues and a lack of measurement in damping parameters, the Raleigh damping coefficients of the ligaments were assumed as $\alpha = 0/\text{s}$ and $\beta = 7.5 \times 10^{-5}$ s, the values were used in our previous middle ear model of the human ear (Gan et al. 2004, 2006). In this study, the stiffness damping coefficient β of the TM and ossicular chain was increased to 1.5×10^{-4} and 1.0×10^{-4} s, respectively, and α was still zero, so that the model-predicted TM displacement matched well with the experimental result (Guan et al. 2014)

For soft tissues in the middle ear, a density of 1000 kg/m^3 was chosen, except for the density of the TM. Considering the higher elastic modulus of chinchilla TM, the TM may have a higher proportion of fibers than those of other middle ear soft tissues. The density of TM was assumed to be 1100 kg/m^3, which is the same as that of cat TM used by Tuck-Lee et al. (2008). Buytaert et al. (2011) provided average density values for the malleus, incus and stapes in gerbil ossicles. They reported the density of 1740 kg/m^3 for the malleus and incus, and 1370 kg/m^3 for the stapes. The mass of malleus–incus complex, manubrium and stapes were, respectively, 11.8 mg, 0.2 mg and 0.4 mg as reported by Vrettakos et al. (1988). Based on these values and the volumes measured in the present model, the approximate density of malleus–incus complex, stapes and manubrium was 2000, 1300 and 1200 kg/m^3, respectively. The density of stapes used for chinchilla model was close to that of gerbil. The density of malleus-incus complex was higher than that of gerbil, but lower than that of human (Gan et al. 2004).

2.5 Finite element analysis

Acoustic-structure coupled FE analysis was conducted to calculate the middle ear transfer function and middle ear admittance when sound pressure was applied in the ear canal. For calculation of the middle ear transfer function, a uniform acoustic pressure over the frequency range of 100–10,000 Hz was applied 2 mm away from the TM and harmonic analysis was conducted using ANSYS (ANSYS Inc., Canonsburg, PA).

For calculation of middle ear admittance, a uniform normal velocity, representing a volume velocity input, was applied at the entrance of the bony ear canal. The canal entrance of the model was a reference location for middle ear admittance in this study. The ear canal pressure and middle ear response were derived. The input admittance Y_{TM} at this reference location is defined as the mean volume velocity of U_C at the location normalized to the sound pressure in the ear canal (P_{Ca}). Y_{TM} can be calculated as: $Y_{TM} = \frac{U_C}{P_{Ca}}$. The unit of acoustic admittance is siemens (S) where 1S equals 1 m^3/Pa/s.

3 Results

3.1 Middle ear transfer function

Figure 4 shows the umbo and FP displacement curves across the frequency range from 100 to 10,000 Hz derived from the BC1 boundary condition of middle ear cavity. The magnitude of the TM and FP displacement along the direction perpendicular to the FP was normalized by the input sound pressure and expressed in units of μm/Pa. The mean TM displacement at the umbo, as shown in Fig. 4a, was 0.14 μm/Pa at low frequencies. At 1600 Hz the TM displacement of the model showed a resonance peak. The mean displacement of

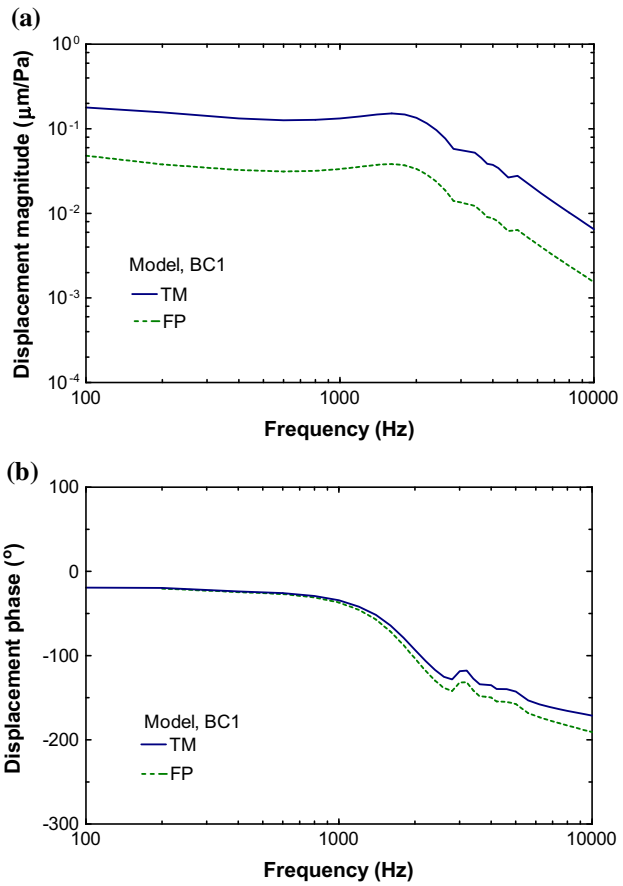


Fig. 4 TM and FP displacement curves derived from the chinchilla ear model under BC1 boundary condition. **a** Magnitude; **b** Phase

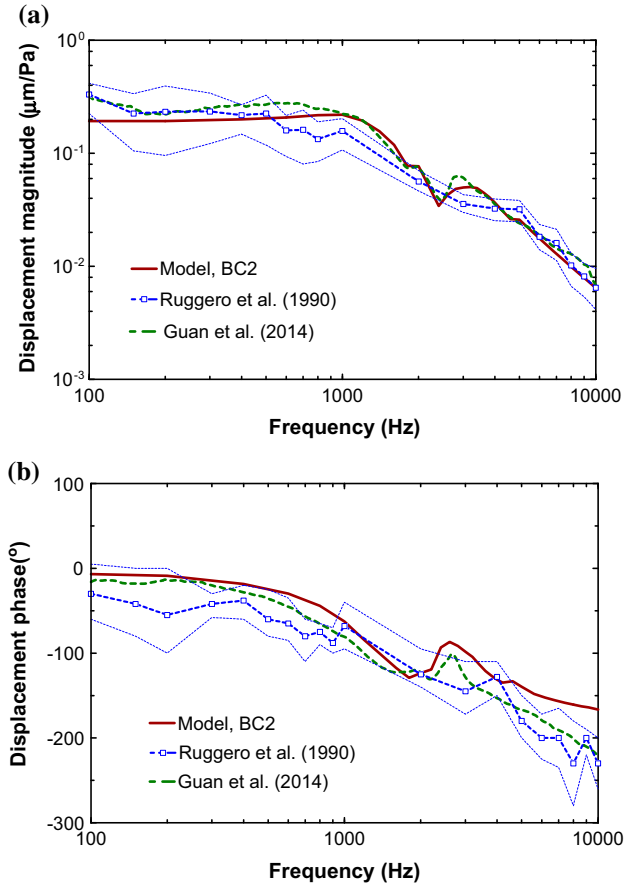


Fig. 5 FE model-derived TM displacement with BC2 acoustic boundary condition in comparison with the published experimental data. The dash-dotted line represents the measurements by Guan et al. (2014). The dashed line with open square symbols represents the mean displacement measured at the tip of the manubrium by Ruggero et al. (1990), and the thin dashed lines denote ±1SD from the mean. **a** Magnitude; **b** Phase.

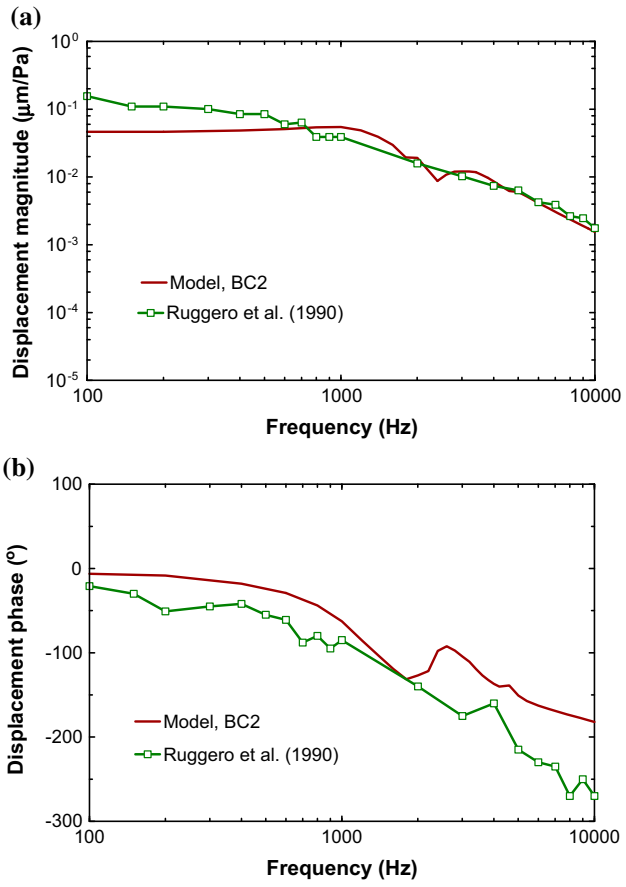


Fig. 6 FE model-derived FP displacement with BC2 acoustic boundary condition in comparison with the published experimental data. The line with open square symbols represents the mean stapes displacement in intact bullas reported by Ruggero et al. (1990). **a** Magnitude; **b** Phase

FP was about 0.037 μm/Pa at frequencies of 100–2000 Hz. The maximum displacement of the FP curve also occurred at 1600 Hz. Figure 4b shows the phase curves of the umbo and FP displacements and these two curves were very similar from 100 to 10,000 Hz. The stapes phase lagged relative to the umbo about 4° at 1000 Hz.

Figure 5 shows the frequency response curve of the TM displacement at umbo derived from the FE model with BC2 boundary condition (solid lines) in comparison with the published measurements in chinchillas by Ruggero et al. (1990) and Guan et al. (2014) in magnitude (Fig. 5a) and phase (Fig. 5b). Note that the scales of the published data were adjusted and normalized by the input sound pressure. As shown in Fig. 5a, the umbo displacement derived from model was about 0.2 μm/Pa at low frequencies, slightly lower than the measurements. At frequencies $f > 800$ Hz, the umbo displacement matched well with the measurements by Guan et al. (2014). At frequencies of 500–4000 Hz, the model-derived TM displacement was a slightly higher than the data by Ruggero et al. (1990). An important feature in the TM displacement measured by Guan et al. (2014) was the notch appearing at about 2400 Hz. The model-derived curve shows a minimum of TM displacement at 2400 Hz which well reflected the feature observed in the experimental results. In addition, the corresponding phase curves displayed in Fig. 5b also generally agreed the experimental data except for the less lag at frequencies above 2000 Hz.

Figure 6 shows the model-derived frequency response curve of the FP displacement with the BC2 boundary condition in comparison with the published data (Ruggero et al. 1990) across the frequency range of 100 to 10,000 Hz. Figure 6a displays the magnitude and Fig. 6b the phase angle. As can been seen in Fig. 6, the FE model-derived FP displacement curve was consistent with Ruggero's data at high frequencies, but the magnitude was lower than the measured displacement at $f < 500$ Hz. Compared with the measured phase curve, the model result showed a small delay, and a flat phase changed above 2500 Hz.

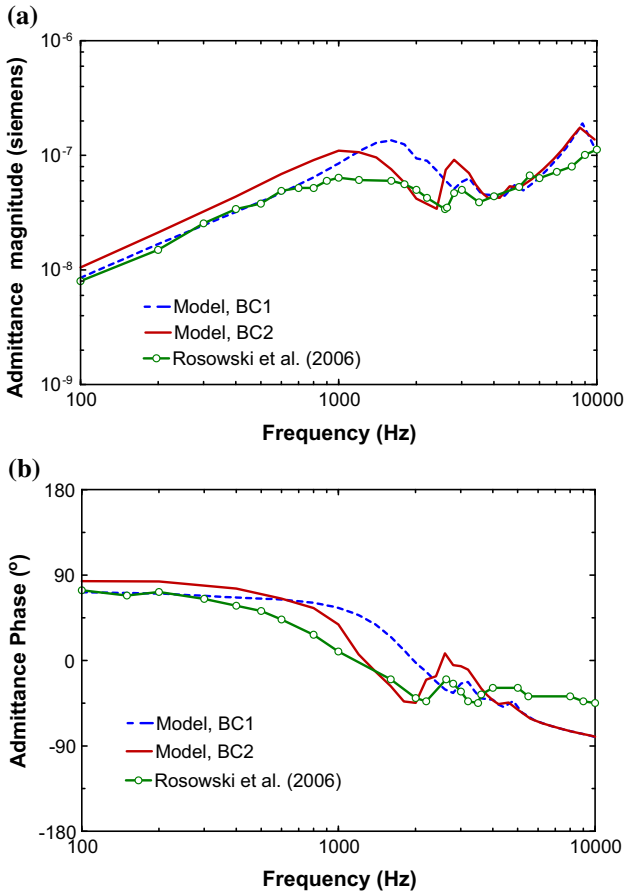


Fig. 7 FE model-derived middle ear admittance with BC1 and BC2 boundary conditions in comparison with the published admittance data measured under the vented cavity condition by Rosowski et al. (2006). The solid line with circle symbols represents the mean admittance measurement by Rosowski et al. **a** Magnitude; **b** Phase

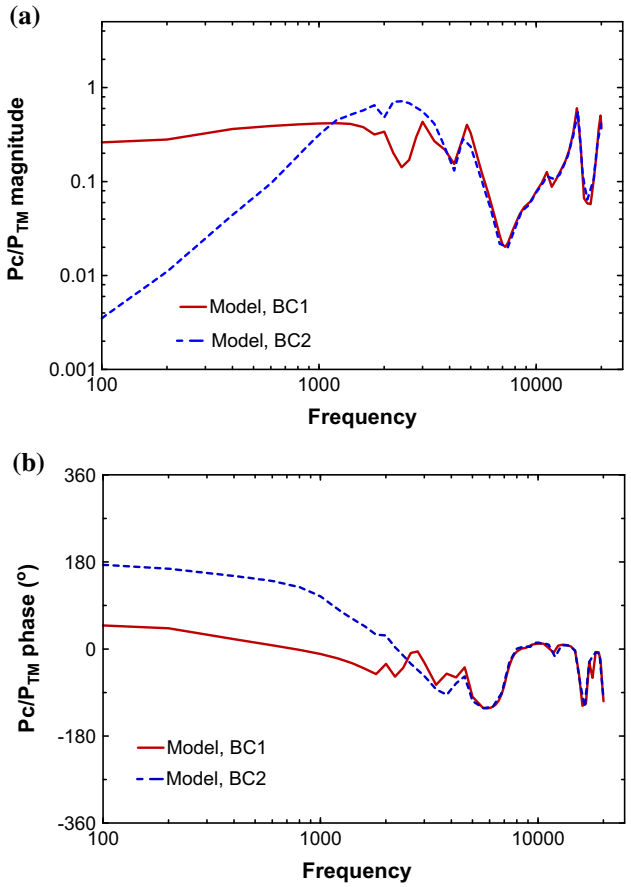


Fig. 8 Comparison of the effect of acoustic boundary conditions on tympanic cavity pressure predicted by the model. The tympanic cavity pressure (P_C) were normalized with respect to the ear canal pressure (P_{TM}) at TM. **a** Magnitude; **b** Phase

Observing Figs. 4, 5 and 6, the results from BC2 boundary condition better reflect the features in the TM and FP displacements.

3.2 Middle ear admittance

The middle ear input admittances calculated from the FE model of chinchilla middle ear with both BC1 and BC2 boundary conditions are shown in Fig. 7. The middle ear admittance measured by Rosowski et al. (2006) of the closed and vented bulla was also included in the figure for a comparison. As can be observed at frequencies below 1000 Hz, the model-derived admittance magnitude increased proportionally with frequency. For BC1 boundary condition, the computed magnitude curve was close to the experimental result at frequencies below 800 Hz, but the magnitude was higher than the experimental data at between 1000 and 3000 Hz. The phase from modeling curve was flatter than the measured one at low frequencies. For BC2 boundary condition, the admittance magnitude reached a maximum of 1.45×10^{-7} S at 1000 Hz and then decreased to a notch at 2400 Hz with a value of 3.42×10^{-8} S. In addition, a small peak at 2800 Hz was apparent which was also shown in the experimental data. At frequencies above 4000 Hz, both boundary conditions had little effects on the admittance.

3.3 Sound pressure in the middle ear cavity

The present study focused on development of a FE model of the chinchilla ear to investigate the middle ear response with various boundary condition models of middle ear cavity. Figure 8 illustrates the tympanic cavity pressure normalized by the ear canal pressure across the frequency range of 100 to 20,000 Hz with BC1 and BC2 boundary conditions. The pressure in the tympanic cavity was computed near the umbo in the cavity side. The cavity pressure for BC1 boundary condition exhibited a flat curve at $f < 2000$ Hz and the local maximum at 3000, 4800, 15,400 and 19,800 Hz, respectively. Compared with BC1 boundary, the BC2 boundary resulted in much low cavity pressure at low frequencies, and the pressure

increased with frequency at $f < 1800$ Hz. BC1 boundary condition produced a middle ear pressure 58 times higher than that of BC2 condition at 100 Hz, and the difference in phase was 115°. At high frequencies ($f > 3500$ Hz), the two boundary conditions had little effect on the tympanic cavity pressure. Therefore, the partially flexible cavity wall only affected the tympanic cavity pressure at low frequencies.

3.4 Acoustical role of the septa

One of the unique features of the chinchilla middle ear cavity is the presence of multiple septa that divide the middle ear air space into multiple air-filled cambers. To gain insight into the role of the septa in acoustic function of the chinchilla middle ear, the admittance was calculated from the model after partial and complete removal of the septa. For the partial removal of the septa, two models were created: one modeled the removal of septa in the superior bulla cavity (superior septa removal), resulting in a connected space of the superior bulla without any bony partitions, but the septa in the tympanic cavity remained intact. The other modeled the removal of the septa in the inferior bulla cavity (inferior septa removal), while the superior septa remained intact. For the complete removal of the septa (no septa), the septa in both the superior bulla and the inferior bulla were removed. The purpose for the stepwise septum removal was an attempt to distinguish the acoustic roles of the septa in the superior bulla from those in the inferior bulla.

Figure 9 shows a comparison of the admittances across frequency range from 200 to 20,000 Hz under the intact, partial septa, and no septa conditions when the BC1 boundary condition was applied to middle ear cavity. Under the superior septa removal condition, the admittance curve (dotted line) became fluctuant and showed a number of minima and maxima accompanied by rapid shifts in phase angles between 650 and 1300 Hz. A small admittance peak at 4900 Hz was observed. When the inferior septa were removed, the admittance (thin line with circles) was little affected by the septa removal. Under the no septa condition, the admittance curve (thin line with asterisk symbols) had little variation from the removal of superior septa, and only the small peak at 4900 Hz appeared to move upward in frequency to about 5400 Hz. The results illustrated in Fig. 8 suggest that the septa in the superior bulla cavity act to smooth the middle ear response at medium frequencies and the septa in the tympanic cavity have little effect on the admittance under the assumed BC1 boundary condition of middle ear cavity.

Figure 10 shows the comparison of model-derived frequency response curves of the middle ear admittance across the frequency range from 200 to 20,000 Hz for the intact, partial septa and no septa under the BC2 boundary condition. The effect of the septa on admittance occurred at 800

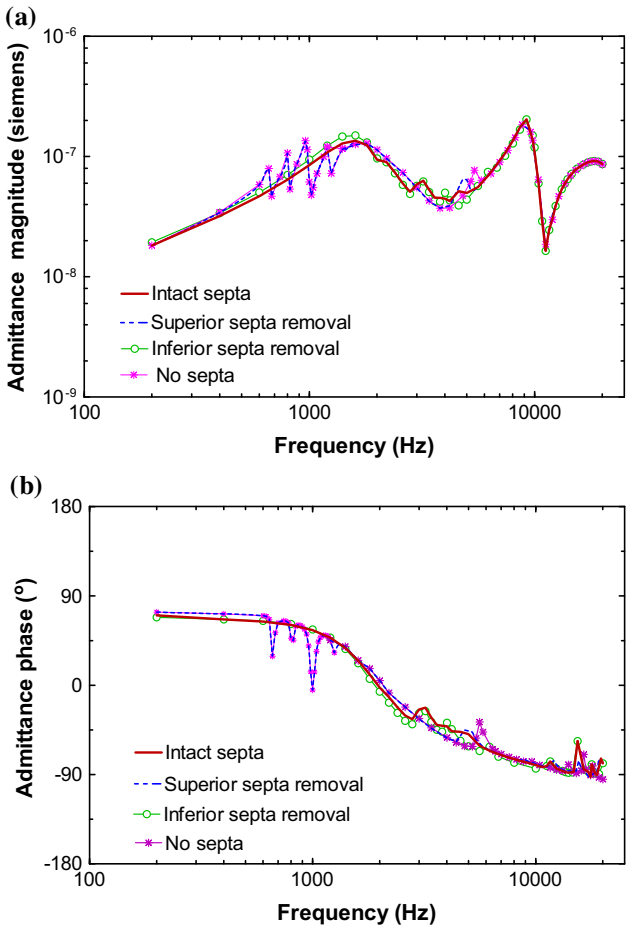


Fig. 9 FE model-derived middle ear admittances with BC1 boundary condition for intact septa (*solid line*), superior septa removal (*dotted line*), inferior septa removal (*thin line* with *circle symbols*), and no septa (*thin line* with *asterisk symbols*). **a** Magnitude; **b** Phase

to 5000 Hz. The removal of the superior septa increased the admittance from 600 to 2400 Hz. The notch at 2400 Hz with the intact septa appeared to move to 3200 Hz and the peak at 2800 Hz appeared to move to 4000 Hz when the septa inside the superior bulla cavity were removed (dotted line). The removal of the inferior septa resulted in a slight increase in the admittance around 1000 Hz (thin line with circle symbols). Further removal of the septa inside both the superior and inferior cavities (thin line with asterisk symbols) leaded to a slight shift in the peak frequency around 4000 Hz from the removal of the superior septa.

4 Discussion

4.1 Model geometry parameters

A 3D FE model of the chinchilla ear was developed based on a complete set of μCT images of a bulla. Compared with

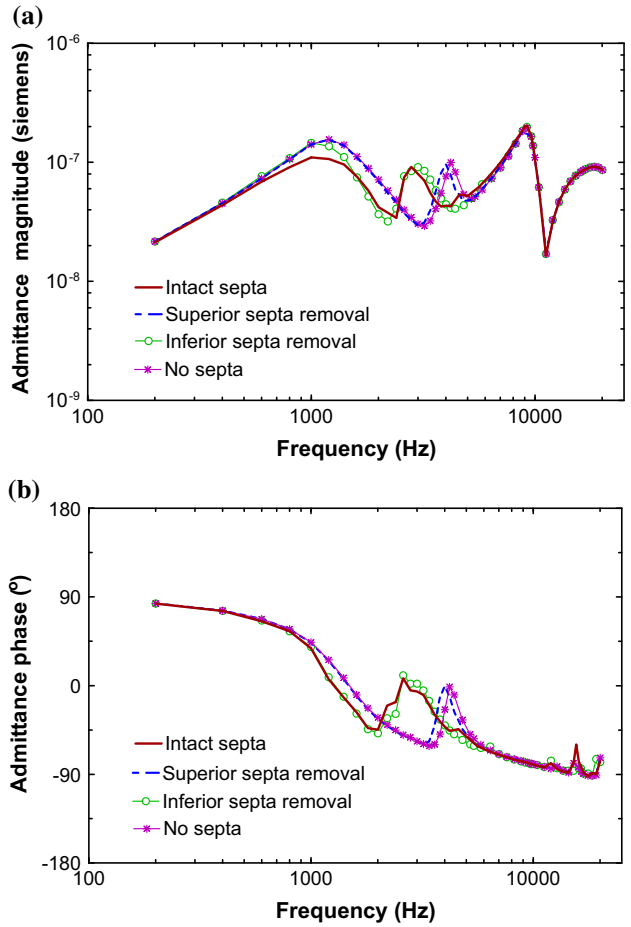


Fig. 10 FE model-derived middle ear admittances with BC2 boundary condition for intact septa (*solid line*), superior septa removal (*dotted line*), inferior septa removal (*thin line* with *circle symbols*), and no septa (*thin line* with *asterisk symbols*). **a** Magnitude; **b** Phase

the anatomical measurements of the chinchilla middle ear reported by Vrettakos et al. (1988), the main differences were the sizes of the TM, FP, and middle ear cavity as listed in Table 1. The TM surface area (74.71 mm^2) in the FE model was larger than the mean surface area (60.44 mm^2) measured by Vrettakos. The volume of middle ear cavity in FE model was 2668.0 mm^3, larger than 1530 mm^3 reported by Vrettakos. Besides Vrettakos' published chinchilla geometry data, the estimated bulla cavity volume of chinchilla varied over a wide range, such as 1600 mm^3 (Rosowski et al. 2006), 2333 mm^3 (Mason 2001), and 2800 mm^3 (Teas and Nielsen 1975). The volume of 2800 mm^3 was very close to the FE model. Overall, the present model had a larger bulla size than that reported mean data in the literature. As a result, the large bulla may contribute to a greater compliance of the middle ear air space for the model.

4.2 Middle ear function derived from the model

The model-derived results from acoustic-mechanical coupling allow us to compare the computed middle ear transfer functions from different cavity models with the experimental data, including the TM and FP displacements. The results shown in Fig. 5 demonstrate that the model can capture the major TM displacement features of the chinchilla. Ravicz and Rosowski (2013) pointed out that the TM displacement notch and phase step near 2500 Hz presented only under the open-hole cavity condition due to a resonance between the bulla air space and the open hole in the bulla wall. In another study of TM vibration by Guan et al. (2014) in which the hole for releasing the middle ear pressure was sealed by dental cement during the TM displacement measurement, the magnitude notch and phase step in the TM displacement curves were still observed. From this study, the BC2 model matched well with the experimental results. The notch in the TM displacement at 2400 Hz may have been associated with either a flexible structure in the cavity wall or a potential for air-leak artifacts from the cavity.

The comparison of stapes FP displacements between the FE model and experimental data shown in Fig. 6 suggests that the displacement curve is similar to the experimental data by Ruggero et al. (1990), except that the model displayed a relatively low displacement magnitude at low frequencies. One of the factors resulting in the low FP displacement was the dimensions of the ossicles in the model. The anatomical ossicular lever ratio, defined as the ratio between the length of the manubrium and the length of the incus long process, was 3.76 in the model as listed in Table 1. The estimated the lever ratio of chinchilla by Ruggero et al. (1990) was 2.94. The anatomical ossicular lever ratio of the model was larger than that of Ruggero's measurement. Given the same umbo displacement, a high ossicular level ratio may theoretically produce a low FP displacement. The high anatomical ossicular lever ratio in the model was one of reasons resulting in the low FP displacement. However, the ossicular lever ratio has a wide range reported in the literature. Vrettakos et al. (1988) measured the anatomical lever ratio of 2.84 and Mason (2001) reported a level ratio of 3.66 in chinchilla. The anatomical lever ratio of 3.76 of the FE model differed little from the level ratio of 3.66 reported by Mason.

The middle ear admittance derived from the FE model with BC2 boundary condition was generally consistent with the experimental results by Rosowski et al. (2006) as shown in Fig. 7. Slightly high middle ear admittance was obtained from the BC2 boundary model compared to the measured admittance. One of the reasons causing the difference may be the larger volume of middle ear cavity in FE model. As

indicated by Rosowski et al. (2006), the chinchilla cavity air space has a significant effect on the middle ear admittance. In the model, the volume of middle ear air space is 1.67 times larger than the estimated value of 1600 mm^3 by Rosowski et al. (2006).

In summary, good agreements between the middle ear function curves obtained from BC2 model and published experiment data displayed in Figs. 5, 6 and 7 suggest that the FE model developed in this study is feasible to characterize middle ear functions in chinchillas.

4.3 Effect of boundary condition of middle ear cavity

Two acoustic boundary conditions of the middle ear cavity were used to represent the acoustic-mechanical coupling in 3D FE model of the chinchilla ear. The model-derived results indicated that the BC2 boundary condition resulted in higher TM and stapes displacements than those from BC1 boundary at low frequencies. The TM displacement magnitude with BC2 boundary was about 1.7 times larger than that of BC1 boundary at $f < 1000$ Hz. Moreover, the BC2 boundary condition also caused a shift of middle ear resonance frequency from 1600 Hz to 1000 Hz and increased the resonance peak displacement from 0.152 to 0.220 μm/Pa as shown in Fig 5. Recently, Maftoon et al. (2014) reported the effect of the middle ear cavity opening on TM vibration in gerbil, and their measurements demonstrated that an open cavity shifted the middle ear resonance frequencies to lower frequencies. The main increase in TM displacement at low frequencies happened upon the smallest (1 mm) hole in the cavity wall and the further progressive enlarging of the opening had little effect on low-frequency vibration magnitude.

Correlating the TM displacement with the cavity pressure, it was found that the low cavity pressure in BC2 boundary was associated with larger TM displacement at low frequencies. In Fig. 8, the BC2 boundary had much lower tympanic cavity pressure than that of the BC1 boundary at frequencies below 1000, while the difference in cavity pressure was not significant at high frequencies ($f > 3500$ Hz). Thus, the TM displacement was not affected by the boundary conditions at high frequencies. This suggests that the increase in low-frequency TM displacement with BC2 boundary resulted from the low cavity pressure.

In Fig. 8, the acoustic pressure in the middle ear cavity was disturbed by the boundary condition. It is noted that several reports in the literature also provided middle ear pressure measurements (O'Connor and Puria 2006; Voss et al. 2007; Bergevin and Olson 2014) and pressure calculation (Gan et al. 2006) in relation to frequency. Voss et al. (2007) reported the middle ear pressure measurements in human temporal bones. Their results showed the pressure was nearly independent of frequency at low frequencies, and the pressure drop across the TM was about −12 dB below 1000 Hz. The nearly frequency-independent feature of pressure difference across the human TM at low frequencies is similar to the result in Fig. 8 of BC1 boundary condition in this study. The pressure change across the TM in gerbils reported by Bergevin and Olson (2014), in which a small ventilation hole was presented in the cavity wall, indicated that the pressure increased with frequency at frequencies below 3000–4000 Hz (estimated from Fig. 3 of Bergevin and Olson). The pressure difference across the TM in chinchilla model also exhibited the frequency-dependent variations under the BC2 boundary condition and the pressure increased with the frequency below 2500 Hz, which was similar to the measured results in gerbils with a ventilation hole in the cavity.

The effects of cavity boundary condition in chinchilla model on middle ear responses were estimated through comparison between the rigid and partially flexible boundary conditions of middle ear cavity. The results demonstrated that the vented middle ear cavity or flexible boundary condition in the cavity wall affected the TM displacement and middle ear cavity pressure at low frequencies and caused the addition of an anti-resonance to the TM and stapes displacements near 2400 Hz.

4.4 Role of the septa

In many small mammals, the middle ear cavity is divided into multiple, connected cavities by bony septa. Some species have a single septum (e.g., cat), while chinchilla has multiple septa. Guinan and Peake (1967) reported that the opening of the septum in cat had a large effect in a rather narrow frequency range from 2000 to 4000 Hz. Rosowski et al. (2000) measured the cat middle ear admittances with intact and removal of the septum. They found that the removal of the septa in cat bulla introduced a notch into the middle ear admittance at 10,000 Hz. Tuck-Lee et al. (2008) demonstrated the presence of the septum shifted in the middle ear resonance from near 10,000 to 4–5000 Hz using a FE model of cat middle ear with an elastic boundary of the middle ear cavity. According to the hypothesis of septum function, the function of the septum was to shift the middle ear resonance away from the useful frequency range, so as not to interfere with sound localization (Puria 1991).

The admittance curves in Fig. 9 indicate that the septa inside the superior bulla cavity acted to smooth the middle ear response at medium frequencies given the BC1 boundary condition of middle ear cavity. The admittance curves in Fig. 10 suggest the superior septa removal caused an upward shift in the resonance frequency of the cavity given the partial flexible boundary condition of middle ear cavity. However, the model results suggest that the septa inside the superior bulla cavity dominated the acoustic effect on middle ear

admittance, and the acoustic role of septa may be affected by cavity boundary.

The best hearing sensitivity range of chinchilla is coincident with the best sensitivity range for human, approximately 125 Hz to 16,000 Hz (Heffner and Heffner 1991). Unlike chinchilla, the cat's hearing spans a range from 48 Hz to 85,000 Hz, and good hearing is from 500 Hz to 32,000 Hz. It is well known that the septum of cat results in a shift of middle ear resonance at medium-high frequencies. The present results indicate that the septa of chinchilla affect the middle ear response at low-medium frequencies. From a comparison between cat and chinchilla, the different frequencies benefiting from septa on middle ear function reveal the role of septa which may be associated with the different audible frequency ranges.

4.5 Effect of model parameters on middle ear admittance

Because of a lack of acoustic property data of the middle ear cavity, the acoustic boundary of the chinchilla middle ear cavity was simulated based on two boundary condition models. The acoustic parameters were approximately determined by fitting the umbo displacement and middle ear admittance curves. Figure 11 displays how the middle ear admittance was affected by boundary parameters. In BC1 boundary condition, the boundary impedance was set to vary from 0.5 to 10 times its original value, and the model-predicted middle ear admittances are shown in Fig. 11a. Further increasing the boundary impedance, the curve almost coincided with that of 10 times impedance (not shown in the figure). The admittance magnitude was reduced with the increase in the boundary impedance of BC1 condition at low frequencies. At frequencies from 2500 to 5000 Hz, the increasing of boundary impedance resulted in the increasing fluctuation of the admittance. At the high frequencies, there was no significant variation of admittance as the boundary impedance increased. In BC2 boundary condition, the main model parameters of the flexible region consist of the Young's modulus, thickness and damping coefficient. Figure 11b shows the variations of middle ear admittance when the model parameters were varied from the original values. As can be seen in this figure, the BC2 model parameters affected the admittance in the frequency range from 500 to 3500 Hz. When the Young's modulus or thickness of the BC2 model was changed to 2 times the original value, the maximum change of admittance was generally less than 5%. Another parameter of the BC2 boundary condition is the damping coefficient. A fivefold increase in the damping coefficient resulted in a change of less than 1.68% in the admittance.

It should be noted that the material properties used for the middle ear components in the model are the best available in the literature, yet there may be some uncertainty in the material properties of individual tissues. The parameters in Table 2 should be considered to be acceptable for function validation of the model, but may not be the absolute values of tissue mechanical properties. Moreover, the FE model-derived results showed that the partially flexible boundary condition provided a better agreement to the experimental measurements in fine structure of the TM and FP displacement and middle ear admittance curves. However, there are two possibilities leading to the partially flexible boundary model based on the present model. One is flexible structure, the other is effect of the vented cavity. Further studies are required to clarify these questions. Additionally, the opened cavity condition used in experimental measurement has not been modeled yet. The effect of the different middle ear cavity conditions on the TM motion needs further studies.

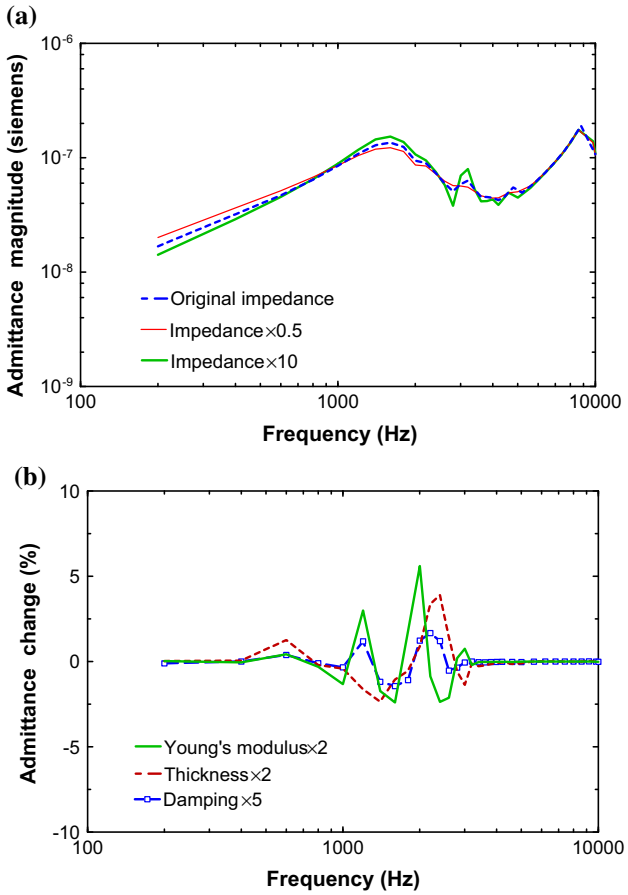


Fig. 11 Effects of the acoustic model parameters on middle ear admittance. **a** FE model-derived middle ear admittance curves with various impedance values in BC1 boundary condition; **b** FE model-derived middle ear admittance changes in response to variations in model parameters of BC2 boundary condition

5 Conclusion

A 3D FE model of the chinchilla ear was developed based on X-ray μCT images to simulate the TM and FP displacements and the middle ear admittance. The FE model of the chinchilla ear consists of the ear canal, TM, middle ear ossicles and suspensory ligaments, and the middle ear cavity. Two boundary conditions of the middle ear cavity were created in the model to simulate the rigid and partially flexible cavity boundaries. Acoustic-mechanical coupled analysis was conducted with these two conditions to characterize the middle ear transfer function of the chinchilla ear. The FE model results were compared with experimental data reported in the literature including the TM and FP displacements and the middle ear input admittance. The model results indicated that the vented middle ear cavity or the flexible boundary increasing TM displacement at low frequencies was due to low pressure in the tympanic cavity. An application of this model was presented to identify the acoustic role of the middle ear septa—a unique feature of chinchilla middle ear cavity. The 3D FE model of the chinchilla ear developed from this study provides a useful research tool for characterizing the middle ear functions through acoustic-mechanical coupled FE analysis.

Acknowledgments The authors thank the former graduate student Dr. Xiying Guan for his work on image processing of the middle ear ossicels and the undergraduate students Rebecca L. Browder and Kegan W. Leckness for their participations in 3D-reconstruction of the chinchilla model at the University of Oklahoma. This work was supported by NIH R01DC011585.

References

Browning GG, Granich MS (1978) Surgical anatomy of the temporal bone in the chinchilla. Ann Otol Rhinol Larynqol 87(6):875–883

Buytaert JAN, Salih WHM, Dierick M, Jacobs P, Dirckx JJJ (2011) Realistic 3D computer model of the Gerbil middle ear, featuring accurate morphology of bone and soft tissue structures. J Assoc Res Otolaryngol 12(6):681–696

Bergevin C, Olson ES (2014) External and middle ear sound pressure distribution and acoustic coupling to the tympanic membrane. J Acoust Soc Am 135(3):1294–1312

Cheng T, Gan RZ (2007) Mechanical properties of stapedial tendon in human middle ear. ASME J Biomech Eng 129(6):913–918

Cheng T, Gan RZ (2008a) Mechanical properties of anterior malleolar ligaments from experimental measurement and material modeling analysis. Biomech Model Mechanobiol 7(5):387–394

Cheng T, Gan RZ (2008b) Experimental measurement and modeling analysis on mechanical properties of tensor tympani tendon. Med Eng Phy 30(3):358–366

Elkhouri N, Liu H, Funnell WRJ (2006) Low-frequency finite element modeling of the gerbil middle ear. JARO 7(4):399–411

Heffner RS, Heffner HE (1991) Behavioral hearing range of the chinchilla. Hear Res 52(1):13–16

Gan RZ, Feng B, Sun Q (2004) Three-dimensional finite element modeling of human ear for sound transmission. Ann Biomed Eng 32(6):847–859

Gan RZ, Sun Q, Feng B, Wood MK (2006) Acoustic-structural coupled finite element analysis for sound transmission in human ear-pressure distributions. Med Eng Phys 28(5):395–404

Guan X, Chen Y, Gan RZ (2014) Factors affecting loss of tympanic membrane mobility in acute otitis media model of chinchilla. Hear Res 309:136–146

Guinan JJ Jr, Peake WT (1967) Middle-ear characteristics of anesthetized cats. J Acoust Soc Am 41(5):1237–1261

Hanamure Y, Lim DJ (1987) Anatomy of the chinchilla bulla and eustachian tube: I. Gross and microscopic study. Am J Otolaryngol 8(3):127–143

Horoshenkov KV, Sakagami K (2001) A method to calculate the acoustic response of a thin, baffled, simply supported poroelastic plate. J Acoust Soc Am 110(2):904–917

Hsu GS, Margolis RH, Schachern PA (2000) Development of the middle ear in neonatal chinchilla. I. Birth to 14 days. Acta Otolaryngol 120(8):922–932

Koike T, Wada H, Kobayashi T (2002) Dynamic frequency characteristic of the middle ear in guinea pig: the finite element analysis. Audiol Jpn 45(4):289–297

Ladak HM, Funnel WRJ (1996) Finite-element modeling of the normal and surgically repaired cat middle ear. J Acoust Soc Am 100(2):933–944

Maftoon N, Funnell WRJ, Daniel SJ, Decraemer WF (2014) Effect of opening middle-ear cavity on vibration of gerbil tympanic membrane. JARO 15(3):319–334

Masaki M, Wright CG, Lee DH, Meyerhoff WL (1989) Experimental cholesteatoma: epidermal ingrowth through tympanic membrane following middle ear application of propylene glycol. Acta Otolaryngol (stockh) 108(1–2):113–121

Mason MJ (2001) Middle ear structures in fossorial mammals: a comparison with non-fossorial species. J Zool Lond 255(4):467–486

Nummela S (1995) Scaling of the mammalian middle ear. Hear Res 85(1–2):18–30

O'Connor KN, Puria S (2006) Middle ear cavity and ear canal pressure-driven stapes velocity responses in human cadaveric temporal bones. J Acoust Soc Am 120(3):1517–1528

Puria S (1991) A theory of cochlear input impedance and middle ear parameter estimation. Ph.D. Thesis, City University of New York

Rabbitt R (1990) A hierarchy of examples illustrating the acoustic coupling of the eardrum. J Acoust Soc Am 87(6):2566–2582

Ravicz ME, Rosowski JJ (2013) Middle-ear velocity transfer function, cochlear input impedance and middle-ear efficiency in chinchilla. J Acoust Soc Am 134(4):2852–2865

Rosowski JJ, Huang GT, Atencio CA, Peake WT (2000) Acoustic effects of multiple middle-ear air spaces: measurements in cats. In: Wada H, Takasaka T, Ikeda K, Ohyama K, Koike T (eds) Recent developments in auditory mechanics. World Scientific, Singapore, pp 15–21

Rosowski JJ, Ravicz ME, Songer JE (2006) Structures that contribute to middle-ear admittance in chinchilla. J Comp Physiol A 192(12):1287–1311

Ruggero MA, Rich NC, Robles L, Shivapuja BG (1990) Middle-ear response in the chinchilla and its relationship to mechanics at the base of the cochlea. J Acoust Soc Am 87(4):1612–1629

Slama MC, Ravicz ME, Rosowski JJ (2010) Middle ear function and cochlear input impedance in chinchilla. J Acoust Soc Am 127(3):1397–1410

Songer JE, Rosowski JJ (2007) Transmission matrix analysis of the chinchilla middle ear. J Acoust Soc Am 122(2):932–942

Sun Q, Gan RZ, Chang HK, Dormer KL (2002) Computer-integrated finite element modeling of human middle ear. Biomech Model Mechanobiol 1:109–122

Takahashi D, Tanaka M (2002) Flexural vibration of perforated plated and porous elastic materials under acoustic loading. J Acoust Soc Am 112(4):1456–1464

Teas DC, Nielsen DW (1975) Interaural attenuation versus frequency for guinea pig and chinchilla CM response. J Acoust Soc Am 58(5):1066–1072

Tuck-Lee JP, Pinsky PM, Steele CR, Puria S (2008) Finite element modeling of acoustic mechanical coupling in the cat middle ear. J Acoust Soc Am 124(1):348–362

Voss SE, Rosowski JJ, Merchant SN, Peake WT (2007) Non-ossicular signal transmission in human middle ears: experimental assessment of the "acoustic route" with perforated tympanic membranes. J Acoust Soc Am 122(4):2135–2153

Vrettakos PA, Dear SP, Saunders JC (1988) Middle-ear structure in the chinchilla: a quantitative study. Am J Otolaryngol 9(2):58–67

Wang X, Wang L, Zhou J, Hu Y (2014) Finite element modelling of human auditory periphery including a feed-forward amplification of the cochlea. Comput Method Biomech Biomed Eng 17(10):1096–1107

Wang X, Nakmali D, Gan RZ (2015) Complex modulus of round window membrane over auditory frequencies in normal and otitis media chinchilla ears. Int J Exp Comput Biomech 3(1):27–44

Yu X, Cheng L, Guyader JL (2014) On the modeling of sound transmission through a mixed separation of flexible structure with an aperture. J Acoust Soc Am 135(5):2785–2796

Yokell Z, Wang X, Gan RZ (2015) Dynamic properties of tympanic membrane in a Chinchilla Otitis media model measured with acoustic loading. ASME J Biomech Eng 137(8):081006-1–081006-9

Zhang X, Gan RZ (2013) Dynamic properties of human tympanic membrane based on frequency-temperature superposition. Ann Biomed Eng 41(1):205–214

Zhang X, Gan RZ (2014) Dynamic properties of human stapedial annular ligament measured with frequency-temperature superposition. ASME J Biomech Eng 136(8):081004-1–081004-7

J. dynamic behavior mater. (2016) 2:59–73
DOI 10.1007/s40870-015-0041-3

Mechanical Properties of a Human Eardrum at High Strain Rates After Exposure to Blast Waves

Huiyang Luo[1] · Shangyuan Jiang[2] · Don U. Nakmali[2] · Rong Zhu Gan[2] · Hongbing Lu[1]

Received: 21 October 2015 / Accepted: 7 December 2015 / Published online: 17 December 2015
© Society for Experimental Mechanics, Inc 2015

Abstract The mechanical properties of a human tympanic membrane (TM) or eardrum were characterized at high strain rates after multiple exposures to blast waves. Human cadaveric temporal bones were subjected to blast waves at first, then TM strip specimens were prepared either along the radial or the circumferential direction. A highly sensitive miniature split Hopkinson tension bar was used for tensile experiments on the human eardrum strip specimens at high strain rates. The mechanical properties of the human TMs before and after exposure to blast waves were compared and discussed. The mechanical properties in the time-domain were subsequently converted to the corresponding properties in the frequency domain to investigate the effect of blast waves on the viscoelastic properties. The results indicate that the blast waves have different effects on the mechanical properties in the radial and circumferential directions. After exposure to the overpressure induced by the blast waves, the mechanical behavior in the radial direction in general becomes stiffened, while it is weakened in the circumferential direction. The results could be analyzed further in an ear simulation model to develop understanding of the effect of blast waves on hearing loss.

Keywords Human eardrum · Blast wave · Young's modulus · High strain rate · Split Hopkinson tension bar · Complex modulus · Frequency domain

✉ Hongbing Lu
hongbing.lu@utdallas.edu

[1] Department of Mechanical Engineering, The University of Texas at Dallas, Richardson, TX 75080, USA

[2] School of Aerospace and Mechanical Engineering, The University of Oklahoma, Norman, OK 73019, USA

Introduction

In the United States and the rest of the world, bombing attacks by terrorists or in battleground impose an increasing risk to personal injuries. A blast injury consists of four phases: primary, secondary, tertiary, and quaternary blast injuries [1, 2], and the greatest concern being the primary blast injuries. The eardrum or tympanic membrane (TM) rupture has been traditionally considered as a biomarker for blast injuries in ear and other organs. Blast induced hearing loss is categorized into TM perforation or rupture, cochlear hair cell damage, and rupture of round window [3]. The TM rupture results in acute hearing loss, tinnitus, pain, and dizziness. Although most injuries can be spontaneously healed through a period of time, permanent hearing loss often occurs [4]. When exposed to blast waves, there is a 16 % chance for a person to have TM perforation to induce damage in both ears. Hearing loss occurs commonly in the middle to high-frequency range [5] and there are more instances of hearing loss reported than vestibular or balance disorders. For curing, the most effective measure is to avoid exposure to other blast waves that might induce additional auditory injuries. However, in conflict zones, exposure to the multi-blast waves is often inevitable, especially for those far away from the blast sites, who are exposed to blast waves at magnitudes near or below a threshold pressure that can still develop hearing loss even if they do not show visible blast injury [6, 7].

The eardrum or tympanic membrane separates the middle ear from the outer ear, receives the sound waves collected by the outer ear, and transmits them to the middle ear. The TM plays an important role in coupling sound pressure wave in the ear canal with ossicular vibration in the middle ear. The damage in the TM caused by various diseases, pathological conditions, and blast wave, can

contribute to different levels of conductive hearing loss [8–13].

The eardrum is a multi-layer membrane including the epidermal, collagen fibrous and mucosal layers. The collagen fibers provide primarily the mechanical stiffness of the TM. It consists of a matrix of ground substance embedding approximately 22 μm thick of collagen fiber layer aligned primarily along the radial direction emanating from the umbo, and approximately 15 μm thick collagen fiber layer along the circumferential direction [14]. A major part of TM is the pars tensa, which is within tympanic annulus ring located at the boundary; the malleus manubrium bone is attached in the central portion at the medial side. The small dimensions of the TM (about 70 μm thick and 9 mm in diameter) make it difficult to measure the mechanical properties. Numerous investigations of the mechanical behavior of human TMs have been performed at low strain rates or low frequencies [15–20]. The Young's modulus of a human TM strip specimen was reported as 10–20 MPa. Some of these property values are often used as input to model sound transmission and hearing sensitivity in middle ear [21, 22]. Accurate measurements of TM dynamic properties will help to understand the effects of structural changes of the TM, such as trauma by blast wave and infection, on the sound transmission and conductive hearing loss through modeling [23, 24].

The eardrum is subjected to loading in the frequency domain. The Young's modulus of the TM at high frequency was reported as 40 MPa in the circumferential direction at a frequency of 890 Hz [25]. Since the TM performs its function in the frequency domain, its mechanical properties must be characterized within the auditory frequency range, or high strain rates, for use to model the acoustic wave transmission in human ear. It is well known that for most biological tissues, the mechanical properties are not sensitive to strain rate under relatively low strain rate range [26]. However, their mechanical properties can change rapidly at high strain rate as tissues are relatively soft materials in which high strain rate behavior corresponds to their behavior towards glassy state. Recently, the Young's modulus of human TMs has been measured at high strain rates, corresponding approximately to the behavior in the higher frequency regime using a split Hopkinson tension bar (SHTB) [27, 28]. The results show a strong rate-dependent behavior for TM. In the study of traumatic blast injuries, the ear is one of the most vulnerable organs affected by the blast wave. Recently, the effects of acute and repeated exposure to blast overpressure in rodents were evaluated in order to help better understand the potential ramifications for injury in humans exposed to blast [29]. A blast chamber was set up to produce blast waves with profiles similar to that induced by explosives, in order to develop a reproducible mouse model to study blast-induced hearing loss [30]. A bench model consisting of a simplified ear canal, eardrum, and middle ear cavity was tested in a blast chamber for high intensity sound transmission, and the experimental data were compared with the simulation results from a finite element model within the CFX/ANSYS environment [31].

In this paper, we use a highly sensitive miniature SHTB to measure the mechanical properties of human eardrum after exposure to blast waves at high strain rates, corresponding approximately to the behavior at high frequencies, and compare the properties with the corresponding results from the control TMs which are not subjected to blast waves. The control and blast-exposed human TM specimens were prepared in the radial and circumstantial directions, and tested on the SHTB to determine the Young's modulus at high strain rates. The results are converted to the complex modulus in the frequency domain. The viscoelastic properties of TMs after exposure to blast waves are compared and discussed with the control (normal) TMs.

Experiments

Exposure of Human TMs to Blast Waves

Fresh human cadaveric temporal bones, including the complete normal organ of the ear, were obtained from Life Legacy Foundation, a certified human tissue supply source for military research. The study protocol was approved by the US Army Medical Research and Material Command (USAMRMC) Office of Research Protections (ORP). All experiments on human temporal bones were performed in the Biomedical Engineering Lab at the University of Oklahoma. A temporal bone containing an intact TM and ossicular chain with the pinna attached was mounted to a specifically designed "head block" inside the test chamber (Fig. 1a, b). A compressed air (nitrogen)-driven blast apparatus located inside the chamber was used to mimic blast exposure in this study. A polycarbonate film (McMaster-Carr, Atlanta, GA) of either 130 or 260 μm thick was used as a diaphragm, the rupture of which under compressed air generated blast overpressure of at least 207 kPa (30 psi, corresponding to 200 dB sound pressure level). The overpressure level applied on a TM was controlled by varying the distance from the blast reference plane.

A pressure sensor (Model 102B16, PCB Piezotronics, Depew, NY) was placed at the entrance of the ear canal (approximately 1 cm off the center of the ear canal opening) to monitor the blast pressure as shown in Fig. 1b. The pressure signal at P_0 was acquired by the cDAQ 7194 and

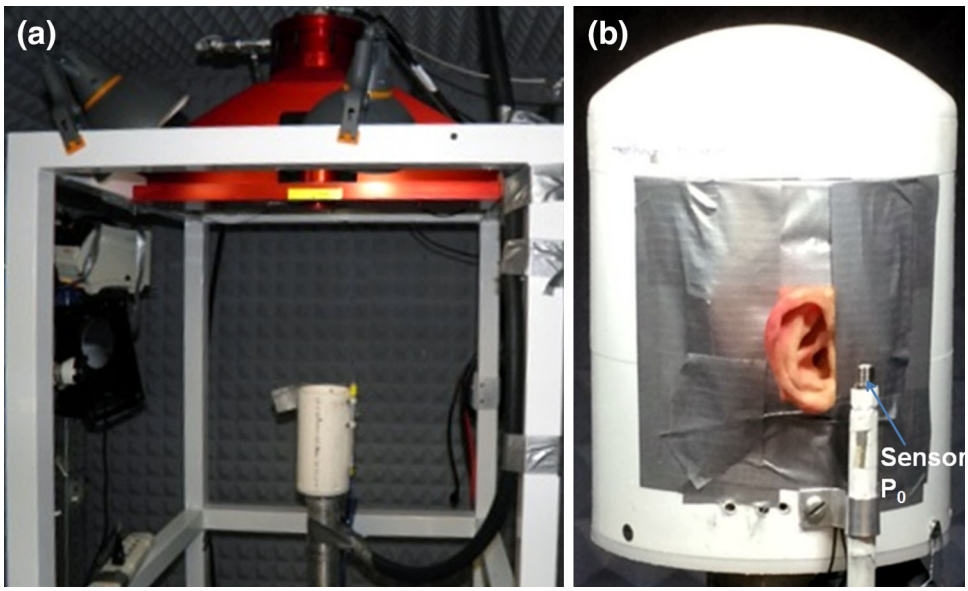


Fig. 1 The setup for the blast chamber that was used to induce blast waves to apply on a human TM bulla. **a** An overview of the blast chamber; **b** A *zoomed-in view* of human temporal bone bulla embedded inside a dummy head

A/D converter 9215 (National Instruments Inc., Austin, TX) with a sampling rate of 100 ks/s (10 μs interval). The LabVIEW software package (NI Inc.) was used for data acquisition and analysis. Before blast test, two control TMs were harvested, the information of which is shown in Table 1. The remaining temporal bones were divided into two groups. One group was exposed to blast waves for four times with an average peak pressure of 33 kPa (4.8 psi, as measured at P_0) without inducing TM rupture. This group of TM information is shown in Table 2. Another group was subjected to three to four times of blast exposure as the peak pressure increases with the number of exposures until reaching a peak value of approximately 66.5 kPa (9.5 psi) to induce rupture in the TM. The information for this group of TMs is shown in Table 3. After exposures to blast waves, the TM was harvested from the temporal bone for preparation of strip specimens for dynamic tensile experiments on the miniature SHTB.

Preparation of Human TM Strip Specimens

The control TMs with the tympanic annulus and malleus attached (Fig. 2), were harvested from two TM bullas. After the TM bullas were exposed to multiple blast waves,

Table 1 Control TM sample information and SHTB results

TM sample	Information	Location	Strain rate (s^{-1})	Modulus E (MPa)	Maximum stress reached σ_m (MPa)	Maximum strain reached ε_m (%)
TB 15-16R	64, F, R	1T	596	25.6	3.9	25
		2T	744	28.2	1.6	24
		3T	368	32.8	6.0	15
		4T	562	27.3	4.1	21
		5T	1365	51.8	19.1	50
		6T*	334	24.3	1.8	14
TB15-17L	79, M, L	1R	1280	39.4	6.2	24
		2R	518	37.7	4.8	22
		3R	885	34.4	2.5	34
		4R	1590	39.0	9.8	22
		5R1*	154	31.6	2.2	7.0
		5R2*	392	55.2	11.5	16
		6R*	171	3.21	1.9	8.0

M male; *F* female; *R* right ear; *L* left ear. Location 1T, 1R, etc. are labeled in Fig. 4. *T* transverse direction, *R* radial direction

* At a lower strain rate, the TM did not rupture and a second SHTB impact experiment was conducted. TB15-xx is the sample code for TM; the number in the information column is the age

Table 2 Blast-exposed (non-ruptured) TM information and SHTB results

TM sample	Information	Location	Strain rate (s^{-1})	Modulus E (MPa)	Maximum stress reached σ_m (MPa)	Maximum strain reached ε_m (%)
TB 15-7L	79, M, L (non-ruptured)	2R	841	55.1	4.4	11
		3R	558	53.2	15.1	20.8
		5R	946	90.2	10.0	9.2
		6T	1168	78.3	6.6	6.6
TB15-8R	58, M, R (non-ruptured)	2R	848	50.5	4.70	20.3
		3R*	359	48.9	7.40	16.2
		4T	913	21.4	8.10	38.3
		5T*	422	26.2	5.80	18.4
TB15-18R	79, M, R (non-ruptured)	1T	1550	24.3	6.50	45
		2T*	312	22.4	3.80	14
		3T	746	39.3	3.50	16
		4T	603	34.8	9.30	18
		5T	544	29.1	6.70	19
		6T*	306	50.9	8.50	14
		7T1*	385	11.7	2.00	16
		7T2*	358	12.6	2.60	15
TB15-19L	75, M, L (non-ruptured)	1T*	305	42.4	6.10	12
		2T	706	18.6	3.20	15
		4T	762	17.6	2.30	34
TB15-20R	75, M, R (non-ruptured)	1T	1578	19.0	3.20	30
		2T	944	29.1	4.90	22
		3R*	246	32.9	3.30	11
		4R*	148	24.3	1.10	6.5
		6R*	212	36.2	8.00	34

The group marked with "non-ruptured" indicates that after 4 times of exposure to the same level of blast waves, the TMs did not rupture

M male; *F* female; *R* right ear; *L* left ear

* At a lower strain rate, the TM did not break and a second SHTB tensile experiment was conducted. TB15-xx is the sample code for TM; the number in the information column is the age

the same procedure was used to harvest the blast-exposed TMs. The harvested TMs were immediately immersed in 0.9 % saline solution. A surgical knife was used to cut the pars tensa of the TM into strip specimens. Each TM strip specimen had dimensions of 1–1.5 mm wide and 4–5 mm long. The axial (length) direction of each strip specimen is along approximately either the radial or circumferential direction. In the case where a TM ruptured, the length direction of a TM specimen was mainly along the crack edge of the ruptured TM, in order to prepare as many strip specimens as possible. The specimens for measurement of Young's modulus in the radial direction were cut along the radial fibers emanating from the umbo to annulus, and the specimens for measurement of the circumferential direction were cut nearly along the local circumferential fiber direction. After cutting, each strip specimen was placed back immediately into the saline solution again, and was used in dynamic tension experiment within 30 min. Unlike the control TMs in which TM strip specimens were cut only for one orientation from one TM, for blast-exposed TMs, TM strip specimens with different orientations were cut from each TM, in order to prepare as many strip specimens as possible. TM strip-specimen orientations for ruptured TMs are shown in Fig. 3, and for un-ruptured TMs the specimen orientations are shown in Fig. 4. In this investigation, two control (healthy, without subjecting to blast exposure) TMs were used in order to compare results. In our previous work, we have conducted experiments on control TMs [27, 28], they were prepared from 11 normal TMs. In this investigation, 9 TMs were subjected to blast waves, they were then used for dynamic tension on SHTB at high strain rates. A list of control TM specimens with the age and side information is given in Table 1. Table 2 includes information for the five non-ruptured TMs after 4 times of exposure to blast waves with consistent pressures, and Table 3 contains information for the four ruptured TMs after 3–4 times of exposure to blast waves with increasing pressures.

Table 3 Blast-exposed (ruptured) TM information and SHTB results

TM sample	Information	Pressure at rupture (kPa)	Location	Strain rate (s^{-1})	Modulus E (MPa)	Tensile strength σ_m (MPa)	Failure strain ε_m (%)
TB 15-4R	64, M, R (ruptured)	84.1	1R	846	48.6	7.1	32.5
TB15-5L	73, M, L (ruptured)	77.6	2R	2756	54.3	17.6	41.2
			3R	935	83.7	26.6	20.5
			4R	1110	76.5	12.5	19.4
			5T	404	66.8	4.0	5.2
TB15-6R	73, M, R (ruptured)	118.6	1T	1405	77.2	30.4	36.2
			2T	1013	20.1	17.0	21.5
			3T	1637	50.9	12.4	19.4
			4T	868	77.2	21.2	20.9
			5T	1226	23.2	3.60	19.2
			6T	931	33.0	12.4	40.6
TB15-15L	64, F, L (ruptured)	108.9	1R	1580	96.0	5.80	6.2
			2R	635	83.0	3.40	5.0
			3R	1410	37.1	7.60	20
			4T	965	37.3	10.8	22
			5R	512	34.5	2.70	8.0

The TMs listed in this table were exposed to increasing levels of blast pressure for 3–5 times until rupture. TB15-xx is the sample code for a TM; the number in the information column is the age

M male, *F* female, *R* right ear, *L* left ear

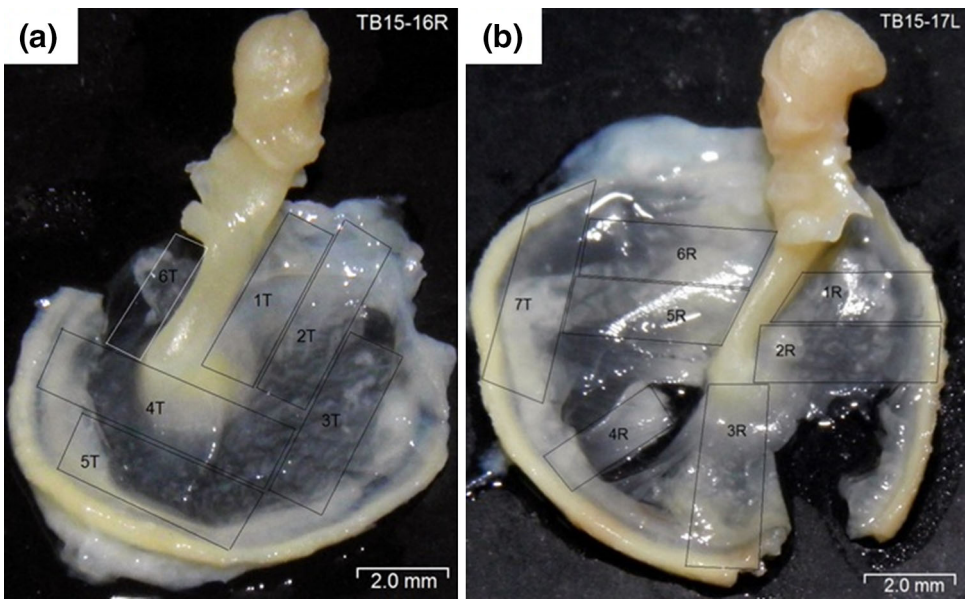


Fig. 2 Control TMs that would be cut into strip specimens as marked. **a** TB15-16R (control, i.e., healthy undamaged TM not exposed to blast waves); **b** TB 15-17L (control). Note, some TMs were damaged during the harvesting procedures, rather than due to exposure to the blast waves

SHTB Experiments

A highly sensitive miniature SHTB was used for tensile tests of TM strip specimen at high strain rates. A schematic diagram for the SHTB setup is shown in Fig. 5. The incident bar was a 3.66 m long aluminum 7075-T6 bar with 6.4 mm diameter. The transmission bar was a 2.74 m long hollow 6061-T6 bar with 5 mm inner diameter and 6.4 mm outer diameter. A pair of clamp fixtures made by 7075-T6 aluminum was used to grip a TM strip specimen. An aluminum tube striker bar was launched to make impact with a flange which was threaded to the incident bar end to load the specimen. Two semiconductor strain gages with a gage factor of 176 were attached on the opposite surfaces of the

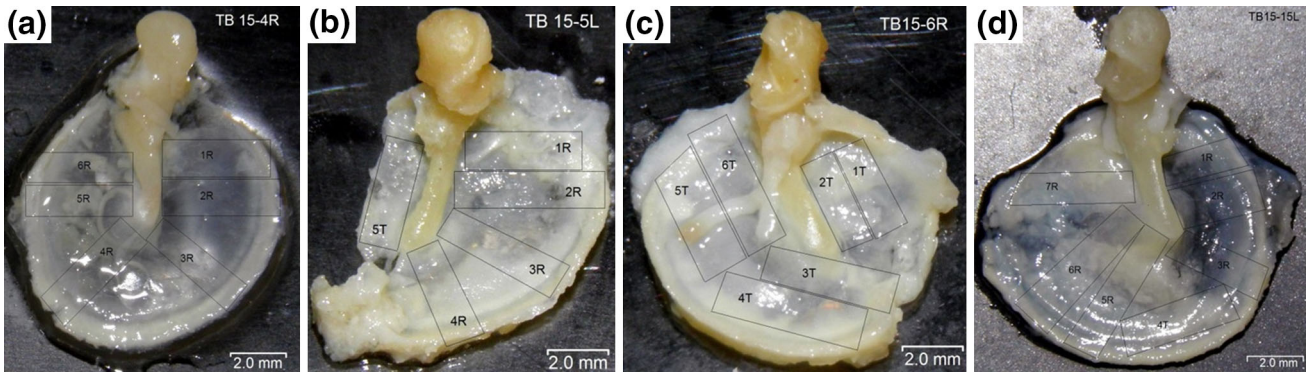


Fig. 3 Blast-exposed TMs (ruptured) that would be cut into strip specimens as marked. **a** TB15-4R; **b** TB 15-5L; **c** TB15-6R; **d** TB 15-15L. Note, the TMs ruptured due to exposure to the blast waves

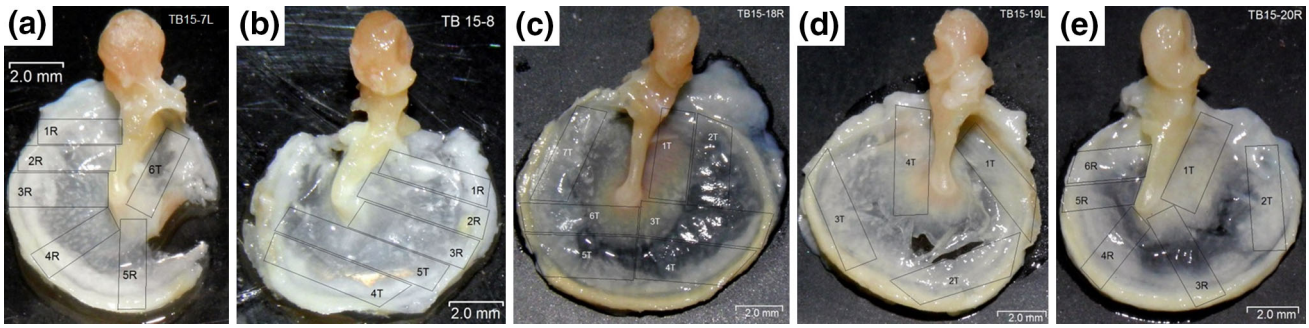


Fig. 4 Blast-exposed (non-ruptured) TMs which would be cut into strip specimens as marked. **a** TB15-7L; **b** TB 15-8R; **c** TB15-18R; **d** TB 15-19L; **e** TB15-20R. Note, the TMs were damaged during the harvesting procedures, rather than due to the blast waves

hollow transmission bar, at a distance of 17.8 cm from the clamping fixture, to measure the transmitted strain signal. A HBM Genesis 5i digital oscilloscope (25 Ms/s, 15-bit resolution, 1 MHz frequency bandwidth) was used to acquire all strain signals on bars through a Wheatstone bridge and Vishay 2310B signal-conditioning amplifier (up to magnification of 11,000, 180 kHz response frequency). A plastic collar was used as a pulse shaper to provide assistance to generate dynamic stress equilibrium on the TM strip specimen and to reach a constant strain rate condition. The miniature SHTB was used to test both control and blast-exposed human TM specimens under high strain rates. Additional details on the SHTB are documented elsewhere [27, 28].

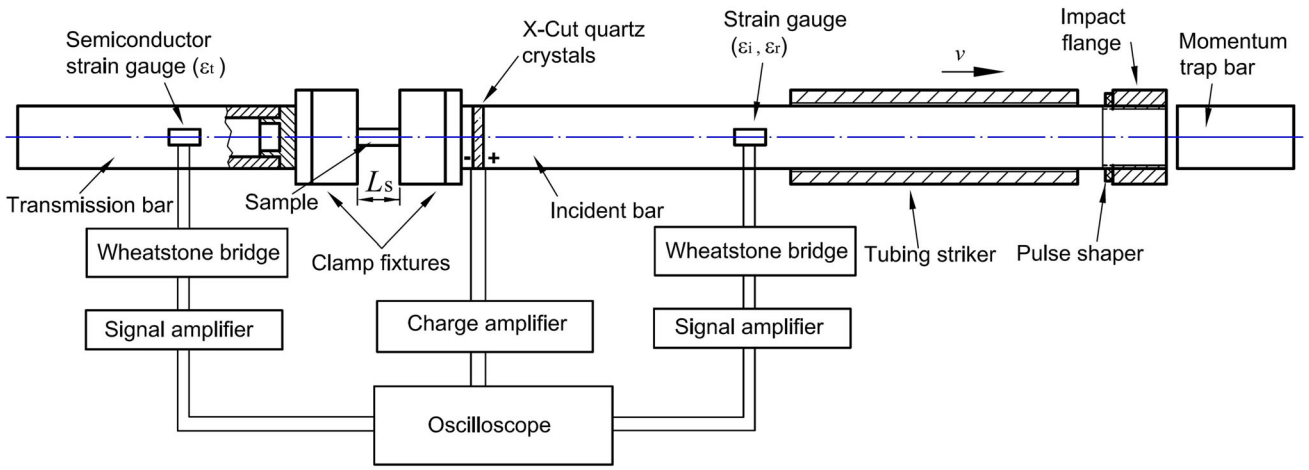


Fig. 5 Schematic diagram of a highly sensitive miniature split Hopkinson tension bar setup

With the use of a clamping fixture between the TM strip specimen and a bar end, in a valid SHTB experiment, the formulas for the stress and strain rate in a specimen are given as [32, 33]

$$\sigma_s(t) = \frac{A_t}{A_s} E_t \varepsilon_t(t) \quad (1)$$

$$\dot{\varepsilon}_s(t) = \frac{1}{L_s}[(c_i - c_t\beta)\varepsilon_i(t) - (c_i + c_t\beta)\varepsilon_r(t)] \quad (2)$$

where $\beta = E_iA_i/(E_tA_t)$; E, c, ε, σ, A and L are Young's modulus, bar wave speed, strain, stress, cross-sectional area, and length, respectively; the subscripts i, t, r represent the incident, transmitted, reflected signals, respectively. The subscript s indicates specimen. The strain history is obtained through the integration of strain rate with respect to time. Note that, for the soft TM tissue with Young's modulus in the neighborhood of tens of MPa, the typical maximum strain in a TM specimen is relatively high, on the order of 10–30 %, and therefore the compliance of the metal clamp fixtures is negligible. On the clamping fixtures mounted on two bar ends, two mini-aluminum bolts were used to tighten aluminum end plates to grip a TM strip specimen. During the gripping of a specimen, a small droplet of saline was added to the TM specimen surface to ensure that it was saturated with saline at all the time. The tensile tests were conducted at 23 ± 2 °C under relative humidity 40 ± 5 %. In this work, in order to apply preconditioning, we slightly stretched the TM strips to flat form for several times by wood sticks with round edge. Then a TM specimen was clamped for tensile test at high strain rates. Tensile tests for the control and the blast-exposed TM strip specimens were conducted within three ranges of strain rates, namely, 100–500, 500–1000 and 1000–2500 s^{-1}.

Experimental Results

TMs After Exposure to Blast Wave

In the blast experiments, the pressure in the compressed air cylinder for the shock tube was set to 2.0 MPa. The intensity of blast wave decreases with the increase of the distance from the blast nozzle. For the group one TMs (Table 2), each TM was subjected to 4 times of consistent pressure profile as shown in Fig. 6 and did not break. For the group two TMs (Table 3), each TM was subjected to increasing pressure with an increment of approximately 15 kPa in peak pressure between neighboring exposures until reaching 66.5 kPa to induce rupture of the TM. As shown in Fig. 6 during the blast duration of 0.7 ms, the four waves were very similar to each other, indicating a good repeatability of the blast chamber. After 1.0 ms, there were fluctuations in pressure waves, and those waves were slightly different, but their magnitudes were much smaller that earlier waves, they are not anticipated to affect results in this study.

It is noted that in Figs. 2, 4, the damages in the TMs were induced during harvesting of the TM, rather than due to the blast waves. In Fig. 3a–d, the damages (cracks) in the 4 blast-exposed TMs were the results of the exposure to the multi-blast waves. In Fig. 3, crack locations are spread out; they are not concentrated at a particular quadrant of the TM. The cracks are in general along the radial direction, indicating that the circumferential fibers fractured.

SHTB Results

The input and output signals from incident bar, transmission bar, and X-cut signals are shown in Fig. 7a. They are similar to the data obtained in our previous work on control TMs [27, 28]. The force at the end of the strip specimen in contact with the incident bar, labeled as "front force", was measured by the X-cut quartz. The data in Fig. 7a is analyzed to evaluate the dynamic stress equilibrium and strain rate history on a TM specimen; these results are shown in Fig. 7b. Both conditions are satisfied, indicating a valid experiment at a high strain rate. The data is processed further to determine the stress–strain relationships. Typical stress–strain curves are plotted in Fig. 8, they are mostly linear until fracture, very similar to our previously reported results. Figure 8 shows typical stress–strain curves of TM strip specimens in the radial and circumferential directions at high strain rates. Note that TM specimens did not necessarily break at these strain rates. The maximum strain experienced in each experiment was limited by the loading duration time of the miniature SHTB. Since this study

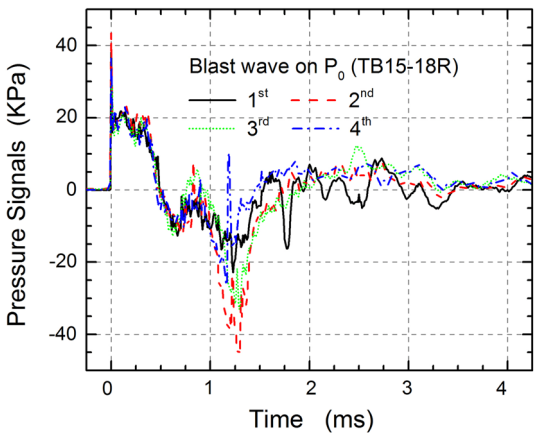


Fig. 6 The pressure histories for typical blast waves on TM measured by pressure sensor P_0

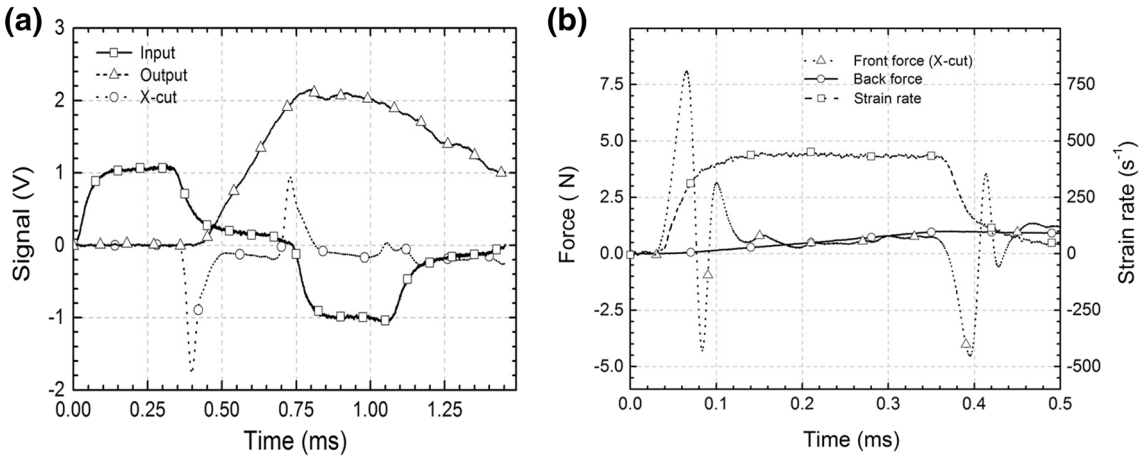


Fig. 7 Typical SHPB results. **a** Recorded signals from incident bar, transmission bar, and X-cut crystal. **b** Examination of dynamic stress equilibrium and constant strain rate history on a TM specimen

focused on the TM properties after exposure to blast wave, two control TMs as shown in Fig. 2a, b were used in SHTB test, to investigate if the TMs in this batch have similar properties as those from our previous batch. For control TM strip specimens in the radial and circumferential directions, the Young's modulus values are summarized in Table 1. The SHTB results include strain rate, maximum stress and strain achieved by the SHTB setup.

In order to compare the experimental data at different strain rates, the Young's modulus values are averaged within one of the three strain rate ranges, 100–500, 500–1000 and 1000–2500 s^{-1}, respectively. The average Young's modulus values of blast-exposed TMs within different strain rate ranges in this work are given in Table 2 for non-ruptured TMs, and Table 3 for ruptured TMs,

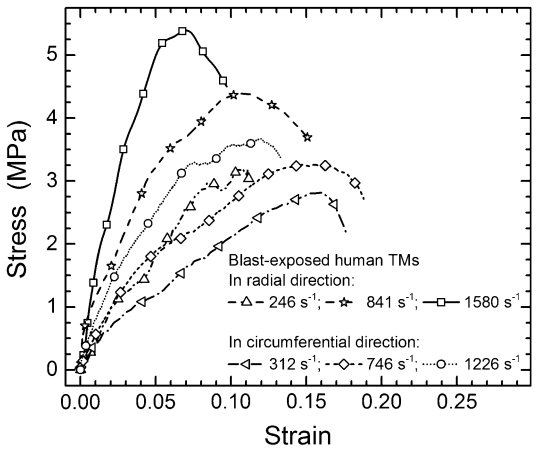


Fig. 8 Typical stress–strain curves of blast-exposed TM strip specimens in the radial and circumferential directions at high strain rates. Note that the TM specimens did not break at strain rates less than 500 s^{-1}. The strain rates of 246, 841, 1580, 312, 746 and 1226 s^{-1} were used for testing TM specimens TB15-20R-3R, TB15-7L-2R, TB15-15L-1R, TB15-18R-2T, TB15-18R-3T, and TB15-6R-5T, respectively

respectively. Within each range of strain rate, the Young's modulus is rather scattered. There is no clear trend to indicate a difference in results from the ruptured or non-ruptured TMs after exposure to blast waves. Since the number of data points in each group is not big enough, we therefore collect all data in both groups and analyze all the data together. Figure 9a, b show our previous results for the Young's modulus of normal TMs at different strain rates in the radial direction and the circumferential directions, respectively. The data shows about 20–30 % variation in Young's modulus obtained from different TM specimens [28]. The data was fitted into a model (in Discussion Section). In Fig. 9a, b, the error bar was plotted, representing 20 % deviation. A summary of the average data obtained in our previous work for control TMs [28] is given in Table 4. For control TMs, the Young's modulus as a function of strain rate is plotted in Fig. 9c, d in the radial and circumferential directions, respectively. The fitted curves in Fig. 9a, b with error bars are plotted to check if the data is in the 25 % deviation range. For two control TMs, one TM was used to cut strip specimens along the radial direction, and the other one was used to prepare strip specimens along approximately the circumferential direction. Each TM was cut into 6 or 7 pieces of strip specimens, and two or three TM specimens were tested under each of three strain rate ranges. The Young's modulus values of this batch of control TMs used in this work are similar to values obtained previously [27, 28], they are still within the range of the fitted curve of the control TMs in previous work [27, 28]. Results indicate that different batches of control human TMs give reasonably consistent results. This provides assurance to use our previous control TM results for comparison with results obtained from blast-exposed TMs, to investigate the effect of the blast wave on the TM mechanical properties.

The Young's modulus data for blast-exposed TMs under high strain rates are summarized in Table 5. Two typical

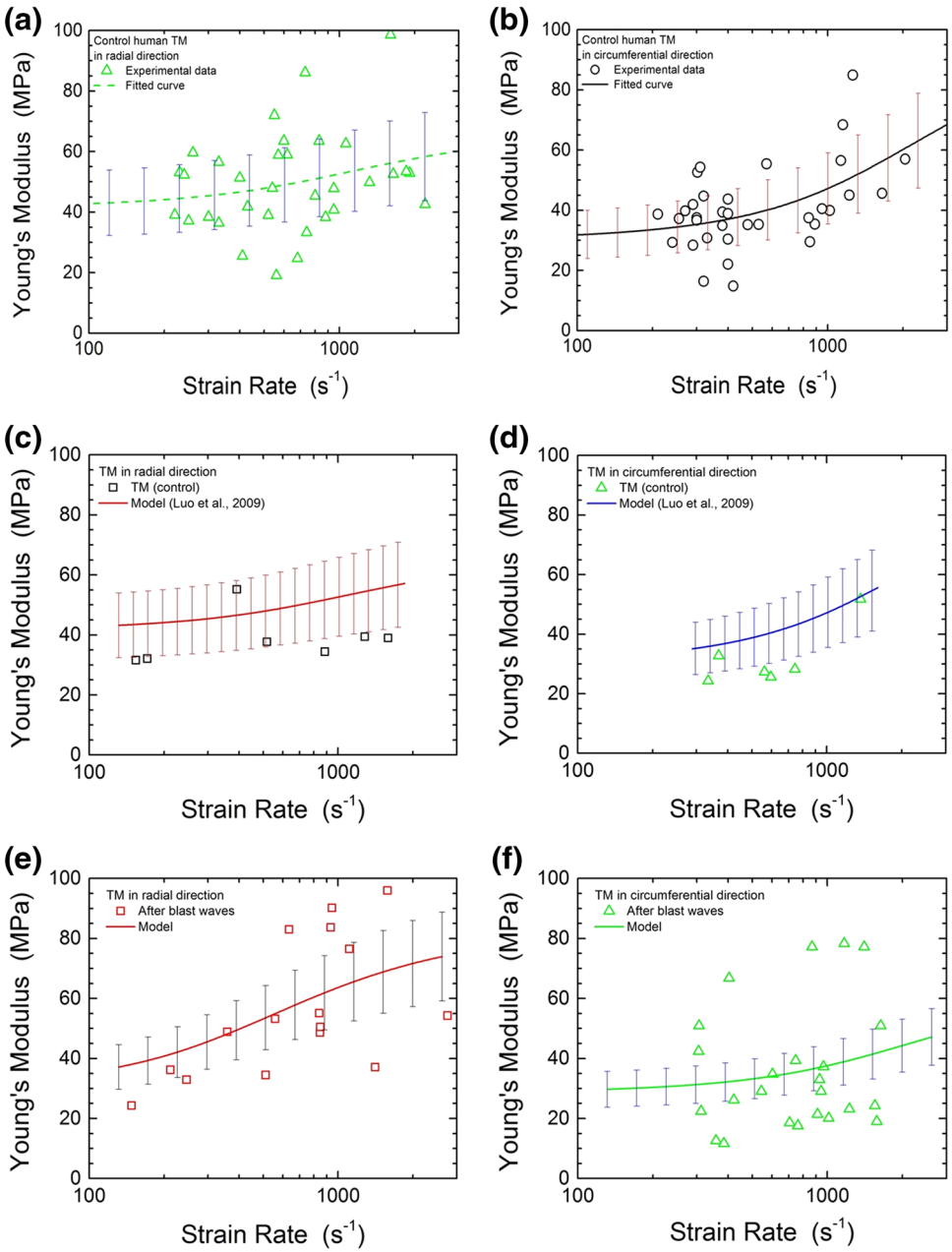


Fig. 9 Comparison of Young's modulus of TMs at different strain rates. **a** Control TMs in the radial direction [28]; **b** control TMs in the circumferential direction [28]; **c** control TMs in the radial direction; **d** control TMs in the circumferential direction; **e** blast-exposed TMs in the radial direction; **f** blast-exposed TMs in the circumferential direction

Table 4 Mechanical properties of healthy (control) human eardrum [28]

Eardrum	Number of TM specimens	Strain rate (s^{-1})	Young's modulus (MPa)	Maximum stress reached (MPa)	Maximum strain reached	Fiber direction
Healthy TM without subjecting to a blast wave	11	309 ± 77	45.2 ± 10.2	6.3 ± 3.4	11 ± 3	R
	15	714 ± 146	51.4 ± 16.6	10.4 ± 3.4	20 ± 7 %	R
	7	1654 ± 381	58.9 ± 18.5	15.9 ± 7.3	41 ± 10 %	R
	21	333 ± 68	34.1 ± 11.2	4.3 ± 1.8	11 ± 2 %	C
	6	772 ± 176	40.6 ± 7.6	7.7 ± 2.5	14 ± 8 %	C
	7	1353 ± 362	56.8 ± 15.7	13.7 ± 5.5	37 ± 10 %	C

R radial direction; *C* circumferential direction

blast-exposed TM strip specimens after tensile testing at strain rates higher than 500 s^{-1} are shown in Fig. 9. From these results, the Young's modulus as a function of strain rate is plotted in Fig. 9c, d for blast-exposed TMs in the radial and circumferential directions, respectively.

Figure 10 shows typical broken TM strip specimens after tensile experiments on SHTB. Figure 10a–d show failure patterns for control TMs in the circumferential direction, control TMs in the radial direction, blast-exposed TMs (TB15-15L-3R) in the radial direction, and blast-exposed TM (TB15-18R-7T) in the circumferential direction, respectively. The control TMs show ductile fracture pattern in both the radial and the circumferential directions (Fig. 10a, b). However, blast-exposed strip TM specimens with length in the radial direction still show ductile failure mode (Fig. 10c) with the fracture surface in a 45 degree inclined with respect to the loading direction, but the blast-exposed TM strip specimens with length along the circumferential direction show a brittle failure pattern (Fig. 10d), as indicated by the orientation of fracture surface which is perpendicular to the fiber direction.

Discussions

Viscoelastic Properties in the Time-Domain

The results obtained for blast-exposed TMs indicate that the Young's modulus values of these TMs depend on the strain rate within high strain rate range. Since data for the Young's modulus has been obtained within three ranges of high strain rates (300–2000 s^{-1}), the mechanical behavior of the TM was described as a standard linear solid with three undetermined parameters. Figure 11 shows the standard linear model consisting of two springs, with spring constants E_∞, E_1, and a dashpot with viscosity η.

The relaxation time of the model is $\tau = \eta/E_1$. For a standard linear solid under the uniaxial tension, the Young's relaxation modulus $E(t)$ is given as

$$E(t) = E_\infty + E_1 e^{-\frac{t}{\tau}} \tag{3}$$

For a linear viscoelastic material loaded at a constant strain rate $\dot{\varepsilon}_0$, the strain history is $\varepsilon(t) = \dot{\varepsilon}_0 t$.

An approach has been developed to convert the relaxation modulus to Young's modulus at different strain rates for eardrum [27, 28], foam [34] and resin [35]. For a linearly viscoelastic material under uniaxial stress state, the uniaxial stress $\sigma(t)$ is calculated from the applied strain history $\varepsilon(t)$, using the Boltzmann superposition principle

$$\sigma(t) = \int_0^t E(t-\xi)\frac{d\varepsilon(\xi)}{d\xi}d\xi \tag{4}$$

where $E(t)$ is relaxation modulus at time t. At a constant strain rate, $\varepsilon(t) = \dot{\varepsilon}_0 t$, where $\dot{\varepsilon}_0$ is the constant strain rate, Eq. (4) becomes

$$\overline{E}(t) = \frac{\sigma(t)}{\varepsilon(t)} = \frac{1}{t}\int_0^t E(\xi)d\xi \tag{5}$$

where $\overline{E}(t)$ is the average uniaxial relaxation modulus from time 0 to t. Eq. (5) indicates that the Young's relation modulus at a given strain rate is equal to the time-averaged relaxation modulus.

From an experimental stress–strain curve, the Young's modulus is determined within the limit of linearity, ε_e. The time t at the limit of linearity is determined by $t = \varepsilon_e/\dot{\varepsilon}_0$. Considering the standard linear solid model given in Eq. (3), the Young's modulus $\bar{E}(\dot{\varepsilon})$ as a function of strain rate $\dot{\varepsilon}_0$, which is also the average relaxation modulus $\bar{E}(t)$ up to time t (i.e., the elapsed time when strain reaches ε_e), is given as

$$\begin{aligned}\bar{E}(\dot{\varepsilon}) &= E_\infty + \frac{E_1(1-e^{-\frac{\varepsilon_e}{\dot{\varepsilon}\tau}})\tau\dot{\varepsilon}}{\varepsilon_e} \text{ and}\\ \bar{E}(t) &= E_\infty + \frac{E_1(1-e^{-\frac{t}{\tau}})\tau}{t}\end{aligned} \tag{6}$$

Table 5 Mechanical properties of blast-exposed human eardrum

Eardrum	Samples	Strain rate (s^{-1})	Young's modulus (MPa)	Maximum stress reached (MPa)	Maximum strain reached %	Specimen orientation
Blast-exposed	4	241 ± 36	35.6 ± 10.2	5.0 ± 3.3	17 ± 12	R
	8	765 ± 171	62.4 ± 20.4	9.3 ± 8.1	15 ± 10	R
	4	1714 ± 721	66.0 ± 25.7	10.9 ± 5.3	21 ± 15	R
	7	356 ± 49	33.3 ± 20.7	4.7 ± 2.3	14 ± 4	C
	10	798 ± 149	33.7 ± 17.1	8.6 ± 5.5	25 ± 9	C
	7	1368 ± 237	41.9 ± 26.8	11.9 ± 9.3	28 ± 13	C

R radial direction; *C* circumferential direction

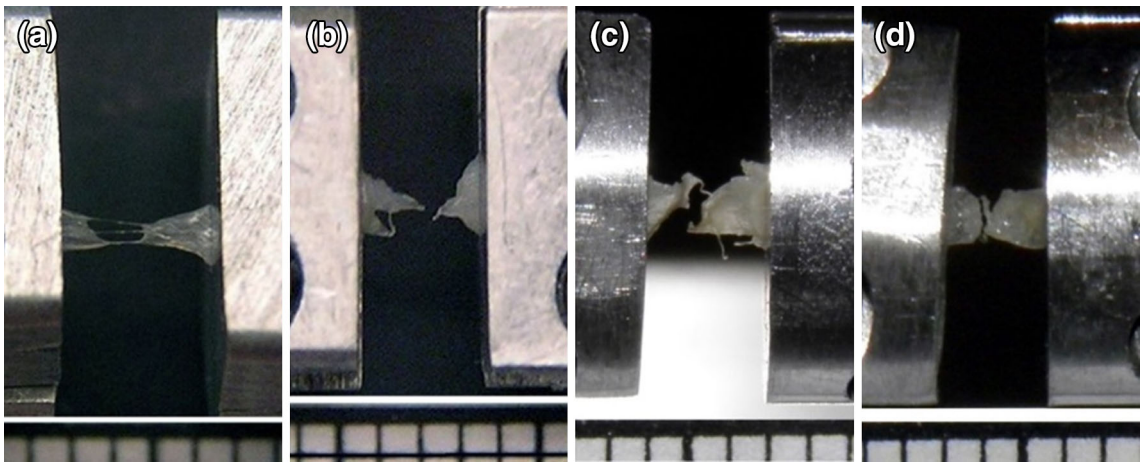


Fig. 10 Typical failed TM strip specimens after SHTB test. **a** A control TM in the circumferential direction; **b** a control TM in the radial direction; **c** TM (TB15-15L-3R) in the radial direction after blast wave; **d** TM (TB15-18R-7T) in the circumferential direction after blast wave

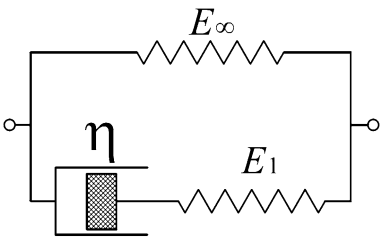


Fig. 11 A standard linear solid model

All the individual Young's modulus data (as shown in Tables 1, 2, 3) at the actual strain rates measured in SHTB tests are used as inputs to fit into Eq. (6), to search for the three best-fit parameters E_∞, E_1, and η. Table 6 summarizes the three best-fit parameters for both control and blast-exposed TMs in the radial and circumferential directions. Hence the best-fit Young's modulus is plotted in Fig. 12 as a function of strain rate (10^2–2×10^4 s^{-1}) for TM in either the radial or the circumferential direction. Although the mechanical property data points are scattered within certain range, which is a common phenomenon for bio-tissues, the curves in general represent the trend reasonably well with the experimental data. With these curves, the Young's modulus can be determined at strain rates within 300–2000 s^{-1}. Figure 12 summarizes all fitting curves for comparison. The y-axis error bars show 20 % deviation, they are plotted to represent the data scattering.

Different phenomena could happen for TMs in the radial direction or in the circumferential direction after exposure to blast waves. At strain rates lower than 300 s^{-1} data for both control and blast-exposed TMs do not show much difference. When the strain rate is higher than 300 s^{-1}, up to 2500 s^{-1}, the Young's modulus becomes in general significantly higher than that of TMs without subjecting to exposure to blast waves. However, for the TMs in the circumferential direction, the Young's modulus of blast-exposed TM decreased in tested strain rate range (300–2500 s^{-1}). As the strain rate becomes higher, the modulus becomes higher as well. These results indicate that the fibers in the radial direction of the TMs become stiffer, while the fibers in the circumferential direction become weaker after exposure to blast waves. This could be due to the fact that there are more collagen fibers along the radial direction (~22 μm thick layer) than in the circumferential direction (~15 μm thick layer) [14], and the blast waves generate a biaxial tensile stress state in a TM. Assuming each collagen fiber has about the same mechanical behavior, the difference in collagen fiber thickness in the radial and circumferential directions can give up to nearly 45 % of difference in mechanical properties (e.g., Young's modulus, tensile strength, etc.) in the two directions (radial vs. circumferential). Thus, under biaxial tension during blast pressure, the collagen fibers in the circumferential direction are expected to experience a higher stress (nearly 45 % higher) than the collagen fibers in the radial direction. When the blast pressure approaches the critical threshold value for rupture, it is easier for collagen fibers in the circumferential direction to rupture. On the other hand, the collagen fibers in the radial direction are expected to experience lower stress, thus will not experience rupture under a blast pressure that induces rupture in the collagen fibers in the circumferential direction. Therefore, the blast wave would cause some circumferential fibers to break, inducing cracks along primarily the radial direction. The radial fibers, however, are largely intact, they have gone through multi-blast waves, and tend to develop crystallization due to increased alignment of the collagen fibers, and as a result, they become stiffer.

Table 6 Best-fit parameters for Young's relaxation modulus

Eardrum	Modulus coefficient E_∞ (MPa)	Modulus coefficient E_1 (MPa)	Relaxation time τ (10^{-5} s)	Specimen orientation
Control	41.5	25.4	5.07	R
Control	30.0	69.1	2.53	C
Blasted	30.1	52.6	10.3	R
Blasted	28.5	35.5	2.61	C

R radial direction; *C* circumferential direction

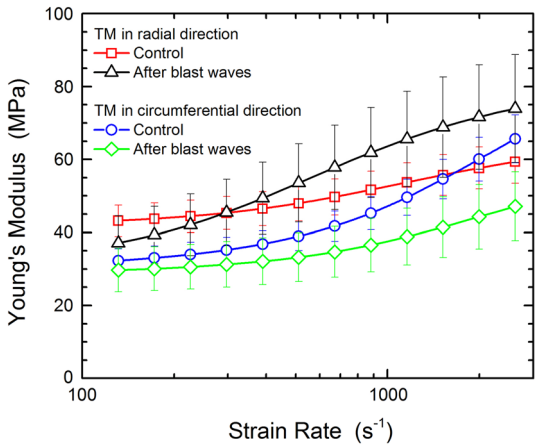


Fig. 12 Summary of fitted curves for the Young's modulus of control and blast-exposed TMs as a function of strain rate

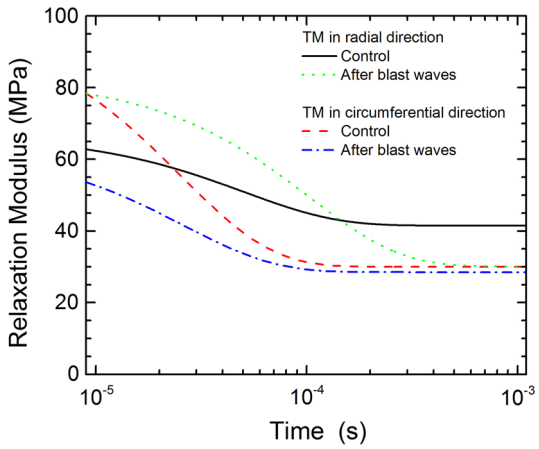


Fig. 13 Comparison of Young's relaxation modulus between control and blast-exposed TMs in the time domain

With the parameters in Eq. (6) determined, the Young's relaxation modulus $E(t)$ can be determined. The Young's relaxation modulus was obtained for TM strip specimens in both the radial and the circumferential directions, as shown in Fig. 13. For the TMs in the radial direction, there is a crossing of the relaxation curves for control and blast-exposed TMs; there exists a critical time, $\sim 1.5 \times 10^{-4}$ s, below which the relaxation modulus of blast-exposed TMs is higher than that without blast; above that time, the relaxation modulus is lower. However, for the TMs in the circumferential direction, the relaxation modulus of blast-exposed TMs is lower than that without blast; the difference in the relaxation modulus beyond the critical time is smaller than that below the time.

Viscoelastic Properties in the Frequency Domain

The relaxation modulus in the time domain was converted to the complex modulus in the frequency domain. The complex modulus and the loss tangent are expressed as

$$\tilde{E}(\omega) = E'(\omega) + iE''(\omega), \text{ and } \tan\theta = \frac{E''}{E'} \tag{7}$$

where $E'(\omega)$ is the storage modulus and $E''(\omega)$ is the loss modulus. For the standard linear solid in the frequency domain, the storage modulus $E'(\omega)$ and the loss modulus $E''(\omega)$ are calculated as [36–38]

$$E'(\omega) = E_\infty + \frac{E_1\tau^2\omega^2}{1+\tau^2\omega^2}, \text{ and } E''(\omega) = \frac{E_1\tau\omega}{1+\tau^2\omega^2} \tag{8}$$

where ω is the angular frequency, $\omega = 2\pi f$, f is the frequency. The frequency f corresponds approximately to the strain rate [27, 28, 39] in the calculation of viscoelastic properties. The storage and loss moduli of TM are shown in Fig. 14a, b as determined using Eq. (8), respectively. The loss tangent values of TM in both the radial and circumferential directions are shown in Fig. 14c.

For TMs in the circumferential direction, the storage modulus, the loss modulus and the loss tangent curves have similar tends, as shown in Fig. 14a–c, respectively. The Young's modulus values of the TMs in the circumferential directions after exposure to blast waves are lower than those for control TMs. As the frequency becomes higher, the corresponding values of TM after blast decrease more rapidly than the control TMs, indicating that the blast waves have resulted in weakening of the circumferential collagen fibers. The blast-exposed TMs show less frequency-dependent viscoelastic effect than the control TMs

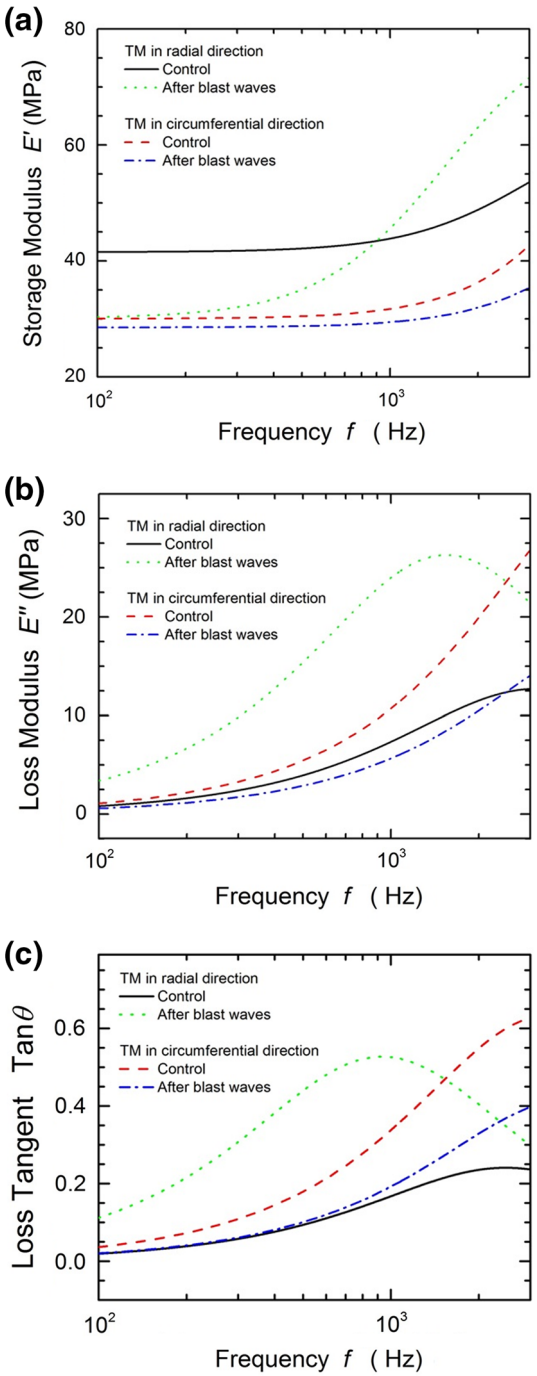


Fig. 14 Comparison of complex modulus between control and blast-exposed TMs in the frequency domain. **a** Storage modulus; **b** Loss modulus; **c** Loss tangent

in the circumferential direction, likely due to the significant damage developed in the collagen fibers in the circumferential direction. An eardrum is a multi-layer membrane including the epidermal, collagen fibrous and mucosal layers. The total thickness of a human eardrum is approximately 70 μm, among which, the collagen fibrous layer is approximately 37 μm (including 22 μm thick of collagen fibers along the radial direction, and 15 μm thick of collagen fibers along the circumferential direction). The thickness of 70 microns was used to calculate the modulus data. Since the combined thickness of the collagen fibers in the radial direction is approximately 7 μm thicker than the combined thickness of collagen fibers in the circumferential direction, the mechanical behavior in the radial direction emanating from the umbo can be different from the corresponding behavior in the circumferential direction. Although the non-raptured TMs did not exhibit visible cracks, damage likely occurred in the collagen fibers along the circumferential directions, especially after exposure to repeated blasts waves, leading to deterioration in mechanical properties. In the radial direction, however, due to the existence of thicker collagen fibers along this direction, the collagen fibers along the radial direction experienced stress levels less than a threshold value to induce permanent damage. Under exposure to repeated blast waves, the TM likely exhibits Mullin's effect, associated likely with the stress-induced crystallization or crosslinking in the collagen fibers. Additional investigation is needed to elucidate the mechanism behind the stiffening phenomenon in the radial direction in the future.

For TMs in the radial direction, the storage modulus, the loss modulus and the loss tangent show significantly different trends than those in the circumferential direction. There exists a critical frequency, ~900 Hz as shown in Fig. 14a, ~1500 Hz in Fig. 14b, and ~900 Hz in Fig. 14c, respectively. In Fig. 14a, below 900 Hz, the storage modulus of TM after exposure to blast waves is lower than that of the control TMs; after that, it becomes higher. It indicates that the blast waves induced higher frequency-dependent viscoelastic effect on TMs in the radial direction. In Fig. 14b, a peak value appears at ~1500 Hz for the loss modulus. The peak frequency decreases as compared to that of the control TM (not shown in Fig. 14b, the peak frequency is higher than 2500 Hz). The loss modulus of TM after exposure to blast waves is twice as high as that of the control TM. The loss tangent of TM after exposure to blast waves shows a much larger change, about three times as high as that of the control TM. This indicates that the blast wave causes very significant frequency-dependent behavior of TMs for TMs in the radial direction.

Conclusion

A blast chamber was used to induce blast wave to rupture TM under 35 kPa wave pressure for four times until the TM in the threshold or ruptures. A highly sensitive miniature SHTB was used to measure Young's modulus of both control TMs and blast-exposed TMs under high strain

rate 300–2000 s^{-1}. In the radial direction, the blast-exposed TMs has Young's modulus of 24.3–96 MPa, higher than the values of 45.2–58.9 MPa of the control TMs. In the circumferential direction, the blast-exposed TMs have Young's modulus of 11.7–78.3 MPa, less than the values of 34.1–56.8 MPa of the control TMs. A standard linear solid viscoelastic model was used to convert Young's modulus in the time domain into the complex modulus in the frequency domain. Blast waves cause significant changes on the mechanical properties of TM mainly due to the damage induced in the circumferential fibers and the stiffening in the radial fibers. From the viscoelastic property changes in the frequency domain, the blast-exposed TM show less viscoelastic effect in the circumferential direction, stronger viscoelastic effect in the radial direction.

Acknowledgments We acknowledge the support of DOD W81XWH-13-MOMJPC5-IPPEHA and W81XWH-14-1-0228, NIH R01DC011585, and NSF CMMI-1031829, CMMI-1132174 and ECCS-1307997. Lu acknowledges the Louis A. Beecherl Jr. Chair for additional support.

References

1. Nakagawa A, Manley GT, Gean AD, Ohtani K, Armonda R, Tsukamoto A, Yamamoto H, Takayama K, Tominaga T (2011) Mechanisms of primary blast-induced traumatic brain injury: insights from shock-wave research. J Neurotrauma 28(6):1101–1119
2. Mathews ZR, Koyfman A (2015) Blast injuries. J Emerg Med 49(4):573–587
3. Choi CH (2012) Mechanisms and treatment of blast induced hearing loss. Korean J Audiol 16:103–107
4. Ritenour AE, Baskin TW (2008) Primary blast injury: update on diagnosis and treatment. Crit Care Med 36(7):S311–S317
5. Shah A, Ayala M, Capra G, Fox D, Hoffer M (2014) Otologic assessment of blast and nonblast injury in returning middle east-deployed service members. Laryngoscope 124:272–277
6. Yeh DD, Schecter WP (2012) Primary blast injuries—an updated concise review. World J Surg 36:966–972
7. Radford P, Patel HDL, Hamilton N, Collins M, Dryden S (2011) Tympanic membrane rupture in the survivors of the July 7, 2005, London bombings. Otolaryngol Head Neck Surg 145(5):806–812
8. Hunter LL, Margolis RH (1997) Effects of tympanic membrane abnormalities on auditory function. J Am Acad Audiol 8:431–446
9. da Costa SS, Paparella MM, Schachern PA, Yoon TH, Kimberley BP (1992) Temporal bone histopathology in chronically infected ears with intact and perforated tympanic membranes. Laryngoscope 102:1229–1236
10. Ruah C, Penha R, Schachern P, Paparella M (1995) Tympanic membrane and otitis media. Acta Oto-rhino-laryngologica Belg 49:173–180
11. Voss SE, Rosowski JJ, Merchant SN, Peake WT (2001) Middle-ear function with tympanic-membrane perforations. I. Measurements and mechanisms. J Acoust Soc Am 110:1432–1444
12. Oktay MF, Cureoglu S, Schachern PA, Paparella MM, Kariya S, Fukushima H (2005) Tympanic membrane changes in central tympanic membrane perforations. Am J Otolaryngol 26:393–397
13. Rosowski JJ, Nakajima HH, Cheng JT (2014) Current topics in the study of sound conduction to the inner ear, Chapter 26 in Perspectives on Auditory Research. In: Popper AN, Fay RR (eds) Handbook of Auditory Research, vol 50. Springer, Berlin, pp 493–511
14. Lim DJ (1995) Structure and function of tympanic membrane: a review. Acta Oto-rhino-laryngolog Belg 49:101–115
15. von Békésy G (1960) Experiments in Hearing. McGraw Hill, New York
16. Dirckx JJ, Decraemer WF (2001) Effect of middle ear components on eardrum quasi-static deformation. Hear Res 157:124–137
17. Fay J, Puria S, Decraemer WF, Steele C (2005) Three approaches for estimating the elastic modulus of the tympanic membrane. J Biomech 38:1807–1815
18. Cheng T, Dai C, Gan RZ (2007) Viscoelastic properties of human tympanic membrane. Ann Biomed Eng 35:305–314
19. Huang G, Daphalapurkar NP, Gan RZ, Lu H (2007) A method for measuring linearly viscoelastic properties of human tympanic membrane using nanoindentation. J Biomech Eng-Trans ASME 130:014501
20. Daphalapurkara NP, Dai C, Gan RZ, Lu H (2009) Characterization of the linearly viscoelastic behavior of human tympanic membrane by nanoindentation. J Mech Behav Biomed Mater 2(1):82–92
21. Gan RZ, Sun Q, Feng B, Wood MW (2006) Acoustic-structural coupled finite element analysis for sound transmission in human ear-pressure distributions. Med Eng Phys 28:395–404
22. Wang X, Cheng T, Gan RZ (2007) Finite-element analysis of middle-ear pressure effects on static and dynamic behavior of human ear. J Acoust Soc Am 122:906–917
23. Puria S (2003) Measurements of human middle ear forward and reverse acoustics: Implications for otoacoustic emissions. J Acoust Soc Am 113:3464–3481
24. Ferris P, Prendergast PJ (2000) Middle-ear dynamics before and after ossicular replacement. J Biomech 33:581–590
25. Kirikae I (1960) The Structure and function of the middle ear. University of Tokyo Press, Tokyo
26. Fung YC (1993) Biomechanics: mechanical properties of living tissues, vol 2. Springer, New York
27. Luo H, Dai C, Gan R, Lu H (2009) Measurement of Young's modulus of human tympanic membrane at high strain rates. J Biomech Eng-Trans ASME 131(6):064501
28. Luo H, Lu H, Dai C, Gan R (2009) A comparison of Young's modulus for normal and diseased human eardrums at high strain rates. Int J Exp Comput Biomech 1(1):1–22
29. Ahlers ST, Vasserman-Stokes E, Shaughness MC, Hall AA, Shear DA, Chavko M, McCarron RM, Stone JR (2012) Assessment of the effects of acute and repeated exposure to blast overpressure in rodents: toward a greater understanding of blast and the potential ramifications for injury in humans exposed to blast. Front Neurol 3:32
30. Cho SI, Gao SS, Xia A, Wang R, Salles FT, Raphael PD, Abaya H, Wachtel J, Baek J, Jacobs D, Rasband MN, Oghalai JS (2013) Mechanisms of hearing loss after blast injury to the ear. PLoS ONE 8(7):e67618
31. Hawa T, Gan RZ (2014) Pressure distribution in a simplified human ear model for high intensity sound transmission. J Fluids Eng 136(11):111108
32. Gray GT (2000) Classic split Hopkinson pressure bar technique', mechanical testing and evaluation. ASM 8:462–476
33. Luo H, Lu H, Leventis N (2006) The compressive behavior of isocyanate-crosslinked silica aerogel at high strain rates. Mech Time-Depend Mater 10:83–111
34. Luo H, Zhang Y, Wang B, Lu H (2009) Characterization of the compressive behavior of glass fiber reinforced polyurethane foam at different strain rates. J Offshore Mech Arct Eng-Trans ASME 132(2):021301

35. Luo H, Lu G, Roy S, Lu H (2013) Characterization of the viscoelastic behavior of bismaleimide resin before and after exposure to high temperatures. Mech Time-Depend Mater 17(3):369–399
36. Knauss WG, Emri I, Lu H (2008) Mechanics of polymers: viscoelasticity. In: Sharpe Jr, William N (eds) Handbook of experimental solid mechanics. Springer, USA, pp 49–96
37. Aerts JRM, Dirckx JJJ (2010) Nonlinearity in eardrum vibration as a function of frequency and sound pressure. Hear Res 263:26–32
38. Zhang X, Gan R (2013) Dynamic properties of human tympanic membrane based on frequency-temperature superposition. Ann Biomed Eng 41:205–214
39. Emri I, von Bernstorff BS, Cvelbar R, Nikonov A (2005) Re-examination of the approximate methods for interconversion between frequency- and time-dependent material functions. J Non-Newtonian Fluid Mech 129:75–84

Pressure Distribution in a Simplified Human Ear Model for High Intensity Sound Transmission

Takumi Hawa[1]
School of Aerospace
and Mechanical Engineering,
The University of Oklahoma,
865 Asp Avenue,
Felgar Hall Room 218,
Norman, OK 73019
e-mail: hawa@ou.edu

Rong Z. Gan
School of Aerospace
and Mechanical Engineering
and OU Bioengineering Center,
The University of Oklahoma,
865 Asp Avenue,
Felgar Hall Room 218,
Norman, OK 73019
e-mail: rgan@ou.edu

High intensity noise/impulse transmission through a bench model consisting of the simplified ear canal, eardrum, and middle ear cavity was investigated using the CFX/ANSYS software package with fluid-structure interactions. The nondimensional fluid-structure interaction parameter q and the dimensionless impulse were used to describe the interactions between the high intensity pressure impulse and eardrum or tympanic membrane (TM). We found that the pressure impulse was transmitted through the straight ear canal to the TM, and the reflected overpressure at the TM became slightly higher than double the incident pressure due to the dynamic pressure (shocks) effect. Deformation of the TM transmits the incident pressure impulse to the middle ear cavity. The pressure peak in the middle ear cavity is lower than the incident pressure. This pressure reduction through the TM was also observed in our experiments that have dimensions similar to the simulation bench model. We also found that the increase of the pressure ratio as a function of the incident pressure is slightly larger than the linear growth rate. The growth rate of the pressure ratio in this preliminary study suggests that the pressure increase in the middle ear cavity may become sufficiently high to induce auditory damage and injury depending on the intensity of the incident sound noise. [DOI: 10.1115/1.4027141]

Introduction

The significant recent increase in terrorist activity and military involvement has resulted in a greater risk to human health from explosions and blast waves. Despite its protective technology, the military has experienced the development of traumatic brain injury (TBI), auditory damages, and the loss of lives due to insufficient blast protection capabilities. For example, TBI has been observed in Iraq and Afghanistan and is a primary injury that impairs brain function and structures temporarily or permanently due to the significant levels of external forces, such as pressure, volumetric tension, and shear stress [1]. TBI cannot be treated by conventional medical technologies. In order to improve personal protection devices against TBI, blast injury mechanics has been an active research topic. Examples of this research include the development of finite element (FE) models for the mechanical response of the head and brain to blast loading [2,3].

Another example is auditory damages to the military service personnel who are exposed to high intensity sound produced by explosions and jet engines. Hearing loss becomes the most common disability in veterans. Auditory damage and injury cause eardrum or tympanic membrane rupture, which requires greater pressure differentials due to high magnitude blast than damage to the inner ear [4]. Therefore, understanding high intensity pressure wave transduction through the ear and proposing advanced hearing protection mechanisms is one of the major challenges in auditory sciences and rehabilitation engineering.

The normal hearing level of a human being is below 130 dB sound pressure level, which results in linear acoustic transmission of sound pressure into the inner ear or cochlea. To understand the mechanisms of auditory function in relation to ear structure changes, creating a physical model of the cochlea has been extensively challenged by many researchers due to the complexity of the geometry and material properties [5–7]. A simplified mathematical model of a guinea pig cochlea, which consisted of a coiled geometry as a straight channel, showed that there is no significant difference in the calculations due to the geometric complexity [8,9]. Recently, various FE models of the human ear have been developed [10–13]. In all published FE models, the ear components are assumed as a linear system with small vibrations for acoustic-mechanical transmission from the TM to the middle and finally to the cochlea. The dominant process used in FE modeling has been harmonic analysis with the acoustic-structure-fluid coupling [12–15].

However, the high intensity noise transmission in the human ear with fluid-structure interaction for modeling elastic TM has not been studied based on the authors' knowledge. In spite of the significant governmental and military resources directed towards reducing the risk to human health from blast waves, it is widely accepted that the effects of blast waves on the human ear canal and middle ear are poorly understood. Therefore, investigation of high intensity sound transduction through the ear is one of the most important research areas in rehabilitation engineering.

The work reported in this paper is focused on understanding the high intensity impulse transmission mechanism from the ear canal to the middle ear cavity. We employ a commercial numerical simulation package, CFX/ANSYS, with fluid-structure interactions to model benchmark geometry of the ear canal, TM, and cavity structure and to simulate the pressure wave propagation through the ear. As a preliminary study to have a basic idea of how high intensity noise transmits through the bench model, the TM is assumed as a linear elastic material. The dimensionless impulse and the nondimensional parameter q derived by Taylor [16] are used to describe the fluid-structure interaction. The relationship between the pressure ratio (the incident pressure to the pressure in the middle ear cavity) and the material properties of the membrane associated with the duration time of the overpressure wave is clarified. The results provide insight into the relationship between q and the pressure ratio. Also, we compare the simulation results with the blast experiments and identify the mechanism of the pressure wave transmission through the TM to the cavity.

[1]Corresponding author.

Contributed by the Fluids Engineering Division of ASME for publication in the JOURNAL OF FLUIDS ENGINEERING. Manuscript received July 30, 2013; final manuscript received February 27, 2014; published online September 4, 2014. Assoc. Editor: John Abraham.

 Copyright © 2014 by ASME

Downloaded From: http://fluidsengineering.asmedigitalcollection.asme.org/ on 09/11/2014 Terms of Use: http://asme.org/terms

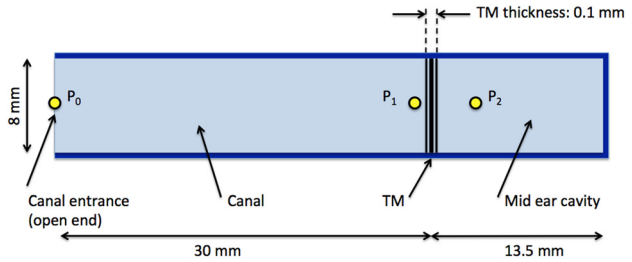


Fig. 1 Geometry of the model

Benchmark Model for the Ear and Simulation Conditions

A benchmark model for the ear consisting of simplified ear canal, TM, and middle ear cavity is presented in Fig. 1. The pipe is divided into two sections by an elastic thin plate, which models the TM. The ear canal and the cavity are sectioned between the open-end and TM, and between the TM and close-end, respectively. The lengths of the ear canal and cavity are 30 mm and 13.5 mm, respectively, based on published ear anatomic structure [11,17]. The thickness of the TM is 0.1 mm, and the diameter of the pipe is 8 mm according to the geometry of the human TM and ear canal [18].

For a simulation of continuous fluid domain, the continuity, momentums, and energy equations from physical principles of classical fluid mechanics have been used to predict the high intensity overpressure propagation in the domain. These equations are given by [19]

$$\frac{\partial \rho_f}{\partial t} + \nabla \cdot (\rho_f v) = 0$$

$$\frac{\partial \rho_f \boldsymbol{V}}{\partial t} + \nabla \cdot (\rho_f \boldsymbol{V}\boldsymbol{V}) = -\nabla p + \nabla \cdot \tau_f$$

$$\frac{\partial (\rho_f h_{\text{tot}})}{\partial t} - \frac{\partial p}{\partial t} + \nabla \cdot (\rho_f \boldsymbol{V} h_{\text{tot}}) = \nabla \cdot (\lambda \nabla T) + \nabla \cdot (\boldsymbol{V} \cdot \tau_f)$$

where t is the time, ρ_f is the fluid density, τ is the stress tensor of the fluid, $\boldsymbol{V}$ is the velocity vector, p is the pressure, T is the temperature, and λ is the thermal conductivity of the fluid. The stress tensor can be defined as

$$\tau_f = \mu\left(\nabla \boldsymbol{V} + (\nabla \boldsymbol{V})^T - \frac{2}{3}\delta \nabla \cdot \boldsymbol{V}\right)$$

where δ is the Kronecker δ, and μ is the viscosity of the fluid. The total enthalpy h_{tot} can be defined as

$$h_{\text{tot}} = h_{st} + V^2/2$$

where h_{st} is the static enthalpy. An arbitrary Lagrangian–Eulerian formulation is used to solve the above equations, allowing the deformation of the fluid domain to be found.

The governing equation for the solid domain can be described by using the second law of motion

$$\rho_s \ddot{\boldsymbol{d}}_s = \nabla \cdot (\boldsymbol{F} \cdot \boldsymbol{S}(\boldsymbol{d}_s)) + \boldsymbol{f}_s$$

where ρ_s is the solid density, $\boldsymbol{d}_s$ is the displacement vector of the structure, $\boldsymbol{f}_s$ is the externally applied body force vector on the structure, $\boldsymbol{S}$ represents the second Piola–Kirchhoff stress tensor, and $\boldsymbol{F}$ represents the deformation gradient tensor. On the fluid-structure interfaces along TM boundaries, the particle velocity is coupled to the flexible TM structure, such that both the displacement compatibility and the traction equilibrium are satisfied.

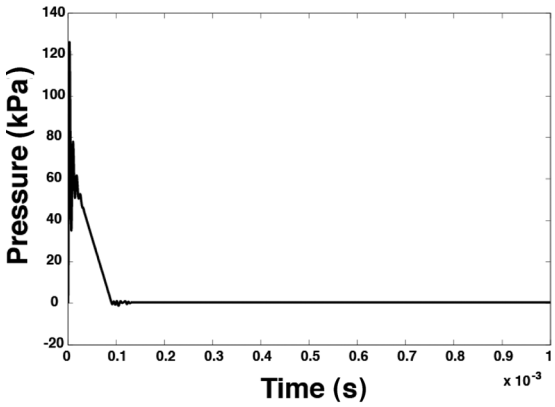


Fig. 2 A typical example of variation of the blast overpressure with time at the entrance of the ear canal model

Thus, the fluid and the structure do not overlap or detach during the motion, and no particle can cross the interface due to the kinematic requirement. The computations of fluid-structure interaction problems coupling computational fluid dynamics analysis with finite element stress analysis are performed using a commercial package, CFX with ANSYS. CFX solves the Navier–Stokes equations for the fluid flow using a finite element control volume formulation to construct the discrete equations. ANSYS is a finite element software package for linear and nonlinear stress analysis that will be used to compute the deformation of the elastic TM due to the overpressure loading. Details of the simulation package can be found in their manual [20].

The boundary conditions along the surfaces are the tangency and no-slip conditions. We consider a high-pressure wave traveling in the positive x direction through the ear canal section towards a thin elastic plate (TM). A typical example of a high-pressure incident wave pulse at the entrance of the ear canal due to the high intensity impulse/blast is presented in Fig. 2. For this particular example, we command that the input pressure is suddenly increased to 70 kPa at $t = 0^+$ and linearly decays with $t_0 = 90\mu$s, where t_0 is the duration time of the input blast overpressure. However, a large initial pressure fluctuation is observed in the figure due to the quick response to the input pressure peak in the CFX control function. Because of the quickly transient response in pressure, the high rate of increase of pressure could cause the pressure to overshoot the target pressure value and be forced by the CFX function to return the target value.

Explosions and Blast Waves

During the explosion, the release of a large amount of energy occurs in a very short period of time on the order of 10^{-6} to 10^{-3} s. Such a fast energy release induces an instantaneous increase in the pressure and temperature (approximately, 100 MPa and 3000 K, respectively) within the explosive materials. The extremely high pressure due to the explosion generates a strong blast wave propagating in the surrounding medium away from the explosion point.

In 1963, Taylor considered a blast wave as a one-dimensional exponentially decaying pressure wave pulse and investigated the interactions between blast waves and plates [16]. The momentum available in the incident pulse is given by $I_0 = \int_0^{t_0} p dt = p_0 t_0$, where p_0 is the incident pressure peak. When this incident pulse impinges on the thin plate, it induces the motion of the plate and is partly reflected. Taylor obtained a relation

$$I/I_0 = 2q^{q/(1-q)} \tag{1}$$

where I is the transmitted impulse and the q is the nondimensional parameter describing the fluid-structure interaction. This nondimensional parameter

Downloaded From: http://fluidsengineering.asmedigitalcollection.asme.org/ on 09/11/2014 Terms of Use: http://asme.org/terms

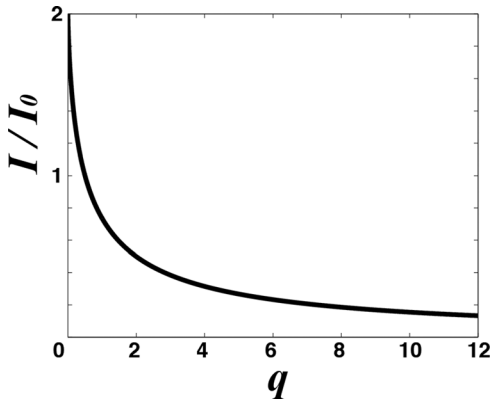


Fig. 3 Taylor's plot (momentum ratio, I/I_0 versus q) for considering fluid-structure interaction

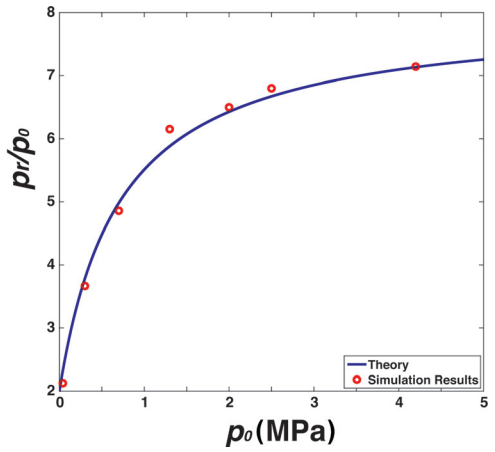


Fig. 4 Reflected pressure wave magnitudes against a solid wall with various inlet or incident pressures

$$q = t_0/t^* \tag{2}$$

compares the characteristic time of the fluid-structure interaction t^* and the incident wave duration time t_0. t^* is given by

$$t^* = \rho_s h/\rho_f c_f \tag{3}$$

where ρ_s, ρ_f, c_f, and h are the density of the TM (1200 kg/m^3) [21], density of the air (1.2 kg/m^3), sound speed of the air (343 m/s), and thickness of the TM (0.1 mm) [22], respectively. The momentum ratio of the transmitted impulse I/I_0 defined in Eq. (1) is a monotonically decreasing function of q, depending on the plate density. The above three equations (Eqs. (1)–(3)) imply that less impulse is transmitted to lighter plates because the lower plate density induces the higher value of q. For example, when the TM is relatively massive, it is hardly moving and the impulse of the pressure wave is reflected with nearly perfect. Thus, the reflected momentum is about $-I_0$, and the TM gains momentum nearly $2I_0$. The momentum ratio asymptotes to a constant value of 2 for small q and $2/q$ for large q (see Fig. 3). Based on the properties suggested by the literature, it is computed that the characteristic time of the fluid-structure interaction is 2.9×10^{-4} s, and our experiments suggest that t_0 is 3 ms (details of the discussions will appear in the Model Validation section). Thus, the time scale ratio q is approximately 10.3. However, since the round trip distance for the pressure pulse between the ear canal entrance and TM is 60 mm, it only takes 1.75×10^{-4} s, which is 1 order magnitude less than our experimental duration time t_0. When the reflected pressure wave comes back to the entrance of the ear canal, the numerical noise generated by the outer flow boundary condition propagates back to the TM and pollutes the simulation results. Thus, we run various cases of simulations for $t_0 < 3$ ms with smaller ρ_s such that the time scale ratio q can maintain its original value 10.3.

The simulation results also depend on the Young's modulus of the TM E_Y. The E_Y of the TM is 2×10^7 N/m^2 [23]. The dimensionless impulse in terms of the Young's modulus can be described as $I/\left(M\sqrt{E_Y/\rho_s}\right)$, where M is the mass per unit area of the TM. For example, when $q = 10.3$, $p_0 = 100$ kPa, $t_0 = 3$ ms, $\rho_s = 1200$ kg/m^3, $E_Y = 2 \times 10^7$ N/m^2, and the mass per unit area of the TM, $\rho_s \cdot h = 0.12$ kg/m^2, the dimensionless impulse is approximately 2.9. In order to maintain the values of the time scale ratio q and the dimensionless impulse for different values of p_0 and t_0, we must choose appropriate values of ρ_s and E_Y for each simulation case.

Model Validation

Sensitivity of Simulation. Before moving on to the fluid-structure interaction (FSI) problem, we have performed a benchmark test against known theoretical results for a wave propagation problem [24]. According to the theory of the blast wave striking a solid massive wall, the value of reflective pressure approaches eight times as high as the incident pressure for very large values of the incident pressure and dynamic pressure under strong shocks [24]. On the other hand, when the incident pressure is negligible compared with the atmospheric pressure, the value of the reflective pressure tends toward twice the incident pressure. The reflected pressure p_r for air is given by

$$p_r = 2p_0 \frac{7p_{\text{atm}} + 4p_0}{7p_{\text{atm}} + p_0}$$

where p_{atm} is the atmospheric pressure. In order to perform this benchmark test problem for the model validation, we have considered our computational domain shown in Fig. 1 with 69,216 nodes; however, the TM has been considered as a solid wall to simulate the benchmark test problem. This implies that the middle ear cavity domain does not contribute to the simulation results in this test. We have used the high-resolution scheme in the CFX options to compute the advection terms in discrete finite volume equations and the second-order backward Euler discretization scheme for transient calculation. The air density = 1.2 kg/m^3 and time step = 10 ns are used to ensure the stability of the scheme. Based on the average spatial step size = 0.3 mm and the speed of sound in the air at the room temperature = 343 m/s, the corresponding Courant-Friedrichs-Lewy number is approximated as 0.01. As for convergence criterion, we have chosen a root mean square option and 0.0001 for residual type and target value, respectively. Simulation results with various inlet pressure p_0 values (0.04, 0.3, 0.7, 1.3, 2, 2.5, and 4.2 MPa) are considered and compared with the theoretical prediction in Fig. 4. The simulation results show excellent agreement with the theoretical prediction, which implies that our model is suitable for the wave propagation analysis.

The sensitivity of the simulations to mesh refinement is investigated. The investigation focuses on $p_0 = 100$ kPa with time duration $t_0 = 10\,\mu$s, TM density $\rho_s = 4$ kg/m^3, and TM Young's modulus $E_Y = 2 \times 10^7$ N/m^2 to maintain values of q and dimensionless impulse parameter. Since the bending stiffness and nonlinear properties of the TM in response to high intensity impulse are currently not available in the literature to our knowledge, we have considered the TM as a linear isotropic elastic material for simplicity. The time step = 10 ns was chosen for all simulation studies to ensure the numerical stability for large mesh displacement.

For the model's grid refinement validation, the pressure ratio p_0/p_2 is measured with various fluid mesh sizes (5472, 13,152,

Downloaded From: http://fluidsengineering.asmedigitalcollection.asme.org/ on 09/11/2014 Terms of Use: http://asme.org/terms

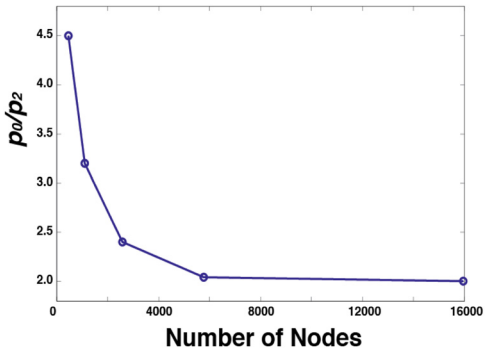


Fig. 5 Pressure ratio dependence of the number of nodes in the flow field

30,912, 69,216, and 191,472 nodes) while fixing the eight-node TM element with 12,792 nodes. Figure 5 summarizes the results obtained with various pressure ratios from simulations. It demonstrates the convergence of the computed pressure ratio results with mesh refinement. It is found that the meshes with 69,216 nodes provide a difference in computations of the pressure ratio within 1%. Moreover, the simulation time for 191,472 nodes requires more than four times longer than that for the mesh with 69,216 nodes. It should be pointed out that such a small variation in the pressure ratio might be due to the presence of a large pressure gradient at the blast wave front. This overpressure wave structural difference diminishes as the number of nodes increases with a refinement of the mesh. We have also studied mesh sensitivity of the solid (TM) domain on the simulation with the eight-node element with reduced order integration method and nonlinear option in ANSYS that are capable to consider geometric nonlinearity and to alleviate locking behavior. The deflection of the TM in the axial direction is measured with various mesh sizes (5184, 12,792, and 26,376 nodes). Figure 6 shows the meshes with 12,792 nodes provide a difference in computations of the TM deflection within 0.2%. Thus, in order to obtain sufficient accuracy for computations within reasonable simulation time, we chose to use 69,216 and 12,792 nodes in the fluid and structure domains for the simulations, respectively.

Experimental Measurement on Bench Model. To validate the FE model for simulating high intensity sound transduction through the ear and to have a better understanding of the overpressure distribution from the ear canal to the middle ear, a simple bench (physical) model with dimensions similar to the FE model of Fig. 1 was created. The bench model was made from hard plastics (i.e., polymethacrylate) with the design of the ear canal and middle ear cavity chambers as shown in Fig. 7(*a*). These two chambers were separated by a membrane of thin latex material (Saf-Care^{TM}) to simulate the TM. The diameter, length, and volume of the ear canal and middle ear cavity components were similar to that of a human ear [12,25,26]. Data of the Young's modulus and density of the latex material are not available; however, an analysis of a few other kinds of gloves estimated E_Y ranging from 0.3 to 3 MPa in the literature [27], which agreed with values obtained from our experimental measurements. Two pressure sensors (Models 102B16 and 105C02, PCB Piezotronics, NY) were inserted in the bench model at the entrance of the canal chamber and inside of the cavity chamber to measure p_0 and p_2, respectively. As shown in Fig. 7(*b*), the bench model with the inserted pressure sensors was placed in a specially designed holder and exposed to blast overpressure in the high intensity sound chamber in Gan's biomedical engineering lab at the University of Oklahoma. The compressed air (nitrogen)-driven blast apparatus is capable of generating an overpressure or impulse of at least 30 psi or 207 kPa inside an anechoic chamber.

Five exposure tests were performed on the bench model, and Fig. 8 illustrates the recorded pressure waveforms of p_0 and p_2.

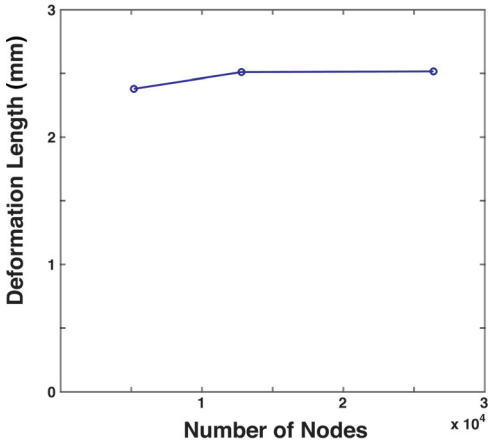


Fig. 6 TM deflection dependence of the number of nodes of the TM structure

Figure 8(*a*) shows the typical overpressure waveform of p_0 measured at the ear canal entrance within the time duration of 3 ms to reach the peak pressure. The waveform of p_2 displayed in Fig. 8(*b*) demonstrates that the impulse pressure transmitted into the middle ear cavity became somewhat similar to an acoustic waveform. The mean peak pressure of p_0 from five tests was 5.29 psi (36.5 kPa) with standard deviation ± 0.71 psi or ± 4.93 kPa. The mean peak-to-peak pressure of p_2 was 1.91 ± 0.47 psi (or 13.17 ± 3.28 kPa). The ratio of p_0 to p_2 ranged from 2.55 to 3.46 with an average of 2.77 ± 0.43. The statistical results for p_0 and p_2 (student t-test, p-value < 0.01 with 95% confidence interval) indicates that the peak pressure measured at the ear canal entrance (p_0) was significantly different from the pressure inside the middle ear cavity (p_2). These pressure results obtained from the bench model tests will be compared with simulation results in the Simulation Results and Discussions section.

Simulation Results and Discussions

Several high intensity noise loadings (between 17 and 135 kPa) induced deformation of the TM, and the changes of the pressure inside the middle ear cavity have been derived with various TM densities (between 1.2 and 36 kg/m^3) and TM Young's moduli (between 2×10^4 and 6×10^5 N/m^2). A typical example of time-history plots of the pressure propagation is shown in Fig. 8. This example is simulated with $p_0 = 49$ kPa, $E_Y = 6 \times 10^5$ N/m^2, and $\rho_s = 36$ kg/m^3. Note that the initial location of the TM is at $x = 30$ mm, and the input target pressure at the inlet of the ear canal is presented in Fig. 2. The peak target pressure was 70 kPa; however, a large initial pressure fluctuation is presented in that figure. The input pressure is damped, and the peak pressure decays to 49 kPa (see Fig. 9). The pressure wave is stabilized at $t = 0.04$ ms and propagates toward the TM with $t_0 = 90\,\mu$s (see Fig. 2). The slight sharp increase of the pressure observed at the location $x = 30$ mm at $t = 0.08$ ms in Fig. 8 indicates the initial contact with the TM. This pressure wave moves the TM front as we see the movement of the sharp increase of the pressure to the middle ear cavity side at $t = 0.10$ ms. At $t = 0.12$ ms, a large pressure discontinuity is observed at the location $x = 32.5$ mm. This indicates that the maximum deformation of the TM is reached at this time. The maximum deformation and the associated pressure are approximately 2.5 mm and 111 kPa, respectively.

At $p_{atm} = 101$ kPa and $p_0 = 49$ kPa, p_r is approximately 117 kPa. However, the maximum pressure obtained from the simulations is $p_r = 111$ kPa, which is slightly less than the predicted value because there is an energy loss at the TM due to its lighter density and elasticity. Also, the pressure value near the TM is slightly higher than twice the incident pressure p_0. The increase of the reflected pressure above the expected value of twice the incident

Downloaded From: http://fluidsengineering.asmedigitalcollection.asme.org/ on 09/11/2014 Terms of Use: http://asme.org/terms

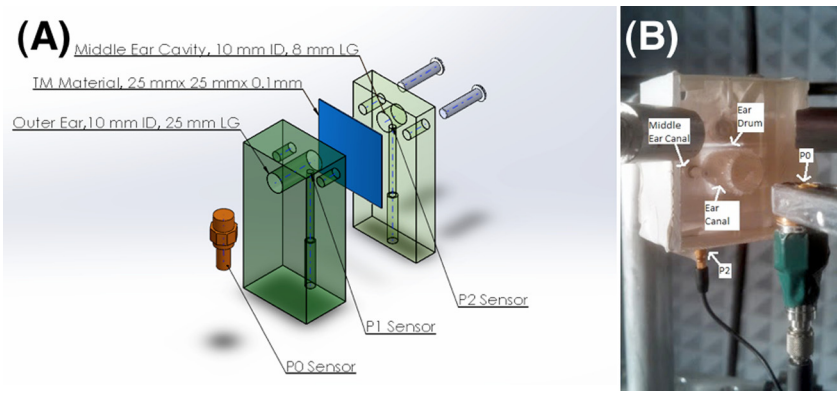


Fig. 7 (*a*) Illustration of the design of the bench model and (*b*) picture of the bench model with inserted pressure sensors placed inside of the blast or high intensity sound test chamber

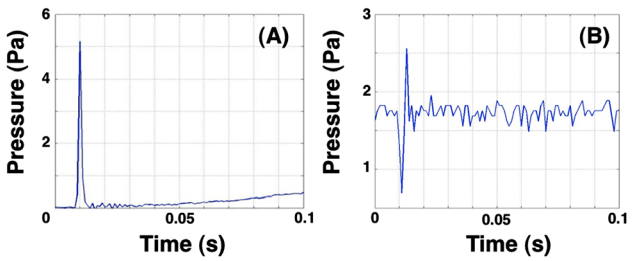


Fig. 8 (*a*) Typical waveform of p_0 (pressure amplitude-time curve) measured in bench model and (*b*) waveform of p_2 measured in bench model

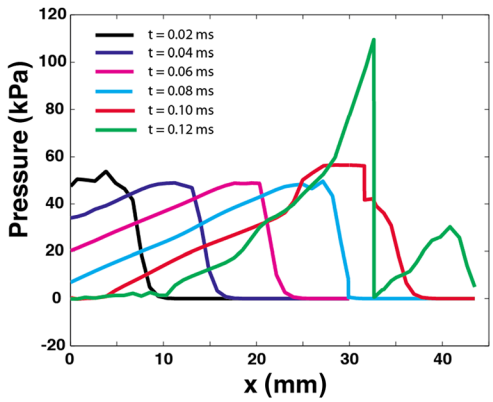


Fig. 9 A simulation of pressure propagation through the ear canal, TM, and cavity at six different times, $t = 0.02$, 0.04, 0.06, 0.08, 0.10, and 0.12 ms when $t_0 = 90\,\mu s$, $\rho_s = 36\,kg/m^3$, and $E_Y = 6 \times 10^5\,N/m^2$

value is due to the dynamic (or shock) pressure. In addition, the deformation of the TM generates another wave propagating downstream inside of the middle ear cavity. The amplitude of the pressure in the cavity (p_2) is approximately 30.5 kPa, which provides the pressure ratio p_0/p_2 approximately 1.63. Due to the presence of the TM, the pressure reduction in the middle ear cavity was observed; however, since the TM is elastic, the pressure reduction is not significantly high but dependent on the intensity of the noise. The pressure increase in the middle ear cavity could be sufficiently high to induce auditory damage and injury. After reaching the maximum deformation of the TM, the incident pressure wave is reflected in the ear canal, and the pressure peak quickly decays to slightly less than the original incident pressure value due to the loss of the energy at the TM.

Table 1 Pressure ratio p_0/p_2 from simulations

t_0 (μs)	ρ_s (kg/m^3)	E_Y (N/m^2)	p_0 (kPa)	p_1 (kPa)	p_2 (kPa)	p_0/p_2
3	1.2	2×10^4	107	142	51	2.098
5	2	3.3×10^4	98	133	50	1.960
10	4	6.7×10^5	102	140	50	2.040
30	12	2×10^5	105	165	51	2.059
60	24	4×10^5	100	170	50	2.000

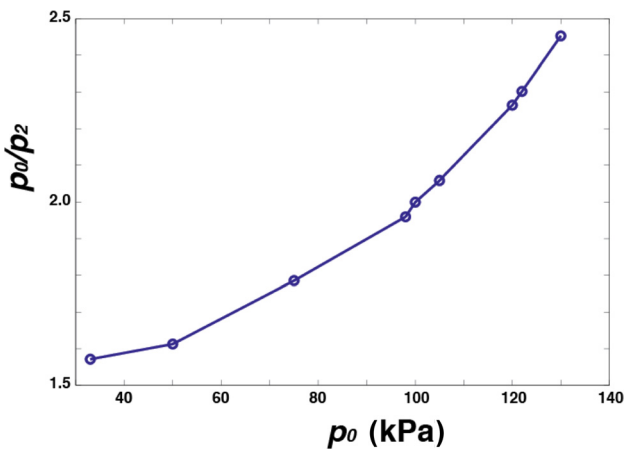


Fig. 10 Pressure ratio p_0/p_2 dependence of input pressure p_0

A summary of the pressure ratios for various duration (t_0), E_Y, and ρ_s values is presented in Table 1. Note that the values of t_0, E_Y, and ρ_s are chosen to maintain the time scale ratio q and the dimensionless impulse. q is set to be 10.3 as described in previous section, which is the value calculated based on t_0 obtained from the experiments and ρ_s of the human TM. It can be seen from the table that in the simulations with the incident pressure value p_0 being approximately the same, the pressure ratio does not change as long as the q value and the dimensionless impulse are maintained at the same values.

The dependence of pressure ratio p_0/p_2 on the incident peak pressure p_0 is shown in Fig. 10. The pressure ratio increases as the incident peak pressure increases with a slightly larger growth rate than the linear growth. This indicates that the p_2 does not increase as much as the p_0 increase. Although the growth rate of the pressure ratio is not significant, the pressure increase in the middle ear cavity could be sufficiently high to induce auditory damage and injury depending on the intensity of the incident pressure noise. Note that the pressure ratio at $p_0 = 36.5$ kPa is approximately 1.6

Downloaded From: http://fluidsengineering.asmedigitalcollection.asme.org/ on 09/11/2014 Terms of Use: http://asme.org/terms

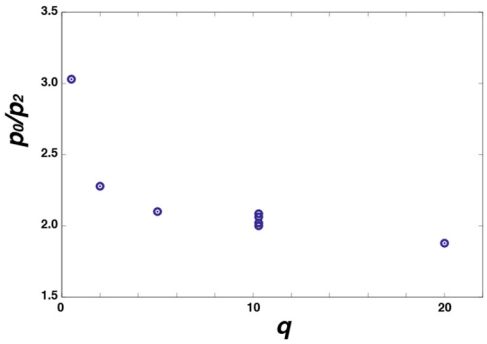


Fig. 11 Pressure ratio p_0/p_2 dependence on q

according to the figure, which indicates the pressure reduction through the TM. This pressure reduction has been seen in our experiments. The pressure ratio of the experimental data ranges from 2.55 to 3.46, which are higher than the simulation results. The difference between the simulation and experimental results is probably caused by neglecting the nonlinearity of the material properties of the TM. Moreover, the pressure ratio might depend on the material properties of the TM, and the use of the latex material may cause the difference in simulation and experimental values of the pressure ratio.

Figure 11 shows the dependence of pressure ratio p_0/p_2 on the time scale ratio q computed by simulations. It can be seen that the pressure ratio increases with a decrease in q exponentially. The trend of the curve is similar to the relationship between the momentum ratio and q (Fig. 3). When the TM is relatively massive, it hardly moves and the amplitude of the pressure wave generated in the cavity becomes smaller. Thus, the pressure ratio becomes larger. On the other hand, when the TM is relatively light, it moves easily and the amplitude of the pressure wave generated in the cavity becomes larger. Thus, the pressure ratio becomes smaller as the q decreases. These simulation results clarify the physical mechanisms of the pressure generation in the cavity.

Conclusion

We have investigated high intensity noise/impulse transmission through a bench model consisting of a simplified ear canal, TM, and middle ear cavity using the CFX/ANSYS software package with fluid-structure interactions. The nondimensional fluid-structure interaction parameter q and the dimensionless impulse are applied to describe the interactions between high intensity pressure impulse and TM. The simulations demonstrate that the pressure impulse is transmitted through the ear canal to the TM, and the reflected overpressure becomes slightly higher than twice the incident pressure. The incident pressure impulse has high enough intensity, which induces the dynamic pressure (shocks) effect. The reflected overpressure deforms the TM, and the deformation transmits the incident pressure impulse into the middle ear cavity. The incident pressure peak is much higher than that of the pressure in the middle ear cavity.

To validate the simulation results, we have conducted experiments on a physical bench model, which has dimensions similar to the simulation bench model. The experimental results show a good agreement with the simulations. It is also found that the increase of the pressure ratio as a function of the incident pressure is slightly larger than the linear growth rate. The growth rate of the pressure ratio in this preliminary study suggests that the pressure increase in the middle ear cavity may become sufficiently high to induce auditory damage and injury if the intensity of the incident sound noise reaches really high levels.

The model and simulation reported in this paper is our first step to investigate the overpressure distribution from the ear canal to the middle ear cavity. In order to understand the details of the high intensity noise transmission through the ear, it is important to consider the nonlinear mechanical properties of ear tissues and the actual geometry of the ear components in the future simulation models.

Acknowledgment

We thank Don Nakmali, M.S. and Zach Yokell, B.S. from the biomedical engineering lab at the University of Oklahoma Bioengineering Center for their expert technical assistance on the bench model test.

Nomenclature

c = sound speed
$\boldsymbol{d}$ = displacement
E_Y = Young's modulus
$\boldsymbol{f}$ = externally applied body force vector
h = static enthalpy
h_{tot} = total enthalpy
I = transmitted impulse
I_0 = momentum available in the incident pulse
M = mass per unit area of the TM
$\mathbf{n}$ = unit normal vector
p = pressure
p_{atm} = atmospheric pressure
p_r = reflected pressure
p_0 = incident pressure peak
P_0 = pressure at inlet
P_1 = pressure at TM
P_2 = pressure in the mid ear cavity
q = nondimensional fluid-structure interaction parameter
t = time
T = temperature
t_0 = duration time of the input blast overpressure
t^* = characteristic time of the fluid-structure interaction
V = velocity magnitude
$\boldsymbol{V}$ = velocity vector
x = Cartesian coordinates in x-direction
δ = Kronecker δ
λ = thermal conductivity
μ = viscosity
ρ = density
$\boldsymbol{\sigma}$ = Cauchy stress tensor
τ = stress tensor

Subscripts

f = fluid
s = solid

References

[1] Taylor, P. A., and Ford, C. C., 2009, "Simulation of Blast-Induced Early-Time Intracranial Wave Physics Leading to Traumatic Brain Injury," ASME J. Biomech. Eng., **131**(6), p. 061007.
[2] Bass, C. R., Panzer, M. B., Rafaels, K. A., Wood, G., Shridharani, J., and Capehart, B., 2012, "Brain Injuries From Blast," Ann. Biomed. Eng., **40**(1), pp. 185–202.
[3] Panzer, M. B., Myers, B. S., Capehart, B. P., and Bass, C. R., 2012, "Development of a Finite Element Model for Blast Brain Injury and the Effects of CSF Cavitation," Ann. Biomed. Eng., **40**(7), pp. 1530–1544.
[4] Mrena, R., Paakkonen, R., Back, L., Pirvola, U., and Ylikoski, J., 2004, "Otologic Consequences of Blast Exposure: A Finnish Case Study of a Shopping Mall Bomb Explosion," Acta Otolaryngol., **124**(8), pp. 946–952.
[5] Steele, C. R., and Taber, L. A., 1979, "Comparison of WKB Calculations and Experimental Results for 3-Dimensional Cochlear Models," J. Acoust. Soc. Am., **65**(4), pp. 1007–1018.
[6] Cancelli, C., Dangelo, S., Masili, M., and Malvano, R., 1985, "Experimental Results in a Physical Model of the Cochlea," J. Fluid Mech., **153**, pp. 361–388.
[7] Lechner, T. P., 1993, "A Hydromechanical Model of the Cochlea With Nonlinear Feedback Using PVF(2) Bending Transducers," Hear. Res., **66**(2), pp. 202–212.

Downloaded From: http://fluidsengineering.asmedigitalcollection.asme.org/ on 09/11/2014 Terms of Use: http://asme.org/terms

[8] Steele, C. R., and Zais, J. G., 1985, "Effect of Coiling in a Cochlear Model," J. Acoust. Soc. Am., **77**(5), pp. 1849–1852.
[9] Loh, C. H., 1983, "Multiple Scale Analysis of the Spirally Coiled Cochlea," J. Acoust. Soc. Am., **74**, pp. 94–103.
[10] Koike, T., Wada, H., and Kobayashi, T., 2002, "Modeling of the Human Middle Ear Using the Finite-Element Method," J. Acoust. Soc. Am., **111**(3), pp. 1306–1317.
[11] Sun, Q., Gan, R. Z., Chang, K. H., and Dormer, K. J., 2002, "Computer-Integrated Finite Element Modeling of Human Middle Ear," Biomech. Model. Mechanobiol., **1**(2), pp. 109–122.
[12] Gan, R. Z., Feng, B., and Sun, Q., 2004, "Three-Dimensional Finite Element Modeling of Human Ear for Sound Transmission," Ann. Biomed. Eng., **32**(6), pp. 847–859.
[13] Zhang, X. M., and Gan, R. Z., 2011, "A Comprehensive Model of Human Ear for Analysis of Implantable Hearing Devices," IEEE Trans. Biomed. Eng., **58**(10), pp. 3024–3027.
[14] Gan, R. Z., Reeves, B. P., and Wang, X. L., 2007, "Modeling of Sound Transmission From Ear Canal to Cochlea," Ann. Biomed. Eng., **35**(12), pp. 2180–2195.
[15] Gan, R. Z., Cheng, T., Dai, C. K., Yang, F., and Wood, M. W., 2009, "Finite Element Modeling of Sound Transmission With Perforations of Tympanic Membrane," J. Acoust. Soc. Am., **126**(1), pp. 243–253.
[16] Taylor, G. I., 1963, *The Pressure and Impulse of Submarine Explosion Waves on Plates*, Cambridge University, Cambridge, UK.
[17] Gan, R. Z., and Wang, X. L., 2007, "Multifield Coupled Finite Element Analysis for Sound Transmission in Otitis Media With Effusion," J. Acoust. Soc. Am., **122**(6), pp. 3527–3538.
[18] Wever, E. G., and Lawrence, M., 1982, *Physiological Acoustics*, Princeton University, Princeton, NJ.
[19] Batchelor, G. K., 1967, *An Introduction to Fluid Dynamics*, Cambridge University Press, Cambridge, UK.
[20] ANSYS, 2010, "ANSYS CFX-PRE User's Guide," Canonsburg, PA.
[21] Wada, H., Metoki, T., and Kobayashi, T., 1992, "Analysis of Dynamic Behavior of Human Middle-Ear Using a Finite-Element Method," J. Acoust. Soc. Am., **92**(6), pp. 3157–3168.
[22] Kirikae, I., 1960, *The Structure and Function of the Middle Ear*, University of Tokyo, Tokyo, Japan.
[23] Von Bekesy, G., 1960, *Experiments in Hearing*, McGraw-Hill, New York.
[24] Mays, G. C., and Smith, P. D., 1995, *Blast Effects on Buildings*, Thomas Telford Publications, London.
[25] Cheng, T., Dai, C. K., and Gan, R. Z., 2007, "Viscoelastic Properties of Human Tympanic Membrane," Ann. Biomed. Eng., **35**(2), pp. 305–314.
[26] Luo, H. Y., Dai, C. K., Gan, R. Z., and Lu, H. B., 2009, "Measurement of Young's Modulus of Human Tympanic Membrane at High Strain Rates," ASME J. Biomech. Eng., **131**(6), p. 064501.
[27] Krutzer, B., Ros, M., Smit, J., and de Jong, W., 2011, "A Review of Synthetic Latices in Surgical Glove Use," http://www.kraton.com/products/cariflex/synthetic_latices.pdf

Downloaded From: http://fluidsengineering.asmedigitalcollection.asme.org/ on 09/11/2014 Terms of Use: http://asme.org/terms